

Lecture Notes in Mechanical Engineering

Ranganath M. Singari  
Pavan Kumar Kankar  
Girija Moona *Editors*


# Advances in Mechanical Engineering and Technology

Proceedings of 6th International  
Conference on Advanced Production  
and Industrial Engineering (ICAPIE) -  
2021

 Springer


# Lecture Notes in Mechanical Engineering

## Series Editors

Francisco Cavas-Martínez , Departamento de Estructuras, Construcción y Expresión Gráfica Universidad Politécnica de Cartagena, Cartagena, Murcia, Spain

Fakher Chaari, National School of Engineers, University of Sfax, Sfax, Tunisia

Francesca di Mare, Institute of Energy Technology, Ruhr-Universität Bochum, Bochum, Nordrhein-Westfalen, Germany

Francesco Gherardini , Dipartimento di Ingegneria “Enzo Ferrari”, Università di Modena e Reggio Emilia, Modena, Italy

Mohamed Haddar, National School of Engineers of Sfax (ENIS), Sfax, Tunisia

Vitalii Ivanov, Department of Manufacturing Engineering, Machines and Tools, Sumy State University, Sumy, Ukraine

Young W. Kwon, Department of Manufacturing Engineering and Aerospace Engineering, Graduate School of Engineering and Applied Science, Monterey, CA, USA

Justyna Trojanowska, Poznan University of Technology, Poznan, Poland

**Lecture Notes in Mechanical Engineering (LNME)** publishes the latest developments in Mechanical Engineering—quickly, informally and with high quality. Original research reported in proceedings and post-proceedings represents the core of LNME. Volumes published in LNME embrace all aspects, subfields and new challenges of mechanical engineering. Topics in the series include:

- Engineering Design
- Machinery and Machine Elements
- Mechanical Structures and Stress Analysis
- Automotive Engineering
- Engine Technology
- Aerospace Technology and Astronautics
- Nanotechnology and Microengineering
- Control, Robotics, Mechatronics
- MEMS
- Theoretical and Applied Mechanics
- Dynamical Systems, Control
- Fluid Mechanics
- Engineering Thermodynamics, Heat and Mass Transfer
- Manufacturing
- Precision Engineering, Instrumentation, Measurement
- Materials Engineering
- Tribology and Surface Technology

To submit a proposal or request further information, please contact the Springer Editor of your location:

**China:** Ms. Ella Zhang at [ella.zhang@springer.com](mailto:ella.zhang@springer.com)

**India:** Priya Vyas at [priya.vyas@springer.com](mailto:priya.vyas@springer.com)

**Rest of Asia, Australia, New Zealand:** Swati Meherishi at [swati.meherishi@springer.com](mailto:swati.meherishi@springer.com)

**All other countries:** Dr. Leontina Di Cecco at [Leontina.dicecco@springer.com](mailto:Leontina.dicecco@springer.com)

To submit a proposal for a monograph, please check our Springer Tracts in Mechanical Engineering at <https://link.springer.com/bookseries/11693> or contact [Leontina.dicecco@springer.com](mailto:Leontina.dicecco@springer.com)

**Indexed by SCOPUS. All books published in the series are submitted for consideration in Web of Science.**

More information about this series at <https://link.springer.com/bookseries/11236>

Ranganath M. Singari · Pavan Kumar Kankar ·  
Girija Moona  
Editors

# Advances in Mechanical Engineering and Technology

Proceedings of 6th International Conference  
on Advanced Production and Industrial  
Engineering (ICAPIE) - 2021

*Editors*

Ranganath M. Singari  
Department of Design  
Department of Mechanical Engineering  
Delhi Technological University  
New Delhi, India

Pavan Kumar Kankar  
Department of Mechanical Engineering  
Indian Institute of Technology Indore  
Indore, Madhya Pradesh, India

Girija Moona  
Physico-Mechanical Metrology  
CSIR - National Physical Laboratory  
New Delhi, India

ISSN 2195-4356

ISSN 2195-4364 (electronic)

Lecture Notes in Mechanical Engineering

ISBN 978-981-16-9612-1

ISBN 978-981-16-9613-8 (eBook)

<https://doi.org/10.1007/978-981-16-9613-8>

© The Editor(s) (if applicable) and The Author(s), under exclusive license to Springer Nature Singapore Pte Ltd. 2022

This work is subject to copyright. All rights are solely and exclusively licensed by the Publisher, whether the whole or part of the material is concerned, specifically the rights of translation, reprinting, reuse of illustrations, recitation, broadcasting, reproduction on microfilms or in any other physical way, and transmission or information storage and retrieval, electronic adaptation, computer software, or by similar or dissimilar methodology now known or hereafter developed.

The use of general descriptive names, registered names, trademarks, service marks, etc. in this publication does not imply, even in the absence of a specific statement, that such names are exempt from the relevant protective laws and regulations and therefore free for general use.

The publisher, the authors and the editors are safe to assume that the advice and information in this book are believed to be true and accurate at the date of publication. Neither the publisher nor the authors or the editors give a warranty, expressed or implied, with respect to the material contained herein or for any errors or omissions that may have been made. The publisher remains neutral with regard to jurisdictional claims in published maps and institutional affiliations.

This Springer imprint is published by the registered company Springer Nature Singapore Pte Ltd. The registered company address is: 152 Beach Road, #21-01/04 Gateway East, Singapore 189721, Singapore

# Contents

<b>Metal Hydride Hybrid Refrigeration System Incorporated with Cloud-Based Remote Monitoring and Control</b> .....	1
Narayan Singh	
<b>A Study on Surface Topography Transformation in Abrasive Slurry Jet Polishing of BK7 Glass</b> .....	15
K. G. Anbarasu, L. Vijayaraghavan, and N. Arunachalam	
<b>Comparative Analysis of Mechanical Behavior of Femur Bone of Different Age and Sex Using FEA</b> .....	27
Dinesh Yadav and Ramesh Kumar Garg	
<b>Performance Analysis of PCM-Integrated Greenhouse Dryer</b> .....	37
Ravin Sehrawat, Ravinder Kumar Sahdev, and Sumit Tiwari	
<b>Numerical Simulation of Frontal Crash for Toyota Yaris Using LS-DYNA</b> .....	45
Tushar Tanwar, Shikhar Gupta, Ashwani Kumar Singh, and Vijay Gautam	
<b>Rail Pad Dynamic Properties: A Review</b> .....	57
Sumeet Padhi, Shubham Sharma, and Yamika Patel	
<b>Design Analysis of an Electric Go-Kart</b> .....	71
Sunny Bhatia, Anshul Gautam, Antash Dhiman, Farhan Mukhtar, and Priyansh Sharma	
<b>Identification and Ranking of Supply Chain Risks Using Fuzzy TOPSIS: A Case Study of Indian Automotive Manufacturing</b> .....	83
Vinod G. Surange and Sanjay U. Bokade	
<b>Thermohydrodynamic Analysis of Journal Bearing Using Non-newtonian Lubricants</b> .....	97
Kedar Deshmukh and Vilas Warudkar	

<b>A Review on Research Aspects and Trends in Ultrasonic Machining . . . .</b>	<b>107</b>
Karun Kant, Prashant Gupta, Shrikant Vidya, Lavepreet Singh, and Anurag Shanu	
<b>Conceptualisation and Modelling of Underwater Remotely Operated Vehicle . . . . .</b>	<b>115</b>
Dhruv and Vikas Rastogi	
<b>Design and Performance of Plate-Fin Heat Exchanger: A Brief Review . . . . .</b>	<b>127</b>
Vivek M. Korde, Gauri S. Gotmare, Priya K. Kachhwah, and Divyanshu Lokhande	
<b>Exploration on Photoluminescence Features in Pr<sup>3+</sup>-Doped Sodium-Calcium Orthosilicate Phosphor for White LEDs . . . . .</b>	<b>141</b>
Subhajit Pradhan and M. Jayasimhadri	
<b>Solar Energy Production Onsite for Battery Swapping Stations in Delhi . . . . .</b>	<b>149</b>
Mukesh Kumar and Sarita Baghel	
<b>Pollination System for Greenhouse Flowering Plants Using Nano Drones . . . . .</b>	<b>157</b>
Manoj Kumar Shukla, Lavepreet Singh, Shrikant Vidya, Haider Quasim, and Rahul Bhandari	
<b>Garbage Classification Using YOLOv3 . . . . .</b>	<b>163</b>
Murlı Manohar Pant, Akanksha, Muskan Gupta, and Madan Mohan Tripathi	
<b>Aerodynamics Characteristics of Compound Delta Wing at High Altitude . . . . .</b>	<b>171</b>
Gaurav Gupta, Pranav Tiwari, Bhanu Pratap Vatsa, Aashish Anand Sahay, K. S. Srikanth, and Shrikant Vidya	
<b>Current Research Aspects and Trends in Electrical Discharge Machining: A Review . . . . .</b>	<b>185</b>
Shivam Rawat, Satyam Tiwari, Tariq Zafar, Abhishek Singh, Anurag Shanu, and Shrikant Vidya	
<b>Current Research Aspects and Trends in Abrasive Water Jet Machining: A Review . . . . .</b>	<b>193</b>
Prabhat Ranjan, Pradumn Chaubey, P. Suresh, and Shrikant Vidya	
<b>Design and Development of Environmental Monitoring AirShip . . . . .</b>	<b>199</b>
Ayush Singh, Ayush Kumar, and Anurag Shanu	
<b>Green Power Generation from Road Traffic Using Speed Breaker . . . . .</b>	<b>209</b>
Rishabh Kumar, Lavepreet Singh, Yuvraj Bhardwaj, Manish Singh, and Rajneesh Kumar	

<b>Analysis of Steering Using Davis Mechanism</b> .....	219
Spandan Shukla, Shravan Sharma, and Pramod Kumar	
<b>Modeling and Simulation of a Bevel Gear</b> .....	231
Priyanshu Choudhary, Alok Niranjan, and Pramod Kumar	
<b>Design and Analysis of Helical Gear</b> .....	249
Priyanshu Choudhary, Aditya Singh, Ankit Kumar, and Pramod Kumar	
<b>Adapting Cam, Automation and FMS to Boost India’s GDP and Economy</b> .....	267
Prajwal Jaiswal, Kushagra, Mayank Singh, and A. K. Madan	
<b>Accident Detection and Prediction with Notification Alert System</b> .....	281
Sajal Gupta, Manish Rawat, and A. S. Rao	
<b>Heat Transfer Analysis of Engine Cylinder Fins by Varying Fin Geometry and Material</b> .....	291
Mmehul Bhayana, Mohit Bhankhar, Neeraj Saini, and N. A. Ansari	
<b>Managing Healthcare Supply Chain During Epidemic and Pandemic</b> .....	307
Amit Kaushik, Shivam Kumar Mishra, Romesh Yadav, and Girish Kumar	
<b>Trajectory Planning and Optimization of Robotic ARM</b> .....	319
Aachman Garg, Aashish Yadav, Abhishek Mishra, and Vikas Rastogi	
<b>Investigation of Flexural Strength of Abaca and Neem Twisted Natural Fiber Composites</b> .....	333
S. J. Rithik, K. Thileepan, R. Dharmaseelan, and B. Vijaya Ramnath	
<b>Investments in the Long-Term Electric System to Encourage the Use of Plug-In Hybrid Electric Vehicles</b> .....	339
Md. Zahid Anwer, Deepanshu Bhatia, and P. Suresh	
<b>Refrigeration Performance Analysis Using Artificial Neural Network</b> .....	349
Lavnish Singh Bisht, Sourav Kumar Singh, Ankit Kumar, and Akhilesh Arora	
<b>Factors Affecting Production System in Additive Manufacturing</b> .....	361
Kamal, Gaurav Deshwal, Ayush Kumar, and Mahendra Singh Niranjana	
<b>Evaluation of Emerging Smartphone Manufacturing Countries by Fuzzy MCDM</b> .....	375
Dhruv Singh Rathore, Sachin Mann, Vaibhav Panchal, and M. S. Niranjana	
<b>Electric Vehicles Challenges, Opportunities, and Future Scope: The Recent Review</b> .....	387
Ranjan Verma, S. K. Srivastava, and Aishvarya Narain	



<b>Robust Control Design of Active Suspension System for Quarter Car with Neural Network and Ziegler–Nichols Tuning Method</b> .....	397
Danish Saifi and Pramod Kumar	
<b>Design of an Unmanned Aerial Vehicle for Search and Rescue Operations</b> .....	407
Ayush Muktibodh, Dinesh Kumar, Vishal Dhiman, and Vikas Rastogi	
<b>Construction and Validation of a Low Cost Thermal Conductivity Measurement Device</b> .....	419
Raviratna Subir, Rishabh Goswami, Vikrant Singh, Deepak Kumar, and Pushendra Singh	
<b>A Statistical Study for Optimizing the Challenges in Vaccine Supply Chain During Critical Times Using DEMATEL Method</b> .....	429
Mukul Suri, Priyam Srivastav, Abhishek Dhiman, and M. Shuaib	
<b>Impact of COVID-19 Lockdown on Noise Levels in Delhi and Mumbai</b> .....	439
Reuben Sewak, Sankalp Kumar, Aviral Agarwal, and Rajeev Kumar Mishra	
<b>Evaluation of Metal Removal Rate in EDM Machining of AISI P20 Steel</b> .....	451
Tariq Zafar, Shivam Rawat, Satyam Tiwari, Abhishek Singh, Anurag Shanu, and Shrikant Vidya	
<b>Floating Solar Power Plant System</b> .....	461
Bhanu Pratap Bhandari, Yati Sharma, and Altaf Hasan Tarique	
<b>Convolution Neural Network for Structural Failure Detection of Wind Turbine Blade: A Review</b> .....	467
Ameya Gajbhiye and Vilas Warudkar	
<b>A Literature Survey on the Design and Development of Work-Holding Fixtures</b> .....	475
Syed Haider Abbas Abidi, Adarsh Kumar Verma, and Abdul Gani	
<b>Design of Storage System for Local Gardeners: A Case Study</b> .....	487
Prakash Kumar and Sirish Taneeru	
<b>A 30-h Observation of Electric-Vehicle-To-Grid Technology in the Presence of Residential and Industrial Inductive Loads</b> .....	499
Raju Chintakindi	
<b>Study and Modal Analysis of Induction Motor by Using ANSYS</b> .....	509
Siddhant Bhadouria, Brahma Nand Agrawal, Sudhir Kumar Singh, and Pawan Kumar Singh Nain	

**The Physical and Chemical Fuel Properties of Jatropha Oil Diesel Blends with Biogas in Dual Fuel Operation** ..... 521  
 Lalit

**Design and Analysis of Overhead Ambulance** ..... 531  
 Sudhir Kumar Singh, Dipul Kumar, Gaurav Kumar Jha,  
 and Pawan Kumar Singh Nain

**Design of Pineapple Peeling Equipment** ..... 545  
 Prakash Kumar and Debkumar Chakrabarti

**Aerodynamic Design of Heavy Transport Vehicles** ..... 557  
 Anuj Vaishnav, Vaibhav Prasad, and Brahma Nand Agrawal

**Design, Fabrication and Cost Analysis of Tri-Star Wheel Stair Climber Trolley Load Carrier on Indian Road Context** ..... 567  
 Rakshit Varshney, Yash Modi, Shrikant Vidya, and Kuldeep Narwat

**Longitudinal Speed Control of Electric Vehicle to Reduce Road Speed Limit Violations** ..... 575  
 Ritanshu Tiwari and A. R. Kulkarni

**Design of Adaptive Wheel Driven Pipeline Inspection Robot** ..... 583  
 Ayush Kaiwart, Nikhil Dhar Dubey, Farman Naseer, Ankush Verma,  
 and Swastik Pradhan

**Designing Mobile App Interfaces for Facilitating Medical Treatment at the Government Hospitals** ..... 597  
 Prakash Kumar

**Finite Element Analysis of Friction Angle in Friction Drilling Process** ..... 609  
 Nitin S. Chityal and Sagar U. Sapkal

**Particle Size Distribution Analysis and Characterization of Cenospheres** ..... 619  
 Pragnya Pradeep, M. Y. Aravind Rao, J. Dharanish, R. Bheemraj,  
 P. Rajeshwari, and S. Seetharamu

## About the Editors

**Dr. Ranganath M. Singari** is a professor in the Department of Mechanical, Production and Industrial Engineering and heads the Department of Design, Delhi Technological University, India. He is a graduate in Industrial Production Engineering from Karnataka University. He completed his M.Tech in Computer Technology and Applications and Ph.D. from the Department of Production Engineering from University of Delhi, India. He has more than 60 international publications in conference and reputed journals. He is also a reviewer for reputed journals. Dr. Singari has organized several international conferences, seminars/workshops, industry-institute interactions and 6 FDP/SDP/STTP. He also serves as Chairman, Production Engineering, Skill India Program, DTTE, Delhi. He is an expert member of several selection committees for technical, teaching and administrative positions. His research interest is materials, manufacturing, industrial management, production management, CAD/CAM, supply chain management, multi-criteria decision making and sustainable lean manufacturing. He has 25 years of research and teaching experience.

**Dr. Pavan Kumar Kankar** is working as Associate Professor in Department of Mechanical Engineering, IIT Indore. His research interests include fault diagnosis and prognosis using machine learning techniques, reliability, bio-medical signal processing and analysis of dynamical systems. He is having more than 15 years of teaching and research experience. He worked with Villanova University for effective discrimination between four kinds of common defects in gears by utilizing the method of recurrence analysis. Dr. Kankar also worked on improving theoretical model of unbalanced shaft-bearing system with researchers of Faculty of Science, University of Yaoundé, Yaoundé, Cameroon. He contributed in various projects awarded by national and international funding agencies under IMPRINT India Initiative by Ministry of Human Resource Development and India–Japan Cooperative Science Program, etc., total worth of Rs. 3.3 crore approx. IIT Indore has been recently awarded a grant of INR 100 Cr. by DST, Govt. of India to establish a Technology Innovation Hub (TIH) on Cyber Physical Systems (CPS) with a focused theme of “System Simulation, Modeling and Visualization.” Dr. Kankar is also a

core committee member of this Technology Innovation Hub (TIH) at IIT Indore. Dr. Kankar has contributed to more than 100 publications which include journal papers, conference papers, books, and book chapters. He is member of International Institute of Acoustics and Vibration, USA. He is a member of various professional bodies like American Society of Mechanical Engineers, Society for Reliability and Safety (SRESA), Tribology Society of India. His work is having more than 2200 citations.

**Dr. Girija Moona** is currently working as Senior Scientist at CSIR-National Physical Laboratory, Delhi. She has more than 15 years of research and academic experience. She has been an active researcher in the area of mechanical measurements and dimensional metrology. Her areas of research also include measurement uncertainty evaluation using Monte Carlo Simulation and hybrid composites. She has participated in various international intercomparisons related to dimensional metrology on behalf CSIR-NPL India, to prove the international equivalence of NPL. She has authored more than 60 publications in peer reviewed journals, conferences and book chapters. She is an active reviewer of many reputed journals related to measurement, metrology and materials.

# Metal Hydride Hybrid Refrigeration System Incorporated with Cloud-Based Remote Monitoring and Control



Narayan Singh

## 1 Introduction

In the contemporary situation, most domestic vapor compression refrigeration systems use R134a due to their favorable thermodynamic properties. Conversely, it is well known for having a high global warming potential. The global warming potential (GWP) and ozone-depleting potential (ODP) are some of the most important criteria considered in the development of new refrigerants. This is due to their impact on ozone layer depletion and global warming. That is what makes it so necessary to find alternative refrigerants to R134a and alternative refrigerant systems altogether [1].

The hybrid refrigeration systems proposed to tackle various environmental issues are termed Envi-hybrid machines. These machines symbolize refrigeration systems and every other type of device that we use and see in our daily lives that should be improved for preventing environmental damage in the form of air pollution, water pollution, and soil contamination. About 90% of machines, big or small, used in the world or we use ourselves, cause harm to the environment in several ways. This approach of technology is far more toxic to us and our future generation than it currently appears.

With Montreal Protocol's order forbidding ozone exhausting substances, there is a restriction in using such technology that produces environment harming by-products. Conventional refrigerants should be supplanted by environment-friendly working fluids and systems. Due to no other alternative currently, countries are forced to use these working fluids and 200-year-old refrigeration methods. Envi-hybrid System mentioned in this research proposes to not use any high-energy consumption device like the compressor in conventional refrigerators. To run on a fraction of energy compared to conventional refrigeration systems is the main idea that is realistically achievable. Besides, the amount of energy used is so less that it could be

---

N. Singh (✉)

Vellore Institute of Technology University, Vellore 632014, India

solicited entirely off-grid by using a minimal investment into a non-conventional power resource such as solar panels [2, 3].

With the assistance of research and exploiting the cloud and IoT revolution, this paper focuses on describing an Envi-hybrid system through theoretical and physical models manufactured during this study. This model utilizes viable techniques, for example, cloud-based computing, control and monitoring, atmospheric water generation system, and single-stage Metal Hydride Refrigeration System or SSRS. These models mentioned above are described individually in this research study and how they contribute together to a single Envi-Hybrid System.

## 2 Operating Principle and Method

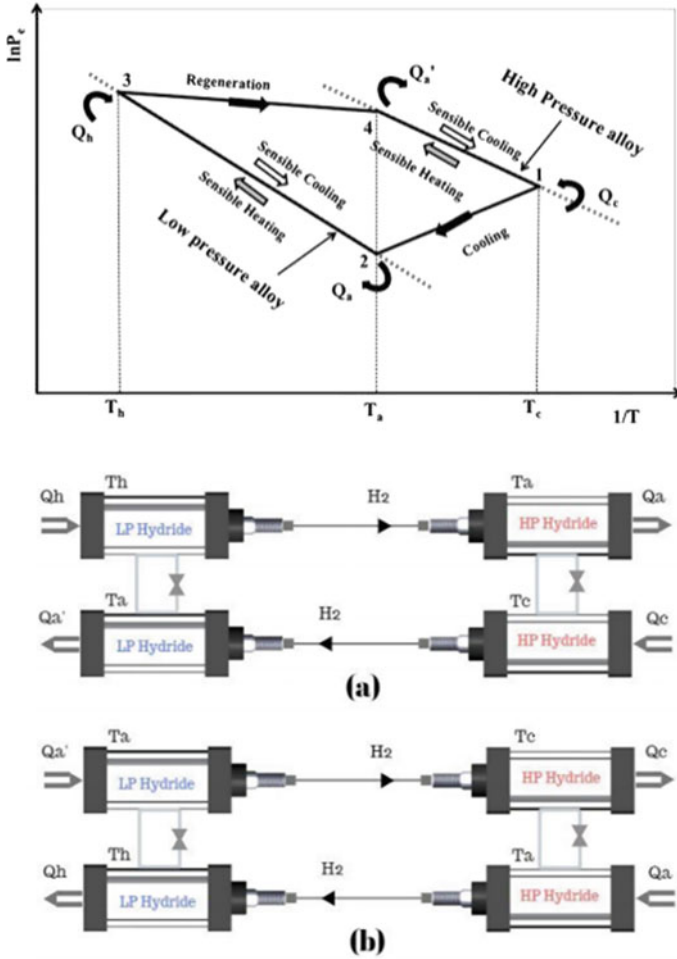
### 2.1 *Envi-Hybrid Metal Hydride Refrigeration System (SSRS)*

Greater demand for conventional refrigeration systems tends to reduce fossil fuel reserves. The refrigeration systems which can run directly on low-grade thermal energy include wet vapor absorption refrigeration, dry solid–gas adsorption, and dry solid–gas thermochemical sorption.

MH refrigeration system works on the principle of endothermic desorption characteristics of metal hydrides. A single-stage SSRS uses two pairs of low-temperature ( $\text{La}_{0.9}\text{Ce}_{0.1}\text{Ni}_5$  and  $\text{La}_{0.8}\text{Ce}_{0.2}\text{Ni}_5$ ) and high-temperature ( $\text{LaNi}_{4.7}\text{Al}_{0.3}$  and  $\text{LaNi}_{4.6}\text{Al}_{0.4}$ )  $\text{LaNi}_5$  hydrides [4]. Water is used as a refrigerant for the thermochemical heat exchange process of the SSRS.  $\text{LaNi}_5$ -based metal hydrides are widely used to produce MHCSs because of their excellent hydrogen storage properties, thermal stability, and reaction kinetics. In this system, the cooling effect is produced by the endothermic reaction of desorbing hydrogen gas from high-pressure MH cells to low-pressure MH cell. For quasi-continuous refrigeration output, SSRS requires four MH beds operating at refrigeration temperature ( $T_c$ ), heat sink temperature ( $T_a$ ), and heat source temperature ( $T_h$ ) [5]. The working of the thermodynamic cycle of the metal hydrides-based cooling system is shown in Fig. 1. Figure 1 shows the structure and design of the SSRS model using the heat recovery principle. The thermodynamic cycle revolves around refrigeration processes, regeneration methods, sensible heating, and sensible cooling processes [6].

The general cooling process of the refrigerant (water) in this Envi-Hybrid system is as follows:

- Net refrigeration effect  $Q_c$ , as shown in Fig. 1, is produced through the refrigeration process (1–2), with the transfer of hydrogen from the LT (low-temperature) hydride at  $T_c$  to the HT (high-temperature) hydride at  $T_a$ . The refrigeration effect ( $Q_c$ ) at  $T_c$  is generated by desorption enthalpy ( $\Delta H_d$ ) of the LT hydride, and the enthalpy of formation ( $\Delta H_a$ ) of the HT hydride is released at  $T_a$ .



**Fig. 1** Thermodynamic cycle for solid sorption refrigeration system (SSRS). X-axis = (1/temperature); Y-axis = (ln (Pressure)) (left), Scheme of SSRS **a** refrigeration and **b** regeneration processes (right) [7–9]

- During the process (2–3), sensible heating of the HT hydride from  $T_a$  to  $T_h$  and through processes (1–4) sensible heating of LT hydride from  $T_c$  to  $T_a$  is carried out.
- The regeneration process (3–4) transpires with hydrogen transfer from HT hydride at  $T_h$  to the LT hydride at  $T_a$ . Here, the HT hydride takes the enthalpy ( $\Delta H_d$ ) at  $T_h$  to desorb hydrogen. The LT hydride absorbs this desorbed hydrogen through rejecting heat ( $\Delta H_a$ ) at  $T_a$ .
- During processes (4–1) sensible cooling process for the LT hydride from  $T_a$  to  $T_c$  and during the process (3–2) sensible cooling of the HT hydride from  $T_h$  to

Ta occur. After each H<sub>2</sub> transfer process, the MH beds are disengaged from the external heat transfer line and heat transfer fluid is supplied through the reactors having the same metal hydrides [10–13].

During this process, water continuously desorbs heat to the MH cell and travels through the refrigerator cooling area or expansion device. Doing so, it simultaneously keeps absorbing heat from hot material in the area and travels back by the pressure applied through a pump towards the MH cell to desorb that heat and in the end completing the cycle. However, in this cycle, refrigerant (water) travels to a secondary expansion device, located on the highest region of the Envi-hybrid refrigeration system. This secondary expansion device is part of the AWG (Atmospheric Water Generator) located at the top face of the enclosure, open to the atmosphere around it.

## 2.2 *Envi-Hybrid Atmospheric Water Generation System (AWG)*

AWG produces fresh drinking water from humid atmospheric air through the cooling condensation method. In this cooling condensation-based AWG, a pump transfers cooled water throughout AWG coils, which then cools the air surrounding it. This step lowers the air's dew point, which causes the ambient humid air to condense in the form of water droplets [14]. A controlled-speed fan impulse the water droplets over the coil. This water is then passed into a collecting tank having a filtration system to purify the water entering the water reservoir. Atmospheric water generating method bids 99.9% pure drinking water throughout the year. It is undeniably an environment-friendly and safe source of sustainable water generation technique, which is explained at the end of this study. Four main factors that affect the generation of water in this type of system are:

*Humidity in the atmosphere, ambient temperature, energy provided to the system.*

The following points provide the fundamental operating process of AWG:

- Using a small electric pump, cooled water passes through the AWG coil with the help of pressure provided.
- This cooled liquid transfers through an expansion coil with a controlled flow of refrigerant (water) concerning the cold suction coil's temperature.
- Due to the cooled refrigerant's temperature range between 10° and 20° Celsius, the water vapor from air condenses into a liquid state at an average of 0.6 L per hour at 60% RH humidity in ambient air. The AWG and water purification apparatus's working schematic are shown in Fig. 2a, b, respectively.

As clearly shown in the figures, the water goes to the collection tank through a purification process which is accepted as fit for producing clean drinkable 99% pure water. The collecting tank and condensation coil CAD, designed in registered software Dassault Systems Solidworks, are shown in Fig. 3.



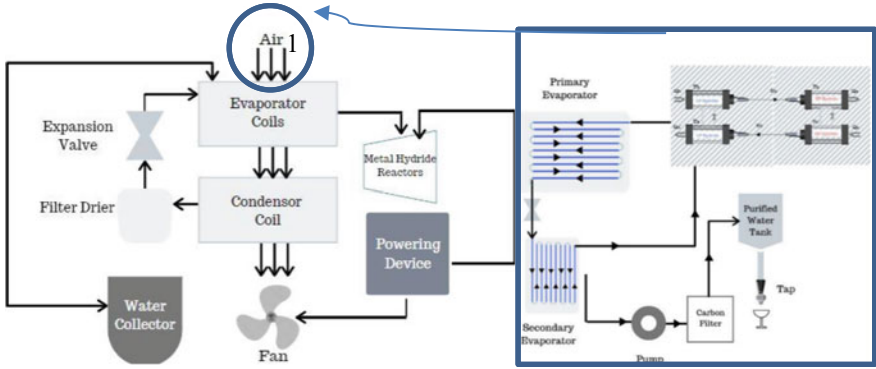


Fig. 2 a Water generation system, water purification system

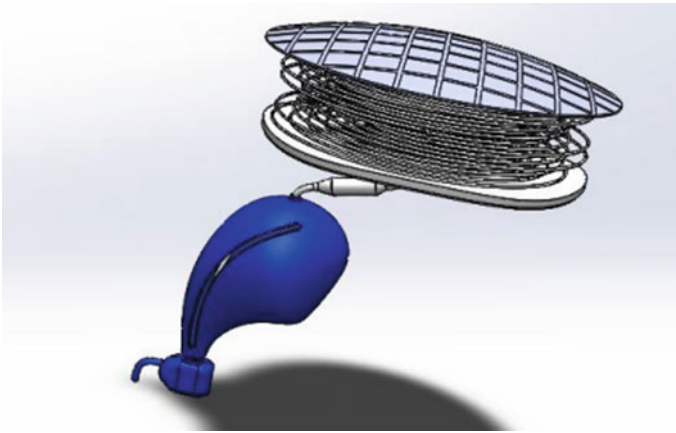


Fig. 3 Water generator/collector

### 2.3 *Envi-Hybrid Cloud Control and Monitoring System (CCAM)*

Machines are made to make human effort lesser. However, if there are underlying effects that may make us face difficulties in the future, then it might not be a much valuable investment for the price paid. Nowadays, remote control and monitoring technology are readily available and easy to integrate due to the age of IoT and the cloud-based tech revolution. The world is shifting towards more advanced methods of automation and safety associated with it. Without safety or guarantee, one would differ from buying a high-investment product. The better the human-machine communication, the better will be the efficiency of work output expected. All of

this with an eye for communicative information and a guarantee that the mechanical systems work according to the user.

The guarantee in this Envi-hybrid system here is provided by the numerous sensors and programmable logic coded in the control and monitoring system. The communication gap is filled up by the “useful” data sent from these sensors and received through a secure internet cloud server to the Envi-hybrid web-app. Some other software, web apps, web application server, android app, etc., are playing their role in the shadows of IoT (Internet of Things). It is essential to understand each component’s role responsible for making this communication medium between an Envi-hybrid system and its user possible. These components are classified into two types: Physical and Digital components.

**Physical Components:** Siemens IOT2000, Siemens PLC s7200 & HMI, WIFI Router, Ethernet Cables, Sensors (Humidity, Temperature, Fluid level, Fluid Pressure), Energy Meter, Industry grade secure component wiring, Wire housing, Support Structure, Plugs and switches, Smartphone.

1. **Siemens IOT2000:** This device is a smart gateway that blends communication between different data sources, analyzes it, and advances it to the comparing recipients. It offers data solutions that can be easily executed for such applications. It can very well be utilized to actualize creation ideas in any event for existing industrial plant projects that are set up to confront what is to come (Fig. 4).
2. **Siemens PLC s7200 and HMI:** SIMATIC S7-1200 Basic Controllers are the perfect selection with regards to deftly and effectively performing automation tasks in the lower to medium execution range. They highlight a complete range of technological functions and integrated I/Os, particularly small and space-saving designs. The S7-1200 CPUs with Safety Integrated handle both standard and safety-related tasks. Smaller design with integrated I/O, communication interfaces that meet the most elevated industry pre-requisites, and a range of integrated programmable logics make this controller a vital piece of an extensive computerization solution.



**Fig. 4** a Siemens IOT2000 (left), b Siemens PLC s7200 (right)

3. **Sensors (Humidity, Temperature, Fluid level, Fluid Pressure):** These sensors provide crucially useful and some unwanted data of humidity, pressure, temperature, and fluid level to the CCAM. The system knows by logic which data is useful and functions accordingly by sending it to the user interface for making a decision (Fig. 5).
4. **WiFi Router:** It creates a WiFi zone around the system surrounding, which avails high-speed internet without the hassle of wires. The MIMO technology in the router supports enhanced 300Mbps wireless transmission rate.
5. **Energy meter:** The meter that is utilized for gauging energy usage through an electric load. Energy is the total power consumed by the load at a certain interval of time (Fig. 6).

**Digital Components:** Node-red, Node.js, MongoDB, Aws cloud, Useful Data (un-processed for User understanding), Useful Data (processed for User understanding), Programmable logic code, Cellular internet connection/WLAN/WIFI, Mode of connectivity, Android Smartphone, Android App, Envi-hybrid System User interface, Web application, and Software.

1. **Node-Red:** Node-RED edits and creates a process flow that demonstrates inject, debug, and function nodes. With Node-RED running with cloud storage, we can open the editor in a web browser on any system. Generally, an inject node is



Fig. 5 Humidity sensor (left), Temperature sensor (middle), & Hydrogen pressure sensor (right)



Fig. 6 a WiFi Router (left), b Energy Meter (right)

added first, and after that, a debug node. After wiring the two or more together, we are ready to deploy our data.

2. **Node.js:** This open-source server environment is free and can be used by any user knowing java scripting. It runs on many platforms (Windows, Linux, Unix, Mac OS X, etc.) and uses JavaScript on the server.
3. **MongoDB:** A cross-platform document-oriented database program. It is defined as a NoSQL database program. It uses JSON or similar class documents with schema, and MongoDB Inc developed it.
4. **AWS Cloud:** Amazon Web Services (AWS) is an all-inclusive and evolving cloud computing platform produced by Amazon. It delivers a mix of infrastructure as a service (IaaS), platform as a service (PaaS), and packaged software as a service (SaaS) offering.
5. **UI-code:**

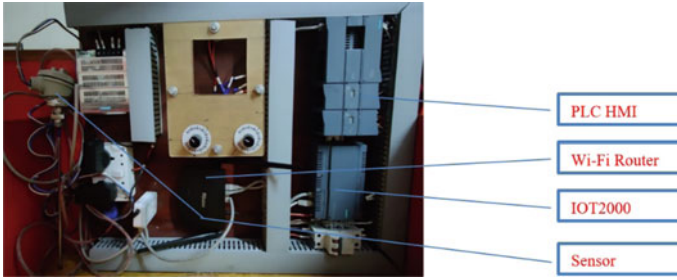
```
>>[{"id":"cb67b901.907ae8","type":"ui_text_input","z":"e9a326cd.3dd118",
"name":"","label":"HYBRID REFRIGERATION SYSTEMS-CONTROL AND
>>MONITORING","tooltip":"","group":"a361458c.596838","order":3,"width":0,"height":0,"passthru":true,"mode":"text","delay":300,"topic":"","x":450,"y":460,"wires":[
[]]},{id":"a361458c.596838","type":"ui_group","z":"","name":"NARAYAN
SINGH","tab":"b220839c.9ab9f","disp":true,"width":"9","collapse":false},{id":"b22
0839c.9ab9f","type":"ui_tab","z":"","name":"HYBRID REFRIGERATION
SYSTEMS-CONTROL AND MONITORING","icon":"dashboard","disabled":false,
"hidden":false}]
```

6. **User Interface for Envi-hybrid System:** this provides an interface to communicate with Envi-Hybrid System and perform various actions such as turning on the water generation system before coming back home, checking the temperature of cooling space in the cooling portion, logging the energy usage pattern of the Envi-hybrid, checking the ambient humidity, and setting the range of water to be generated according to that, turning the refrigerator on/off remotely from anywhere, and for checking the safety of the area for any type of gas or other leaks at all times.

### 3 Experimental Setup

#### 3.1 *Envi-Hybrid Working Model Apparatus of CCAM (Cloud Control and Monitoring)*

Cloud control monitors an immense range of performance measurements naturally and contrasts them with predefined metric data. It provides cloud control issue alerts at whatever point performance metric qualities, surpassing particular limit esteem, which fills in as the triggers for alerts. It indicates both fundamental and caution alerts following the intersection of ready limits by monitored measurements. Thus, it



**Fig. 7** CCAM working model setup

can set up an extensively ready system that tells you when performance is moderate or when an objective is down. Here, the AWS (Amazon Web Services) is used for hosting the web application data so that it can be accessed by any system even without Node-red installed.

1. In the CCAM system, Siemens PLC (Programmable Logic Controller) acts as the system's logic brain.
2. Siemens IOT2000 helps carry this information to the cloud using AWS.
3. This information is then converted into useful and controlled data on the web application and android application. The entire setup is shown in Fig. 7.

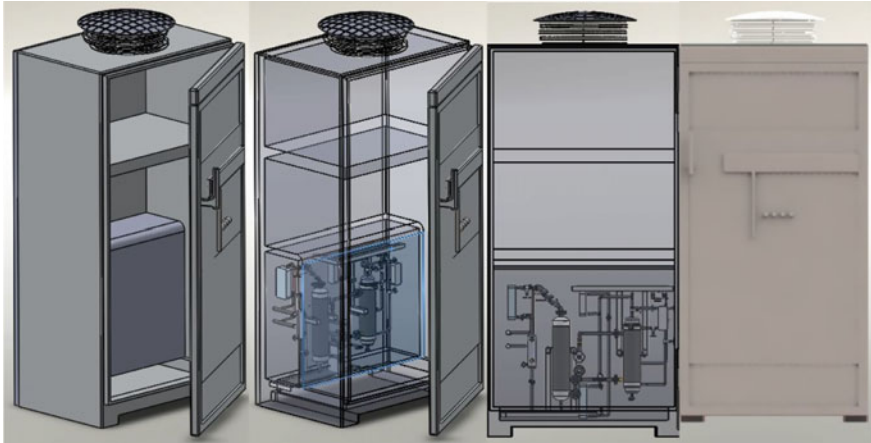
Major components visibly are Siemens IOT2000, Siemens PLC s7200 & HMI, WIFI router, ethernet cables, sensors (Humidity, Temperature, Fluid level, Fluid Pressure), energy meter, industry-grade secure component wiring, Wire housing, support structure, plugs, and switches.

### ***3.2 CAD Design of Envi-Hybrid Refrigeration System***

See Fig. 8.

## **4 Result and Discussion**

This study proposed to keep the emissions and harmful effects produced by refrigeration systems as low as mathematically and experimentally possible. For this purpose, we must shift our focus to a different method of the cooling process. Metal hydride cooling systems fall into this category. By exploiting the chemical properties of metal hydrides to absorb and desorb hydrogen and produce a cooling effect in the said process, we are practically able to achieve our goal with a leap of energy-saving units. This process uses a lesser amount of work input than previous cooling systems, i.e., saving a vast amount of energy resources.



**Fig. 8** Envi-Hybrid enclosure, Envi-Hybrid enclosure transparent view, Envi-Hybrid enclosure front view, Envi-Hybrid enclosure rendered view [15–23]

This study is oriented to promote new generation refrigeration systems and the machines used in our daily lives that produce no harmful emissions, do not contaminate the environment, and do not deplete the ozone layer.

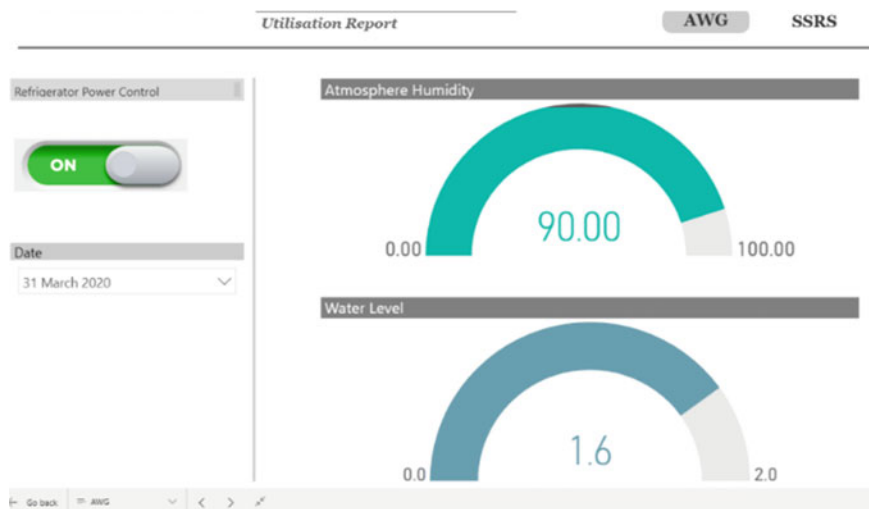
SSRS does not use any harmful chemical refrigerant in the entire cooling process, eliminating the concept of ODP and GWP risks entirely. It uses the atmospheric water generation system to produce 99% pure treated water. Also, the amount of electricity used in this system is minuscule compared to conventional refrigeration systems (Fig. 9).

## 5 Conclusion

With the help of this study, initial target issues such as atmospheric pollution, ozone desolation, energy wastage and loss (electric energy, heat energy, useful cooling, and heating temperatures), lacuna due to different machines of different applications, issue of water-saving and wastage of acquirable water resource were proposed to be solved by propounding Envi-Hybrid system as discussed.

Further research is necessary for this field to take a significant and forward step towards practically sustainable machines in the future. Metal hydrides can be viably used as working materials in various thermal machines, contributing fundamentally towards environmentally clean energy technologies. These systems utilize low-grade thermal energy, for instance, waste heat from industries, solar energy, and heat from exhaust gases to create excellent heating and cooling outputs.

Research and development of such devices require profoundly advanced computational design techniques for a complete simulation before investing in the final



**Fig. 9** CCAM Web app MH cell monitoring page, web app atmospheric humidity monitoring page, web app AWG monitoring page

design. Two significant restrictions of these devices are the high initial expense of the hydride alloy and difficulty in achieving optimized heat and hydrogen transfer in the reaction bed. However, as mentioned earlier, through the combined study of research already present in this field, affordable bulk production of such components is much possible.

Investment in MH systems is comparative to investment in renewable energy for making more energy-efficient machines as its applications lies not only in refrigeration but also several other technology fields such as fabrication of small pneumatic actuators for rehabilitative systems which have constraint of space and volume and cannot support mechanical compressors [24]. Also, in a recent research, MH's radiation shielding sensitivity was studied and was found to be one of best products to shield gamma rays and neutron in nuclear and fusion reactors [25]. MH alloys were also used to produce an innovative conversion reaction high-capacity anode for lithium batteries that abetted in reducing the volume variation and poor electronic conductivity of LiH [26]. Similarly, another recent breakthrough research in metal borohydrides proposed wide range of structural flexibility, composition, and physical properties. It also gained interest in solid-state ion conductors and energy storage due to very high hydrogen density [27].

## References

1. Barode S, Tiwari A (2012) Performance analysis of vapour compression refrigeration systems using hydrofluorocarbon refrigerants. *Int J Sci Eng Res* 3(12)

2. Choudhari M, Ahuja K, Thakkur S, Bardhan S, Sharma V (2019) Performance investigation of metal-hydride based heat transformer. *Energy Storage*. <https://doi.org/10.1002/est2.56>
3. Kumar A, Mishra D, Sharma V (2018) Estimation of enthalpy of formation of metal hydrides—effect of different measurement parameters. *Adv Energy Res* 1271–276
4. Sharma V, Kumar E (2014) Studies on La based intermetallic hydrides to determine their suitability in metal hydride based cooling systems. *Inter-metallics* 60–67
5. Sharma V, Kumar E (2013) Effect of measurement parameters on thermodynamic properties of La-based metal hydrides. *Int J Hydrogen Energy* 5888–5898
6. Sharma V, Kumar E, Murthy S (2014) Influence of dynamic operating conditions on the performance of metal hydride based solid sorption cooling systems. *Int J Hydrogen Energy* 1108–1115
7. Sharma V, Kumar E (2016) Thermodynamic analysis of novel multi-stage multi-effect metal hydride based thermodynamic system for simultaneous cooling, heat pumping and heat transformation. *Int J Hydrogen Energy* 1–11
8. Sharma V, Kumar E (2014) Measurement and simulation of hydrogen storage and thermodynamic properties of LaNi<sub>4.7</sub>Al<sub>0.3</sub> hydride. *Int J Appl Eng Res* 985–994
9. Sharma V (2017) Static and dynamic measurement-based thermodynamic analysis of solid sorption refrigeration system. *Int J Energy Res* 553–564
10. Rao K, Gopal M, Bhattacharyya S (2012) Thermodynamic analysis of a sorption refrigeration system with and without internal heat recovery. *Int J Low-Carbon Technol* 124–133
11. Zhong Y, Critoph R, Thorpe R (2005) Evaluation of the performance of solid sorption refrigeration systems using carbon dioxide as refrigerant. *Appl Therm Eng* 1807–1811
12. Sharma V, Kumar E (2014) Measurement and analysis of reaction kinetics of La e based hydride pairs suitable for metal hydride e based cooling systems. *Int J Hydrogen Energy* 19156–19168
13. Mohan M, Sharma M, Sharma V, Kumar E, Sathesh E, Muthukumar P (2019) Performance analysis of metal hydride based simultaneous cooling and heat transformation system. *Int J Hydrogen Energy* 10906–10915
14. Pavithra S, Anbarasu T (2011) Vapour compression refrigeration system generating fresh water from humidity in the air, Chennai and Dr. MGR University. In: *Second International Conference on Sustainable Energy and Intelligent System*, 20–22
15. Delhomme B, Rango P, Marty P, Bacia M, Zawilski B, Raufast C, Miraglia S, Fruchart D (2012) Large scale magnesium hydride tank coupled with an external heat source. *Int J Hydrogen Energy* 37:9103–9111
16. Magnetto D, Mola S, DaCosta DH, Golben M, Rosso M (2006) A metal hydride mobile air conditioning system. *SAE Int*
17. Nakamura H, Nakamura Y, Fujitani S (1997) A method for designing a hydrogen absorbing LaNi<sub>5-x-y</sub>MnxAl<sub>y</sub> alloy for a chemical refrigeration system. *J Alloy Compd* 252(1–2):83–87
18. Kang BH, Park CW, Lee CS (1996) Dynamic behavior of heat and hydrogen transfer in a metal hydride cooling system. *Int Hydrogen Energy* 21:769e74
19. Lototsky M, Tolj I, Davids MW, Bujlo P, Smith F, Pollet BG (2015) “Distributed hybrid” MH–CGH<sub>2</sub> system for hydrogen storage and its supply to LT PEMFC power modules. *J Alloys Comp* 645:S329–S333
20. Bjurström H, Suda S (1989) The metal hydride heat pump: dynamics of hydrogen transfer. *Int J Hydrogen Energy* 14:19
21. Kim KJ, Feldman KT Jr, Lloyd G, Razani A (1997) Compressor-driven metal-hydride heat pumps. *Appl Thermal Eng* 17:551–560
22. Paya J, Linder M, Laurien E, Corbera JM (2009) Dynamic model and experimental results of a thermally driven metal hydride cooling system. *Int J Hydrogen Energy* 34:3173–3184
23. Dehouche Z, de Jong W, Willers E, Isselhorst A, Groll M (1998) Modelling and simulation of heating/air conditioning systems using the multi-hydride-thermal-wave concept. *Appl Thermal Eng* 18:457e80
24. Kim K, Kim SH, Kim SH, Yu CH (2018) Hydrogen-absorbing alloy-based metal-hydride actuation for application in rehabilitative systems. *Technol Health Care* 26(S1):43–53. <https://doi.org/10.3233/THC-174063>. PMID:29689754; PMCID:PMC6004936



25. Muth B, Jung WS, Kwak JK, Kim SJ, Park CJ (2020 Sep) A radiation shielding sensitivity analysis based on metal hydrides multilayers. *J Radiol Prot* 40(3):774–789. <https://doi.org/10.1088/1361-6498/ab9a08> PMID: 32503019
26. Aymard L, Oumellal Y, Bonnet JP (2015 Aug) Metal hydrides: an innovative and challenging conversion reaction anode for lithium-ion batteries. *Beilstein J Nanotechnol* 31(6):1821–1839. <https://doi.org/10.3762/bjnano.6.186> PMID:26425434;PMCID:PMC4578386
27. Paskevicius M, Jepsen LH, Schouwink P, Černý R, Ravnsbæk DB, Filinchuk Y, Dornheim M, Besenbacher F, Jensen TR (2017) Metal borohydrides and derivatives—synthesis, structure and properties. *Chem Soc Rev* 46(5):1565–1634. <https://doi.org/10.1039/c6cs00705h> PMID: 28218318

# A Study on Surface Topography Transformation in Abrasive Slurry Jet Polishing of BK7 Glass



K. G. Anbarasu , L. Vijayaraghavan, and N. Arunachalam 

## 1 Introduction

The presence of high-frequency surface error or surface roughness causes high-angle scattering of light, which in turn affects the functional performance of the optical components [1]. Generally, the required surface characteristics for the optical parts are obtained by the polishing process. Thus, the role of the polishing process is very crucial in optics manufacturing industries. The polishing processes commonly used for polishing optical components are conventional polishing process, magnetorheological polishing process, laser polishing process, and abrasive slurry jet polishing process (ASJP). Among all polishing processes, the ASJP is preferred for polishing complex shapes, owing to its ability for polishing complex shapes, with nano-level surface roughness [1–3]. In addition to that, the ASJP process has attractive features such as very less tool wear, low cost of processing, cooling, and flushing of the working zone [1–3].

On the other hand, the ASJP process is a complex process due to more process variables and different mechanisms of material removal. Thus, to understand the process, few works have been carried out to investigate the effect of process parameters on surface roughness generation of different glasses such as K9, Quartz, N-BK7, and BK7 [1, 4–8]. In that, the pressure of the jet, angle of impact, polishing time or the jet exposure time, size of the particle, type of particle, and concentration of particle have a major influence on surface roughness generation. Especially the polishing time or jet exposure time plays a crucial role in the polishing process, since the surface roughness reduction rate varies with respect to time [5–8]. Furthermore, Huu Loc et al. [5] and Wang et al. [6] have reported that the raise in surface roughness of N-BK7 and K9 glasses were noticed, beyond a certain time of polishing. In addition,

---

K. G. Anbarasu (✉) · L. Vijayaraghavan · N. Arunachalam  
Department of Mechanical Engineering, Indian Institute of Technology Madras, Chennai 600036, India

Wang et al. [6] have reported that the rough surface of K9 glass shows the large change in  $R_a$  in the initial duration of polishing and then saturates, but in the case of smooth surface, there was no change in  $R_a$  in the initial duration of polishing and then raises with an increase in time.

From the literature, certain works were performed to study the effect of process parameters on surface roughness generation. However, only limited works have been reported on the time-dependent surface roughness generation of BK7 glass. Especially the mechanism of removal as well as the surface topography transformation of BK7 glass with respect to time is not much explored, hence to produce the desired optical surface quality on BK7 glass at shorter processing time and low cost. The detailed understanding of the time-dependent surface topography transformation is required, since the polishing process is a time-dependent process. In that perspective, the present work focuses on understanding the physical insights on the surface topography transformation of BK7 glass with respect to time.

## 2 Experiment Details

The ground BK7 glass disk of 30 mm diameter and 8 mm thick was used for the present study. The experiments were carried out with the ASJP setup [8]. For polishing, initially, the abrasive slurry was prepared by adding a fixed weight percentage of the aluminum oxide particle on water, and the mixture was continuously stirred to obtain homogenous slurry. The prepared abrasive slurry was pumped to the nozzle using an air-operated double diaphragm pump. The abrasive slurry jet coming out from the nozzle impacts the BK7 glass disk rotating at a certain speed. Further to polish the entire surface area of the work material, the nozzle linearly traverses over the surface at a certain traverse speed. The abrasive slurry, after polishing, was collected and sent back to the slurry tank for continuous processing.

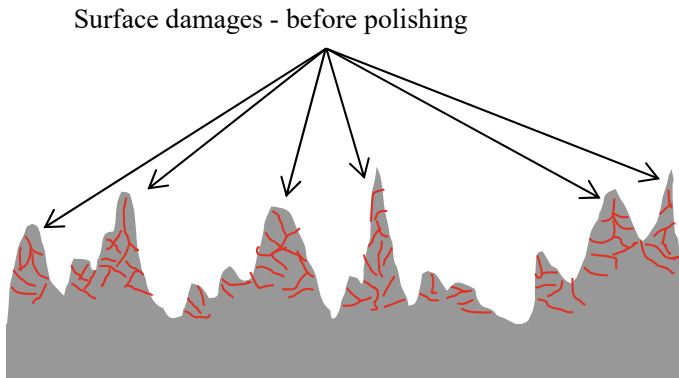
The experiment was conducted by following the experimental condition given in Table 1, and the surface topography transformation with respect to time was studied by using a confocal microscope (OLYMPUS LEXT 4000). The measurements were taken at three different selected areas ( $640 \mu\text{m} \times 640 \mu\text{m}$ ) of the workpiece, and the surface topography transformation was assessed at a fixed interval of 10 min. The most often used surface roughness parameters, such as average surface roughness ( $R_a$ ) and maximum peak to lowest valley height ( $R_t$ ), were used to define the surface topography transformation with respect to time. In addition to that, the surface image (Confocal microscope image) was taken to analyze the surface morphology transformation with respect to time.

**Table 1** Experimental conditions

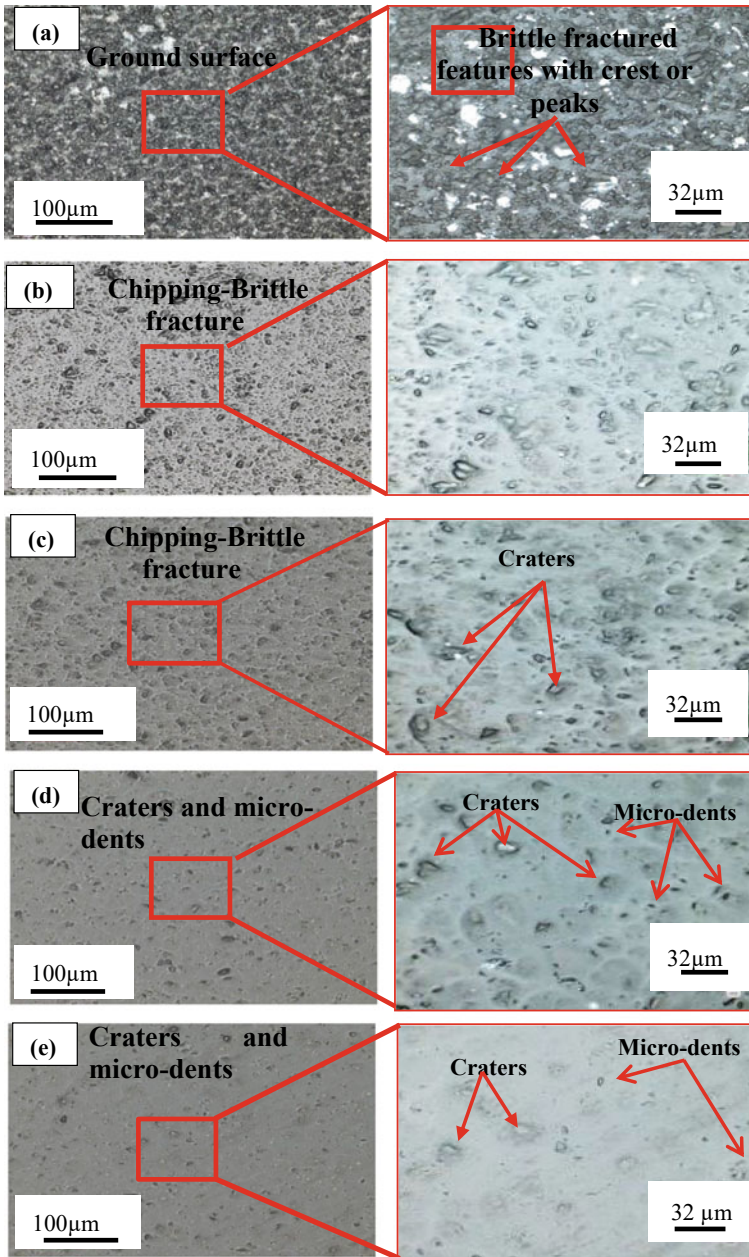
S. No	Parameters	
1	Pressure (bar)	5
2	Traverse speed of nozzle (mm/min)	3
3	Workpiece speed (rpm)	300
4	Size of the particle( $\mu\text{m}$ )	1
5	Concentration of particle (wt %)	10
6	Angle of impact (Deg)	30
7	Stand-off distance (mm)	10
8	Jet exposure time (min)	10, 20, 30, 40, 50, 60, 70, 80, and 90
9	Abrasive particle	$\text{Al}_2\text{O}_3$

### 3 Results and Discussion

The surface topography transformation with respect to jet exposure time was discussed in this section. Figure 1 shows the schematic of the ground glass surface before polishing, and the surface changes with respect to time are shown in Fig. 2. Besides, the schematic of the different mechanisms of material removal is illustrated in Fig. 3. The reduction in  $R_a$  and the rate of reduction in  $R_a$  with respect to time is shown in Fig. 4. In the beginning, the ground glass surface contains brittle fracture features with surface damages, as well as more crest or peak (Figs. 1 and 2a). Thus, during initial duration of polishing, the collision of the abrasive particle on the ground glass surface results in edge chipping of the surface peaks (Fig. 3). Owing to the presence of brittle fracture features with surface damages as well as weak geometry of the surface peaks. This, in turn, results in a steep reduction in  $R_a$  ( $0.58 \mu\text{m}$



**Fig. 1** Schematic of the ground glass surface



**Fig. 2** Confocal microscope images—surface changes with respect to time **a** Initial, **b**  $t = 10$  min, **c**  $t = 20$  min, **d**  $t = 30$  min, **e**  $t = 40$  min, **f**  $t = 50$  min, **g**  $t = 60$  min, **h**  $t = 70$  min, **i**  $t = 80$  min, and **j**  $t = 90$  min

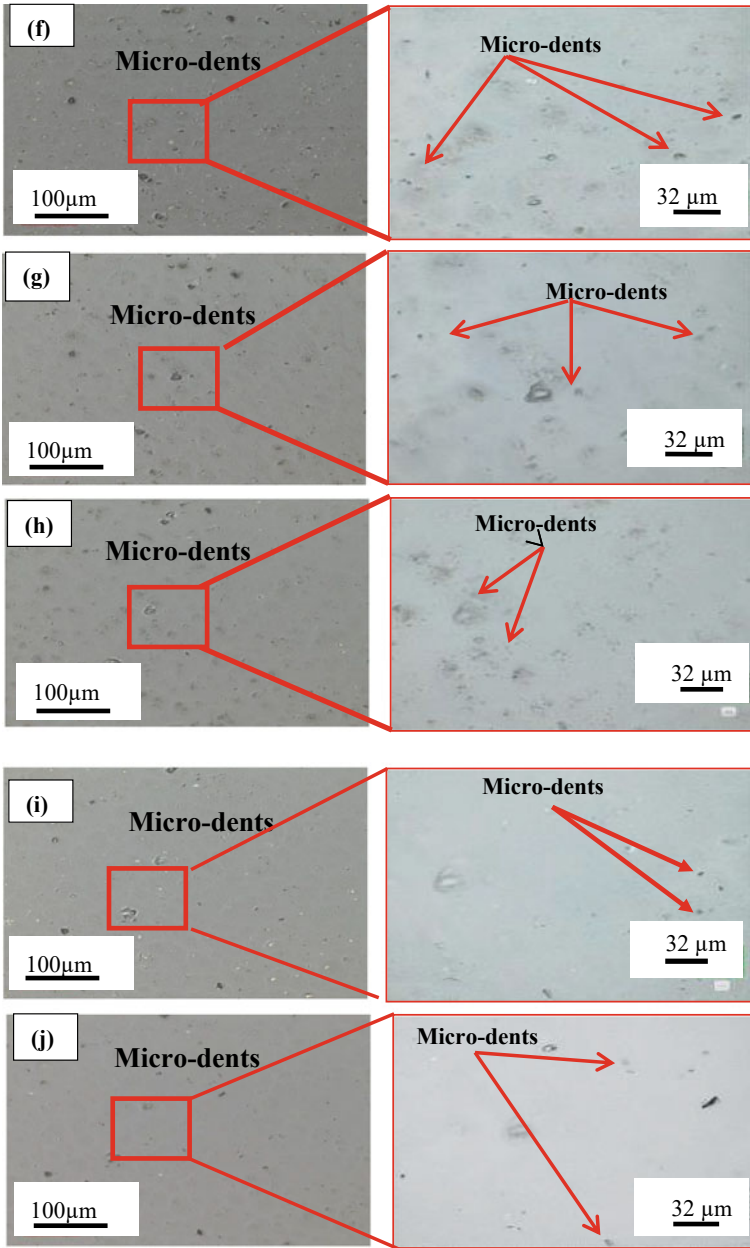
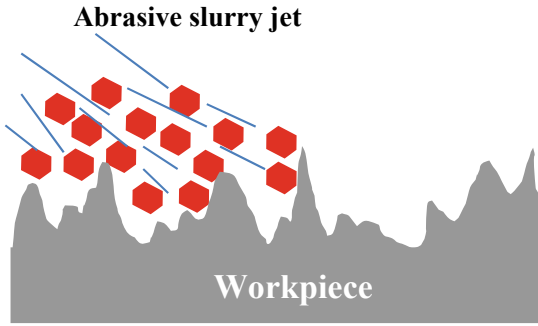
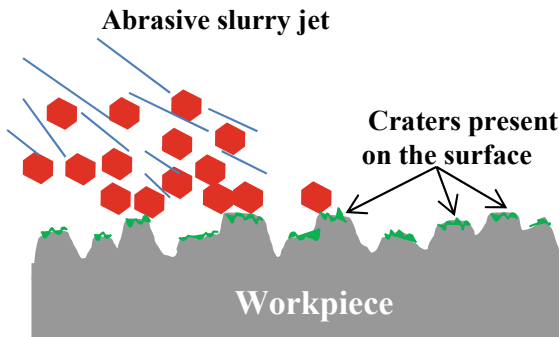


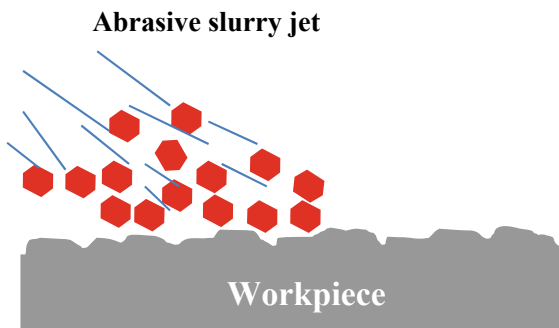
Fig. 2 (continued)



**Edge chipping mechanism-** due to the collision of the abrasive particle over the surface peaks

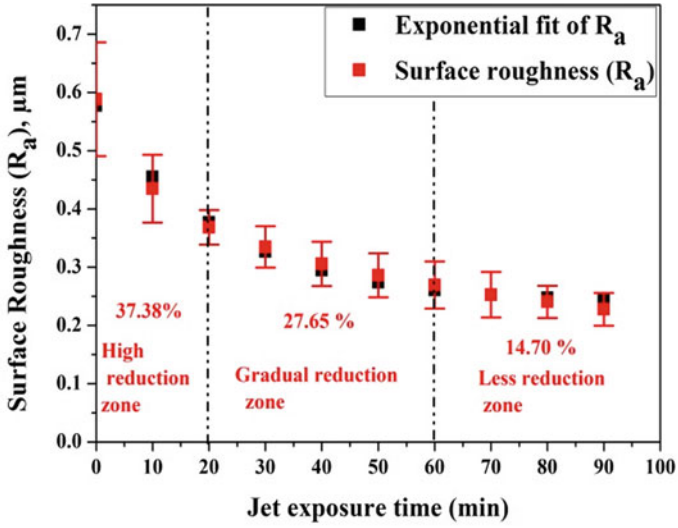


**Micro cutting mechanism-** due to the sliding of the abrasive particle over the craters present on the surface

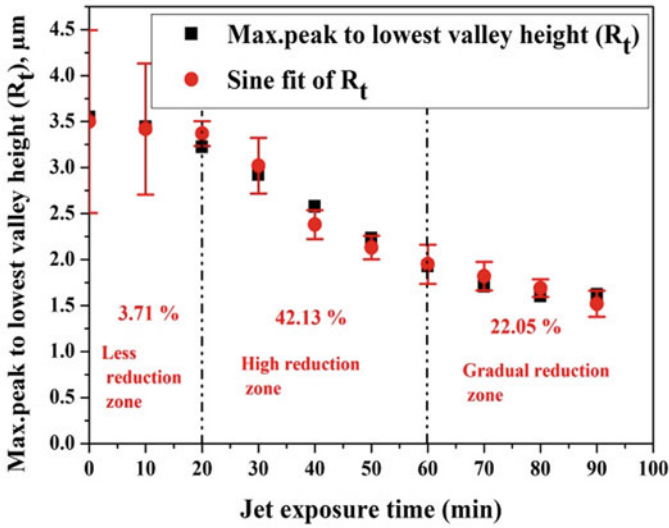


**Micro cutting and ball impact effect –** due to the impact of the abrasive particle over the flattened surface peaks

**Fig. 3** Schematic of transition in mechanism of material removal with change in time



(a)



(b)

**Fig. 4** a Surface roughness ( $R_a$ ) with respect to time b Maximum peak to lowest valley height ( $R_t$ ) with respect to time



to 0.43  $\mu\text{m}$ ) shown in Fig. 4a. However, small reduction in  $R_t$  (3.5  $\mu\text{m}$  to 3.42  $\mu\text{m}$ ) was observed (Fig. 4b) after 10 min of polishing. This is due to the consideration of the maximum height of the surface profile, in the case of  $R_t$  evaluation. On the other hand,  $R_a$  was evaluated by taking the average of surface profile height. Thus, there was a high reduction in  $R_a$ . Furthermore, from Fig. 2b, it was observed that the foremost mode of material removal occurs due to brittle chipping of surface peaks by the impact of the abrasive particle. Thus, the observed high reduction in  $R_a$ , as well as the brittle mode of material removal, is due to the edge chipping mechanism (Fig. 3) in the initial duration of polishing [9].

After 10 min of jet exposure time, the abrasive particles collide with the partially removed peaks (shown in Fig. 2b) and results in chipping of those peaks. This causes a further reduction in  $R_a$  (0.43  $\mu\text{m}$ –0.36  $\mu\text{m}$ , shown in Fig. 4a), but less reduction in  $R_t$  (3.42–3.37  $\mu\text{m}$ ), and the rough surface change to a partially smooth surface with the more brittle mode of material removal craters after 20 min (shown in Fig. 2c). The observed change is due to the knocking of the abrasive particle over the peaks left out after 10 min of polishing, which leads to brittle mode chipping of material similar to the initial stage of polishing (first 10 min). Moreover, high % reduction in  $R_a$  (37.38%), as well as less % reduction in  $R_t$  (3.71%), was observed in the first 20 min of polishing (Fig. 4). After 20 min of polishing, the abrasive slurry jet interacts with the craters present on the flattened surface peaks and removes the material via sliding action of the abrasive particle over the work material surface (Fig. 3) since the surface peaks were knocked off (Fig. 2c). Thus, there was a gradual reduction in  $R_a$  (0.36–0.26  $\mu\text{m}$ ) from 20 to 60 min of polishing (Fig. 4a).

In addition, from Fig. 4a, a considerable % reduction in  $R_a$  (27.65%) was observed after 60 min. However, from Fig. 4b, during 20–60 min polishing, the reduction in  $R_t$  was high (3.37–1.95  $\mu\text{m}$ ) and also a high % reduction in  $R_t$  (44.28%) was observed after 60 min. The observed high reduction in  $R_t$  is due to the removal of peak left out in the previous phase of polishing. Moreover, it is evident from Figs. 2d–g, during 20–60 min of polishing, the flattened surface peaks with craters were removed, and more micro-dents were evolved during these stages of polishing. This may due to the sliding type mechanism of material removal (Fig. 3) and its results on the ductile mode or plastic mode of removal. A similar observation of micro-dents was reported by Cai et al. [10], that the micro-dents were produced due to the impact of small size particles on the surface at low angle of impact. In addition to that, Peng et al. [4] have reported different mode of material removal based upon the size of the cerium oxide particle. From their work, it was found that the 3  $\mu\text{m}$  particle produces plastic pits on the surface, and the 100 nm particle produces a smooth surface, but there is no report on brittle mode of material removal. In the present work, the alumina particle was used. The kinetic energy of the particle is  $5.5407 \times 10^{-3}$  nJ (calculated using the following Eq. (1)), which is less than the threshold kinetic energy (0.44364 nJ) of the impacting particle for crack formation in the case of glass [11, 12] (calculated using the Eq. (2)):

$$\text{K.E} = \frac{1}{2} \times m_a \times u^2 \times \cos^2\theta \quad (1)$$

where K.E is the kinetic energy of the particle (nJ),  $m_a$  of the abrasive particle (kg),  $u$  velocity of the particle (m/s), and  $\theta$  is the impact angle ( $^\circ$ ) (only tangential velocity component was considered for calculation since the impact angle considered is shallow).

$$U_{th} = C_{\sigma v} \times \frac{E_w^{3/2} \times K_{Ic}^6}{H_w^{13/2}} \quad (2)$$

where  $U_{th}$  is the kinetic energy of the particle at which still the cracks occurs,  $C_{\sigma v}$  is the constant ( $2.3 \times 10^4$ ),  $E_w$  is the young's modulus (82 Gpa),  $K_{Ic}$  is the fracture toughness (0.84 Mpa.  $m^{1/2}$ ), and  $H_w$  is the hardness (6.166 Gpa) of the BK7 glass.

Thus, the observed micro-dents may be due to less kinetic energy of the impacting particle as well as the shallow angle of impact. Beyond 60 min of polishing, the abrasive slurry jet interacts with the smooth surface consists of micro-dents (Fig. 2g) and results in less reduction in  $R_a$  during 60–90 min of polishing (0.26–0.22  $\mu m$ ) as well as gradual reduction in  $R_t$  (1.95–1.52  $\mu m$ ). In addition, less % reduction in surface roughness (14.70%, Fig. 4a) as well as considerable % reduction in  $R_t$  (22.07%). was observed, during 60–90 min of polishing (Fig. 4b).

Furthermore, from Figs. 2h–j, there is no significant change in the surface, during 60–90 min of polishing. This may be due to the domination of the ball impact effect over the sliding mechanism. The phenomena of ball impact effect were reported in Tsai et al. [13]. The ball impact effect induces compressive residual stress and results on rise in the strength and hardness of the work material [13]. Thus, the less reduction in  $R_a$  is may be due to the ball impact effect (Fig. 3), and the gradual reduction in  $R_t$  is due to the removal of surface craters left out in the previous phase of polishing. Overall, from this study, it was observed that the reduction in  $R_a$  shows time-dependent nonlinear behavior (Fig. 4a). On the other hand, ASJP is a stochastic process, and material removal occurs due to multiple mechanisms (edge chipping and sliding) with respect to time. Owing to the complexity of the process, the curve-fitting model was preferred to define the relationship between the surface roughness ( $R_a$ ) and jet exposure time or polishing time; for that, an exponential fit was used (Fig. 4a). The curve fitting was done using ORGIN software and the best fit was obtained ( $Adj.R^2 = 0.98$ ). The equation obtained from curve fitting is given in Eq. (3).

$$R_a = y_0 + A \times e^{D_R t} \quad (3)$$

where  $R_a$  is the average surface roughness ( $\mu m$ ),  $y_0$  is the offset value (0.2375),  $A$  is the amplitude (0.3398),  $D_R$  is the decay rate ( $-0.0446$ ), and  $t$  is the jet exposure time. Similarly, to establish the relationship between the maximum peak to lowest valley height ( $R_t$ ), and jet exposure time, the sine curve fit was used (Fig. 4b) and the best fit ( $Adj. R^2 = 0.96$ ) was obtained. The equation obtained from the fit is given below:

$$R_t = y_0 + A \times \sin\left(\pi \times \frac{(t - x_c)}{w}\right) \quad (4)$$

where  $y_0$  is the offset (2.5748),  $A$  is the amplitude (0.98),  $x_c$  is the phase shift ( $-46.98$ ), and  $w$  is the period (87.01).

## 4 Conclusions

From this study, the surface topography transformation during abrasive slurry jet polishing of BK7 glass with respect to time were revealed and the conclusions drawn from the study is given below.

- Three different stages of reduction in surface roughness ( $R_a$ ) and maximum peak to the lowest valley height ( $R_t$ ) were observed with respect to time. Along with that, different mechanisms of material removal (edge chipping and sliding) as well as craters and micro-dents were observed with respect to time.
- Especially, in the case of  $R_a$ , there was high reduction during initial duration of polishing, then the reduction is gradual, and, finally, the reduction was almost in steady state. However, there was less reduction in  $R_t$  during initial duration of polishing, then reduced massively, and, finally, the reduction was gradual. The observed changes in surface roughness, is due to the removal of peaks, followed by the removal of craters.
- Moreover, the change in surface roughness ( $R_a$ ), with respect to time, is similar to the exponential function, and the change in maximum peak to lowest valley height ( $R_t$ ) with respect to time is similar to the sine function. This study brought out the stochastic nature of the process, along with information about the saturation limit in surface roughness generation. This is very much essential to plan for subsequent processing steps to reduce the surface roughness of the given component.

**Acknowledgements** The authors would like to acknowledge Industrial Consultancy and Sponsored Research, Indian Institute of Technology Madras for funding the project through New Faculty Initiation Grant- MEE/13-14/817/NFIG.

## References

1. Fang H, Guo P, Yu J (2006) Surface roughness and material removal in fluid jet polishing. *Appl Opt* 45:4012–4019
2. Kim WB, Nam E, Min BK et al (2015) Material removal of glass by magnetorheological fluid jet. *Int J Precis Eng Manuf* 16:629–637
3. Liu H, Wang J, Huang CZ (2008) Abrasive liquid jet as a flexible polishing tool. *Int J Mater Prod Technol* 31:2–13

4. Peng W, Guan C, Li S (2013) Material removal mode affected by the particle size in fluid jet polishing. *Appl Opt* 52:7927–7933
5. Huu Loc P, Shiou FJ, Yu ZR, Hsu WY (2013) Investigation of optimal air-driving fluid jet polishing parameters for the surface finish of N-BK7 optical glass. *J Manuf Sci Eng Trans ASME* 135:1–7
6. Wang RJ, Wang CY, Wen W, Wang J (2017) Experimental study on a micro-abrasive slurry jet for glass polishing. *Int J Adv Manuf Technol* 89:451–462
7. Anbarasu KG, Vijayaraghavan L, Arunachalam N (2018) Experimental study on surface generation in optical glass with fluid jet polishing process. *Int J Abras Technol* 8:245–260
8. Anbarasu KG, Vijayaraghavan L, Arunachalam N (2019) Effect of multi stage abrasive slurry jet polishing on surface generation in glass. *J Mater Process Technol* 267:384–392
9. Mohajerani A, Spelt JK (2010) Erosive wear of borosilicate glass edges by unidirectional low velocity impact of steel balls. *Wear* 269:900–910
10. Cai DH, Qi H, Wen DH, Zhang L, Yuan QL, Chen ZZ (2016) Effect of fluid motion on the impact erosion by a micro-particle on quartz crystals. *AIP Adv* 6:085203–085211
11. Slikkerveer PJ, Beuten PCP, In't Veld FH, Schollen H (1998) Erosion and damage by sharp particles. *Wear* 217:237–250
12. Wensink H, Elwenspoek MC (2002) A closer look at the ductile-brittle transition in solid particle erosion. *Wear* 253:1035–1043
13. Tsai FC, Yan BH, Kuan CY, Hsu RT, Hung JC (2009) An investigation into superficial embedment in mirror-like machining using abrasive jet polishing. *Int J Adv Manuf Technol* 43:500–512

# Comparative Analysis of Mechanical Behavior of Femur Bone of Different Age and Sex Using FEA



Dinesh Yadav  and Ramesh Kumar Garg 

## 1 Introduction

Biomechanics is a branch of mechanics responsible for analyzing the biological structure using mechanical engineering principles [1]. Initially, the mechanical laws cannot be easily applied to biological structures because of their non-linear and anisotropic behavior. Still, the advent of FEM simplifies the modeling, analysis, and simulation of linear and non-linear biological structures. In the human skeleton system, femur is the longest and strongest bone present between the hip joint and knee joint [2]. Femur structure is dynamic in nature and having a highly complex composition [3]. It can withstand a high compressive force of between 8000 and 11000 N and helps the human body in day-to-day movements such as walking, hopping, dancing, and standing [4]. In Indian-based population, the length of femoral bone is approximately one-fourth of the human height. The thickness of bone varies between 6 and 50 mm depending upon humans' bone health, sex, and age [5].

Modeling and analysis of human femoral bone under different boundary conditions like load, age, and sex has been conducted using various finite element techniques [6]. Finite element analysis (FEA) is an evolving technique for estimating various bone properties in a specific patient on computed tomography (CT)-extracted DICOM images [7]. FEA and CT images have been used to determine the stress–strain analysis, bone rigidity, failure load, and deformation-induced in bone in a different position [8].

The time-intensive and computationally extensible design of models is one of the critical restrictions making clinical trials challenging to implement. Each FE model almost took 10–12 h, depending upon the model's nature and type [9].

---

D. Yadav · R. K. Garg (✉)  
Deenbandhu Chhotu Ram University of Science and Technology, Murthal, Haryana, India  
e-mail: [drkrgarg.me@dcrustm.org](mailto:drkrgarg.me@dcrustm.org)

In the present study, a 3D model of the femoral bone is produced by CT scan and MRI scan-based DICOM images using Materialize MIMICS, and 3D slicer software. Wall thickness analyses of created models have been completed to establish its relation with induced stress and deformation within the femur bone [10]. After the pre- and post-processing of the designed femur models as per age, sex, and weight of humans, FEA has been done for the mechanical property analysis on the created femur model using ANSYS by assigning only the real-time isotropic property of the bone material [11]. The force, i.e., four times the weight (mg) of the patient, has been applied to the head of the femur and the base of the femur is preserved in order to examine the stress distribution and total deformation [12].

## 2 Material and Method

### 2.1 Image Rendering Using Mimics

Digital Imaging and Communications in Medicine (DICOM) files containing patient and scan attributes are saved for CT scanning images [13]. The scanning attributes such as the thickness of the slice, number of slices, and internal space between slices can affect the scan and final cad model’s quality. Three views, i.e., coronal, sagittal, and axial, are visible in the mimics-22 window and the fourth view is for the 3D model, as shown in Fig. 1. Femur mask is created with a pre-defined threshold limit of HU region, i.e., “Bone CT” and then segmentation is conducted and extra noises are removed from created femur model using edit mask command then the 3D model of femur bone has been edited to prevent possible pitfalls during meshing and also affect the FEM results. The value of HU in bone CT changes itself concerning the input scanned data of femur bone [14]. The last “Region Growing” tool has been applied to remove separate geometries from the bone; this leads to the development

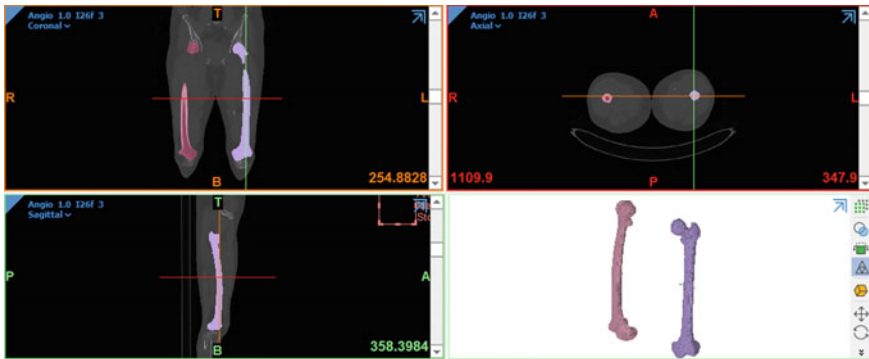


Fig. 1 Coronal, sagittal, axial, and 3D model in mimics-22 window

of a new mask. Multiple 3D Edit and Edit Slice Mask command has been utilized to erase the extra flesh from the distal and proximal end. Then femur model has been intended using the “Calculate 3D” tool. The models still have some impurities and holes with a range of up to 7 mm, which are removed using the Wrap and smooth command [15].

3-Matic is a software tool that comes with Mimics. Its purpose is to simplify and edit further the designed femur model. Using the “Fix Wizard” tool under the “Fix” command, many errors such as stitching, holes, shells, overlap and intersecting triangles are marked and eliminated manually or automatically [16]. Under the “analyze” command, wall thickness analysis is performed for every designed model with pre-defined maximum and minimum wall thickness [17]. This analysis shows the wall thickness variation of the model concerning its length.

The smoothed wrapped model is exported to 3-Matic for meshing purposes. In 3-Matic, the model’s shading mode is set to fill with triangle edges under the view tab for visualizing the surface mesh. Then the smooth function under the fix tab is applied to reduce the number of details. Under the remesh tab, the mesh’s quality and size were inspected by using inspect part function [18]. Then the quality preserving reduces triangles function was applied for preserving the quality of the model. Adaptive remesh was also done before applying the create volume mesh function to creating mesh volume. The final model has been exported to the ANSYS Workbench for FEA [19]. In the Workbench, real-time isotropic bone material properties (Young’s Modulus of elasticity 16000 MPa, Poisson ratio 0.36, Bulk Modulus 19,048 MPa, Shear Modulus 5882.4 MPa) have been assigned to the designed model under the static structure tool.

## 2.2 *Ansysis*

ANSYS is an FEA tool for linear, non-linear, and dynamic structural analysis. In order to support a wide variety of mechanical design concerns, ANSYS computer modeling product supplies final parts for model behavior and supports material models and equation solutions [20].

Workbench manages the dynamic communications and data transmission from one point to another to overcome complex interaction from the importation of CAD geometry to meshing, from meshing to loading and boundary constraints, from analysis to optimization post-processing [21]. The specialists are presently expected to ensure that the data from one separate domain is reformatted and converted to the next properly using a standard and separate framework. ANSYS allows the user to connect all required resources into the common model for various mechanical modeling problems and equation solvers. For each process, simulation activities are made up using building blocks. Link the outputs and inputs of each other and provide a true generalization. Although Workbench would not eliminate the expert’s need, it does not mean that people can immerse themselves in the process and that the expert will work better. To have a single user interaction method and allow the user to

connect all required resources into the single, common model workflow use ANSYS Workbench [22].

### 2.3 Finite Element Analysis

The human body has been influenced by a number of external and internal forces and other physiological conditions [23]. It is necessary to analyze these physiological conditions to understand the femur bone's failure mechanism and guide the implant and bone orthosis designers for the fracture fixation of bone [24]. In this study, the femur bone is analyzed using FEA by considering the age, sex, and weight of human beings. Stress and deformation have been analyzed by considering all thicknesses of bone using FEA under real-time conditions. FEA effectively and efficiently considers the effect of these forces and physiological conditions and shows the induced stress and deformation in femur bone by applying force, i.e., four times the bodyweight [25]. Femur bone has highly heterogeneous and non-linear in nature, which means that the distribution of material properties in all senses of the bone model is difficult [26]. To overcome this problem, here bone is assumed isotropic in nature and healthy bone with bone mineral density<sup>1</sup>, in different age groups for both male and female is considered for analysis [27]. Figure 2 demonstrates the detailed steps involved in FEA analysis of femur bone. DICOM images from CT scan are segmented in Mimics and 3D computer-aided design (CAD) model is prepared. Then the designed model is processed and wall thickness analysis has been performed in 3-Matic software. Further analysis has been performed using ANSYS and SolidWorks softwares.

## 3 Result and Discussion

The static structure of 3D femoral bone models for different age and sex with isotropic material properties has been analyzed using ANSYS 18.0 Workbench. In this analysis, the femur bone's wall thickness, stress, and deformation induced on the femoral bone have been evaluated for both males and females having the same weights 65 kg, 70 kg, and 70 kg with age 40, 45, and 65, respectively.

Wall thickness of created models has been evaluated using 3-Matic 13 software in order to analyze the bone strength concerning the age and sex of human beings. It is observed that males have a higher bone thickness than females in the same-age group. In males, the bone thickness increases up to 50 years and then starts decreasing in old ages, the value for the same as shown in Fig. 3. But in females, bone thickness and bone strength are affected by the menstruation cycle. In old age, the bone thickness in females is decreasing rapidly, as shown in Fig. 4.

The correlation between wall thickness and stress induced in bones is also validated using the basic stress equation below:



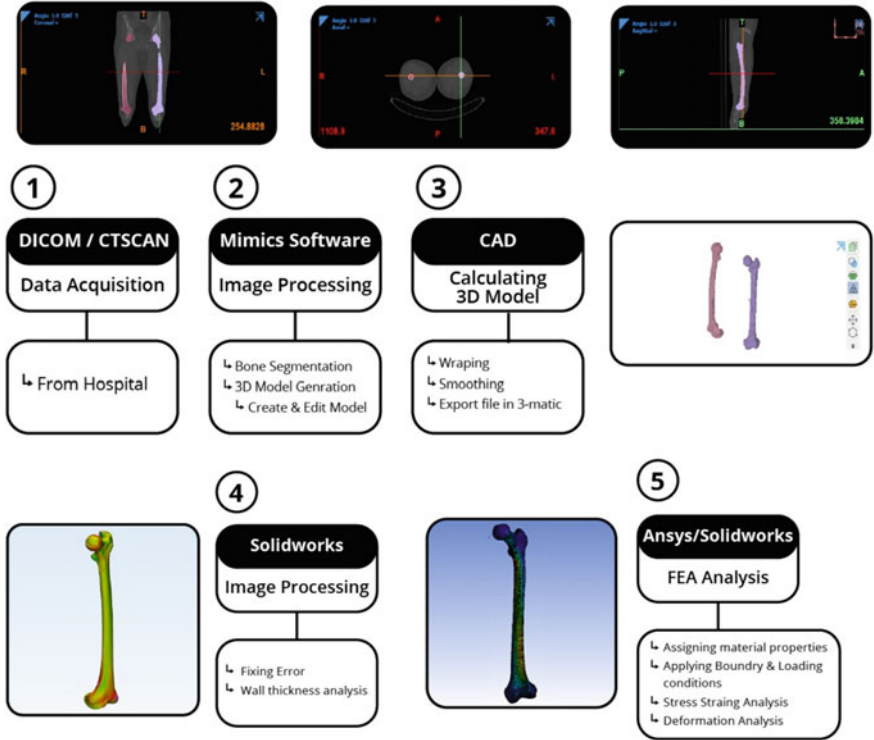


Fig. 2 FEA analysis methodology of femur bone

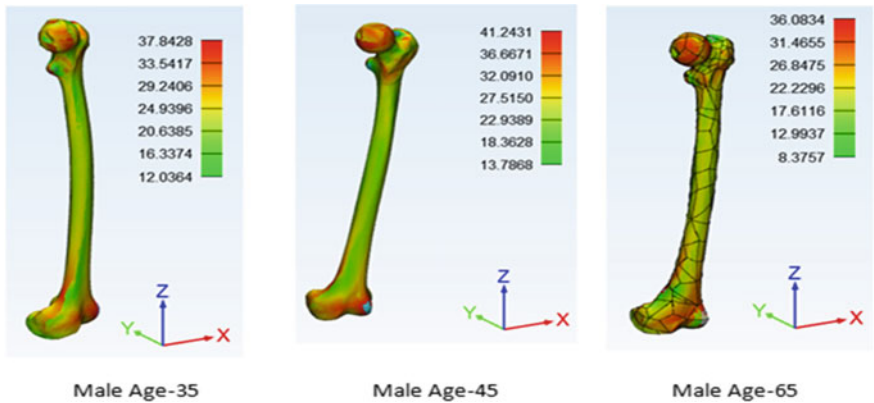
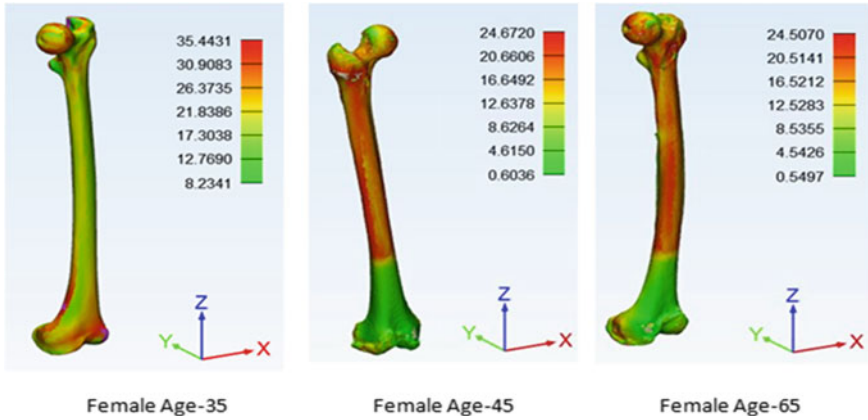


Fig. 3 Wall thickness analysis of male femur bone



**Fig. 4** Wall thickness analysis of female femur bone

$$\sigma = \frac{P}{A} \quad (1)$$

$$A = \frac{\pi}{4}(D^2 - d^2) \quad (2)$$

$$t^2 = \frac{(D^2 - d^2)}{4} \quad (3)$$

$$\sigma \propto \frac{1}{t^2} \quad (4)$$

$$P_{ind} \leq \sigma_{Per} * \pi t^2 \quad (5)$$

For a safe design, materials have to follow the above equation. It is observed from the equations that increase in thickness ( $t$ ) of the femur bone, the load bearing capacity, and the model's strength has been increased. Males bone has a larger thickness of bone than women, which offers a larger area and leads to high strength.

For the structural analysis of bones, "four" is taken as a factor of safety to consider the other uncalculated forces on bone due to bone mass and attached arteries and veins. First of all, edge meshing of all the femur bone models with element size 5 mm is performed in ANSYS-18 Workbench. For the stress and deformation analysis of created 3D models, the distal end of femur bone has been treated as fixed support and a force (four times of bodyweight) has been applied to the proximal end. The maximum stress is induced in the femur bone's shaft with a minimum value at the distal end. As stress concentration is higher in the shaft and proximal end, the chance of fracture is also high for the same.

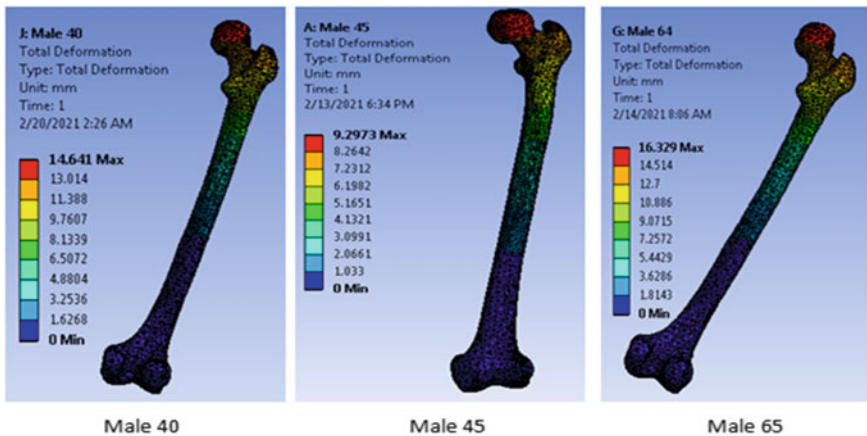
At the time of the modeling process, the 3D models are constructed using Mimics-22 and edge sizing mesh is performed with element size 5 mm. FEA is carried out on

**Table 1** Simulation results of femur bone models

Sr. No	Sex	Age	Nodes	Elements	Stress		Deformation		Wall thickness	
					Max MPa	Min MPa	Max MPa	Min MPa	Max mm	Min mm
1	Male	40	22,289	12,477	57.79	0	14.64	0	37.84	12.03
2		45	39,092	22,386	45.02	0.023	9.29	0	41.24	13.78
3		65	22,289	12,477	62.85	0.05	16.39	0	36.84	8.37
4	Female	40	20,165	11,208	53.94	0.01	4.62	0	35.44	8.23
5		45	5905	6535	75.01	0	3.08	0	24.67	0.60
6		65	12,932	11,044	82.22	0	12.01	0	24.50	0.54

the 3D bone model with the distal end as fixed support. The simulation results reveal that the most significant deformation occurs at the top of the femoral head and that the least deformation occurs at the bottom of the femoral bone. Simulation results for all the created models with boundary conditions are shown in Table 1.

Total deformation and stress induced in male femur bone of different age groups is shown in Figs. 5 and 6, respectively. It is observed as the wall thickness increased, the induced stress and deformation decreased and bone offers high bone strength. Similarly, in case of females, the similar analysis is performed and the results are simulated in Table 1. The optimum stress induced in male femur bone at 45 years is 45.02 MPa with a deformation 9.29 mm. But in case of female, the optimum deformation is achieve at 40 years with minimum deformation as shown in Table 1.



**Fig. 5** Total deformation induced in male femur bone of different age groups

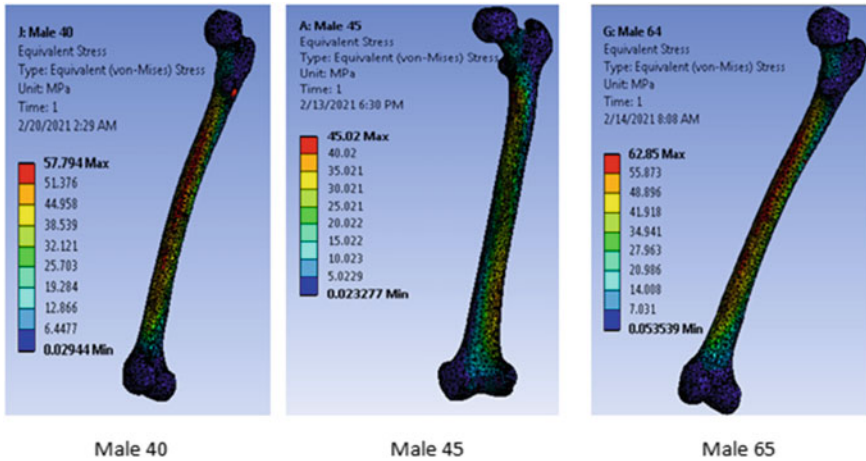


Fig. 6 Equivalent stress induced in male femur bone of different age groups

## 4 Conclusion

FEA has been used to determine the forces on the 3D femoral bone model. The present study concludes that the induced stress, overall deformation, and bone strength would increase with human's weight. Age and sex of human beings also affect the same. This study also discusses the effect of the wall thickness of bone, age, and sex on von Mises stress and deformation in femur bone. The findings conclude that in females' case, the maximum bone strength is offered in 30–40 years age group and the case of males 40–50 years age group. Females offer lower bone strength than males because of the degradation of bone properties in the female with the start of the maturation cycle.

## References

1. Ethier CR, Simmons CA (2007) *Introductory biomechanics: from cells to organisms*. Cambridge University Press
2. Fantoni I, Lozano R, Sinha SC (2002) Non-linear control for underactuated mechanical systems. *Appl Mech Rev* 55(4):B67–B68
3. Petit MA, Beck TJ, Shults J, Zemel BS, Foster BJ, Leonard MB (2005) Proximal femur bone geometry is appropriately adapted to lean mass in overweight children and adolescents. *Bone* 36(3):568–576
4. Karwowski W, Ostaszewski K, Zurada JM (1992) Applications of catastrophe theory in modeling the risk of low back injury in manual lifting tasks. *Le Travail Humain* 259–275
5. Lombardi RM (2012) Bone density as a source of error measuring body composition with the BOD POD and iDXA in female runners (Doctoral dissertation, The Ohio State University)

6. Trabelsi N, Yosibash Z, Wutte C, Augat P, Eberle S (2011) Patient-specific finite element analysis of the human femur—a double-blinded biomechanical validation. *J Biomech* 44(9):1666–1672
7. Poelert S, Valstar E, Weinans H, Zadpoor AA (2013) Patient-specific finite element modeling of bones. *Proc Inst Mech Eng [H]* 227(4):464–478
8. Engelke K, van Rietbergen B, Zysset P (2016) FEA to measure bone strength: a review. *Clin Rev Bone Miner Metab* 14(1):26–37
9. Taylor CA, Hughes TJ, Zarins CK (1998) Finite element modeling of blood flow in arteries. *Comput Methods Appl Mech Eng* 158(1–2):155–196
10. Van den Broeck J, Vereecke E, Wirix-Speetjens R, Vander Sloten J (2014) Segmentation accuracy of long bones. *Med Eng Phys* 36(7):949–953
11. San Antonio T, Ciaccia M, Müller-Karger C, Casanova E (2012) Orientation of orthotropic material properties in a femur FE model: a method based on the principal stresses directions. *Med Eng Phys* 34(7):914–919
12. Lotz JC, Cheal EJ, Hayes WC (1995) Stress distributions within the proximal femur during gait and falls: implications for osteoporotic fracture. *Osteoporos Int* 5(4):252–261
13. Pianykh OS (2009) Digital imaging and communications in medicine (DICOM): a practical introduction and survival guide. Springer Science & Business Media
14. Lee DC, Hoffmann PF, Kopperdahl DL, Keaveny TM (2017) Phantomless calibration of CT scans for measurement of BMD and bone strength—inter-operator reanalysis precision. *Bone* 103:325–333
15. Gargiulo P (2011) 3D modeling and monitoring of denervated muscle under Functional Electrical Stimulation treatment and associated bone structural change. *Eur J Transl Myol-Basic Appl Myol* 21:31–94
16. Walter DJ, Sirinterlikci A (2017) Utilization of freeware and low cost tools in a rapid prototyping and reverse engineering course. In: ASEE Annual Conference Exposition, Columbus, USA
17. Hsu CE, Shih CM, Wang CC, Huang KC (2013) Lateral femoral wall thickness: a reliable predictor of post-operative lateral wall fracture in intertrochanteric fractures. *Bone Joint J* 95(8):1134–1138
18. Chen X, Liu Y (2018) Finite element modeling and simulation with ANSYS Workbench. CRC press
19. Yassine RA, Elham MK, Mustapha S, Hamade RF (2017) A detailed methodology for FEM analysis of long bones from CT using Mimics. In: ASME 2017 international mechanical engineering congress and exposition. American Society of Mechanical Engineers Digital Collection
20. Stolarski T, Nakasone Y, Yoshimoto S (2018) Engineering analysis with ANSYS software. Butterworth-Heinemann
21. da Silva GA, Beck AT, Sigmund O (2019) Stress-constrained topology optimization considering uniform manufacturing uncertainties. *Comput Methods Appl Mech Eng* 344:512–537
22. Madenci E, Guven I (2015) The finite element method and applications in engineering using ANSYS®. Springer
23. Saibene F, Minetti AE (2003) Biomechanical and physiological aspects of legged locomotion in humans. *Eur J Appl Physiol* 88(4):297–316
24. McKibbin B (1978) The biology of fracture healing in long bones. *J Bone Joint Surg Br* 60(2):150–162
25. Keyak JH, Sigurdsson S, Karlsdottir G, Oskarsdottir D, Sigmarsdottir A, Zhao S, Kornak J, Harris TB, Sigurdsson G, Jonsson BY, Siggeirsdottir K (2011) Male–female differences in the association between incident hip fracture and proximal femoral strength: a finite element analysis study. *Bone* 48(6):1239–1245
26. Dobaré M, Garcia JM, Gómez MJ (2004) Modeling bone tissue fracture and healing: a review. *Eng Fract Mech* 71(13–14):1809–1840
27. Mccreadie BR, Goldstein SA (2000) Biomechanics of fracture: is bone mineral density sufficient to assess risk? *J Bone Miner Res* 15(12):2305–2308

# Performance Analysis of PCM-Integrated Greenhouse Dryer



Ravin Sehrawat, Ravinder Kumar Sahdev, and Sumit Tiwari

## 1 Introduction

Food and energy availability are the two key problems faced by the world in the existing time. Drying is a traditional method used to conserve food; it means lowering the moisture content to a reasonable limit to preserve food for a long time [1]. However, the drying of agro-products is an energized process propelled largely by energy demand with high operating costs. The need for energy can be met by renewable and non-renewable sources of energy. Solar energy is an inexpensive option that can also virtually eradicate CO<sub>2</sub> and CO emanation and other adulterants from the drying process [2]. One of the drawbacks of solar energy is that availability depends on seasons and geographical location like latitude and longitude—for example, solar energy compilation decrease during winter, particularly in upper latitudes [3, 4]. Similarly, solar energy is available only for a few hours of the day. Therefore, the main challenge is to run the greenhouse dryer (GHD) after non-sunshine hours. The problem can be minimized by integrating a TES system, which extends the period of available energy, allowing the drying air to be heated for an extended amount of time. PCMs are broadly used for TES for their significant enthalpy of fusion and high energy storage density [5, 29]. In recent years, PCM-based solar energy systems are in focus. Low thermal conductivity is the key barrier to the use of PCMs [30]. The authors performed a lot of work and the result highlights the future of the PCM-integrated system [3–6].

---

R. Sehrawat · R. K. Sahdev

Department of Mechanical Engineering, University Institute of Engineering & Technology,  
Maharshi Dayanand University, Rohtak, Haryana 124001, India

S. Tiwari (✉)

Department of Mechanical Engineering, Shiv Nadar University, Dadri, Uttar Pradesh 201314,  
India

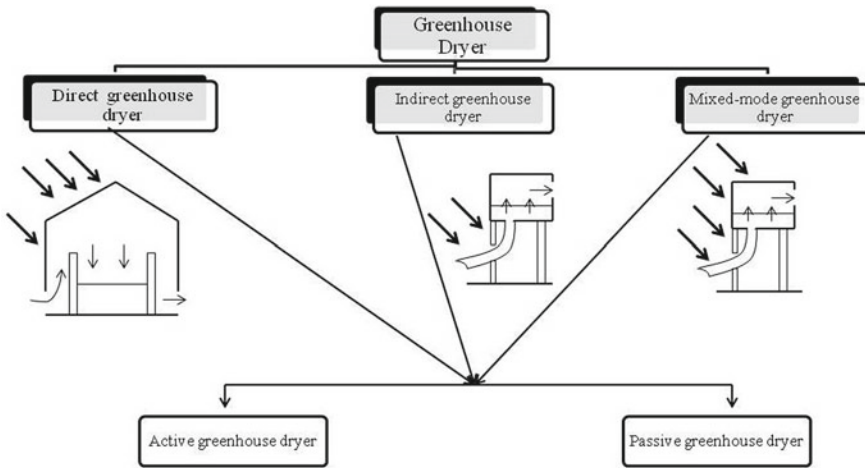


Fig. 1 Greenhouse dryer classification

## 2 Greenhouse Dryer

In the GHD, the substance to be dried is kept in an enclosure with a translucent shell. The absorption of direct/indirect solar radiations generates heat inside the drying chamber [7–9]. These solar radiations are the amount of absorbed solar radiations both on the object and the drying chamber’s internal surfaces. It improves product quality and uses optimal resources and time. It also makes the operation more effective and saves the environment [10, 27]. GHD is classified into various categories based on the mode of operation, geometry, etc., as shown in Fig. 1.

## 3 Phase Change Material

Latent heat storage is named as PCM energy storage [11, 25]. When the material gets heat, the material’s chemical bond breaks up, and the material changes phase as per particular interest (solid–liquid, solid–gas, liquid–gas) [12, 13, 26]. This phase transition is an endothermic mechanism, as the phase transition temperature is reached, the material begins to melt. The temperature then remains steady until the process of melting is done. The heat accumulated during the process of phase shift (melting process) is called latent heat [14, 15]. There are two key benefits of PCM storage as vast volumes of heat can be retained with only minor temperature shifts and hence have a high storage density. Various PCM groups were defined based on latent heat of fusion and melting temperature as shown in Fig. 2. [10–14].

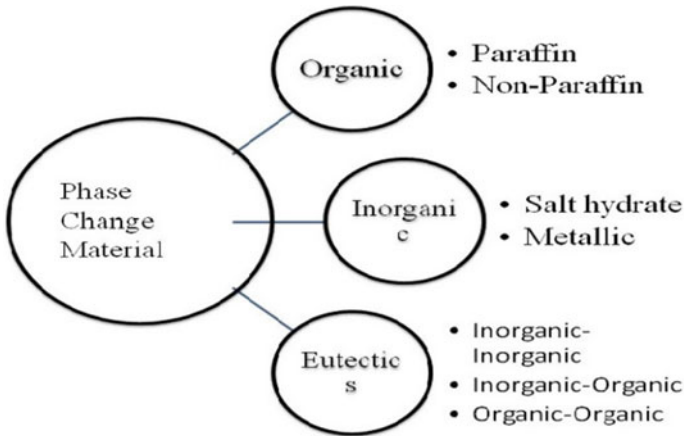


Fig. 2 Phase change materials classification

## 4 PCM-Integrated Greenhouse Dryer

The recent development on GHD has mainly concentrated on improving drying efficiency, effectual use of solar energy, minimizing the drying period, and improve running time in non-sunshine hours [31]. Incorporation of the solar air dryer, automatic close loop process, integration of PCM, etc., are some techniques introduced to support GHD. This paper focuses on the performance measurement of the PCM-integrated GHD.

### 4.1 Analysis Based on Performance

The performance of GHD includes the assessment of the significant parameters, such as drying rate, energy payback period, drying rate, thermal efficiency, coefficient of performance, etc.

A reviewed study was performed on TES-integrated greenhouse dryer. The study’s outcome suggests that sensible heat storage was a viable option for intermediate thermal operation but the key problem of low thermal density and cost. PCMs offered high thermal density [15]. Slices of strawberry of thickness 3 mm were dried in paraffin wax as a PCM-integrated industrial size greenhouse dryer. The system was incorporated with two air collectors, an energy storage system of 2 m long, 1 m wide, and 1 m deep, which contain 300 kg PCM of paraffin wax, and two fans were installed at the drying unit’s outlet and inlet, as well as an energy storage medium. When the system was analyzed for environmental impact, the energy payback time was determined to be approximately 6.82 years. CO<sub>2</sub> mitigation was measured as 99.60 tones for the predicted device lifetime. It was also discovered that the PCM box supplies



heat to the drying product in between sunshine and non-sunshine hours [16]. Various solar energy-based system integrated with PCM was observed. The most widely used PCM was paraffin which appeared to be productive in solar thermal application devices only for low- and medium-temperature operating systems. PCM built-in solar energy systems had significant reliability and performance improvements [17].

A greenhouse dryer integrated with a photovoltaic panel, solar accumulator, and paraffin-based energy storage system was analyzed. Further, black-colored zinc fins were installed with a solar panel to increase heat transfer. The solar accumulator was loaded with 300 aluminum soft drink can, which hold 56 kg PCM. The PCM was loaded with 4.8 kg strips to increase thermal conductivity. Kiwifruit and mushroom were dried during the study and experimental results positively related to the mathematical model [18]. Piper nigrum (black pepper) was dried with two active horizontal solar dryers integrated with PCM (paraffin wax) and compared with open sun drying. The TES consists of a 4 mm thick galvanized iron sheet with has a length of 200 mm, and outer and inner diameter was 205 mm and 197 mm, respectively, 38 kg paraffin wax has been melted and pumped into the heat exchanger. The drying time were 14 h and 23 h. For achieving the optimal humidity content of 0.14 (d.b) from 3.46 (d.b) in mixed mode and indirect mode of drying, it took 59 h to dry in the open sun. Mixed-mode dryers have high carbohydrate and protein values as compared to two other cases [19]. Three dryer systems, namely open sun drying, solar dryer with PCM, and solar dryer without PCM, were used to dry chili. Paraffin wax as a PCM was filled into a rectangular tube. The rectangular tubes of each module were attached in parallel. To maximize solar radiation absorption, the top surface and sides of each module are painted dark. During low solar radiation time, all PCM thermal storage device surfaces supply heat to the air inside the dryer to begin the drying process.

Chili has been dried to 10.0 percent (w.b.) moisture content from 74.7 percent (w.b.) moisture content in 2.5 days, 3.5 days, and 11 days with the combined PCM-integrated SD, PCM-free SD, and open sun dryer [20].

Various SDs arrangements (direct heating, indirect heating, mixed-mode dryer, PCM/PVT-integrated SD, etc.) were studied. It was observed that direct dryers in remote areas are affordable and easy to mount, though indirect dryers have better drying control and improved efficiency. It was also noted that, the drying rate is largely determined by the heat transfer coefficients of evaporative (he) and convective (hc). Hybrid dryers were autonomous and can also work during the off-sunshine hours [21]. Grapes were dried in three different drying arrangements, namely hot air oven dryer, solar dryer, and SD with PCM. For energy preservation, paraffin wax was used as a PCM. The study concludes that the use of TES enhanced the device's reliability and performance [22]. Valeriana Jatamansi was dried inside a PCM-integrated indirect SD. The study was also compared with the heat pump dryer and shade dryer. Paraffin RT-42 was used as PCM in the dryer, where a blend of gravel, iron scrap, and engine oil was used as a TES medium in the collector. Results indicate that the drying time using PCM was decreased by 37.50% and 64.29% relative to heat pump drying and shade drying, respectively [23]. Modeling, simulation, and experiment of various sustainable SDs were studied. Based on a detailed description, it was proposed that

**Table 1** Remarks from the various study

Sr. No	Author	Remarks
1	[15]	PCM make a better combination with greenhouse dryer performance
2	[19]	PCM-integrated greenhouse dryer performed better and provide high efficiency
3	[20]	TES overcomes the downside of the intermittent supply of solar energy
4	[21]	Proposed a mathematical model for TES-integrated SD
5	[22]	Drying temperature remains uniform with the integration of TES
6	[23]	Integration of PCM helped to dry commodities in unfavorable environmental conditions
7	[24]	Proposed hybrid dryers during the off-sunshine season.
8	[25]	PCM boost efficiency with the supply of energy in low to non-sunshine hours
9	[26]	The addition of PCM helped to provide hot air in the greenhouse dryer until midnight

the introduction of combined heat and power systems powered by biomass might be a successful solution to post-harvest waste [24]. A lot of work has been performed by authors and Tables 1 and 2 detailed various remarks and governing equations, respectively.

## 5 Conclusion

Solar energy play a significant role in the present era as clean energy. The major problem with solar energy is its intermittent nature (non-availability during non-sunshine hours). The use of fossil fuel to supply heat in non-sunshine hours is not feasible due to limited availability on earth and environmental aspects. PCM-integrated SD is an optimal alternative to minimize the issue of energy demand during sunshine and non-sunshine hours. An important role in reducing post-harvest losses, particularly in low sunshine hours, will be played by the PCM-integrated SD for the drying of agricultural products. Following conclusions are made.

- Integration of PCM in SD enhances the system performance in terms of efficiency, drying time, operating time.
- PCM with enhanced thermal conductivity will be more effective.
- Integration of PCM raises the initial cost but lowers running cost.

**Table 2** The governing equation is used to solve the mathematical model

Sr. No	Authors	Governing equation
1	[19]	<p>1. Energy balance equation for drying unit  <math>Q_U = A_c F_R [I - U_L (T_i - T_o)]</math>  The heat loss coefficient  <math>U_L = \frac{I(\tau a_a)}{T_i - T_o}</math>  Factor for removing heat <math>F_R</math>  <math>F_R = \frac{m C_p}{A_c U_L} \left( 1 - \exp\left(\frac{A_c U_L F'}{m C_p}\right) \right)</math></p> <p>2. Exergy balance equation for drying unit  <math>\dot{E}_{x_{out}} = \dot{m}_a \bar{C}_{p,a} \left[ (T_{out,a} - T_a) - T_a \ln \frac{T_{out,a}}{T_a} \right]</math>  <math>\dot{E}_{x_{out}} = \dot{m}_a \bar{C}_{p,a} \left[ (T_{out,a} - T_a) - T_a \ln \frac{T_{out,a}}{T_a} \right]</math></p> <p>3. Energy balance of PCM energy storage system  <math>Q = m [C_{SP}(T_m - T_i) + a_m \Delta h_m + C_{IP}(T_f - T_m)]</math></p> <p>4. Entropy generation calculation  <math>S_{gen} = m_{PCM}(S_l - S_s) + \dot{m}_a (S_{a,out} - S_{a,in}) t_p</math></p> <p>5. Exergy analysis of PCM energy system  <math>\dot{E}_{x_{stored}} = \dot{m}_{HTF} C_{HTF} (T_{HTF,in} - T_{HTF,out}) \left[ 1 - \left( \frac{T_o}{T_{PCM}} \right) \right]</math></p>
2	[21]	<p>1. The energy balance on the absorber plate  <math>\rho_b A_b S P \delta_b C_b \frac{dT_b}{dt} =</math>  <math>A_b S P h_{c,bf} (T_f - T_b) + A_{g,sp} h_{r,bg} (T_g - T_b) + A_g U_b (T_a - T_b) + A_b S P t_g a_b I</math></p> <p>2. Energy balance in PCM  <math>\lambda_w m_w \frac{d\theta}{dt} + m_w C_w \frac{dT_w}{dt} = A_w h_{c,wf} (T_f - T_w) + A_g h_{r,wg} (T_g - T_w) + A_w t_g a_w I</math></p> <p>3. Solar accumulator efficiency  <math>\eta_{SA} = \frac{Q_{abs,f}}{Q_{abs,w}} 100\%</math></p> <p>4. Energy balance of the air  <math>\rho_f V_f (C_f + C_v H_2) \frac{dT_{f2}}{dt} =</math>  <math>W_{f3} (C_f + C_v H_1) T_{f3} - W_{f3} (C_f + C_v H_2) T_{f2} + A_p h_{c,pf} (T_{f2} - T_p)</math></p>
3	[22]	<p>1. Net amount of energy fall on SAH  <math>Q_{in,SAH1} = \alpha \times \tau \times I \times A_{SAH1}</math></p> <p>2. The rate of heat energy charging and discharging to TES is expressed as  <math>e_{ch} = \dot{m}_a C_{pa} (T_{ies,air} - T_{oes,air})</math>  <math>e_{disch} = \dot{m}_a C_{pa} (T_{ies,air} - T_{oes,air})</math></p> <p>3. Overall efficiency of the SD with PCM  <math>\eta_{over} = \frac{m_{water} \times h_{fg}}{(E_s + E_{TES} + E_b)}</math></p>

## References

1. Kant K, Shukla A, Sharma A, Kumar A, Jain A (2016) Thermal energy storage based solar drying systems: a review. *Innov Food Sci Emerg Technol* 34:86–99
2. Khan MA, Karmakar R, Sarker MRI, Tuly SS, Beg RA (2019) Experimental investigation of single basin solar still using phase change material (PCM) as an energy storage medium.

- In: AIP Conference Proceedings (vol 2121, No. 1, p 120002)
3. Ayyappan S, Mayilsamy K, Sreenarayanan VV (2016) Performance improvement studies in a solar greenhouse drier using sensible heat storage materials. *Heat Mass Transf* 52(3):459–467
  4. Azaizia Z, Kooli S, Hamdi I, Elkhali W, Guizani AA (2020) Experimental study of a new mixed-mode solar greenhouse drying system with and without thermal energy storage for pepper. *Renew Energy* 145:1972–1984
  5. Berrow F, Lakhali EK, El Omari M, Faraji M, El Qarnia H (2011) Thermal performance of a greenhouse with a phase change material north wall. *Energy Buildings* 43(11):3027–3035
  6. Huang BK, Toksoy M, Cengel YA (1986) Transient response of latent heat storage in greenhouse solar system. *Sol Energy* 37(4):279–292
  7. Jain A, Kumar A, Shukla A, Sharma A (2017) Development of Phase Change Materials (PCMs) for solar drying systems. In: *Solar drying technology* (pp 619–633). Springer, Singapore
  8. Kaizawa A, Kamano H, Kawai A, Jozuka T, Senda T, Maruoka N, Akiyama T (2008) Thermal and flow behaviors in heat transportation container using phase change material. *Energy Convers Manage* 49(4):698–706
  9. Sahdev RK, Kumar M, Dhingra AK (2016) A review on applications of greenhouse drying and its performance. *Agric Eng Int CIGR J* 18(2):395–412
  10. Sharma SD, Sagara K (2005) Latent heat storage materials and systems: a review. *Int J Green Energy* 2(1):1–56
  11. Lin Y, Jia Y, Alva G, Fang G (2018) Review on thermal conductivity enhancement, thermal properties and applications of phase change materials in thermal energy storage. *Renew Sustain Energy Rev* 82:2730–2742
  12. Kürklü A (1998) Energy storage applications in greenhouses by means of phase change materials (PCMs): a review. *Renew Energy* 13(1):89–103
  13. Pielichowska K, Pielichowski K (2014) Phase change materials for thermal energy storage. *Prog Mater Sci* 65:67–123
  14. Saman W, Bruno F, Halawa E (2005) Thermal performance of PCM thermal storage unit for a roof-integrated solar heating system. *Sol Energy* 78(2):341–349
  15. Shukla A, Sharma A, Kant K (2016) Solar greenhouse with thermal energy storage: a review. *Curr Sustain Renew Energy Rep* 3(3–4):58–66
  16. Dwivedi VK, Tiwari P, Tiwari S (2016) Importance of Phase Change Material (PCM) in solar thermal applications: a review. In: *2016 International Conference on Emerging Trends in Electrical Electronics & Sustainable Energy Systems (ICETEESES)* pp 42–45
  17. Farid MM, Khudhair AM, Razack SAK, Al-Hallaj S (2004) A review on phase change energy storage: materials and applications. *Energy Convers Manage* 45(9–10):1597–1615
  18. Xu B, Li P, Chan C (2015) Application of phase change materials for thermal energy storage in concentrated solar thermal power plants: a review to recent developments. *Appl Energy* 160:286–307
  19. Atalay H, Cankurtaran E (2020) Energy, exergy, exergoeconomic and exergo-environmental analyses of a large scale solar dryer with PCM energy storage medium. *Energy* 119221
  20. Kalidasan B, Pandey AK, Shahabuddin S, Samykano M, Thirugnanasambandam M, Saidur R (2020) Phase change materials integrated solar thermal energy systems: global trends and current practices in experimental approaches. *J Energy Storage* 27:101118
  21. Vásquez J, Reyes A, Pailahueque N (2019) Modeling, simulation and experimental validation of a solar dryer for agro-products with thermal energy storage system. *Renew Energy* 139:1375–1390
  22. Lakshmi DVN, Muthukumar P, Nayak PK (2020) Experimental investigations on active solar dryers integrated with thermal storage for drying of black pepper. *Renew Energy*
  23. Pankaew P, Aumporn O, Janjai S, Pattarapanitchai S, Sangwan M, Bala BK (2020) Performance of a large-scale greenhouse solar dryer integrated with phase change material thermal storage system for drying of chili. *Int J Green Energy* 17(11):632–643
  24. Singh P, Gaur MK (2020) Review on development, recent advancement and applications of various types of solar dryers. *Energy Sources Part A Recovery Utilization Environ Eff* 1–21

25. Bharani Priya A, Dineshkumar M, Naveen Romi J, Vijay Nepolean A, Kirubakaran V (2020) Solar dryer integrated with thermal energy storage systems for the preparation of dry grapes in the farmyard: sustainable rural farming approach
26. Bhardwaj AK, Chauhan R, Kumar R, Sethi M, Rana A (2017) Experimental investigation of an indirect solar dryer integrated with phase change material for drying *Valeriana jatamansi* (medicinal herb). *Case Studies in Thermal Engineering* 10:302–314
27. Lamidi RO, Jiang L, Pathare PB, Wang Y, Roskilly AP (2019) Recent advances in sustainable drying of agricultural produce: A review. *Appl Energy* 233:367–385
28. Tiwari S, Tiwari GN, Al-Helal IM (2016) Performance analysis of photovoltaic–thermal (PVT) mixed-mode greenhouse solar dryer. *Sol Energy* 133:421–428
29. Salve, S. and Fulambarkar, A.M., 2021. A solar dryer for drying green chili in a forced convection for increasing the moisture removing rate. *Materials Today: Proceedings*.
30. Das S, Biswas A, Das B (2021) A review on solar drying applications using latent heat as energy storage media. In: *Recent Advances in Mechanical Engineering* (pp 305–317). Springer, Singapore
31. Chaturvedi R, Islam A, Sharma K (2021) A review on the applications of PCM in thermal storage of solar energy. *Mater Today Proc*
32. Sinhmar N, Singh P (2021) Progress and latest developments in hybrid solar drying with thermal energy storage system. In: *Advances in Electromechanical Technologies* (pp 487–498). Springer, Singapore

# Numerical Simulation of Frontal Crash for Toyota Yaris Using LS-DYNA



Tushar Tanwar, Shikhar Gupta, Ashwani Kumar Singh, and Vijay Gautam

## 1 Introduction

The safety of passengers under crash conditions is a special concern for a vehicle in the automobile industry nowadays. Here, instead of performing an actual crash test, simulation is carried out in LS-DYNA software for crash analysis of the Toyota Yaris FE model which is less time-consuming and is economical [1]. Several factors affect the performance of the vehicle during crash analysis, one of them is lightweighting and the other is crashworthiness [2]. Crashworthiness is the measure of the ability of a car structure to absorb energy to prevent its occupant during a collision. Before the simulation could be carried out, several pre-processing conditions need to be specified and the results obtained from the software are verified from actual crash test reports.

To reduce the weight, conventional materials are being replaced with lightweight materials like aluminium alloys because they provide better strength-to-weight ratio. Although, in many cases, lightweight material may be costlier than conventional materials due to requirement of new processes and equipment [3] but if they provide better crashworthiness then they become a priority because passenger safety is the primary concern. The application of new lightweight materials like aluminium, magnesium and high strength steel is playing an important role in the automobile industry because of higher strength but lower ductility compared to conventional materials. However, in the construction of vehicle components, the use of lighter substitutes to steel is playing important role in the automotive industry, and aluminium is considered as one of the best substitutes for steel. The reduction of vehicle weight also brings additional benefits such as better acceleration, better handling of the vehicle and more comfort for the occupants in the vehicle. Content of aluminium has been continuously increasing in the vehicle structure and it had

---

T. Tanwar (✉) · S. Gupta · A. K. Singh · V. Gautam  
Delhi Technological University, Delhi, India

been studied from the vehicle market in China that emission of dangerous substance will be reduced if aluminium content used in the vehicle structure will be more than 330 kg [4].

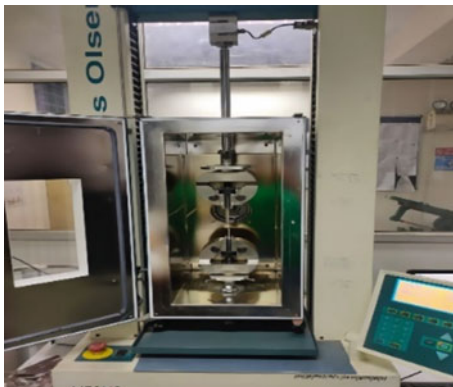
## 2 Material Characterization

6000 and 7000 series of aluminium are of particular interest in the automobile industry. The use of aluminium alloys for the construction of vehicle structure is one of the methods of reducing the weight of the vehicle as the density of aluminium ( $2700 \text{ kg/m}^3$ ) is one-third of the steel ( $7600 \text{ kg/m}^3$ ) and it is attracting many different sectors especially automobile and aeronautical due to their low density and high strength [5]. In this study, AA6082-T6 material is used as this aluminium alloy has the highest strength in the 6000 series. This alloy is mostly supplied in plate or sheet, since this aluminium alloy has not been in much use in the automobile industry, this may be due to lack of knowledge about this alloy. Aluminium alloy 6082 is a medium-strength alloy with excellent properties such as lightweight, corrosion resistance, ductility and easy machining [6]. Low content of copper in 6082 compared to 6061 results in excellent corrosion resistance. This alloy is also known as structural alloy [7]. This grade substitutes the conventional 6061 alloys in many structural applications as it has 10–15% higher tensile strength. It is widely used in structural applications in which high-stress resistance is required. The tempering designation of T6 represents that the material is solution heat treated and then artificially aged. The machining of tensile specimen was done using HS-G3015C laser cutting machine as shown in Fig. 1.

**Fig. 1** Preparation of tensile specimen using HS-G3015C laser cutting machine



**Fig. 2** Tensile testing using H50KS UTM



**Fig. 3** Untested and tested specimens as per ASTM standard



### 3 Testing and FEA Simulation

In this study, the material was tensile tested and the simulation was carried out in LS-DYNA software. LS-DYNA software is a multi-functional simulation software that is strongly used to analyse the non-linear physical processes with large deformations that occur in a short time. It is an industry-standard software originally developed by Lawrence Livermore National Laboratory for impact and defence applications [8]. For the application of material AA6082-T6, Cowper–Symonds model is used in the LS-DYNA software. The reason for doing so is the ease and simplicity of this model as compared to the Johnson–Cook and Zerilli–Armstrong models [9]. Also, this model was originally used in the Toyota Yaris FE model which was designed by the George Washington University National Crash Analysis Centre.



### 3.1 Tensile Testing of the Specimen

The strain rates used in the testing have significant influence on the flow stress behaviour of the material and it is expressed in units of per second (Figs. 2 and 3). Uniaxial tension tests at strain rates ( $10^{-4}$  to  $10^{-1} \text{ s}^{-1}$ ) were performed on H50KS UTM. The reason for tensile testing is to generate the true stress versus true strain curve. This curve will give the yield point for AA6082-T6 so that further simulation could be carried out. The tensile test performed was according to the ASTM standards which involves specimens cut in dog-bone shape. The specimens had a thickness of 2 mm and gauge length of 84.16 mm and were cut in the rolling direction by laser cutting.

$$\text{StrainRate} = \frac{\partial \varepsilon}{\partial t} = \frac{\Delta L}{L \cdot \partial t} = \frac{V}{L} \quad (1)$$

where V is the cross-head velocity of the UTM, and  $\Delta L$  and L depict the change in length and original gauge length of the specimen. Tests were conducted at cross-head velocities of 0.505, 5.05, 50.5 and 505 mm/min, which correspond to strain rates of  $10^{-4}$ ,  $10^{-3}$ ,  $10^{-2}$  and  $10^{-1} \text{ s}^{-1}$ , respectively.

The plot (Fig. 4) shown below is the true stress-true strain plot of AA6082-T6 for varying strain rates. From the plot, the yield stress at reference strain rate of  $10^{-3} \text{ s}^{-1}$  is coming out to be 242.32 MPa.

The reason for performing the test at different strain rates is to check the behaviour of the material at different strain rates. From the plot, it can be seen that yield stress is increasing with an increase in strain rate.

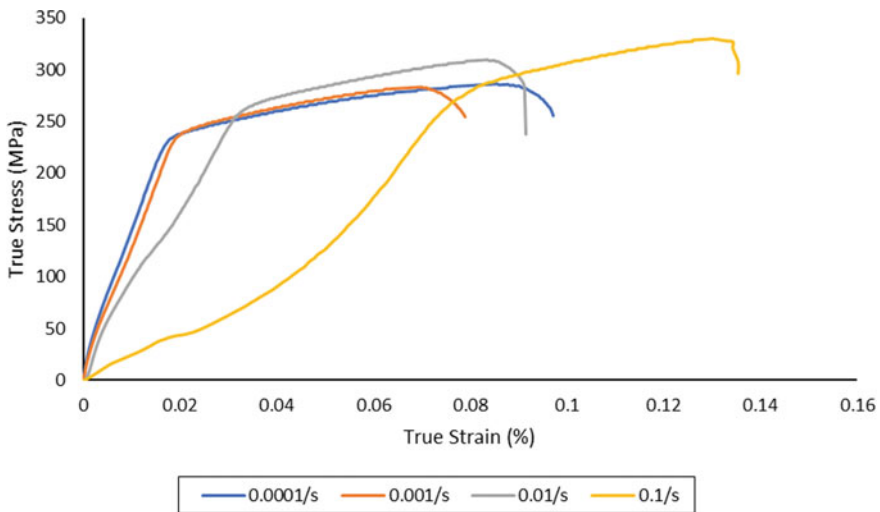
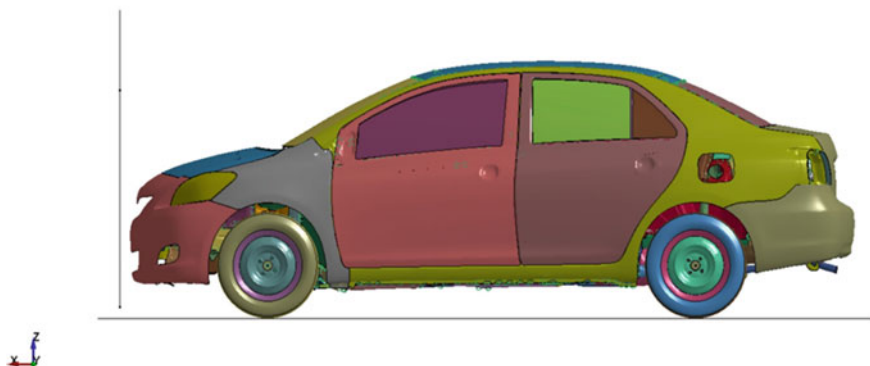
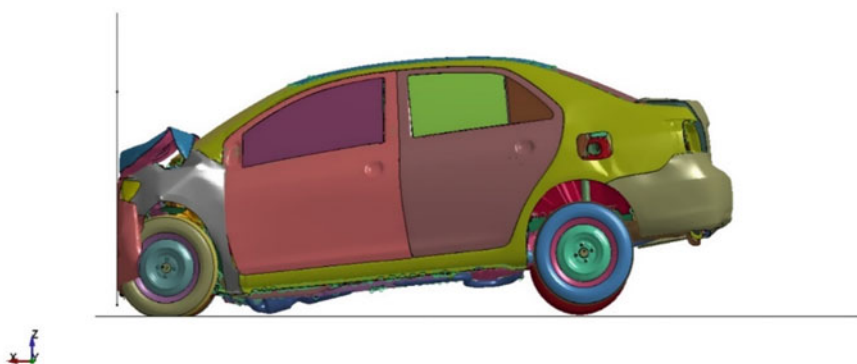


Fig. 4 True Stress versus True Strain plot for varying strain rates



**Fig. 5** Position of car before the crash at 0.0 s



**Fig. 6** Position of car during the crash at 0.1 s

### **3.2 Modelling and Simulation**

The FEM model and its constraints were already defined by the George Washington University National Crash Analysis Centre [10]. This model was made and assembled for use by NHTSA (National Highway Transportation and Safety Authority), USA which incorporates crash testing by adopting the NCAP regulations according to their country standards. The simulation performed was all set on standard values. The Toyota Yaris FE model (2010) was taken from the NHTSA and the standard speed of the car is 56.33 KMPH or 35 MPH for the crash test. The frontal crash simulation was done for this model using LS-DYNA software. This speed has been defined according to the regulations of NCAP, so there have been no changes made in the speed while simulating the crash.

For this simulation, a tonne-mm-s system of unit is used in which mass is in tonnes, length in millimetres, time in seconds, force is in newtons and stress in MPa. The ratio for velocity in this system is  $1.56E + 04$ . The simulation was completed in 42

steps, i.e. there were total of 42 stages in which the data was written of d3plot for the crash simulation. The simulation time, i.e. 0.2 s was divided in 42 parts as required by user to write d3plots. Shown below are three stages, starting, intermediate and ending by which a general idea can be formed regarding the crash simulation (Figs. 5 and 6).

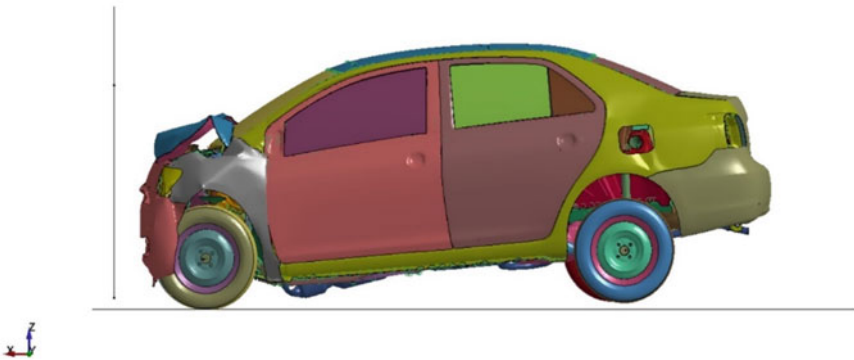
In Fig. 7, the car had been moved back after colliding with the wall and this is because of the fact that the momentum is conserved during the collision, since the wall is rigid so when the car exerted a force in the direction of the wall, the wall also exerted an equal and opposite force back on the car. The piecewise linear plasticity material model is used for the simulation of crash of this car. This model is also known as Cowper–Symonds material model and it works on the principle of the behaviour of elasto-plastic materials.

The Cowper–Symonds material model is frequently used to determine the material behaviour at different strain rates [11]. This model scales the yield stress ( $\sigma_y$ ) which considers the effect of strain factor and strain rate factor only as shown in Eq. (2) where  $\sigma_o$  is the initial yield stress;  $\dot{\epsilon}$  is the strain rate; C and P are the Cowper–Symonds strain rate parameters;  $\beta$  is the strain hardening parameter, which adjust the contribution of isotropic and kinematic hardening;  $\epsilon_p^{eff}$  is the effective plastic strain and  $E_p$  is the plastic hardening modulus which is given in terms of the elastic modulus E and the tangent elastic modulus  $E_{tan}$  as shown in Eq. (3).

$$\sigma_y = [1 + \left(\frac{\dot{\epsilon}}{C}\right)^{1/P} (\sigma_o + \beta E_p \epsilon_p^{eff})] \quad (2)$$

$$E_p = E_{tan} \frac{E}{(E - E_{tan})} \quad (3)$$

MAT\_024 PIECEWISE\_LINEAR\_PLASTICITY model was selected as shown in Fig. 8 and the required material properties were entered. Instead of finding out the Cowper–Symonds strain rate parameters C and P, we had inserted a combined true



**Fig. 7** Position of car after the crash at 0.2 s

Keyword Input Form

NewID  MatDB  RefBy  Pick  Add  Accept  Delete  Default  Done

Use \*Parameter  Comment (Subsys: 1 YarisD\_V2g.key)

\*MAT\_PIECEWISE\_LINEAR\_PLASTICITY\_(TITLE) (024) ( 811)

**TITLE**  
AI6082-T6

1	<b>MJD</b>	<b>RQ</b>	<b>E</b>	<b>PR</b>	<b>SIGY</b>	<b>ETAN</b>	<b>FAIL</b>	<b>TDEL</b>
	h	2.700e-09	6.900e+04	0.3300000	242.32001	0.0	1.000e+21	0.0
2	<b>C</b>	<b>P</b>	<b>LCSS</b>	<b>LCSR</b>	<b>VP</b>			
	0.0	0.0	2101005	0	0.0			
3	<b>EPS1</b>	<b>EPS2</b>	<b>EPS3</b>	<b>EPS4</b>	<b>EPS5</b>	<b>EPS6</b>	<b>EPS7</b>	<b>EPS8</b>
	0.0	0.0	0.0	0.0	0.0	0.0	0.0	0.0
4	<b>ES1</b>	<b>ES2</b>	<b>ES3</b>	<b>ES4</b>	<b>ES5</b>	<b>ES6</b>	<b>ES7</b>	<b>ES8</b>
	0.0	0.0	0.0	0.0	0.0	0.0	0.0	0.0

Fig. 8 MAT\_024 PIECEWISE\_LINEAR\_PLASTICITY keyword file in LS-DYNA

stress versus true strain curve of varying strain rates ( $10^{-4}$ ,  $10^{-3}$ ,  $10^{-2}$ ,  $10^{-1}$  s<sup>-1</sup>) in a table as shown in Fig. 9. This Table ID was inserted in the LCSS of the keyword input dialogue box of MAT\_024 PIECEWISE\_LINEAR\_PLASTICITY model. The strain rate parameters: C and P, the curve ID, LCSR, EPS1-EPS8 and ES1-ES8 are ignored if a Table ID is defined.

For comparable mechanical properties of aluminium parts with that of steel, the cross-sectional area of car parts shown in Table 1 has been increased.

Keyword Input Form

NewID  Draw  RefBy  Pick  Add  Accept  Delete  Default  Done

Use \*Parameter  Comment (Subsys: 1 YarisD\_V2g.key)

\*DEFINE\_TABLE\_(TITLE) ( 1)

**TITLE**  
Strain Rate Table

1	<b>TRID</b>	<b>SFA</b>	<b>OFFA</b>
	2101005	1.0000000	0.0

Repeated Data by Button and List

<b>VALUE</b>	<b>LCDID</b>
0.1	2101004

1 1.0000e-04 2101001  
2 1.0000e-03 2101002  
3 1.0000e-02 2101003  
4 1.0000e-01 2101004

Data Pt. 4

Fig. 9 DEFINE\_TABLE keyword file in LS-DYNA

**Table 1** List of modified parts

Part number	Part name	Yield stress (MPa)
2,000,001	Fender wheel bracket right	270
2,000,061	Radiator frame bottom	270
2,000,078	Radiator frame rear	270
2,000,097	Frame upper main left	270
2,000,098	Fender wheel bracket left	270
2,000,115	Rail lower plate right	270
2,000,118	Frame upper main right	270
2,000,119	Rail lower plate left	270
2,000,120	Rail lower connector left	270
2,000,123	Rail lower connector right	270
2,000,130	Front frame upper support left	270
2,000,133	Bumper bracket right	270
2,000,134	Bumper bracket left	270
2,000,138	Frame front right	380
2,000,139	Radiator frame front	270
2,000,140	Front frame upper support right	270
2,000,142	Frame front left	380
2,000,159	Housing support front left	270
2,000,160	Housing support front right	270
2,000,163	Rail outer right	380
2,000,164	Rail inner right	350
2,000,166	Rail inner left	350
2,000,168	Rail outer left	380

## 4 Result and Discussions

The parts shown in Table 1 are replaced with AA6082-T6 material and so the energy absorption of the vehicle is affected due to the change of material. The focus of this study was to examine the effect of the changed material on the crashworthiness of the vehicle during a crash test. The above parts have individually shown a change in energy absorption which ultimately resulted in overall change of energy absorption of the vehicle. The graphs below are showing an overall effect on the energy absorption and crash pulse of the vehicle and the velocity of driver's seat during a crash. A comparison is drawn based on the increase or decrease of the energy absorption and crash pulse. Some individual parts had showed a decrease in the energy absorption but the overall effect on the car had been considered which is explained below.

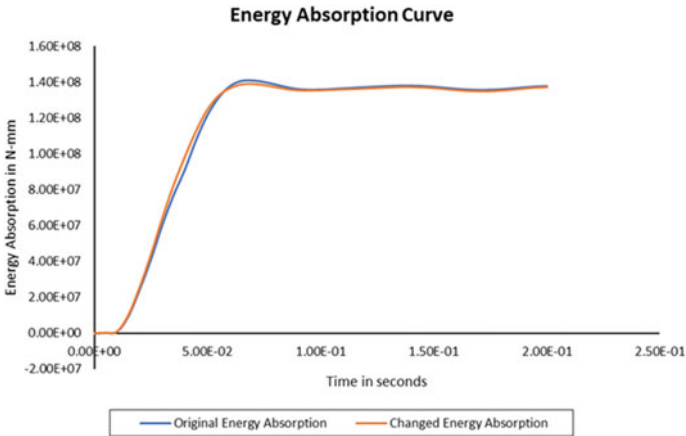


Fig. 10 Energy absorption curve for the whole car body, i.e. internal energy plot

### 4.1 Energy Absorption Curve

In the plot (Fig. 10) shown below, it can be seen that there is a slight increase of **1.99%** in energy/shock absorbed by the car which is generated during a crash. This means that AA6082-T6 absorbs more energy of the crash than conventional materials used in the car.

### 4.2 Crash Pulse

The plot (Fig. 11) shown below is the deceleration curve of the car. The lower the negative peak of the crash pulse, lesser will be the impact of the crash on the driver. As shown in the plot (Fig. 11) if the peak points of original and changed acceleration are compared, a massive decrease in the acceleration and deceleration of the car could be seen. The curve of changed acceleration is much smoother than original acceleration. So, the net decrease in negative acceleration or deceleration is approximately **31.48%**. In an ideal condition, this curve is smooth and has a constant decrease with the least negative slope possible so that the driver and passengers don't get fatally injured.

### 4.3 Velocity Curve

The plot (Fig. 12) shown below depicts the velocity time curve of the driver's seat. Here, more gradual decrease in the changed velocity as compared to original velocity

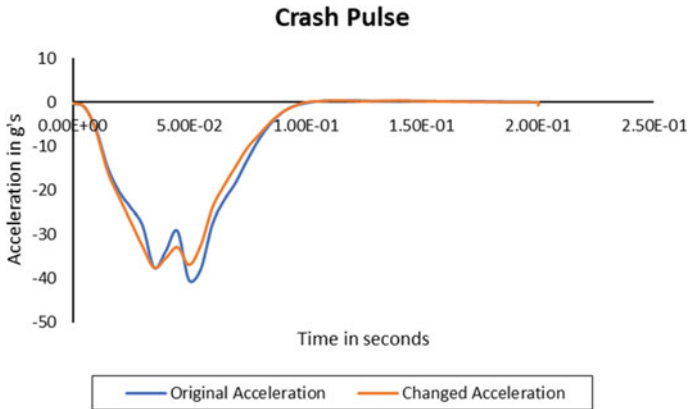


Fig. 11 Crash pulse or deceleration curve of the car

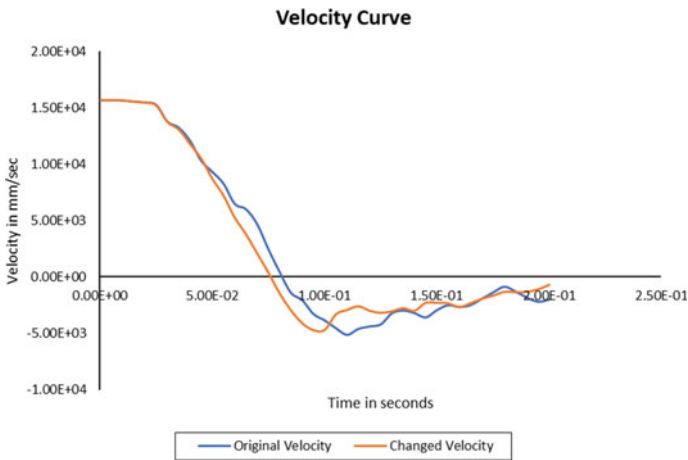


Fig. 12 Velocity–time curve of the driver seat

can be seen. The average decrease in the velocity is **19.80%**. This means that the driver is travelling with much lesser velocity during the crash with changed material. So, the chances of fatal injury are decreased in case of changed material.

## 5 Conclusions

This study had shown the effect of change of material on the crashworthiness of the vehicle. The world is moving towards enhancing the safety provided to the occupants of a vehicle during a crash and one of the methods for doing this is by changing the

material of some parts of the vehicle, which ultimately enhances the shock absorption capability of the vehicle. This study had been done in the same way; the material had been changed to AA6082-T6 for the parts shown in Table 1. For some individual parts, the energy absorption is coming out to be positive and for some parts, it is coming out to be negative but an overall positive effect can be seen in the plot above. It is also seen that the driver seat is retarding a bit slower than before which means that the peak deceleration and velocity have been reduced which ultimately leads to increased safety of the occupants in the vehicle than before. Since aluminium is lighter in weight than steel so an overall weight reduction of 1.30% is seen in the vehicle.

## References

1. Kiran CS, Sruthi J, Balaji SC (2017) Design and crash analysis of a passenger car using ANSYS workbench. 13:5
2. Singh AK, Gautam V, Kumar D (2020) Numerical simulation of crashworthiness of a saloon car. *Solid State Technol* 63(1):12
3. Tisza M, Czinege I (2018) Comparative study of the application of steels and aluminium in lightweight production of automotive parts. *Int J Lightweight Mater Manuf* 1(4):229–238. <https://doi.org/10.1016/j.ijlmm.2018.09.001>
4. Du JD, Han WJ, Peng YH, Gu CC (2010) Potential for reducing GHG emissions and energy consumption from implementing the aluminum intensive vehicle fleet in China. *Energy* 35(12):4671–4678. <https://doi.org/10.1016/j.energy.2010.09.037>
5. Ho C, Nor MM (2020) Tensile behaviour and damage characteristic of recycled aluminium alloys AA6061 undergoing finite strain deformation. 9
6. Lin CF, Chen TH, Tsai L, Hsieh TH, Su WC, Wang IH (2020) Investigation into quasi-static and dynamic tensile mechanical properties of aluminium–scandium alloy. *Mater Sci Technol* 36(17):1820–1828. <https://doi.org/10.1080/02670836.2020.1838709>
7. Mo W (2012) Dynamic properties of aluminium alloys used in automotive Industry. p 7
8. Sandner V, Ellway J, van Ratingen M (2017) Euro NCAP frontal impact working group report. 10
9. Estimating the Strain-Rate-Dependent Parameters of the Cowper-Symonds and Johnson-Cook Material Models using Taguchi Arrays.pdf (2016)
10. Center for collision safety and analysis (2016) 2010 Toyota Yaris finite element model validation detail mesh. <https://doi.org/10.13021/G8CC7G>
11. Marangoni AL, Massaroppi Junior E (2017) Cowper-Symonds parameters estimation for ABS material using design of experiments with finite element simulation. *Polímeros* 27(3):220–224. <https://doi.org/10.1590/0104-1428.04016>



# Rail Pad Dynamic Properties: A Review



Sumeet Padhi, Shubham Sharma, and Yamika Patel

## Nomenclature

$\varepsilon$ :	Strain
$\varepsilon_0$ :	Max. amplitude of strain
$\sigma$	Stress
$\sigma_0$	Max. amplitude of stress
$w$	Angular velocity( $=2\pi f$ )
$t$	time
$\delta$	Phase lag
$E'$	Storage modulus
$E''$	Loss modulus
$E^*$	Dynamic modulus
$i$	$\sqrt{-1}$
$\zeta$	Damping ratio
$E$	Young's modulus
$\eta$	Dynamic viscosity
$K_R$	Rail pad stiffness
$D^\alpha$	Fractional derivative operator
$\Gamma$	Gamma function

---

S. Padhi (✉) · S. Sharma · Y. Patel  
Delhi Technological University, New-Delhi 110042, India  
e-mail: [sumeetpadhi\\_2k18me227@dtu.ac.in](mailto:sumeetpadhi_2k18me227@dtu.ac.in)

© The Author(s), under exclusive license to Springer Nature Singapore Pte Ltd. 2022  
R. M. Singari et al. (eds.), *Advances in Mechanical Engineering and Technology*,  
Lecture Notes in Mechanical Engineering,  
[https://doi.org/10.1007/978-981-16-9613-8\\_6](https://doi.org/10.1007/978-981-16-9613-8_6)

# 1 General Background

The railway is one of the essential aspects of any nation's development. Economically, it is the best means for transporting large amount of goods and people over long land routes. Railway is a solution to growing air pollution and traffic congestion [1], it is even considered as a lifeline in various overpopulated cities over the world. Its major drawback is the problem of noise and vibration which causes discomfort to passengers and disturbance to people and buildings near its surroundings [1]. It also poses a threat to the safety of operation. With excess vibration, derailment is always a possibility. With increased globalization and population, dependency on railway increased manifolds in recent years, and thus understanding vibration becomes important.

Rail pad is one of the critical components for any type of track. They are inserted between sleepers and rails. It was first introduced on Amtrak and on British rail to reduce the effect of impact loading on sleepers and to prevent cracking of rail seat area [2]. The interest in resilient pads sparked around (1970–1980) period. Initial pads were made up of natural rubber and later shifted to synthetic rubber and polymers with development in material science. Some initial experiments were performed in Battelle Columbus Laboratories [2]. Several field experiments were also carried out by Pandrol International Limited during 1984–85. It considers different speeds ranging from (70–160) km/hr, different rail pad materials (natural rubber, synthetic rubber, plastics, composites, etc.), and different surface profiles (plain, grooved, and studded patterns). For accurate recording data, these field experiments were conducted usually for one whole day under average freight traffic and with varying speed for one single type of rail pad. Different internationally standardized experimental way of determining the dynamic stiffness of resilient material was developed later, which was broadly classified into direct and indirect methods [3]. Using numerical methods to solve track dynamics and vibrations accelerated with improved computer's efficiency and dedicated software's which were able to solve complex differential equations in minutes. Finite Element Method (FEM), Boundary Element Method (BEM), Infinite Element Method (IFEM), etc. are different techniques for simulating, based on the exact problem statement. Sometimes, a combination of this method is also used for simulating problems.

## 1.1 Basic Theories and Equations

Rail pad is known to be made up of viscoelastic material. Such materials exhibit properties of both elastic and viscous material upon deformation. Such material has damping that is highly frequency dependent and is typically characterized by Dynamic Mechanical Analysis [DMA]. In a perfectly elastic material, stress and strain occur in phase, whereas, in a perfectly viscous material, there is a phase difference of 90 degrees between stress and strain. A viscoelastic material's behaviour

is somewhere between that of purely elastic and purely viscous material and exhibits some phase lag of [0–90] degree, and mathematically it can be represented as Eqs. (1) and (2):

$$\varepsilon = \varepsilon_0 * \sin(\omega t) \quad (1)$$

$$\sigma = \sigma_0 * \sin(\omega t + \delta) \quad (2)$$

The stored energy, representing the elastic portion of the material, is represented as ‘Storage Modulus’ ( $E'$ ) which is defined and given by Eq. (3):

$$[E' = \frac{\sigma_0}{\varepsilon_0} * \cos\delta] \quad (3)$$

The energy dissipated as heat, representing the viscous portion of the material, is represented as ‘Loss Modulus’ ( $E''$ ) and given by Eq. (4):

$$[E'' = \frac{\sigma_0}{\varepsilon_0} * \sin\delta] \quad (4)$$

The overall ‘Dynamic Modulus’ ( $E^*$ ) shown in Eq. (5) is expressed as the ratio of stress to strain under vibratory conditions:

$$[E^* = E' + iE''] \quad (5)$$

Loss tangent ( $\tan\delta$ ), expressed as the ratio of storage modulus to loss modulus, gives the value of damping for such materials. For low levels of damping, the damping ratio ( $\zeta$ ) can be inferred as shown in Eq. (6):

$$(\zeta = \frac{\tan\delta}{2}) \quad (6)$$

Another mathematical way to describe the behaviour of viscoelastic materials is by the use of fractional calculus. A perfectly elastic material follows Hook’s law which is given by Eq. (7):

$$\sigma(t) = E * \varepsilon(t) \quad (7)$$

A perfectly viscous material follows Newton’s law of viscosity which is presented in Eq. (8):

$$\sigma(t) = \eta * \frac{d\varepsilon(t)}{dt} \quad (8)$$

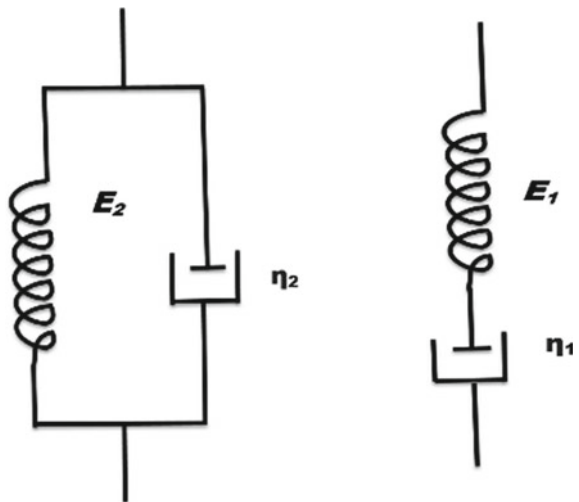
These equations are not universal law; they are just mathematical model that represents an ideal solid material. In real world, no material is perfectly elastic or

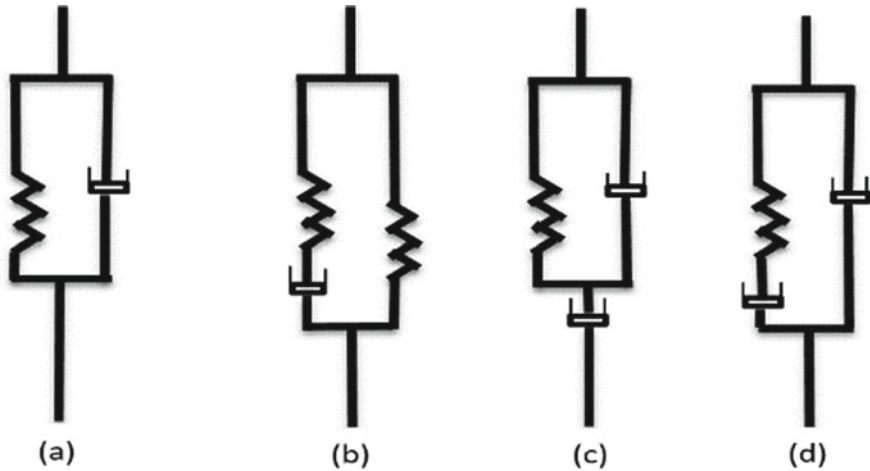
viscous. For a viscoelastic material, derivative of  $\epsilon(t)$  lies between 0 and 1 [ $\epsilon(t)$ :  $0 < (n) < 1$ ]. The driving law for a viscoelastic material is thus given in Eq. (9),

$$\sigma(t) = \eta^n \frac{d^n \epsilon(t)}{dt^n} \text{ where } (0 < n < 1) \tag{9}$$

This fundamental fractional derivative equation is known as ‘Scott Blair Element’ or ‘Abel Dashpot’. Fractional calculus usually works well for dielectrics and viscoelastic materials over the extended frequency range and time ranges. There are numerous different ways or rules to compute the fractional derivative, unlike the classical Newtonian derivatives. Other material models are also defined to aid in the numerical modelling of the rail pad. These material models are usually combined with fractional calculus to determine elastic stiffness and viscous coefficient of the track system. Some basic material models are ‘Kelvin-Voigt Model’ (spring and dampers are in parallel), ‘Maxwell material Model’ (spring and dampers are in series) and ‘Zener model’ (spring parallel to a damper and spring in series), as shown in Figs. 1 and 2. But these material models alone satisfy poorly to experimental data and fail to explain the actual behaviour of such materials [4, 5]. Some fractional derivative models that are frequently used for the theoretical study are ‘Fractional Derivative Kelvin-Voigt (FDKV)’, ‘Fractional Derivative Maxwell (FDM)’ and ‘5-Parameter Fractional Derivative (FDV)’ models. In the next section, all experimental techniques which were used to calculate complex stiffness and damping values of rail pad and how rail pad properties changes with temperature and frequency have been covered.

**Fig. 1** Kelvin-Voigt element, Maxwell element [6]





**Fig. 2** Representation of different Zener models **a** Spring in series with Voigt, **b** spring in parallel with Maxwell, **c** dashpot in series with Voigt, **d** dashpot in parallel with Maxwell [7]

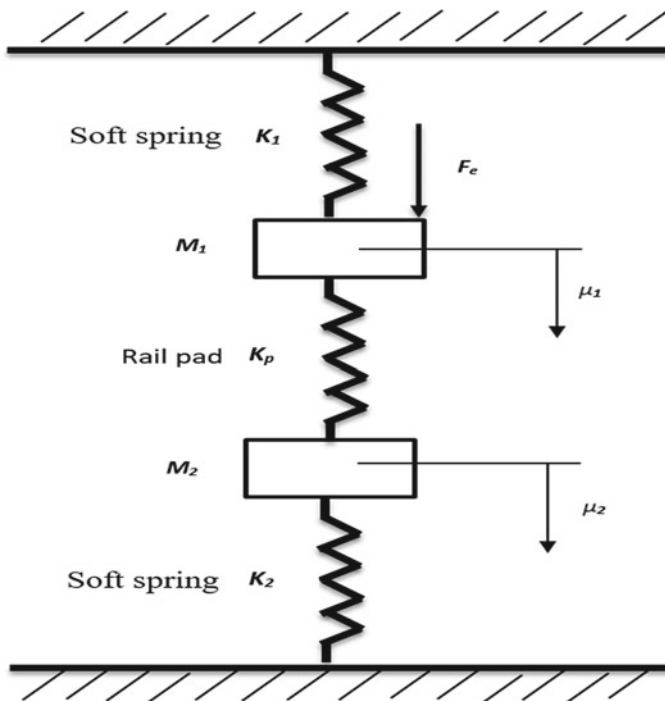
## 2 Different Experimental Techniques Used to Determine Rail Pad Properties

From the early 80 s, many researchers performed field and laboratory experiments to understand the dynamic properties of rail pad. One of them was **SL Grassie (1989)**, who performed two field experiments and some laboratory experiments to find out to what extent different rail pads attenuate the dynamic strain. The main concern at that time was to minimize the damage incurred to sleeper and rail joints. One field experiment was conducted at Coppull on B.R.’s West Coast Main Line (WCML) under regular traffic with speeds varying from 80 km/h to 160 km/h. 13 different rail pads with different material and surface shape were put into test. Another field experiment was conducted in Australia and New Zealand (ANZ). In this, rail with irregularities and joint defects was incorporated with four different rail pads. One of the earliest experimental apparatuses was developed by Battelle for measuring impact strains. The apparatus consisted of a short section of rail, rail pads and concrete sleeper. Dropping a tub from a height on the railhead, the test was performed. Using strain gauges, the rail pad’s attenuation was determined. The test was unable to yield any useful result. Some modifications to the setup also proved ineffective. It took several years to develop experimental apparatus that can apply static/harmonic loads with frequencies of interest (resonance frequencies) [2].

Fenander [8] determined the stiffness and damping of rail pads under different frequency and preload conditions. Field experiment was carried out on Sweden track, which consisted of UIC60 rails, rail pads, concrete sleepers and ballast. Both static loads and dynamic loads were applied by servo hydraulic cylinders placed on a

specifically designed railway wagon. A number of soft rail pads and stiffer (polymer-based rail pads) were used for the test, and pad compression was measured. Force versus displacement graphs were plotted for different rail pads. Although both field and laboratory experiment results should coincide, stiffness is calculated from field experiments which were higher than the stiffness calculated from laboratory experiments. Different reasons like inaccurate preload value from field measurements, different temperature conditions, different surface conditions between which rail pads are placed, etc. may cause this discrepancy. From both types of measurements, it was seen that stiffness of the rail pad increased with an increase in preload, but only increased slightly with frequency. For low preloads, loss factor was also seen growing with an increase in frequency for high frequency [8].

Thompson et al. [3] proposed an indirect method for measuring complex stiffness. It was a more reliable method than the direct method as it could measure stiffness at higher frequencies and for more degree of freedoms. Equivalent mass-spring system for the apparatus can be seen in Fig. 3. Direct method measured stiffness directly by using force transducer and displacement transducer. Common indirect methods like ‘T.U. Delft’, ‘TU Berlin’, ‘TNO’, etc., were used for measuring dynamic rail pad properties, but the direct method, despite its limitations, was a fast and efficient measuring method [3].



**Fig. 3** Equivalent mass-spring system of measurement apparatus (indirect method) [3]

Maes et al. [4] used direct method setup at Vrije Universiteit Brussel (VUB) to find dynamic stiffness and loss factor for different rail pads and compared it with a reference Ethylene–Vinyl Acetate (EVA) pad. The reason for considering EVA as a reference is that it is a highly elastic material with a very high stiffness value, and all other materials considered for rail pad are softer than this. It was observed from the experiment that the stiffer the rail pad, the lesser it is frequency dependent. Also, with increase in preload, dynamic stiffness increases, whereas the loss factor hardly changed with preload [4].

Remennikov et al. [10] studied ageing's effect on stiffness, damping and resonance frequency using the 'Instrumented Impact Hammer' technique. The apparatus was developed at the University of Wollongong. Vibration response was measured in a frequency range (0–1000) Hz using Bruel & Kjaer PULSE Vibration Analyser system. It was concluded that static stiffness degrades with increased ageing of the rail pad. The resonance frequency of worn pads was observed to be (5–15) % lower than new pads. Stiffness and damping also decreased with ageing. The experiment was performed with only three types of rail pads (two worn and one new) and thus was able to show the approximate relationship between rail pad properties and ageing [10].

Kaewunruen et al. [11] presented an alternative rail pad tester that can apply large preloads. It highlighted the importance of accounting effects of preload on dynamic properties of rail pad. The tester could apply a maximum preload of 400KN. The test setup consisted of a concrete block supporting steel mass, preloading bolt system and rail pad. Both new and worn 'HDPE 5.5 mm' and 'studded 6.5 mm' rail pads were used as a specimen. It was observed that at moderate preload values (<100KN), resonance frequencies change with preloading but with higher preloads, there was the negligible effect on resonant frequencies. From the load–deflection curve, stiffness decreases with a decrease in preload and with an increase in age of the pad. The results were compared with experimental data of 'Track Testing Centre (TTC)' and 'TU Delft (DUT)' [11].

'Dynamic mechanical analysis (DMA)' is a technique in which sinusoidal stress or strain is applied and it measures the corresponding displacement to find complex stiffness. This technique was significantly less complex than other rail pad test setups and considered the effect of preload, temperature and frequency on the specimen. The apparatus also be used to find the glass transition temperature. Not many researchers have worked on DMA. Qiao et al. [12] presented dynamic mechanical analysis using 'T.A. Instruments DMA 2980'. In the apparatus, the specimen was held fixed with both ends cantilevered and excited by a constant strain amplitude of 15  $\mu\text{m}$ . The experiment was performed with different temperature ranging from  $-80\text{C}$  to  $70\text{C}$  and frequency ranging from 1 to 20 Hz. Results obtained showed a similar trend as to how complex modulus and loss factor vary with temperature and frequency. The loss factor reached its maximum at glass transition temperature due to particle–particle contact interaction. Using this theory, glass transition temperature was also determined [12]. Using the same DMA technique, Oregui et al. [13] experimented on three rail pads (FC9, FC1530, Orange). The dynamic properties of rail pads were

determined using the time–temperature superposition (TTS) and William-Landel-Ferry (WLF) formula over a broad frequency range, temperature and preloads, and also a Prony series material model was proposed, which was in good agreement with experimental data [13].

Wei et al. [14] used a ‘Universal Testing Machine’ fitted with a control box that can regulate temperature ( $-70\text{C}$  to  $120\text{C}$ ) and is capable of exerting a maximum load of  $110\text{KN}$  with a maximum loading speed of  $80\text{KN/sec}$  ( $0.8\text{ Hz}$ ) [15]. The apparatus consisted of a section of rail, a loading steel plate, two supporting steel plates, some emery cloths and a rail pad, and for the experiment, a large-amplitude quasi-static load was simulated, and dynamic force–displacement curves were plotted at  $30\text{KN/sec}$  ( $0.3\text{ Hz}$ ) for three commonly used rail pads in the Chinese high-speed rail network and using the TTS technique and WLF formula the dynamic properties for higher frequency and under different temperature were predicted [15]. Results revealed that the complex stiffness of the rail pad is sensitive at low temperatures and increased frequency, and the complex stiffness increased as temperature decreased, with the loss factor peaking at glass transformation temperatures [15].

It has been observed that ‘Universal Testing Machine’ with temperature control box was emerged as latest technology. Next section covers various numerical method to study the properties of rail pad stiffness and damping at different running conditions.

### 3 Analytical/Numerical Techniques to Understand Rail Pad Properties and Their Effect on Track Vibrations

For the last few decades, various numerical techniques have been developed to study the material properties of rail pad. Bagley et al. [9] presented the fractional calculus approach for determining the macroscopic behaviour of viscoelastic material. Many researchers like A. Gemant, P.G. Nutting and M. Caputo, who worked in a similar domain, agreed that fractional calculus should be used to model viscoelastic behaviour. The stress and strain are related by Eq. (9). Mathematically, the model was represented as

$$\sigma(t) = E_0 \cdot \varepsilon(t) + E_1 \cdot D^\alpha[\varepsilon(t)] \quad (10)$$

Riemann and Liouville formula is generally used to define the fractional derivative portion of the equation ( $D^\alpha[\varepsilon(t)]$ ).

$$D^\alpha[\varepsilon(t)] = \frac{1}{\Gamma(1-\alpha)} \frac{d}{dt} \int_0^t \frac{\varepsilon(\tau)}{(t-\tau)^\alpha} d\tau, 0 < \alpha < 1 \quad (11)$$



To characterize the frequency-dependent properties of the material, Fourier transform was used, and by the least-square method, various parameters of the model were determined. The results were impressive and accurately predicted the frequency-dependent stress–strain relationship. The author also discussed molecular theories and how the concept of the fractional derivative relationship between stress and strain originated from these basic molecular theories [9].

Fenander [8] used the four-parameter fractional derivative model for rail pad. The model described the connection between tensile force  $F(t)$  to corresponding elongation  $x(t)$  as shown in Eq. (12)

$$F(t) + lD^\alpha F(t) = k_0x(t) + k_1D^\alpha x(t), 0 < \alpha < 1 \quad (12)$$

The above equation terms ‘ $\alpha$ ’, ‘ $k_0$ ’, ‘ $k_1$ ’ and ‘ $l$ ’ are the four unknown parameters that are determined by the help of experimental data. The fractional derivative operator [ $D^\alpha x(t)$ ] was described similar to Eq. (11). Expression for complex stiffness was derived by applying Fourier transformation. To solve the differential equation and determine the unknown parameters, the ‘Rosen Brock Optimization Algorithm’ was used. Measured stiffness from the fractional derivative model was accurate compared to available data [8].

Maes et al. [4] used a computational numerical programme to model a rail pad using the Poynting-Thompson material model (i.e. spring connected parallel to damper and spring connected in series). The material model has the power to separate the influence of frequency from the effects of preload [4] and this adapted material model was developed by Dynatrack [16]. The adapted Poynting-Thompson model was unable to accurately explain the damping behaviour of the rail pad and failed to satisfy experimental results. Up to 2000 Hz, the stiffness predicted was in good agreement with the measured result from the experiment, but after that the model was unable to predict stiffness increase above 2000 Hz [16].

Galvin et al. [17] developed a 3D model and solved it using numerical techniques to analyse train-induced vibrations. The focus of this work was to analyse how vibration of the track is affected by soil conditions and by discontinuous structures like underpass, bridge or buildings near the track. The model is numerically solved using Boundary Element Method (BEM) integrated with the Finite Element Method (FEM). By use of an iterative algorithm, coupling of both methods into a single model is carried out. The fastening system and rail pad are modelled as a viscous material damping element [17].

Koroma et al. [18] used a nonlinear Poynting-Thomson viscoelastic model involving three parameters to investigate the effects of preload and frequency. Rail was discretely assisted on rail pads in the model and was subjected to static and dynamic loads, also FEM and time integration scheme were used to solve it in the time domain and to determine static displacements and preloaded stiffness of rail pads, a Newton–Raphson iterative technique was used and this was followed by dynamic load analysis, in which the track was subjected to a load while travelling at a certain speed, the stiffness distribution, in this case, was dependent on the speed of

the load and it was observed that reaction force amplitude and dynamic amplification reduces, but dynamic stiffness increases with increase in preload [18].

Oregui et al. [19] developed a frequency-dependent model (Prony series) to study effect of rail pad on vertical track dynamics. The author also did sensitivity analysis to find out which variable has more influence on output and mainly focus on it. A three-dimensional finite element model with frequency-dependent rail pads was developed. It consisted of a long track with 24 NS90 sleepers, UIC54 rails, FC9 rail pads and clamps. A frictional contact ( $\mu = 0.75$ ) was defined between the rail and the upper surface of the rail pad. Preload was simulated by considering two springs per clip. The author also simulated hammer tests on the track by using 'LS-Dyna' software. The vertical track response was barely affected in high frequency range (2000–3000 Hz) but showed a significant difference in low frequency range (0–100 Hz). Rail pad properties changed with temperature, but the temperature had very less influence on the track's vertical response. Also, with decrease in preload, the rail resonance shifts to lower frequencies. The ageing of the rail pad also affects track response; more the rail pad is worn out, the more the rail resonance shifts to lower frequency because it loses its damping capacity with time [19].

Wei et al. [14] used Fractional Derivative Kelvin-Voigt (FDKV) to analyse frequency and temperature-dependent dynamic properties of rail pad theoretically. The FDKV model is represented similar to Eq. (10). The fractional derivative operator ( $D^\alpha$ ) was also defined by a similar Eq. (11), known as Riemann and Liouville formula. However, for a numerical solution for the FDKV model, the Grunwald–Letnikov formula is preferred over the Riemann–Liouville formula. The storage stiffness, loss stiffness and loss factor of rail pad in frequency domain were calculated by applying the Fourier transformation on FDKV model. The FDKV model was coupled with the Euler beam differential equation of rail to obtain a vertical train-track-coupled dynamic model. Numerical techniques solved the tedious calculation part, and vertical vibration against frequency was plotted. The author also compared the FDKV model to K.V. model and observed that vertical vibrations levels calculated with the FDKV model were higher than the model using KV model [14].

Khajehdezfuly [20] developed a 2-D model of vehicle sub-model and slab-track sub-model and connected them with nonlinear Hertz spring and solved the model analytically using Newmark-beta method and Newton–Raphson iterative scheme. An implicit approach was used to solve differential equations of motion for given time domain. The slab-track sub-model consisted of rail, rail pad, concrete sleeper, resilient layer, continuous concrete base and subgrade. Rail was modelled as Timoshenko beam element, which is a much accurate way of modelling rail, especially when large deflection is expected. Concrete sleeper, on the other hand, is modelled as Euler–Bernoulli beam, the rest of the slab-track components are modelled as a spring-dashpot element. The vehicle sub-model, simulated as a multi-body system and suspension, was modelled as a spring-dashpot element. Rail irregularity of wavelength 0.25, 0.5, 1 and 4 m with different amplitude was also included in the model. The term 'Dynamic Impact Factor(DIF)' was defined to understand the severity of the wheel/rail contact force and wheel jumping phenomenon. From results, it was observed that, in general, with an increase in stiffness of the rail pad, the rail/wheel

force (DIF) increases. With the increase in velocity, DIF increases up to critical velocity and then decreases. Low-amplitude irregularity didn't have any significant effect on rail/wheel force, but the high amplitude irregularity does have, depending upon the wavelength of irregularity [20].

Ping Wang et al. [21] studied the impact of rail pad's frequency and temperature-dependent properties on rail's vibrations and rolling noise. The fractional derivative Zener (FDZ) model was considered for modelling the rail pad. The unknown parameters of the FDZ model were approximated from experimental results. Full track model with Vossloh 300 rail pad, ballast less track and rail (as Timoshenko beam) was made. Using a combination of the semi-implicit Euler method (Symplectic method) and spectral element method, in short known as SEM-SM method, vertical rail receptance and decay rate were calculated. Basic modal analysis was also carried out by the author. It was observed that the inclusion of frequency- and temperature-dependent stiffness and damping had a significant impact on track dynamic characteristics below 500 Hz and  $-20^{\circ}\text{C}$ . The first-order bending resonance was also affected by this, whereas pinned-pinned resonance hardly changed. The rail's LF high attenuation frequency band widened, and the decay rate appeared to increase with the inclusion. The author finally concluded that at low temperatures (below  $-20^{\circ}\text{C}$ ), the rail decay rate increases sharply in the entire frequency domain and it becomes important to take in consideration the temperature-dependent and frequency-dependent properties of rail pad (especially trains working in cold regions) while modelling [21].

Kedia et al. [22] Using a track interaction model of train, this paper was focussed on investigating the effects of irregularities in rail-rail pad, which may produce noises and track vibrations and for this the ballast-track structure was modelled as an infinite rail, rested on a viscoelastic foundation, and an Indian vehicle rail was modelled which acted as an analogous spring mass damper system [22]. The data for the long wavelength track irregularity was developed using the Sato-track spectrum, and the data for the short-wavelength track irregularity was collected from the field, and it was found that shorter wavelength vibrations and noise levels were found to be greater than long wavelength vibrations and noise levels, with magnitudes beyond the limitations set by Indian Railways standards, also the track properties were changed to address this problem, and it was discovered that stiffer pads decreased vibration levels in the range of 6 dB–23 dB and the noise level in the range of 7dBA–15dBA, which lead the author to recommend stiffer pads for the ballast-track structure [22].

Ulu et al. proposed unnecessary movements on the railroad structure and inside the vehicle are caused by a rapid shift in superstructure stiffness of railway lines, such as transfer areas, during crossings at the beginning and finishing points of tunnels, bridges or railway switches. To reduce the dynamic effects of transition zones on railway vehicles, the author studied four separate scenarios, as shown in the Table 1, which were created to illustrate the controllers' success and stability. As the success of the control algorithms was compared to the Integral Square Error (ISE) efficiency indices and Power Spectral Density (PSD) in both time and frequency domains, it was discovered that the superstructure transition zone effects were nearly eliminated by both controllers, and the rail irregularity effects were much more powerful than transitional effects for displacement. In contrast to the unloaded situation, the transfer

**Table 1** Situations of created scenarios

Situation of scenarios	1	2	3	4
Transition zone	Exist	Exist	Exist	Exist
Load condition of rail vehicle	Unloaded	Unloaded	Fully- loaded	Fully- loaded
Rail irregularity	Absent	Exist	Absent	Exist
Longitudinal velocity of rail vehicle	50 km/h	50 km/h	80 km/h	80 km/h

results improved by almost two times in a fully loaded scenario, but control achievements remained constant as the same control gains were used, while control forces increased by two times. The vibrations in the fully loaded scenario under the effects of rail superstructure change and rail irregularity at high speed was not substantially different from the irregularity-existing unloaded rail scenario, indicating that the track irregularity was the most dominant influence in terms of vibration. Aside from transfer zones, certain track problems such as swing rail pads, pumped ballast and rail deformations often cause passenger discomfort and can result in increased service, maintenance costs and, most importantly, derailment risks [23].

## 4 Conclusion

This paper tried to cover most of the methods and techniques used to understand the dynamic properties of rail pads. It also covered a brief history of rail pads and why there was a need to study them and an approach has been made to understand the behaviour of rail pad and their effects on track vibration. In this paper, author tried to chronologically illustrate the developments that took overtime from the 1980s to the present day. The paper also extensively discussed how dynamic properties of rail pad vary with frequency, temperature, preload and ageing. In recent years, the focus has slightly been shifted. Researchers are working more on the interrelationship between rail pad, wheel and rail irregularities and combined effect of these two on wheel jumping phenomenon and track vibrations. Though a limited literature has been found which focussed on the behaviour of rail pad with the irregularities.

## References

1. Kouroussis G, Connolly DP, Verlinden O (2014) Railway-induced ground vibrations—a review of vehicle effects. *Int J Rail Transp* 2(2):69–110
2. Grassie SL (1989) Resilient railpads: their dynamic behaviour in the laboratory and on track. *Proc Inst Mech Eng Part F J Rail Rapid Transit* 203(1):25–32
3. Thompson DJ, van Vliet WJ, Verheij JW (1998) Developments of the indirect method for measuring the high frequency dynamic stiffness of resilient elements. *J Sound Vib* 213(1):169–188

4. Maes J, Sol H, Guillaume P (2006) Measurements of the dynamic railpad properties. *J Sound Vib* 293(3–5):557–565
5. Eldred LB, Baker WP, Palazotto AN (1995) Kelvin-Voigt versus fractional derivative model as constitutive relations for viscoelastic materials. *AIAA J* 33(3):547–550
6. Greco R, Marano GC (2015) Identification of parameters of Maxwell and Kelvin–Voigt generalized models for fluid viscous dampers. *Journal of Vibration and Control*, 21(2):260–274. <https://doi.org/10.1177/1077546313487937>
7. Dai Z, Peng Y, Mansy HA, Sandler RH, Royston TJ (2015) A model of lung parenchyma stress relaxation using fractional viscoelasticity. *Medical Engineering and Physics*, 37(8)
8. Fenander Å (1997) Frequency dependent stiffness and damping of railpads. *Proc Inst Mech Eng Part F J Rail Rapid Transit* 211(1):51–62
9. Bagley RL, Torvik PJ (1983) A theoretical basis for the application of fractional calculus to viscoelasticity. *J Rheol* 27(3):201–210
10. Remennikov A., Kaewunruen S., Ikaunieks K (2006) Deterioration of dynamic rail pad characteristics. In: *Conference on Railway Engineering*, Melbourne. pp 174–179
11. Kaewunruen S, Remennikov AM (2007) An alternative rail pad tester for measuring dynamic properties of rail pads under large preloads. *Exp Mech* 48(1):55–64
12. Qiao J, Amirkhizi AV, Schaaf K, Nemat-Nasser S (2010) Dynamic mechanical analysis of fly ash filled polyurea elastomer. *J Eng Mater Technol* 133(1)
13. Oregui M, de Man A, Woldekidan MF, Li Z, Dollevoet R (2016) Obtaining railpad properties via dynamic mechanical analysis. *J Sound Vib* 363:460–472
14. Wei K, Wang F, Wang P, Liu Z, Zhang P (2016) Effect of temperature- and frequency-dependent dynamic properties of rail pads on high-speed vehicle–track coupled vibrations. *Veh Syst Dyn* 55(3):351–370
15. Wei K, Yang Q, Dou Y, Wang F, Wang P (2017) Experimental investigation into temperature- and frequency-dependent dynamic properties of high-speed rail pads. *Constr Build Mater* 151:848–858
16. de Man (2002) A survey of dynamic railway track properties and their quality, Delft, TU Delft
17. Galvín P, Domínguez J (2009) Experimental and numerical analyses of vibrations induced by high-speed trains on the Córdoba–Málaga line. *Soil Dyn Earthq Eng* 29(4):641–657
18. Koroma SG, Hussein MF, Owen JS (2015) Influence of preload and nonlinearity of railpads on vibration of railway tracks under stationary and moving harmonic loads. *J Low Frequency Noise Vibr Act Control* 34(3):289–306. <https://doi.org/10.1260/0263-0923.34.3.289>
19. Oregui M, Núñez A, Dollevoet R, Li Z (2017) Sensitivity analysis of railpad parameters on vertical railway track dynamics. *J Eng Mech* 143(5):04017011. [https://doi.org/10.1061/\(ascem\).1943-7889.0001207](https://doi.org/10.1061/(ascem).1943-7889.0001207)
20. Khajehdezfuly A (2019) Effect of rail pad stiffness on the wheel/rail force intensity in a railway slab track with short-wave irregularity. *Proc Inst Mech Eng Part F J Rail Rapid Transit* 233(10):1038–1049
21. Ping W, Yinling D, Shaohua W, Feng W, Wei K (2020) Influence of the temperature- and frequency-dependent dynamic properties of rail pads on the vibration characteristics of rails at low temperature. *Proc Inst Mech Eng Part F J Rail Rapid Transit* 095440972091376. <https://doi.org/10.1177/0954409720913767>
22. Kedia NK, Kumar A, Singh Y (2021) Effect of rail irregularities and rail pad on track vibration and noise. *KSCE J Civ Eng* 25(4):1341–1352
23. Ulu A, Metin M (2020) Control of railway vehicle vibrations due to the effect of different superstructure stiffness in transition zones with rail irregularities. *Pamukkale Univ J Eng Sci* 26(4):709–719
24. Ashter SA (2014) *Thermoforming of single and multilayer laminates*. William Andrew publications
25. Zhai W, Wei K, Song X, Shao M (2015) Experimental investigation into ground vibrations induced by very high speed trains on a non-ballasted track. *Soil Dyn Earthq Eng* 72:24–36
26. Wei K, Wang P, Yang F, Xiao J (2014) The effect of the frequency-dependent stiffness of rail pad on the environment vibrations induced by subway train running in tunnel. *Proc Inst Mech Eng Part F J Rail Rapid Transit* 230(3):697–708

27. He Z, Zhu Z, Wu N, Wang Z, Cheng S (2016) Study on time-dependent behaviour of granite and the creep model based on fractional derivative approach considering temperature. *Math Probl Eng* 2016:1–10
28. Ge X, Ling L, Yuan X, Wang K (2020) Effect of distributed support of rail pad on vertical vehicle-track interactions. *Constr Building Mater* 262:120607
29. Wu TX, Thompson DJ (2001) Vibration analysis of railway track with multiple wheels on the rail. *J Sound Vib* 239(1):69–97
30. Kaewunruen S, Remennikov A (2008) Dynamic properties of railway track and its components: a state-of-the-art review, part of the acoustics, dynamics, and controls commons, civil engineering commons, structural engineering commons, and the structural materials commons
31. Lei X, Zhang B (2011) Analysis of dynamic behaviour for slab track of high-speed railway based on vehicle and track elements. *J Transp Eng* 137(4):227–240
32. Heunis JJ (2011) Material models for rail pads, (Thesis). Prof J.L. van Niekerk, University of Stellenbosch, Supervisor
33. Liu Y, Luo Y, Yin HP (2014) Numerical analysis of nonlinear properties of rail fastening systems
34. Sarawade SS, Agarwal SK, Gawarshettiwar PN, Patil SA, Yeole AR, Jain SA (2019) Determination of non-linearity in rail pad. *IOSR J Eng (IOSR JEN)* 11–17

# Design Analysis of an Electric Go-Kart



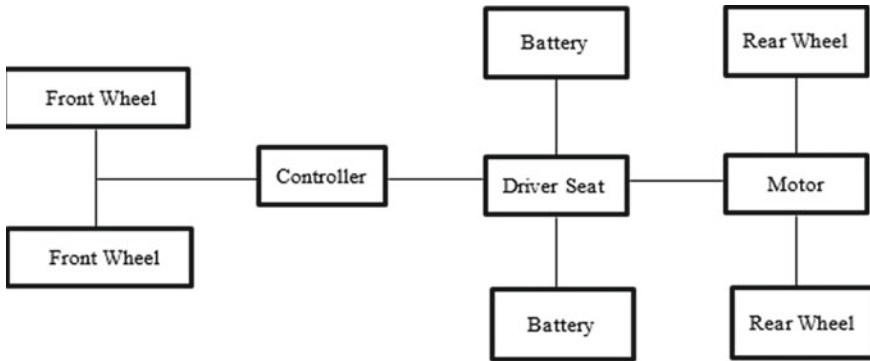
Sunny Bhatia, Anshul Gautam, Antash Dhiman, Farhan Mukhtar,  
and Priyansh Sharma

## 1 Introduction

Electric vehicle technology has been around since the late 1800s [10]. The electric-powered Go-Kart is a four-wheeled conveyance that is compact in design, facile to run, and light in weight. The Go-Karts are small and open four-wheel vehicles [7]. The Go-Kart is a vehicle that is simple, lightweight, and compact, and easy to operate [9]. It is particularly utilized for racing purpose on a flat track [1]. Go-Kart is a diminutive four-wheeled conveyance with no suspension and differential. It is mild-powered conveyance which is normally applied for racing purpose. The basic difference between an electric Go-Kart and a conventional kart is that the environment is polluted by the conventional kart because these karts run by petrol engines, so there is an important need to find the alternatives and an electric Go-Kart is one of the best possible alternatives. Owing to the go-green concept [7], this paper endeavors to offer an observation into the strategy and production measures this is obligatory while engineering large acquirement electrical power train [2]. So, verbalizing its floor clearance is far very low which is why it cannot run on hard roads. The chassis is impartial of suspension to experience the thrill. Electric Go-Kart is a low maintenance conveyance. We make use of the lead-acid battery in place of a lithium-ion battery. Electric Go-Kart is more secure when there may be any collision or contingency transpire because there are no gasoline tanks in it and lead-acid battery is safer than lithium-ion battery because lithium can still catch fire on exploding if several damaged is transpire in contingency or collision after utilizing lead-acid battery we will surmount but there is moreover major downside of it. That the lead-acid battery life may be very short. Because of this, a greater path of work is to be devised and increases a more secure and useful conveyance predicted primarily based on a torsion loss and inflexible body. Although plenty of

---

S. Bhatia · A. Gautam · A. Dhiman · F. Mukhtar (✉) · P. Sharma  
Manav Rachna International Institute of Research and Studies, Faridabad, Haryana, India



**Fig. 1** Basic layout of electric Go-Kart

paintings have been maintained on the Electric Go-Kart, a systematic observation on imposing the contemporary technology in the Go-Kart is required to be done. The chassis is designed in such a way that it requires fewer materials and the ability to withstand loads applied on it [9]. This work offers to grow a retrofit Go-Kart with reduced weight by way of selecting a suitable material for the chassis. The design stage is very crucial because of various dynamic problems. So the proper analysis should be done because of safety purposes [7]. These chassis have been modeled and analyzed using a software program like BLENDER and FUSION 360.

## 2 Design Section with Layout

An electric Go-Kart is powered by electric motors and batteries, as opposing to a classic petrol engine. The drivetrain consists of the motor, transmission, and any drive wheels. Drivetrain components need to be mounted robustly and operate efficiently to be safe and effective [8]. It is cheaper and its running cost is very low than the conventional IC engine. Electric Go-Karts required low maintenance, they require only lead-acid batteries of the Go-Karts to be plugged into an array of chargers after each run and they are free of impurities and do not emit smoke. Electric Go-Karts do not have fuel tanks or other combustible materials that could be safe in the event of an accident. The basic layout of electric Go-Kart is shown in Fig. 1.

## 3 Basic Components of Electric Go-Kart

There are three main components of electric Go-Kart by which the electric Go-Kart is run which are.



1. Motor.
2. Controller.
3. Battery.

### ***3.1 Motor***

It is an electrical device that converts electrical energy into mechanical power. Most electric automobiles manipulate through the reciprocal action among the magnetic field and electric current in a twine winding to create force in the form of power applied on the controller. So, we use a BLDC (brushless direct current) motor which is of 48 V and 1000 watts so it can withstand with driver weight and material weight.

### ***3.2 Controller***

A controller is a corresponding contrivance that seizes an input sign from a quantified transform variable, examines this price with that of a deliberate manage point price (set point), and whole congruous significance of the output signal demanded through the final manipulate issues to offer to heal action within a manipulate loop. An electronic controller uses electrical signals and an analog end to obtain its amenable, correlative, and corrective functions, an electric sensor (thermocouple, RTD, or transmitter) established at the quantified position continuously sends an input signal to the controller. So we use a 48-V and 1000-W controller to control the current and speed of a motor. The main motive and the purpose of a controller is to control and regulate the speed and the current of the motor, but in this electric Go-Kart we have used a separate controller for this purpose.

### ***3.3 Battery***

A battery is a device that stores chemical energy and coverts it into the electrical energy. We use four lead-acid batteries of 12 V and 24 Ah (ampere-hour) because it is cheap and reliable. It is found to run the electric-powered motor by way of giving it electrical power. The purpose of using these type of batteries is that the material is easily available in the market, the material is not expensive and can be easily transported.

The specifications of electric Go-Kart components, weight and load distribution are tabulated in Tables 1 and 2.

**Table 1** Specification of components

Components	Volt	Watt	Ampere
Motor	48 V	1000 W	–
Controller	48 V	1000 W	–
Battery	12 V (4-Pack)	–	32 AH

**Table 2** Components weight and weight and load distribution

Components	Weight (Kg)	Load (N)
Motor	28	274.8
Controller	7.9	77.4
Battery	0.6	5
Driver	70	686.7

**Table 3** Material requirement for electric Go-Kart

Components	Material	Safety factor
Body 1	Iron, Gray Cast ASTM A48 Grade 35	Yield strength
Body 2	Iron, Gray Cast ASTM A48 Grade 35	Yield strength

## 4 Materials and Methodology

The actual graft started from the assortment and examination of the material after considering all the aspects regarding the designing of the Go- Kart and simulation has been done on Fusion360 and based on the literature work and the results attained the design was completed. Go-Kart wants to be mild for correct dealing with material and manages the chassis or body is what needs to be mild and stiff. The high-grade content plays very important role to determine the hardness, strength, machining, and weld ability characteristics. Material selection for chassis plays a vital role in building up entire vehicle in providing reliability, safety, and endurance [9]. The material requirement for an electric Go-Kart is tabulated in Table 3.

## 5 Design

The basic considerations to be considered while designing an electric Go-Kart include strength and lightweight. The selection of material is very important. The materials selected are iron, Gray Cast ASTM A48 Grade 35. It is one of the proper materials for kart chassis and is used because it possesses high tensile strength and is light in weight [12]. The chassis is designed in such a way that it includes factors like density, elasticity, elongation, the strength-to-weight ratio, thermal expansion, and

**Table 4** Specifications of iron, Gray Cast ASTM A48 Grade 35

Specifications	Values
Density	7.395E-06 kg/mm <sup>3</sup>
Young's modulus	109,626 MPa
Poisson's ratio	0.244
Yield strength	251.7 MPa
Ultimate tensile strength	334 MPa
Thermal conductivity	0.04804 W/(mm C)
Thermal expansion coefficient	1.206E-05/C
Specific heat	450 J/(kg C)

yield stress. The specifications of iron, Gray Cast ASTM A48 Grade 35 are tabulated in Table 4.

### 5.1 CAD Design of Go-Kart Chassis

The Go-Kart chassis material is considered depending upon the various factors such as stress during impact, strain during impact, and displacement. After understanding the parameters, the design is given to the Go-Kart with the help of the software used. The chassis of Go-Kart is a skeleton frame made up of hollow pipes and other materials of different cross sections. The chassis of Go-Kart must be stable with high torsional rigidity, as well as it should have relatively high degree of flexibility as there is no suspension. So that it can give enough strength to withstand with grub load as well as with other accessories [9]. The chassis is designed in such a way that it should ride safe and the load that applies does not change the structural strength of the chassis [9]. The design of the chassis of Go-Kart is designed in CAD software with the help of the different types of load conditions, constraints, and induced von Mises stress and strain is calculated for which Fusion 360 software is used [6]. The gravity makes an important role in this modeling, so we take the weight of a driver on an average 70 kg and take different component weights and convert thermo to Newton and then applied on the Go-Kart chassis.

### 5.2 Top View of Chassis

The chassis top view is shown in Figs. 2 and 3.

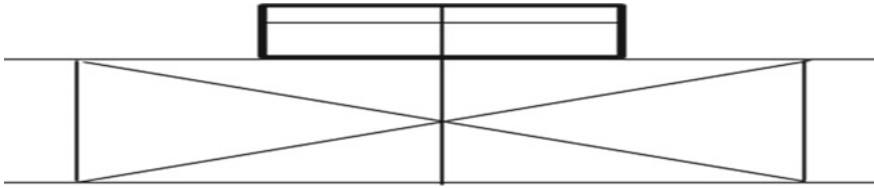


Fig. 2 Chassis top view

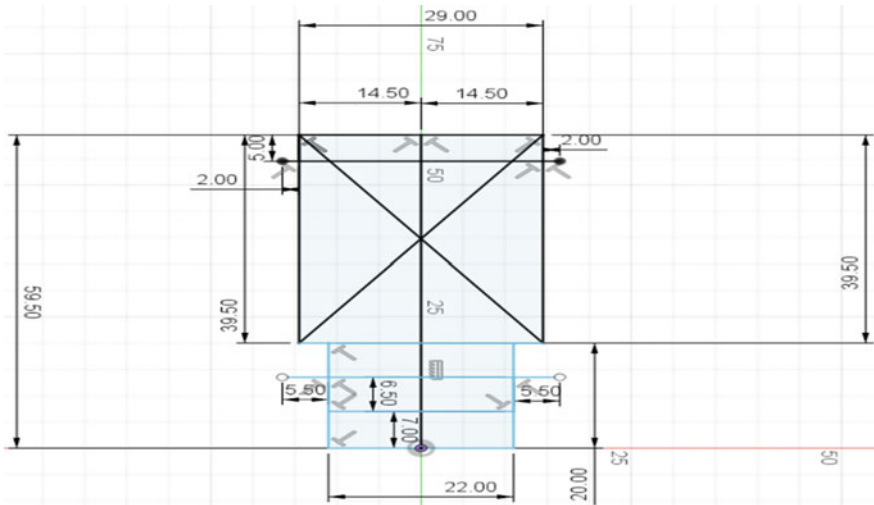


Fig. 3 Chassis top view

### 5.3 Chassis Dimension

This is the basic size of the chassis design. So, the Go-Kart chassis should be balanced with immense torsional strength and should have a high degree of flexibility as there is no suspension in it. The iron gray cast is more economic and durable but it is slightly heavier in weight. So we calculate stress, strain, and displacement on material by applying different constraints, loads, and von Misses. The stress, strain, and displacement are shown in Figs. 4, 5 and 6.

### 5.4 Stress During Impact

See Fig. 4.



Fig. 4 Stress

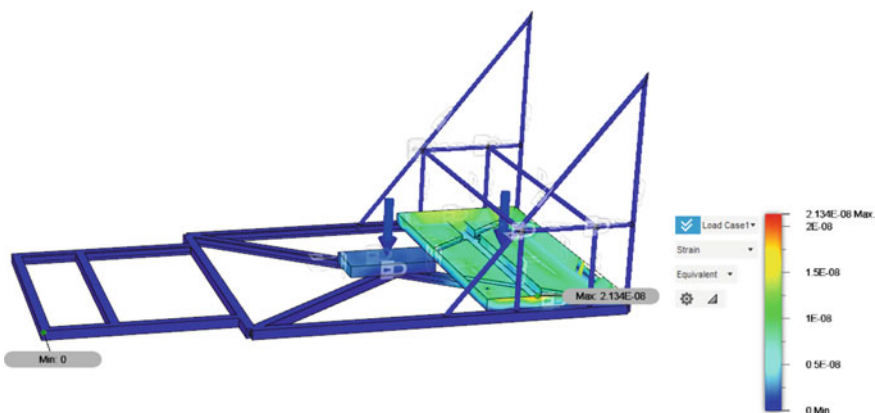


Fig. 5 Strain

### 5.5 Strain During Impact

See Fig. 5.

### 5.6 Displacement

See Fig. 6.

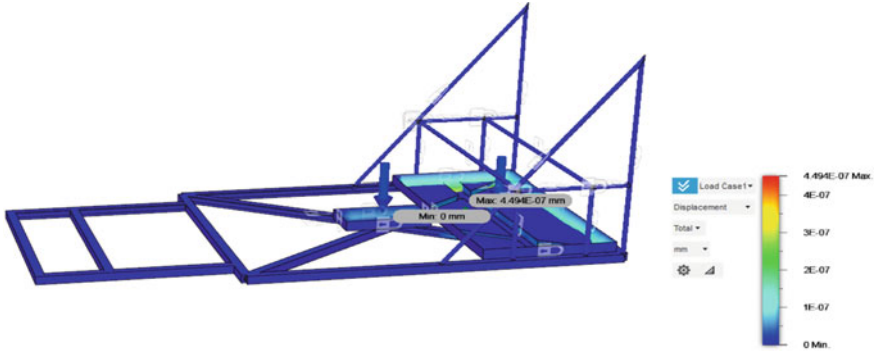


Fig. 6 Displacement

Fig. 7 Electric Go-Kart front view



### 5.7 3D Modeling of Go-Kart

In designing a Go-Kart, the 3D modeling of the Go-Kart frame can be done using any 3D CAD software, but we use a blender for this. While designing a vehicle like a Go-Kart one of the important steps is 3D modeling. 3D modeling Go-Kart frame allows us to make all possible iterations on the vehicle in the virtual world. By making all possible modifications before passing to fabrications, mistakes and wastage of materials can be reduced.

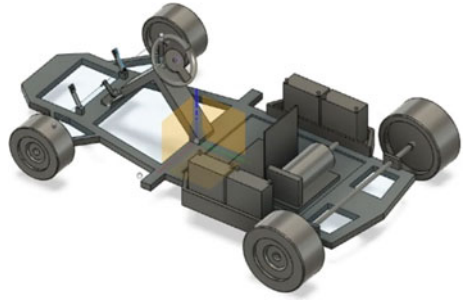
#### 5.7.1 Front View

The front view of electric Go-Kart is shown in Fig. 7.

#### 5.7.2 Back View

The back view of electric Go-Kart is shown in Fig. 8.

**Fig. 8** Electric Go-Kart  
back view



## 6 Result and Discussion

The result clearly shows the slight difference of stress and strain in Iron, Gray Cast ASTM A48 Grade 35 because of the material weight and its physical properties and is tabulated in Table 5. The material is light in weight; it is cheaper and more durable. So, we choose this material to construct an electric Go-Kart. The material selected for the chassis building withholds strength and more durability.

## 7 Conclusion

The electric Go-Kart was finally evaluated and concluded and by considering all the possible factors while designing and analyzing it was found that Iron Gray Cast ASTM A48 Grade 35 material is more economic and durable for designing a Go-Kart. The priority in this paper was to build a Go-Kart with least cost without negotiating the safety and performance of the vehicle. The final result is a desired Go-Kart design meeting all the above factors above in this paper. The design of chassis for Go-Kart can broaden many skills. By use of modeling software like fusion 360 or blender are vital to obtaining our choice design. By using this software, we design a 3D model of a Go-Kart and analyzes the stress and strain when different types of the load are acting on it. Designing of electric Go-Kart chassis was made on this paper which offers a brief conception approximately how electric power kart may be made for commercial and research purposes. Designing of electric Go-Kart is facile, affordable, and effectively authorized of next technology as a source of clean and sustainable electricity.

**Table 5** Results

Name	Minimum	Maximum
Safety factor		
Safety factor (per body)	15	15
Stress		
von Mises	0 MPa	0.001415 MPa
First principle	-5.955E-04 MPa	9.518E-04 MPa
Third principle	-0.001894 MPa	7.153E-05 MPa
Normal XX	-6.889E-04 MPa	3.915E-04 MPa
Normal YY	-6.657E-04 MPa	3.145E-04 MPa
Normal ZZ	-0.00188 MPa	1.544E-04 MPa
Shear XY	-1.512E-04 MPa	1.97E-04 MPa
Shear YZ	-4.779E-04 MPa	6.704E-04 MPa
Shear ZX	-5.42E-04 MPa	8.127E-04 MPa
Displacement		
Total	0 mm	4.494E-07 mm
X	-4.076E-08 mm	4.29E-08 mm
Y	-4.894E-08 mm	5.107E-08 mm
Z	-4.485E-07 mm	4.698E-09 mm
Reaction force		
Total	0 N	4.636 N
X	-0.4584 N	0.4423 N
Y	-0.5612 N	0.5669 N
Z	-1.768 N	4.634 N
Strain		
Equivalent	0	2.134E-08
First principle	-2.325E-10	1.926E-08
Third principle	-1.768E-08	0
Normal XX	-4.499E-09	3.359E-09
Normal YY	-2.085E-09	2.03E-09
Normal ZZ	-1.478E-08	1.375E-09
Shear XY	-3.432E-09	4.471E-09
Shear YZ	-1.085E-08	1.521E-08
Shear ZX	-1.23E-08	1.844E-08
Contact pressure		
Total	0 MPa	1.885E-04 MPa
X	-2.358E-05 MPa	1.73E-05 MPa
Y	-3.693E-05 MPa	4.715E-05 MPa
Z	-1.238E-04 MPa	1.884E-04 MPa



## References

1. Hajare K, Shet Y, Khot A (2016) A review paper on design & analysis of a go-kart chassis. 2349–4476
2. Burrige M, Alahakoon S (2017) The design and construction of a battery electric vehicle propulsion system-high performance electric kart application. *Earth Environ Sci* 73. <https://doi.org/10.1088/1755-1315/73/1/012016>
3. Johnson J, Kola Y (2017) Design, modeling and developing of a go kart vehicle. <https://doi.org/10.1109/amiams.2017.8069197>
4. Saheb SH, Reddy G, Hameed M (2016) Design report of a go kart vehicle. *IJEAST* 2455–2143
5. Singh H, Sagar P, Singh K (2016) Development of electric go-kart, “Development of Electric Kart,” SAE Technical Paper, 2016–28–0149. <https://doi.org/10.4271/2016-28-0149>
6. Saini NK, Rana R, Hassan MN, Goswami K (2019) Design and impact analysis of Go-kart chassis. *Int J Appl Eng Res* 0973–4562
7. Manish KK (2017) Design failure modes and effects analysis of an electric kart. Bachelor in Technology, Department Of Mechanical Engineering, College Of Engineering and Technology, Odisha, eISSN: 2319–1163. pISSN: 2321–7308
8. Davis EM (2012) Design and performance evaluation of an electric Go-Kart and custom permanent magnet brushless DC.
9. Raghunandan D, Pandiyan A, Majeed S (2016) Design and analysis of go-kart chassis. *IJESRT* 5(11) ISSN: 2277–9655. CODEN: IJESS7
10. Abhijeet Pareek B, Boobesh S (2019) Design and implementation of electric go kart veicleIndia. *IJARIII* 5(2) ISSN(O)-2395–4396
11. Lal K, Abhishek OS (2017) Design, analysis and fabrication of GO-KART. *Int J Sci Eng Res* 429–434
12. Sahu A, Panda MR, Ranjan S, Khara M, Senapati SR, Parida S, Rao B (2020) Design and analysis of electric Go-Kart chassis. *J Xi’an Univ Architect Technol* 4739–4745
13. Kanherkar KL (2017) Design and analysis of a GO-KART. *J Mater Sci Mech Eng (JMSME)* 198–201

# Identification and Ranking of Supply Chain Risks Using Fuzzy TOPSIS: A Case Study of Indian Automotive Manufacturing



Vinod G. Surange  and Sanjay U. Bokade 

## 1 Introduction

The automotive supply chain is a complex network of multiple associated agents. The globalization trend and dependencies of numerous activities involved in an integrated process of planning, sourcing, manufacturing, delivering and returning makes entire SC susceptible to multiple risks with adverse impact [1, 2, 3]. The internal supply chain encompasses activities involved within an enterprise like purchase, process, make, warehousing and sell, while the external supply chain includes all the agents involved in transforming raw material to finished products which are received by customers [4]. Figure 1 shows internal and external SC along with the flow of information, money and logistics across SC.

This research aims to identify risks predominant to the automotive supply chain and rank them according to their adverse impact severity on five different criteria (C) using the Technique for Ordered Preference and Similarity to Ideal Solution (TOPSIS) under fuzzy environment (FTOPSIS) [6, 7]. Authors [8] introduced the theory of fuzzy sets. It is helpful under an uncertain environment for effective decision-making [9, 10, 11]. Financial Aspects, Operations/Activities, Brand/Reputation, Schedule/Timeline, Product Quality and Reliability are the five criteria for this study.

---

V. G. Surange (✉)

Research Scholar, Department of Mechanical Engineering, Rajiv Gandhi Institute of Technology, Mumbai, Maharashtra, India

Assistant Professor, Department of Mechanical Engineering, St. John College of Engineering and Management, Palghar, Maharashtra, India

S. U. Bokade

Rajiv Gandhi Institute of Technology, Mumbai, Maharashtra, India

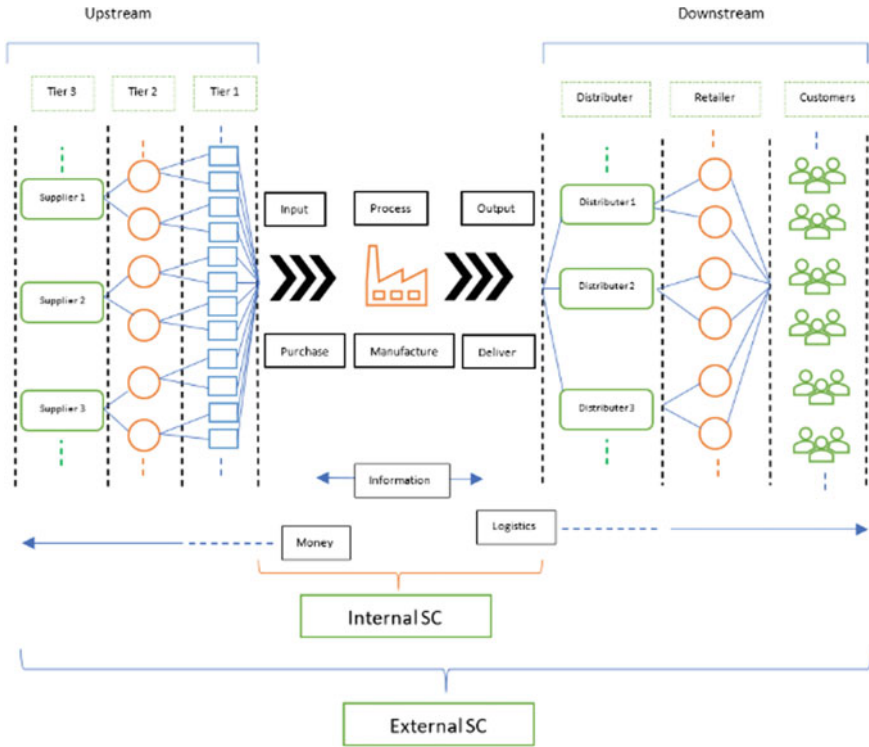


Fig. 1 Supply chain network [5]

## 2 Risk Factors Identified Through Literature Review

Table 1 enlisted the risk factors identified from the literature and confirmed after discussion with automotive manufacturing industry experts.

## 3 Industry Input

Table 2 presents industry experts' profile for obtaining a linguistic assessment of the importance of criteria selected for study and the impact severity of each risk factor on criteria.

**Table 1** Critical risk factors to automotive supply chain

Code	Risk factor	Description	Reference
R1	Natural disasters	External unforeseeable environmental risks such as flood, drought, tsunami, earthquake, hurricane, disease outbreak	[4, 12, 13]
R2	Manmade disasters	Blunders, system failure with the intent of human, strikes, political unrest	[4, 12]
R3	Risks related to ICT	Cyber-attacks, virus intrusion, failure of IT systems, vulnerability due to complex network, data alteration/loss	[4, 12]
R4	Risks related to competition/competitive risks	Merger and acquisitions of significant brands, strategies of competitors	[14–17]
R5	Risks related to raw materials	Scarcity of raw material, inferior quality of raw material, price fluctuations	[4, 12, 18, 19]
R6	Risks related to suppliers	Transactional relationship, poor process quality, improper supplier selection process, the bankruptcy of supplier, an inadequate response	[4, 12, 18, 20–23]
R7	Risks due to delays	Complicated processes in obtaining clearance from regulatory bodies, strikes, delay because of suppliers' internal issues, delay due to critical part/process failure	[4, 12]
R8	Market demand risks	Error in the forecast, market uncertainty, Bullwhip effect	[4, 12, 18, 24]
R9	Economic risks	Tax laws changes, exchange rate variations, issues related to payment processing, untimely/less than market standard payment to employees	[18, 20, 22, 25–28]
R10	Risks related to management	Lack of top management commitment, strategic and tactical imbalance, inability to resolve conflicts, delay in decision-making, lack of transparency	[4, 29, 28, 30–36]

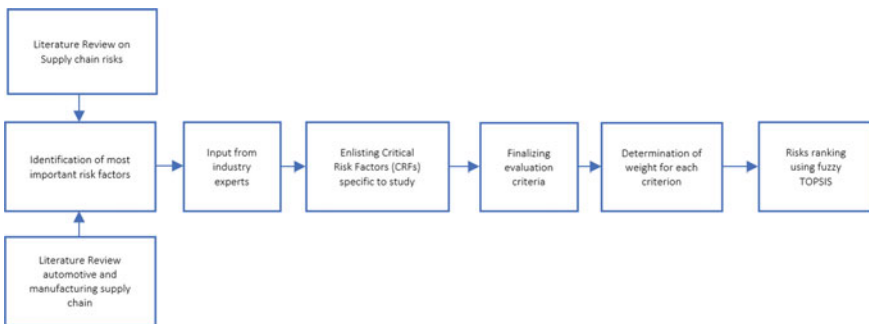
(continued)

**Table 1** (continued)

Code	Risk factor	Description	Reference
R11	Risks related to tools and techniques	Inability to adopt new technology, adhering to the traditional approach, no encouragement for advanced tools adoption	[4, 26, 37]
R12	Risks related to employees	Incompetence, low skill sets, no training, poor attitude	[4, 18, 34, 37, 38]
R13	Risks related to the impact of product/processes on the environment	Pollution, waste creation, no concern about the environment	[19]

**Table 2** Industry experts profile

Industry expert (IE) no	Designation	Total experience in years	Industry type
1	Design Engineer	5	Automobile
2	Supply chain analyst	5	Research Associate
3	Sr. Project Manager	22	Steel, cladding and framing industry
4	Sr. Project Manager	12	Technical consultancy
5	Manager	12	Compressors and pumps manufacturing
6	Senior Design Engineer	8	Automotive seating design and manufacturing
7	ISO Consultant (Risk Management)	10	Consultancy (certification)



**Fig. 2** Process of CRFs ranking

**Table 3** Fuzzy linguistic expressions and fuzzy triangular numbers for criteria and risk ratings

Weight of each criteria linguistic variables		Ratings of risks linguistic variables	
Linguistic expression	Fuzzy triangular number	Linguistic expression	Fuzzy triangular number
Extreme less	(0, 0, 0.1)	Very poor	(0, 0, 1)
Less	(0, 0.1, 0.3)	Poor	(0, 1, 3)
Moderately less	(0.1, 0.3, 0.5)	Moderately poor	(1, 3, 5)
Moderate	(0.3, 0.5, 0.7)	Fair	(3, 5, 7)
Moderately high	(0.5, 0.7, 0.9)	Moderately risky	(5, 7, 9)
High	(0.7, 0.9, 0.10)	Risky	(7, 9, 10)
Extreme high	(0.9, 1.0, 1.0)	Very risky	(9, 10, 10)

## 4 Methodology

Figure 2 presents a flowchart of steps followed to obtain the ranking of critical risk factors using FTOPSIS.

Table 3 presents the linguistic variables used for evaluating criteria (C) weights and the associated Triangular Fuzzy Numbers (TFNs). The evaluation is obtained from seven decision-makers (DM).

The impact severity of each risk (R) on each criterion (C) by DMs was evaluated using variables. Table 3 presents the membership function for risk impact ratings.

## 5 Steps in Fuzzy TOPSIS

### 5.1 Step I: Criteria and Risk Factors Rating Allocation

Let,

$j$  = Critical risk factors (R) ( $j = 1, 2, 3...n$ );

$k$  = Number of industry decision-makers (DM) ( $k = 1, 2, 3...0.7$ );

$R = \{R_1, R_2, R_3, \dots, R_j\}$  to be rated against ‘m’ criteria (C);

$C = \{C_1, C_2, C_3, \dots, C_m\}$ ;

$W_i$  = Weights of criteria, where  $i = 1, 2, 3, \dots, m$ .

Table 4 presents aggregate linguistic assessment made by decision-makers from the industry. ‘DM<sub>k</sub>’ denotes rating given by each DM ( $k = 1, 2, 3, \dots, k$ ) for each risk factor  $R_j$  ( $j = 1, 2, 3, \dots, n$ ) against criteria of evaluation  $C_i$  ( $i = 1, 2, 3, \dots, m$ ) which are indicated by  $\tilde{R}_k = \tilde{x}_{ijk}$  ( $i = 1, 2, 3, \dots, m$ ;  $j = 1, 2, 3, \dots, n$ ,  $k = 1, 2, 3, \dots, k$ ) with the

**Table 4** Aggregate fuzzy weight of linguistic assessment by DMs for each criterion

	L-FW	M-FW	H-FW
C 1	0.3000	0.7571	1.0000
C 2	0.5000	0.8429	1.0000
C 3	0.3000	0.7143	1.0000
C 4	0.5000	0.8571	1.0000
C 5	0.5000	0.9000	1.0000

membership value  $\mu_{\tilde{R}_k}(x)$ . Linguistic assessment of all 13 CRFs with DMs input is as shown in Table 6. The assessment was done for all 13 CRFs based on their adverse impact severity—higher the rating, severe is the impact of CRFs on criteria.

### 5.2 Step II: Development of Combined Fuzzy Rating for Criteria

Triangular fuzzy numbers are assigned to fuzzy rating valuation by all DMs.

$$[\tilde{V}_k = (a_k, b_k, c_k), k = 1, 2, 3 \dots k].$$

$$\tilde{V}_k = (a, b, c), k = 1, 2, 3 \dots k, a = \min_k \{a_k\}, b = \frac{1}{k} \sum_1^k b_k, c = \max_k \{c_k\}.$$

The aggregated fuzzy decision matrix for the weight of criteria  $\tilde{W}_i = (\tilde{w}_1, \tilde{w}_2, \tilde{w}_3 \dots \tilde{w}_m)$  is presented in Table 4.

### 5.3 Step III: Generation of the Decision Matrix Under Fuzzy Environment

A decision matrix under a fuzzy environment for risk factors is computed as follows:

$$\bar{D}_R = \begin{bmatrix} \tilde{x}_{11} & \tilde{x}_{12} & \dots & \tilde{x}_{1m} \\ \cdot & \cdot & \cdot & \cdot \\ \cdot & \cdot & \cdot & \cdot \\ \tilde{x}_{n1} & & & \tilde{x}_{nm} \end{bmatrix}$$

### 5.4 Step IV: Fuzzy Decision Matrix Normalization

The normalization is done as shown in Table 5 by utilizing linear scale transformation using the following formulae:

**Table 5** Normalized fuzzy decision matrix

	C1			C2			C3			C4			C5		
R1	0.5000	0.8714	1.0000	0.3000	0.7571	1.0000	0.0000	0.3143	0.9000	0.3000	0.8286	1.0000	0.0000	0.5429	1.0000
R2	0.1000	0.8143	1.0000	0.3000	0.7286	1.0000	0.0000	0.4714	0.9000	0.3000	0.7571	1.0000	0.0000	0.5571	1.0000
R3	0.1000	0.7000	1.0000	0.5000	0.8143	1.0000	0.0000	0.6286	1.0000	0.3000	0.8000	1.0000	0.0000	0.5571	1.0000
R4	0.3000	0.6429	1.0000	0.0000	0.4429	1.0000	0.1000	0.7286	1.0000	0.1000	0.6000	1.0000	0.1000	0.6429	1.0000
R5	0.3000	0.7857	1.0000	0.3000	0.7143	1.0000	0.1000	0.5286	1.0000	0.3000	0.7857	1.0000	0.3000	0.6857	1.0000
R6	0.1000	0.7000	1.0000	0.0000	0.6429	1.0000	0.0000	0.6571	1.0000	0.3000	0.8429	1.0000	0.1000	0.8143	1.0000
R7	0.3000	0.8143	1.0000	0.1000	0.7429	1.0000	0.5000	0.8857	1.0000	0.5000	0.8857	1.0000	0.1000	0.7000	1.0000
R8	0.3000	0.8143	1.0000	0.1000	0.6857	1.0000	0.0000	0.5286	1.0000	0.0000	0.5000	1.0000	0.0000	0.4714	1.0000
R9	0.3000	0.8286	1.0000	0.0000	0.6000	1.0000	0.0000	0.6571	1.0000	0.0000	0.5714	1.0000	0.0000	0.3857	1.0000
R10	0.5000	0.8571	1.0000	0.1000	0.7571	1.0000	0.5000	0.8429	1.0000	0.3000	0.7286	1.0000	0.3000	0.7000	1.0000
R11	0.0000	0.6857	1.0000	0.0000	0.7000	1.0000	0.0000	0.6571	1.0000	0.0000	0.7714	1.0000	0.0000	0.7286	1.0000
R12	0.0000	0.5571	1.0000	0.0000	0.7000	1.0000	0.0000	0.7143	1.0000	0.0000	0.7000	1.0000	0.0000	0.7143	1.0000
R13	0.1000	0.5714	1.0000	0.0000	0.6000	1.0000	0.0000	0.7429	1.0000	0.0000	0.5857	1.0000	0.0000	0.6286	1.0000



**Table 6** Weighted normalization of fuzzy decision matrix

Weight	C1		C2		C3			C4			C5				
	0.3	0.7571	1.0	0.5	0.8428	1.0	0.3	0.7142	1.0	0.5	0.8571	1.0	0.5	0.9	1.0
R1	0.1500	0.6598	1.0000	0.1500	0.6382	1.0000	0.0000	0.2245	0.9000	0.1500	0.7102	1.0000	0.0000	0.4886	1.0000
R2	0.0300	0.6165	1.0000	0.1500	0.6141	1.0000	0.0000	0.3367	0.9000	0.1500	0.6490	1.0000	0.0000	0.5014	1.0000
R3	0.0300	0.5300	1.0000	0.2500	0.6863	1.0000	0.0000	0.4490	1.0000	0.1500	0.6857	1.0000	0.0000	0.5014	1.0000
R4	0.0900	0.4867	1.0000	0.0000	0.3733	1.0000	0.0300	0.5204	1.0000	0.0500	0.5143	1.0000	0.0500	0.5786	1.0000
R5	0.0900	0.5949	1.0000	0.1500	0.6020	1.0000	0.0300	0.3776	1.0000	0.1500	0.6735	1.0000	0.1500	0.6171	1.0000
R6	0.0300	0.5300	1.0000	0.0000	0.5418	1.0000	0.0000	0.4694	1.0000	0.1500	0.7224	1.0000	0.0500	0.7329	1.0000
R7	0.0900	0.6165	1.0000	0.0500	0.6261	1.0000	0.1500	0.6327	1.0000	0.2500	0.7592	1.0000	0.0500	0.6300	1.0000
R8	0.0900	0.6165	1.0000	0.0500	0.5780	1.0000	0.0000	0.3776	1.0000	0.0000	0.4286	1.0000	0.0000	0.4243	1.0000
R9	0.0900	0.6273	1.0000	0.0000	0.5057	1.0000	0.0000	0.4694	1.0000	0.0000	0.4898	1.0000	0.0000	0.3471	1.0000
R10	0.1500	0.6490	1.0000	0.0500	0.6382	1.0000	0.1500	0.6020	1.0000	0.1500	0.6245	1.0000	0.1500	0.6300	1.0000
R11	0.0000	0.5192	1.0000	0.0000	0.5900	1.0000	0.0000	0.4694	1.0000	0.0000	0.6612	1.0000	0.0000	0.6557	1.0000
R12	0.0000	0.4218	1.0000	0.0000	0.5900	1.0000	0.0000	0.5102	1.0000	0.0000	0.6000	1.0000	0.0000	0.6429	1.0000
R13	0.0300	0.4327	1.0000	0.0000	0.5057	1.0000	0.0000	0.5306	1.0000	0.0000	0.5020	1.0000	0.0000	0.5657	1.0000

$$\tilde{R} = [\tilde{r}_{ij}]_{n \times m} \text{ (} i = 1, 2, 3 \dots m; j = 1, 2, 3 \dots n \text{), where.}$$

$$\tilde{r}_{ij} = \left( \frac{a_{ij}}{c_j^*}, \frac{b_{ij}}{c_j^*}, \frac{c_{ij}}{c_j^*} \right), c_j^* = \max \{c_{ij}\}, j \in B, B = \text{important criteria.}$$

**5.5 Step V: Formation of the Weighted Normalized Matrix**

Table 6 shows the computation of the weighted normalized matrix by multiplying each member of the normalized matrix by the weight of the respective criterion.

$$\tilde{Y} = [\tilde{y}_{ij}]_{n \times m} \text{ (} i = 1, 2, 3 \dots m; j = 1, 2, 3 \dots n \text{).}$$

$$\tilde{y}_{ij} = \tilde{r}_{ij}(\cdot) \tilde{w}_i.$$

**5.6 Step VI: FPIS (A + ) and the FNIS(A-) Calculation**

The Positive Ideal Solution (PIS A + ) and Negative Ideal Solution (NIS A-) under fuzzy environment are calculated as follows:

$$A + = ( \tilde{v}_1^+, \tilde{v}_2^+ \dots \dots \tilde{v}_m^+ )$$

$$A - = ( \tilde{v}_1^-, \tilde{v}_2^- \dots \dots \tilde{v}_m^- )$$

$$\tilde{v}_i^+ = [(1,1,1), (1,1,1), (1,1,1)].$$

$$\tilde{v}_i^- = [(0,0,0), (0,0,0), (0,0,0)] \text{ } i = 1,2,3 \dots m.$$

**5.7 Step VII: Distance Calculation of Each Risk Factor from FPIS and FNIS**

The distance between two fuzzy numbers  $\tilde{x} (a_1, a_2, a_3)$  and  $\tilde{y} (b_1, b_2, b_3)$  is calculated as.

$$d ( \tilde{x}, \tilde{y} ) = \sqrt{\frac{1}{3}[(a_1 - b_1)^2 + (a_2 - b_2)^2 + (a_3 - b_3)^2]}$$

$$d_j^+ = \sum_{i=1}^m d(\tilde{v}_{ji}, v_i^+) \text{ } j = 1,2,3 \dots n.$$

$$d_j^- = \sum_{i=1}^m d(\tilde{v}_{ji}, v_i^-) \text{ } j = 1,2,3 \dots n.$$

Table 7 presents calculated distances, where d (..) denotes computed distance between two fuzzy numbers, i.e. Risk Factor (RF) and FPIS/FNIS.

**5.8 Step VIII: Determining Closeness Coefficient (CC<sub>i</sub>) of Each Risk Factor**

The closeness coefficient (CC<sub>i</sub>) represents the simultaneous distance of the FPIS  $d_j^+$  and FNIS  $d_j^-$  as shown in Table 8.

**Table 7** Computation of distances

	C1	C2	C3	C4	C5		C1	C2	C3	C4	C5
d (R1, d + )	0.5286	0.5334	0.7329	0.5185	0.6485	d (R1, d-)	0.6971	0.6904	0.5355	0.7134	0.6426
d (R2, d + )	0.6022	0.5390	0.6952	0.5309	0.6451	d (R2, d-)	0.6785	0.6830	0.5548	0.6937	0.6459
d (R3, d + )	0.6223	0.4694	0.6592	0.5232	0.6451	d (R3, d-)	0.6537	0.7150	0.6329	0.7054	0.6459
d (R4, d + )	0.6032	0.6814	0.6247	0.6160	0.6000	d (R4, d-)	0.6442	0.6163	0.6511	0.6499	0.6676
d (R5, d + )	0.5751	0.5419	0.6654	0.5257	0.5382	d (R5, d-)	0.6738	0.6794	0.6174	0.7014	0.6840
d (R6, d + )	0.6223	0.6351	0.6536	0.5162	0.5698	d (R6, d-)	0.6537	0.6567	0.6378	0.7175	0.7164
d (R7, d + )	0.5701	0.5894	0.5346	0.4548	0.5886	d (R7, d-)	0.6802	0.6818	0.6887	0.7391	0.6830
d (R8, d + )	0.5701	0.6002	0.6801	0.6650	0.6662	d (R8, d-)	0.6802	0.6675	0.6171	0.6281	0.6272
d (R9, d + )	0.5677	0.6440	0.6536	0.6482	0.6895	d (R9, d-)	0.6835	0.6470	0.6378	0.6429	0.6111
d (R10, d + )	0.5309	0.5869	0.5419	0.5365	0.5352	d (R10, d-)	0.6937	0.6855	0.6794	0.6862	0.6878
d (R11, d + )	0.6406	0.6240	0.6536	0.6096	0.6106	d (R11, d-)	0.6505	0.6703	0.6378	0.6922	0.6904
d (R12, d + )	0.6669	0.6240	0.6429	0.6218	0.6131	d (R12, d-)	0.6266	0.6703	0.6482	0.6733	0.6864
d (R13, d + )	0.6488	0.6440	0.6378	0.6450	0.6294	d (R13, d-)	0.6293	0.6470	0.6536	0.6460	0.6633

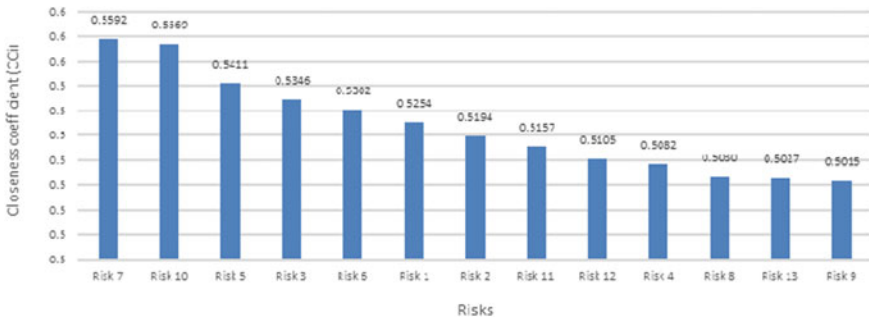
**Table 8** Closeness coefficient of each risk factor

Risks	$d_j^+$	$d_j^-$	$CC_i$
R1	2.9618	3.2790	0.5254
R2	3.0124	3.2559	0.5194
R3	2.9192	3.3527	0.5346
R4	3.1254	3.2291	0.5082
R5	2.8463	3.3560	0.5411
R6	2.9970	3.3820	0.5302
R7	2.7376	3.4728	0.5592
R8	3.1815	3.2201	0.5030
R9	3.2030	3.2223	0.5015
R10	2.7315	3.4327	0.5569
R11	3.1384	3.3412	0.5157
R12	3.1687	3.3048	0.5105
R13	3.2050	3.2392	0.5027

$$CC_i = \frac{d_j^-}{d_j^+ + d_j^-} \quad j = 1, 2, 3, \dots, n.$$

### 5.9 Step IX: Ranking of the Alternatives

The 13 CRFs are ranked (Fig. 3) concerning the descending order of  $CC_i$ . The most severe risk factor is nearer to the FPIS and away from the FNIS.



**Fig. 3**  $CC_i$  of risk factors (CRFs) in descending order of preference

## 6 Results and Discussion

A thorough literature review was done to identify significant risk variables in the Indian automotive manufacturing supply chain. Considered risk factors were analysed using fuzzy TOPSIS. As discussed in section one, five criteria were considered for the assessment of risks impact. The criteria selected are crucial for decision-makers. The results conclude that the risk factor 'Risk due to delay (R7)' is ranked first among the considered factors. The organization should examine all potential mitigation strategies to avoid the detrimental consequences of delay risks. 'Risks related to management (R10)' and 'Risks related to raw materials (R5)' are ranked second and third, respectively. The subsequent ranking order of analysed risk factors is presented in Sect. 5.9. Top management commitment, decision-making and support are imperative for minimizing disruptions. Raw material availability, quality and price fluctuations should be monitored to avoid delivery delay, reliability-related issues and cost overrun. Reliance on a single supplier, poor process quality at the supplier's end and internal issues may adversely impact the manufacturing supply chain.

## 7 Conclusion

This article identified the risk factors critical to the Indian automotive supply chain and modelled risk factors prioritization using the FTOPSIS approach. For sustainability in the dynamic situation of today's industrial scenario, remaining prepared in advance for uncertain situations is vitally important. The study put forth the systematic approach of prioritization of critical risk factors to the Indian automotive supply chain. This study's outcome is expected to assist forefront managers of the Indian automotive sector in adopting a systematic approach for risk mitigation.

## References

1. Gupta A, Mau RR, Marion JW (2015) Supply chain risk management in aviation and aerospace manufacturing industry - an empirical study. *Int. J. Supply Chain Oper. Resil.* 1(3):300. <https://doi.org/10.1504/ijscor.2015.072624>
2. Salleh Hudin N, Abdul Hamid AB, Chin TA, Habidin NF (2017) Exploring supply chain risks among Malaysian automotive Smes. *IJASOS- Int E-J Adv Soc Sci III*(8):666–674. <https://doi.org/10.18769/ijasos.337330>
3. Chand M, Raj T, Shankar R (2015) A comparative study of multi criteria decision making approaches for risks assessment in supply chain. *Int J Bus Inf Syst* 18(1):67–84. <https://doi.org/10.1504/IJBIS.2015.066128>
4. Gautam A, Prakash S, Soni U (2018) Supply chain risk management and quality: A case study and analysis of Indian automotive industry. *Int J Intell Enterp* 5(1–2):2–17. <https://doi.org/10.1504/IJIE.2018.091189>
5. Sun C, Xiang Y, Jiang S, Che Q (2015) A supply chain risk evaluation method based on fuzzy topsis. *Int J Saf Secur Eng* 5(2):150–161. <https://doi.org/10.2495/SAFE-V5-N2-150-161>

6. Mavi RK, Goh M, Mavi NK (2016) Supplier selection with Shannon entropy and fuzzy TOPSIS in the context of supply chain risk management. *Procedia Soc Behav Sci* 235:216–225. <https://doi.org/10.1016/j.sbspro.2016.11.017>
7. Rahim AAA, Musa SN, Ramesh S, Lim MK (2021) Development of a fuzzy-TOPSIS multi-criteria decision-making model for material selection with the integration of safety, health and environment risk assessment. *Proc Inst Mech Eng Part L J Mater Des Appl* 1464420721994269. <https://doi.org/10.1177/1464420721994269>
8. Zadeh LA (1965) Fuzzy sets. *Inf Control* 8(3):338–353. <https://doi.org/10.1061/9780784413616.194>
9. Gupta R, Shankar R (2016) Ranking of collusive behaviour in Indian agro-supply chain using interval 2-tuple linguistic TOPSIS method. *J Model Manag* 11(4):949–966. <https://doi.org/10.1108/JM2-03-2015-0006>
10. Kirkire MS, Rane SB, Abhyankar GJ (2020) Structural equation modelling—FTOPSIS approach for modelling barriers to product development in medical device manufacturing industries. *J Model Manag* 15(3):967–993. <https://doi.org/10.1108/JM2-09-2018-0139>
11. Al Zubayer MA, Mithun Ali S, Kabir G (2019) Analysis of supply chain risk in the ceramic industry using the TOPSIS method under a fuzzy environment. *J Model Manag* 14(3):792–815. <https://doi.org/10.1108/JM2-06-2018-0081>
12. Thun JH, Hoenic D (2011) An empirical analysis of supply chain risk management in the German automotive industry. *Int J Prod Econ* 131(1):242–249. <https://doi.org/10.1016/j.ijpe.2009.10.010>
13. Dias GC, Hernandez CT, de Oliveira UR (2020) Supply chain risk management and risk ranking in the automotive industry. *Gest e Prod* 27(1):1–21. <https://doi.org/10.1590/0104-530X3800-20>
14. Silva ES, Wu Y, Ojiako U (2013) Developing risk management as a competitive capability. *Strateg Chang* 22(5–6):281–294. <https://doi.org/10.1002/jsc.1940>
15. Mehrjerdi YZ, Dehghanbaghi M (2013) A dynamic risk analysis on new product development process. *Int J Ind Eng Prod Res* 24(1):17–35
16. Kidane TT, Sharma RRR (2016) Relating supply chain risks to supply chain strategy. *Proc Int Conf Ind Eng Oper Manag* 8–10:70–78
17. Simons R (1999) How risky is your company?. *Harv Bus Rev* 77(3)
18. Prakash A, Agarwal A, Kumar A (2018) Risk assessment in automobile supply chain. *Mater Today Proc* 5(2):3571–3580. <https://doi.org/10.1016/j.matpr.2017.11.606>
19. Nunes B, Bennett D (2008) Environmental threats and their Impacts on the automobile industry. *Int Conf Manag Technol*. <https://doi.org/10.13140/2.1.2227.0248>
20. Deep S, Gajendran T, Jefferies M (2019) A systematic review of “enablers of collaboration” among the participants in construction projects. *Int J Constr Manag* 1–13. <https://doi.org/10.1080/15623599.2019.1596624>
21. Alikhani R, Torabi SA, Altay N (2019) Strategic supplier selection under sustainability and risk criteria. *Int J Prod Econ* 208:69–82. <https://doi.org/10.1016/j.ijpe.2018.11.018>
22. Babu H, Bhardwaj P, Agrawal AK (2020) Modelling the supply chain risk variables using ISM: a case study on Indian manufacturing SMEs. *J Model Manag* <https://doi.org/10.1108/JM2-06-2019-0126>
23. Pitchaiah DS, Hussaiah M, Sateesh N, Govardhan D (2020) Prioritization of supply chain risk by multi attribute decision making method for manufacturing of automobiles. *Mater Today Proc* 39:201–205. <https://doi.org/10.1016/j.matpr.2020.06.490>
24. Kumar G, Singh RK, Jain R, Kain R (2020) Analysis of demand risks for the Indian automotive sector in globally competitive environment. *Int J Organ Anal* <https://doi.org/10.1108/IJOA-03-2020-2076>
25. Islam A, Tedford D (2012) Risk determinants of small and medium-sized manufacturing enterprises (SMEs)—an exploratory study in New Zealand. *J Ind Eng Int* 8(1):1–13. <https://doi.org/10.1186/2251-712X-8-12>
26. Dandage RV, Mantha SS, Rane SB (2019) Strategy development using TOWS matrix for international project risk management based on prioritization of risk categories. *Int J Manag Proj Bus* 12(4):1003–1029. <https://doi.org/10.1108/IJMPB-07-2018-0128>

27. Dey PK, Ogunlana SO (2004) Selection and application of risk management tools and techniques for build-operate-transfer projects. *Ind Manag Data Syst* 104(3):334–346. <https://doi.org/10.1108/02635570410530748>
28. Batkovskiy AM, Konovalova AV, Semenova EG, Trofimets VY, Fomina AV (2015) Risks of development and implementation of innovative projects. *Mediterr J Soc Sci* 6(4):243–253. <https://doi.org/10.5901/mjss.2015.v6n4s4p243>
29. Czuchry AJ, Yasin MM (2003) Managing the project management process. *Ind Manag Data Syst* 103(1–2):39–46. <https://doi.org/10.1108/02635570310456887>
30. Ojiako U, Johansen E, Greenwood D (2008) A qualitative re-construction of project measurement criteria. *Ind Manag Data Syst* 108(3):405–417. <https://doi.org/10.1108/02635570810858796>
31. Cao Q, Hoffman JJ (2011) A case study approach for developing a project performance evaluation system. *Int J Proj Manag* 29(2):155–164. <https://doi.org/10.1016/j.ijproman.2010.02.010>
32. Dandage RV, Mantha SS, Rane SB, Bhoola V (2018) Analysis of interactions among barriers in project risk management. *J Ind Eng Int* 14(1):153–169. <https://doi.org/10.1007/s40092-017-0215-9>
33. Maya RA (2016) Performance management for Syrian construction projects. *Int J Constr Eng Manag* 5(3):65–78. <https://doi.org/10.5923/j.ijcem.20160503.01>
34. Keil M, Cule PE, Lyytinen K, Schmidt RC (1998) A framework for identifying software project risks. *Commun ACM* 41(11):76–83. <https://doi.org/10.1145/287831.287843>
35. Abdolshah M, Moradi M (2013) Fuzzy Quality function deployment: an analytical literature review. *J Ind Eng* 2013:1–11. <https://doi.org/10.1155/2013/682532>
36. Islam A, Tedford D (2012) Implementation of risk management in manufacturing industry- an empirical investigation. *Int J Res Manag Technol* 2(3):258–267. <http://www.ircast.org/ijrmt/papers/vol2no32012/1vol2no3.pdf>
37. Shevtshenko E, Mahmood K (2015) Analysis of machine production processes by risk assessment approach. *J Mach Eng* 15(1):112–124
38. Shin J, Lee S, Yoon B (2018) Identification and prioritization of risk factors in R&D projects based on an R&D process model. *Sustain* 10(4):1–18

# Thermohydrodynamic Analysis of Journal Bearing Using Non-newtonian Lubricants



Kedar Deshmukh and Vilas Warudkar

## 1 Introduction

The hydrodynamic journal bearings are used to support rotating shafts in high-speed equipment, electric motors, turbines, and other applications. Journal bearings support the external load with the help of thin film between the journal and the bearing surface. The fluid film's hydrodynamic pressure aids in preventing metal-to-metal contact between rotating machinery parts and bearing surfaces. Because of the high journal speed, variations in temperature of the lubricant have a major impact on the properties of the lubricant during bearing operation. Thus, the performance of the journal bearing depends upon the temperature and pressure distribution within the bearing. As a result, investigating bearing performance using thermohydrodynamic analysis necessitates solving complex equations of lubricant flow. Reynolds equation and energy equation solved simultaneously while taking into account the effects of conduction and convection. Previously researchers investigated the performance of journal bearing by solving complex equations over finite difference method. Many scholars began using commercial CFD software to solve complex equations as analysis software improved. Instead of solving Reynolds equations, CFD codes use Navier–Stokes equations to solve flow problems. As a result of advancements in modern machinery and the demands of different operating conditions, the expanding use of non-Newtonian fluids as lubricants has attracted a lot of attention in recent years. Polymer thickened oil, grease, and natural lubricants, among others, are used as lubricants for modern machines that display non-Newtonian behavior. First and foremost, “Hughes and Osterle [1] did outstanding work on thermohydrodynamic analysis of journal bearings. The authors discovered the relationship between the viscosity of the lubricant within the journal bearing as a function of temperature

---

K. Deshmukh (✉) · V. Warudkar

Department of Mechanical Engineering, Maulana Azad National Institute of Technology Bhopal, Bhopal, India



and pressure under adiabatic conditions. Oliver [2] did an experimental study and found that addition of dissolved polymer to the lubricant increases the load-carrying capacity and decreases the friction coefficient in short journal bearings. B Chetti [3] investigated performance of finite circular journal bearing lubricated with micro-polar fluids by considering the effect of elastic deformation on the bearing liner. Many authors have recently begun to use commercial CFD codes in their study. Montazeri [4] studied the hydrodynamic properties of lubricant in ferro fluid-lubricated journal bearings. The Navier–Stokes equations were numerically solved using the CFD approach. Gertzos et al. [5] studied performance of hydrodynamic journal bearing lubricated with a Bingham fluid using CFD techniques. Liu et al. [6] investigated the performance of a rotor bearing device using computational fluid dynamics and fluid structure interaction methods. Czaban [7] simulated and calculated the hydrodynamic pressure distribution in the lubrication gap of a sliding contact bearing with non-Newtonian lubricating oil. ANSYS Fluent, a commercial CFD program, was used to perform the investigation. THD study of journal bearings was carried out by Sahu et al. [8] using CFD as a method. The pressure and temperature distribution of the lubricating film were calculated by the authors. Panday et al. [9] used ANSYS Fluent software to perform numerical unsteady analysis of thin film journal bearings, calculating bearing parameters such as pressure distribution and wall shear stress at various eccentricity ratios. Using computational fluid dynamics, Chauhan [10] calculated circular bearing performance parameters using an isothermal and thermo-hydrodynamic approach. Pratomo et al. [11] studied tribological characteristics of polymer-thickened oil in lubricated sliding contacts by considering cavitation effect. The analysis was carried out using commercial CFD software ANSYS Fluent.”

However, there was no analysis presenting the effect of viscosity index on the performance of journal bearing. This paper presents the results of pressure, temperature, and shear stress distribution obtained at different viscosity indexes.

## 2 Mathematical Modeling

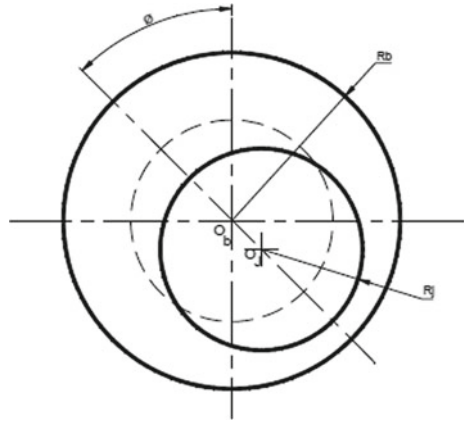
### 2.1 Geometry

The relative rotational velocity is created by the journal rotating inside the bearing. When the journal is in a stable position, it assumes an eccentric position with respect to the bearing. The produced pressure within the converging lubricant film, which balances the external load, adjusts the amount of eccentricity (Fig. 1).

“The eccentricity, viscosity, and clearance space between the journal and the bearing can influence the generation of hydrodynamic pressure within the journal bearing. The hydrodynamic pressure of the lubricant film is determined by the film thickness equation for circular journal bearings, which is as follows:

$$h(\theta) = C + e\cos\theta = C(1 + \varepsilon\cos\theta)$$

**Fig. 1** Schematic diagram of circular journal bearing



$\epsilon$  represents the eccentricity ratio of the journal bearing and  $C$  is radial clearance between journal and bearing. From the maximum film thickness,  $\theta$  is the value of film thickness along the circumferential path” [10].

### 2.2 Momentum Conservation Equation

“The underlying lubrication theory is based on the solution of a specific form of the Navier–Stokes equation, as shown below, in which viscosity varies with shear rate and temperature. The Navier–Stokes equations are as follows:” [11]

$$\rho(u \cdot \nabla)u = -\nabla p + \eta \nabla^2 u$$

$$\nabla \cdot u = 0$$

### 2.3 Conservation of Energy Equation

Energy equation for incompressible viscous fluids is shown here. Net heat flux is denoted by  $q$ . In this equation, surface and body forces are taken into consideration.

$$\begin{aligned} \rho \frac{D}{Dt} \left( e + \frac{V^2}{2} \right) &= \rho \dot{q} + \frac{\partial T}{\partial x} \left( k \frac{\partial T}{\partial x} \right) + \frac{\partial}{\partial y} \left( k \frac{\partial T}{\partial y} \right) + \frac{\partial}{\partial z} \left( k \frac{\partial T}{\partial z} \right) \\ &- \frac{\partial(u p)}{\partial x} - \frac{\partial(v p)}{\partial y} - \frac{\partial(w p)}{\partial z} + \frac{\partial(u \tau_{xx})}{\partial x} \\ &+ \frac{\partial(u \tau_{yx})}{\partial y} + \frac{\partial(u \tau_{zx})}{\partial z} + \frac{\partial(v \tau_{xy})}{\partial x} + \frac{\partial(v \tau_{yy})}{\partial y} \\ &+ \frac{\partial(v \tau_{zy})}{\partial z} + \frac{\partial(w \tau_{xz})}{\partial x} + \frac{\partial(w \tau_{yz})}{\partial y} + \frac{\partial(w \tau_{zz})}{\partial z} + \rho \vec{f} \cdot \vec{V} \end{aligned}$$

## 2.4 Shear Stress Variation

“Oil shear stress was believed to vary with share rate based on the Ostwald–de Waele equation (power-law lubricant) [12], which is shown as

where  $\zeta$  is shear stress,  $\gamma$  is shear strain, and  $K$  and  $n$  are coefficients. The coefficients for the lubricant can be determined experimentally [13]; however, in this paper, we have assumed viscosity index to be varying in the range of 0.75–1.3. When  $n > 1$  the fluid is called dilatant and when  $n < 1$ , it is called pseudoplastic.”

## 3 CFD Simulation

### 3.1 CFD Model Description

For simulation, the ANSYS fluent CFD package was used. 3D fluid domain model has been developed in the Design Modeler. Clearance space between journal and bearing surface has been kept as 0.8 mm. The eccentricity ratio of 0.8 has been considered. 3D swept mesh method has been used (Figs. 2 and 3).

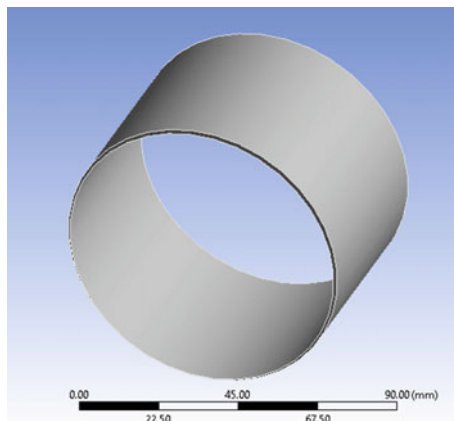
For meshing, hexahedral elements are used. Five divisions in the radial direction have been considered for better results. Named selections for inlet, outlet, moving, and fixed wall are done in meshing.

Table 1 lists the dimensions of the journal bearing as well as the lubricant properties. The test was carried out at various shaft speeds ranging from 500 to 3000 rpm.

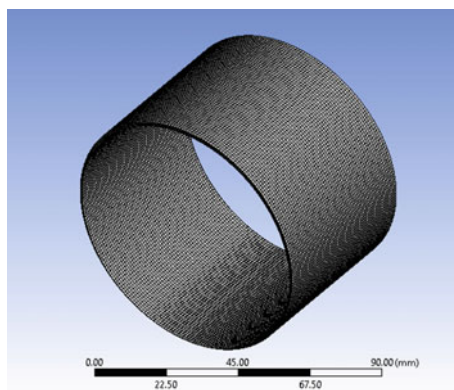
A steady-state condition has been assumed for simulation purposes. Laminar flow is considered for fluid flow. Viscosity of the lubricant is considered to be varying according to non-Newtonian power-law equation.

For analysis viscosity index  $n$  is considered to be varying in the range of 0.75–1.3. Consistency index  $k$  is kept at 1.06 Pa·s. Viscous heating effect has been taken into account. At the inlet and outlet of the bearing lubricant pressure is considered

**Fig. 2** 3D model of the fluid domain



**Fig. 3** Hexahedral mesh on fluid domain



**Table 1** Journal bearing operating parameters

Parameters	Value
Shaft radius $R_j$	40 mm
Bush inner radius $R_b$	40.8 mm
Min oil film thickness	0.16 mm
Clearance $C$	0.8 mm
Eccentric distance	0.64 mm
Eccentricity ratio $\varepsilon$	0.8
Viscosity $\mu$	1.06 kg/m-s
Viscosity index $n$	0.75–1.3
Density of lubricant $\rho$	887 kg/m <sup>3</sup>
Specific heat of lubricant $C_p$	1845 J/kg-K
Thermal conductivity of lubricant $k$	0.145 W/m-K
Rotational speed $\omega$	500–3000 rpm

to be atmospheric. Moving (inner wall) has been considered to be rotating at the speed in the range of 500–3000 rpm. Gravitational forces have been considered on the journal bearing. Convergence criteria is kept at  $10^{-6}$  for all residuals. 3D Navier–Stokes equations are solved for analysis.

## 4 Results and Discussion

The bearing performance characteristics are investigated at different journal speeds in the range of 500–3000 rpm. Viscosity index has been varied in the range of 0.75–1.3.

### 4.1 *Static Pressure*

Static pressure profile at journal speed of 500 rpm obtained at viscosity index at 0.99, 1, and 1.01 is shown in the figure below.

Figure 4a shows the pressure distribution in the bearing at the viscosity index of 0.99. The maximum static pressure obtained was 879,244 Pa. Figure 4b shows a pressure distribution at constant viscosity. The maximum static pressure in this case was observed to be 967,050 Pa. Figure 4c shows pressure distribution in the bearing at viscosity index of 1.01. The maximum static pressure was observed to be 1,063,580 Pa. Figure 4d shows the graph of maximum static pressure versus different journal speeds by using lubricant with viscosity index varying from 0.75 to 1.3. We can observe from this graph that maximum static pressure increases as the viscosity index increases. Significant rise in static pressure is seen at higher journal speeds.

### 4.2 *Static Wall Temperature*

Temperature profile at journal speed of 500 rpm obtained at viscosity index at 0.99, 1, and 1.01 is shown in the figure below. Figure 5a shows the temperature distribution in the bearing at the viscosity index of 0.99. The maximum temperature obtained was 330.12 K. Figure 4b shows a temperature distribution at constant viscosity. The maximum temperature in this case was observed to be 332.8 K. Figure 5c shows temperature distribution in the bearing at viscosity index of 1.01. The maximum temperature was observed to be 335.65 K. Figure 5d shows the graph of maximum temperature versus different journal speeds by using lubricant with viscosity index varying from 0.75 to 1.3. We can observe from this graph that maximum temperature increases as the viscosity index increases. Significant rise in temperature is seen at higher journal speeds. Rise in temperature at higher viscosity index is due to increase in viscous heating.

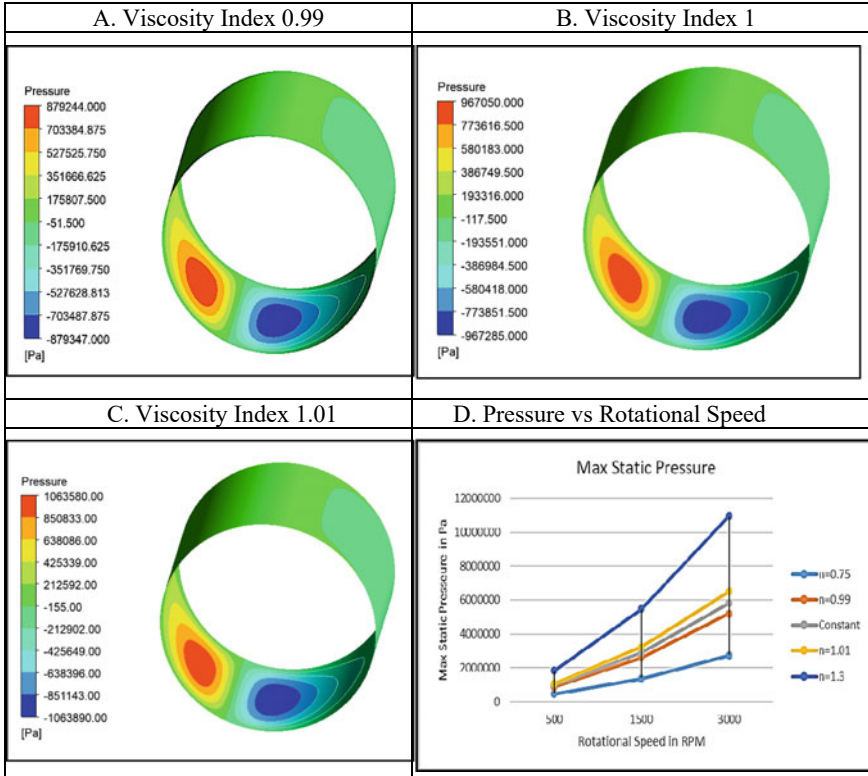


Fig. 4 CFD results of static pressure analysis with lubricant viscosity varying from 0.75 to 1.3

### 4.3 Wall Shear Stress

Wall shear stress profile at journal speed of 500 rpm obtained at viscosity index at 0.99, 1, and 1.01 is shown in the figure below. Figure 6a shows the wall shear stress distribution in the bearing at the viscosity index of 0.99. The maximum wall shear stress obtained was 20,518.8 Pa. Figure 6b shows a wall shear stress distribution at constant viscosity. The maximum wall shear stress in this case was observed to be 22,593.3 Pa. Figure 6c shows wall shear stress distribution in the bearing at viscosity index of 1.01. The maximum wall shear stress was observed to be 24,877 Pa. Figure 6d shows the graph of maximum wall shear stress versus different journal speeds by using lubricant with viscosity index varying from 0.75 to 1.3. We can observe from this graph that maximum wall shear stress increases as the viscosity index increases. Significant rise in wall shear stress is seen at higher journal speeds.

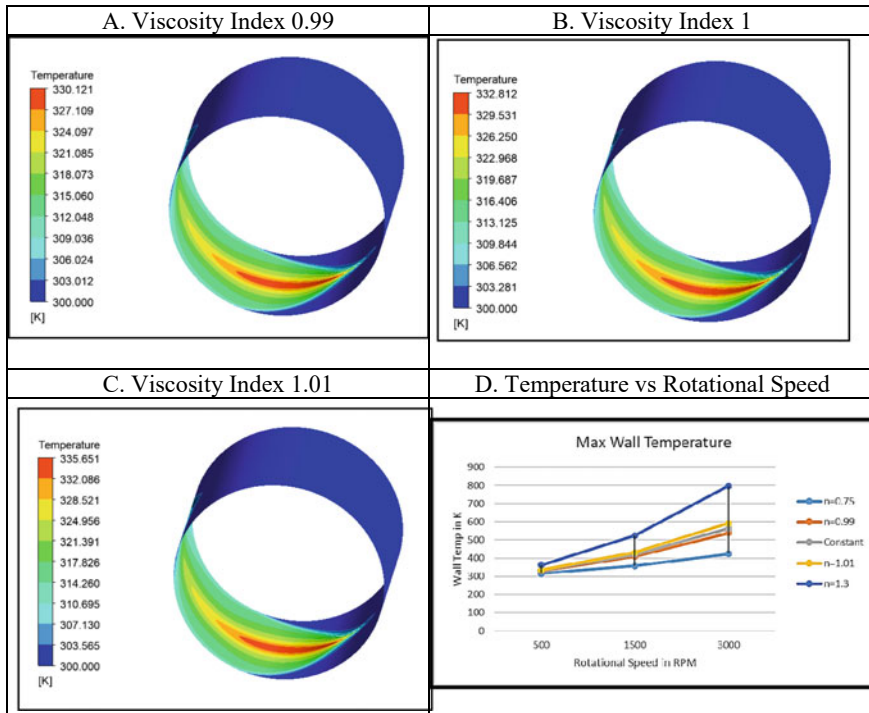


Fig. 5 CFD results of temperature analysis with lubricant viscosity varying from 0.75 to 1.3

## 5 Summary and Conclusion

Thermohydrodynamic analysis of the journal bearing was carried out using lubricants with viscosity index varying from 0.75 to 1.3. The analysis was carried out using ANSYS Fluent CFD software. At journal speeds ranging from 500 to 3000 rpm, bearing performance parameters such as maximum static pressure, wall temperature, and wall shear stress were evaluated, with eccentricity ratio = 0.8 and radial clearance = 0.8 mm.

From the analysis, it was observed that viscosity index has great impact on performance characteristics of the journal bearing. Shear-thinning fluids, i.e., viscosity index < 1 tends to decrease the maximum static pressure in the bearing which in turn decreases the load-carrying capacity of the bearing, and there is a significant reduction in shear stress and temperature rise. At very high speeds and low loads, lubricant blended with shear-thinning fluids can be beneficial.

Shear-thickening fluid, i.e., viscosity index > 1 tends to increase the maximum static pressure in the bearing which in turn enhances the load-carrying capacity of the bearing, and a significant rise in temperature and shear stress is seen. It can be concluded that shear-thickening fluid can be blended with the lubricant to increase the load-carrying capacity for low-speed and high-load applications.

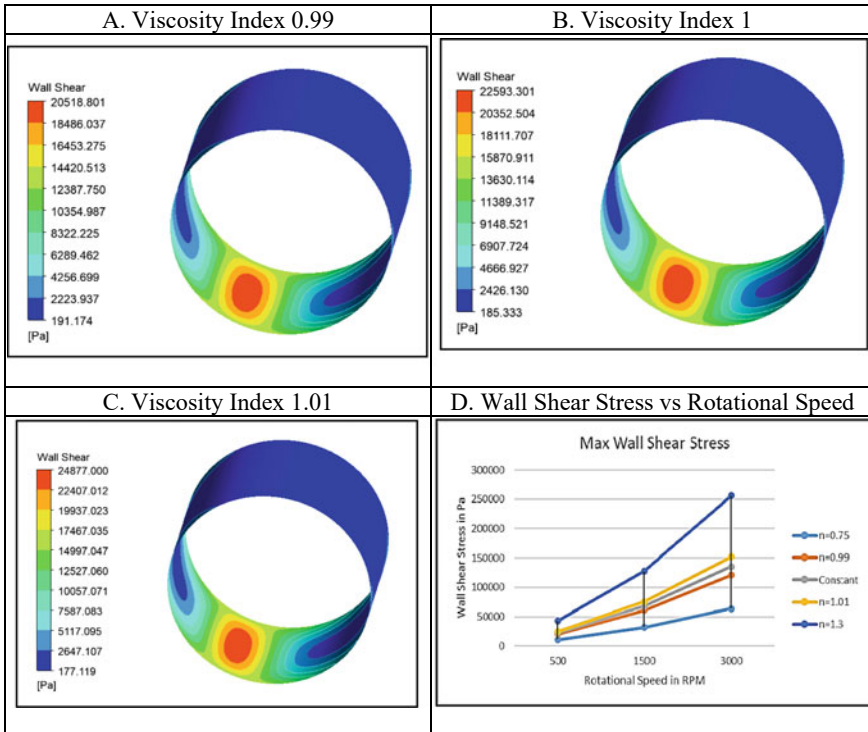


Fig. 6 CFD results of wall shear stress analysis with lubricant viscosity varying from 0.75 to 1.3

## References

- Hughes WF, Osterle F (1958) Temperature effects in journal bearing lubrication. *ASLE Trans* 1(1):210–212. <https://doi.org/10.1080/05698195808972331>
- Oliver DR (1988) Load enhancement effects due to polymer thickening in a short model journal bearing. *J Nonnewton Fluid Mech* 30(2–3):185–196. [https://doi.org/10.1016/0377-0257\(88\)85024-9](https://doi.org/10.1016/0377-0257(88)85024-9)
- Chetti B (2014) Analysis of a circular journal bearing lubricated with micropolar fluids including EHD effects. *Ind Lubr Tribol* 66(2):168–173. <https://doi.org/10.1108/ILT-12-2011-0114>
- Montazeri H (2008) Numerical analysis of hydrodynamic journal bearings lubricated with ferrofluid. *Proc Inst Mech Eng Part J J Eng Tribol* 222(1):51–60. <https://doi.org/10.1243/13506501JET314>
- Gertzos KP, Nikolakopoulos PG, Papadopoulos CA (2008) CFD analysis of journal bearing hydrodynamic lubrication by Bingham lubricant. *Tribol Int* 41(12):1190–1204. <https://doi.org/10.1016/j.triboint.2008.03.002>
- Liu H, Xu H, Ellison PJ, Jin Z (2010) Application of computational fluid dynamics and fluid-structure interaction method to the lubrication study of a rotor-bearing system. *Tribol Lett* 38(3):325–336. <https://doi.org/10.1007/s11249-010-9612-6>
- Czaban A (2015) CFD analysis of hydrodynamic pressure distribution in non-newtonian oil in journal bearing lubrication gap. *Solid State Phenom* 220–221:37–42. <https://doi.org/10.4028/www.scientific.net/SSP.220-221.37>



8. Sahu M, Giri AK, Das A (2012) Thermohydrodynamic analysis of a journal bearing using CFD as a tool. *Int J Sci Res Publ* 2(9):1–7
9. Panday KM, Choudhury PL, Kumar NP (2012) Numerical unsteady analysis of thin film lubricated journal bearing. *Int J Eng Technol* 4(2):185–191. <https://doi.org/10.7763/ijet.2012.v4.346>
10. Chauhan A (2014) Circular bearing performance parameters with isothermal and thermo-hydrodynamic approach using computational fluid dynamics. 2(7):46–52
11. Pratomo AW, Muchammad, Tauviquirrahman M, Jamari, Bayuseno AP (2016) Tribological characteristic enhancement effects by polymer thickened oil in lubricated sliding contacts. *AIP Conf Proc* 1725. <https://doi.org/10.1063/1.4945514>
12. Ramírez-González PV, Aguayo JP, Quiñones-Cisneros SE, Deiters UK (2009) Non-newtonian viscosity modeling of crude oils-comparison among models. *Int J Thermophys* 30(4):1089–1105. <https://doi.org/10.1007/s10765-009-0578-2>
13. Czaban A (2013) The influence of temperature and shear rate on the viscosity of selected motor oils. *Solid State Phenom* 199:188–193. <https://doi.org/10.4028/www.scientific.net/SSP.199.188>

# A Review on Research Aspects and Trends in Ultrasonic Machining



Karun Kant, Prashant Gupta, Shrikant Vidya, Lavepreet Singh, and Anurag Shanu

## 1 Introduction

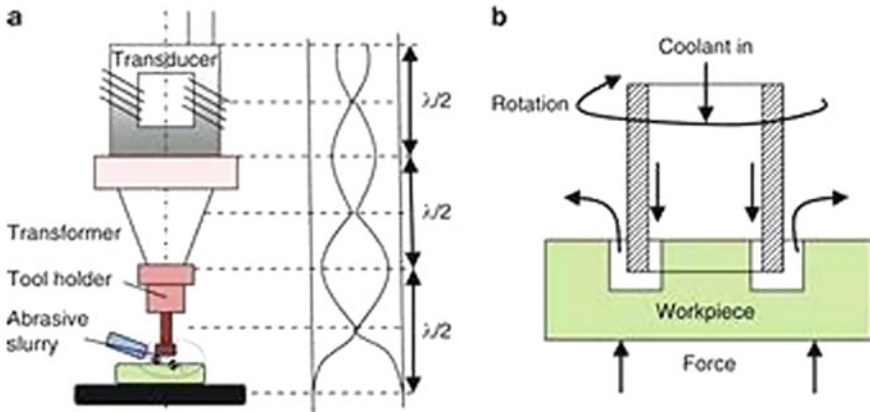
Ultrasonic machining is a mechanical sort non-customary machining measure with boundless use in machining of amazingly hard-fragile materials. This material is generally created by powder metallurgy. USM could be a reasonable option for machining of wide range of WC–Co materials, as the cycle is liberated from numerous issues related with warm base machining. USM has been differently named ultrasonic penetrating, ultrasonic cutting, ultrasonic rough machining, and slurry boring. USM is a non-customary powered substantial evacuation measure. Both electrically conductive and non-metallic materials can be machined through this tool. In USM, high recurrence electric oomph is changed over into mechanical sensations through a transducer supporter mix, which are then sent to an energy centering just as intensifying gadget known as horn or sonotrode. Machining of hard and fragile materials is acquiring significance because of its developing usage in numerous ventures like hardware, optical, and bio-clinical fields. Ultrasonic-helped processing (UAM) joins the material evacuation system of granulating, processing kinematics, and ultrasonic help.

### 1.1 Principle of Ultrasonic Machining

It deals with a similar guideline of ultrasonic welding. This machining utilizes ultrasonic waves to create high recurrence power of low plentifulness, which goes about as main impetus of grating. Ultrasonic machine creates high recurrence vibrating wave of recurrence around 20,000 to 30,000 Hz and adequacy around 25–50  $\mu\text{m}$ .

---

K. Kant · P. Gupta · S. Vidya (✉) · L. Singh · A. Shanu  
Department of Mechanical Engineering, Galgotias University, Greater Noida, Uttar Pradesh, India



**Fig. 1** Ultrasonic machining process [1]

This high recurrence vibration move to rough molecule contains in grating slurry. This leads space of grating molecule to fragile workpiece and eliminates metal from the contact surface (Fig. 1).

## 1.2 Applications

- This machining is utilized to machine hard and fragile material like carbide, earthenware, glass, and so on.
- This is utilized in machining of pass on and apparatus of drill, wire drawing machine, and so forth.
- Used in creation of silicon nitrite turbine sharp edge.
- It is utilized to cut jewel fit as a fiddle.
- It is utilized machining of machining non-conductive hard material which can't be machined by ECM or EDM because of helpless conductivity.

## 1.3 Advantages

- Hard material can be effectively machined by this strategy.
- No heat produced in work so there is no issue of work solidifying or change in construction of workpiece.
- Non-conductive metals or non-metals, which can't be machined by ECM of EDM can be machined by it.
- It doesn't shape chips of huge size.

## 2 Reviews on Ultrasonic Machining

Abdo et al. [2] defined that pocket processing has been viewed as quite possibly the most generally utilized tasks in machining. The target of this exploration was to examine the impact of the device covering boundaries on a superficial level unpleasantness, exterior sound structure as well as the machined pocket profiles. The trial results give proof that the surface harshness and MRR have been altogether as a consequence of the considered device covering and the device way approaches. In this examination, the impacts of the device covering and the instrument way procedures were tentatively investigated on a superficial level harshness using RUM, MRR, and profiles of pouches machined on alumina ( $Al_2O_3$ ) clay were calculated.

Saqib Anwar et al. [3] elaborated the rotating ultrasonic machining (RUM) that has demonstrated its abilities in a few assembly applications, specifically for the fabrication of large highlights on fired material. Surface cracking and edge chipping, on the other hand, are the most common issues encountered throughout the RUM of artistic materials. The exhibition estimates such as surface unpleasantness, surface sound structure, and apparatus dress are dissected to assess machinability. Furthermore, the sidewalls of channels have a coarse machined section close to the top control and a relatively flat region of machined surface active near the bed of channel. Using RUM interaction to the bio lox specialty material, fantastic surface completion of  $R_a = 0.21$  m and  $R_t = 2.3$  m can be achieved. To improve the surface unpleasantness of micro-channels, lower feed rates and cut depths are optional, while higher degrees of shaft rapidity and vibration sufficiency with acceptable vibration recurrence estimation should be nominated.

Jagadish et al. [4] concluded that the feed rate affects the material expulsion rate, while the slurry affects the form point and over-cut focus.

Cong et al. [5] examined the power utilization in rotary ultrasonic machining of CFRP. It outlines an analysis of the effects of information factors (ultrasonic force, apparatus turn speed, and CFRP type) on the power utilization of each portion including the ultrasonic force supply, axle motor, air blower and coolant siphon and the whole system. It was reported that the power utilization of the coolant pump was consistently the best.

Kai Ding et al. [6] conclude that the penetrating power and force for RUM were diminished by 23%, 47.6% individually of those for CD. The reduction in boring power and force diminished step by step with speeding up, while they changed somewhat with expanding feed rate. Nonetheless, it is reported that contrasted with CD, rotary ultrasonic machining can deliver lesser surface roughness of openings under comparable working conditions and the most extreme decrease rate is 23%.

Yasmine El-Taybany et al. [7] stated that the ultrasonic-helped processing of pop glass is researched and contrasted with regular processing (CM). It shows a decrease of hub cutting power and second at higher shaft speed and lesser feed rate and profundity of cut. Subsequently, the effect of UAM boundaries has been concentrated to decide their impact on the pivotal cutting power and the occasion.

Pabla et al. [8] elaborated that present examination is pointed toward considering the effect of various exploratory condition (by shifting thickness of the workpiece, cobalt material, instrument profile, apparatus material, rough coarseness size, and force rating) on reactions of premium (material expulsion rate and device wear rate) in ultrasonic penetrating of WC–Co composite material. The key boundaries for machining attributes were found to be force rating, rough coarseness scale, and apparatus content (MRR and TWR). The best material evacuation rate was achieved by combining a high-power rating with a coarse coarseness size.

Ravinder Kataria et al. [9] mentioned that the lower CR of a composite material (WC–Co) with a higher cobalt satisfied (24%) was due to a higher estimate of break resilience, which counteracts the turn of events and proliferation of breaks. In terms of CR, the silver steel instrument performed the highest. As far as CR was concerned, machines with no measurement bore unrivaled execution. Force rating and rough coarseness size were discovered to be the main boundaries for CR.

Yun-Hyuck Hong et al. [10] concluded that test was performed regarding machining boundaries, like crushing velocity, feed rate, and so forth, to contemplate impact of ultrasonic vibration in pounding. For an ideal state of ultrasonic-assisted crushing, which can restrict the pounding services, the design of experiment method was used. The major machining factors in DOE were ultrasonic sufficiency strength, feed rate, and shaft revolution speed. The ultrasonic crushing decreased the granulating power to 23% than the customary pounding and this could diminish the device wear.

Jatinder Kumar [11] concluded that ultrasonic machining is perhaps the most broadly utilized non-customary cycles, particularly for business machining of hard, weak, and delicate materials. There is colossal extension aimed at use of USM for setting up savvy machining answers for moderately extreme and malleable metals like titanium, nickel compounds. The quality and nature of USM measurements are based on the work material properties like crack sturdiness, hardness as well as the instrument properties (hardness, sway strength, and finish). The impediments of USM, holes saw from the writing survey, and the headings for future examination have likewise been introduced.

Yan Wang et al. [12] discussed the fiber-supported earthenware framework composite has been generally utilized in aviation and other high-innovation fields because of their brilliant mechanical and actual properties. Be that as it may, FRCMC is a sort of commonplace material with inhomogeneous and anisotropic design; in this manner, it is hard to ensure the exactness and surface quality utilizing customary machining. Contrasted and CG, the pounding power can be decreased somewhat, there is more uniformity in surface microstructure, all the more short-fiber chips are framed, the profundity of the cutting notch is all around conveyed, little surface unpleasantness has been accomplished, and the improvement in crushing quality can be done using UAG which is a viable technique for the machining of fiber-supported earthenware framework composite.

Treadwell et al. [13] discussed that paper revealed the correlations between turning ultrasonic machining (RUM) and pounding of CFRP interestingly. Five yield factors were looked at, including cutting power, force, surface unpleasantness, opening

distance across, and material expulsion rate (MRR). Rotational ultrasonic machining, a half-breed machining measure consolidating ultrasonic machining and crushing, has likewise been effectively utilized in penetrating of CFRP mixtures.

Vineet et al. [14] discussed the impact of interaction boundaries, specifically release flow, beat on schedule, and electrical release machining with ultrasonic-assisted cryogenically cooled cathode, has been concentrated on duty cycle and hole voltage, on terminal wear proportion, material evacuation rate, and surface unpleasantness. On M2-grade HSS workpiece material, the UACEDM test was successfully completed. In UACEDM, measurable models for predicting MRR, EWR, and surface roughness have been created connecting the info boundaries, specifically release current, beat on schedule, obligation cycle, and hole voltage.

Shaolei Wang et al. [15] illustrated that the pounding powers and ground surfaces are analyzed among CG and UAG methods. Upgrades in granulating powers and quality of surface might be ascribed to the high recurrence and huge abundance variety in the elements of the crushing cycle. Ultrasonic vibration creates sway loads, more modest single grain track covering, surface of contact, and inter-granular track covering prompts change in pounding powers and quality of surface. The impacts of framework coordinating on pounding power and surface unpleasantness are concentrated tentatively. The plan of analyses and trial gear are portrayed in detail. A five-variable and four-level partial factorial plan is utilized here to lead tests.

Hao Shen et al. [16] elaborated that turning RUM is a well-known and effective tool for assembling openings in weak materials. Improved material evacuation speeds, decreased cutting forces, and smaller edge piece sizes at the opening way out are all signs of RUM. Intriguingly, a basic feed rate was accounted for in order to ensure the viability of the RUM contact. When the forage rate is at a relatively low level, the ultrasonic force/adequacy diminishes and the hurtful power increments step by step with an expanding feed rate.

Jianjian Wang et al. [17] elaborated that ultrasonic shuddering is thought to be steady or unchanged through the cycle of turning ultrasonic machining (RUM) on fragile supplies, ignoring the impacts of various handling boundaries. Be that as it may, no test proof has been accounted for to approve this supposition. The impacts of thermomechanical stacking happening in the solidness of ultrasonic abundance through RUM cycle were examined in probes quartz crystal and cobalt. The consistency of ultrasonic vibration during the machining cycle was tested using ultrasonic force.

Ravinder Kataria et al. [18] stated that the edge chipping was seen at the leave side of the opening because of extreme corruption of the instrument face for longer machining activity. In any case, the edge of the bored opening showed great surface quality.

PKSC Fernando et al. [19] concluded that the revolving ultrasonic machining can bore openings of top caliber on rocks of various hardness with a much lower cutting power and at an entrance pace of around multiple times quicker than percussive drilling. Instrument pivot ultrasonic power, pace, and feed rate insignificantly affected outward irregularity.

Palamandadige Fernando et al. [20] concluded that the rotational ultrasonic machining (RUM) is a non-traditional besides financially savvy machining strategy for tough and weak resources, like pottery, complex things, etc. RUM is a half-breed measure that consolidates the substantial evacuation instruments of precious stone grating pounding and ultrasonic machining. A trial examination of turning ultrasonic machining of K9 glass utilizing both irregular and conti PKSC Fernan.

Ping Zou et al. [21] elaborated the tests for turning the workpiece of ASS 304 are led with and without ultrasonic vibration utilizing the planned MS-UAT, and afterward the 3D morphology assessment boundaries  $S_a$  and  $S_q$  are applied to portray and examine the machined surface. A point by test examination is introduced for the impacts of ultrasonic abundance, profundity of cut, and cutting velocity on the machined surface quality in UAT of ASS 304 with solidified carbide-covered cutting apparatus.

Weiming Zeng et al. [22] discussed the rotating ultrasonic machining (RUM) has pulled in ample consideration and around are various distributions on the interaction. Notwithstanding, not many examinations on device costume in the RUM cycle have been accounted for. This daily, without precedent used for writing, presents a test perception on apparatus wear in RUM of alumina.

Hang Gao et al. [23] discussed the revolving ultrasonic machining (RUM) of KDP. Information of a few yield boundaries (like crushing power and force, surface harshness, and edge chipping) were gathered and investigated. As an examination, precious stone boring (without ultrasonic vibration) was additionally tried. It very well may be seen that the force in RUM had a higher most extreme worth than that in precious stone boring, and had a bigger variety as well. In the writing, there could be no different reports on force in RUM for any materials.

Wang et al. [24] proposed a mechanistic model for rotation-based ultrasonic machining of CFRP composites utilizing elliptical ultrasonic vibration, calculated effective cutting time, and also investigated MRR. It was reported that the projected values of cutting forces are in line with the experimental value of results.

In a nutshell, most of the literatures dealt with the parametric optimization, better tool design as well as support addition at the hole exit while the novel method of rotary ultrasonic elliptical machining is promising area of research and development in the quality machining of brittle materials.

### 3 Conclusion

Ultrasonic machining is quite possibly the maximum generally utilized non-customary cycles, particularly for business machining of hard, weak, and delicate materials settings (input power, static burden, plentifulness, and recurrence of vibration). The factual expulsion USM takes remained discovered near happen through proliferation then crossing point of middle then sidelong breaks that remain initiated because of rehashed effects of grating grains. Plan of the instrument is a pivotal reason influencing the profitability of USM measure. Apparatuses with higher frame

will in general smother the adequacy of vibration along these lines lessening the machining rate. Instruments with extreme tip distance will in general experience mishappening and miniature breaking during machining. Exhaustion disappointment of the instrument happens if there's a small misalignment between the two, apparatus and the horn. WC-Co, a composite substance with a higher cobalt content (24 percent) displayed lesser machining percentage because of greater estimation of break strength that opposed turn of events and spread of breaks. The most noteworthy material expulsion rate was gotten at mix of high strength assessment and abrasive coarseness size.

## References

1. Joshi SS (2016) Ultrasonic machining. In: Bhushan B (eds) Encyclopedia of nanotechnology. Springer, Dordrecht. [https://doi.org/10.1007/978-94-017-9780-1\\_366](https://doi.org/10.1007/978-94-017-9780-1_366)
2. Abdo BMA, El-Tamimi A, Nasr EA (2020) Rotary ultrasonic machining of alumina ceramic: an experimental investigation of tool path and tool overlapping. *Appl Sci* 10:1667. <https://doi.org/10.3390/app10051667>
3. Abdo BMA, Anwar S, El-Tamimi A (2019) Machinability study of biolox forte ceramic by milling microchannels using rotary ultrasonic machining. *J Manuf Process* 43(Part A):175–191. ISSN 1526–6125. <https://doi.org/10.1016/j.jmapro.2019.05.031>
4. Biswas JH, Jagadish, Ray A (2019) Experimental investigation and optimisation of ultrasonic machining parameters on zirconia composite. *Int J Mach Mach Mater* 21(1–2):115–137
5. Cong WL, Pei ZJ, Deines TW, Srivastava A, Riley L, Treadwell C (2012) Rotary ultrasonic machining of CFRP composites: a study on power consumption. *Ultrasonics* 52(8):1030–1037. ISSN 0041–624X. <https://doi.org/10.1016/j.ultras.2012.08.007>
6. Ding K, Fu Y, Su H, Chen Y, Yu X, Ding G (2014) Experimental studies on drilling tool load and machining quality of C/SiC composites in rotary ultrasonic machining. *J Mater Process Technol* 214(12):2900–2907. ISSN 0924–0136. <https://doi.org/10.1016/j.jmatprotec.2014.06.015>
7. El-Taybany Y, Hossam M, El-Hofy H (2017) Experimental investigation of ultrasonic-assisted milling of soda glass using factorial design of experiments. *Procedia CIRP* 58:381–386. ISSN 2212–8271. <https://doi.org/10.1016/j.procir.2017.03.238>
8. Kataria R, Kumar J, Pabla BS (2015) Experimental investigation into the hole quality in ultrasonic machining of WC-Co composite. *Mater Manuf Process* 30(7):921–933. <https://doi.org/10.1080/10426914.2014.995052>
9. Kataria R, Kumar J, Pabla BS (2016) Experimental investigation and optimization of machining characteristics in ultrasonic machining of WC-Co composite using GRA method. *Mater Manuf Process* 31(5):685–693. <https://doi.org/10.1080/10426914.2015.1037910>
10. Kim KT, Hong YH, Park KH, Choi YJ, Lee SW, Choi HJ (2012) An experimental investigation of ultrasonic assisted grinding in DOE approach. *Adv Mater Res* 565:129–134. <https://doi.org/10.4028/www.scientific.net/amr.565.12>
11. Kumar J (2013) Ultrasonic machining—a comprehensive review. *Mach Sci Technol* 17(3):325–379. <https://doi.org/10.1080/10910344.2013.806093>
12. Li H, Lin B, Wan S, Wang Y, Zhang X (2016) An experimental investigation on ultrasonic vibration-assisted grinding of SiO<sub>2</sub>/SiO<sub>2</sub> composites. *Mater Manuf Process* 31(7):887–895. <https://doi.org/10.1080/10426914.2015.1090586>
13. Ning FD, Cong WL, Pei ZJ, Treadwell C (2016) Rotary ultrasonic machining of CFRP: a comparison with grinding. *Ultrasonics* 66:125–132. ISSN 0041–624X. <https://doi.org/10.1016/j.ultras.2015.11.002>



14. Srivastava V, Pandey PM (2013) Experimental investigation on electrical discharge machining process with ultrasonic-assisted cryogenically cooled electrode. *Proc Inst Mech Eng Part B J Eng Manuf* 227(2):301–314. <https://doi.org/10.1177/0954405412469487>
15. Wang Y, Lin B, Cao X, Wang S (2014) An experimental investigation of system matching in ultrasonic vibration assisted grinding for titanium. *J Mater Process Technol* 214(9):1871–1878. ISSN 0924–0136. <https://doi.org/10.1016/j.jmatprotec.2014.04.001>
16. Wang J, Feng P, Zhang J, Shen H (2017) Experimental investigation on the effects of thermo-mechanical loading on the vibrational stability during rotary ultrasonic machining. *Mach Sci Technol* 21(2):239–256. <https://doi.org/10.1080/10910344.2017.1283962>
17. Wang J, Feng P, Zhang J, Cai W, Shen H (2017) Investigations on the critical feed rate guaranteeing the effectiveness of rotary ultrasonic machining. *Ultrasonics* 74:81–88. ISSN 0041–624X. <https://doi.org/10.1016/j.ultras.2016.10.003>
18. Kataria R, Kumar J, Pabla B (2017) Ultrasonic machining of WC–Co composite material: experimental investigation and optimization using statistical techniques. *Proc Inst Mech Eng Part B J Eng Manuf* 231(5):867–880. <https://doi.org/10.1177/0954405416629586>
19. Fernando PK, Zhang M, Pei Z (2018) Rotary ultrasonic machining of rocks: an experimental investigation
20. Fernando P, Zhang M, Pei Z, Cong W (2017) Intermittent and continuous rotary ultrasonic machining of K9 glass: an experimental investigation. *J Manuf Mater Process* 1:20. <https://doi.org/10.3390/jmmp1020020>
21. Zou P, Xu Y, He Y et al (2015) Experimental investigation of ultrasonic vibration assisted turning of 304 austenitic stainless steel. *Shock Vibrat* 501:817598
22. Zeng WM, Xu XP, Pei ZJ (2009) Experimental investigation of tool wear in rotary ultrasonic machining of alumina. *Key Eng Mater* 416:182–186. <https://doi.org/10.4028/www.scientific.net/kem.416.182>
23. Wang Q, Pei ZJ, Gao H, Churi NJ, Kang R (2009) Rotary ultrasonic machining of potassium dihydrogen phosphate (KDP) crystal: an experimental investigation. *Int J Mechatron Manuf Syst* 2(4):414–426
24. Wang H, Pei ZJ, Cong W (2020) A feeding-directional cutting force model for end surface grinding of CFRP composites using rotary ultrasonic machining with elliptical ultrasonic vibration. *Int J Mach Tools Manuf* 152:103540. ISSN 0890–6955. <https://doi.org/10.1016/j.ijmachtools.2020.103540>

# Conceptualisation and Modelling of Underwater Remotely Operated Vehicle



Dhruv and Vikas Rastogi

## 1 Introduction

According to the OECD, oceans contribute \$1.5 trillion in value-added to the world economy. There are various resources available underwater that can be tapped. Nowadays, conventional methods of exploring seabeds are being replaced by automated approaches using small-scale AUVs and ROVs for underwater monitoring and surveying. Underwater vehicles can come in many shapes. Torpedo-shaped vehicles minimise surface area and result in a low drag coefficient, as was the case with Minesniper MkII ROV [1]. For smaller scale ROVs, the torpedo design is, however, inefficient with insufficient space for payload. Under strong aquatic currents and heavy payload missions, a stronger control system and an optimised vehicle design are required [2]. A hydrodynamic design similar to that of the KOS ROV and the IES ROV ensures a low drag configuration and symmetry to facilitate robust control while simultaneously having components placed away from the centre of buoyancy and centre of mass which increased stability and has been followed here [3].

Despite being remotely operated, taking power, and telemetry from a tether, automation is still needed, such as position tracking and depth holding. There are various control strategies available to an ROV, like sliding mode control, vision servoing control, PID control, etc. [4–6]. In this paper, we follow PID tuning as a control strategy. A custom connector was designed for underwater connections to detach tether with ease for debugging and troubleshooting [7, 11]. Taking references from both industrial ROVs and student ROVs created for the MATE ROV competition, the design finally obtained is one optimised for a small-scale ROV with robust control capable of being equipped with various manipulators for a variety of tasks [3,

---

Dhruv (✉) · V. Rastogi

Mechanical Engineering Department, Delhi Technological University, Delhi 110042, India

6, 8, 9]. The electrical calculations have been done, taking into account the problem statement posed by one of the MATE ROV competitions for an explorer class vehicle [10].

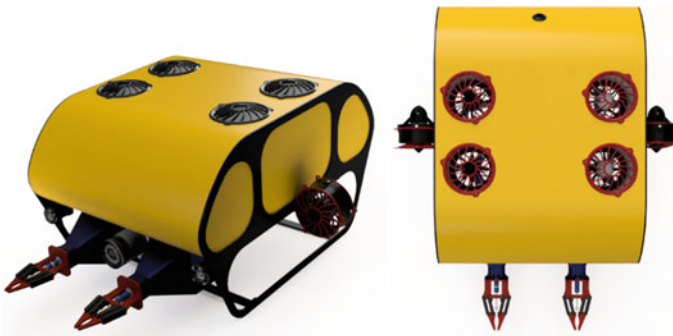
## 2 Design Rationale

All the individual components and subsystems have been engineered and placed to keep the centre of gravity's optimal relative locations and the centre of buoyancy. The ROV has been designed and assembled in *SolidWorks*, following which the simulations were carried out both in *SolidWorks* and *Ansys*. The ROV is positively buoyant, with sufficient restoring torque to orient itself in case of disturbance along with roll motion (Fig. 1).

The system is designed, and the subsystems are placed keeping in mind that the heavier parts are close to the bottom and the lighter ones on the top to keep the centre of gravity below the centre of buoyancy. The magnitude of the buoyant force acting on an object is equal to the fluid's weight displaced by the object, i.e.

$$F_b = \rho g V_f \quad (1)$$

The frame has been modelled, ensuring optimum strength and stiffness, lightweight, ease of construction, maintenance repair, and cost of raw material availability. Rather than designing a frame as a single part, it constitutes multiple parts assembled to serve the frame's purpose. Each piece is made of an aluminium plate machined by a water jet cutting process to produce the required shapes, and custom clamps and fixtures are manufactured using high-precision FDM 3D printing. Latches and L-brackets are used to assemble various systems. The latches are used to increase accessibility and ease in assembly without compromising the joint strength. For optimising weight, the parts were topologically optimised while maintaining sufficient strength to meet the requirements. The frame directly supports all essential systems



**Fig. 1** CAD render for the proposed design of ROV



**Fig. 2** Different parts of the proposed ROV design

like electronic hull, gripper and dropper mechanisms, and camera hulls. The parts have been analyzed structurally in SolidWorks (Fig. 2).

While designing a watertight enclosure, things like least cross-sectional area, use of pressure-resistant shape, and material with high strength to weight ratio are selected. Also to gain the upper hand on the waterproofing front, the vessel was built to open outward rather than inward, allowing us to take advantage of the outside pressure.

## 2.1 Structural Frame

For the structural frame, aluminium alloy 6061 is chosen to make a lightweight structure and provide it with the required strength and rigidity. Since most components require custom assembly brackets and mounts, they are designed considering 3D printing as the manufacturing method. For the watertight enclosure of electronic components, the built dimensions capable of operating at a depth of around 50 m are chosen, which makes it ideal for shallow water applications. For depth rating simulation, pressure vessel software was used, and iterations were performed with varying hydrostatic pressure values with time-dependent depth. Deformation was calculated against the depth value before the tube buckled (Figs. 3 and 4).

$$\text{Hydrostatic pressure}(P) = \rho gh \quad (2)$$

## 2.2 Hydrodynamics

Since the vehicle invests in its run most of the time, it manoeuvres along its surge axis. Hence, the shape of the vehicle chosen for this translational motion is very similar to the ship's streamlined shape. This ensures a smooth and uniform flow of fluid besides the vehicle. The acrylic lid has been given gradual bends about each

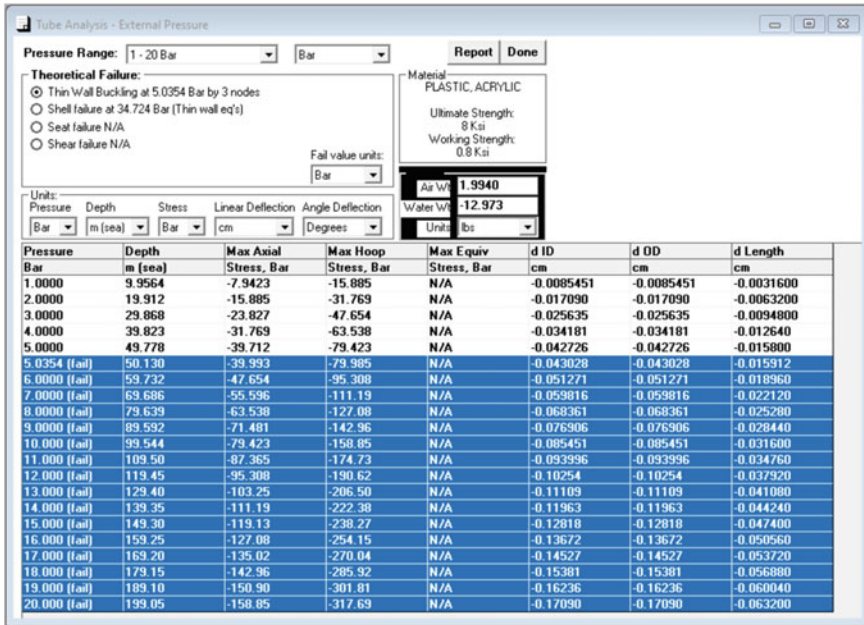


Fig. 3 Tube analysis data

face’s edges to facilitate such flow in other remaining translational motions. This makes the fluid deviate gradually along the frame’s surface, decreasing the pressure developed and eventually minimising the drag force for the respective translational motion. The velocity contours have been shown below for each possible translational motion.

$$Drag = 1/2\rho v^2 AC_d \tag{3}$$

For predicting the value of the drag coefficient with varying velocity and to assess the hydrodynamic performance, a data set has been created of the most traversed motion, which surges for the values of coefficient of drag against varying velocity. This data set has been plotted, and the poly-curve fit technique has been implemented to predict a relation between these two variables. Using the polynomial equation-based relation the drag coefficient at any velocity can be predicted easily without the need to revise the simulations again and again. Figure 5 presents the graph on which the data set has been plotted, and the blue curve depicts the fourth-degree polynomial equation represented as

$$y = 0.16x^4 - 0.62x^3 + 0.9x^2 - 0.55x + 0.65 \tag{4}$$

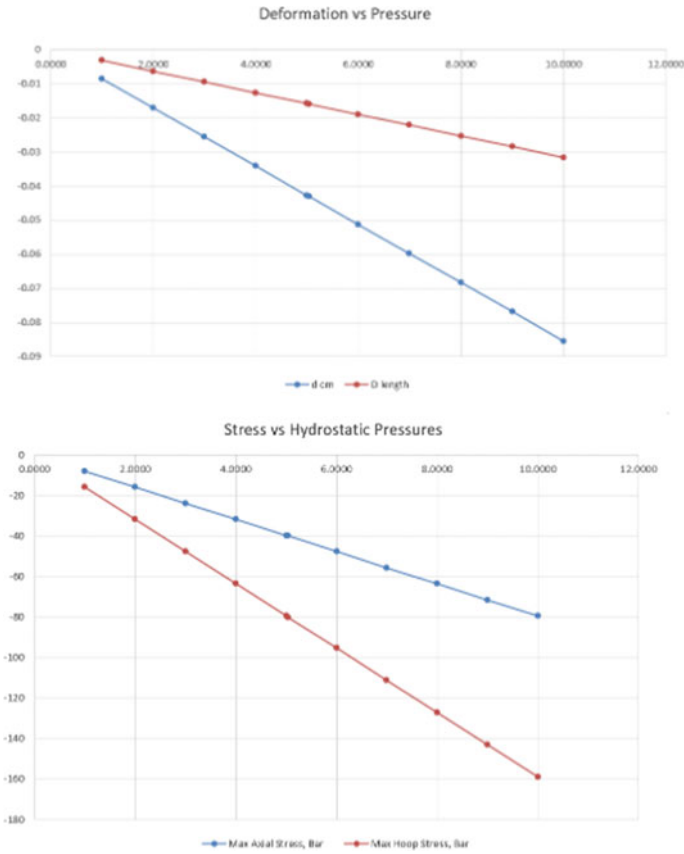


Fig. 4 Deformation and stress curves

### 2.3 Power Connector for Underwater Applications

**Motivation.** Because of the high hydrostatic pressure and corrosive nature of the marine environment, it is difficult to secure reliable electrical connections. IP67 and IP68 connectors have to be used for transmitting electrical signals and power. Therefore, the reliability of the whole system during deployment, lifetime, and maintenance becomes dependent on its connector (Fig. 6).

**Design Considerations.** One has to consider the material properties suitable for the marine environment and the thermal, mechanical, and electrical characteristics required by the connection.

**Material Selection.** The harshness of the operational environment makes it impractical to use copper or brass connectors. Thus, gold-plated 4 mm bullet connectors are used as a power connector for the ROV tether. Acrylonitrile butadiene styrene

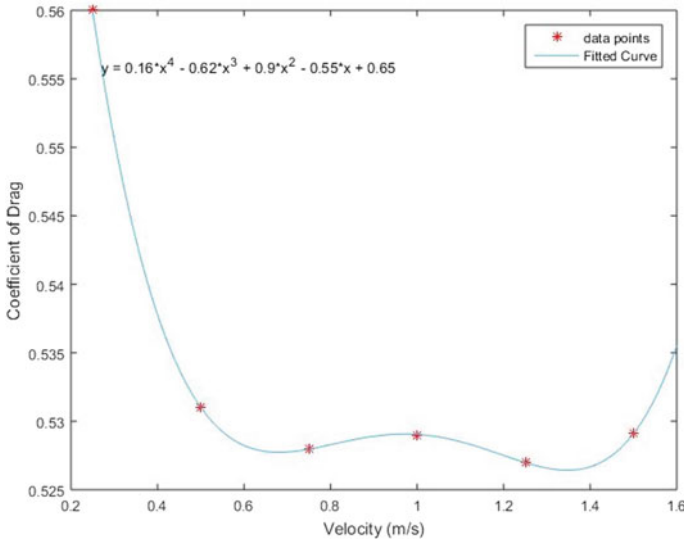


Fig. 5 Coefficient of drag versus velocity plot

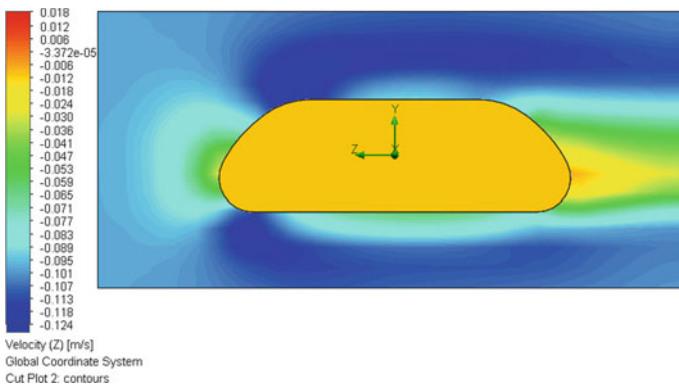


Fig. 6 Velocity contours for acrylic lid

(ABS) is used for the connector’s outer ring. O-rings are used to produce a leakproof plug and socket assembly. To suit shallow water applications, low-pressure O-rings, i.e., least seal hardness, is chosen.

*Selecting a Cost-effective Manufacturing Process.* Fused deposition modelling, a type of additive manufacturing process, is used to manufacture the connector body. The internal structure of FDM is similar to the fibre-reinforced composite structure, with vertically stacked cross-sections of polymer.

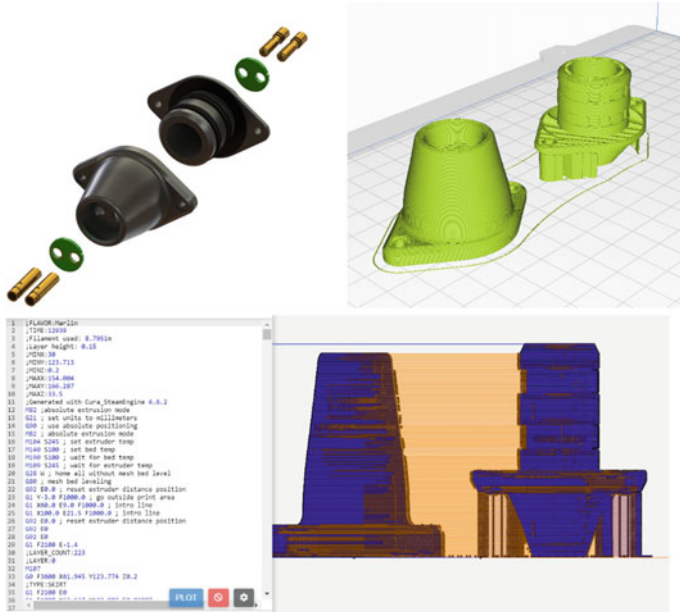


Fig. 7 Watertight connector design and analysis

*Fabrication.* The connector was designed in *SolidWorks*. G-codes were prepared in *Ultimaker-Cura* and simulated on *Autodesk Netfabb*. Metal pins or bullet connectors were soldered on a custom-designed PCB and assembled with the rest of the body. Marine-grade epoxy resin was used to seal the bullet connectors inside the plastic body. The issue with 3D printing a waterproof connector is that since the part is produced by a continuous stacking of polymer layers, the resultant parts are highly porous. The connector body was post-processed to tackle the issue by treating it with Acetone ( $C_3H_6O$ ) vapours, which melts the surface layers and thus produces a shiny surface finish and fill up the air gaps properly (Fig. 7).

### 3 Embedded and Controls System

#### 3.1 Power Distribution Unit

The main power is supplied to the ROV via 12 AWG silicone wires. The two output wires are routed into the ROV to the power distribution board via the tether.

**Power Distribution Board.** A PCB was designed and manufactured for voltage conversion from 48 to 12 V and power distribution. The PDB has three outputs: outputs for ESCs, outputs for DC/servo motors, and outputs for the USB hub. The

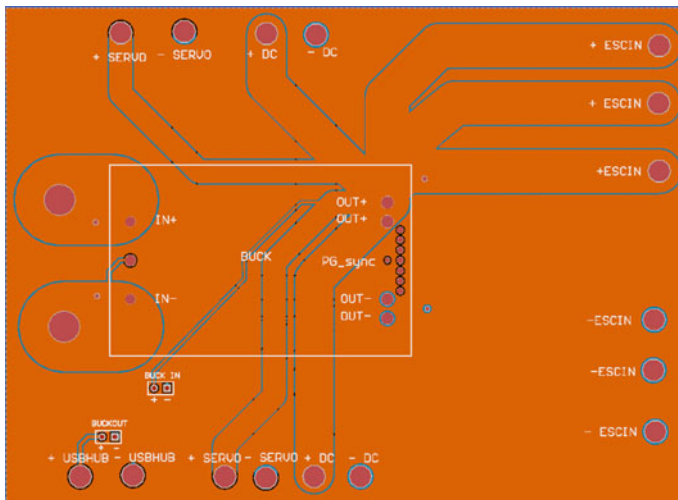


three outputs for ESCs from the PDB are fed into the custom-designed Arduino Mega Shield, on which the input 12 V power is split into six outputs for six ESCs. The USB hub powers Arduino Mega and the cameras. The trace widths were chosen using the IPC recommended trace width chart (Fig. 8 and Table 1).

$$P_{Tot} = \sum (V_{Load} I_{Drawn} N) \tag{7}$$

$$P_{Tot} = (72) \times 6 + 3 + 0.00625 + (48) \times 2 + (15.54) \times 3 + 0.0015 \tag{7}$$

$$P_{Tot} = 577.63 \text{ W} \tag{8}$$



**Fig. 8** Schematic for power distribution board

**Table 1** Current and voltage readings of various components

Component name	Current rating (Amp)	Voltage rating (V)	Power required (W)	Current drawn
T200 thruster	6A	12	72	6A
Arduino mega	0.6A	5	3	0.25A
Pressure sensor	1.25 mA	5	0.00625	0.00052A
Servo motor HS100WP	4A	12	48	4A
Servo motor HS5646WP	2.1A	7.4	15.54	2.1A

### 3.2 Control System

**Microcontroller.** Arduino MEGA (2560) 32-bit was used because it is relatively fast and has several serial communication (UART) ports to communicate with several devices at once. A custom Arduino Mega shield was designed to mount the Arduino and attach all the sensors to it. It is connected with different components like the RS485 communication board, the logic level converter (I2C) for a pressure sensor, six ESCs and IMU. It also has power outputs to run six Blue Robotics T200 thrusters. At the surface, a Red-gear gaming controller is connected to the laptop. This controller serves as the entire control unit for the ROV. It is connected with an Arduino UNO board and gives the commands to the ROV via RS485 communication (Figs. 9 and 10).

**Proportional Integral Derivative Controls.** For stability, PID is used for depth. The BlueRobotics Bar30 pressure sensor, connected to the Arduino is used for depth sensing. The PID controller is tuned via the Ziegler-Nichols method.

$$U(s) = [K_p + K_i/s + sK_d] * E(s) \tag{9}$$

where  $U(s)$  is the output signal,  $E(s)$  is the error signal, and  $K_p$ ,  $K_i$ , and  $K_d$  are the constants for each of the three terms.

**Manipulators.** Our ROV has two grippers. Two of the servo motors are used in a gear-based claw, while the other two are used for a direct motor-controlled arm.

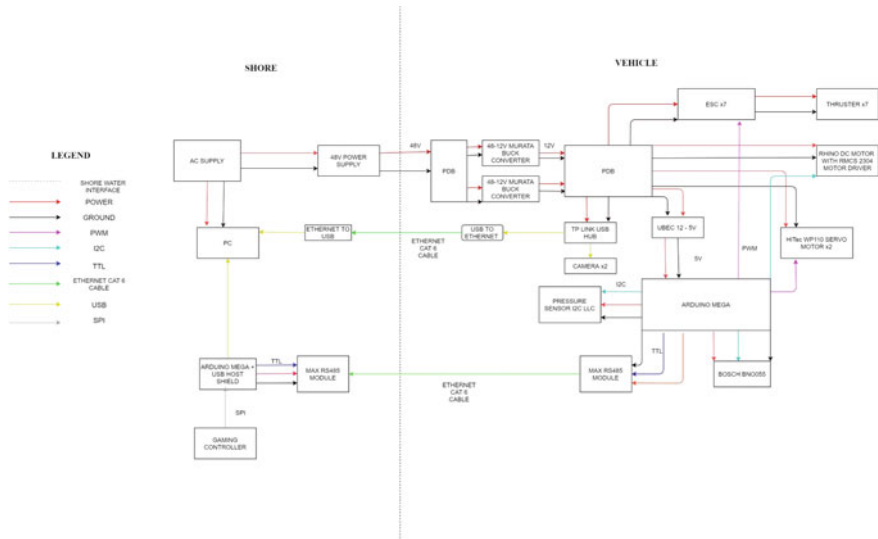
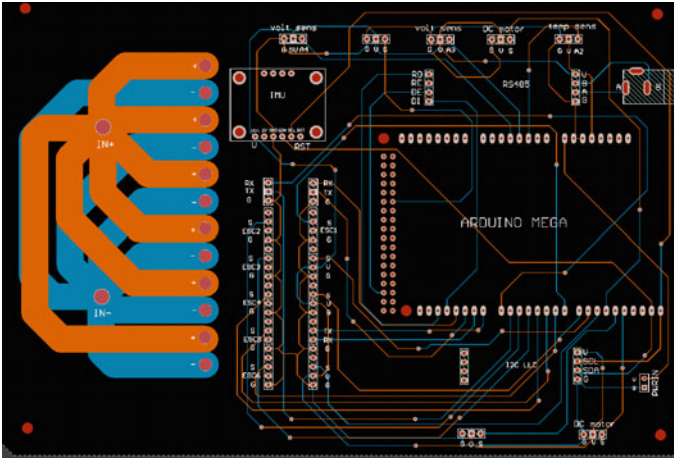


Fig. 9 ROV control stack



**Fig. 10** Proposed schematic for controller shield

In the vehicle, HS1100WP and HS5646WP servos were used, both rated IP67 waterproofing.

**Power loss.**

Resistance of 4 mm copper wires = 4.3  $\Omega$ /km.

Total length of tether = 15 m  $\times$  2.

Total resistance of power cables = 4.3 \* 30/1000 = 0.129 Ohms.

Total power requirement = 577.63 W

$$\text{Total current requirement} = 577.63/48 = 12.033 \text{ A} \quad (10)$$

$$\text{Voltage drop at maximum current (25A)} = IR = 0.129 * 12.033 = 1.552 \text{ V} \quad (11)$$

$$\text{Power loss at maximum current (25A)} = I^2R = 12.033 * 12.033 * 0.129 = 18.678 \quad (12)$$

$$\text{Minimum voltage at ROV} = 46.448 \text{ V} \quad (13)$$

$$\text{The power efficiency of cable (E)} = (P_{\text{tot}} - P_{\text{loss}})/P_{\text{tot}} = 96.766\% \quad (14)$$

**Table 2** Technical specifications of vehicle

Coefficient of drag	0.5275–0.56
Depth rating	50 m
Total power consumption	577.63 W
Power efficiency of cable	96.766%
Internal surge current	75.83 A
Voltage drop across tether	1.552 V
Power loss in tether	18.678 W

### 3.3 Sensors

**Pressure sensor.** The Bar30 pressure sensor is used to determine the depth at which the vehicle must operate. It employs piezo-resistive semiconductor gel and a sensor interface IC. It has a pressure resolution of 0.2 mbar and a depth resolution of 2 mm.

## 4 Results

As discussed above, the paper’s objective is to find the parameters for the development of an underwater ROV model. It has been found that the results are consistent with the simulation conditions. The vehicle’s CFD analysis was done and the velocity contours were drawn with the coefficient of drag vs velocity graph being plotted. The Cd value varies from 0.56 to 0.5275 at different velocities. The maximum power consumption was calculated and the tether efficiency was evaluated and came out to be 96.766%.

The underwater connectors prepared were fabricated and extensively tested at depth for an extended amount of time. Stress analysis for waterproof enclosure was carried out and a reliable depth rating of 50 m was obtained. The result was a hydrodynamic and statically stable vehicle capable of being equipped with different payloads for different mission requirements (Table 2).

## 5 Conclusion

The six degrees of freedom model of an underwater remotely operated vehicle has been successfully created considering the required parameters and design considerations. The model was simulated using multiple simulation tools for reliable results. The conceptual designs in this paper can be produced physically and implemented for a range of applications. The watertight connector’s proposed design was developed and tested for many hours, and it functioned well without any fail. It has the potential to be expanded to support the different forms of cables to allow for quick

separation of tether and vehicle. The design allowed for robust depth control and smooth surge operations allowing the vehicle to grip and release with much ease. The final product was a cost-effective solution to resolve underwater problems at a low depth. However, there is further scope of research on this design based on functional and efficiency parameters and using physical scaled models under actual conditions.

## References

1. Refsnes JE, Sorensen AJ (2004) Design of control system of torpedo-shaped ROV with experimental results. *Oceans' 04 MTS/IEEE Techno-Ocean'04* (IEEE Cat. No. 04CH37600), vol 1. IEEE, pp 264–270
2. Gomes R, Borges Sousa J, Pereira L (2003) Modelling and control of the IES project ROT. In: *Proceedings of the European control conference*. Cambridge, VK
3. Gomes RM, Martins A, Sousa A, Sousa JB, Fraga SL, Pereira FL (2005) A new ROV design: issues on low drag and mechanical symmetry. In: *Europe oceans*, vol 2. IEEE, pp 957–962
4. García-Valdovinos LG, Salgado-Jiménez T, Bandala-Sánchez M, Nava-Balanzar L, Hernández-Alvarado R, Cruz-Ledesma JA (2014) Modelling, design and robust control of a remotely operated underwater vehicle. *Int J Adv Robot Syst* 11(1):1
5. Vossoughi GR, Meghdari A, Borhan H (2004) Dynamic modeling and robust control of an underwater ROV equipped with a robotic manipulator arm. In: *Proceedings*, pp 19–21
6. Ahern AM, Gillig RP, Julius J, Walker W (2017) The systems and design philosophy of mosquito 2.0. In: *Proceedings of the wisconsin space conference*, vol 1, No 1
7. Wang G, Zhou JQ, Zhao YT, Feng J, Sun Q (2021) Performance degradation modeling and reliability analysis of aviation connectors in marine environment. In: *IOP conference series: materials science and engineering*, vol 1043, No 3. IOP Publishing, p 032029
8. Natu A, Garg V, Gaur P, Raj P, Dhruv SS, Biswas U, Bansal et al D, Design and Development of an Autonomous Underwater Vehicle VARUNA 2.0
9. Brundage HM, Cooney L, Huo E, Lichter H, Oyebode O, Sinha P, Stanway MJ, Stefanov-Wagner T, Stiehl K, Walker D (2006) Design of an ROV to compete in the 5th annual MATE ROV competition and beyond. In: *Oceans*. IEEE, pp 1–5
10. Sani MI, Siregar S, Kurnia MM, Hasbialloh D (2019) An electrical power control system for explorer-class remotely Operated Underwater Vehicle (ROV). *TELKOMNIKA Telecommun Comput Electron Control* 17(2):928–936
11. Painter H, Flynn J (2006) Current and future wet-mate connector technology developments for scientific seabed observatory applications. IEEE, pp 1–6

# Design and Performance of Plate-Fin Heat Exchanger: A Brief Review



Vivek M. Korde, Gauri S. Gotmare, Priya K. Kachhwah,  
and Divyanshu Lokhande

## Nomenclature

$Re_H$	Reynolds number based on height
$f$	Friction factor
$A_c$	Minimum free flow area, $m^2$
$Da$	Darcy number, $K/H^2$
$L$	Length of porous fin, m
$H$	Height of channel, m
$A_0$	Total heat transfer surface area of porous fin, $m^2$
$j^*$	Modified j factor
$s$	Flow maldistribution parameters
$h$	Velocity ratio
$j$	Colburn factor
CFD	Computational fluid Dynamics
$Re$	Reynolds number
$h$	Fin height, m
$s$	Fin spacing, mm
$A$	Wave amplitude, mm
$L$	Fin wavelength, m
VG	Vortex generator
CFU	Common flow up
EG	Ethylene glycol
$Nu$	Nussult number
$JF_i$	Thermal Hydraulic performance Factor
$\Phi$	Nanoparticles weight fraction

---

V. M. Korde · G. S. Gotmare (✉) · P. K. Kachhwah · D. Lokhande  
Department of Mechanical Engineering, Yeshwantrao Chavan College of Engineering, Nagpur  
441110, India

Pr	Prandtl number
$\mu_w$	Wall fluid viscosity
$\mu_m$	Average fluid viscosity
l	Lance length of fin, m
t	Thickness, m
s	Fin spacing, m
H	Height of fin, m
HTE	Heat transfer enhancement
PPF	Plain plate fin
JF	Thermal hydraulic performance factor
R	Humped radii
$\epsilon$ NTU	Effective number of transfer units
s1	Non-louvered inlet and exit
s2	Redirection length of fin
Kc	Total heat transfer coefficient of cold fluid
CFD	Common flow down
IRW	Inline row winglet
SRW	Staggered rows of winglets
PFHE	Plate-fin heat exchanger
WFP	Wavy plate fins
E	Friction power per unit surface area, w/m <sup>2</sup>
$E\beta$	Core Volume Goodness Index
$\eta_{aha\beta}$	Friction power
$\eta_a$	Overall surface efficiency
$h_a$	Coefficient of heat transfer at air side ,wm <sup>2</sup> °c
$F_p$	Fin pitch, mm
$D_e$	Hydraulic diameter
$F_h$	Fin height, m
t	Thickness of fin, m
h	Coefficient of heat transfer , wm <sup>2</sup> °c
$\Delta P$	Pressure drop
$\theta$	Crease angle
$\lambda$	Crease cycles

## 1 Introduction

Heat exchangers with plate fins are a form of heat exchangers that is small and compact in which the surface area of heat transfer is increased by extending metal surfaces known as fins. Plate-fin heat exchangers are distinguished by their high efficiency, compactness, lightweight, and moderate price. The plate-fin heat exchanger is suitable for gas–liquid, gas–gas, and multi-phase applications across a broad variety

of temperatures and pressures. They are primarily used in the field of air separation and liquefaction, the refining and liquefaction of natural gas, petrochemicals manufacturing, and massive cooling systems.

The heat exchangers with plate and fins are primarily used for applications such as gas to gas and liquid to gas. Extended surfaces are preferred in such heat exchange systems because of the low coefficient in gas flows. Additionally, the coefficient of heat transmission can be improved by employing specially configured extended surfaces which have a significantly higher thermal transfer coefficient than extended surfaces, the pressure drop penalties are high as well, but are not sufficiently extreme to mitigate.

## 2 Performance Enhancement of Plate-Fin Heat Exchanger

Kang et al. [1] determined the heat transfer properties of 12 cores with three rows and four different fin configurations. The four fin designs used in the experiment were a slotted plain, plate plain, wavy-fin having a sinusoidal section, and wavy-fin having a triangular section. The heat transmission and pressure loss properties of four fin configurations are compared using the factor for friction ( $f$ ) and Nusselt number curves. For identical fin spacing in the Reynolds number range evaluated, the slotted fin cores have the maximum factor for friction ( $f$ ) and Nusselt number, while the plain plate-fin core has a minimum factor for friction ( $f$ ) and Nusselt number, while the factor for friction ( $f$ ) and Nusselt number of the fin (wavy) cores of two types are similar, according to the experimental results. For the investigation of the influence of a porous fin in a simplified PFHE model, Kim et al. [2] conducted an experimental examination employing six porous fins of varied permeability and porosities fabricated of aluminium alloy. When Reynolds numbers are low, the louvred fin has a somewhat greater friction factor than the porous. Porous fins have far higher friction factors than louvred fins at higher Reynolds numbers. Correlations for the porous fins for the friction and heat transfer was developed by using the Darcy number ( $Da$ ) as well as geometrical features like  $A_c/A_o$  and  $L/H$ .

Friction factors for porous fins are correlated.

$$f = \frac{2}{Re_H} \frac{A_c}{A_o} \frac{L}{H} + \frac{0.21}{Da^{1/2}} \frac{A_c}{A_o} \frac{L}{H} \quad (1)$$

Modified j-factor correlation

$$j^* = 13.73(Re_H^{-0.489} Da^{0.451}) \quad (2)$$

Wen et al. [3] Zhang has presented the results of numerical and experimental research to demonstrate that fluid maldistribution efficiency has deteriorated in traditional entrances, whereas a better configuration with pierced baffles can improve performance both radially and axially. Then there is the small hole baffle. The best



choice for change is to space it out in a staggered manner. When the right length baffle is chosen, the holes are staggered and the punched ratio slowly rises from the central axis, lowering the ratio of velocity and parameter  $S$  for flow maldistribution. Sheik Ismail et al. [4] examine the impact of the different fin constraints and build a correlation between non-dimensional quantities like the Fanning factor for friction ( $f$ ) and the Colburn  $j$  factor geometrical parameters, and flow parameters. To assess the thermohydraulic parameters, a CFD strategy was used for numerical analysis of various fin configurations. The findings include a look at flow dynamics in laminar and turbulent regimes, as well as data validation. The wavy fins, except for the offset fins, do not have a generalized correlation in terms of the influence of the  $f$  and  $j$  variables on geometrical parameters. The evolution of the  $j$  and  $f$  relation for wavy fins is examined in this work. To create the correlation, a CFD analysis was performed with fluent software which produced design data for 18 different fin geometries. The power-law expressions were then used to create general pressure drop and heat transfer correlation. De Schampheleire et al. [5] looked at the impact of non-uniformities on a plate water/air heat exchanger's thermal efficiency that is commercially available in the wind tunnel by taking three different non-uniform flow conditions. 2D hotwire tests are used to verify the wind tunnel's uniformity. Three non-uniformities are produced when a plate is placed 10 cm above the exchanger; one is for the exchanger's right side, the upper half portion of the heat exchanger is covered by the second, and the third obstacle is a circular void in the centre of the plate with a diameter of 150 mm. CFD tools are further used to implement the above cases. Two obstructions occupy half of the overall flow area, occupying the vertical or horizontal halves of the heat exchanger, respectively. A circular hole is the most extreme obstacle, covering 78% of the overall flow space. A major thermal effect is not generated by obstructions that cover 50% of the total flow area. Because of the obstruction's minor effect, this is the case. Because the rise in the local velocity of air is minimal, the coefficient of convection rises dramatically, allowing a constant rate of heat transfer to be maintained. To increase the transfer of heat in a PFHE, Sinha et al. [6] used vortex generators of winglet type with two rows. Jeong et al. [7] presented a study for the development of a new PFHE shape in which holes and creases were provided to boost heat exchanger efficiency which is utilized where there is a lot of dust. The overall performance was calculated with the help of the volume along with factors for area goodness. The PFHE's innovative shape is compared to the heat exchanger with louvre fin and PFHE for the phenomena of flow and heat on the surface for heat transfer. A novel PFHE form with the optimum shape of holes and creases provided at the fin that can improve the PFHE's heat transmission and reduce the drop of pressure can be designed. According to the numerical analysis results and the thermal flow field optimization for the surrounding PFHE, increasing the crease angle improves the factor for the volume goodness while lowering the factor for the area goodness. Aliabadi et al. [8] create correlations for drop in pressure and heat transmission for wavy PFHE employing water, air, and ethylene glycol as operating fluids (PFHEs). Other prototypes with various geometric properties should be studied to demonstrate general characteristics. The current thesis is separated into three sections: a complete 3D simulation of wavy plate fins (WPFs) with

enough validation; a sufficient description of the simulation work; and the introduction of new PFHE-WPF correlations. Simulation findings are compared and tested against usable experimental evidence, and a satisfactory agreement is achieved. The variances of the  $j$  and  $f$  factors are 9.07 and 3.74%, respectively, among numerical conclusions and experiment data. The usefulness of geometric parameters, fin thickness, length, height and pitch, wavelength width, and amplitude was defined in the literature for output and level of the WPF. To devise the simulation work, the Taguchi approach is used. Finally, the geometrical parameters, Reynolds and Prandtl number are proposed as functions of the current  $f$  and  $j$  factor associations built on the simulation performance. The correlations for air presented and the data available are in agreement, with 95% of the experimental data associated within 712%. Junji et al. [9] perform an experimental investigation on a PFHE with aluminum wavy fins. There are 16 distinct fin heights, pitches, distances, wavy amplitudes, and lengths among the experimental samples. The multiple regression techniques are utilized to establish correlations between the wavy fine for heat transmission and pressure loss. The Taguchi approach is used to do a parametric analysis of the results of wavy fins. The experimental link between friction factor and heat transfer is developed, capable of predicting 90% of the data in the test with 15% of errors. The absolute divergence of the friction factor and Nusselt number association equations is 7.6% and 7.8% correspondingly. The quality management approach with Taguchi is used for the investigation of the impact of each element on a drop in pressure and transmission of heat. The most significant effect on thermal-hydraulic efficiency, with a contribution ratio of 38.7% has been demonstrated to be the wavy amplitude/length ( $2A/L$ ) geometrical parameter. The thermal-hydraulic efficiency is much better with a low fin length and fin pitch. Khoshvaght Aliabadi [10] performed a comparative analysis of the efficiency of a PFHE with dissimilar plate-fin channels and working fluid as water. Plain, offset strip, pin plate-fin channels, louvred perforated, wavy, and VG are fabricated and evaluated. To assess the efficiency of the PFHE using different channels, various performance assessment parameters are used, including the  $ji/fi$  1/3 ratio, the thermohydraulic factor of performance,  $J-Fi$ , the  $Ai/A$  plain and VG-I criterion. The pin, offset strip, vortex generator, wavy, louvred, plain channels, and perforated, respectively, have the highest  $j$  factor and coefficient of heat transfer. The pin, offset strip, vortex generator, wavy, louvred, plain channels, and perforated, respectively, provide better heat transfer with pressure drop from the  $ji/fi$  1/3 ratio viewpoint. The pin, offset strip, VG, louvred, lock, plain channels, wavy and perforated, respectively, have a decent thermohydraulics output and the maximum value of  $JFi$  factor as compared to plain channels. In contrast to the vortex generator, wavy fin, pin channels, perforated fin, offset strip, and louvred have the greatest capacity to minimize the surface area of PFHE. Aliabadi [11] investigated the effects of two different passive techniques of enhancement, the nanofluid flow, and the VG on the thermal and hydraulic performance of PFHE individually and simultaneously. It was shown that both the passive techniques can individually enhance thermohydraulic performance. The lowest weight-fraction nanofluids gives the best performance both individually and combined with VG channels. The thermal-hydraulic performance was enhanced by about 64.3% with the use of the vortex generator channel in its

place of plain one as it rises the coefficient of heat transmission as well as the drop in pressure. The performance enhancement of PFHE by use of the VG channel is more significant than the nanofluid. The correlations were presented for evaluation of factor for friction ( $f$ ) and Nusselt number for the combined passive technique.

$$f = 0.3586\text{Re}^{-0.150}(1 - \Phi)^{-24.644} \quad (3)$$

$$\text{Nu} = 0.3141\text{Re}^{0.037} \text{Pr}^{0.705} (1 - \Phi)^{-15.393} \quad (4)$$

$$1850 < \text{Re} < 4560, 5.1 < \text{Pr} < 6.3, \Phi < 0.4\%$$

Du et al. [12] performed numerical simulation and an experiment to study the thermohydraulic characteristics for the exchanger with offset PFHE having double-flow oil-air for cooling lubricating oil. To explain the flow characteristics and heat transfer, correlations were established. The  $j$  and  $f$  factors experimental correlations were established. The suggested correlations for the oil side had a strong prognostic potential against the current results, predicting 95% of research data and having less than 3% of the average variance for  $j$  factor.

$$\text{oil side : } j = 0.2899 \cdot \text{Re}^{-0.604} \left( \frac{\mu_w}{\mu_m} \right)^{-0.14} \quad (5)$$

$$f = 11.45 \cdot \text{Re}^{-0.6975} \left( \frac{\mu_w}{\mu_m} \right)^{-0.14} \quad (6)$$

$$\text{Air side : } j = 0.0388 \cdot \text{Re}^{-0.1932} \quad (7)$$

$$f = 3.8266 \cdot \text{Re}^{-0.5253}$$

Kuchhadiyaa et al. [13] experimented to determine the thermal characteristics of cross-flow PFHE having fin of offset strip. Experiments were conducted for the determination of the thermohydraulic efficiency of the exchanger at distinct input parameters and mass flow rates such as cold and hot fluid inlet temperatures. The difference in per cent amid coefficient of heat transmission values derived through the experiments conducted and those proposed in the literature ranges from 5.24% to 5.82% for hot fluid and 2.59% to 6.76% for cold fluid. Praveen kumara et al. [14] designed a rectangular fin having different grooves such as trapezoidal, rectangular, semi-circular, and triangular, analysed and compared for its heat transfer performance. Rectangular grooves on the fin will provide a higher rate of heat transmission of about 30% in contrast to other grooves. The numerous grooves on the fins allowed for greater heat transfer than other types of fins with the same geometry, ranging from 13 to 30%. Grooves are used to maximize the fin's surface area. More surface area allows more fluid interaction, which means faster heat transfer from the root.

Rectangular grooved fins were observed to have improved efficacy and heat transfer than other grooves of the same dimensions added to the finned body. Grooves on the fin can be used as a way to minimize the weight of the material, which lowers the expense of producing the fin. Khoshvaght-Aliabadi et al. [15] studied the impacts of various three passive HTE approaches related to the flow needs and WPF heat transmission: winglets, perforations, and nanofluids. Two improved WPFs (winged and perforated WPFs), in addition to two different boosted coolants (0.3% and 0.1% Al<sub>2</sub>O<sub>3</sub> and water nanofluids), are utilized for enhancing the efficiency and reducing the extent of PFHE. It is observed that the Nusselt number for the PPF is less than WPFs, and it attempts to strengthen by improving the aspect ratio of waviness. The factor of friction ( $f$ ) for the plain plate fin (PPF) is less than WPFs. Lastly, it indicates the techniques of projected HTE may be better than the distinctive WPFs. Ozturk et al. [16] accomplished a numerical investigation to determine the effect of fins on the efficiency of a compact heat exchanger using the CFD programmed FLUENT. The tests are carried out for simple, louvred, and offset fin forms in 2D models of the determined cases. Concerning changing velocities, the findings for the coefficient of heat transfer, drop in pressure, Colburn  $J$  and friction factors  $f$  are summarized. The results are shown for different fin pitches to see how they affect heat exchanger efficiency. As the frontal velocity is increased, both the friction factor and the Colburn  $J$ -factor decrease. Juan et al. [17] presented a numerical model for the research on the distribution of the flow of the impacts of dynamic viscosity and inlets and outlets tube situations. As the fluid viscosity was increased, it was observed that the distribution of flow increased more uniformly but the pressure declines at the same time. In porous media of PFHE, as the resistance (viscous) is improved, the influence of the  $Re$  on the distribution of flow was also reduced. When the number of Reynolds was about 1000, the analytical findings showed that the procedure proposed would considerably improve the oil flow distribution by about 79%. Xilong et al. [18] investigate the heat transmission and fluid flow characteristics of fins (wavy and humped) with varied radii of the hump and reusing experimental and computational methods. In the process of recirculation using the humped fin, valley phenomena are eliminated for either turbulent or laminar flows. As compared to the triangular fin pattern, where high temperatures are uniformly distributed, the temperature fields close to the peak and valley zones for the humped fin pattern were found to be increased. Javaherdeh et al. [19] used the  $\varepsilon$ -NTU technique to evaluate the features of pressure drop and heat transmission for a louvred fin exchanger having varied geometric constraints of louvred fins. It was found that when the louvred angle increases simultaneously the flow speed also increases which increases heat transmission and pressure drop. As the louvred pitch increases simultaneously the louvred number is decreasing, affecting the increase in pressure loss and heat transmission. The optimal value for non-louvred outlet and inlet length is  $S1 = 1.25$  mm and  $S2 = 2.5$  mm as the redirection length of a fin. Samadifar and Toghraie [20] analysed the heat transfer enhancement in PFHE utilizing a passive method of adding six different vortex generators on a triangular channel cross-section, using a finite volume method. A finite volume method of analysis reveals that a rectangular vortex generator can increase the heat transfer performance by 7% with a 45° angle of attack. Yang et al. [21]

used R113 refrigerant as the working fluid to examine the fluid friction and heat transmission in vertical channels which are heated on a single side with serrated, perforated, and plain fins. The  $j$  factor (Colburn factor) for the serrated fin is found 20% lesser as compared to the Manglik and Bergles results from correlation, whereas the friction factor  $f$  shows similar results as Manglik and Bergles expression values having a comparative error of 10%. The performance assessment criterion  $j/f$ ,  $j/f^{1/3}$ , and  $j/f^{1/2}$  of the serrated fin are the finest amid these fin geometries under current experimentation. Furthermore, the data obtained of serrated, plain, and perforated fins are extremely valuable for designing and optimizing the PFHE. Fumin et al. [22] presented a method to enhance the heat transmission efficiency of the exchanger by upgrading the heat exchanger's interior structure to solve the problem of high oil temperature in a certain engineering machinery transmission device, enabling the machine to operate in the normal temperature range. Based on the study of the impact factor of the cold fluid passage coefficient of heat transfer  $K_c$ , it is found that increasing the cross-sectional area  $A_c$  of the cold fluid passage may effectually raise the coefficient of heat transmission  $K_c$  of the cold fluid passage, which is useful for heat exchanger structure optimization in engineering. Morteza et al. [23] examined the thermohydraulic properties of a PFHE providing chevron plate fins in the turbulent flow regime ( $4000 < Re < 10,000$ ), and experimental investigation is performed at three different aspect ratios of waviness and four types of winglet with holes arrangements with a fixed hole diameter, and width or height of winglets are features of the enhanced heat transfer in chevron plate fins. The new inquiry is motivated by the possibility of using winglets and holes in chevron plates at the same time. The  $Al_2O_3-H_2O$  nanofluid flow is evaluated on the basis of an optimum geometric parameter of improved chevron plate fine as the next passive technique. Thus the combination of holes and winglets has a direct impact on the efficiency of chevron plate fins, resulting in significant improvement in a drop in pressure and heat transfer. Furthermore, using the optimally improved chevron plate fins and nanofluid at the same time could increase the Nusselt number. At a weight fraction of 0.3%, the nanofluid exhibits the strongest operating conditions of this device. Ma'arof et al. [24] examines the effects of different fin designs arrangements, the total surface area of fins, and surface condition on the degree of heat transfer by fabricating and testing fin heat exchangers. The HTR was found to be impaired by modifying the structure and condition of the fins. The configuration of the fin was found to be one of the utmost vital factors influencing the fin heat exchanger efficiency. At all fan speeds, the fin coating was found to reduce the temperature by a much greater margin. Haoa et al. [25] established the thermal current approach, which merged heat exchanger thermal resistance with traditional heat exchange correlations, to get a global remedy for the modelling and evaluation of heat exchangers with offset strip fin having cross-flow arrangement. Improving the thermohydraulic efficiency of compacted exchangers is vital for highly efficient IC engines or hybrid fuel cell cars. They employed the tree traversal procedure to maximize and achieve the new thickness, breadth, and height while maintaining the limits on the transfer of heat and flow resistance. The modified heat exchanger's airflow length is reduced by 21% from 140 to 110 mm as compared to the original structure. Meanwhile, the thermal resistance decreases by

nearly 1.8%, suggesting improved heat transfer efficiency. Consequently, the experimental validation allows for a comparison of experimental and theoretical findings, demonstrating that with a modest inaccuracy of not more than 3.23%, the thermal current technique is suitable for the design of heat exchangers and performance enhancement. Also, the investigational findings demonstrate that the overall coefficient of heat transmission rises by nearly 7.43% and reduction in pressure drop on the airside decreases by almost 29.7%. Jiaming et al. [26] perform a numerical simulation of a PFHE with an oblique wavy surface having V-shaped to enhance the thermohydraulic characteristics. The effects of the V shape's pointing direction, angle of obliquity, and wave amplitude are fully investigated to determine the geometry that provides the best thermal performance. At the same Reynolds number, it has been determined that the heat exchanger with V shapes representing downflow offers low  $f$  and  $j$  values, however, greater  $j/f$  compared to V shapes indicating up the flow. As a result, the flow pattern induced by the wavy oblique surface is the primary cause of the enhanced transfer of heat in the heat exchanger with oblique wavy surfaces having V-shaped. A large secondary flow often results in a large pressure loss. Ozturk [27] carried out the experimentation to improve the performance in a commercial refrigerator by using plate fin. Three various types of fins were investigated having single and double intermediate, and mini channel flat tube having a constant frontal area and a very narrow flow depth. To evaluate the prominence of the type of fin on the performance, the factor which is defined by heat transfer such as volume goodness factors,  $j$  and  $f$  factors, core volume goodness index ( $E\beta$ ) versus factor which is defined by friction power ( $\eta$  aka  $\beta$ ) are used. Kuldip et al. [28] provide a detailed analysis of louvred-fin heat exchangers to better acknowledge the flow characteristics and various structural parameters impacts. It was mentioned that the growth of the boundary layer is disrupted by louvred fins, which increases the thermohydraulic characteristics of the louvred fin heat exchanger. Thermal efficiency can be improved by increasing louvre height and length, however, resistance can also be increased. A larger depth of flow has a significant impact on pressure loss and the compactness of the exchanger. In comparison to a PFHE, a louvred fin exchanger is projected to increase heat transmission by 25% while decreasing pressure by 110%.

### 3 Research Gap

This review has discussed some of the latest areas regarding PFHE. Substantial scope for the research work is exposed in this field as mentioned below:

- The use of nanofluids and nanomaterials is the latest emerging field where more research is necessary while designing the PFHE [29].
- New techniques should be searched to reduce the fouling in PFHE, especially when they are used in food processing [29].

- High operational cost is paid to overcome the critical corrosion problems in industries where PFHE are used to severe process conditions, hence this is the area where the research should be focused [29].
- More generalized heat transfers and correlations of pressure drop are required for the thermal–hydraulic calculations, and the suitable optimization in design methodologies of the plate type heat exchanger is required to be focused on while improving the efficiency of the design model [30].
- The investigations for appropriate Nusselt number for two-phase and the correlations for friction factors for various configurations and types of fins will serve a great help in obtaining the proper optimization methodology of plate-type heat exchanger design with phase change [30].
- Augmentation of the heat transmission processes in increasing the air-side heat transmission efficiency of the heat exchanger such as perforation, serration, and breaking technology regarding fins should be investigated in-depth [31].

## 4 Conclusion

This study aims to provide an overview of the numerical and experimental investigations that have been conducted on PFHE. The review is concentrated on the passive method's ability to improve heat transmission. The following are the findings of this study:

- Both the passive techniques, use of nanofluids (low weight fraction) and the VG channel might contribute to more compact PFHEs being designed. The increase in thermal–hydraulic performance of about 1.67 times can be obtained by combining the two improvement approaches for the thermal exchange. The perforations, winglets, and nanofluids enhance thermal performance. In the compound approach (Cu/water nanofluid in the VG channel), the thermal–hydraulic efficiency factor increase compared with the plain channel is 67.4%.
- The CHX where the fin is required to enhance the performance in a narrow flow depth range, especially where the compactness is considered, louvre fin with single intermediate is the best and achieves better heat transfer indexes than the other fin geometries. Thus, for such types of PFHEs, the combined effect of conventional parameters and factors ( $h$ ,  $\Delta P$ ,  $j$ ,  $f$ , and  $j/f^{1/3}$ ) and the rarely chosen factors ( $\eta_a$ ,  $h_a\beta$ ,  $E\beta$ ,  $\eta_a h_a \gamma$ , and  $E\gamma$ ) that consider the compactness and unit depth, respectively, should be considered carefully to provide higher performances.
- The heat transfer performance of PFHE can be enhanced by 7% with the use of a simple rectangular vortex generator as compared to others. The installation at  $45^\circ$  of the attack angle is at the best for the vortex generator. Further, the heat transmission may be enhanced by improving the height of VG. But pressure loss in the PFHE also increases with the use of a vortex generator.
- The thermoaerodynamic performances of the PFHE, which are used in surroundings where extraneous materials are generated, can be augmented by applying the

optimum shape of holes and creases to the plate fin. The most superior thermal performance falls under  $\theta$  (crease angle) =  $15^\circ$ ,  $\lambda$  (crease cycle) = 3, and N (holes number) = 5. The angle has the largest impact on the drop in pressure and heat transmission efficiency of the changed plate style heat exchanger, and the effect of the  $\lambda$  and the N grows as the crease angle grows.

- When related to a PFHE, a louvred fin heat exchanger will provide a 25% improvement in thermal transmission and a 110% growth in pressure drop. The manufacturing, performance, operational, and design aspects of a well-proposed louvred fin compact heat exchanger are influenced by geometric and flow parameters. The flow speed increases as the louvred angle increases and the boundary layer on the louvred do not expand as much, resulting in increased heat transfer and pressure decrease. Doing numerical simulations for various louvre angles reveals that by using appropriate louvre angles ranging from  $\theta L = 24$  to  $32^\circ$ , with  $\theta L = 28^\circ$  as the optimum louvre angle.
- Correlations are available with strong predictive potential against the specific conditions of heat exchangers which can be used for evaluation of the j & f factor. More appropriate correlations for two-phase systems are required for performance enhancement and the accurate design of PFHE.
- Due considerations should be given for fouling and corrosion effects while designing and maintenance of the PFHE as high operational costs are paid by the industries to overcome the problems induced because of parameters.

The following points should be considered regarding the selection of fin configuration and type while designing PFHE:

- Porous fins having less permeability (high pore density) and lower porosity should be used to make the heat exchanger compact.
- The increase in fin pitch improves the thermohydraulic efficiency of PFHE.
- Coefficient of heat transfer is enhanced by using louvred and slit fins as it disturbs the development of the boundary layer.
- Providing grooves on the fin minimizes the weight of the fin. Typically, rectangular grooved fins are found to have better thermal effectiveness.

## References

1. Kang HJW, Li HZ, Li RC, Xin WQ (1994) Tao experimental study on heat transfer and pressure drop characteristics of four types of plate fin-and-tube heat exchanger surfaces. *J Thermal Sci* 3
2. Kim SY, Paek JW, Kang BH (2000) Flow and heat transfer correlations for porous fin in a plate-fin heat exchanger thermal/flow control research center. Korea Institute of Science and Technology, Seoul, Korea, pp 130–650
3. Wen J, Li Y, Zhou A, Zhang K (2005) An experimental and numerical investigation of flow patterns in the entrance of plate-fin heat exchanger. Department of Refrigeration and Cryogenics Engineering, School of Energy and Power Engineering, Xi'an Jiaotong University, Xi'an, p 710049





4. Sheik Ismail L, Ranganayakulu C (2008) Heat transfer and flow friction correlations for compact wavy plate fin heat exchangers aeronautical. Development Agency, Bangalore, p 560 017
5. De Schampheleire S, De Kerpel K, Ameer B, Huisseune H, De Paep M (2016) Thermal analysis of a commercial plate fin heat exchanger with non-uniform inlet flow conditions. Heat and Combustion Mechanics, Ghent University, Ghent, Belgium, Department of Flow
6. Anupam Sinha K, Raman A, Chattopadhyay H, Biswas G (2011) Effects of different orientations of winglet arrays on the performance of plate-fin heat exchangers. Central Mechanical Engineering Research Institute (CSIR), Durgapur, India, p 713209
7. Jeong CH, Kim HR, Ha MY, Son SW, Lee JS, Kim PY (2013) Numerical investigation of thermal enhancement of plate-fin type heat exchanger with Creases and holes in construction machinery. Appl Thermal Eng S1359–4311(13)00678–9
8. Aliabadi MK, Hormozi F, Rad EH (2013) New correlations for wavy plate-fin heat exchangers: different working fluids. Int J Numer Methods Heat Fluid Flow 24(5):1086–1108. Emerald Group Publishing Limited 0961–5539
9. Junqi D, Yi Z, Gengtian L, Weiwu X (2013) Experimental study of wavy fin aluminum plate fin heat exchanger. Experimental Heat Transfer 26:384–396. 2013 Copyright © Taylor & Francis Group, LLC ISSN: 0891–6152 print/1521–0480
10. Khoshvaght-Aliabadi M, Hormozi F, Zamzamin A (2013) Role of channel shape on the performance of plate-fin heat exchangers: Experimental assessment. School of Chemical, Petroleum, and Gas Engineering, Semnan University, Semnan, Iran, pp 35131–19111
11. Khoshvaght-Aliabadi M (2015) Thermal performance of plate-fin heat exchanger using passive techniques: vortex-generator and Nanofluid. Heat Mass Transfer. Springer, Berlin. <https://doi.org/10.1007/s00231-015-1603-6>
12. Du J, Qian Z-Q, Dai Z-Y (2015) Experimental study and numerical simulation of flow and heat transfer performance on an offset plate-fin heat exchanger. Springer, Berlin. <https://doi.org/10.1007/s00231-015-1695>
13. Kuchhadiyaa BB, Rathod PP (2016) Experimental investigation of thermal behaviour of cross-flow plate-fin heat exchanger with offset strip fin. In: 3rd international conference on innovations in automation and mechatronics engineering, ICIAME
14. Praveen kumara BM, Kaushik ND, Ajith P (2016) A study on the heat transfer enhancement of fin with grooves by natural convection 5(8). an ISO 3297: 2007
15. Khoshvaght-Aliabadi M, Jafari A, Sartipzadeh O, Salami M (2016) Thermal–hydraulic performance of wavy plate-fin heat exchanger using passive techniques: perforations, winglets, and Nanofluids. Int Commun Heat Mass Transfer 78:231–240
16. Mete Ozturk M, Dogan B, Erbay B (2017) Thermo-hydraulic performance assessment of a compact heat exchanger by varying plate fins. In: 6th international conference on renewable energy research and application
17. Juan D, Hai-Tao Z (2017) Numerical simulation of a plate-fin heat exchanger with offset fins using porous media approach. Springer, GmbH Germany Heat Mass Transfer. <https://doi.org/10.1007/s00231-017-2168-3>
18. Zhang X, Wangb Y, Li M, Wang S, Li X (2017) Improved flow and heat transfer characteristics for heat exchanger by using a new humped wavy fin. Appl Therm Eng 124:510–520
19. Javaherdeh K, Vaisi A, Moosavi R, Esmaeilpour M (2017) Experimental and numerical investigations on louvered fin-and-tube heat exchanger with variable geometrical parameters. J Thermal Sci Eng Appl. <https://doi.org/10.1115/1.4035449>
20. Samadifar M, Toghraie D (2018) Numerical simulation of heat transfer enhancement in a plate-fin heat exchanger using a new type of vortex generators. Appl Therm Eng S1359–4311(17):36306–36308
21. Yang H, Wen J, Wang S, Li Y (2018) Effect of fin types and prandtl number on performance of plate-fin heat exchanger: experimental and numerical assessment. Appl Therm Eng S1359–4311(18):30778–30786
22. Xiaoxiang L, Anlin W, Fumin L (2019) Research and structural optimization of heat dissipation performance plate-fin heat exchanger. In: 2019 2nd world Conference on mechanical engineering and intelligent manufacturing

23. Morteza K-A, Mortazavi S (2019) Combined effects of holes and winglets on chevron plate-fins to enhance the performance of a plate-fin heat exchanger working with Nanofluid. *J Thermal Energy Gener Transp Storage Conversion*. <https://doi.org/10.1080/08916152.2019.1569176>
24. Ma'arof MIN, Chala GT, Husain H, Mohamed MS (2019) Influence of fins designs, geometries and conditions on the performance of a plate-fin heat exchanger-experimental perspective. *J Mech Eng Sci* 13(1):4368–4379. ISSN: 2289–4659; e-ISSN: 2231–8380
25. Haoa J-H, Chena Q, Rena J-X, Zhanga M-Q, Aic J (2019) An experimental study on the offset-strip fin geometry optimization of a plate-fin heat exchanger based on the heat current model. *Appl Thermal Eng* 154:111–119
26. Gong J, Onishi J, He A, Kametani Y, Hasegawa Y, Shikazono N (2020) Heat transfer enhancement and pressure loss in a plate-fin heat exchanger with V-shaped oblique wavy surface. *Int J Heat Mass Transfer* 161:120263
27. Ozturk MM (2020) Effect of fin type on performance of compact heat exchangers with mini-channel. *Heat Transfer Eng* <https://doi.org/10.1080/01457632.2020.1860522>
28. Dodiya K, Bhatt N, Lai F (2020) Louvered fin compact heat exchanger—a comprehensive review. *Int J Ambient Energy* <https://doi.org/10.1080/01430750.2020.1839549>
29. Abu-Khader MM (2012) Plate heat exchangers: recent advances. *Renew Sustain Energy Rev* 16(4):1883–1891. <https://doi.org/10.1016/j.rser.2012.01.009>
30. Guo K (2015) Optimization of Plate/Plate-Fin Heat Exchanger Design, A thesis submitted to The University of Manchester for the degree of Doctor of Philosophy, Centre for Process Integration, School of Chemical Engineering and Analytical Science
31. Xue Y, Ge Z, Du ID X, Yang L (2018) On the heat transfer enhancement of plate fin heat exchanger. *Energies*

# Exploration on Photoluminescence Features in Pr<sup>3+</sup>-Doped Sodium-Calcium Orthosilicate Phosphor for White LEDs



Subhajit Pradhan  and M. Jayasimhadri 

## 1 Introduction

In recent times, energy conservation has become a matter of great concern due to a myriad of motives such as economic, security, and environmental safety. The greater demand for efficient use of energy made it more important to look forward to better lighting options as lighting systems are used everywhere, i.e., from industries to large sports complexes. Properties like higher efficiency, low power loss, and longevity made phosphor-converted white LEDs (pc-w-LEDs) an advanced lighting system [1]. Other than lighting, LEDs are also used as indicators, plant growth systems, and displays [2–9]. Several rare earth elements like Eu, Er, Sm, and Tb ions were incorporated in the efficient hosts and investigated recently for pc-w-LED applications [10–13]. In general, a mixture of red–green–blue phosphors excited via UV and near (n)-UV LED chips or a combination of green and red phosphors pumped using blue LED chip is the preferred choice for the realization of white light [14]. Both the approaches require superior red light-emitting phosphors, which should also be chemically and thermally stable. Red emission obtained from Pr<sup>3+</sup>-doped in an appropriate host can be harnessed to fabricate pc-w-LEDs. The narrow-band activators, Pr<sup>3+</sup> ions, show superb emission spectrum with luminescent color modulation and single 4f–4f Pr<sup>3+</sup> ion has advantages for its use in LEDs, displays, and various photonic devices [15]. More importantly, Pr<sup>3+</sup> ions own rich emission levels like <sup>3</sup>P<sub>0</sub> and <sup>1</sup>D<sub>2</sub>, which are generally attributed to red emission lines. Here, due to its high stability, low cost, and environmental friendliness, a silicate host has been preferred over the other inorganic host lattice. Also, these properties have motivated

---

S. Pradhan · M. Jayasimhadri (✉)

Luminescent Materials Research Lab (LMRL), Department of Applied Physics, Delhi Technological University, Bawana Road, Delhi 110 042, India

e-mail: [jayasimha@dtu.ac.in](mailto:jayasimha@dtu.ac.in)

the present work to select and synthesize the pure phase of  $\text{Na}_2\text{CaSiO}_4$  (NCSO) doped with  $\text{Pr}^{3+}$  ion to disclose its potential in w-LED applications.

In this work, single-phase  $\text{Na}_2\text{CaSiO}_4:\text{Pr}^{3+}$  phosphor was prepared via sol–gel technique. Further, the crystallinity, morphology, and luminescent features are investigated employing sophisticated characterization methods like X-ray diffraction, scanning electron microscopy, and spectrophotometer for revealing the potentiality of  $\text{Pr}^{3+}:\text{NCSO}$  phosphors as a red-emitting component in w-LEDs.

## 2 Experimental

### 2.1 Sample Synthesis

Sol–gel synthesis of  $\text{Na}_2\text{Ca}_{1-x}\text{SiO}_4:x\text{Pr}^{3+}$  ( $x = 0.0\text{--}1.0$  mol%) phosphors has been described in this section. The stoichiometric quantities of starting materials tetraethylorthosilicate (TEOS:  $\text{Si}(\text{OC}_2\text{H}_5)_4$ ),  $\text{Ca}_2(\text{NO}_3)_2 \cdot 4\text{H}_2\text{O}$ ,  $\text{NaNO}_3$  are taken as constituent raw material without treating further purification. The constituent raw materials are individually dissolved in ethanol and de-ionized (DI) water and then mixed together to form a clear solution (A). As-prepared solution “A” includes the stoichiometric composition of constituent elements for the host matrix (NCSO). For the host matrix to be activated with  $\text{Pr}^{3+}$  ions, a light green and transparent Praseodymium nitrate ( $\text{Pr}(\text{NO}_3)_3$ ) solution (B) was prepared by mixing a fixed amount of  $\text{Pr}_6\text{O}_{11}$  as per the mole concentration in a sufficient amount of nitric acid ( $\text{HNO}_3$ ). As-prepared solution B is added to solution A and kept at  $65^\circ\text{C}$  under continuous stirring for a few hours for homogenization. Then the final solution is kept in an oven for 18 h at  $90^\circ\text{C}$  to produce a clear green gel followed by drying it at  $110^\circ\text{C}$  for 5 h. At last, the dried sample is sintered for 3 h at  $1150^\circ\text{C}$ , cooled down naturally to room temperature, and ground daintily for subsequent characterizations.

### 2.2 Sample Characterizations

The X-ray diffraction patterns have been observed using Bruker D8 advance model working over  $2\theta$  ranging from  $10^\circ$  to  $80^\circ$  operated at an accelerated voltage of 40 kV and applied current of 40 mA. The SEM images have been obtained using the Carl Zeiss EVO 40 scanning electron microscope machine operated at 20 kV to render the morphological aspects of the as-synthesized sample. The photoluminescence measurements have been recorded using Jasco FP-8300 spectrofluorometer aided with Xenon lamp for excitation.

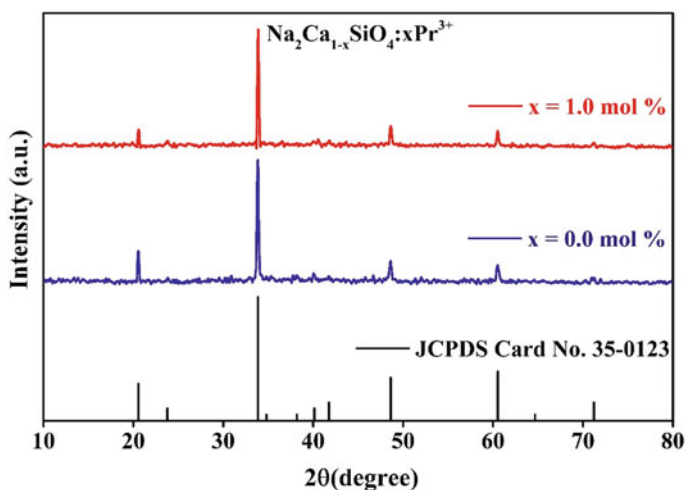
### 3 Results and Discussion

#### 3.1 Diffraction Analysis of the Na<sub>2</sub>Ca<sub>1-x</sub>SiO<sub>4</sub>:xPr<sup>3+</sup> (X = 0.0 to 1.0 mol%)

Figure 1 presents the XRD pattern of Na<sub>2</sub>CaSiO<sub>4</sub> phosphor doped with 0.0 and 1.0 mol% Pr<sup>3+</sup> ion annealed at 1150° for 3 h. The obtained diffraction peaks are matched completely with JCPDS data (card no.35-0123), confirming its monophasic cubic structure and better incorporation of Pr<sup>3+</sup> dopant in silicate host. Scherer formula has been implemented to measure the crystallite size from X-ray diffraction data [16] given by

$$D = \frac{K\lambda}{\beta \cos \theta} \quad (1)$$

where K symbolizes the shape factor;  $\beta$  symbolizes the FWHM of diffraction peak at a particular angle ( $\theta$ ). Here,  $\lambda$  is the X-ray wavelength used. Crystallite size calculated using all the major XRD peaks were found to be 30.85 and 29.29 nm for undoped and 1.0 mol% Pr<sup>3+</sup>-doped Na<sub>2</sub>CaSiO<sub>4</sub>, respectively.



**Fig. 1** XRD patterns for Na<sub>2</sub>Ca<sub>1-x</sub>SiO<sub>4</sub>:xPr<sup>3+</sup> (x = 0.0–1.0 mol %) samples compared with standard JCPDS data

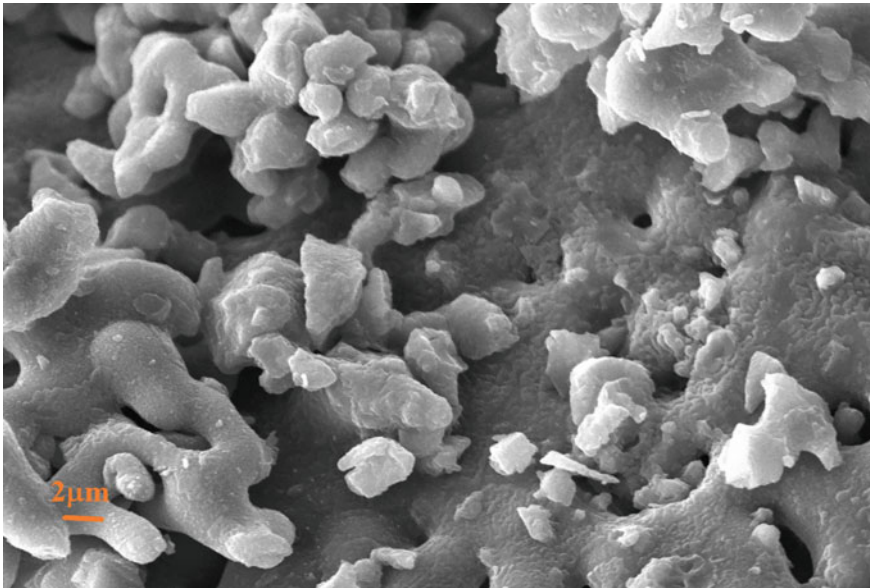


Fig. 2 SEM micrograph of undoped Na<sub>2</sub>CaSiO<sub>4</sub> phosphor

### 3.2 SEM Micrograph Analysis

Figure 2 shows the SEM image of the undoped Na<sub>2</sub>CaSiO<sub>4</sub> phosphor. The SEM image acknowledges the microcrystalline structured Na<sub>2</sub>CaSiO<sub>4</sub> sample and its irregular and non-uniform particle formation due to some agglomeration. Since many other commercially phosphors are available in the range of micrometer size, the above prepared micro-sized particles are convenient to make phosphor-converted (pc) w-LEDs [17].

### 3.3 Photoluminescence Properties

Figure 3 presents the photoluminescence excitation (PLE) spectra for 1 mol % Pr<sup>3+</sup>-doped Na<sub>2</sub>CaSiO<sub>4</sub> phosphor measured at 610 nm emission depicting high-intensity excitation peak near 252 nm and a less intensity band accompanied with three peaks between 445 and 490 nm range. The higher intensity band at 252 nm is accredited to 4f to 5d transition of Pr<sup>3+</sup> [18]. This transition happens due to the transition of an electron from Pr<sup>3+</sup> ions to the conduction band [19]. Also, the peaks near 445 to 490 nm can be attributed to <sup>3</sup>H<sub>4</sub> → <sup>3</sup>P<sub>2</sub>, <sup>3</sup>H<sub>4</sub> → <sup>3</sup>P<sub>1</sub>, and <sup>3</sup>H<sub>4</sub> → <sup>3</sup>P<sub>2</sub> transitions of Pr<sup>3+</sup> ions, respectively [20].

**Fig. 3** PLE spectra measured at 610 nm emission wavelength for the Na<sub>2</sub>Ca<sub>1-x</sub>SiO<sub>4</sub>:xPr<sup>3+</sup> (x = 1.0 mol%) phosphor

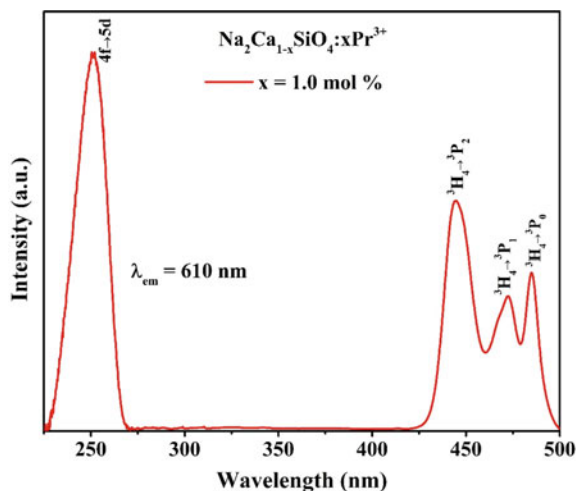
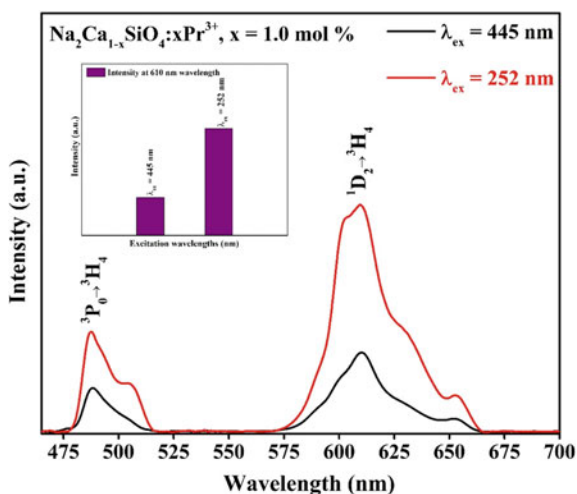
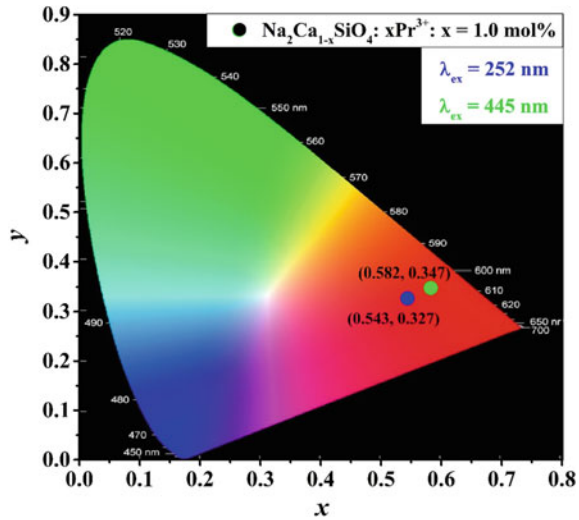


Figure 4 depicts the emission spectra measured under 252 and 445 nm excitations, which mainly consist of a band at 487 nm (blue) corresponding to  ${}^3P_0 \rightarrow {}^3H_4$  transition and a higher intensity band at 610 nm (red) corresponding to  ${}^1D_2 \rightarrow {}^3H_4$  transition [19]. Moreover, the inset of Fig. 4 shows that the intensities at 487 and 610 nm emission peaks are higher for 252 nm excitation as compared to the intensity for 445 nm excitation.

**Fig. 4** Emission spectra of Na<sub>2</sub>Ca<sub>1-x</sub>SiO<sub>4</sub>:xPr<sup>3+</sup> (x = 1.0 mol%) phosphor under 252 nm and 445 nm excitation (Inset: Comparison of intensities under different excitations at 610 nm emission wavelengths)



**Fig. 5** CIE diagram of 1.0 mol% Pr<sup>3+</sup>-doped Na<sub>2</sub>CaSiO<sub>4</sub> phosphor under 252 and 445 nm excitations



### 3.4 CIE Chromaticity Coordinates

Commission International de l'Eclairage (CIE) 1931 standards have been utilized for estimating the color coordinates of Na<sub>2</sub>CaSiO<sub>4</sub> phosphors under 252 and 445 nm excitation. Figure 5 presents the CIE coordinates (x, y) found to be (0.543, 0.327) and (0.582, 0.347) for 252 and 445 nm excitations, respectively. It can be observed that both calculated coordinates are present in the red region of the CIE plot. To determine the clarity of emission color exactly, correlated color temperature (CCT) was computed employing the formula [21]:

$$\text{CCT} = -449\eta^3 + 3525\eta^2 - 6823.3\eta + 5520.33 \quad (2)$$

where  $\eta = \frac{x-x_e}{y-y_e}$ ; ( $x_e = 0.3320$ ,  $y_e = 0.1858$ ) represents chromaticity at epicenter [22]. Using evaluated coordinates (0.543, 0.327) and (0.582, 0.347), the CCT value is calculated to be 1861 K and 1910 K for as-synthesized Na<sub>2</sub>CaSiO<sub>4</sub> phosphor. The obtained CCT values are lower than 5000 K, which suggest that Pr<sup>3+</sup>-doped Na<sub>2</sub>CaSiO<sub>4</sub> is suitable for fabricating cool w-LEDs.

## 4 Conclusions

Silicate host lattice, i.e., Na<sub>2</sub>CaSiO<sub>4</sub> has been chosen for Pr<sup>3+</sup> doping due to its chemical stability, cost-effectiveness, and environmental-friendly composition. Single-phase undoped and Pr<sup>3+</sup>-doped Na<sub>2</sub>CaSiO<sub>4</sub> samples were successfully prepared using



sol-gel technique. The cubic structure was affirmed by X-ray diffraction pattern with an average crystallite size of 30.85 and 29.29 nm for undoped and 1.0 mol% Pr<sup>3+</sup>-doped Na<sub>2</sub>CaSiO<sub>4</sub> phosphors, respectively, as evaluated by the Scherer formula. The morphology of irregular and non-uniform microcrystalline particles was depicted by SEM micrograph. Excitation spectra measured at 610 nm emission wavelength for the Na<sub>2</sub>Ca<sub>1-x</sub>SiO<sub>4</sub>:xPr<sup>3+</sup> (x = 1.0 mol%) phosphor shows a high intensity peak at 252 nm due to 4f → 5d transition. Also, the peaks at 445, 472, and 485 nm can be attributed to <sup>3</sup>H<sub>4</sub> → <sup>3</sup>P<sub>2</sub>, <sup>3</sup>H<sub>4</sub> → <sup>3</sup>P<sub>1</sub>, and <sup>3</sup>H<sub>4</sub> → <sup>3</sup>P<sub>0</sub> transitions of Pr<sup>3+</sup> ions, respectively. The emission spectra for Pr<sup>3+</sup>-doped Na<sub>2</sub>CaSiO<sub>4</sub> phosphor at 1 mol% Pr<sup>3+</sup> ion concentration exhibit intense emission at 487 and 610 nm wavelength under both 252 and 445 nm excitations accredited to <sup>3</sup>P<sub>0</sub> → <sup>3</sup>H<sub>4</sub> and <sup>1</sup>D<sub>2</sub> → <sup>3</sup>H<sub>4</sub> transitions, respectively. The CIE chromaticity coordinates for Pr<sup>3+</sup>-doped Na<sub>2</sub>CaSiO<sub>4</sub> are located in the red region of CIE 1931 diagram under 252 and 445 nm excitation. This red emission obtained from Pr<sup>3+</sup>-doped Na<sub>2</sub>CaSiO<sub>4</sub> phosphors can be harnessed to fabricate pc w-LEDs. Hence, the above-mentioned results signify that the designed phosphor material can be potentially used for w-LEDs applications.

## References

1. Pulli T, Donsberg T, Poikonen T, Manoocheri F, Karha P, Ikonen E (2015) Advantages of white LED lamps and new detector technology in photometry. *Light: Sci Appl* 4:2047–7538
2. Gaffuri P, Stolyarova E, Llerena D, Appert E, Consonni M, Robin S, Consonni V (2021) Potential substitute for critical materials in white LEDs: technological challenges and market opportunities. *Renew Sustain Energy Rev* 143:110869
3. Dutta Gupta S, Agarwal A (2017) Artificial lighting system for plant growth and development: chronological advancement, working principles, and comparative assessment. *Light emitting diodes for agriculture*, 1st edn. Springer, Singapore, pp 1–25
4. Ye S, Xiao F, Pan YX, Ma YY, Zhang QY (2010) Phosphors in phosphor-converted white light-emitting diodes: recent advances in materials, techniques and properties. *Mater Sci Eng R* 71:1–34
5. Sun Q, Wang S, Li B, Guo H, Huang X (2018) Synthesis and photoluminescence properties of deep red-emitting CaGdAlO<sub>4</sub>:Mn<sup>4+</sup> phosphors for plant growth LEDs. *J Lumin* 203:371–375
6. Rajendran M, Vaidyanathan S (2020) Systematic investigation of Eu<sup>3+</sup> activated Na<sub>2</sub>Ln<sub>4</sub>(MoO<sub>4</sub>)<sub>7</sub> [Ln = La, Gd and Y] narrow band red emitting phosphors for hybrid white LEDs and plant growth. *New J Chem* 44:14823–14836
7. Huang X, Sun Q, Devakumar B (2020) Novel efficient deep-red-emitting Ca<sub>2</sub>LuTaO<sub>6</sub>:Mn<sup>4+</sup> double perovskite phosphors for plant growth LEDs. *J Lumin* 222:117–177
8. Fu Y, Xiong P, Liu X, Wang X, Wu S, Liu Q, Peng M, Chen Y (2021) A promising blue-emitting phosphor CaYGaO<sub>4</sub>:Bi<sup>3+</sup> near-ultraviolet (NUV) pumped white LED application and the emission improvement by Li<sup>+</sup> ions. *J Mater Chem* 9:303–312
9. Poelman D, Van Haecke JE, Smet PF (2009) Advances in sulfide phosphors for displays and lighting. *J Mater Sci Mater Electron* 20:134–138
10. Venkataravanappa M, Nagabhushana H, Prasad BD, Darshan GP, Basavaraj RB, Vijayakumar GR (2017) Dual color emitting Eu doped strontium orthosilicate phosphors synthesized by bio-template assisted ultrasound for solid state lighting and display applications. *Ultrason Sonochem* 34:803–820
11. Li YC, Chang YH, Lin YF, Lin YJ (2006) High color purity phosphors of LaAlGe<sub>2</sub>O<sub>7</sub> doped with Tm<sup>3+</sup> and Er<sup>3+</sup>. *Appl Phys Lett* 89:081110

12. Liu X, Lin J (2009) Synthesis and luminescent properties of  $\text{LaInO}_3: \text{RE}^{3+}$  (RE = Sm, Pr and Tb) nanocrystalline phosphors for field emission displays. *Solid State Sci* 11:2030–2036
13. Jisha PK, Prashantha SC, Nagabhushana H (2017) Luminescent properties of Tb doped gadolinium aluminate nanophosphors for display and forensic applications. *J Sci Adv Mater Dev* 2:437–444
14. Wang L, Wang X, Kohsei T, Yoshimura K, Izumi M, Hirosaki N, Xie RJ (2015) Highly efficient narrow-band green and red phosphors enabling wider color-gamut LED backlight for more brilliant displays. *Opt Express* 23:28707–28717
15. Zhao M, Liao H, Ning L, Zhang Q, Liu Q, Xia Z (2018) Next-generation narrow-band green-emitting  $\text{RbLi}(\text{Li}_3\text{SiO}_4)_2: \text{Eu}^{2+}$  phosphor for backlight display application. *Adv Mater* 30:1802489
16. Kaur H, Jayasimhadri M, Sahu MK, Rao KP, Reddy NS (2020) Synthesis of orange emitting  $\text{Sm}^{3+}$  doped sodium calcium silicate phosphor by sol-gel method for photonic device applications. *Ceram Int* 46:26434–26439
17. Qin L, Wei DL, Huang Y, Qin C, Cai P, Il Kim S, Seo HJ (2014) Ortho-vanadates  $\text{K}_3\text{RE}(\text{VO}_4)_2$  (RE = La, Pr, Eu, Gd, Dy, Y) for near UV-converted phosphors. *Mater Chem Phys* 147:1195–1203
18. Xu H, Wang J, Hu W, Wang W, Zhang J, Li H (2011) Luminescent colour modulation of a multicolour praseodymium activated phosphor. *Ceram Int* 45:9306–9309
19. Yua H, Xuan C, Zhanga Y, Lia Q, Gong C (2017) Structure and photoluminescence of polymer derived Pr-doped  $\text{SiAlON}$  red phosphor. *Ceram Int* 43:6898–6903
20. Wen W, Ya-wen X, Jiang-nong Y (2014) Luminescent characteristics of  $\text{Sr}_0.95\text{MoO}_4: 0.05\text{Ln}^{3+}$  (Ln = Eu, Tb, Pr) phosphors. *J Chem Pharma Res* 6(11):590–594
21. McCamy CS (1992) Correlated color temperature as an explicit function of chromaticity coordinates. *Color Res Appl* 17:142–144
22. Sreeja E, Mohan PR, Gopi S, Joseph C, Unnikrishnan NV, Biju PR (2019) Structural and photoluminescence properties of UV-excited  $\text{Er}^{3+}$  doped  $\text{Ba}_2\text{CaWO}_6$  yellowish- green phosphors. *Physica B Condens Matter* 555:74–80

# Solar Energy Production Onsite for Battery Swapping Stations in Delhi



Mukesh Kumar and Sarita Baghel

## 1 Introduction

Delhi is one of the 10 world's most polluted cities in 2020 (PM2.5) as per IQAir, and this led the Government of NCT of Delhi to announce the Delhi Electric Vehicle Policy on August 7, 2020, with a vision to promote the adoption of electric vehicles in the city and to make Delhi, the EV Capital of India.

This policy aims to improve Delhi's air quality and create an entire supply-chain ecosystem for this new segment of vehicles, i.e., electric vehicles at this time. The number of motor vehicles on Delhi's roads is estimated at 10.986 million, 70% of which being two-wheelers as of March 31, 2018, as per Delhi's Economic Survey 2018–19 report [1].

The phase of change of energy source from conventional fuel to electric for motor vehicles can produce high energy demand [2]. To supply the increased demand with conventional power plants might not be feasible and would increase pollution. There has been advancement in battery technology for swapping, which can be used in two-wheelers and four-wheelers with an increase in the number of batteries but maintaining universal size and capacity. The advancements in battery technology make the battery swapping station demands go higher for swap since every vehicle's battery can be swapped.

Battery swapping stations provide the same level of convenience as refueling the conventional liquid or gaseous fuels provide. They are much more convenient and of practical importance than charging stations in densely populated cities like Delhi.

An implementation of a PV system array on a petrol pump's rooftop is analyzed to estimate how this proposal could work. Also, an estimate of how many batteries

---

M. Kumar (✉)

Delhi Technological University, Shahbad Daulatpur, Delhi 110042, India

S. Baghel

Department of Applied Physics, Delhi Technological University, Delhi, India

of standard capacity can be charged per day is estimated. The energy produced could serve the resident with clean energy, leading to a clean energy source for the vehicles.

In practice, the proposal's results could help the government and the residents get through the phase of the drastic change of energy source for the vehicle smoothly. This proposal could also provide an alternate source of income for the fuel industry, like petrol pumps, to get on with clean energy on the sidelines. The future of clean energy does not seem far now, as we discover more and more disadvantages and come to the end of conventional energy sources.

There has always been a great fear of change unless we do not get compelled to do so. Moreover, the time has come for us to change to sources of energy that can no longer contribute to the ever-increasing harmful effects of conventional energy sources.

## 2 Literature Review

### 2.1 Battery Swapping Station (BSS)

Battery swapping stations refers to the concept of replacing partially or entirely discharged batteries with fully charged batteries. BSS implementation can help metropolitan areas to cope with the energy demands. BSS can provide instant refueling to avoid long queues and waiting times that charging stations cannot [3]. Earlier publications show how dependency on national grid connections can be reduced by utilizing electric vehicles' batteries for energy storage by the community [4]. Electric vehicles' charging in an uncontrolled manner could even influence the distribution grid and pose other disadvantages, which requires pervasive research [5]. At the same time, the BSS can be a boon. There have been advancements in fast charging systems, and they could be utilized where vehicles can be put to charge. Fast charging systems require space for vehicles, which cannot be a feasible solution for densely populated cities like Delhi for large-scale electrification vehicles [6].

The energy storage systems like BSS can help the transition from fossil fuel to renewable energy to a large extent [7].

Due to a large number of vehicles in the city, completely off-grid implementation of the BSS alone cannot meet the continuously rising demands [8]. Also, charging batteries is time-consuming, which contradicts the current system of refueling fossil fuels since both are sources of energy for motor vehicles.

The metropolitan area like Delhi can provide electric vehicle owners the facility of BSS at petrol pumps and other public places like parking centers, stadium, etc. for ease of access and utilize the current infrastructures of related use.

## 2.2 *Onsite Energy Production*

The energy demands rapidly increase in household and industrial use as population and urbanization advance. The transport sector alone accounts for 12% of the country's overall carbon dioxide emission and pollutants. Vehicle electrification is required to reduce CO<sub>2</sub> and pollutant emissions [9]. Fossil fuels cannot meet the energy demand due to their limited resources in India and the effect of their use on climate and air [10]. People and the government have realized the necessity of renewable energy. The solar energy sector has seen wide applications in India, and favorable policies have been designed to take advantage of solar energy [11].

The integrated solar charging of electric vehicles can be applied. However, considering factors affecting a non-stationary PV module and high added cost due to extra components, a wide application might seem far-fetched [12].

Researchers have found specific sites in Delhi where charging infrastructures can be designed for lower costs based on different factors [13]. However, the cost-effectiveness for these sites is undoubtedly more than this proposal since we can use already in place infrastructure for PV module installation. Here the petrol pump rooftop is taken as an example due to minimal to no shading, ideal and plain rooftop, adaptability of technology, ease of system installation and maintenance, etc. However, ideal rooftops of other public buildings like stadiums, health centers, educational institutes, and many more, which have similar characteristics, can be utilized. Comparing energy produced using ideal rooftops with fossil fuel sources shows how economic solar energy production can be and takes us toward sustainability [14].

For the onsite generation of energy, photovoltaic panels of appropriate configuration and standard can be used. The solar energy generated could be used for charging the batteries of the BSS. One of the essential factors would be to use the ideal rooftops of public places, mainly petrol pumps.

## 2.3 *Electric Vehicles*

The type of vehicles present in Delhi has more than 70% of two and three-wheelers under the category of light vehicles. Moreover, without light vehicle electrification, there cannot be any recognizable development in terms of change in the source of energy of vehicles [15].

The battery swapping stations can provide a better environment for charging and its lifecycle due to the presence of cooling systems [16].

When the battery is charged at normal temperature, its capacity can be maintained for an extended period and, when put into vehicles, can remain in the optimal temperature range for some time too.

### 3 Analysis and Result

Location (28.732796813585868, 77.19832208470727) refers to a petrol pump with the ideal rooftop of area 248 m<sup>2</sup>, by taking into account some dimensions and specifications as provided in Table 1 (Fig. 1).

The area of the rooftop and the estimate of the number of solar panels of standard dimensions to be installed were made by PVWatt web application version 6 [17]. The application estimates the number of PV panels based on the rooftop's dimensions.

Based on the efficiency of monocrystalline PV panels, the estimate of system capacity given by the application is about 47.2 kW, which signifies about 130 PV panels of 365 W (Fig. 2).

The analysis of data has been made using the system advisor model [18]. Thus for the photovoltaic module of area 1.673 m<sup>2</sup> and rooftop of area 248 m<sup>2</sup>, a PV system of about 47 kW can be installed. This system could provide about 235 kWh on average per day. The energy of 235 kWh can be stored in 117 battery modules of 2 kWh capacity.

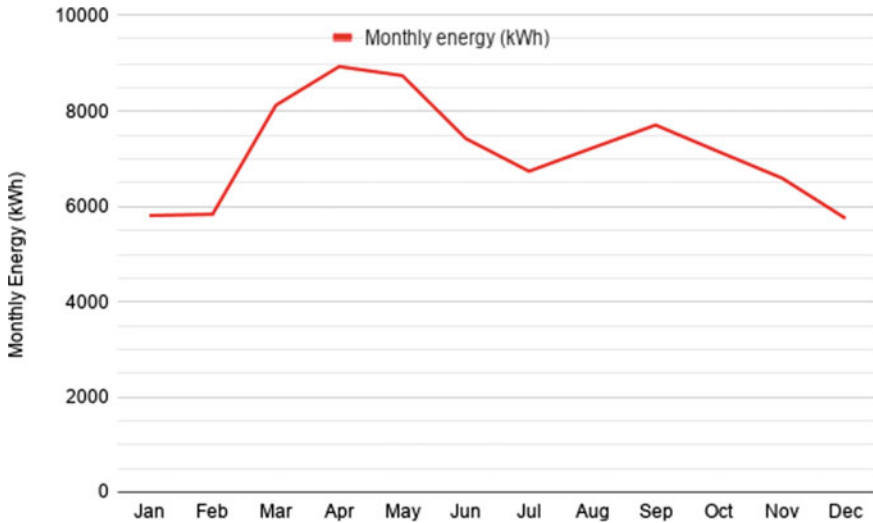
The data for the analysis has been taken from National Solar Radiation Database (NSRDB). The data is generated at the station (28.75, 77.15). Solar data is of 2014 typical year.

**Table 1** Standard dimensions and specifications

Component	Dimensions	Specifications
Photovoltaic module	1.68 m * 0.996 m	LG365Q1C-A5, 365 W, monocrystalline, 6*10cells
Petrol pump's rooftop	248 m <sup>2</sup>	Single storey, no shading
Battery module	Generic dimensions	Generic type, 2 kWh capacity



**Fig. 1** The available rooftop area calculation using PVWatt web application version 6.1.4



**Fig. 2** The monthly energy production for the example site from the simulation is obtained

In Delhi, more than 400 petrol pumps operate, and if the solar system on their rooftop gets installed, there will be the production of about 94 MWh energy on average per day. However, the public places with ideal rooftops have a very high number in Delhi. Here only one implementation is taken into account.

## 4 Discussion

The ever-declining quality of air and drastic changes in the climate, and even rapidly diminishing fossil fuel reserves generate the need for adopting new and renewable energy sources. However, if we use grid electricity generated using conventional energy sources to charge electric vehicles, we need to rethink [19]. In contrast, this paper is all about implementing renewable sources of energy.

The policy-makers and government are trying hard to implement renewable energy sources on a large scale, but the peoples are yet to be involved. The success of large-scale policies can only be realized with the involvement of the residents. Policy-makers need to assure them of at least the same experience and usability as fossil fuels provide to involve the residents. However, this could be done through technologies that can provide similar or better experiences like battery swapping stations (BSS) along with this proposal [20].

The solution to “how the change of energy source to the vehicles can be implemented so the purpose and the results could be justified” is given through this proposal. There have been developments for designing new systems, but the already in place infrastructure use is emphasized, which can reduce initial costs.

There are limitations too like if this proposal is implemented on the petrol pump's rooftop, the safety from electricity spark from wires and other electrical hazards need to be addressed. However, if the proposal is implemented on the local healthcare rooftops, it can provide energy resources in an emergency.

## 5 Conclusion

This proposal can benefit the people of Delhi even if public sector undertaking companies (PSUs) like Indian Oil Corporation Limited (IOCL) can implement this on their petrol pumps. Even recent hikes in taxes on fossil fuels all over the country encourage people to search and adopt other sources of energy for motor vehicles. For that, this proposal can prove to be affordable. This idea can be fruitful for both government or companies and residents, i.e., users.

Renewable energy has been utilized from ancient times, and as of November 27, 2020, 38% of India's installed electricity generation capacity is from renewable sources (136 GW out of 373 GW). Although if we continue to use fossil fuels in vehicles, our environment will go on degrading. Thus we urgently need to switch to renewable energy sources on motor vehicles too.

There has been the adaptation of electric vehicles but only to a certain extent, even when the government introduces a new electric vehicle policy with some incentive and relaxation. Though with the help of this proposal and advancements in battery technologies and battery swapping stations (BSS), a large-scale implementation can be achieved.

To develop Delhi as a smart city in the true sense, we need to focus more on renewable and sustainable energy sources and stop further degradation of the environment [21]. We know solar energy would only be harnessed during the daytime; thus, the requirement of an alternative source for charging batteries can be grid electricity with a unity power factor [22]. Urbanization and smart city development do not mean the development is sustainable. Even the cities of developed Western countries are not sustainable [23]. To attain true sustainability, we must use renewable energy as much as possible and even use electric vehicles to supply the emergency needs using the vehicle to home (V2H) approach [24].

The development of micro-smart grids for renewable sources exploitation for agriculture can take the cities and the country toward sustainability due to significant energy demand in the sector [25]. A better approach for developing smart cities would be by considering the technological, social, economic, and environmental points of view [26]. The policy-makers are taking steps to implement renewable energy sources, but we should also rethink the policy's adaptability and feasibility [27]. The Covid-19 pandemic has also influenced the present scenario of India in the transition of energy sources, and the effectiveness of the policy cannot be seen [28].



## References

1. India environment portal <http://www.indiaenvironmentportal.org.in/node/461437/>. Last accessed 17 April 2021
2. Deshmukh RR, Ballal MS (2018) An energy management scheme for grid connected EVs charging stations. In: 2018 international conference on power, instrumentation, control and computing (PICCC), Thrissur, pp 1–6 IEEE. <https://doi.org/10.1109/PICCC.2018.8384741>
3. Ban M et al (2019) Battery swapping: an aggressive approach to transportation electrification. *IEEE Electrification Mag* 7(3):44–54. <https://doi.org/10.1109/MELE.2019.2925762>
4. Hasan ASMM (2020) Electric rickshaw charging stations as distributed energy storages for integrating intermittent renewable energy sources: a case of Bangladesh. *Energies* 13(22):6119. <https://doi.org/10.3390/en13226119>
5. Qureshi U et al (2021) Real-time control for charging discharging of electric vehicles in a charging station with renewable generation and battery storage. In: 2021 International conference on sustainable energy and future electric transportation (SEFET), pp 1–6. <https://doi.org/10.1109/SeFet48154.2021.9375717>
6. Thakre MP et al (2020) Fast charging systems for the rapid growth of advanced Electric Vehicles (EVs). In: 2020 international conference on power, energy, control and transmission systems (ICPECTS), pp. 1–6. <https://doi.org/10.1109/ICPECTS49113.2020.9336979>
7. Kalair A et al (2010) Role of energy storage systems in energy transition from fossil fuels to renewables. *Energy Storage* 3(1):e135. <https://doi.org/10.1002/est2.135>
8. Krishna A, Sebastian S, Design of an off-grid photovoltaic electric vehicle charging station, p 26
9. Sugathan M (2021) Road transportation emissions in India: adopting a ‘Hub’ and ‘Spoke’ approach towards electric-driven decarbonization. In: Brewer T (ed) *Transportation air pollutants: black carbon and other emissions*. Springer International Publishing, Cham, pp 43–54. [https://doi.org/10.1007/978-3-030-59691-0\\_4](https://doi.org/10.1007/978-3-030-59691-0_4)
10. Muneer T et al (2005) Sustainable production of solar electricity with particular reference to the Indian economy. *Renew Sustain Energy Rev* 9(5):444–473. <https://doi.org/10.1016/j.rser.2004.03.004>
11. Sahoo SK (2016) Renewable and sustainable energy reviews solar photovoltaic energy progress in India: A review. *Renew Sustain Energy Rev* 59:927–939. <https://doi.org/10.1016/j.rser.2016.01.049>
12. Sehgal L et al, Proposal of integral mounted solar charging and external solar charging station for an electric rickshaw in Delhi, p 4
13. Sheppard CJR et al (2016) Cost-effective electric vehicle charging infrastructure siting for Delhi. *Environ Res Lett* 11(6):064010. <https://doi.org/10.1088/1748-9326/11/6/064010>
14. Shakya AK, Shrestha JN (2015) Case study on grid integrated solar PV for National Dasarath Stadium 11
15. Jerome S, Udayakumar M (2021) Assessment of gasoline consumption and greenhouse gas emission reduction on using battery electric two-wheeler in India. *J Braz Soc Mech Sci Eng* 43(1):40. <https://doi.org/10.1007/s40430-020-02756-x>
16. Sasidharan C et al (2021) Light electric vehicles and their charging aspects. In: Patel N et al (eds) *Electric vehicles: modern technologies and trends*. Springer, Singapore, pp 33–51. [https://doi.org/10.1007/978-981-15-9251-5\\_2](https://doi.org/10.1007/978-981-15-9251-5_2)
17. PVWatts calculator web application version 6.1.4, released 2021.03.19: Accessed 15 April 2021. <https://pvwatts.nrel.gov>
18. System Advisor Model Version 2020.11.29 (SAM 2020.11.29): National Renewable Energy Laboratory: Golden, CO.: Accessed 15 April 2021. <https://sam.nrel.gov>
19. Khan S et al (2018) A comprehensive review on solar powered electric vehicle charging system. *Smart Sci* 6(1):54–79. <https://doi.org/10.1080/23080477.2017.1419054>
20. Zheng Y et al (2014) Electric vehicle battery charging/swap stations in distribution systems: comparison study and optimal planning. *IEEE Trans Power Syst* 29(1):221–229. <https://doi.org/10.1109/TPWRS.2013.2278852>

21. Shahidehpour M et al (2018) Smart cities for a sustainable urbanization: illuminating the need for establishing smart urban infrastructures. *IEEE Electric Mag* 6(2):16–33. <https://doi.org/10.1109/MELE.2018.2816840>
22. Singh B et al (2020) Implementation of solar PV-battery and diesel generator based electric vehicle charging station. *IEEE Trans Ind Appl* 1–1. <https://doi.org/10.1109/TIA.2020.2989680>
23. Tanguay GA et al (2010) Measuring the sustainability of cities: an analysis of the use of local indicators. *Ecol Ind* 12
24. Verma A, Singh B (2019) Control and implementation of renewable energy based smart charging station beneficial for EVs, home and grid. In: 2019 IEEE energy conversion congress and exposition (ECCE). IEEE, Baltimore, MD, USA, pp 5443–5449. <https://doi.org/10.1109/ECCE.2019.8913253>
25. Fabrizio E et al (2017) Monitoring and managing of a micro-smart grid for renewable sources exploitation in an agro-industrial site. *Sustain Cities Soc* 28:88–100. <https://doi.org/10.1016/j.scs.2016.08.026>
26. Kuru K, Ansell D (2020) TCitySmartF: a comprehensive systematic framework for transforming cities into smart cities. *IEEE Access*. 8:18615–18644. <https://doi.org/10.1109/ACCESS.2020.2967777>
27. Lu Y et al (2020) A critical review of sustainable energy policies for the promotion of renewable energy sources. *Sustainability* 12(12):5078. <https://doi.org/10.3390/su12125078>
28. Mishra S et al (2021) A comprehensive review on developments in electric vehicle charging station infrastructure and present scenario of India. *Sustainability* 13(4):2396. <https://doi.org/10.3390/su13042396>

# Pollination System for Greenhouse Flowering Plants Using Nano Drones



Manoj Kumar Shukla, Lavepreet Singh, Shrikant Vidya, Haider Quasim, and Rahul Bhandari

## 1 Introduction

Pollination is one of the important factors for the purpose of seed generation in plants to keep their species alive. But we know that plants will not be able to move from one place to another unlike animals so they have to depend on others for the purpose of pollination like wind, water, birds, insects and many other factors. But these factors are not enough for the purpose of mass production or for agricultural purposes; therefore, we have to introduce new efficient method to increase the productivity.

The existing artificial methods for pollination are labor-consuming and have low productivity depending upon the type of pollinators used, and they cause injuries and also not much ineffective. By using modern technique, these defects mitigate in pollination in the open and closed soil by using nano copters, which acts as a pollinating agent by means of an automatic control system [1]. For the characterization of these drones, various criteria had been set up like their size, weight and maneuverability. There are various programming references for an automatic flight control of drones and also onboard computing platform [2]. These copters can be equipped with various inventories like microphone, different sensors as well as cameras, and they can transport small weight containers [3, 4]. The programming control of a copter allows to make various operations with inventories attached, and they can be equipped with other transportable accessories to transport the pollens from one place to another [5, 6].

Scientists investigating a possibility of implementing swarm technology for pollination of plants [7]. In past few years, researchers have discovered a nano copter that has been accepted all over the world [8]. This nano copter has lesser weight and differs in dimensions in comparison to general copter. Its size varies from the range 10–15 cm, and weight is less than 120–150 g. Nano copters are cheaper than the

---

M. K. Shukla · L. Singh · S. Vidya · H. Quasim (✉) · R. Bhandari  
Galgotias University, Greater Noida, India

normal models available in the market [8]. Due to heavy weight and rigid housing of copters, its propellers rotate quickly and it leads to chance of collision when power supply is suddenly cutoff so handling of it becomes difficult in such circumstances [9].

The operating flight controller of nano copter faces the difficulty in adjustment during various flight modes that make risky environment for its management [10].

The use of nano copters started increasing due to their smaller weight about 40–50 g and its smaller size of about 10–15 cm. The size of these nano copters was similar to that of large insects like butterfly or humming bird. These dimensions and size allow drones to do the same movements as the natural pollinators do, and it is possible by the automatic control of these drones [11].

## 2 Process of Pollination

These nano copters can artificially pollinate the pollen grains taking it from one flower transferring these pollens to another flower at the same time like insects do. There are total four stages involved in the pollination as they are below:-

1. The first stage involves the climbing of drone from a certain height to the stalk of a plant and reaches that height within 2–3 s [11].
2. In second stage, the nano copters are automatically controlled for collecting or releasing the pollens from the stalk of flower.
3. Automatic controller processes a pestle by the hanged equipment for pollen collecting/transfer due to lag over a flower in third stage.
4. Automatic controller analyzes the data and lifts the copter to transfer the pollen to another flower in the fourth stage.

Automatic control uses the coordinates obtained from the central control unit for the analysis of flower position and if the pollen was dropped their by that drone then it will move in search for the flower according to the coordinates sent through the central control unit. All the send by central control unit was analyzed by the program mapping system, and it will implement these coordinates in real-time positioning of drone (Figs. 1, 2 and 3).

Nano copter uses the photographs of arrangement of flowers taken from aerial mode to identify its trajectory with respect to the positioning of plant during the flight and stimulates the pollination of plants in automatic control by collecting and delivering the pollen. The simulated pollination for these nano drones can be seen by simply modifying its design to standard basis as well as changing its working programming and changing of a control unit for computer processing interface.

The important modifications that are required to be done were its automated flight control algorithm, return to its initial position, automated landing; deduction of its height and position [4].

All the changes are aimed to a possibility of automated control flight operations and implemented on the software termed as Netlogo and Ready Software solutions.

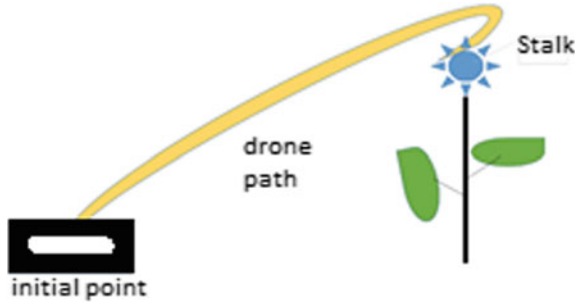


Fig. 1 Stage 1: High arc path taken by copter to reach the flower

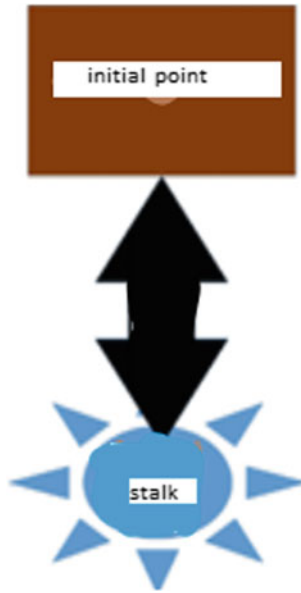


Fig. 2 Stage 3: Pollination by copter

Nano copters are suitable to use for greenhouses and hotbeds on the closed soil due to its low resistance to demolition downwind and small size [4].

The use of a nano copter will automate the simulated pollinations of plants and will increase the effectiveness of process of simulated pollination. Dependency on insect pollinators and weather conditions can also be eliminated by the use of nano copters.

Reprogramming of computer interface for the nano copter facilitates the auto-landing and return to a take-off point.

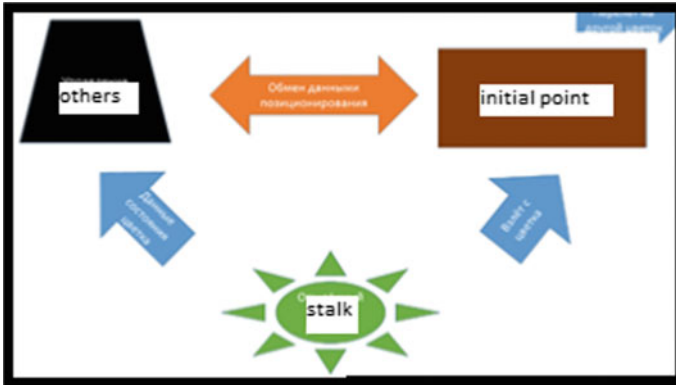


Fig. 3 Stage 4: Automatic control of data positioning and copter movement to the next flower

### 3 Experimental Studies and Results

All the above proposed analysis was tested on a swarm intelligence simulation software *NetLogo*. We have evaluated the model on three basic behaviors to utilize the proposed approach (i) Random fly of drone towards flower (‘R’), (ii) stigmergic behavior (‘S’) and (iii) Both flocking and stigmergic behavior (‘S + F’). For each observation, we have taken 10 trials in the interval at which 90–95% of targets were detected. We also plotted the graph showing the resulting performance indicator samples. The result of each case was summarized by Table 1 in the form of “mean ± confidence level”.

Table 1 Mean ± confidence level for different Scenario

Scenario	Number of targets/clusters	Type/Number of Obstacle	Drones	Completion time (ticks)
Plane Field flowers	55/5	Tress = 10 flowers = 50	84	R 1743 ± 140 S 806 ± 140 S + F 686 ± 143
Densely polluted flowers area	25/1	Trees = 40 Flowers = 250	84	R 742 ± 186 S 740 ± 192 S + F 670 ± 75
Farm field	120/2	Trees = 20 Flowers = 500	42	R 1440 ± 105 S 856 ± 148 S + F 806 ± 98

### 4 Experimental Results

The five targets scattered over the synthetic area are called scenario. Each scenario contains per group 12 targets. Figure 4a represents the initial arrangement of almost 84 drones grouped into four swarms. These swarms have placed as antipodes represented by triangular symbol in the shown area. Targets have been represented as cluster of dots.

Figure 4 shows the distribution of various swarms with different sizes. The stigmergic formation has shown in Fig. 5. From the table and figures, we conclude that stigmergic formation will reduce the time for target search as well as for pollination process.



Fig. 4 Basic Scenario a Initial State b Flocking c Stigmergic and Flocking

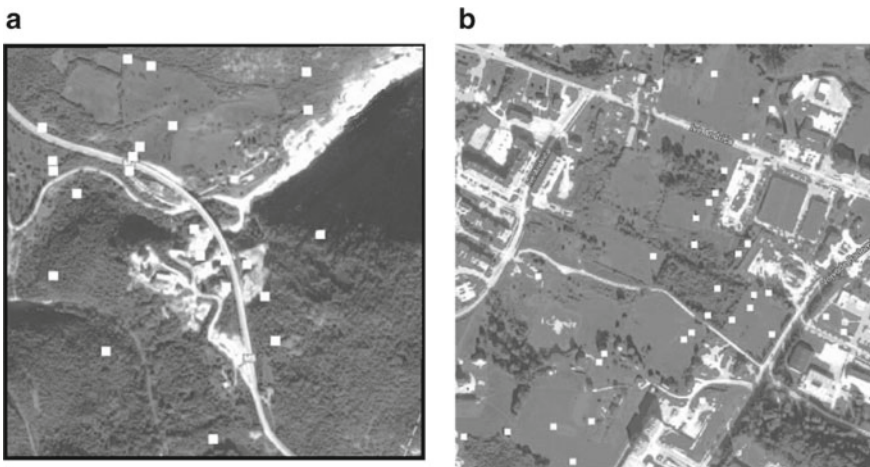


Fig. 5 Models of plane field flowers and forest scenarios a Plane field flower b Farm

## 5 Conclusion

In this article, we are trying to use flocking and stigmergic behavior to improve the target search operation as well as to improve the pollinating efficiency using these behaviors in swarm for farming process. The drones use stigmergy behavior to attract drones towards potential targets and uses flocking behavior to organize other drones into swarm and guide each other towards the movement of flower stalk. The results of stigmergic and flocking behavior in both real and simulated worlds are satisfactory. If these results are suitably implemented then they will help to increase the overall search operation of the drones. But these accurate results are not an easy work but if implemented correctly it will improve the performance. Thus, using appropriate parameters, we can improve the target search operations of the present drones working on swarm technology, and they can be implemented to increase the pollination efficiency thereby helping farmers for the agricultural purpose.

## References

1. Brambilla M, Ferrante E, Birattari M, Dorigo M (2013) Swarm robotics: a review from the swarm engineering perspective. *Swarm Intell* (7):1–41
2. Abutalipov RN, Bolgov YV, Senov HM (2016) Flowering plants pollination robotic system for greenhouses by means of nano copter (drone aircraft). In: 2016 IEEE international conference quality management, transport and information security, information technologies. IEEE, pp 7–9
3. Valin H, Sands RD, Van der Mensbrugge D, Nelson GC, Ahammad H, Blanc E, Bodirsky B, Fujimori S (2014) The future of food demand: understanding differences in global economic models. *Agri Econ* 1(45):51–67
4. Ermacorra G, Toma A, Bona B, Chiaberge M, Silvagni M (2013) A cloud robotics architecture for an emergency management and monitoring service in a smart city environment. In: 2013 IEEE/RSJ international conference of intelligent robots and systems, vol 3, No 8
5. Bernon MP, Picard GG (2007) Enhancing self-organising emergent systems design with simulation. In: *Engineering societies in the agents World VII*. Springer, Berlin, pp 284–299
6. Kuyucu T, Tanev I, Shimohara K (2015) Superadditive effect of multi-robot coordination in the exploration of unknown environments via stigmergy. *Neurocomputing* 148:83–90
7. Dasgupta P (2008) A multiagent swarming system for distributed automatic target recognition using unmanned aerial vehicles. *IEEE Trans Syst Man Cybern—Part A: Syst Humans* 3(38):549–563
8. Kerr J, MostrovsKy T (2003) From space to species: ecological applications for remote sensing. *Trends Ecol Evol* (18):299–305
9. Richardson AD, Braswell BH, Hollinger DY, Jekins JP, Ollinger SV (2009) Near-surface remote sensing of spatial and temporal variation in canopy phenology. *Ecol Appls* (19):1417–1428
10. Vander Walt S, Colbert SC, Varoquaux G (2011) The NumPy array: a structure for efficient numerical computation. *Comput Sci Eng* (13):22–30



# Garbage Classification Using YOLOv3



**Murli Manohar Pant, Akanksha, Muskan Gupta,  
and Madan Mohan Tripathi**

## 1 Introduction

Overpopulation is one of the major problems faced by our society in recent times. There are many other problems that originate due to overpopulation and increase in garbage, and inability to process the garbage properly is one of them. The littering of garbage is a problem, which may seem small but when we look at the bigger picture this accumulates the garbage and harms our environment at a large scale. The amount of waste generated is increasing every day and a proper disposal of waste is used to ensure the process of garbage management [1]. Now the garbage is also of different kinds and is majorly classified into biodegradable and non-biodegradable wastes. The amount of waste generated in both categories is huge, and the need for classification and proper management of garbage is high. People litter the garbage here and there and don't even care about segregating it but segregation is the major part of the garbage disposal.

Technology can be used to segregate the garbage by classifying it into the respective categories. Classification is important so as to decide which waste has to be recycled, reduced or reused, and these play a major role in waste management. In this paper, an innovative algorithm is used to detect a garbage and hence classify it into respective categories, i.e., biodegradable and non-biodegradable. The dataset of 12,000 images containing both the types of waste was created with 10 classes of both categories and was used for the training of the model. The algorithm used is YOLOv3 (You only look once), which majorly focuses on the convolutional neural networks and is one of the fastest object detection algorithms used for real-time detection with high accuracy. Object detection algorithms majorly use convolutional neural networks for extracting the features from an image. R-CNN [2], Fast R-CNN [3] and Faster R-CNN [4] are methods, which improve the mean average precision

---

M. M. Pant (✉) · Akanksha · M. Gupta · M. M. Tripathi  
Electrical Engineering, Delhi Technological University, New Delhi, India

and reduce the time for training. It is used in this paper to detect the garbage and hence classify it into biodegradable and non-biodegradable categories. After training the model with the dataset using YOLOv3 and testing it, the model was able to detect the garbage and classify it with an MAP accuracy of 99.57%.

This type of model can be effectively used in industries and can be used to reduce the human efforts to classify the garbage. Classification of garbage plays a major role where production of garbage is high as in big industries where a huge amount of garbage is produced, and if the garbage there is not classified and disposed properly, it can cause a lot of harm to the environment.

The remainder of the paper is organized in the following manner: Sect. 2 explains the preparation and processing of the dataset in which it is explained how the dataset was created, which involved clicking of pictures, processing of pictures and annotations of pictures and finally the creation of dataset. Section 3 talks about the image capture through the raspberry pi cam. Section 4 talks about the algorithm, which is YOLOv3, how it operates and how it is used in this study for detection and classification of garbage while the conclusion of the study and the future scope is presented in Sect. 5 with the acknowledgments presented.

## 2 Preparation and Processing of Dataset

The preparation of dataset to train on YOLOv3 was done by the following process.

### 2.1 *Clicking the Images*

The first step was collecting wastes for both the categories and clicking their pictures from various angles. 10 objects were taken for each of the categories, i.e., biodegradable and non-biodegradable categories, and 300 images of each object were taken. The pictures were clicked by a mobile camera and taken with different angles and with different surroundings and then were put together and then processed.

### 2.2 *Processing of Images*

Images were cropped and resized (compressed), their contrasts were changed and augmented to increase the number of these images to 600. These images contained a variety of biodegradable and non-biodegradable wastes, which are generally found in the household. The processing of the images included increasing the number of images and naming them in sequential order. The contrasting of images was done, and filters (Gaussian, negative) were applied. The images were then augmented. For enhancing the performance of deep convolutional neural networks, the expansion of

the dataset is required, and data augmentation methods are used for the same [5]. The number of images was increased for each item from 300 to 600, which created modified versions of images, and this process also improves the performance of the model and also the ability of the model to generalize the result. Now, we had a total of  $(600 * 10) + (600 * 10) = 12,000$  images. Now these images were clubbed together in the same folder. Now using a python program, all of these images were renamed in a sequence.

### 2.3 Annotations of Images

The next step was the annotation of images. Labeling is the software that was used to annotate these images, and a total of 20 classes were created, a class for each item. Labeling is a tool available online that can be used for annotations of images and for dataset preparations and using it the images can be annotated in the form of either txt file or xml file. It is a very useful tool, which labels the images and saves the coordinates of the frames of the annotated image in one of the two formats as per requirement. Image annotation is basically a computer vision process in which labels are given to the images so that the machine learns about the images and once it is trained it will be able to identify the particular image. For our study, we saved the files in xml files in the YOLOv3 format. All the 12,000 images with their xml files were saved in the same folder to be trained. Now after we had this complete dataset of images with annotations, the machine was ready to be trained and was trained using YOLOv3 code, which was done on the Google Colab platform (Fig. 1).



**Fig. 1** Images of biodegradable and non-biodegradable waste

### 3 Image Capturing

Raspberry cam was used to capture the image. The raspberry pi, a single board computer series that runs on Linux is a cheap and easy to handle multipurpose programmable computer and has various learning as well as industrial applications. In IoT vision, there are a wide range of research applications of raspberry pi [6]. It has set of GPIO pins (General Purpose Input Output pins) for hardware components, which are to be run using raspberry pi. The raspberry pi cam is connected using this GPIO pins. The raspberry pi cam connections are made with raspberry pi, and then it has to be enabled by running Raspi-config and selecting the camera option (Figs. 2 and 3).

The model that was trained through YOLOv3 was run on the image that was captured by the cam and was tested if the model was able to identify the image and then classify it accordingly into biodegradable and non-biodegradable waste. The image is first captured and stored in the memory of raspberry pi. Then it runs a custom trained YOLOv3 model to find the garbage in the captured image. If it finds



**Fig. 2** Image of a Raspberry Pi



**Fig. 3** Connecting Raspberry Pi cam with Raspberry Pi

garbage, it tries to identify the garbage in the image if it's one of the 20 classes of garbage in the dataset. If it detects and identifies the garbage, it tries to classify the image on the basis of the two categories, i.e., biodegradable and non-biodegradable wastes.

### 4 Algorithm Used for Detection and Classification of Garbage

The You Only Look Once (YOLO) v3 uses k cluster model and is one of the most used deep learning techniques [7]. A lot of research is being conducted for object detection in computer vision [8]. Deep learning techniques are being used for object detection [9]. High-level features are formed using low-level features to improve object detection capability [10]. It is used in various fields such as medical imaging [11], robot vision [12], industrial detection [13], autonomous driving [14], etc. In this paper, we are hereby using this object detection technique to detect and classify our garbage.

YOLOv3 has a 53 layer network and for detection, 53 more layers are stacked and so there are a total of 106 convolutional layers, which are underlying in the architecture of YOLOv3. This makes the detections at three different scales. In the network, the detection is done at three different places in the maps of three different sizes. The first 81 layers downsample the images, and the 82nd layer makes the first detection using  $1 \times 1$  detection kernel. The second detection is done at the 94th layer and at the 106th layer, third detection is done. Detections at different layers help in detecting small images, which is a feature improved as compared to the YOLOv2. Logistic regression is used in YOLOv3 for object confidence and class prediction. It is a fast method as compared with some other methods, which can be indicated through a plot of inference time of this method and other methods (Fig. 4).

Now coming to the study, the dataset that is being created is trained using YOLOv3 on Google Colab platform. While training, to find the accuracy of the model, MAP

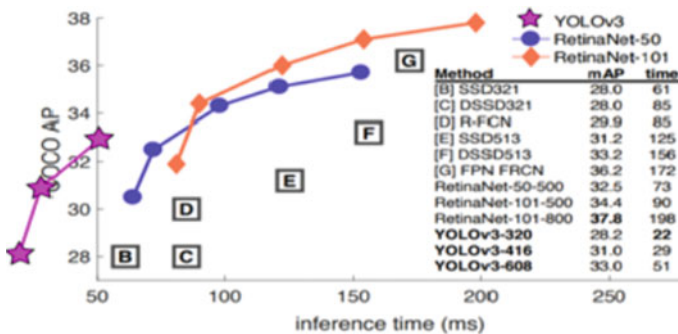


Fig. 4 COCO AP v/s Inference time comparisons

(mean average precision) was calculated. The Mean Average Precision is simply referred as Average Precision or (AP), which is used to measure the performance of the different PASCAL algorithms and models [15]. MAP is a quality measure for the proposed study. After being trained for 20 objects that are of both kinds, biodegradable and non-biodegradable wastes, the model is being tested. An image is being captured by using Raspberry pie cam, and the image is tested using the model.

The model was able to recognize the image and classify it efficiently. The proposed model was able to recognize garbage of 10 different types of non-biodegradable waste, i.e., plastic bottles, wrappers of biscuits, chips and chocolates, milk packets, empty packs of frooti and appy, polythene bags and cans. It was also able to detect biodegradable waste like tissue, paper bags, paper plates and bowls, banana peels, pizza boxes, paper cups and newspaper. The bot detects the garbage and changes its alignment towards garbage. Apart from detecting and recognizing these wastes, it was also able to classify them properly as biodegradable and non-biodegradable wastes.

## 5 Conclusions and Future Scopes

Among different models, the YOLOv3 is one of the fastest and most reliable algorithms. The precision we have obtained from this study verifies the same, and it detects and classifies the garbage at a fast speed. The custom-trained YOLOv3 model was able to detect and classify garbage of 10 bio-degradable and 10 non-biodegradable. The mean average precision of the model is 99.57%. The image from raspberry pi was captured efficiently and after running the custom trained YOLOv3 model, the garbage was detected if present in the image. It was further classified into biodegradable and non-biodegradable. The high mean average precision and correct classification of garbage show how effectively this model can be used in practical use.

This study of classifying the garbage on the basis of biodegradable and non-biodegradable using YOLOv3 model can have various industrial advantages. Using this model for image detection and classification, a bot can be developed that can be used to detect, collect and segregate the garbage and can classify it correctly. Hence, using such a bot will reduce human dependence for classification and segregation of garbage. In a bigger picture, this could be seen as a small step towards a smart city in which bots are used for waste management of the city in which this classification technique can be used in bots to classify the garbage and hence process the garbage accordingly.



**Acknowledgements** This research was supported by IoT Lab of the Department of Electrical Engineering, Delhi Technological University. We would like to thank the members of IoT Lab of the Department of Electrical Engineering, Delhi Technological University for their support.

## References

1. Thung G, Yang M, Classification of Trash for Recyclability Status. <https://www.semanticscholar.org/paper/Classification-of-Trash-for-Recyclability>
2. Girshick R, Donahue J, Darrell T, Malik J (2014) Rich feature hierarchies for accurate object detection and semantic segmentation. In: Proceedings of the IEEE conference on computer vision and pattern recognition. Columbus, OH, USA, pp 125–138
3. Girshick R (2015) Fast R-CNN. In: Proceedings of the IEEE international conference on computer vision. Santiago, Chile, pp 127–135
4. Ren S, He K, Girshick R, Sun J (2017) Faster R-CNN: towards real-time object detection with region proposal networks. *IEEE Trans Pattern Anal Mach Intell* 39:1137–1149
5. Shijie J, Ping W, Peiyi J, Siping H (2017) Research on data augmentation for image classification based on convolution neural networks. In: 2017 Chinese automation congress (CAC). <https://doi.org/10.1109/CAC.2017.8243510>
6. Maksimovic M, Vujovic V, Davidović N, Milosevic V, Perisic B (2014) Raspberry Pi as Internet of Things hardware: performances and constraints. *IcETRAN 2014*
7. Zhao L, Li S (2020) Object detection algorithm based on improved YOLOv3. *Electronics* 9(3):537. <https://doi.org/10.3390/electronics9030537>
8. Hanchinamani SR, Sarkar S, Bhairannawar SS (2016) Design and implementation of high speed background subtraction algorithm for moving object detection. In: Proceedings of the IEEE international conference on advances in computing, communications and informatics. Jaipur, India, pp 367–374
9. Zhou X, Gong W, Fu W, Du F (2017) Application of deep learning in object detection. In: Proceedings of the IEEE/ACIS 16th international conference on computer and information science. Wuhan, China, pp 631–634
10. Zhao Z, Zheng P, Xu S, Wu X (2019) Object detection with deep learning: a review. *IEEE Trans Neural Netw Learn Syst* 30:3212–3232
11. Christ PF, Kaissis G, Ettliger F, Kaissis G, Schlecht S, Ahmaddy F, Grün F, Menze B, Valentinsch A, Ahmadi S-A et al (2017) SurvivalNet: Predicting patient survival from diffusion weighted magnetic resonance images using cascaded fully convolutional and 3D convolutional neural networks. In: Proceedings of the IEEE international conference on international symposium on biomedical imaging. Melbourne, Australia, pp 839–843
12. Senicic M, Matijevic M, Nikitovic M (2018) Teaching the methods of object detection by robot vision. In: Proceedings of the IEEE international convention on information and communication technology, electronics and microelectronics. Opatija, Croatia, pp 558–563
13. Weimer D, Scholz-Reiter B, Shpitalni M (2016) Design of deep convolutional neural network architectures for automated feature extraction in industrial inspection. *CIRP Ann* 65:417–420
14. Chen X, Ma H, Wan J, Li B, Xia T (2017) Multi-view 3D object detection network for autonomous driving. In: Proceedings of the IEEE conference on computer vision and pattern recognition. Hawaii, HI, USA, pp 6526–6534
15. Yinghao C, Huang C, Xie X (2018) Multilayer hybrid deep-learning method for waste classification and recycling. *Computational intelligence and neuroscience* 1–9. <https://doi.org/10.1155/2018/5060857>

# Aerodynamics Characteristics of Compound Delta Wing at High Altitude



Gaurav Gupta , Pranav Tiwari, Bhanu Pratap Vatsa, Aashish Anand Sahay, K. S. Srikanth , and Shrikant Vidya 

## 1 Introduction

Delta wing configuration was galvanized from the birds to fabricate a higher-performing air-vehicle, which can land and take-off in an exceedingly little space to assist in stealth missions and perform completely different operations; however, because the delta wing produce vortex that facilitates them to achieve high speed and vortex flow depend extremely on the lift and drag value, which, in turn, can be controlled by the ever-changing angle of attack.

The phenomenon of vortex generation emerges as a result of flow separation that starts from the leading edge and leads to flow separation in a spiral vortex that, if positioned properly will facilitate achieving a super-cruising state without sending a large sum of fuel within the thruster.

T. Lee and his team studied delta wing vortex breakdown and declared that, with lowered lift and drag forces, the 65°-sweep reverse delta wing conjointly exhibited delayed stall compared to its delta wing configuration [1, 2].

Delta wing configuration employed in the experiment has a trailing edge that helps in controlling the flow as when the velocity is high the air spins very fast around the top and bottom contour of the wing creating a low-pressure region at the center of the vortex and the air, which separates from cutting edge to forward sweep can separate without adding the shock impact on the trailing edge, thus reducing pressure over the contour of the wing, which helps in reducing drag.

Delta wing configurations are used in many multi-purpose aircraft due to their very high-performance value, so this study will help to achieve better performance with the help of better maneuverability by changing the angle of attack.

---

G. Gupta (✉) · P. Tiwari · B. P. Vatsa · A. A. Sahay · K. S. Srikanth · S. Vidya  
School of Mechanical Engineering, Galgotias University, Greater Noida, Uttar Pradesh, India



The experimental study aims to determine the range of AOA for compound delta-wing aircraft with a double sweep to generate an invariable flow separation point by computational method to improve the potential of the aircraft.

## 2 Experimental Methodology and Design Modeling

Wing geometry is designed in SolidWorks with leading edge beveled at the angle of  $14^\circ$  for 53 cm from the chord of the wing with a first sweep angle of  $50^\circ$  and a second sweep angle of  $62.5^\circ$  with a trailing edge in the forward sweep at an angle of  $4^\circ$  (Fig. 1).

Flow on both wings is assumed to be computationally aligned with the chord of the wing so only half of the domain is studied.

Boolean Tetrahedral Meshing of the rectangular domain is utilized in Ansys Fluent with 2,317,894 cells, computational flow experiment and numerical calculations are done on the contour of the wing in CFD using 'k- $\epsilon$  2nd Equation Model' simulating mean flow conditions.

Simulations were performed at attack angles of  $5^\circ$ ,  $10^\circ$  and  $15^\circ$  with pressure-based model in case of Mach No.—0.78 as in low-velocity air stream sweep from the wings and density-based model for Mach No.—2.0 as in high-velocity phase air

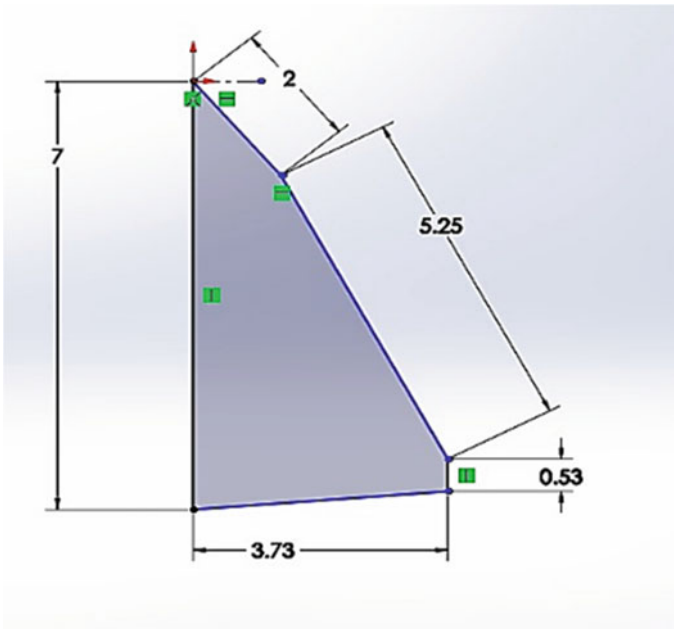


Fig. 1 Wing Geometry

particles compresses the molecules due to less time to undergo flow distortion, and the flow distribution on the surface contour was studied to understand the pressure distribution on the wing created by vortex to identify the angle of attack for better pressure distribution on wing and stability of vortex to help attain super-cruising.

## 3 Result

### 3.1 *Airflow Interpretation*

Airflow interpretation of the double sweep delta wing was done on three ranges of AOA for both subsonic and supersonic velocity. This led us to study the surface contour for pressure distribution.

CFD images show the pressure dissemination from Fig. 2 to Fig. 7. Numerical values of lift coefficient and drag coefficient were obtained, which were illustrated through graphical representation from Fig. 8 to Fig. 17.

The following results were obtained:

#### **Airflow Interpretation for Subsonic Velocity**

In Fig. 2, the flow separation at AOA  $5^\circ$  starts at the cutting edge, which forms an initial vortex. Due to this, the value of the lift was increased. Drag was also increased. There was no significant improvement in the L/D ratio, and the initial vortex density was low with higher pressure at the cutting edge and forward sweep edge. In Fig. 4, at AOA  $10^\circ$ , a dominated vortex is created over the edge connecting to the initial vortex, and L/D was greater than in AOA  $5^\circ$  with high-pressure density at forward sweep edge. In Fig. 6, at AOA,  $15^\circ$  dominant vortex is created starting from the cutting edge. Here, the shock impact reduced the vortex stability near the center of the wing. This resulted in a weak vortex. The increment in lift force was quite significant with the corresponding increase in drag force.

#### **Airflow Interpretation for Supersonic Velocity**

In Fig. 3, a dominant vortex is created at AOA  $5^\circ$  starting from the cutting edge to the chord line with higher pressure at the cutting edge. A great amount of lift increase was observed with the corresponding higher increase in drag. L/D ratio was better compared to the subsonic part. In Fig. 5, at AOA  $10^\circ$ , a violent vortex was created from the cutting edge forming a powerful initial vortex. The value of L/D was higher compared to the subsonic velocity part. Lift force gained a boost of about 5 times resulting in better, improved, and stable flow regime for super cruising. In Fig. 7, at AOA  $15^\circ$ , a short length but dominant vortex is formed connecting to the cutting edge and reduced in the center of the wing resulting in higher pressure density at the forward sweep edge. Here, the higher AOA helped in early vortex formation but led to the increment in drag force. Thus, a lower L/D and high shock wave impact was observed.

### 3.2 Distribution of Pressure Contours

The observation of pressure dissemination for subsonic velocity and supersonic velocity is observed to be quite similar but at supersonic velocity, the air compresses upon impact lead to a denser and stable flow of vortex with higher pressure density on the wing at the point of vortex distortion.

The pressure scattering contours of the wing are represented in Figs. 2, 3, 4, 5, 6 and 7.

In Fig. 2, at AOA  $5^\circ$ , pressure is observed to be high at the cutting edge and tail of the wing, and the vortex is seen to have a lower density, the shock impact was also low in this case of subsonic due to lower velocity whereas in Fig. 3, at AOA  $5^\circ$ , a denser and more stable vortex is formed from the leading edge with the consistent vortex density.

In Fig. 4, at AOA  $10^\circ$ , the pressure density on the trailing edge was very high, a sustaining vortex is formed above the wing. In Fig. 5, due to greater velocity, the vortex flow was more stable, and shock impact was low, which helped to maintain super-cruising but the pressure density was increased in the wing towards the trailing edge and the leading edge of the wing.

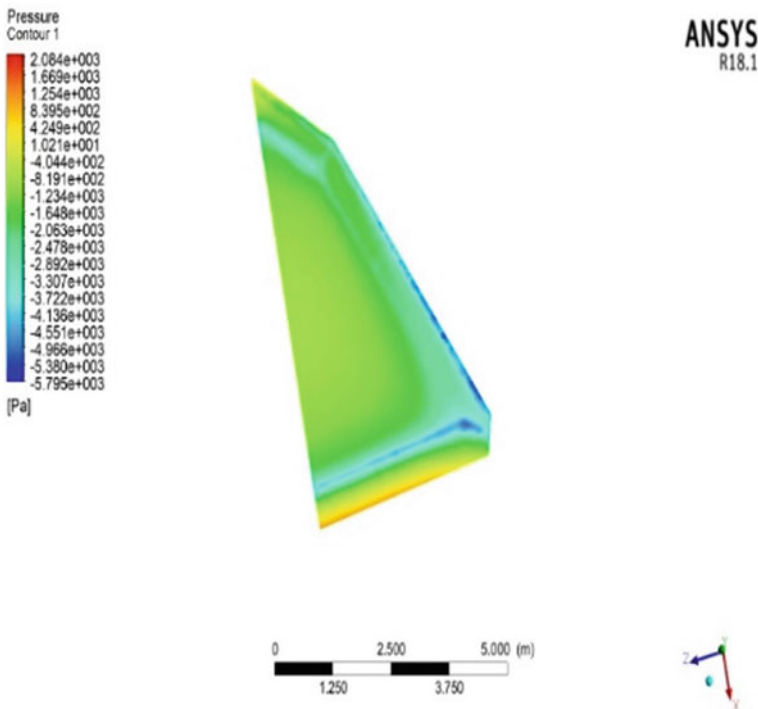


Fig. 2  $5^\circ$  AOA at Mach No 0.78

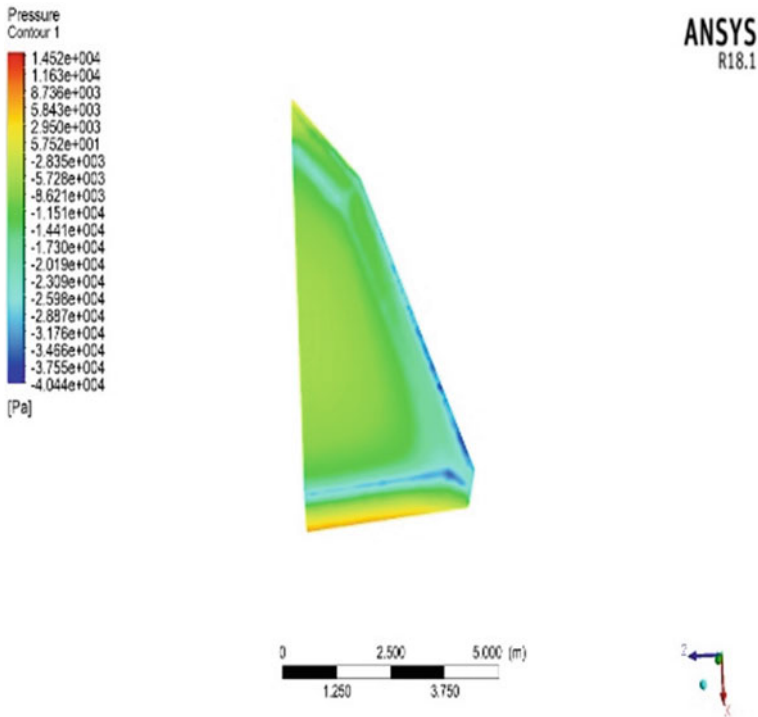


Fig. 3 5° AOA at Mach No 2.0

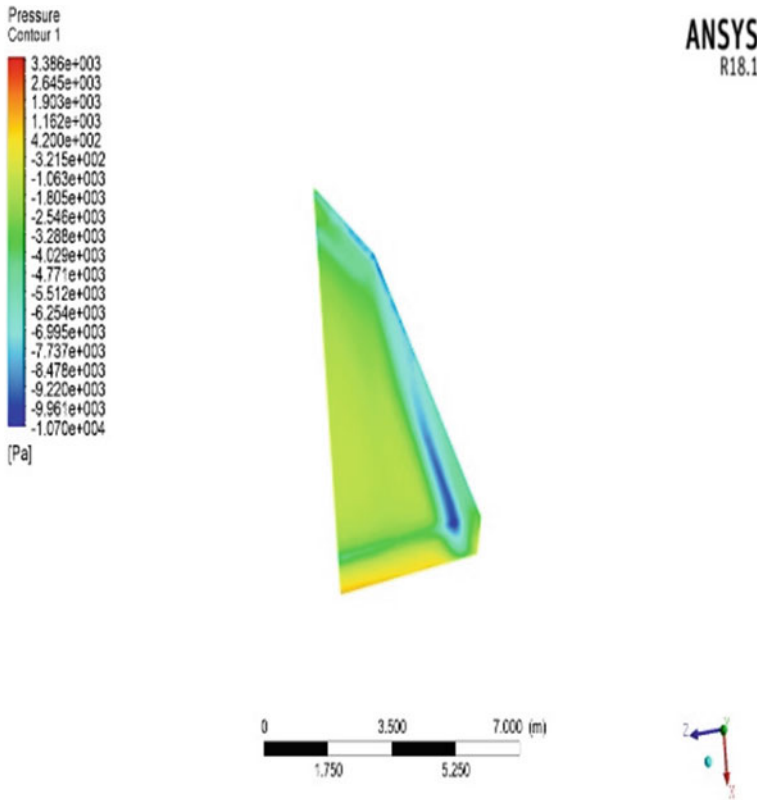
In Fig. 6, at AOA 15°, a dominant vortex is created quite early upon the cutting edge and reduces in the center of the wing. The pressure density was high at the forward sweep whereas in Fig. 7, vortex formation was early, and the drag is seen to be quite high. The shock impact was increased, which led us to distorted vortex flow, and pressure density was higher at the forward sweep.

### 3.3 Variation of Values

During the experiment, the values of lift, drag, lift coefficient and drag coefficient were studied. The graphical illustration below shows the changing values between subsonic velocity and supersonic velocity.

In Fig. 8, the lift coefficient increases linearly with an increase in AOA.

In Fig. 9, the lift coefficient is more linearly inclined but the slope is much smoother resulting in better flow separation in the supersonic speed case while changing attack angle.



**Fig. 4** 10° AOA at Mach No 0.78

In Fig. 10, steep variation is seen in the drag coefficient ( $C_d$ ) at the start for subsonic and after 10° attack angle, the variation becomes somewhat smoother.

In Fig. 11, steep variation is observed in the drag coefficient ( $C_d$ ), which shows an increment with the AOA.

Drag force is observed to increase very slowly for transitioning from 0° to 5° with a much greater increase in drag force as the AOA increases 5°. The massive increases in drag are observed.

In Fig. 12, the rate of change of drag increases heavily with a change in AOA.

In Fig. 13, the rate of change of drag is increasing linearly after a range, thus resulting in the stable increase of lift with drag improving transitioning in higher AOA with a stable flow regime.

L/D ratio is observed to be highest for the 5° AOA then continues to decline till 10° and reaches a state of stability.

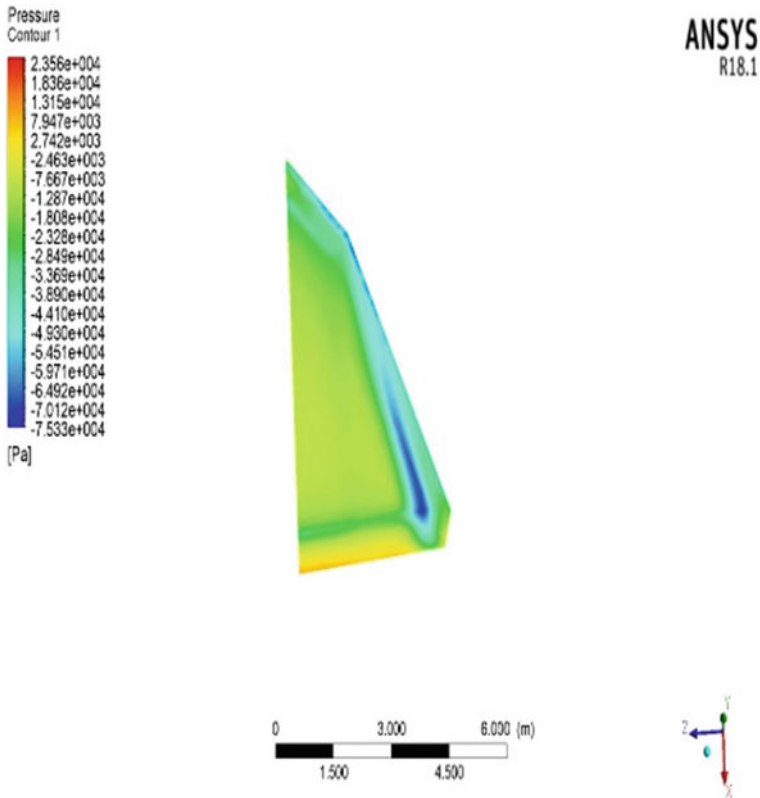
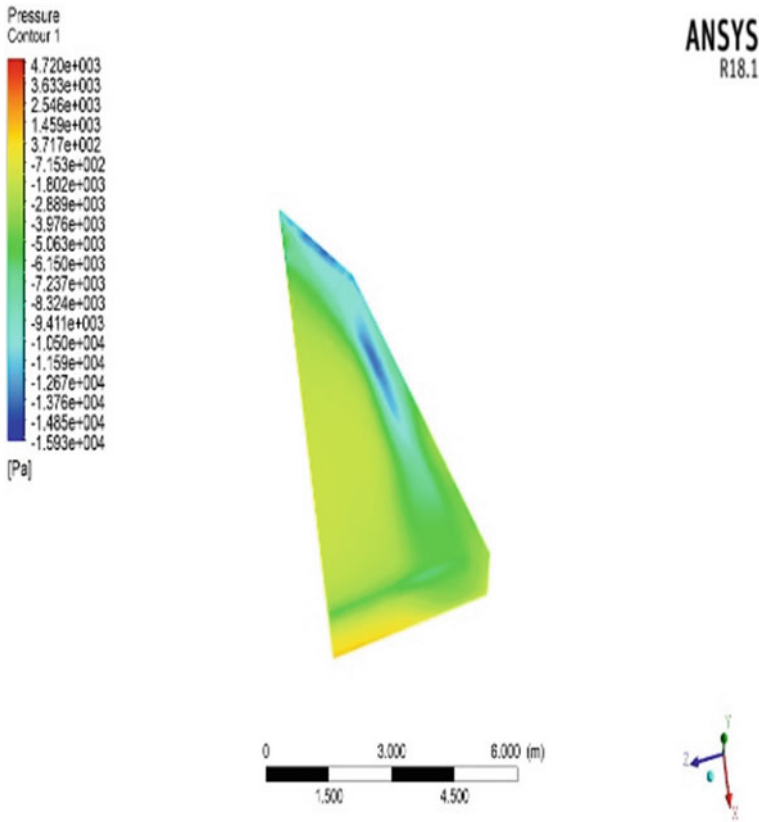


Fig. 5 10° AOA at Mach No 2.0

In Fig. 14,  $L/D$  is high, and stability in the value of  $L/D$  is seen to be linear, which signifies the lift force and drag force are stable after an attack angle of 10°.

In Fig. 15, the highest value of  $L/D$  is lower as compared to subsonic velocity, the ratio of  $L/D$  is seen to decrease slightly after 10°, which signifies an increase in lift is more as compared to drag.

In Fig. 16, following speed and AOA, the lift is observed to be in constant change at subsonic velocity. A steep increase in drag is been observed. In Fig. 17, the lift is constant and linear for supersonic velocity. Compared to the subsonic, speed value is high as a supersonic part. Thus, a stable and denser vortex is seen, resulting in better super-cruising conditions.



**Fig. 6** 15° AOA at Mach No 0.78

## 4 Conclusion

In this experiment, the airflow interpretation is conducted in subsonic velocity and supersonic velocity regimes at high altitude conditions for AOA of 5°, 10° and 15° on the compound delta wing to study the characteristics of the wing. The result achieved is discussed below.

The CFD results explain that the changing AOA, drag, lift and shockwave impact the characteristics of vortex generation. Upstream movement can be boosted with the increase in AOA. This led to the generation of the initial vortex toward the first sweep of the wing. During the experiment, we observed that AOA can contribute primarily to the generation of the vortex. Here, the lift was highly sensitive and variable with AOA. The drag force was observed to increase with the AOA as more surface area causes drag to increase thus compromising the lift force. The value of L/D was observed to be inversely proportional to AOA. This explains that the density of the vortex remains compatible with the increasing AOA.

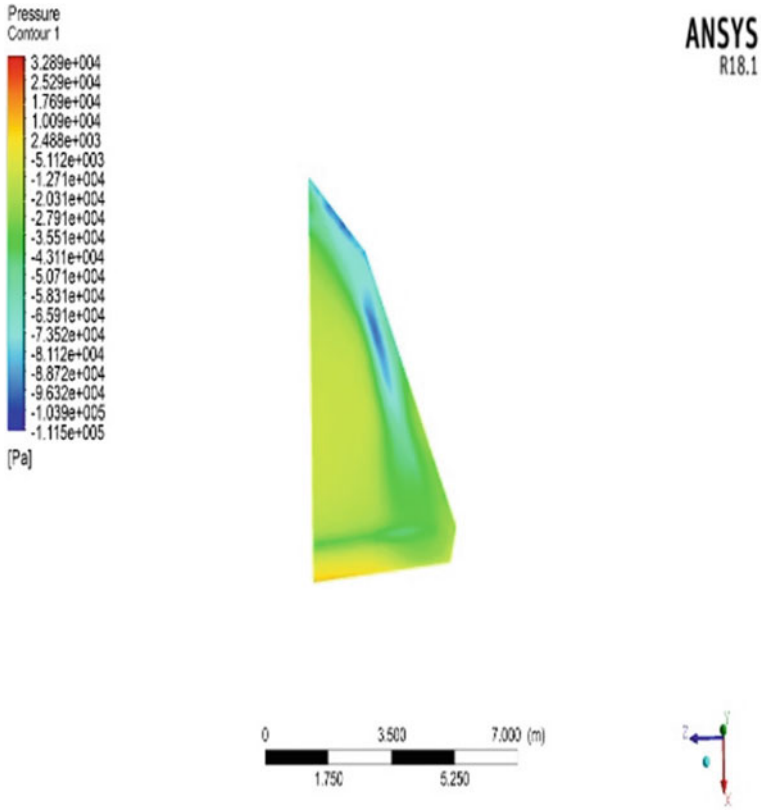
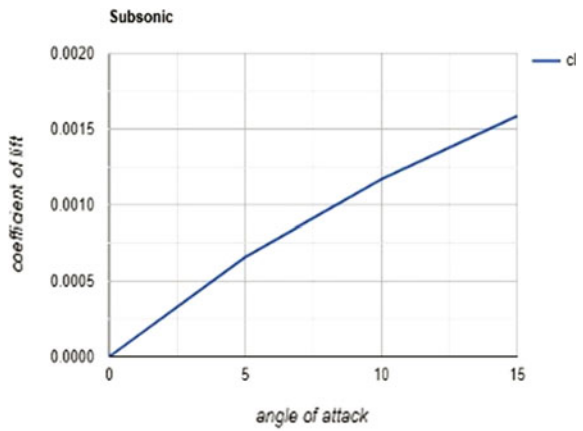


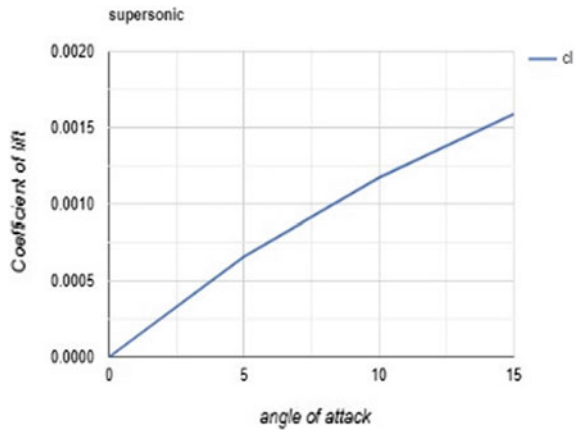
Fig. 7 15° AOA at Mach No 2.0

Fig. 8  $C_l$  versus AOA (at Mach No 0.78)

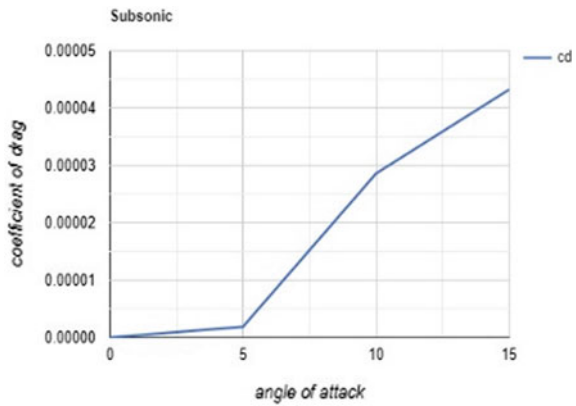




**Fig. 9**  $C_l$  versus AOA (at Mach No 2.0)



**Fig. 10**  $C_d$  versus AOA (at Mach No 0.78)



This experiment proves that the flight of the plane can be more stable if the AOA is steered between  $5^\circ$  and  $12^\circ$ . Airflow separation can be controlled, and shock waves can be reduced if the backend of the wing has a forward sweep. This forward sweep also lowers the pressure at the tail of the wing.

The present CFD analysis of flow separation of double sweep delta wing for subsonic velocity and supersonic velocity can be inciting to dissertate about vortex generation over the wing at the right position to maximize thrust and lift output helping to maintain super-cruising state.

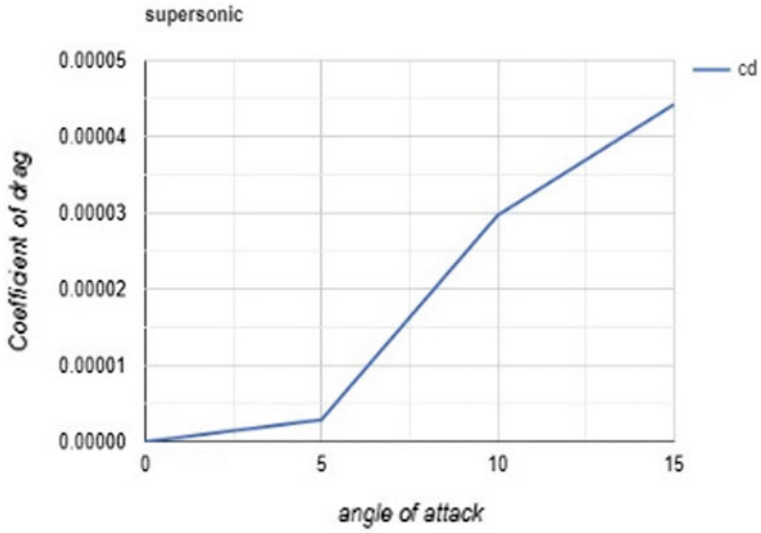


Fig. 11  $C_d$  versus AOA (at Mach No 2.0)

Fig. 12 D versus AOA (at Mach No 0.78)

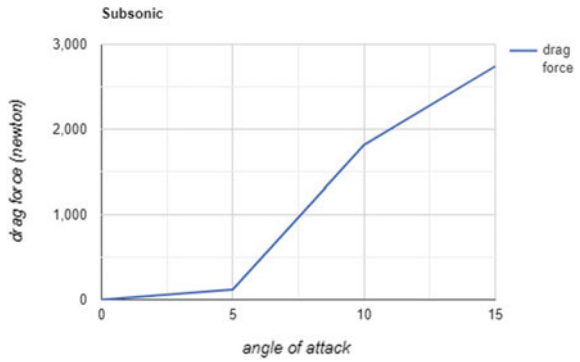
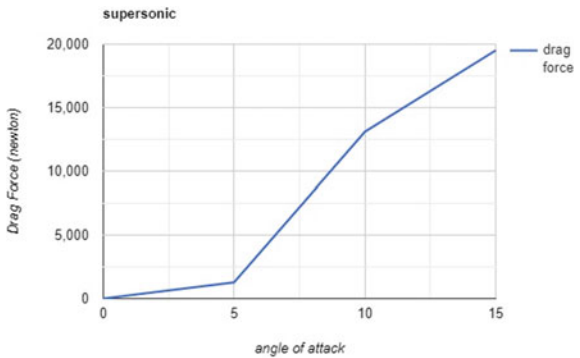
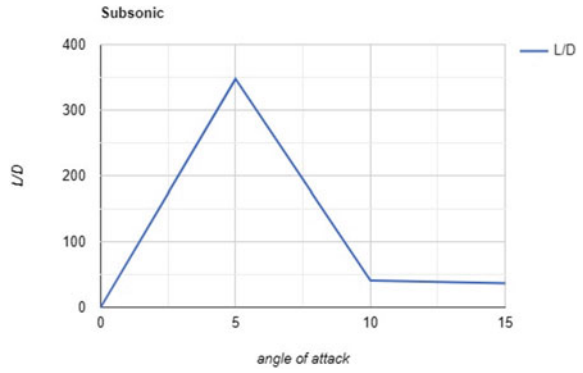


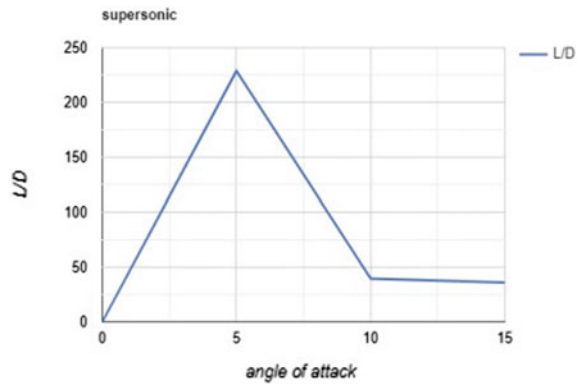
Fig. 13 D versus AOA (at Mach No 2.0)



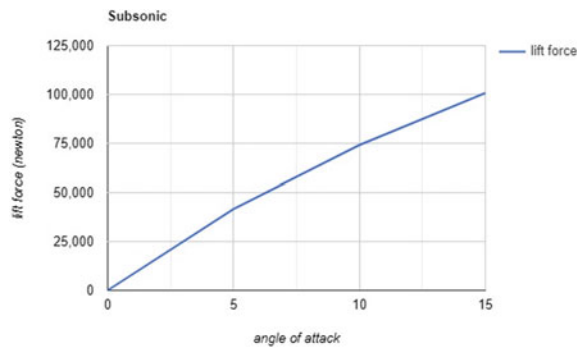
**Fig. 14** L/D versus AOA (at Mach No 0.78)



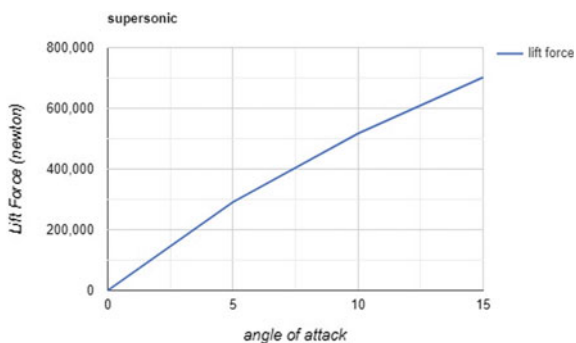
**Fig. 15** L/D versus AOA (at Mach No 2.0)



**Fig. 16** L versus AOA (at Mach No 0.78)



**Fig. 17** L versus AOA (at Mach No 2.0)



## References

1. Lee T, Tremblay-Dionne V, Ko LS (2019) Ground effect on a slender reverse delta wing with anhedral. Proc Inst Mech Eng Part G: J Aerosp Eng 233(4):1516–1525
2. Gupta G, Tiwari P, Vatsa BP, Sahay AA, Srikanth KS, Vidya S (2021) Aerodynamics characteristics of compound delta wing at sea level. In: IOP conference series: materials science and engineering

# Current Research Aspects and Trends in Electrical Discharge Machining: A Review



Shivam Rawat, Satyam Tiwari, Tariq Zafar, Abhishek Singh, Anurag Shanu, and Shrikant Vidya

## 1 Introduction

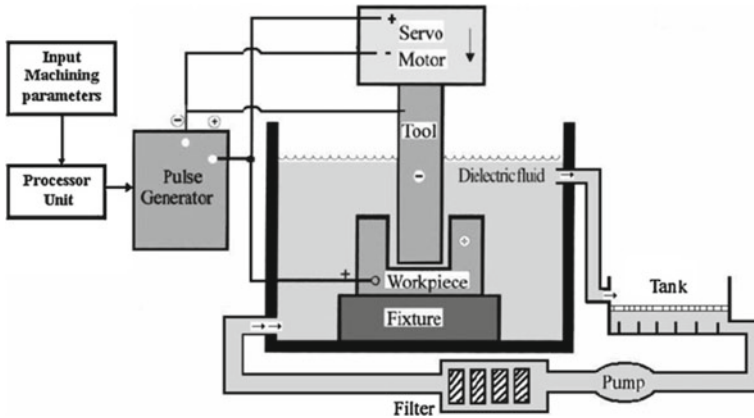
EDM refers to non-conventional machining procedures. EDM is a machining alternative for producing geometrically complicated or hard material pieces, which are exceedingly tough to manufacture using traditional machining methods. The non-contact machining technology has evolved from a simple tool and die fabrication method to a very small-scale application machining alternative, creating a great deal of research interest. EDM is most often utilized in unconventional substance removal techniques. Its particular capability in the fabrication of mould, cast, automobile, aeronautics, and surgical parts has been its unique property of employing heat energy to create electrically conductive components irrespective of hardness.

Metal removal in EDM is because of erosion caused by continuous spark discharge, which occurs amongst tool electrodes and workpieces. Generally, tool electrode is made negative whereas workpiece is made positive. The servo mechanism sustains a very narrow gap of a few micrometers amongst tool electrode and the workpiece. Tool and workpiece dipped into dielectric medium. EDM oil or kerosene is a common type of dielectric liquid used, whereas gaseous dielectrics are also used (Fig. 1).

In precision manufacturing, electrical discharge machining (EDM) plays an important role [1–3]. EDM is widely used when precision is of great importance in the processing of conductive materials. Roughing is a complex procedure in EDM because it measures more than one improvement in processing performance, namely, the MRR along with surface cleanliness (SF), which are both needed to achieve a precision function [4, 5]. EDM is an unconventional process in which the corresponding profile is obtained using the energy of sparks. EDM has evolved from a

---

S. Rawat · S. Tiwari · T. Zafar · A. Singh · A. Shanu (✉) · S. Vidya  
Department of Mechanical Engineering, Galgotias University, Greater Noida, India  
e-mail: [anurag.shanu@galgotiasuniversity.edu.in](mailto:anurag.shanu@galgotiasuniversity.edu.in)



**Fig. 1** Schematic of the EDM process [1]

simplified tool and die manufacturing process to the best choice for the production on small-scale components by the ultimate level of dimension exactness [6–8]. EDM's reputation and performance are due to its uniqueness in producing a variety of components that are very difficult to process, such as titanium, tungsten carbide, Inconel materials, etc., and offers an environment for producing complex shapes that are often impossible to process with conventional machining methods [9, 10].

Machining of materials to the required shape using conventional cutting tool is generally harder than the work material for the production of materials in industries. It is usually noticed that there has been frequent geometrical changes being found in the tools, and also tool wear is also found in the conventional tools during operation. The tools used conventionally for this problem are costly and hence alternate choice for ease of machining with low cost would lead to the usage of EDM [11–13]. EDM is a well-known machining technique that is used in modern industries to create geometrically complex or solid parts from substances, which are difficult to manufacture using older methods.

Non-contact machining is receiving a lot of research attention as it evolves from a basic tool and die production technique to an alternate processing of micro-scale applications. EDM experts have been exploring a number of methods for enhancing sparking efficiency in recent years, including many innovative experimental ideas that vary from the standard EDM sparking phenomenon. The aims of this new study are the same, regardless of the methods used to achieve more effective metal removal while reducing tool wear and enhancing surface quality [14–16].

Marashi et al. [17] provided a research for analyzing the dielectric changes by addition of powder to dielectric. They utilized powder dielectric in the process in the name of powder mixed EDM (PMEDM). Their results show that the PMEDM helps the manufactured parts with primarily high surface quality. They also explained in detail about the role of powder addition and their improved performance in discharge

characteristics during machining operation. Eventually, they discussed the concentration of powder particles and physical—thermal properties in detail. They narrated the suitable technique to select the form of suitable powder for further studies.

Dimla et al. [18] described how rapid prototyping led to the development of fast EDM electrodes. “Copper covering of stereo lithography models and copper covering of direct metal laser sintered (bronze) models” were two different techniques they used. Finally, they demonstrated that the required copper was not deposited on the electrode’s inner side. They also proved that the electrodes were not suitable for performing EDM operation.

Kunleda et al. [19] milled three-dimensional cavity using EDM. They employed gas in the form of working fluid. They also generated high-pressure gas flow with which molten workpiece materials were removed. They also demonstrated that the electrodes were ineffective for EDM operations.

Newton et al. [20] used Inconel 718 with high nickel content super alloy. Super alloy generally contains high strength at higher temperatures. They also discovered oxidation and corrosion resistance. During the production of Inconel 718 parts, they demonstrated that non-traditional EDM has numerous advantages over conventional machining. The experiment was primarily carried out to determine the parameters responsible for the formation of recast layers in Inconel 718.

Spedding et al. [21] perform an experiment and attempted modeling using Response Surface Methodology (RSM) and Artificial Neural Networks (ANN). They remarked that the performance responses were surface roughness and surface waviness. They also did validation experiment and concluded that the proposed models produced accurate results.

Ramasamy et al. [22]. They stressed that this EDM process generally used in places where highly complex shapes of the workpiece with high hardness such as hardened steel. It has also been reported that during high MMR, the surface finish degrades. They also found some cracks like microcracks in the finished workpiece. They also studied the 3D surface characterization to study the various surface texture parameters. They finally discovered that one of the most significant variables affecting surface texture was pulse current.

## 2 Latest Trends in EDM

Meena et al. [23] researched the EDM machining of Ti-6Al-4 V alloy along aid of GRA as well as studied the impact of polarity shifting along with ultrasonic vibration in dielectric fluid medium at micro-EDM phase and found substantial improvement in MRR and Ra.

Valaki et al. [24] suggested a bio-dielectric fluid based on waste vegetable oil for sustainable EDM machining, focusing on eco-friendly processes to mitigate environmental contaminants. They were also able to improve the MRR with the aid of this new technique.

Niamat et al. [24] suggested a new dielectric medium and explored the impact of paraffin with purified water as dielectrics on EDM. They examined how the results of MRR, TWR, and Ra changed over with the addition of new dielectric medium.

Sadagopan and Mouliprasanth et al. [25] discovered that machining high speed steel (HSS) in EDM with the help of water and compressed air as dielectric enhanced the MRR by 62% over traditional EDM.

Das et al. [26] highlighted the importance of environmentally sustainable machining in all ways, and they also proposed using neem oil as a dielectric medium in EDM. Their experiment was carried out on a Sparkonix EDM computer equipped with a Servomax DC motor.

The EDM of  $\alpha$ - $\beta$  brass was studied by Marichamy et al. [27], and its process parameters were improved employing Taguchi methods. They observed that the peak current had been the most essential part impacting the responses (MRR, TWR, and Ra), and the percentage proportion of each parameter was calculated by using ANOVA.

Azhiri et al. [28] replaced the liquid electrode with the help of gaseous medium to improve the WEDM process in machining Al-SiC MMC. They also identified that the addition of gaseous electrode medium improved surface quality but produced lower MRR. GRA was used to enhance cutting velocity (CV) and lower the Ra. As per ANOVA, pulse on time was the important item impacting the CV and Ra.

EDM machining on hybrid metal matrix composite was performed by Gopalakannan et al. [29]. As the method parameters, they chose the pulse current, the pulse time, and the distance voltage. Taguchi-based GRA has been used to manufacture greys for various relational properties (MRR, TWR, SR). ANOVA has defined the critical factors that adjust the output reactions (pulse current, pulses on time).

Ugrasen et al. [30] employed optimization technique with WEDM of HCHCr. Taguchi's L27 OA was utilized for dealing out the parameters. Along with current, Pon time, Poff time bed speed was also changed. Outcome responses were Ra and MRR. ANOVA was also part of their experiment to know the values of the affecting parameters.

Ni55.8Ti shape memory alloy was allowed for machining with the help of WEDM process by Magabe et al. [31]. Empirical modeling with ANOVA tool had been used with Taguchi's L16 OA. They found very good improvement in the formation of cracks over the surface layers. Their enhanced MRR was 0.021 g/mm, and surface finish was Rz-6.2  $\mu$ m.

Khundrakpam et al. [32] proposed a near dry EDM by using Taguchi-based GRA method towards minimizing the surface roughness. They used only minimum quantity of lubrication amongst the anode and cathode. GRA converted five various responses into single grey grade and identified the most favorable parameters (pulse-on time, discharge current).

Balasubramanian et al. [33] performed machining of high-temperature Ni44Ti50Cu4Zr2 shape memory alloy using coated wire EDM. It reveals that MRR raises as the pulse on time and current raises but decreases as pulse off time and servo voltage rise.



MartynaElwira and Biliska [34] examined the impact of EDM variables on the outside structure of different materials (30HHS heat treating steel, 4H13 stainless steel, Ti-6Al-4 V titanium alloy and NC6 tool steel). Pulse on time (Ton), pulse off time (Toff) and current (I) were taken for all different materials, and statistical analysis was carried out for 24 EDM experiments. Major impacting parameters over surface quality have been presented in the experiment.

Soundhar et al. [35] conducted an experiment on titanium alloy (Ti-13Zr-13Nb (TZN)), and they prepared the alloy with the help of powder metallurgy. They state that traditional machining of TZN alloys produces poor surface with a greater tool wear rate, and hence, they adopted EDM process. Their selected parameters (pulse on time, pulse off time, voltage, and current) were analyzed for optimum results of MRR, Ra, and TWR. They adopted RSM empirical model and ANOVA.

Parsana et al. [36] formulated a mathematical model with the help of RSM through Box-Behnken. They studied MRR, TWR, and roundness of the hole by analyzing the parameters (pulse-on time, pulse-off time and peak current). They executed the accuracy through confirmation runs. They adopted weighted sum approach as well as multi-purpose PVS optimum solutions. Eventually, they arrived at the solution through the level diagrams.

### 3 Conclusion

This paper focused on the emerging EDM technologies that have been built to help users fulfill their demands for optimum efficiency and quantity. The primary aim of this paper is to give an idea about EDM operation used mainly for the workpiece, which are difficult to cut, and similarly, various parameters associated with EDM process have also been discussed in detail. This review paper may be useful to those who wish to conduct experiment using EDM machine. Since conventional machining is not being used in industries as they are not suitable for the modern industry requirements.

There are different process variants of EDM like wire EDM, near dry EDM, which may be utilized for machining and characterization of advanced materials like metal matrix composites (MMCs). Recent research shows that the machining performance like MMR and surface integrity improved with the process variation like rotary tool EDM. Fabrication of ceramic materials with EDM is another key research area. Many researchers have tried to fabricate it using EDM and discovered considerable improvements in process performance.

The authors agree that the challenge for EDM producers is to continue to push the envelope in terms of producing EDM that is environmentally friendly and can be used for unattended machining. Key research areas include achieving high conductivity and strength without losing fracture toughness.

## References

1. Shagbark MR et al (2013) Fuzzy approach to select machining parameters in electrical discharge machining (EDM) and ultrasonic-assisted EDM processes. *J Manuf Syst* 32(1):32–39
2. Chattopadhyay KD et al (2008) Analysis of rotary electrical discharge machining characteristics in reversal magnetic field for copper-en8 steel system. *Int J Adv Manuf Technol* 38(9):925–937
3. Hung J-C, Yang T-C, Li K-C (2011) Studies on the fabrication of metallic bipolar plates—using micro electrical discharge machining milling. *J Power Sources* 196(4):2070–2074
4. Thoe TB, Aspinwall DK, Wise MLH (1998) Review on ultrasonic machining. *Int J Mach Tools Manuf* 38(4):239–255
5. Joshi SN, Pande SS (2009) Development of an intelligent process model for EDM. *Int J Adv Manuf Technol* 45(3):300–317
6. Kar S, Patowari PK (2018) Electrode wear phenomenon and its compensation in micro electrical discharge milling: a review. *Mater Manuf Process* 33(14):1491–1517
7. Mahendran S et al (2010) A review of micro-EDM. In: *Proceedings of the international multi conference of engineers and computer scientists*, vol. 2
8. Sheil B (ed) (2014) *High definition: zero tolerance in design and production*. Wiley, New York
9. Hagedorn-Hansen D (2017) *The effects of developed selective laser melting strategies on titanium hybrid parts*. Stellenbosch University, Diss. Stellenbosch
10. Fotovvati B (2020) *Direct metal laser sintering of Ti-6Al-4V alloy: process-property-geometry empirical modeling and optimization*. The University of Memphis, Diss
11. Komanduri R (2000) *Tool materials*. Kirk-Othmer encyclopedia of chemical technology
12. Shokrani A, Dhokia V, Newman ST (2012) Environmentally conscious machining of difficult-to-machine materials with regard to cutting fluids. *Int J Mach Tools Manuf* 57:83–101
13. Padhee S et al (2012) Multi-objective parametric optimization of powder mixed electro-discharge machining using response surface methodology and non-dominated sorting genetic algorithm. *Sadhana* 37(2):223–240
14. Xavior MA, Adithan M (2009) Determining the influence of cutting fluids on tool wear and surface roughness during turning of AISI 304 austenitic stainless steel. *J Mater Process Technol* 209(2):900–909
15. Zhang, Julie Z., Joseph C. Chen, and E. Daniel Kirby. “Surface roughness optimization in an end-milling operation using the Taguchi design method.” *Journal of materials processing technology* 184.1–3 (2007): 233–239.
16. Ho KH, Newman ST (2003) State of the art electrical discharge machining (EDM). *Int J Mach Tools Manuf* 43(13):1287–1300
17. Marashi H et al (2016) State of the art in powder mixed dielectric for EDM applications. *Precision Eng* 46:11–33
18. Dimla DE, Hopkinson N, Rothe H (2004) Investigation of complex rapid EDM electrodes for rapid tooling applications. *Int J Adv Manuf Technol* 23(3):249–255
19. Kunleda M et al (2003) High speed 3D milling by dry EDM. *CIRP Ann* 52(1):147–150
20. Newton TR et al (2009) Investigation of the effect of process parameters on the formation and characteristics of recast layer in wire-EDM of Inconel 718. *Mater Sci Eng A* 513:208–215
21. Spedding TA, Wang ZQ (1997) Study on modeling of wire EDM process. *J Mater Process Technol* 69(1–3):18–28
22. Ramasawmy H, Blunt L (2004) Effect of EDM process parameters on 3D surface topography. *J Mater Process Technol* 148(2):155–164
23. Meena VK, Azad MS (2012) Grey relational analysis of micro-EDM machining of Ti-6Al-4V alloy. *Mater Manuf Process* 27(9):973–977
24. Valaki JB, Rathod PP (2016) Assessment of operational feasibility of waste vegetable oil based bio-dielectric fluid for sustainable electric discharge machining (EDM). *Int J Adv Manuf Technol* 87(5):1509–1518
25. Niamat M et al (2017) Effect of different dielectrics on material removal rate, electrode wear rate and microstructures in EDM. *Procedia Cirp* 60:2–7

26. Sadagopan P, Mouliprasanth B (2017) Investigation on the influence of different types of dielectrics in electrical discharge machining. *Int J Adv Manuf Technol* 92(1):277–291
27. Das S, Paul S, Doloi B (2019) Investigation of the machining performance of neem oil as a dielectric medium of EDM: a sustainable approach. *IOP conference series: materials science and engineering*, vol 653, no 1. IOP Publishing
28. Marichamy S et al (2016) Parametric optimization of EDM process on  $\alpha$ - $\beta$  brass using Taguchi approach. *Russian J Non-Ferrous Metals* 57(6):586–598
29. Azhiri RB et al (2014) Application of Taguchi, ANFIS and grey relational analysis for studying, modeling and optimization of wire EDM process while using gaseous media. *Int J Adv Manuf Technol* 71(1–4):279–295
30. Gopalakannan S, Senthilvelan T, Ranganathan S (2013) Statistical optimization of EDM parameters on machining of aluminium hybrid metal matrix composite by applying taguchi based grey analysis
31. Ugrasen G et al (2015) Optimization of process parameters in wire EDM of HCHCr material using Taguchi's technique. *Mater Today: Proc* 2(4–5):2443–2452
32. Magabe R et al (2019) Modeling and optimization of Wire-EDM parameters for machining of Ni 55.8 Ti shape memory alloy using hybrid approach of Taguchi and NSGA-II. *Int J Adv Manuf Technol* 102(5):1703–1717
33. Khundrakpam NS, Brar GS, Deepak D (2018) Grey-Taguchi optimization of near dry EDM process parameters on the surface roughness. *Mater Today: Proc* 5(2):4445–4451
34. Balasubramanian C, Rajkumar K (2021) Wire-EDM machinability investigation on quaternary Ni<sub>44</sub>Ti<sub>50</sub>Cu<sub>4</sub>Zr<sub>2</sub> shape memory alloy. *Mater Manuf Process* 1–10
35. Bilska ME (2021) Study of the influence of selected EDM machining parameters on performance and surface texture for selected materials. PhD diss., Instytut Techniki Wytwarzania
36. Soundhar A, Zubar HA, Sultan MTBHH, Kandasamy J (2019) Dataset on optimization of EDM machining parameters by using central composite design. *Data Brief* 23:103671
37. Parsana S, Radadia N, Sheth M, Sheth N, Savsani V, Prasad NE, Ramprabhu T (2018) Machining parameter optimization for EDM machining of Mg-RE-Zn-Zr alloy using multi-objective passing vehicle search algorithm. *Arch Civil Mech Eng* 18:799–817

# Current Research Aspects and Trends in Abrasive Water Jet Machining: A Review



Prabhat Ranjan, Pradumn Chaubey, P. Suresh, and Shrikant Vidya

## 1 Introduction

Using traditional machining, components are machined to the expected component geometry. Turning, milling, grinding and forming processes have very little advantages [1, 2]. Also, they have limitations like heat-affected zones and the need to configure a cutting tool for each application and work material. Water jet machining was introduced in the middle of 1800, and later, it was converted into abrasive water jet machining (AWJM) with the help of abrasive particles such as silicon dioxide, silicon carbide, aluminum oxide in order to speed up the rate of material removal [3]. Abrasive water jet (AWJ) is indeed a widely desired unconventional manufacturing technology used throughout modern industries [4]. Its uses in the manufacturing industries for the processing of different materials, especially those that are difficult to cut, are commonly used [5].

AWJ machining is highly favored because it produces little to no heat in the cutting field, as well as the material percentage removal is higher relative to other unorthodox machining such as WEDM, etc. [6–8]. Surface roughness is minimal with AWJ and as it does not generate much heat near the cutting zone, it causes very little microstructural changes to the surface of the work piece [9, 10]. However, it still has some disadvantages such as high initial cost and more noise associated with machining [11–13]. AWJM, in which particles of abrasives are mixed with a high-speed jet of water, hit the work surface [14, 15]. As the cutting movements of the AWJM are controlled by the computer, their operations are efficiently executed. AWJM are often employed in automotive industries, aerospace, sports, mining industries and electronics industries [16–19]. Figure 1 [20] portrays a schematic diagram of the AWJM process.

---

P. Ranjan · P. Chaubey · P. Suresh · S. Vidya (✉)  
Department of Mechanical Engineering, Galgotias University, Greater Noida, Uttar Pradesh, India

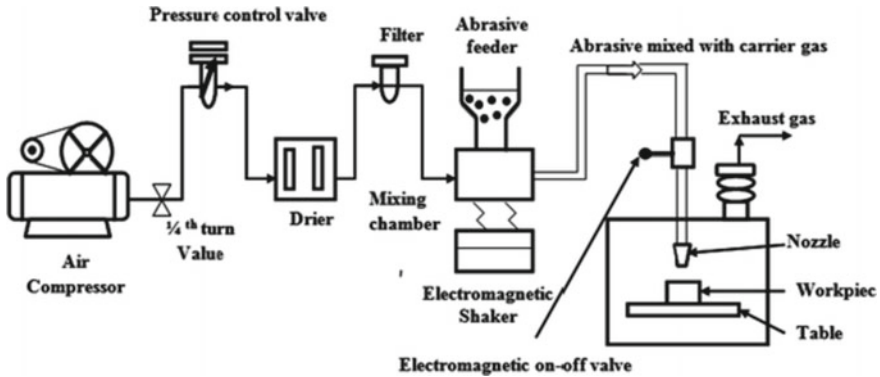


Fig. 1 Schematic diagram of the AWJM process [20]

## 2 Research Prospects and Trends

Material removal and accuracy of manufacturing are greatly connected to the type of abrasive used in the AWJM process [21]. Hardness of the abrasive materials plays a major role. Most widely used abrasives are silicon dioxide (Silica), boron carbide, silicon carbide, sodium bicarbonate, and garnet and aluminum oxide. Abrasive materials with high hardness could reduce the surface roughness and increase the MRR [22–24]. Abrasive grain particle size determines the operations of the AWJM [25]. For polishing operations, very fine particle abrasives are used, and for cutting operations, coarse grain particle size is used.

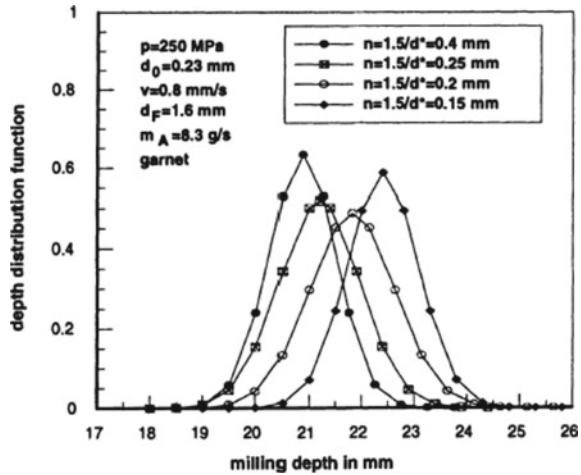
Agus et al. [26] identified the parameters to evaluate the abrasive particles such as hardness of abrasive material, density, shape, abrasive particle diameter and mass flow rate. They also stressed that for cutting the hard materials such as granite and porphyry, hardness of the abrasive materials plays the major role and for cutting the soft materials such as marble, particle shape plays the vital factor.

Momber et al. [27] identified that the rate of material removal improves greatly with an optimum grain size distribution, which is shown in Fig. 2. The AWJM performs machining under the influence of high-pressure water mixed with the particles of abrasive, which makes it an eco-friendly process of machining.

Most widely used abrasives are silicon dioxide (Silica), boron carbide, silicon carbide, sodium bicarbonate, and garnet and aluminum oxide [28]. Mardi et al. [29] analyzed the effects of the jet traverse speed on the surface of the Alumina nanoparticle reinforced with the metal matrix composite (MMC) machined by the AWJM. They concluded that high level of transverse speed could damage the surface of the work piece machined by the AWJM.

Arola and Ramulu et al. [30] investigated the material removal rate in AWJM of metal surface integrity and texture. They also conducted the microhardness test and carried out microstructure analysis. Their results suggest that the deepness of the

**Fig. 2** Influence of particle distribution parameter on milling depth variations [27]



surface plastic deformation is inversely relative to the co-efficient of the strength of the metals.

Zhao and Guo [31] studied the microstructure and topography of the abrasive water jet machined surface. They observed that the very high smooth surface is more possible with the hard materials and erosions on the soft materials pose very serious problems. Vigneshwaran et al. [32] studied the “AWJM of fiber-reinforced composite materials” as composite materials are vital parts in the manufacturing industry. They found that the AWJM is very suitable methodology for machining the fiber-reinforced composite materials.

Wang et al. [33] investigated the performance of machining and process of erosion of AWJM of polymer matrix composites (PMCs). They reported that the cutting parameters can decide the quality of kerf with increased rate of production. Traverse speed and pressure of the water play the key role in the depth of the cut and kerfs taper angle. Scanning electron microscope (SEM) revealed the intergranular cracking. They also created the mathematical model for verification.

Shanmugam et al. [34] employed a new technique of compensation in machining of alumina ceramics using AWJM and worked to minimize kerf tapers. They carried out the experiment to minimize the taper angle of kerf taper with the help of kerf taper compensation practice. They also stressed that the KTC angle 4–5° minimizes the kerf taper angle to zero. A predictive model with the help of dimensional analysis was used to verify the technique.

Srinivasu et al. [35] investigated the kinetic operating factors and their influence on the geometry of kerf during the machining of silicon carbide ceramics. They found that by changing  $\alpha$  (90°–40°), the geometry of kerf is closely reliant on the difference of stand-off distance, velocity distributions of abrasive element and their local blow angle.

Shukla et al. [36] demonstrated the application of the optimization technique in AWJM. They conducted experiment on AA6351 Al-alloy with the help of AWJM.

Their main aim was to get optimum values of the parameters involved in the machining performance. They also developed the regression model from the experimental results. Their responses were kerf and taper angle. They adopted Taguchi method along with the optimization technique.

Kumar et al. [37] reported the characterization and optimization of AWJM parameters of aluminum/tungsten carbide composite. They optimized the AWJM on machining the aluminum/tungsten carbide (2, 4, 6, 8 and 10 wt%) composite. Response surface methodology (RSM) was applied to explore the significance of the AWJM parameters on MRR. The most vital parameter affecting the MRR was transverse speed followed by the percentage of reinforcement particles and standoff distance. SR was mainly influenced by the percentage of tungsten carbide.

Gupta et al. [38] investigated the kerf characteristics in AWJM of marble. Water pressure, nozzle transverse speed and abrasive flow rate have been selected as process parameters. Experiments were performed on the basis of Taguchi's design of experiments (DoE) have been carried out for conducting the experiments in their study. Evaluation of data's has been carried out with the help of analysis of variance (ANOVA) by them. They also identified the most vital factor affecting the kerf characteristics. They concluded that the poor kerf width and kerf taper angle are greatly influenced by transverse speed.

Maneiah et al. [39] optimized the machining parameters for surface roughness during AWJM of aluminum/magnesium hybrid metal matrix composites. They chose the parameters such as standoff distance feed rate and flow rate of abrasive grain. The Taguchi method and ANOVA had been taken for optimization purposes to improve surface quality. Their results suggested that the vital factors affecting the quality of the surface were feed rate and flow rate of abrasive grain.

### 3 Conclusion

This paper deals with the AWJM processes and attempts have been made to help the researchers who perform nonconventional machining operation for application. The various process parameters associated with the AWJM have been discussed in detail. The MRR and its effectiveness improvement have also been narrated. Various optimization techniques with significant parameters have been analyzed and presented. Papers based on AWJM of ceramics, AWJM of polymer composite materials and AWJM of metallic materials have been discussed. It can be noted as besides drilling, slicing, and milling, Abrasive water jet machining can be effectively utilized for boring as well as straight and taper turning operation with fine tolerance, lesser burr formation and bending free process. This review paper would indeed help understanding the researches for their future research.

## References

1. Neugebauer R et al (2012) Resource and energy efficiency in machining using high-performance and hybrid processes. *Procedia CIRP* 1:3–16
2. Ramesh R, Mannan MA, Poo AN (2000) Error compensation in machine tools—a review: part I: geometric, cutting-force induced and fixture-dependent errors. *Int J Mach Tools Manuf* 40(9):1235–1256
3. Abbatelli D (2014) Material flows in the waterjet industry: an environmental perspective
4. Vijay MM, Babu NR (eds) *Proceedings of the 5th Pacific rim international conference on water jet technology*. Allied Publishers
5. Hloch S et al (2014) Abrasive waterjet (AWJ) titanium tangential turning evaluation. *Metalurgija* 53(4):537–540
6. Yuvaraj N, Pradeep Kumar M (2017) Investigation of process parameters influence in abrasive water jet cutting of D2 steel. *Mater Manuf Process* 32(2):151–161
7. Jain NK, Jain VK (2001) Modeling of material removal in mechanical type advanced machining processes: a state-of-art review. *Int J Mach Tools Manuf* 41(11):1573–1635
8. Natarajan Y et al (2020) Abrasive water jet machining process: a state of art review. *J Manuf Process* 49:271–322
9. Hascalik A, Çaydaş U, Gürün H (2007) Effect of traverse speed on abrasive waterjet machining of Ti–6Al–4V alloy. *Mater Des* 28(6):1953–1957
10. Arola D et al (2001) Waterjet and abrasive waterjet surface treatment of titanium: a comparison of surface texture and residual stress. *Wear* 249(10–11):943–950
11. Kulekci MK (2002) Processes and apparatus developments in industrial waterjet applications. *Int J Mach Tools Manuf* 42(12):1297–1306
12. Kim G, Denos BR, Sterkenburg R (2020) Influence of different piercing methods of abrasive waterjet on delamination of fiber reinforced composite laminate. *Compos Struct* 240:112065
13. Alberdi A, Rivero A, López de Lacalle LN (2011) Experimental study of the slot overlapping and tool path variation effect in abrasive waterjet milling. *J Manuf Sci Eng* 133(3)
14. Fowler G, Pashby IR, Shipway PH (2009) The effect of particle hardness and shape when abrasive water jet milling titanium alloy Ti6Al4V. *Wear* 266(7–8):613–620
15. Jerman M et al (2011) Measuring the water temperature changes throughout the abrasive water jet cutting system. In: 2011 WJTA American waterjet conference
16. Momber AW, Kovacevic R (2012) *Principles of abrasive water jet machining*. Springer Science & Business Media
17. Kovacevic R et al (1997) State of the art of research and development in abrasive waterjet machining 776–785
18. Liu X et al (2019) Waterjet machining and research developments: a review. *Int J Adv Manuf Technol* 102(5):1257–1335
19. Kechagias J, Petropoulos G, Vaxevanidis N (2012) Application of Taguchi design for quality characterization of abrasive water jet machining of TRIP sheet steels. *Int J Adv Manuf Technol* 62(5–8):635–643
20. Bhowmik S, Ray A (2017) Abrasive water jet machining of composite materials. In: *Advanced manufacturing technologies*. Springer, Cham, pp 77–97
21. Unde PD et al (2015) Experimental investigations into abrasive waterjet machining of carbon fiber reinforced plastic. *J Compos*
22. Gopal AV, Venkateswara Rao P (2003) Selection of optimum conditions for maximum material removal rate with surface finish and damage as constraints in SiC grinding. *Int J Mach Tools Manuf* 43(13):1327–1336
23. Khodaii J et al (2019) Influence of grinding parameters on phase transformation, surface roughness, and grinding cost of bioceramic partially stabilized zirconia (PSZ) using diamond grinding wheel. *Int J Adv Manuf Technol* 105(11):4715–4729
24. Jahan MP, Wong YS, Rahman M (2009) A study on the fine-finish die-sinking micro-EDM of tungsten carbide using different electrode materials. *J Mater Process Technol* 209(8):3956–3967



25. Kuttan AA, Rajesh R, Dev Anand M (2021) Abrasive water jet machining techniques and parameters: a state of the art, open issue challenges and research directions. *J Brazilian Soc Mech Sci Eng* 43(4):1–14
26. Agus M et al (1995) Abrasive performance in rock cutting with AWJ and ASJ. In: 8th American water jet conference, vol 26
27. Momber AW, Eusch I, Kovacevic R (1996) Machining refractory ceramics with abrasive water jets. *J Mater Sci* 31(24):6485–6493
28. Mort GA (1995) Results of abrasive water jet market survey. In: Proceedings of 8th American water jet conference, vol 1
29. Mardi KB et al (2017) Surface integrity of Mg-based nanocomposite produced by Abrasive Water Jet Machining (AWJM). *Mater Manuf Process* 32(15):1707–1714
30. Arola D, Ramulu M (1997) Material removal in abrasive waterjet machining of metals surface integrity and texture. *Wear* 210(1–2):50–58
31. Zhao W, Guo C (2014) Topography and microstructure of the cutting surface machined with abrasive waterjet. *Int J Adv Manuf Technol* 73(5–8):941–947
32. Vigneshwaran S, Uthayakumar M, Arumugaprabu V (2018) Abrasive water jet machining of fiber-reinforced composite materials. *J Reinf Plast Compos* 37(4):230–237
33. Wang J (1999) Abrasive waterjet machining of polymer matrix composites—cutting performance, erosive process and predictive models. *Int J Adv Manuf Technol* 15(10):757–768
34. Shanmugam DK, Wang J, Liu H (2008) Minimisation of kerf tapers in abrasive waterjet machining of alumina ceramics using a compensation technique. *Int J Mach Tools Manuf* 48(14):1527–1534
35. Srinivasu DS et al (2009) Influence of kinematic operating parameters on kerf geometry in abrasive waterjet machining of silicon carbide ceramics. *Int J Mach Tools Manuf* 49(14):1077–1088
36. Shukla R, Singh D (2017) Experimentation investigation of abrasive water jet machining parameters using Taguchi and Evolutionary optimization techniques. *Swarm Evol Comput* 32:167–183
37. Kumar K, Ravi V, Sreebalaji S, Pridhar T (2018) Characterization and optimization of abrasive water jet machining parameters of aluminium/tungsten carbide composites. *Measurement* 117:57–66
38. Gupta V et al (2014) Minimization of kerf taper angle and kerf width using Taguchi's method in abrasive water jet machining of marble. *Procedia Mater Sci* 6:140–149
39. Maneiah D et al (2020) Optimization of machining parameters for surface roughness during abrasive water jet machining of aluminium/magnesium hybrid metal matrix composites. *Mater Today: Proc* 27:1293–1298

# Design and Development of Environmental Monitoring AirShip



Ayush Singh, Ayush Kumar, and Anurag Shanu

## 1 Introduction

In recent years the use of unmanned aerial vehicle has increase dramatically. The purpose of UAV varies from crowd control, official government operations, several types of surveys, remote areas accessibility, relief during natural disasters, etc. scientists developing policies for government and other human policies are rather perplexed by the lack of data and inaccurate information about environment, specially densely sampled volumetric data. Ground-based monitoring stations can only provide ground level data and measurement, while satellite can only provide summed regional data. In order to develop a more matured, effective, and cost reduced system we are developing airship capable of collecting and handling these tasks.

The first recorded remote control airship 'Simon' was two decades ago [1]. The start of twenty-first century gave the research on airship a new perspective as it merged airship research with robotics and automation including path finding and visual servo control [2] and maneuvering flight path using GPS [3] for small indoor airship. And researchers have developed and experimentally demonstrated automatic control system [4] for an outdoor airship. The design of the airship discussed in this paper is driven by factors such as longevity, cost effectiveness, long-range and high-speed transmission, etc. Applications of drones for environmental surveillance are quite common, primarily because commercially available multi-rotor drones are noisy and with low endurance and a limited air time and costly also. Airships provide an elegant and feasible solution for long-term monitoring such as rural areas and places where people cannot go and monitor things that cannot be monitored without being present. Airships are much larger compared to conventional drones. But their extremely large size could be used for advertising and marketing, airships are much

---

A. Singh · A. Kumar · A. Shanu (✉)

Department of Mechanical Engineering, Galgotias University, G.B.Nagar, Greater Noida, India  
e-mail: [anurag.shanu@galgotiasuniversity.edu.in](mailto:anurag.shanu@galgotiasuniversity.edu.in)

more safe than other UAVs in case of malfunctioning they will descend gradually rather than crash landing.

Introduction of IOT dramatically changed the world as it connected several places, it completely revolutionized human society connecting physical and cyber world, devices like mobile phones started to emerge. LPWANs are the type of IOT system which provide energy efficient, inexpensive, and long-range communication network. The family of technology purpose to support large-scale IOT network sprawling over vast industrial and commercial purpose. LPWANs can be used for applications such as asset tracking and environmental monitoring, not all LPWANs are equal. There are multiple types of technologies operating in licensed like NB-IOT LTE-M and unlicensed like LoRa Sigfoxetc spectrum with varying degrees of performance in key network factors. The main aim of this paper is to build an airship which is cost effective, could work for an indefinite period of time (theoretically), taking real scenario and maximizing the time duration of flight, better maneuvering and control.

## 2 Assumptions

If we are talking about solar panels then we can assume that we can only get the sunlight half of the days' time which is nearly 12 h (assumed), and the other 12 h is night time. We assumed a constant supply of  $1000 \text{ W/m}^2$  for the first hours of the day. And it maintains a constant velocity ( $V$ ) which means it uses the stored power in the batteries during night time. We assumed that the airship has length ( $L$ ) and its diameter ( $D$ ) which is also its height to be  $L/3$ . For the purposes of calculating volume, surface area, and drag, we assume that the airship has a aerodynamic airship hull shape as in GNVR profile, the details are given in [5, 6, 7] (Fig. 1).

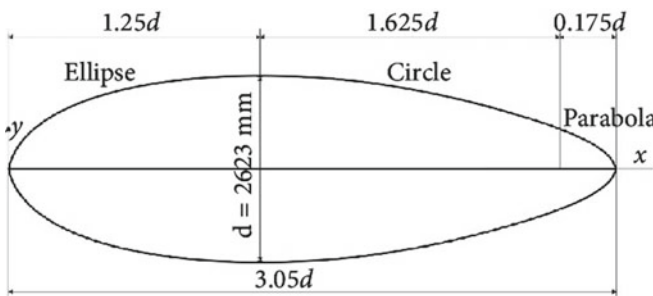


Fig. 1 GNVR

### 3 Envelop Profile

The envelop is the largest and most crucial component of the airship as it determines its aerodynamics and lifting capacity. Theoretically the envelop should have a high volume and low surface area ratio and low drag. This shape of envelop is aerodynamically better and produces low drag. There is more optimized shape but for easy calculation we will be choosing this design. The data of aerodynamic of GNVR aerostat are available below.

$$L = 3.05D.$$

$$\text{Surface area (SA)} = 7.4488D^2.$$

$$\text{Volume (V)} = 1.47926D^3.$$

$$\text{Center of volume location from nose (CV)} = 1.3834741 D.$$

The selection of material is very important as it contains and retains the lifting gas and support the gondola. Approximately 40% of the weight of the ship is that of envelop without air. Usually it is impossible to have all of these qualities in one type of material, hence a complex material or a laminated material is used.

The desired quality needed for the envelop is as follows:

Low fabric density.

High tear resistance.

Resistance to environmental degradation, UV rays, etc.

High strength to mass ratio.

Several materials from which the materials can be chosen.

PVC—Polyvinyl Chloride.

MPET—Metalized polyethylene terephthalate.

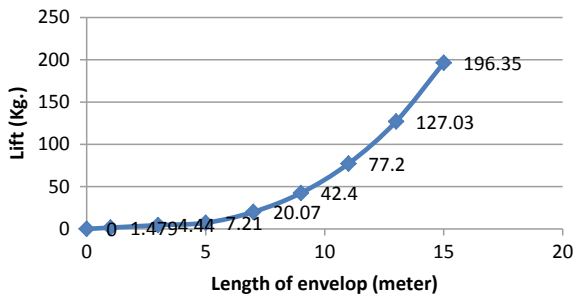
VMPET—Vacuum metalized polyethylene terephthalate.

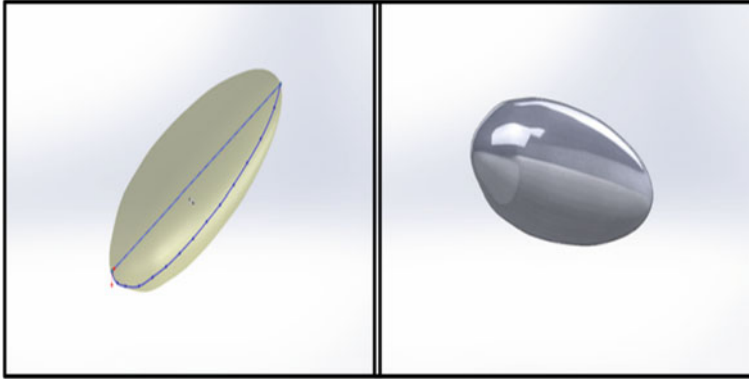
LDPE—Low density polyethylene (Table 1 and Figs. 2, 3 and 4).

**Table 1** Properties of some material

	PVC 1	PVC-PET Blend	MPET-1	MPET-2
Fabric density(g/m <sup>2</sup> )	200	180	100	105
Wear resistance	Good	Good	Good	satisfactory
strength	Excellent	Good	Good	Excellent

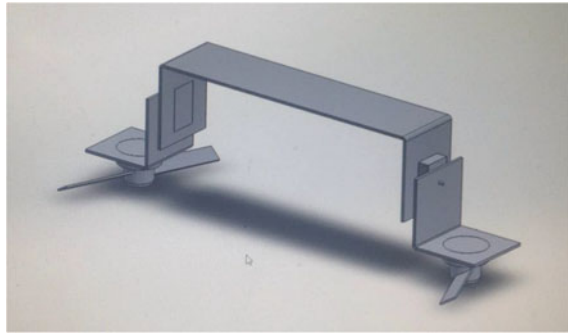
**Fig. 2** Variation of lift with respect to airship length





**Fig. 3** CAD model of airship

**Fig. 4** Fabricated Gondola



### 3.1 Payload

The volume of hull multiplied by unit lift  $10.36 \text{ N/m}^3$  is the assumed gross lift

$$B_{\text{gross}} = \frac{10.36\pi}{54} L^3$$

The theoretical density of the chosen material is  $0.2 \text{ kg/m}^2$  but we will assume  $0.5$  which will adjust itself in the long run.

The hull weight is

$$W_{\text{hull}} = A_{\text{hull}} \cdot \rho_{\text{hull}} \cdot g = 0.800730986L^2 * 0.5 * 9.8 = 3.9236L^2$$

Assuming the mass of the required hardware like sensor, gondola, complete LPAWNs module setup is approximately  $4 \text{ kg}$  but instead we will use  $5 \text{ kg}$  so as to reduce the error in the flight test

$$B_{\text{net}} = 9.8 * 5 = 49\text{N}$$

### 3.2 Solar Cell and Battery

To drive the airship at a constant velocity ( $V$ ) the amount of power required is given by the formula.

$$P_{\text{flight}} = 0.5C_D * \rho_{\text{air}} * A_s * V^3$$

$$A_s = \text{surface ar}$$

$$C_D = \text{drag coefficient} = 0.0510$$

$$\rho_{\text{air}} = 1.225 \text{ kg/m}^3$$

$$V = \text{velocity}$$

$$P_{\text{flight}} = (0.5 * 0.0510 * 1.225 * 0.8007)L^2V^3 = 2.5019 * 10^{-2}L^2V^3(\text{watt})$$

To calculate the total energy of the flight for a day multiply the above by 24

$$E_{\text{flight}} = 24P_{\text{flight}} = 0.6005L^2V^3(\text{watt hours})$$

Assuming the solar cells to be flat and pointed directly toward the sun, and receiving the sunlight of  $12 \text{ h/m}^2$  is

$$E_{\text{incident}} = \int_0^{12} 1000 \sin \frac{\pi t}{12} dt = 7639 \text{ watt hours/m}^2$$

$$\begin{aligned} \text{Required solar surface area} = A_{\text{array}} &= \frac{E_{\text{flight}}}{\varepsilon E_{\text{incident}}} \\ &= \frac{0.6005L^2V^3}{7639\varepsilon} = \frac{7.861 * 10^{-5}L^2V^3}{\varepsilon} \text{m}^2 \end{aligned}$$

where  $\varepsilon$  = efficiency of solar cells.

The average efficiency of solar cells is 15–20% while commercially available cells have up to 28%. The highest recorded efficiency is 42%. The thin solar cell that we are going to use has an average efficiency of 12–20%. The highest recorded thin

solar panel has 22.5% efficiency in this case we will take 15%. The area density of these solar cells is  $1.5 \text{ kg/m}^2$ , now we can calculate the wt. required for the minimum solar cells

$$W_{\text{array}} = 6.981 * 10^{-2} L^2 V^3 \text{ N}$$

For a continuous flight the batteries need to store double the amount of power with this the total weight of batteries is

$$W_{\text{batt}} = \frac{0.5 E_{\text{flight}} * g}{\rho_{\text{batt}}} = 2.9425 \frac{L^2 V^3}{\rho_{\text{batt}}} \rho_{\text{batt}}$$

= specific energy of the batteries (watt hours/kg)

$$W_{\text{motor}} = 2.835 * 10^{-4} P_{\text{flight}} = 7.099 * 10^{-6} L^2 V^3 \text{ (N)}$$

$Y = 2.834 * 10^{-4} \text{ N/watt}$  (assumed for the battery).

Total weight of power system is given by adding the above

$$W_t = \left\{ \frac{2.9425}{\rho} + 6.981 * 10^{-2} \right\} L^2 V^3$$

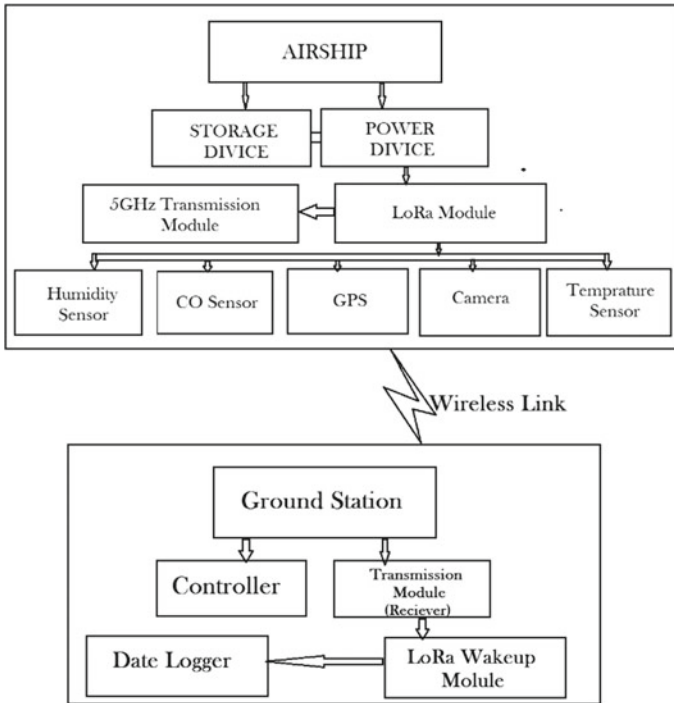
## 4 Monitoring Sections

The basic components of monitoring section are data logger, controller unit, several sensors, high-speed 5 GHz transmission module, a long distance low-power LoRa wireless module high-speed data storage module, high-speed transmission module. The 5 GHz wireless module is set as a default router, 5 GHz wireless adapter (Fig. 5 and Table 2).

## 5 Overall Feasibility

In order for the airship to be able to fly the weight of the power system  $W_t$  must at least be equal to net lift  $B_{\text{net}}$  in addition to this problem there is also a constraint of the solar array as it can not exceed the total surface area of the ellipsoid part of the airship which is

$$7.86 * 10^{-5} \frac{L^2 V^3}{\varepsilon} \leq \frac{\pi L^2}{12}$$



**Fig. 5** Block diagram of configuration of sensors and hardware for airship

**Table 2** Comparison of platform for environmental monitoring

Comparison of commonly used platform for Environmental Monitoring		
Blimp	Low deployment cost Low energy consumption Large Coverage area Large Capacity of throughput	Be susceptible to the weather High latency for data collection Low flexibility
Drone	High flexibility for monitoring Large coverage area Large capacity of throughput	Be susceptible to the weather Limited terminal access High latency for data collection

The function of square becomes an absolute constraint of the velocity of the airship solar cells available in market that have an average efficiency of 13% and allow the maximum velocity of 10 m/s. With slightly more efficient cells, 10 m/s flight becomes feasible the governing factor being the area of required cell should be a little less than cross-sectional area of the blimp.



1 L of helium can generate 1.02 g of lift and the volume of helium contained in the envelop is  $84.82 \text{ m}^3$  which means it can completely lift up to 42.4 kg and total calculated weight is 5 kg  $B_{\text{net}}$  and 14.5 kg  $W_{\text{array}}$  the total mass for the battery available is 22.5 kg which is 22 kg approximately.

The power needed for a continuous velocity of 5 m/s is 253.34 W hours which is 6080.16 W for 24 h. And the total weight of battery can be kept at 22 kg. The total power generated by a solar cell is approximately  $130 \text{ W/m}^2$  with the efficiency of 13%. Counting 12 h of sunlight is  $5 \text{ m}^2$  solar panel which can overwhelmingly generate enough power to supply the airship for 24 h.

## 6 Conclusion

The number of technical challenges is numerous to complete the design of the airship, making the ship autonomous and continuous is one such challenge. Solar power is the only source which has a remote possibility to make this happen. From the analysis above, we can say that under idealized condition continuous flight of the airship is feasible. Realistically the amount of sunlight, a day is different throughout the year; during the main three seasons, during summer season does not have any problem, in winter, except for few days when sun does not rise there are at least 8–10 h of sunlight. The problem arises during rainy season when there is not only the least amount of sunlight but also harsh weather which is not suitable for the airship to remain in air. From the statement, it is clear that complete continuous flight of the airship is impossible as it has to come down during storm, harsh weather, and rain. Our future will include work on better maneuvering so as the airship could withstand complicated control, improving landing, trajectory following, and developing the necessary intelligence for airship autonomy.

## References

1. Lutz C, Ruegg M (1998) The airship simon-design and construction of a radio controlled blimp. A Research Project
2. Zhang H, Ostrowski (1999) Visual servoing with dynamics and control of an unmanned blimp. In: Proceedings of the 1999 IEEE international conference on robotics and automation, pp 618–623
3. Corazzini T, Robertson A, Adams JC, Hassibi A, How JP (1998) GPS sensing for spacecraft formation flying. Fall Issue J Inst Navigat 45(3):195–208
4. Suvama S, Adeel SA, Pant RS, Design and development of an easily deployable indoor finless airship. In: 11th international airship convention and regatta
5. Biju M, Pant RS (2017) Design and development of an indoor autonomous airship. In: 23rd AIAA lighter-than-air systems technology conference
6. Narayana CL, Srilatha KR (2000) Analysis of aerostat configurations by panel methods. In: BLISS project document CF, vol 10
7. Sundaram S (2000) Wind Tunnel tests on 1: 7 and 1: 28 scale Aerostat Models. Experimental Aerodynamics Divisions, National Aerospace Laboratories, Bangalore, India

8. Kantor G et al (2001) Collection of environmental data from an airship platform. In: Sensor fusion and decentralized control in robotic systems IV, vol 4571. International Society for Optics and Photonics
9. Elfes A et al (1998) A semi-autonomous robotic airship for environmental monitoring missions. In: Proceedings. 1998 IEEE International conference on robotics and automation (Cat. No. 98CH36146), vol 4. IEEE
10. Dowling K (1997) Power sources for small robots. Carnegie Mellon University, The Robotics Institute

# Green Power Generation from Road Traffic Using Speed Breaker



Rishabh Kumar, Lavepreet Singh, Yuvraj Bhardwaj, Manish Singh, and Rajneesh Kumar

## 1 Introduction

As the population continues to grow and the ability to spend on transport is increasing, daily traffic on the roads of India is increasing significantly. Kumar et al. [1] explain that pollution from fossil fuel emissions is increasing in cities such as Delhi, especially in, and this makes the use of renewable power a top priority. M. Ramadan et al. [2] discussed the increasing need to devise power recovery methods, as such developments today limit even fossil fuels and require wise use. In addition, such a recovery system will be the answer to what Sorrell [3] has called a long-term problem of climate change. In this article an idea to reuse the power loss from a vehicle that passes through a speed breaker. When the vehicle's mass and momentum press the speed bump, the crank slider mechanism is triggered. The bump reciprocator motion is translated to the crank in the form of rotating motion. This movement is transmitted to the generator through the gear train assembly, and the generator can then generate power. Thus, the "Generation Speed Breaker" makes good use of the kinetic energy of today's high traffic and converts it into electrical power as suggested by Rao. et al. [4]. Adaptive CAD and CAE analysis-its importance is also emphasized by Ho et al. [5]. In recent times with increasing demand for living and industrialization, electricity demand is also increasing every day. In Bangladesh, data shared by the government show that only 31% of the population uses electricity. Conversely, in rural areas, only 23% of the population does not have electricity. To attain sustainable development goals and meet this unfulfilled demand, Renewable energy sources including biogas, the solar, wind, and tidal synchronization concepts [6], which can be used for fulfilling future needs perspectives.

---

R. Kumar · L. Singh (✉) · Y. Bhardwaj · M. Singh · R. Kumar  
Department of Mechanical Engineering, Galgotias University, Greater Noida, India

© The Author(s), under exclusive license to Springer Nature Singapore Pte Ltd. 2022  
R. M. Singari et al. (eds.), *Advances in Mechanical Engineering and Technology*,  
Lecture Notes in Mechanical Engineering,  
[https://doi.org/10.1007/978-981-16-9613-8\\_21](https://doi.org/10.1007/978-981-16-9613-8_21)

209

## 2 Design Calculation

The main concept of design is to provide an application of renewable power resources that can bring the best benefits for the ecosystem, as emphasized by Fatima et al. [7]. This leads to a self-contained roadway as it is proven to be an easy way to generate power that can be easily reused for working with CCTVs, street lights, and other road accessories. It can be done using various types of sensors and microcontrollers which can better utilize the generated power as suggested by Gunti et al. [8].

### 2.1 Design of Vibration-Struts

The main part of the configuration is speed breaker should get back to its typical position after the specific time stretch when the vehicle disregards it. Likewise, the speed switch should not surpass its normal position. To make the mechanism efficient, the framework is stringently damped. The framework is rearranged as demonstrated in Fig. 1a and the examination of a solitary level of opportunity of the vibration, the estimation of the framework is finished to ascertain the regular recurrence of the damper, firmness, and damping coefficient. As indicated by control [9], the speed of the vehicle on the speed switch is 20 km/h, and the wheelbase of the bike is 1.8 m. Subsequently, the knock should get back to its central situation within 0.25 s. For a fundamentally damped framework, the damping factor  $n = 1$  and the condition of movement is

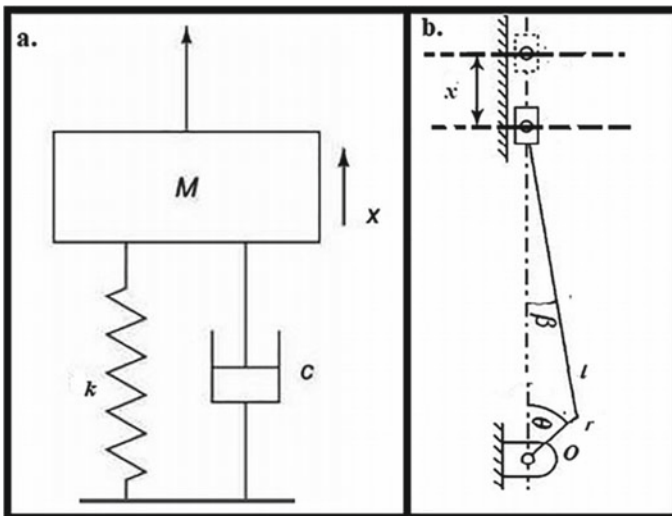


Fig. 1 a Spring-damper system b Slider crank mechanism

$$x = (C + Dt)e^{(-\omega xnt)} \tag{1}$$

where

$xn$ —regular recurrence of the framework (rad/sec).

$x$ —the displacement of the mass from its normal location (taken negatively in descending course) (m).

$C$  and  $D$  are the constants that can be assessed from the given boundary conditions and.

$t$  is the time in seconds.

According to the imperatives referenced over, the limit conditions are

$$\text{at } t = 0 : x = 10\text{cm and } x' = 0 \tag{2}$$

$$\text{at } t = 0.25 \text{ sec} : x = 0 \tag{3}$$

Subbing Eq. (2) in Eq. (1), we get  $C = -0.1$  m and  $D = -0.01xn$ .  
Subsequently, the condition of movement

$$X = -(0.1 + 0.01\omega t)e^{(-\omega xnt)} \tag{4}$$

Presently, subbing Eq. (3) in Eq. (4) and accepting 99.1% of unwinding in the spring Rao [4], we get,

$$-0.001 = -(0.1 + 0.01\omega t)e^{(-\omega xnt)} \tag{5}$$

using the above condition, characteristic recurrence  $\omega = 7.80$  rad/s. [10] recommends the standard components of a hindrance. Using those characteristics to determine the mass of the knock and the knock’s composition as Mild Steel, we get.

The speed bump’s volume =  $0.05900 \text{ m}^3$ .

The thickness of steel is =  $7850 \text{ kg/m}^3$ .

Mass of the bump =  $0.05900 * 7850 = 463.41\text{kg}$ .

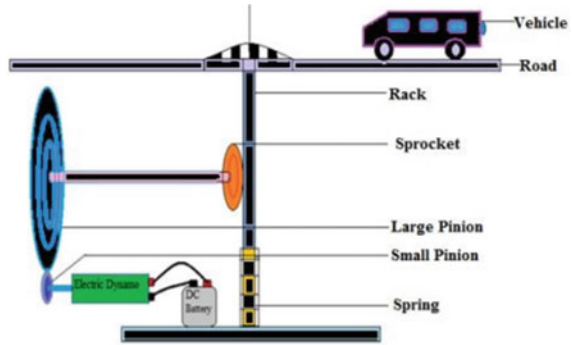
We realize that  $\omega = \sqrt{k/m}$  where  $m = 463.1 \text{ kg}$ .

We get  $k = 28,000.5 \text{ N/m}$ .

Likewise, damping co-efficient,  $c = 2k/\omega = 2 * 28000.5/7.80 = 7179.6$ .

For general estimations of wheelbase for a bike, various estimates of stiffness and damping co-efficient have been determined.

**Fig. 2** The detailed construction of the speed breaker



### 2.2 Construction

As any of the vehicles pass on the road through the speed breaker, the rack will automatically move in a downward direction. It will continuously rotate the sprocket and the pinion that will connect to Rack [5]. In the same manner, as we see in the diagram the Pinion is directly connected to the DC generator shaft, so that it will generate [4] the electricity. The time and the position will depend on the speed and the time taking by the moving vehicle on the road when it passes through the speed breaker (Fig. 2).

### 2.3 CAD Models

The segments of the speed breaker framework are planned and gathered to build up a model of the framework. The plan occurred in Solid works 2016 Student Edition. The parts are effectively accessible and are planned with affordable sizes and materials. The reason for the PC helped plan (CAD) is to.

- (1) Obtain the right direction of the segments and their measurements for assembling purposes.
- (2) Review complex subtleties to help segment producing and create segment and gathering diagrams.

The components are as follows (Fig. 3)

## 3 Connecting Rod

The connecting rod is the link pump and the crank. Mounting on bump and disc cranks with M12 bolts is possible on both ends. The critical buckling load was calculated using the recommended dimensions.

**Fig. 3** CAD model of connecting rod



**Fig. 4** CAD model of strut



### **3.1 Strut**

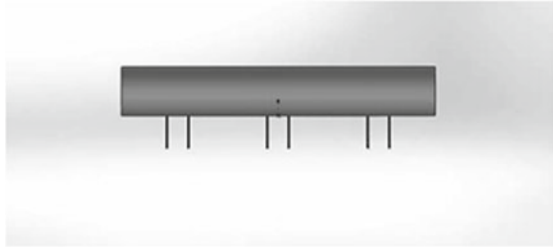
See Fig. 4

## **4 The MacPherson Strut**

It is designed in a McPherson strut type consisting of a damper and a spring. There are suitable installation positions on the top and bottom and M12 bolts are used to tighten the bump and bottom platform.

### **4.1 Bump**

See Fig. 5

**Fig. 5** CAD model of strut**Fig. 6** CAD model of disc crank

## 5 The Designed Speed Bump

It has three mount arrangements, two at each end for fixing the supports and one in the middle for mounting the slider wrench component's associated bars. The knock is 50 cm long, 15 cm broad, and has a semi-circular cross section. The mount is manufactured from a 3 mm thick IS2062 sheet with an E250 grade.

### 5.1 Disc Crank

See Fig. 6

## 6 The Disk with the Crank Arrangement

The plate wrench is a circle-type wrench as demonstrated in the figure. There is an opening 4 cm away from the middle to join the interfacing pole utilizing M12 bolts. It is intentionally mounted on a shaft with an external measurement of 24.4 mm. The width of the circle is 10 cm. Utilizes a one-plate wrench that is not difficult to plan and fabricate. Made on a 4 mm thick IS2062 Grade E250 sheet.



**Table 1** Comparison between two mechanisms

S No	Parameters	Roller method	Rack-pinion method
1	Cost	Low	Moderate
2	Mechanism setup	Very easy	Difficult
3	Maintainability	Difficult	Easy
4	Efficiency	~55%	~75%
5	Design	Easy	Depends upon the weight of sustaining capacity
6	Height	5.05 cm	12.2 cm
7	Dependency	Roller	Spring

## 7 Comparison Between Rack-Pinion and Roller

Rack-Pinion Rack-The lone strategy used to remove a voyaging vehicle M.E that converts power into another type of force by a pinion instrument. The force created as the vehicle goes through the street in the reducer slips under the shaft, which goes about as a specialist for the revolution of the shaft of the DC generator [11]. Then again, in the roller component, squandered force assists with producing power (Table 1).

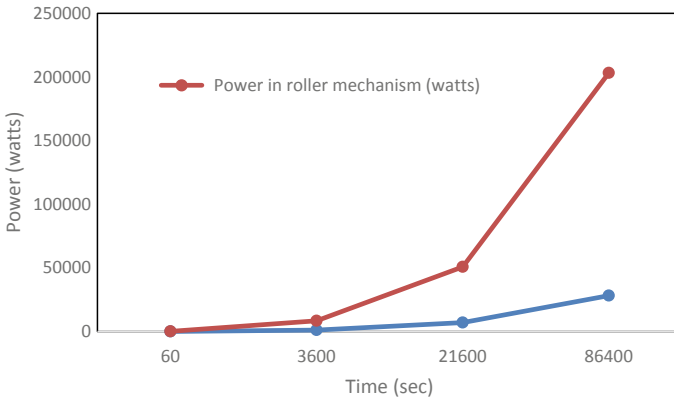
Rack-Pinion procedure will rely upon the spring however roller doesn't rely upon the spring. While utilizing the spring their strength is some issue. That will be the significant hindrance of various sprocket freewheel will be the freewheel board is joined by drive-side bearing [6]. This will show the outcome as axel will be under full pressure. That will break the axel.

## 8 Data comparison

In the system of Rack-Pinion, when any vehicle is passing out and about for 1 min on the speed breaker, it will give 19.61 watts. In any case, in the component of Roller, when any vehicle is passing on the street for 5 s then it will give 8.1 watts of force. For the 1 min, it expanded to 121.5 watts of force. Allow us to think about the information in 1 day, just the 6 h will be the season of a speed breaker. The accompanying table will show the information (Fig. 7 and Table 2).

The above graph is showing the data over the 24 h. In this graph, 6 h will be considered for the useful assumption.

We can also predict from this graph that Rack-Pinion [12] is always less than the roller mechanism. To get the best result we can predict it by joining both techniques. In this paper comparative study of both the mechanism is done to get the most efficient solution for the same.



**Fig. 7** Graph showing power versus Time of Two mechanisms

**Table 2** Power generated by rack-pinion and roller

S. NO	Time (s)	Power generated by rack-pinion mechanism(watts)	Power generated by roller mechanism (watts)
1	60	19.62	122
2	3600	1177.20	7290
3	21,600	7063.20	43,740
4	86,400	28,252.80	174,960

## 9 Block Diagram of Both Mechanism

The block diagrams for both mechanisms are shown in the diagram below. This will help to improve the system’s efficiency [13] by combining two mechanisms at the same time, but the maintenance costs will be very high [3, 14, 15] (Fig. 8).

## 10 Conclusion

In this paper, we planned an advanced speed breaker that proposes a strategy for creating power utilizing the force of a moving vehicle. In the current situation, the plausibility of the thought is checked by considering vehicle traffic streams, and so on, and power is assessed from it. The power sizes examined can be utilized in the domain of different street embellishments. The determined electrical force produced in 24 h in the planned framework is 1.602 kWh.

Time investment funds and effectiveness gains can be accomplished by utilizing the two components simultaneously. The vast majority of the outcomes give more proficient ability to meet our future necessities. Around here, more exploration is

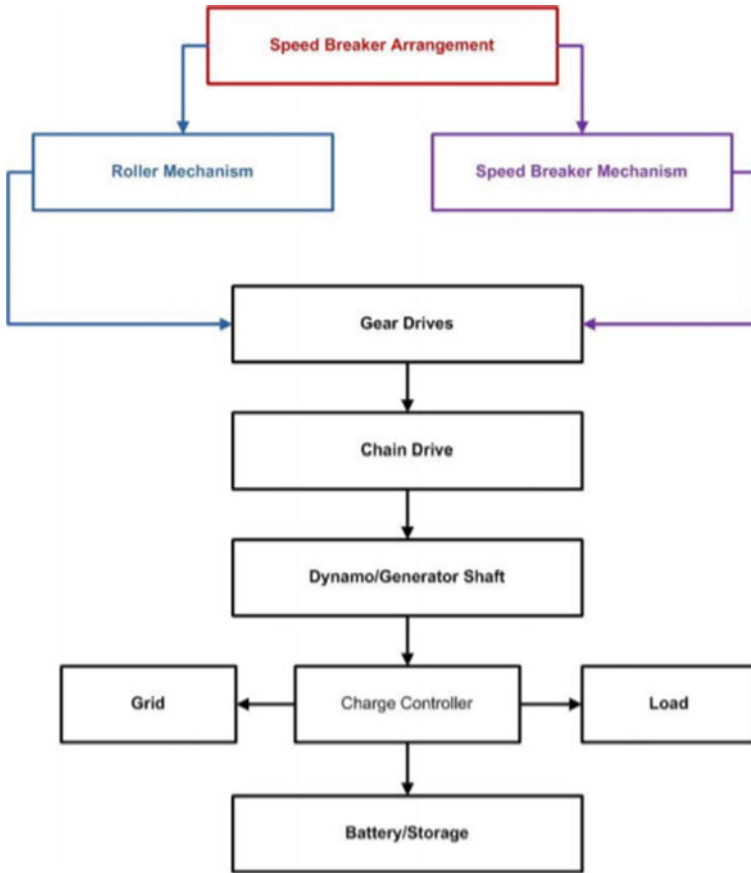


Fig. 8 Block Diagram of speed breaker Mechanism

being accomplished for the proficient turn of events. Our papers and undertakings have been effectively executed as a Green Power Project that helps convert dynamic force into power.

### References

1. Kumar S, Rawat MK, Gupta S (2019) An evaluation of current status of renewable power sources in India. *Int J Innovative Tech Explor Eng IJITEE* 8(10):1234–1239
2. Ramadan M, Khaled M, Hage EH (2015) Using speed bump for power generation - experimental study. *Int Conf Appl Power- ICAE* 75:867–872
3. Sorrell S (2015) Reducing power demand: a review of issues, challenges and approaches. *Renew Sustain Power Rev Elsevier* 47:74–82

4. Rao DV, Rao KP, Rao SC, Rao RU (2014) Design and fabrication of power generating system using speed breakers. *Int J Curr Eng Tech* 4(4):2697–2702
5. Ho MS, Tan YC, Ong CW, Chuah YD, Lee JV (2016) Modeling and simulation of crank slider mechanism using bond graph approach: a case study. *Int J Appl Eng Res* 11(6):4187–4189
6. Sinha A, Mittal S, Jakhmola A, Mishra SK (2021) Green energy generation from road traffic using speed breakers. *Mater Today: Proc* 38:160–168
7. Fatima N, Mustafa J (2014) Production of electricity by the method of road power generation. *Int J Adv Electr Electron Eng* 1(1):9–14
8. Gunti K, Kulkarni S, Angre H, Kamble V, Barve SS, Shukla D (2017) Innovative layout of the gear for the innovative layout of gearbox of a levelling machine. In: *International conference on advances in thermal sciences, materials and design engineering – ASTMDE*
9. Tentative guidelines provision of speed breakers for control of vehicular speeds on minor road, *The Indian Road Congress*, New Delhi, 1996
10. Design of Shaft, Version 2, Department of Mechanical Engineering, Indian Institute of Technology, Kharagpur
11. Abraham A, Jacob CG, Thomas GM, George J, Tom J (2017) Eco friendly power generation from speed breakers. *Int J Innovative Res Sci Technol-IJIRST* 3(11):227–230
12. Mishra A, Kale P, Kamble A (2013) Electricity generation from speed breakers. *Int J Eng Sci* 2(11):25–27
13. Raju SS, Naresh H, Raghuvardhan N (2017) Fabrication of a system for harnessing power from road traffic. *Int Conf Mater Process Charact* 5:6189–6194
14. Singh L, Kumar S, Raj S, Badhani P (2021, May) Aluminium metal matrix composites: manufacturing and applications. In: *IOP Conference Series: Materials Science and Engineering*, vol 1149, no 1. IOP Publishing, p 012025
15. Singh L, Kumar S, Raj S, Badhani P (2021) Development and characterization of aluminium silicon carbide composite materials with improved properties. *Mater Today: Proc* 46:6733–6736

# Analysis of Steering Using Davis Mechanism



Spandan Shukla, Shravan Sharma, and Pramod Kumar

## 1 Introduction

Davis steering system or Davis steering gear is the most used power steering system. Almost all cars are installed with the power steering system [1]. In this type of mechanism sliding guides are attached to the setup of the rack and these guide slide on the rod which is extended from wheel hub king pin, it is a front side wheel operated mechanism. Davis mechanism creates friction between guides and rod which increases steering effort [2].

The motive of steering mechanism is to empower the direction of the automobile to the motorist.

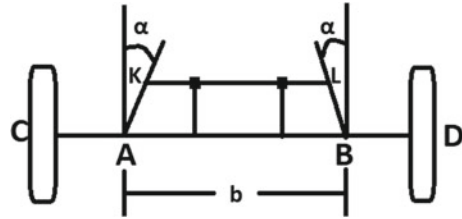
In today's era latest car uses rack-and-pinion mechanism as it turns circular motion into linear motion some of the older mechanism uses the recirculating ball mechanism as it gives benefits of greater mechanical advantage, so that is the reason we sometimes still found those mechanism on heavy vehicles like truck, but for lighter automobiles we use Davis and Ackerman mechanism [3]. Ackerman steering is simpler famous and then Davis steering. Ackerman steering has only turning pair, its wear and tear are very less, its life is too high but the problem with this mechanism is that it can be exact only at three positions which is midpoint and the other two position which is extreme right an extreme left but this is not the case in Davis steering mechanism as it is exact at all positions and also it has one pair and one sliding pair. There is one more mechanism that is Rapson mechanism which is used in ships; it has having one turning pair and one sliding pair [4].

The instantaneous centre (can also be called the instant centre of rotation for a vehicle) is a 2D figure, which is a point in its plane around which all the point rotates except itself for an instant as shown in Figs. 2 and 5 [5].

---

S. Shukla (✉) · S. Sharma · P. Kumar  
Galgotias University, Greater Noida, U.P., India

**Fig. 1** Davis steering mechanism



All the observations and calculations are done with respect to the instantaneous centre.

The Davis gear mechanism consists of a cross-link KL sliding parallel to another link AB and is connected to the stub axles of the two front wheels by means of two similar bell crank levers CAK and DBL pivoted at A and B respectively. The cross-link KL slides in the bearing and carries pins at its end K and L. The slide blocks are pivoted on these pins and move with the turning of bell crank levers as the steering wheel is when the vehicle is running straight, the gear said to be in its mid-position. The short arms AK and BL are inclined at an angle of 90 plus alpha to their stub axles AC and BD as shown in Fig. 1.

In Davis steering mechanism the accurate steering depends upon our right selection of cross-arm angle ( $\alpha$ ).

The correct steering depends upon a suitable selection of cross-arm angle alpha and is given by

$$\tan(\alpha) = b/2I \tag{1}$$

where  $b = AB =$  distance between the pivots of front axles.

$I =$  wheel base.

The range of  $b/I$  is 0.4–0.5,

Hence, angle  $\alpha$  lies between  $11.3^\circ$  and  $14.1^\circ$  [7, 9].

Let,  $a =$  wheel track,  $I =$  wheel base,  $b =$  distance between pivots A and B of the front axle.

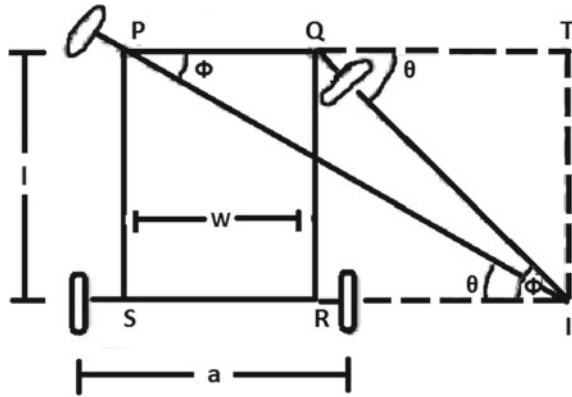
Davis mechanism has sliding pair which mean it has more friction and easy wearing as we know that analysis of Davis steering can be done for 4 wheels and 6 wheels. In Davis mechanism if we try to increase the number of wheels, the turning angle will decrease which means small automobiles can turn easily as compared to bigger automobiles with more number of wheels [10] (Fig. 2).

$$\text{Then, } \cot \Phi - \cot \theta = \frac{b}{I} \tag{2}$$

This is the fundamental equation for correct steering.

If this condition is satisfied, there will be no skidding of the wheels, when the vehicle takes a turn.

**Fig. 2** Instantaneous Centre for Davis steering mechanism



### 1.1 Analysis Using MechAnalyzer

MechAnalyzer is learning software for various models of many mechanisms. In this a user can select from any of the available mechanism and change the input parameters. A 3D model of the selected mechanism with linkages and joints are generated and shown to the user in a 3D environment, whose motion can be animated and seen [6].

The software has the built-in feature which allows creating and studying graphs in a very convenient way. Simulation and study of the graphs help us to compare and validate the theoretical values [11].

Learning about the software, we performed variations in input parameters and calculated the accurate  $\Phi$  and  $\theta$  values to satisfy the equation and get the accurate results [8].

The parameters in which the equation got satisfied were as follows:

- $L_1 = 0.0500$
- $L_2 = 0.3700$
- $L_3 = 0.5000$
- $B = 20.000$

Joint -> Min. value = 0, Max. Value = 0.015.

## 2 Observations

In our work, we are taking the instantaneous centre of the model into our consideration. For effective turning of the vehicle, the instantaneous centre should be nearer to the shaft, which means the length of the shaft should be decreased.

In Fig. 3,

We see two wheels connected with shaft with various joints and links

$L_2$  is the length of shaft from  $J_2$  to  $J_3$ .

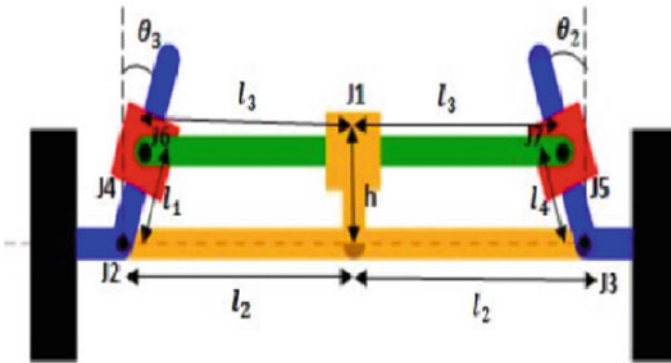


Fig. 3 Davis steering mechanism

- $L_1=L_4$  is the distance between the parallel shafts.
- $L_3$  is the length of the shaft parallel to the main shaft.
- $J_1, J_2, J_3, J_4, J_5$  are the joints.
- $\Theta_1$  and  $\theta_2$  are the angles with vertical.
- $h$  is the vertical distance between the two shafts.

Here, in Fig. 4, we are seeing the 3D representation of Davis steering mechanism before our analysis being initiated. Parameters such as length of shafts and value of joints can be varied. Also, the trajectory for the graph can be selected in this.

In Fig. 5, we observe the 3D representation of the mechanism after the analysis is made. The encircled portion shows the point which is called Instantaneous Centre.

The point where the two parallel dotted lines meet is known as instantaneous centre. For effective turning, it should be closer to the wheels. From this, we calculated the value of  $\Phi$  and  $\theta$  as mentioned in Fig. 2, and put the value in the equation (ii).

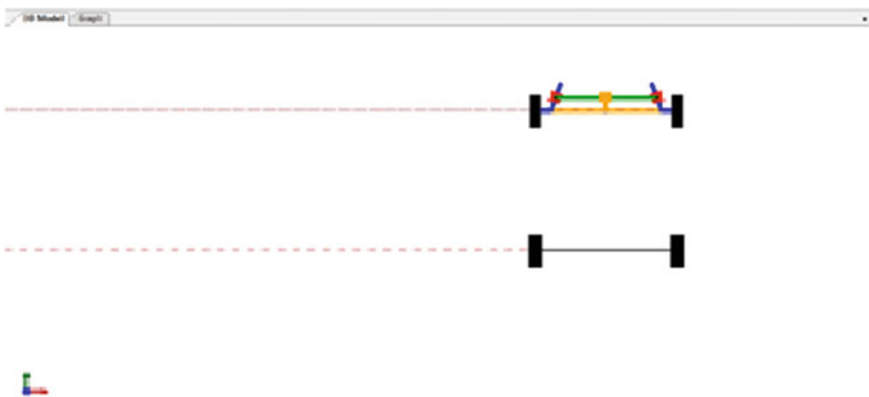


Fig. 4 3D Representation of Davis steering mechanism in mechAnalyzer



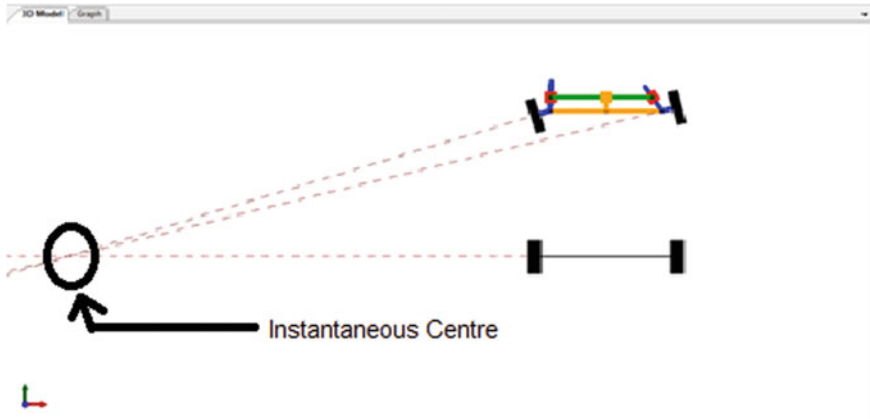


Fig. 5 Instantaneous Centre

The calculated value was approximately in the range of given parameters and the fundamental equation for steering was satisfied.

### 3 Results and Discussions

After our analysis on mechAnalyzer, we obtained various graphs for all the joints and links with respect to the 3D model of the Davis Steering Mechanism. All the graphs are obtained in the software itself. Let us study all the graphs one by one. Firstly, we will discuss the joints.

Figure 6 shows a graphical representation of Time vs Value of position, velocity, acceleration, and Force. In this, the position curve increases with time along axis, the velocity first increases and later decreases along the axes, acceleration gradually increases and decreases and come along axis, the Force acting is constant.

Let us take the example of Joint 1 for comparing the outcome in simulation and in analytical method.

Figure 6 shows the graph of joint 1 that came as an outcome in mechAnalyzer.

1. Considering the distance curve, Theoretically, the values obtained by formulating were (Table 1).  
 In MechAnalyzer, after obtaining the values from graph, we noticed similar values of the respective co-ordinates.
2. For velocity curve, on comparing the calculated values and obtained values we made a comparison and find very slight differences (Table 2).
3. Considering the acceleration curve, the calculated and obtained values were (Table 3).

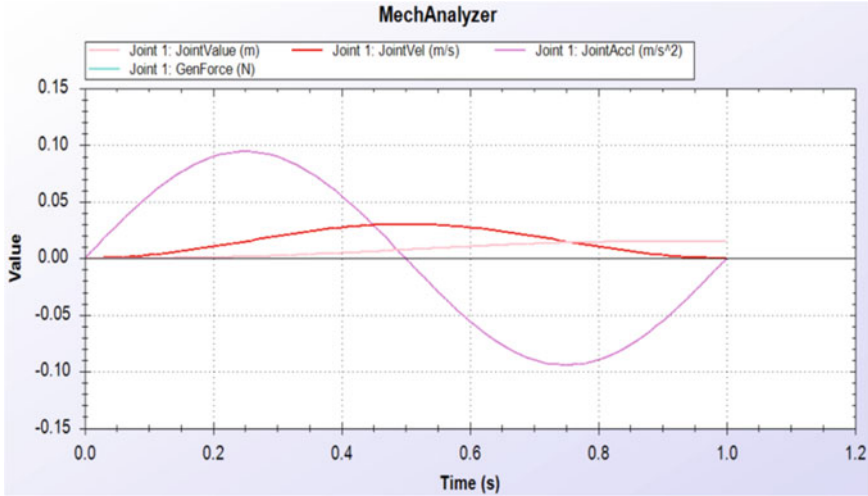


Fig. 6 Graph of position, velocity and acceleration for Joint 1

**Table 1** Values of Position (m) curve in X- and Y-directions

S.No	X-Axis	Y-Axis
1	0.00	0.00
2	0.17	0.00
3	0.20	0.001
4	0.40	0.005
5	0.60	0.010
6	0.80	0.014
7	1.00	0.015

**Table 2** Values of Velocity (m/s) curve in X- and Y-directions

S.No	Th.(X,Y)	Sim.(X,Y)
1	(0,0)	(0,0)
2	(0.18,0.010)	(0.20,0.010)
3	(0.35,0.027)	(0.40,0.027)
4	(0.50,0.030)	(0.50,0.030)
5	(0.62,0.027)	(0.60,0.027)
6	(0.80,0.010)	(0.80,0.010)
7	(1.0,0)	(1.0,0)

\* Th. Stands for theoretical values of X- and Y-axis; \* Sim. Stands for simulated values of X- and Y-axis

**Table 3** Values of Acceleration ( $m/s^2$ ) curve in X- and Y-directions

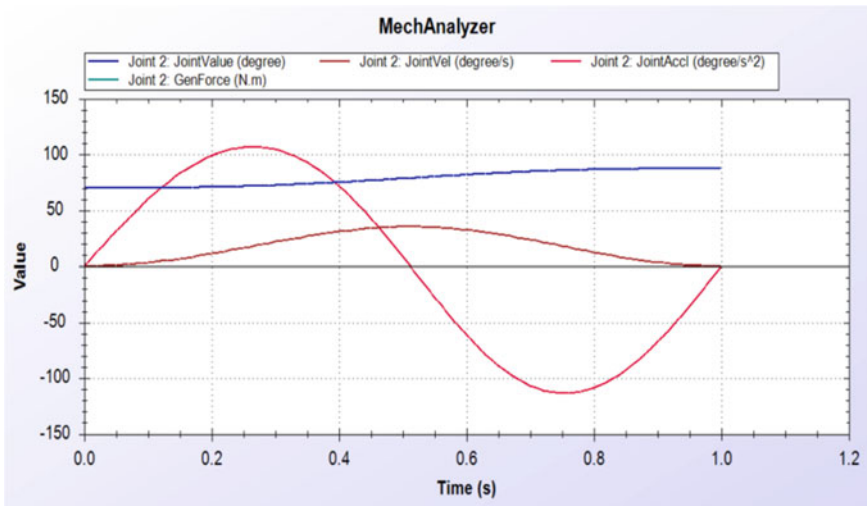
S.No	Th.(X,Y)	Sim.(X,Y)
1	(0,0)	(0,0)
2	(0.10,0.055)	(0.09,0.051)
3	(0.25,0.098)	(0.25,0.094)
4	(0.42,0.055)	(0.41,0.051)
5	(0.50,0.0)	(0.50,0.0)
6	(0.60,-0.055)	(0.59,-0.051)
7	(0.75,-0.098)	(0.75,-0.094)
8	(0.92,-0.055)	(0.91,-0.051)
9	(1.0,0.0)	(1.0,0.0)

\*Th. Stands for theoretical values of X- and Y-axis; \*Sim. Stands for simulated values of X- and Y-axis

Here, we noticed slight differences in theoretical values and simulated values. The curves are similar and the differences in values are due to the slight differences in calculations.

Similarly, we noticed similar results for all the joints and links. We compared the theoretical and simulation values of X- and Y-axes, respectively, for all the joints and links and results were observed.

For Joint2, as shown in Fig. 7, the position curves increase a little with time and become constant at some point, the velocity and acceleration behave the same as in joint 1.



**Fig. 7** Graph of position, velocity, and acceleration for Joint 2

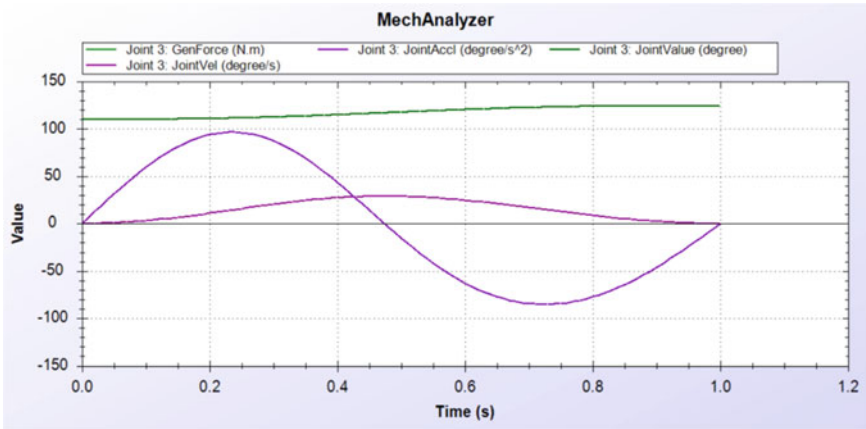


Fig. 8 Graph of position, velocity, and acceleration for Joint 3

Joint 6 has the same properties as joint 2 and graphs are similar since both the joints are at similar position of their respective arms and are on the same line. Therefore, their motions are similar and values of position, velocity, and acceleration are similar.

In joint 3, the velocity and acceleration acting the same as joint 1 and the position curve has changed with time (Fig. 8)

Joint 7 has the same properties as Joint 3 and graphs are similar since both the joints are at a similar position of their respective arms and are on the same line. Therefore, their motions are similar and values of position, velocity, and acceleration are similar.

In Fig. 9, joint 4, the position curve starts decreasing with time, the velocity curve now first decreases then increases with time and the acceleration curve is now reversed that is, it first decreases then increases along the axis with time.

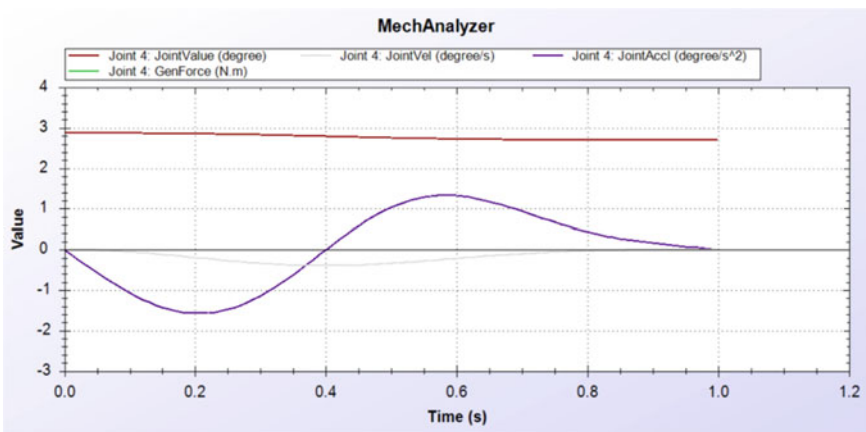


Fig. 9 Graph of position, velocity, and acceleration for Joint 4

Now, in joint 5, the position curve increases a little, the velocity curve increases to some point and then falls, the acceleration curve increases to a point then decreases along the axis as shown in Fig. 10.

Now, we will discuss the links.

In Fig. 11, we are observing value time graph for position velocity and acceleration in X- and Y-direction linearly as well as angularly.

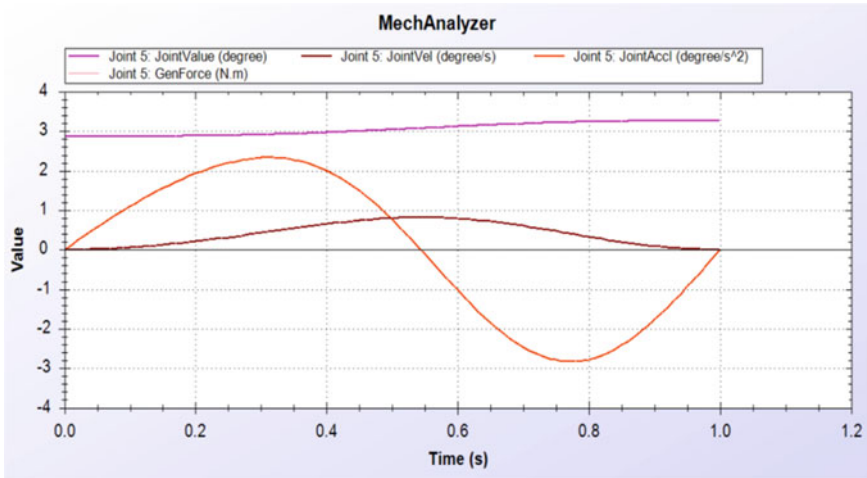


Fig. 10 Graph of position, velocity and acceleration for Joint 5

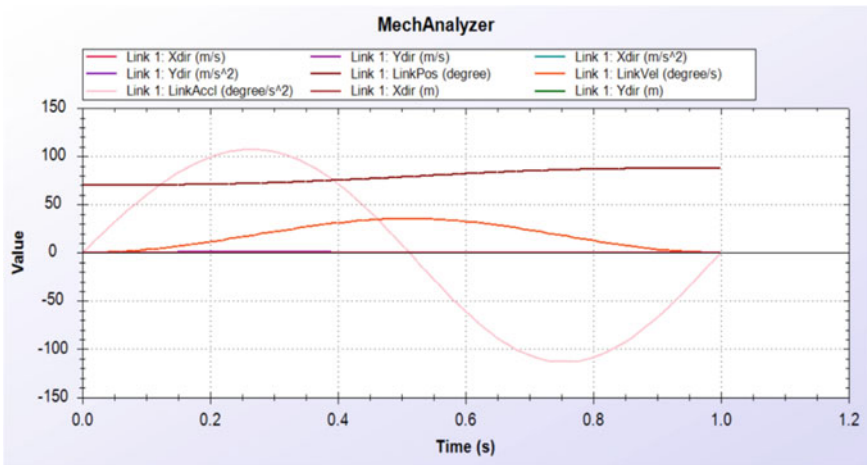


Fig. 11 Graph of position, velocity, and acceleration for Link 1

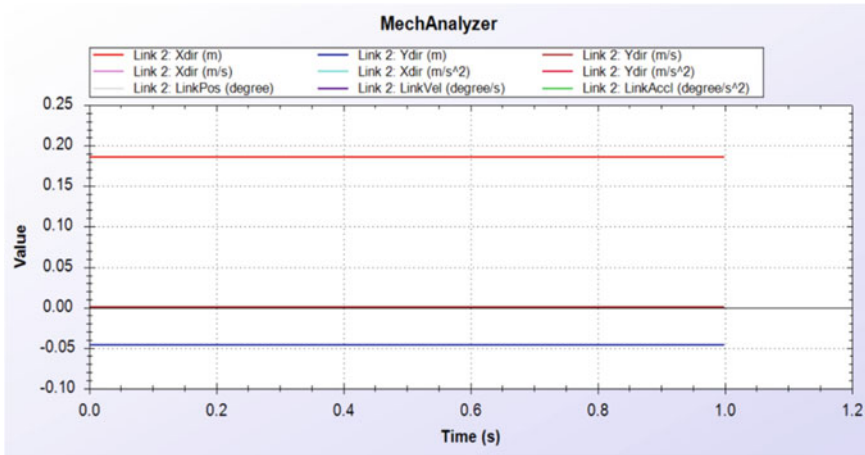


Fig. 12 Graph of position, velocity and acceleration for Link 2

From the graph as shown in Fig. 11, we can see that for link 1, the position curve slowly raises to a level linearly as well as angularly. The velocity and acceleration curve shows normal behaviour along the axes.

Link 5 has the same properties as link 1 and graphs are similar since both the links are at a similar position of their respective arms and are on the same position. Therefore, their motions are similar and values of position, velocity and acceleration are similar.

Here, in Fig. 12, we see constant straight lines for position, velocity, and acceleration both linearly and angularly. Here, position is constant, the velocity is zero, and acceleration is in a state of retardation (Fig. 13).

In link 3, we get negative values of position, also, velocity is negative and decreases and acceleration first decreases to a point and then increases w.r.t both linear and angular.

Now, from Link 4, we started coming to the initial state where position, velocity, and acceleration curve behave the same as joint 7 for both linearly and angularly (Fig. 14).

Link 6 has the same properties as link 4 and graphs are similar since both the links are at a similar position of their respective arms and are on the same position. Therefore, their motions are similar and values of position, velocity, and acceleration are similar.

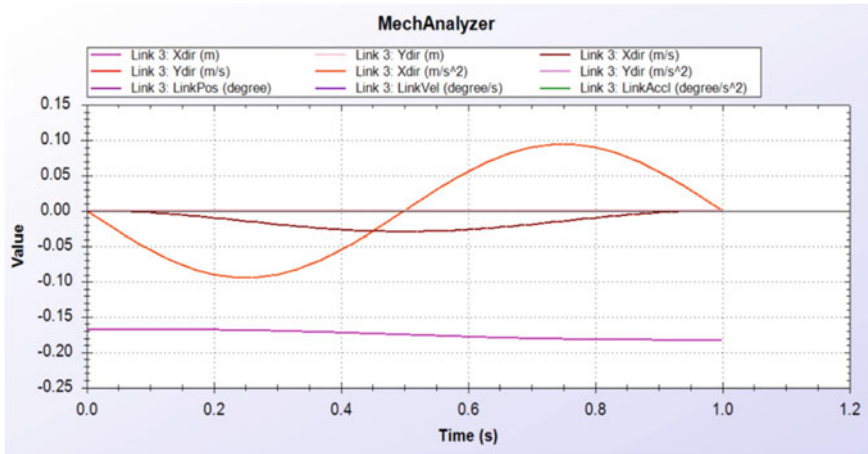


Fig. 13 Graph of position, velocity, and acceleration for Link 3

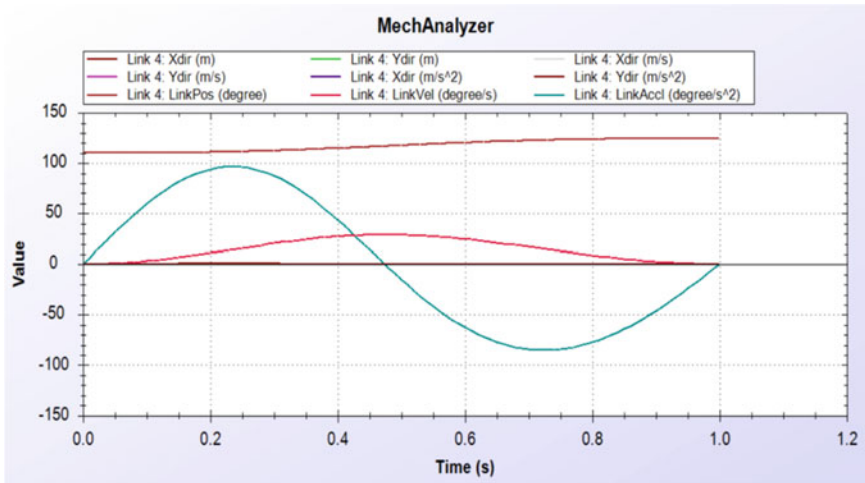


Fig. 14 Graph of position, velocity, and acceleration for Link 4

### 4 Conclusion

From the above observations and studying the graphs, we came to know the changes in position, velocity, and acceleration both linearly and angularly. The graph shows that the values which we gave as input in the mechAnalyzer were accurate. The acceleration and velocity decreases on curves, whilst the position shows considerable variations. We get the accurate steering equation by calculating the values of theta and phi.

The graphs were compared in the mechAnalyzer between the predefined values and variable values which were calculated using formulae for accurate steering systems.

We obtained the values of corresponding axes by calculating the formulae theoretically and the values which we obtained on simulation software (MechAnalyzer). We compared them and concluded that most of the values are same and there are slight differences in theoretical and simulated values. These differences may be the result of minute errors in calculations.

The input parameters were  $L_1 = 0.0500$ ,  $L_2 = 0.3700$ ,  $L_3 = 0.5000$ ,  $B = 20.000$   
The calculated values were put in the equation

$$\text{Cot}\Phi - \text{Cot}\theta = \frac{b}{I}.$$

We concluded that, on decreasing the length of shaft, we obtained an instantaneous centre closer to the wheels and the effective turning of the steering was achieved.

## References

1. Zhao JS, Liu X, Feng ZJ, Dai JS (2013) Design of an Ackermann-type steering mechanism. Proc Inst Mech Eng C J Mech Eng Sci 227(11):2549–2562
2. Zaremba A, Davis RI (1995) Dynamic analysis and stability of a power assist steering system. In: Proceedings of 1995 American control conference-ACC'95, vol 6. IEEE, pp 4253–4257
3. Chiaravalloti F, Gross L, Rieder KH, Stojkovic SM, Gourdon A, Joachim C, Moresco F (2007) A rack-and-pinion device at the molecular scale. Nat Mater 6(1):30–33
4. Babu VC, Rao PG, Santa Rao K, Krishna BM (2020) Design of accurate steering gear mechanism. Mech Mech Eng 22(1):93–104
5. Bevinkatti K et al (2015) Four wheel steering system for Automobile. IJIERT, ISSN 2394–3696
6. Hampali S, Chittawadigi RG, Saha SK (2015) Mechanalyzer: 3d model based mechanism learning software. In: Proceedings of 14th world congress in mechanism and machine science
7. Badawy A, Zuraski J, Bolourchi F, Chandy A (1999) Modeling and analysis of an electric power steering system (No. 1999-01-0399). SAE Technical Paper
8. Pandey D, Kushwah JS, Chittawadigi RG, Krishna KR, Saha SK (2019) Effective teaching of mechanism synthesis using mechAnalyzer software. In: IFToMM world congress on mechanism and machine science. Springer, Cham, pp 3237–3244
9. Weinstein AJ, Moore KL (2010) Pose estimation of Ackerman steering vehicles for outdoors autonomous navigation. In: 2010 IEEE international conference on industrial technology. IEEE, pp 579–584
10. NeelaKrishna DS Analysis and improvement of the steering characteristics of ATV
11. Kumar R, Vantmuri SD, Chittawadigi RG, Saha SK (2016) Dynamic analyses of four-bar mechanism in MechAnalyzer software



# Modeling and Simulation of a Bevel Gear



Priyanshu Choudhary, Alok Niranjana, and Pramod Kumar

## 1 Introduction

The history of the gears is probably as old as the civilization itself. Still today, the importance of gears in the manufacturing industry is undiminished and even continues to grow [1]. The design, analysis, and manufacturing of gear is still a hot topic of research that is vital for the application of such gears in helicopter transmissions, reducers, motorcycle gears, and in other branches of industry [2]. A gear is a rotating circular machine part having teeth and will work with another toothed part that will transmit torque. This device can change the torque and speed. Gears of different sizes produce a change in torque creating a mechanical advantage through their gear ratio and thus may be considered a simple machine.

Study and Simulation of gears have been an important topic for researchers in recent times as different gear mechanism plays very valuable role in big industries. Because of this fault and failure diagnosis and structural monitoring of gears became important and to make it possible and easier many analysts worked on 3D gear modeling and simulation [3]. For finite element analysis and dynamic simulation of different gears, precise modeling with proper parameters is very important. Also it helps in proper CNC production. To increase the efficiency and grade of design of gear, making a program module with proper parameters is very important [4]. By using design software for modeling, purpose of visual study of proportions and fits is also completed. Forces generated because of top land balance, slot width tapers, spiral angle adjustments, etc. are difficult to imagine for visual point of view hence difficult to work on hence 3D software plays an important to overcome these problems [5]. Not only simulation of gears is important for analysis point of view but also important for many applications as shown in detail study done by Wan-Soo Kim and his partners in reference [6] showing “Fatigue Life Simulation of

---

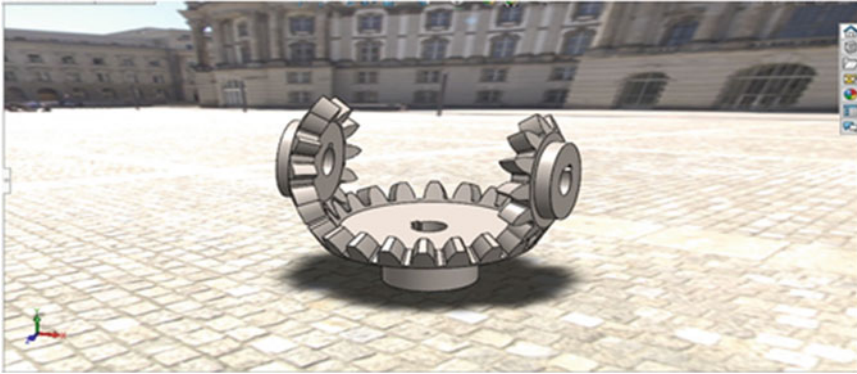
P. Choudhary · A. Niranjana (✉) · P. Kumar  
Galgotias University, Greater Noida 203201, India

Tractor Spiral Bevel Gear According to Major Agricultural Operations”. This study is completely practical application-based showing simulation and analysis of the use of bevel gear for tractors. Similarly in reference [7] simulation of spiral bevel gear has been studied and a bolted or welded joint has been eliminated which links the spiral bevel gear and shaft to reduce complex design and cost in production. Further movement of spiral bevel machine was developed and simulated for practical purpose and successful integral shaft designs for helicopter were achieved. This study also shows how 2D modeling of existing related topic was revised and developed by 3D modeling which was more effective [7]. Dynamic study and modeling of gear can help in the evolution and growth of technology and will help us to achieve higher force bearing capacity, increase in rotating speed, decreased vibration, and decreased noise. For this Yangshou Xiong and his partners worked on analysis and simulation of micro-segment of gears [8]. All these studies show the importance of simulation and analysis of gears.

Similar kind of work has been recorded showing the calculation and analysis of bevel gear on different software like solidworks, Ansys, Lingo, etc. Studies like optimization of a bevel gear in terms of reduction of noise performance can be seen in a study done by Christian Brecher [9], modeling and dynamic analysis of spiral bevel gear for transmission system in a helicopter trail. They have done analysis on bevel gearbox coupling system [10]. Also reference [11] shows different conference papers that show modeling and simulation work done on spiral bevel gear and hypoid gears which uses Gleason Face Hobbing process. Till now a lot of new and development research has been done on all the different types of gears. Other than stress analysis, our paper offers deep information about different steel and iron grades that should be used for bevel gear specially considering gearbox for Baja rulebook.

Two key concepts of gearing and its calculation are pitch surface and pitch angle where pitch surface is normally a cylindrical shaped surface which is a complete theoretical concept. It is considered as an imaginary circular boundary which is considered crucial for a calculation point of view. It is used so that an average calculation of peaks and valleys can be done, while the pitch angle in a bevel gear is the angle between the pitch surface and axis of the face of pinion [12].

Our primary focus for modeling and simulation is bevel gear which is a basic gear for usage in the automobile sector, aerospace sector, and making engineering-related machines for power transmission [4]. Its geometry is hard to explain mathematically. The bevel gear is a pair of gears where the two shafts have axes intersecting and they have conical shaped tooth-bearing faces. They are mostly placed at 90 degrees but can also be placed at some other angles. They have a conical pitch surface. They have a pitch angle of mostly less than 90 degrees. Gears having tooth pointing in the outward direction are called external bevel gears while those facing inwards are called internal bevel gears and one with pitch angle exactly 90 degrees are called crown gears. Miter gears are types of bevel gears with pitch angle as 90 degrees as well as having an equal number of teeth. Involute straight bevel gears are also widely used in automobile differential mechanism and other parts of intersecting axis transmission [13] (Fig. 1).



**Fig. 1** Bevel gear geometry (made in solidworks)

## ***1.1 Types of Bevel Gears***

**Straight bevel gear:** Their teeth placed straight and have to taper toward the apex with a conical pitch surface.

**Spiral bevel gear:** In these types of gear tooth contact is slow and smooth because of curved teeth which are placed at an angle.

**Zero bevel gears:** They have curved teeth with each tooth is axis which are coplanar but the middle portion of the tooth rotates around the circumference of the gear. It can be imagined as spiral bevel gears with zero spiral angles which makes teeth end align to the axis.

**Hypoid bevel gear:** They have a hyperbolic pitch surface and resemble spiral bevel gear. It allows a larger pinion diameter and smoother mesh. They have a longer life as compared to others.

## ***1.2 Applications***

It can be used at places where power is transmitted to two different axles running at different velocities like in the case of cornering automobiles.

For a hand drill, bevel gear plays an important mechanism.

Straight bevel gears are used for pre-heater gearboxes.

They are also used in the aerospace industry for 16,000 rpm jet application.

They are used in ground and lapped cooling towers at lower noise and vibration.

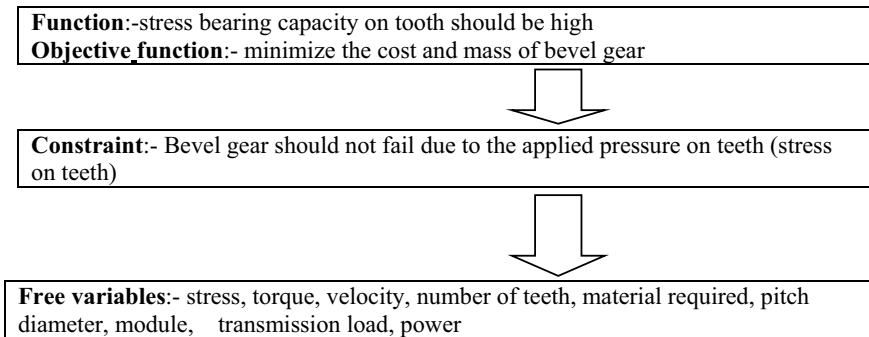
Heavy military defence vehicles like tankers rely on these gears made with special grade materials which can bear high-density application.

### 1.3 Advantages Over Other Gears

- Useful at high torque and high speed.
- Less cost on maintenance for long-term working.
- Less heat is produced compared to others.

## 2 Methodology for Material Selection and Simulation of Bevel Gear

Nowadays, a lot of materials with properties required for gears are available and even some materials are always in development to enhance their characteristics, and as a result, a lot of confusions are created between different types of materials, which are further divided into different grades, their economic factor, serving the purpose and a question arises even till the end that whether the material used is fully optimized or not. To solve this, there are different methods like decision matrix, pugh method, etc. One such most used method is the Ashby material selection method which is better in comparison to others as it does not require much experience and judgment rather needs correct weight factors to evaluate the required material. An example is the form of a flowchart is given below for stress analysis on a tooth of bevel gear.



**Flow chart 1:** Ashby selection method [14]

There are many materials available in the market for making gears. These include low-stress drive gears to heavy stress duty gears. Material selection of any product is important and pragmatically is done by keeping in mind its utility, strength, durability, cost. Similarly, for gears, strength and durability are two such factors that cannot be compromised. Based on its use it can be made of materials like Plastics—areas where light stress material could be used like the toy industry. Wood—areas of complicated woodworking projects. Steel places where stress and durability play an important

role like in the vehicle industry. Talking about the materials used of gears in the gearbox is also of a wide range. So, to make it easy for study and choose the right material of gear we took steel as our primary component. Many software are available in the market for stress simulation like CFD, ANSYS, CATIA, NX, MATLAB, etc. One basic 3D designing software is solidworks on which we performed our stress analysis [15].

## ***2.1 Characteristics of Materials for Gear Selection of a Gear Box (Heavy Duty Gears)***

The material should have high dynamic properties like high tensile, compression strength. Its hardening ability after heat treatment should be good as in the case of many steel types. It should be resistant to corrosion and heat, a lot of heat is created due to stress and friction in the gears of the gearbox. The material should be non-magnetism. Manufacturing properties while going under different processes should be good like précised edges while designing complex parts.

## ***2.2 Types of Steel Available in the Market Which Matches the Requirement for Gear Making for Gear Box***

Plain carbon steel, Alloy steel, Stainless steel, Tool steel are different types of steel. Among these, mostly plain carbon steel and alloy steels are used for gear manufacturing for heavy stress due to their mechanical properties. Some differences between them are as follow. Ductile and gray iron are the two types of cast iron which is the most suitable in gear manufacturing [16].

### **Heat-Treated Plain Carbon Steel**

Common and mostly used after heat treatment.

Quite economical and give a satisfactory result.

### **Heat-Treated Alloy Steel**

Mainly used in the industrial field and is seldom to use untreated alloy steel.

In most cases, they are more expensive than carbon but give a better result based on strength comparison.

### **Advantages Of Using Alloy Steel Over Plain Carbon Steel**

Penetration depth increases with an increase in surface hardness for the same carbon per cent.

In some cases less distortion is achieved as the quenching temperature of some alloy steel is low.

Impact toughness and wear resistance are more.

Higher Toughness level.

### 2.3 Use of Different Types of Steel for Analysis

Cast steel as it is difficult to fabricate, it is only used at places with high stress.

Plain carbon steel-areas which require high toughness and strength, these grades can be used.

Alloy steel-used in places with less tooth wear and much tooth strength is required.

Based on the characteristics and information given above some commonly used gear material for gearbox with their chemical composition, physical properties, and cost are given below (Table 1).

Other than chemical composition, physical properties like tensile stress, yield strength, elastic modulus, Poisson's ratio, Brinell hardness number, etc. are some important properties of the material that tells about its capacity to bear the load. Properties of some of the materials given above are mentioned in the table given below (Table 2).

**Table 1** The chemical composition of material used in gears

Material	C %	Mn %	Si %	Ni %	Cr %	Mo %
AISI 4130	0.28–0.30	0.40–0.60	0.20–0.35	–	0.80–1.1	0.15–0.25
AISI 4140	0.38–0.43	0.75–1.0	0.20–0.35	–	0.80–1.1	0.15–0.25
AISI 4340	0.38–0.43	0.60–0.80	0.20–0.35	1.65–2.0	0.70–0.90	0.20–0.30
AISI 316	0.03–0.08	1.00–2.00	–	–	–	–
AISI 1020	0.17–0.23	0.30–0.60	0.75	10.0–14.0	16.0–18.0	2.0–3.0
Nitralloy Type $N^b$	0.20–0.27	0.40–0.70	0.20–0.40	3.2–3.8	1.0–1.3	0.20–0.30
SAE-0022	0.12–0.22	0.50–0.90	0.60 Max	–	–	–
SAE-0050	0.40–0.50	0.50–0.90	0.80 Max	–	–	–
SAE-8620	0.180–0.230	0.700–0.900	0.150–0.350	0.400–0.700	0.400–0.600	0.150–0.250
Gray cast iron	2.5–4%	0.1–1.2%	1–3%	–	–	–

**Table 2** The physical properties of materials used in gears

Properties	AISI 4130	AISI4140	AISI 4340	AISI 316	AISI 1020	SAE-0050	SAE-8620	Gray cast iron
Tensile strength	560 MPa	655 MPa	745 MPa	500-700 MPa	394 MPa	690 MPa	530 MPa	620 MPa
Yield strength	460 MPa	415 MPa	470 MPa	200 MPa	294 MPa	485 MPa	385 MPa	414 MPa
Elastic modulus	190-210 GPa	190-210 GPa	210 GPa	193 GPa	205 GPa	200-215GPa	190-210 GPa	-
Poisson's ratio	0.27-0.30	0.27-0.30	0.27-0.30	0.265-0.275	0.290	0.29	0.27-0.30	0.211
Brinell's Hardness no	217	197	217	215	111	207-225	149	220

**Table 3** The cost of different material used in gears

Material	Approx. cost/kg in Rs
AISI 4130	150
AISI4140	130
AISI 4340	110
AISI 316	270
AISI 1020	65
SAE-8620	68
Gray cast iron	60

*Note* All these factors are the primary concern to choose any material for gear selection in the heavy-duty industry

Cost of material also plays an important role, so below is the list of the cost of material which can be used for selection of material based on budget (economic factor) (Table 3).

### 3 Theoretical Method

There are different types of forces that act on a bevel gear which are tangential force, axial force, and radial force which occurs due to velocity and torque.

#### 3.1 *Some Basic Terminologies Related to Calculation is Given Below*

**Pitch circle:** Imaginary circle which has common center as tooth wheel and pith of teeth is calculated along with it.

**Circular pitch(p):** It is the measurement between any two similar points on abutting teeth. Can be calculated using  $p = \frac{\pi d}{N}$  where d is the diameter of pitch circle and N is the number of teeth.

**Module addendum:** Ration between pitch diameter and number of teeth ( $M = \frac{d}{N}$ ).

**Addendum:** Distance between pitch circle and peak of tooth.

**Dedendum:** Distance between pitch circle and bottom root of tooth.

**Base circle:** Circe on which involute profile is generated.

**Backlash:** Distance between circular thickness and width of space between teeth.

**Face width:** Axial length of teeth.



### 3.2 Formulas [17]

Force acting on the teeth is resolved into three components  $F_t, F_r, F_a$ , which represents tangential, radial, and axial components;  $\alpha$  is pressure angle and  $\gamma$  is pitch cone angle.

Now, radial and axial components can be calculated using tangential component

$$F_r = F_t \times \tan\alpha \times \cos\gamma$$

$$F_a = F_t \times \tan\alpha \times \sin\gamma$$

And tangential component can be calculated using the formula

$$F_t = 2 \times \frac{M_t}{r_m}$$

where  $M_t$  represents transmitted torque and  $r_m$  represents radius of pinion at midpoint along the face width.

By Lewis Equation

$$M_b = F_t \times h$$

$$I = \frac{1}{12} B \times t^3$$

$$y = \frac{t}{2}$$

$M_b$  = bending moment.

$h$  = height from root of tooth.

$I$  = moment of inertia about neutral axis of tooth.

$y$  = measurement of neutral axis from edge.

$t$  = width of tooth at bottom land.

Bending stress can be calculated by

$$\sigma_b = \frac{P_t}{m \times b \times y \times \left(1 - \frac{b}{A_o}\right)}$$

$m$  = Module.

$y$  = Lewis form factor.

$b$  = Face width.

$\left(1 - \frac{b}{A_o}\right)$  = Bevel factor, where  $A_o$  is

$$A_o = \sqrt{\left(\frac{D_p}{2}\right)^2 + \left(\frac{D_g}{2}\right)^2}$$

## 4 Simulation of Bevel Gear

We can calculate the strength in two different ways, by calculating the bending stress of the tooth or by tooth surface strength. Analysis of both of them is important for proper assurance of strength. We have calculated tooth strength in terms of yield strength of different materials taken from the above table based on required characteristics and their properties, namely, AISI4130 steel normalized at 870C, AISI4340 steel normalized, AISI316 Stainless steel, AISI1020.

### 4.1 Tooth Bending Strength Analysis

Tooth in bevel gears generally breaks from the height of the tooth above the pitch circle known as dedendum, when a large force is applied.

This analysis is done to assure whether the tooth does not break easily and proper measures could be taken to prevent it, like, enhancing the module, widening the tooth width, magnifying pressure angle, etc.

### 4.2 Tooth Surface Strength Analysis

Peeling and abrasion is created due to large surface pressure.

This analysis is done to assure whether tooth surface does not damage due to heavy load and proper measures could be taken to it like, heat-treating the surface, widening tooth width, polishing tooth surface to have a smoother surface

### 4.3 The Objective of Analysis

- To have stress analysis of some basic alloys on bevel gear.
- To choose the required material keeping the economic factor in mind.
- To optimize the use of a gear pair.
- Maximization of power delivered by the gear pair
- Minimization of the cone distance [18].

## 5 Result and Discussion

**Tool used /parameters:** We have used solidworks for designing of different parts. All these parts were aligned to form a bevel gear and different materials were chosen for simulation of stress to test the yield strength of different materials. Simulation was also performed on solidworks. The upper part is known as the pinion and the lower part is the bevel. The parameter of both the pinions is the same. Few parameters that were taken into considerations were pitch angle, inner and outer radius of extruded part of pinion, etc. [15, 19].

Figure 2 shows the upper part of the bevel gear also known as pinion. It has to be placed very properly with bevel gear for smooth and long life functioning. Its parameters have been shown in Table 4. It also has a key hole whose dimensions have also been provided in the same table. We designed two sets of these pairs each

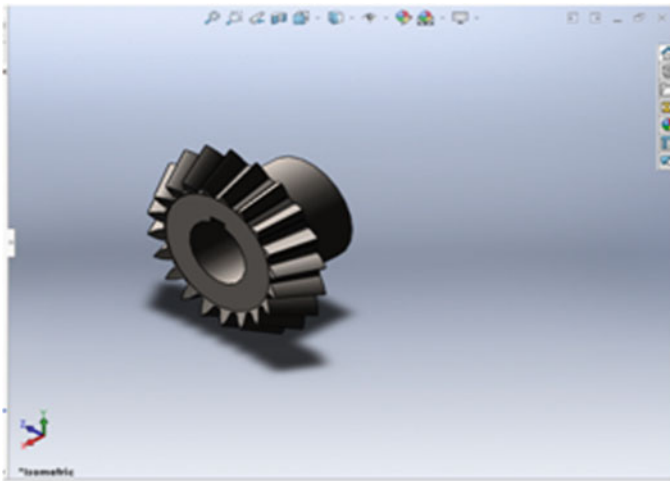
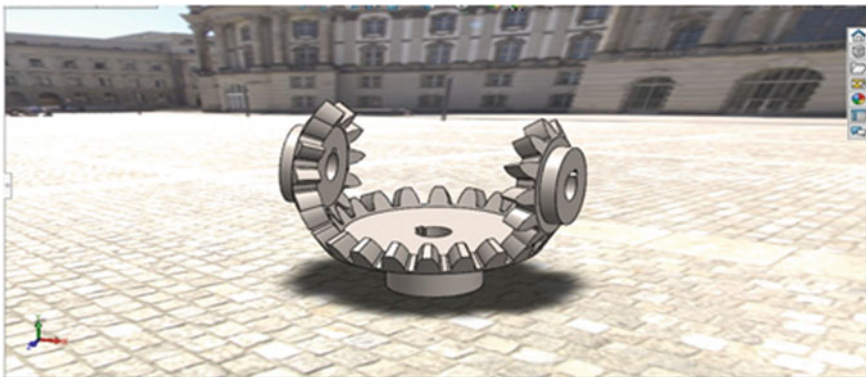


Fig. 2 Design of one part of bevel gear

**Table 4** Parameters for designing of bevel gear

Parameters	Value
Pitch angle	90 degree
Inner radius of extruded part of pinion	0.95 cm
Outer radius of extruded part of pinion	3.05 cm
Radius of pinion cylinder	4.59 cm
Side surface area of pinion cylinder	7.05 cm <sup>2</sup>
Number of tooth of pinion	20
Distance between each tooth	0.89 cm
Key length	0.48 cm
Inner radius of extruded part of bevel	0.95
Outer radius of extruded part of bevel	3.81 cm
Radius of disk on bevel	9.72 cm
Area of disk on bevel	41.8 cm <sup>2</sup>
Number of tooth of bevel	40

with 20 teeth. All the dimensions of these two pairs are similar. Both of them are placed perpendicular to the bevel hence their pitch angle is 90 degrees. Figure 3 shows the complete assembly of bevel gear. The bottom part has 40 teeth and its diameter is bigger than the pinion part. Design of all the parts is done on solidworks and after that all these parts are placed accordingly. All the parameters related to design are given in Table 4. After completion of design and assembly of different parts of bevel gear, we started testing for stress on teeth taking different materials. There are various types of steel available in the market which matches the requirements for gear making but for modeling and simulation of bevel gear we have chosen material depending on the cost and yield strength, etc. Out of all the commonly used materials that we have given in Table 1, we chose AISI4130, AISI 4340, AISI 316, AISI 1020,



**Fig. 3** Assembly of bevel gear

with per Kg cost of 150, 110, 270, 65, respectively. For different materials, chemical composition is represented in (Table 1) Other than chemical composition, there are physical properties also like tensile strength, yield strength, elastic modulus, Poisson's ratio, Brinell hardness, etc. The physical properties of materials used in gears are represented in (Table 2). So from here we got physical, economical, and chemical values by which we can decide which material is best for use according to the requirement. Figures 4, 5, 6, 7 represent the simulation analysis of different

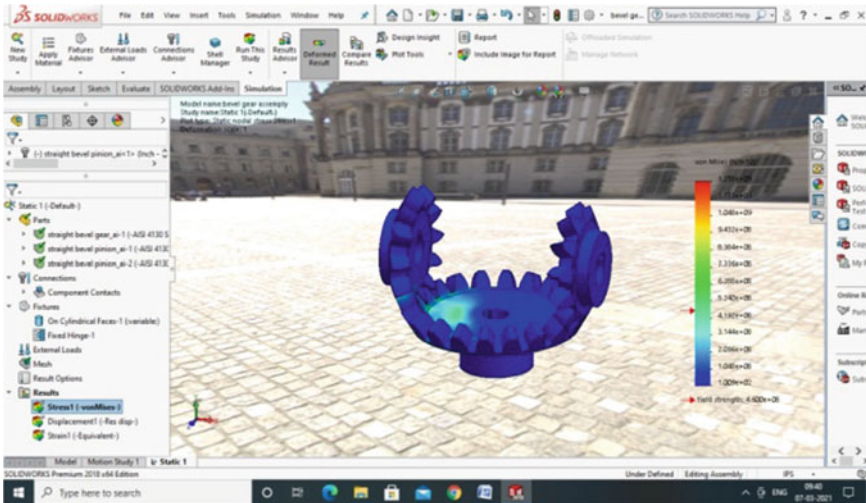


Fig. 4 Stress analysis on material 1

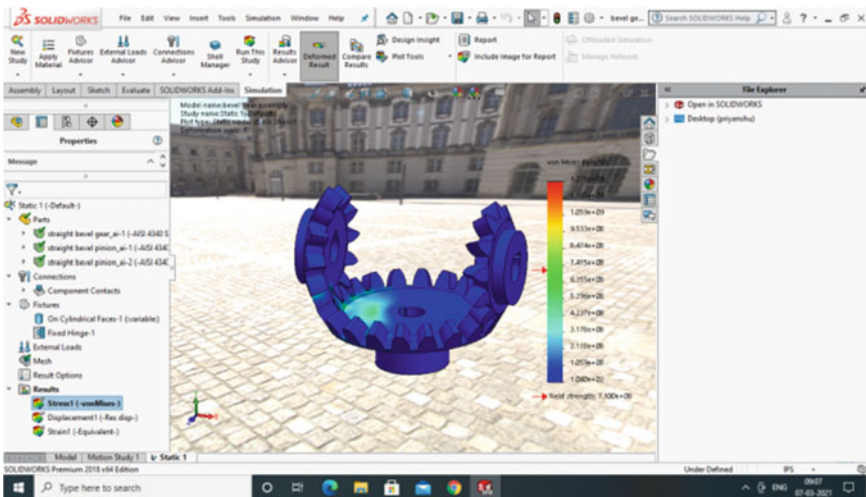


Fig. 5 Stress analysis of material 2

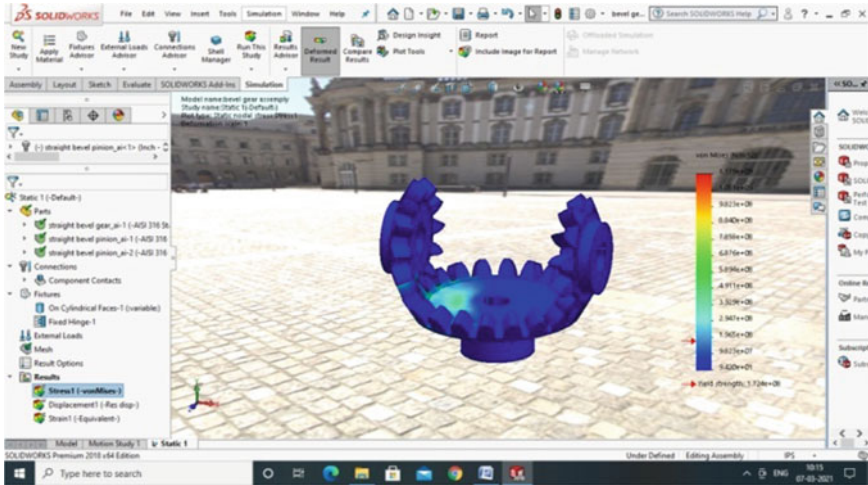


Fig. 6 Analysis of material 3

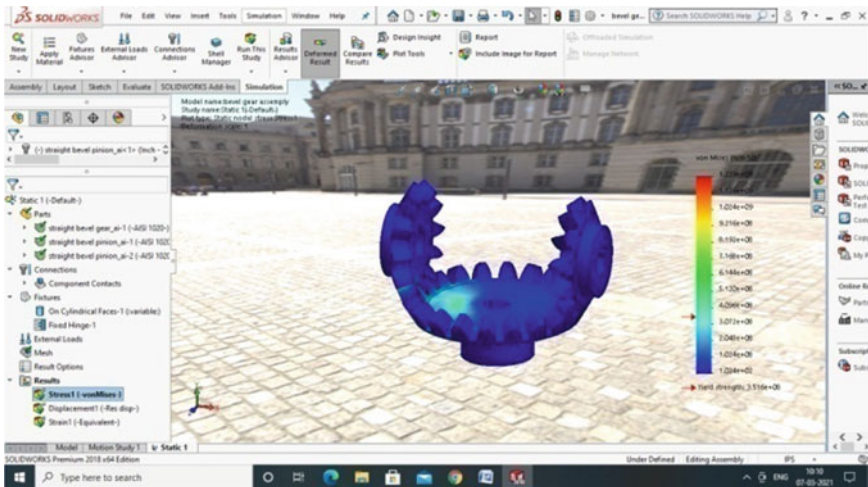


Fig. 7 Stress analysis on material 4

material selected and also properties of each material provided in solidworks has been given below them. Based on the simulation result, we found out that material AISI 4130 has maximum yield strength while material AISI 316 has lowest yield strength. Table 5 shows the representation of yield strength of all the different materials which are taken for simulation with their respective cost per Kg.

Material used- AISI4130 steel normalized at 870C	Material used- AISI4340 steel normalized
<i>Default failure criterion in solidworks:</i>	<i>Default failure criterion in solidworks:</i>
Elastic Modulus-	2.05e + 11 N/m <sup>2</sup> Elastic Modulus- 2.05e + 11 N/m <sup>2</sup>
Poisson's Ratio- 0.285	Poisson's Ratio- 0.32
Shear Modulus- 8e + 10 N/m <sup>2</sup>	Shear Modulus- 8e + 10 N/m <sup>2</sup>
Mass Density- 7850 kg/m <sup>3</sup>	Mass Density- 7850 kg/m <sup>3</sup>
Tensile Strength- 731000000 N/m <sup>2</sup>	Tensile Strength- 1,110,000,000 N/m <sup>2</sup>
Yield Strength- 460,000,000 N/m	Yield Strength- 710,000,000 N/m <sup>2</sup>
Thermal Conductivity- 42.7 W/(m-K)	Thermal Conductivity- 44.5 W/(m-K)
Specific Heat- 477 J/(kg-K)	Specific Heat- 475 J/(kg-K)

Material used AISI 316 stainless steel	Material used AISI1020
<i>Default failure criterion in solidworks:</i>	<i>Default failure criterion in solidworks:</i>
Elastic Modulus- 1.929999974e + 11	N/m <sup>2</sup> Elastic Modulus- 2e + 11 N/m <sup>2</sup>
Poisson's Ratio-0.27	Poisson's Ratio- 0.29
Mass Density- 8000 kg/m <sup>3</sup>	Mass Density- 7900 kg/m <sup>3</sup>
Tensile Strength- 580,000,000.8 N/m <sup>2</sup>	Tensile Strength- 420,507,000 N/m <sup>2</sup>
Yield Strength- 172,368,932.3 N/m <sup>2</sup>	Yield Strength- 351,571,000 N/m <sup>2</sup>
Thermal Conductivity- 16.3 W/(m-K)	Thermal Conductivity- 47 W/(m-K)
Specific Heat- 500 J/(kg-K)	Specific Heat- 420 J/(kg-K)

## 6 Conclusion

The objective of the article of modeling and simulation of bevel gear for stress analysis was achieved. It was observed that material AISI 4340 has maximum yield strength that is  $7.100 \pm 08$ . We have selected this material for gearbox of our ATV as it fits in our budget and has maximum yield strength. Article also provides information about how to select material and what are the advantages of different materials based on their

**Table 5** Yield strength and cost of different material

Material	Yield strength	Approx. cost of material/kg (Rs)
AISI 4130 steel normalized at 870C	$4.600 \pm 08$	150
AISI 4340 steel normalized	$7.100 \pm 08$	110
AISI 316 Stainless steel	$1.724 \pm 08$	270
AISI 1020	$3.516 \pm 08$	65

characteristics. Results of simulation done on bevel gear to check the stress on teeth provide knowledge in which material can be used based on stress-bearing capacity. The result shows that material AISI 4340 has the most stress-bearing capacity among all the materials used hence it can be used at heavy stress duty drives places; while places with low budget and lesser stress duty material can use AISI 1020. Also, this study shows different methods that are used to calculate the stress on teeth that is tooth surface strength and tooth bending strength to get assured of how much stress can tooth of different materials can bear so that could be used at their optimum level at different places.

### Future scope

Study of all these properties for different types of gears within bevel gear is given in 1.1.

Study of different types of gears like spur, rack, and pinion or bevel gear for stress and deformation on solidworks software (1).

Harmonic analysis of gear can be done to find out the mode.

Simulation of bevel gearbox can be done.

## References

1. Chime ERO et al Design, Modeling, application and analysis of Bevel Gears
2. Jadeja RM, Chauhan DM (2013) A review on design, analysis and manufacturing of spiral bevel gear. *Int J Eng Res Technol (IJERT)* 2
3. Wan Z et al (2020) Dynamic modeling of gear system based on 3D finite element model and its application in spalling fault analysis. *Math Probl Eng*
4. Yuxia S, Wei Z (2012) Parametric design of straight bevel gears based on solidworks. In: *The 2nd international conference on computer application and system modeling*
5. Bijonowski B (2015) A practical approach for modeling a bevel gear. *Gear Technol* 32(2):68–75
6. Kim W-S et al (2020) Fatigue life simulation of tractor spiral bevel gear according to major agricultural operations. *Appl Sci* 10(24):8898
7. Davidson SR (2019) Simulation of spiral bevel gear tooth manufacturing to aid in one-piece gear shaft design. *Gear Technol* 70–74
8. Xiong Y et al (2015) Dynamic modelling and analysis of the microsegment gear. *Shock Vib*
9. Brecher C, Löpenhaus C, Knecht P (2016) Design of acoustical optimized bevel gears using manufacturing simulation. *Proc CIRP* 41:902–907
10. Zhu H et al (2019) Modelling and dynamic analysis of the spiral bevel gear-shaft-bearing-gearbox coupling system. *Math Probl Eng*
11. Fan Q (2006) Computerized modeling and simulation of spiral bevel and hypoid gears manufactured by Gleason face hobbing process 1315–1327
12. Tiwari PK, Singh ENN, Sinha PK (2017) Modeling, design & analysis of straight bevel gear and pinion by FEM, solid works & ansys benchwork 14.0. *Int J Eng Manag Res (IJEMR)* 7(4):415–422
13. Zhang F, Tian X, Cui H (2012) The modification design of involute straight bevel gear. *IERI Proc* 3:52–59
14. Delibaş H, Çağrı UZ, Geren N (2017) Advanced material selection technique for high strength and lightweight spur gear design. *Eur Mech Sci* 1(4):133–140



15. Patel N, Gupta T (2016) Methodology for designing a gearbox and its analysis. *Int J Eng Res Technol* 5(1):2278–181
16. O'Rourke R, Grander M (1999) Cast iron: a solid choice for reducing gear noise. *Gear Tech* 16:46–49
17. Patil AV, Gambhire VR, Patil PJ (2014) Analysis of bending strength of bevel gear by FEM (2014)
18. Padmanabhan S et al (2011) Design optimisation of bevel gear pair. *Int J Des Eng* 4(4):364–393
19. Mahato KK, Bhimavarapu SR (2021) Calculation, design and analysis of two stage single speed gearbox for all terrain vehicle for bajasae. *Mater Today: Proc*
20. Motahar H, Samani FS, Molaie M (2016) Nonlinear vibration of the bevel gear with teeth profile modification. *Nonlinear Dyn* 83(4):1875–1884

# Design and Analysis of Helical Gear



Priyanshu Choudhary, Aditya Singh, Ankit Kumar, and Pramod Kumar

## 1 Introduction

The major things of gear box and gear analysis deals with noise, transmission errors, failure of gear tooth, analysis of gear stresses, dynamic loads, and gear ratios which are helpful for design of gears and gear box [1]. A helical gear also known as “dry fixed gear” is a rotating machine that meshes with other gear to transmit torque and rotation between shaft axes [2]. It is also used to change in velocity, direction of the power source, and torque. Helical gear is similar to that of spur gear but their teeth alignment on the cylindrical surface is diagonally placed hence the axis of teeth is angular from the axis of rotation. The teeth are at an angle and slash to face of the gear hence they appear like the segment of a helix. Helical gear transfer power between parallel and right-angle direction. When teeth of a helical gear engaged with each other, contact between gears starts from one side of the teeth and constantly increases as the gears move. Two mating helical gears must have equal helix angle but opposite hand. They can bear more load then spur gears and are smoother in movement while creating less noise because they have greater surface contact in this assembly and teeth are more gradually engaged to each other [2]. Other than parallel arrangement they can also be placed with teeth crossed to each other and are known as skew gears [3]. If the arrangement is parallel, gear with opposite teeth direction is selected for meshing while same handed gears are selected when gear teeth are placed in cross alignment to each other. Commonly used in automotive industries and industrial machinery. Much dealer advice to take helical gear for heavy load bearing capacity and noiseless operation. The most common use of this gear is in transmitting power. Lots of machine industries such as wind turbines helicopters,

---

P. Choudhary · A. Singh · A. Kumar · P. Kumar (✉)  
Galgotias University, Noida 203201, India  
e-mail: [pramodkumar@galgotiasuniversity.edu.in](mailto:pramodkumar@galgotiasuniversity.edu.in)

© The Author(s), under exclusive license to Springer Nature Singapore Pte Ltd. 2022  
R. M. Singari et al. (eds.), *Advances in Mechanical Engineering and Technology*,  
Lecture Notes in Mechanical Engineering,  
[https://doi.org/10.1007/978-981-16-9613-8\\_24](https://doi.org/10.1007/978-981-16-9613-8_24)

249

marine powertrains, and motor vehicles have a heavy usage of these gears, as these applications are often highly condemnatory [4].

### ***1.1 Helical Gear Types***

**Skew gears:** In this, teeth of two skew helical gears are aligned crossed to each other. For these types of pair pressure angle and normal pitch should be same but not necessarily handedness and helix angle. This type of arrangement has point contact between the pairs hence it has to be very accurate in the arrangement.

**Double helical gear:** They have two sets of teeth which are placed slanted and in opposite direction. This is a modified helical gear to solve the issue of axial thrust. They are mounted together on a common axle. Axial thrust is cancelled out in this arrangement because each half produces thrust in opposite direction hence nullifying each other giving a net axial force of zero. Although it has some advantages of its own, it is difficult to manufacture due to its complex shape.

**Herringbone Gear:** They are a special type of double helical gears without any groove between them. It resembles as two mirror helical gears placed side by side forming a V-shaped teeth. More than two teeth are meshed at any instance resulting in smooth power transfer ability. They have an advantage over normal helical gear as there is no requirement of thrust bearing when used at places like torque gearboxes.

For designing and simulation we have used a normal pair of helical gear which is similar to spur gear but have teeth arranged at angle which appears to be like segments of helix. It has many advantages over spur gear few of which are listed below.

### ***1.2 Advantages of Helical Gear***

Noise produced by this gear is less which is caused by gear power transfer. The teeth of gear contact in small areas oppose the entire face contacting at once [1].

It is used in transferring power between non-parallel shafts [2].

The merit of helical gear is that it provides strength output over spur gears [5].

It handles more load than spur gear because its tooth is diagonally positioned and effectively larger.

It provides superior strength due to its same tooth size and equivalent width [3].

### ***1.3 Terminology***

**Pitch Circle:** An imaginary circle that is pure rolling and gives the same motion.

**Pitch Circle diameter:** Size of gear is known by this.

**Pitch Point:** Same point of two pitch circles.

**Pitch Surface:** Surface of rolling discs.

### 1.4 Helix Angle

It is the angle between the helix and the axis of line of its circular helix angle. The helix angle is important in mechanical applications which is used in power transfer and movement modification (Fig. 1).

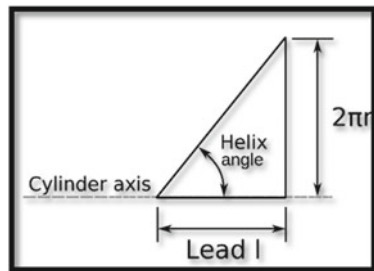
$$\text{Helix angle} = \arctan \left\{ \frac{2\pi r}{l} \right\}$$

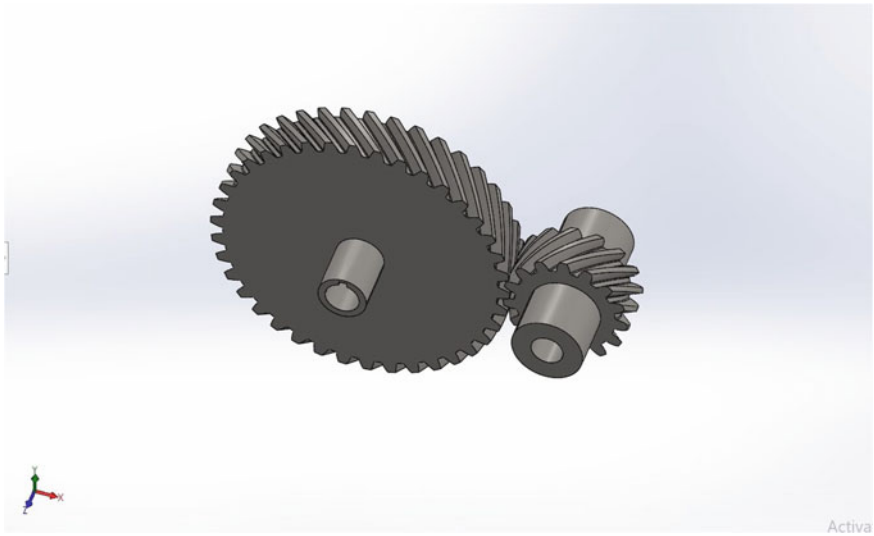
The amount of friction depends on the components of the screw and the interaction with us, but ultimately the efficiency is controlled by the helix angle. Efficiency can be adjusted relative to the helix angle for constant friction [6]. The most effective is the helix angle between 40 and 45 degrees; however, the available efficiency is found above 15° as shown in the Fig. 1.

## 2 Methodology

Designing of helical gear has been done in solidworks as shown in Fig. 2. Standard values have been given by American Gear Manufacturer’s Association (AGMA) as shown in Table 1. After designing of helical gears with different parameters as shown in Table 1, the arrangement was imported to Ansys for further simulation of properties like elastic strain, stress, deformation, and safety factor. Different torque—2000 Nm, 2500 Nm, 3000 Nm, respectively, were applied to analyze the result. The designing was started by outlining the base circle using relations and parameters and after the extrude part is created, the curve is generated and related to that tooth profile is generated [2].

Fig. 1 Helix angle





**Fig. 2** Design in solidworks

**Table 1** Standard values/parameters

Standard values/parameters	Values
Pressure angle	14–26°
Angle of Helix	19–46°
Addendum	0.7 m (Maximum)
Dedendum	0.9 m (Minimum)
Depth(minimum)	1.9 m
Clearance(minimum)	0.3 m
Tooth thickness	1.499 m
Number of teeth	20

Materials used in manufacturing helical gears are Structural Steel (S45C). S45C is easily available and is used to make spur, helical, racks, bevel, and worm gears. Its chemical and mechanical properties and physical properties have been given in Tables 2, 3, and 4, respectively.

### 3 Calculations of Contact Stress of Helical Gear

There are several types of gear but when we talk about spur gear of contact ratio less than 2 then theoretical length is assumed to be  $L$  ( $L = \text{Contact Length}$ ). In case of

**Table 2** Chemical composition of s45c

Elements of S45C	Percentage %
Carbon(C)	0.42–0.50
Nickel(Ni) maximum	0.25
Sulfur(S) maximum	0.035
Silicon(Si)	0.17–0.37
Chromium (Cr) maximum	0.25
Manganese(Mn)	0.50–0.80
Phosphorus(P) maximum	0.35

**Table 3** Mechanical properties of s45c

Quantity	Value
Young’s modulus	200,000–200000 Mpa
Tensile strength	650–880 Mpa
Elongation	8–25%
Fatigue	275–275 Mpa
Yield strength	350–550 Mpa

**Table 4** Physical properties of s45c

Quantity	Value
Thermal expansion	10–10
Thermal conductivity	25–25
Specific heat	460–460
Melting temperature	1450–1510
Density	7700–7700
Resistivity	0.55–0.55

helical gear contact length per tooth is  $L/\cos\alpha$  ( $\alpha$  is helix angle). Because of helical action, total length of contact is always approximately  $L/\cos\alpha$  times contact ratio.

AGMA recommends the value of contact length which is 95% of the contact ratio. Contact stress equation is given as

$$\sigma = C_p \sqrt{\left( \frac{F_t * \cos\alpha * y}{b * d * l * 0.95 * CR} \right)}$$

$$y = K_v * K_o * (0.93 * K_m)$$

where  $F_t$ —Transverse load,  $b$ —Contact length,  $d$ —diameter of pinion/Gear,  $K_o$ —Overload factor,  $K_m$ —Load distribution factor,  $C_p$ —Elastic co-efficient factor

$$C_p = 0.564 \sqrt{\left( \frac{E_1 * E_2}{(E_2(1 - \nu_1^2) + E_1(1 - \nu_2^2))} \right)}$$

where E—Modulus of elasticity,  $\nu$ —Poisson’s Ratio,  $l$ —Geometry factor

$$l = \frac{\sin\beta \cos\beta * i}{2(i + 1)}$$

where  $i$ —Speed ratio( $\frac{n_1}{n_2}$ ),  $\beta$ —transverse pressure angle

$$CR = \frac{\sqrt{((r_1 + a)^2 - r_{b1}^2)} + \sqrt{((r_2 + a)^2 - r_{b2}^2)} - (r_1 + r_2)\sin\beta}{\pi * m * \cos\alpha}$$

where  $r$ —pitch circle radius,  $r_b$ —base circle radius,  $a$ —Addendum,  $K_v$ —Velocity factor

$$K_v = \left[ \frac{78 + (200 * V)^{0.5}}{78} \right]^{0.5}$$

### 4 Background

The transfer of power has always been very important. The efficiency and effectiveness of any method analyzes the amount of power loss in the process. All types of gears can be spur gear, bevel gear, rack and pinion gear, or worm and worm gear, used to produce torque and angular velocity. These gears have important functions in many areas of automotive. Folded and rotating tooth gears are widely used in the industry due to their low production costs. Significant evaluation of the performance of advanced gears design therefore plays an important role in monitoring and evaluating the success rate of such gears in terms of pressure and flexibility produced with high-speed gears and continuous improvement in terms of research work. Helical Gear is more powerful than other gears especially it promotes gears as it has a smooth commitment between targets, produces low noise, can carry a lot of load and energy that can be transferred between incompatible, efficient shafts, etc. a wide variety of applications with great speed and power of machine systems [5]. Our main focus was on designing highly loaded helical gears for good power transmission systems and producing a small sound suitable for the analysis method. Analysis methods, such as Ansys, can be easily used and provide useful information on contact and pressure conversion. So to study the same we have analyzed different

properties which are important to look for gear wear namely equivalent strain, equivalent stress, total deformation, and safety factor applying different torque which are 2000Nm, 2500Nm, 3000Nm taking material as S45C. The outcome from different torques will help us to observe and analyze the significant changes that occur at different stages of simulation.

### 5 Modeling of Gear

Splitting the gears leads to separation of the gear teeth and size as well as altering power distribution and contact stress, which can accelerate the emergence of other types of failures such as scoring and pitting. Decrease Stiffness is often used in dynamic gear mesh models to indicate teeth surface deformities [4]. The gear which we have to design has 20 teeth with mix of parameters, which is in the solid work and other gears are made in a similar way [7]. Part parameter is the most important thing for defining the gear [8]. The part parameter defines all other parameters given in Table 1, which require for the gear tooth profile by using the tool menu. We chose basic helical gears out of all which has line contact between them.

By using Ansys the teeth bending stress and contact stress of helical gear are calculated. This is called Fem analysis [8]. The gear in solidworks is exported to Ansys for analysis and then mesh is generated. The mesh is non-uniform and a finite element model [9]. The geometry is made in solidworks and is imported in the geometry section of Ansys 19 and then in the Mesh section the mesh is created. Design in solidworks, geometry in Ansys after importing from solidworks, and meshing in Ansys has been displayed in Figs. 2, 3, and 4, respectively.

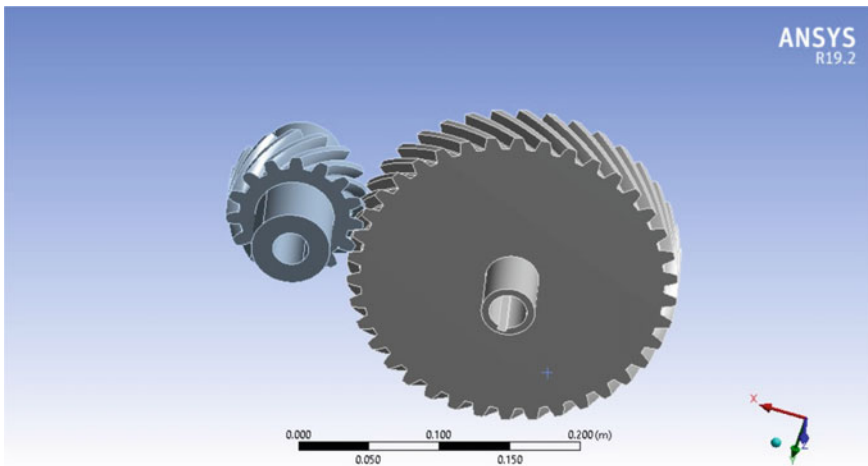
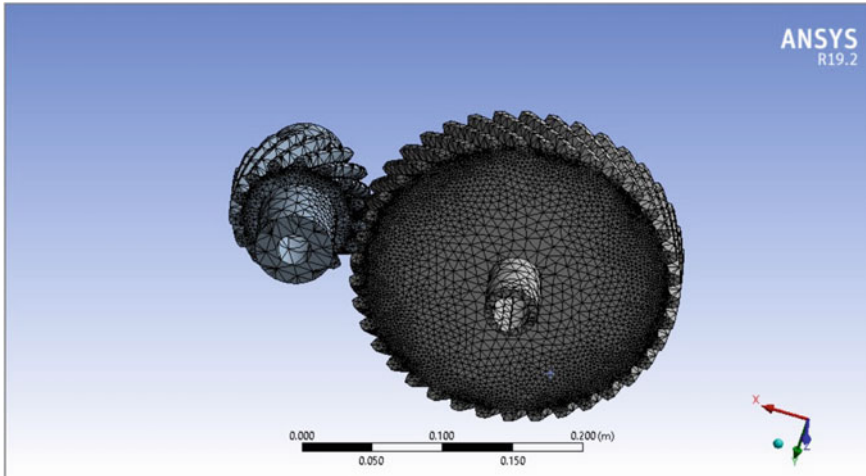


Fig. 3 Geometry in ansys19





**Fig. 4** Mesh generated in ansys 19

## 6 Result and Discussion

The simulation is done on Ansys 19 by fixing the smaller gear and giving motion to the bigger gear. The pinion tooth and gear tooth surfaces are in point contact, the bearing contact is restricted and oriented lengthwise, edge contact is steered clear of, to significantly reduce the effectiveness of the error, the adjustment of bearings, contact the shift key, as well as vibration and noise [10]. Simulation was done to calculate equivalent elastic strain which basically means the limit of material till which it regains its original shape, equivalent stress of Von-Mises type which basically tells that whether the given material will yield or gets fracture and it states that if the Von-Mises stress of any material when applied certain force is equal or greater than the yield limit under simple tension than the material will yield; also total deformation and safety factor for different values of torque that are applied on the bigger gear were calculated. Torque of 2000 Nm, 2500Nm, and 3000Nm are applied and based on that we got different values which are shown in Figs. 5, 6, 7, 8, 9, 10, 11, 12, 13, 14, 15 and 16.

Firstly torque of 2000 Nm has been applied on bigger gear tooth which gives us the maximum and minimum values of elastic strain as  $1.4261e-003$  m/m and  $5.5164e-008$  m/m which is shown in Fig. 5 and the average of two comes out to be  $2.8732e-005$  m/m which means up to  $2.8732e-005$  m/m average value our designed helical gear will regain its original shape, while maximum and minimum elastic stress are  $2.4203e + 008$  Pa and 3951.7 Pa whose average comes out to be  $5.3885e + 006$  Pa as shown in Fig. 6 which means that this helical gear will yield and not crack until  $5.3885e + 006$  Pa value. The deformation for 2000Nm torque comes out to be  $2.919e-005$  m which is the maximum value and 0 m which is the minimum value and the average comes out to be  $1.7937e-005$  m as shown in Fig. 7, while

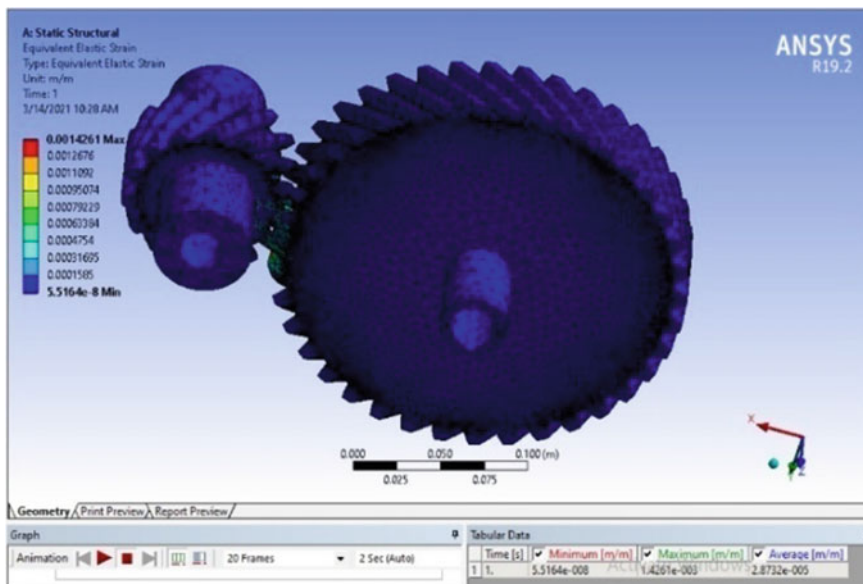


Fig. 5 Equivalent elastic strain (m/m)

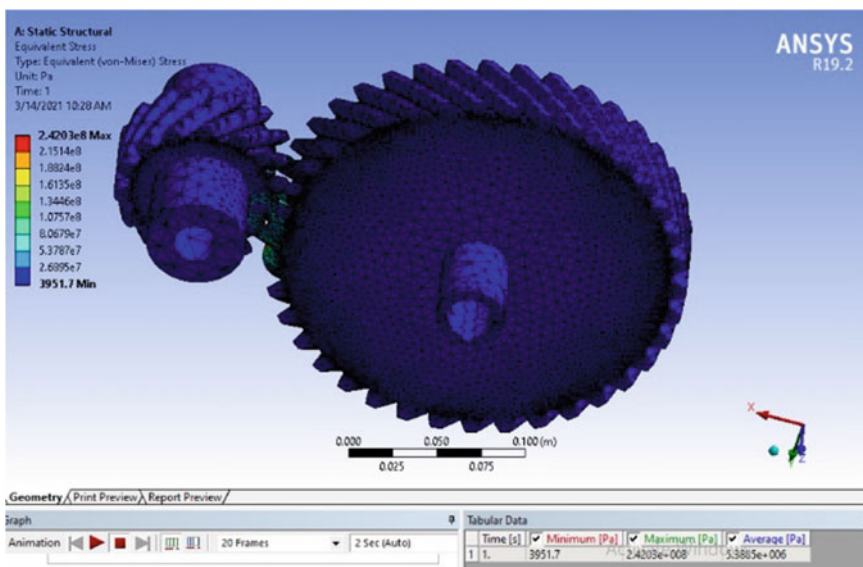


Fig. 6 Equivalent stress (pa)

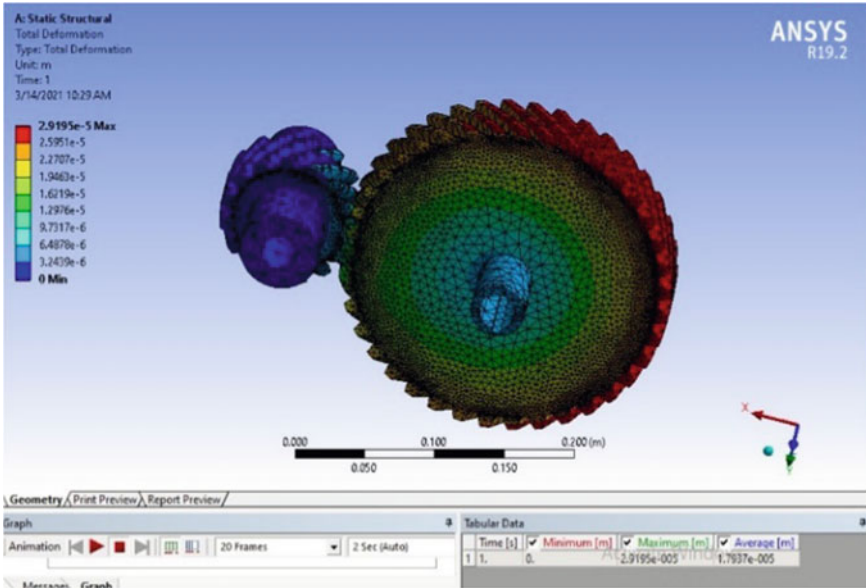


Fig. 7 Total deformation(m)

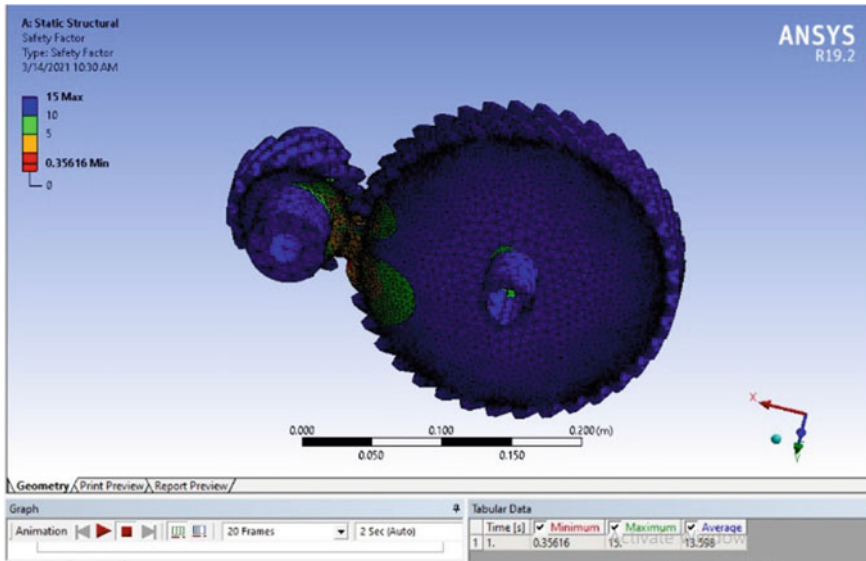


Fig. 8 Safety factor

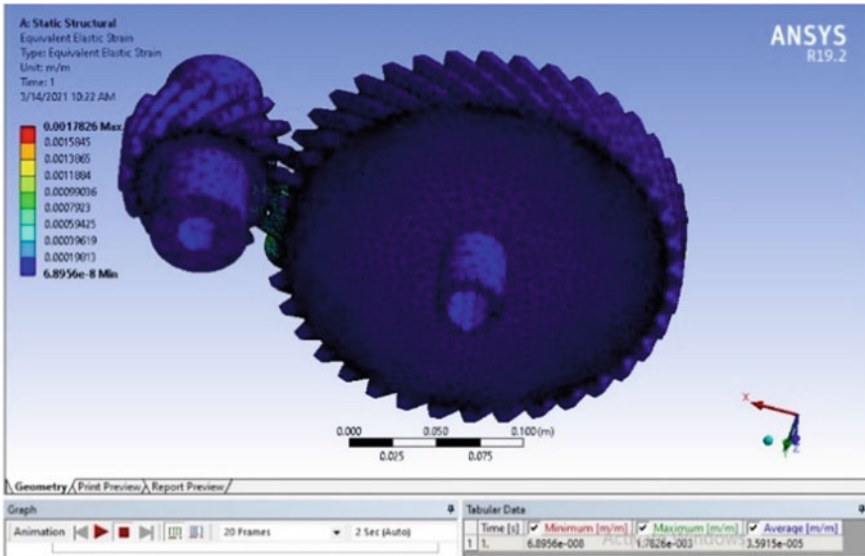


Fig. 9 Equivalent elastic strain (m/m)

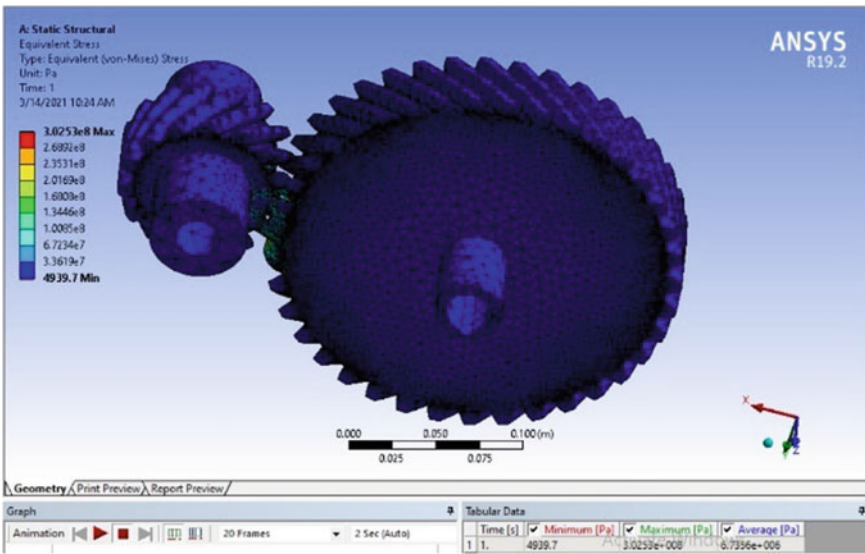


Fig. 10 Equivalent stress (pa)

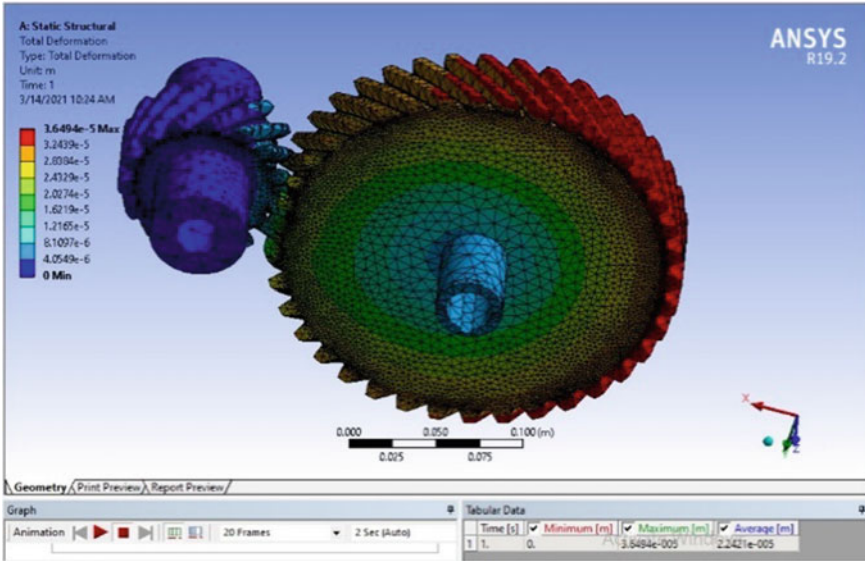


Fig. 11 Total deformation(m)

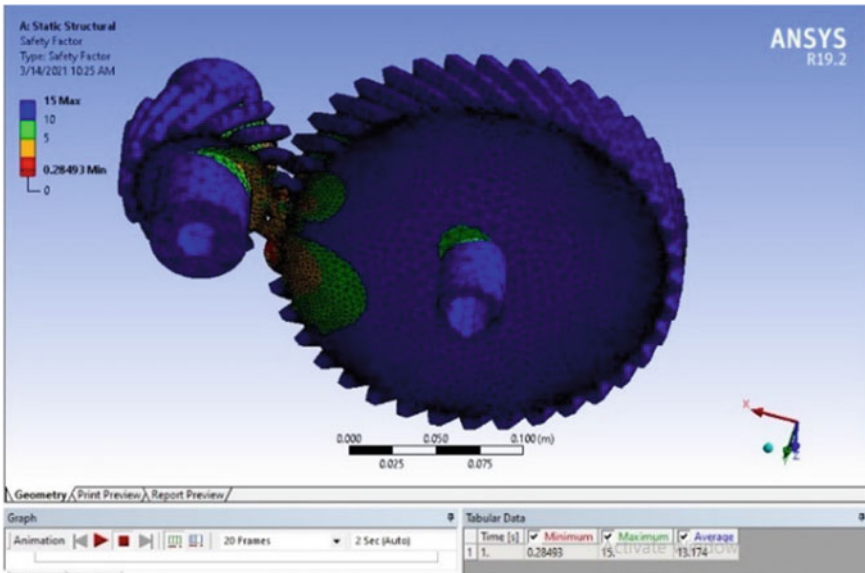


Fig. 12 Safety factor

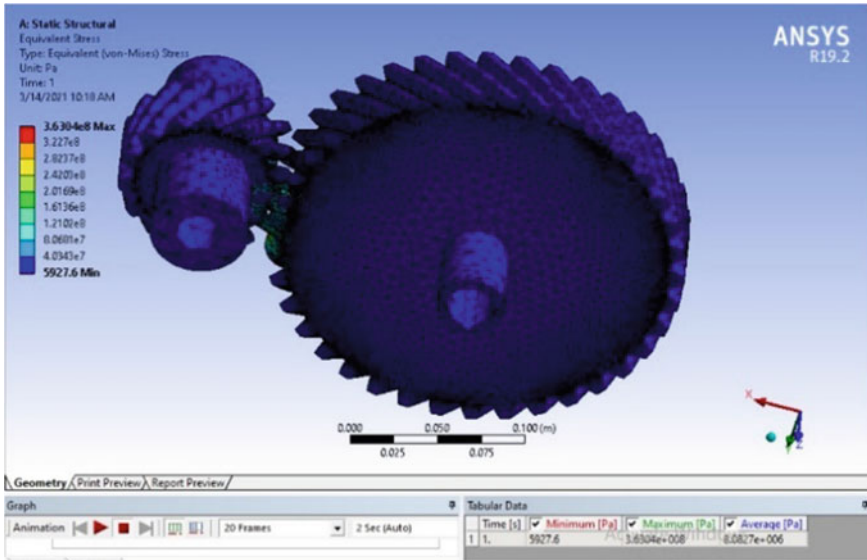


Fig. 13 Equivalent elastic strain (m/m)

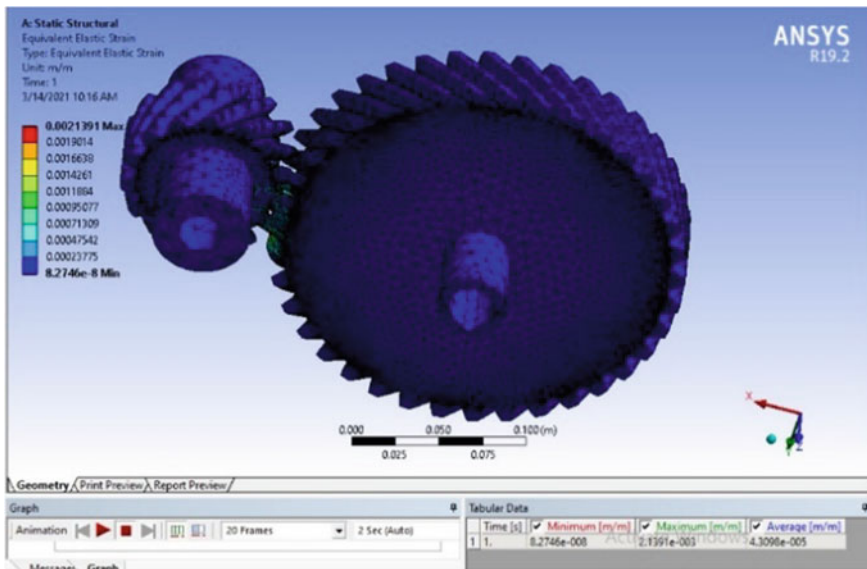


Fig. 14 Equivalent stress (pa)

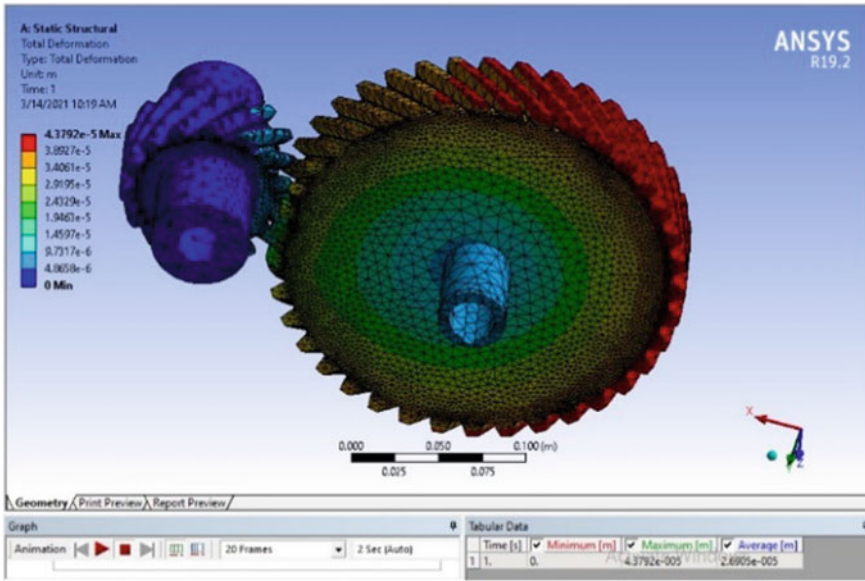


Fig. 15 Total deformation(m)

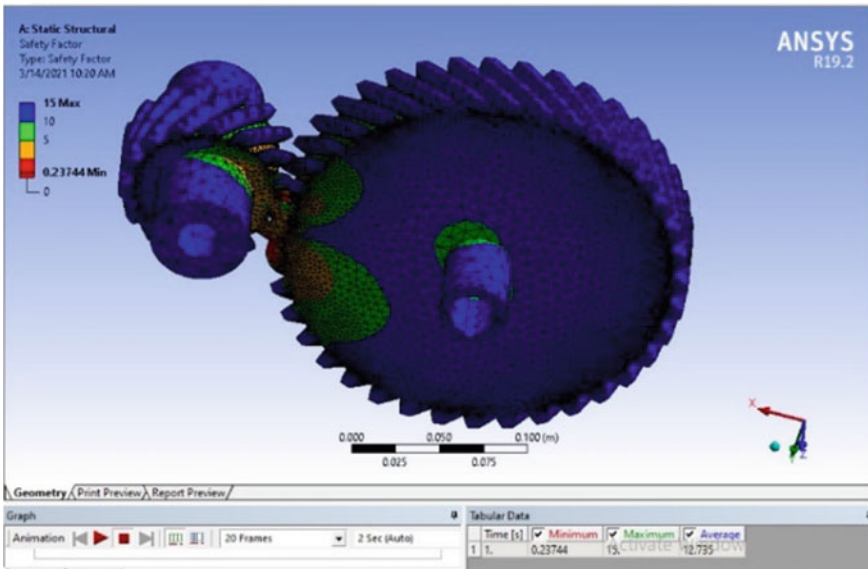


Fig. 16 Safety factor

minimum and maximum values for safety factor comes out to be 0.35616 and 15, respectively, giving an average of 13.598 as shown in Fig. 8.

When the value of torque was increased to 2500Nm, the maximum and minimum values of elastic strain come as  $1.7826e-003$  m/m and  $6.8956e-008$  m/m which is shown in Fig. 9 and the average of two comes out to be  $3.5915e-005$  m/m, while maximum and minimum elastic stress are  $3.0253e + 0008$  Pa and 4939.7 Pa whose average comes out to be  $6.7336e + 006$  Pa as shown in Fig. 10. The deformation for 2000Nm torque comes out to be  $3.5494e-005$  m and 0 m as maximum and minimum, respectively, and average comes out to be  $2.2421e-005$  m as shown in Fig. 11, while minimum and maximum values for safety factor comes out to be 0.28493 and 15, respectively, giving an average of 13.174 as shown in Fig. 12.

When the torque is again increased by 500Nm and the total torque becomes 3000Nm, the maximum and minimum values of elastic strain come as  $2.1391e-003$  m/m and  $8.2746e-008$  m/m which is shown in Fig. 13 and the average of two comes out to be  $4.3098e-005$  m/m, while maximum and minimum elastic stress are  $3.6304e + 008$  Pa and 5927.6 Pa whose average comes out to be  $8.0827e + 006$  Pa as shown in Fig. 14. The deformation for 2000Nm torque comes out to be  $4.3792e-005$  m and 0 m as maximum and minimum, respectively, and the average comes out to be  $2.6905e-005$  m as shown in Fig. 15, while minimum and maximum values for safety factor comes out to be 0.23744 and 15, respectively, giving an average of 12.735 as shown in Fig. 16.

Maximum values of stress, strain, and deformation can be seen when 3000Nm of torque was applied whereas minimum can be observed when 2000Nm of torque was applied. This shows a direct relation of torque with these properties as increment in torque's shoes increase in these values while the opposite holds true for safety factor as observed in Table 5.

### ***6.1 Applying 2000 Nm of Torque***

See Figs. 5, 6, 7 and 8.

### ***6.2 Applying 2500 nm of Torque***

See Figs. 9, 10, 11 and 12.

### ***6.3 Applying 3000Nm of Torque***

See Figs. 13, 14, 15 and 16 and Table 5.



**Table 5** Torque, stress, strain, deformation, safety factor

Torque	2000 Nm	2500 Nm	3000Nm
Equivalent elastic strain(m/m)	2.873e-005	3.5915e-005	4.3098e-005
Equivalent stress(Pa)	5.3885e+006	6.7356e+008	8.0827e+006
Total deformation(m)	1.7937e-005	2.2421e-005	2.6905e-005
Safety factor	13.598	13.174	12.735

## 7 Conclusion

The result from Ansys was obtained by changing torque by the increment of 500 Nm each time, the resulted value has a big difference. From this we can say that Ansys is used to predict the value of stress easily in compared to solving complex problem and design of gears.

In this we examine that on one point load is acted and stress calculated. But, in FEM continuous variable load is considered that why pressure is act on teeth of gear.

By observation it is clear that the bending and compressive stresses of structural steel will be suitable for manufacturing of gear due to increased factor of safety.

As increasing helix angle increases contact stresses because area of contact increases hence helix angle is critical for contact stress [5].

### Future Scope

Study of all these properties for different types of gears within helical gear is given in 1.1.

Study of different types of gears like spur, rack, and pinion or bevel gear for stress and deformation on Ansys software [7].

Harmonic analysis of gear can be done to find out the mode [3].

Simulation of helical gearbox can be done.

## References

1. Venkatesh B, PrabhakarVattikuti SV, Deva Prasad S (2014) Investigate the combined effect of gear ratio, helix angle, facewidth and module on bending and compressive stress of steel alloy helical gear. *Proc Mater Sci* 6:1865–1870
2. Jyothirmai S et al (2014) A finite element approach to bending, contact and fatigue stress distribution in helical gear systems. *Procedia Mater Scia* 6:907–918
3. Mulla NA, Bicha K (2014) Design, modeling and structural analysis of helical gear for ceramic and steel material by using ANSYS. *Int J Eng Technol Sci* 1(2):28–32
4. Brethee KF et al (2017) Helical gear wear monitoring: modelling and experimental validation. *Mech Mach Theory* 117:210–229
5. Prashant M (2017) A review paper on design and analysis of helical gear using ANSYS, FEM & AGMA Standards
6. Sarkar GT, Yenarkar YL, Bhope DV (2013) Stress analysis of helical gear by finite element method. *Int J Mech Robot Res* 2(4):322–329

7. Venkatesh J, Pbgns M (2014) Design and structural analysis of high speed helical gear using Ansys. *Int J Eng Res Appl* 2(3):215–232
8. Ahirwar M, Sen N Study the design and analysis of helical gear using ANSYS
9. Jadhav PP, Bhaskar SV (2016). Design and analysis of helical gear made of stainless steel and nylon under different loading conditions. *Int J Eng Res Technol* 5(10)
10. Litvin FL et al (2003) Modified involute helical gears: computerized design, simulation of meshing and stress analysis. *Comput Methods Appl Mech Eng* 192(33–34):3619–3655

# Adapting Cam, Automation and FMS to Boost India's GDP and Economy



Prajwal Jaiswal, Kushagra, Mayank Singh, and A. K. Madan

## 1 Introduction

Production has emerged as one of India's fastest-growing industries. Mr. Narendra Modi, India's Prime Minister, has initiated the "Make in India" initiative to bring India on the global map. By 2022, the government wants to generate employment for about a hundred million in the sector; moreover, the ameliorate demands of employment are the salient attributes for the youth. Today we know that India has most of the GDP% because of the agriculture industry, so it has become pertinent to have growth in this sector so that it could have lucrative outcomes. AM is the empirical tool in terms of technology; many machines, as well as equipment, can be made with the help of computer numerical control. Today, the approach can be applied to almost every field of engineering, as well as emerging technology and computers. Furthermore, the use of these applications is critical in the design of agricultural mechanization systems.

Soil cutting and tillage are also studied using the F.E.M. The aim of today's farming system is to minimize farming costs by reducing energy use. In order to achieve this aim, the optimal design of agricultural machines proportionate to current tractor power must be considered. In agricultural fields, a variety of tillage equipment designs can be seen, each of which is used for a different purpose. Because of the deep tillage, the tillage equipment's construction is subjected to reaction forces from the soil. If the structure does not compensate for the soil reaction forces, elements of the tillage implement can be subjected to forces that cause deformation under these working conditions. Aside from advanced machines, which are the foundation for precision agriculture, a much smaller tool, a computer with appropriate software, can be very useful, particularly in the area of keeping production planning. A PC is no longer

---

P. Jaiswal (✉) · Kushagra · M. Singh · A. K. Madan  
Department of Mechanical Engineering, Delhi Technological University, Delhi 110042, India  
e-mail: [prajwaljaiswal\\_2k17me162@dtu.ac.in](mailto:prajwaljaiswal_2k17me162@dtu.ac.in)

advanced in precision agriculture, where everything is assisted by computerization, microprocessors, automation, and other high-tech, and it may end up being the least expensive system in a holding. Computers are most often associated with information technology, but they are often used in banks, schools, offices, and other institutions. It also has a growing number of uses. In terms of the entire country's population, 54 percent of households have a computer, and 41 percent of households use the internet. In cities with more than 100,000 residents, 60 percent of households use computers, while in rural areas, 46 percent do. In our country, there is a problem with computer network growth. While the situation is steadily improving, with an increasing number of households having access to the Internet, the process is still slow. The explanation for this is that significant funds must be invested in the construction of a network with internet connectivity. Lowering computer equipment prices results in a rapid increase in the number of computers in villages and thus in holdings, among other things. Apart from using entertainment devices, a farmer who owns a machine begins to search for ways to use I.T. to help him with his farming.

Despite the fact that there is an increasing amount of software dedicated to agriculture, there has been little research in our country to determine what types of applications farmers need.

### ***1.1 Major Factors Making the Production Sector Sharp***

**Market Size:** In the manufacturing sector, India is a popular destination for foreign investment. Many different types of mobile phones, luxury vehicles, and other products have been produced or are planning to be developed in the region.

By 2025, India's manufacturing industry has the potential to be worth \$1 trillion. With a G.D.P. of \$ 2,500,000,000,000 and a population of almost 1.3 billion, Goods and Services Tax (G.S.T.) would make India a similar sector, which will attract a lot of investors. According to the Indian Cellular and Electronics Association (I.C.E.A.), policy initiatives could increase India's laptop and tablet production ability to \$100,000,000,000 by 2025 [1]. Government seeks to ensure the nation's complete growth by encouraging the development of economic corridors and smart cities. The routes would also help to consolidate, track, and create an ecosystem that is favorable to economic growth, as well as strengthen productive practices.

**Investments:** With the support of the Make in India initiative, India is on track to become a technologically advanced manufacturing hub, as Multinational Corporations such as General Electric Company, H.M.D. Global, Samsung, Tesla, Toshiba, and Boeing develop or are about to establish their production in India, attracted by the Indian markets over a billion customers and rising buying capability [2]. According to the United Nations Conference on Trade and Development (U.N.C.T.A.D.), India is one of the top 10 FDI champions in South Asia in 2019, drawing \$ 49,000,000,000.

**Initiatives by the government:** The Indian government has made a variety of attempts to foster a stable atmosphere for the growth of the country's manufacturing

sector, and it has become critical for the government to improve the agriculture sector in order to ratify this industry's growth [3].

## 2 What Can Be the Formula for the Growth of Manufacturing in India?

If India's manufacturing sector is specialized, it has the potential to be the driver of economic growth and employment. Eleven high-value sectors will be benefited by almost  $2 \times$  their G.D.P. supply in a matter of years. COVID-19 outbreak has demonstrated the deterioration of the global supply of drugs and medicinal devices, food, oil, automobile, telecommunications, physics, and a wide range of other products. Creating structures that foster global competitiveness poses one of the most significant avenues for Asian nations to stimulate economic growth and job development in the coming decade.

### 2.1 Raising Productivity

To succeed internationally, India's supply chain chains must increase their production.

- in terms of G.V.A. with full-time equivalent jobs—to near-world levels. They need more appreciation in this regard because their labor product and their goods are both poor. In comparison to India, Indonesian output has doubled; in China and the Republic of Korea, production has quadrupled. The Indian capital has almost two-thirds of its producers, such as China, to reach a high-income economy. The advancement of main manufacturing processes has the potential to improve the competitiveness of Indian firms within the determined price chains by a factor of five
- by doubling worker output and increasing cash production by a factor of two and a half. Policy changes that promote infrastructure development and better provision will help Indians become more efficient. Many property developers are concerned about the environment of local suppliers. Industries that manufacture devices with advanced technology such as software and electronics, computers, and telecommunications tools, for example, need consistent access to some materials [4].

## **2.2 *Securing Power and Technology***

Although India's value chain of development has the infrastructure and strength to go in for its overseas counterparts, the chain values are less defined. Of necessity, the suppliers should have sourcing and coordination skills. The government should assist. Alternatively, develop a system of management and conditional inducements to attract foreign firms to operate in India, either on one's own or in collaboration partnership.

## **2.3 *International Market Overview***

The Computer Production demand will increase from \$ 2.3 billion in 2018 to \$ 3.4 billion in 2023, with a compound annual growth rate (CAGR) of 7.6 percent over the given span. Robotic and automatic manufacturing development is projected to fuel business growth in a variety of industries around the world. Businesses may use.

C.N.C. equipment to design and produce goods using the C.A.M. solution. C.A.M. assists companies in reducing defects in the design and manufacturing processes. Computer software systems can be effectively combined with the modeling tool, resulting in better transformational capability and increased development process performance. The approach allows companies to handle linking modifications in a straightforward and timely manner. Organizations will reduce overall expense related to the solution, I.T. hardware, technical personnel by using a cloud-based C.A.M. solution [5]. Cloud-based systems are an excellent choice for companies with small budgets because the cloud improves speed and durability.

## **3 *Computer-Aided Design (CAD): A New Era in Design of Farm Machines***

In the construction industry, Computer-Aided Design (CAD) is developing as the major demanding popular software resource. Simply put, CAD programmers allow a designer to draw an object on a computer screen rather than on paper with a pencil. It employs machine systems to aid in the development, transformation, and improvement of design [6]. The agricultural sector has a wide range of agricultural machinery ventures that are used for a variety of purposes. When working with agricultural machinery, the reaction force from the soil is a factor because of deep tillage. If manufacturing does not remunerate for the return of the soil under these operating conditions, land practices will be exposed to the forces that trigger the deficit. Changes to H.L. may result in mechanical failure during service. As a result, the start-up's foundations must be strong enough to survive plowing. As a result, proper machine design is needed to extend machine life and reduce farming costs.

Although more research into the effects of farming or soil contact conditions is needed, it can be concluded that structural design and the use of C.A.E. systems have gotten little attention. Strong constructional analysis of the rotavator blade, clayey, and M.B. plow for these farming tools is performed using Creo models and A.N.S.Y.S. 3D software, while vertical and precise structural analysis is performed using A.N.S.Y.S. software [7].

### ***3.1 The Difference Between Traditional and Relative Farming***

#### *Farming in the Old Style*

1. Crop-farming practice are uniform throughout the world.
2. Mistakes can occur when the whole area and financial data are maintained separately.
3. The use of fertilizers and pesticides across the entire field.
4. No use of geolocation tracking is feasible.
5. Impossible to prospect the weather.

#### *Smart Agriculture*

1. Farm is evaluated to decide the best crop and water needed for maximum efficiency.
2. Early identification and use of the affected area save money.
3. Field and financial data in hand increase efficiency, with clear reports showing benefit, yield, and trends.
4. Satellite imagery identifies various farm locations.
5. Climate forecasting and review.

## **4 Methods that Can Be Opted to Ameliorate the Agriculture Sector**

### ***4.1 Computer-Controlled Devices (Automated Systems)***

Computer-controlled processes that produce milk from cows without human intervention are as autonomous as automated milking systems. An agricultural robot, advanced livestock management software, and specialized computers are used to automate the milking process [8]. Automatic milking frees up the farmer's time to track the farm and herd by removing him from the actual milking process. Computer-generated data can also help farmers handle their livestock better.

## 4.2 *Automatic Milking*

Milking animals, especially dairy cows, without human intervention is known as automatic milking. In the late twentieth century, automated milking systems (A.M.S.), also known as voluntary milking systems (VMS), were developed. Robotic milking is another name for automatic milking. To track the health status of cattle, standard programs depended on the use of computers and advanced livestock management systems [9].

## 4.3 *Agricultural Drone*

A type of unmanned aircraft carrier used to expand agricultural activities, increase crop production, and track crop growth is known as an agricultural drone. Farmers can see their fields from the air thanks to agricultural drones [10]. A bird's eye view can show a variety of issues, including irrigation issues, soil variations, insects, and fungal attacks. Intimate details can be seen in multispectral images.

### **Benefits:**

**Termination of employment**—With a strict structure in place, the farmer is excluded from the milking process, and the employee is dedicated to animal care, feeding, and other duties.

**Consistency of milking**—Different milkers has no effect on the milking process, which is the same for all cows and visits. Four different milking cups are withdrawn separately, resulting in a lower risk of injury since the empty quarter is not still attached when the other three are full. The pulsation of newer types of automatic milkers can differ.

**Increased milking frequency**—Milking frequency can be increased to three times a day, but a 2.5-times-per-day frequency is also available. Since only a small amount of milk is stored on average, this can reduce stress on the udder and the cow's growth.

The most popular milking method increases each cow's milk production, but the majority of this increase is liquid milk rather than solid milk.

**Increased Growth**—Although mechanical pressure is an unavoidable part of technological progress, the increasing complexity of the A.M.S. milking unit compared to traditional systems increases dependency on manufacturers' repair services and potentially raises operating costs. In the event of a complete device failure, the farmer is exposed because he relies on the service provider's prompt response.



## 5 Smart Farm

Smart farming focuses on the management of farm activities using data from different sources (historical, geographical, and operational). Technological progress does not always imply that a machine is wise [11]. Smart systems are distinguished by their ability to collect and interpret data. To monitor all farm activities, both pre-and post-harvest, smart farmers use hardware, and software to capture data to provide insight into what is happening [12]. Integrating new technology and existing farming practices to improve the production and quality of agricultural products is part of organic farming and agricultural precision. By the amount of hard work and repetitive work, they increase the productivity of farm workers. Almost every aspect of farming can benefit from technological advances, from planting and irrigation to plant health and harvesting.

### *5.1 Technological Changes with the Use of C.A.M. to Revolutionize the Agriculture Sector*

#### *Tractors*

A tractor is the heart of a farm, and its configuration varies depending on the type of farm and supporting equipment. It can be used for a variety of tasks. Tractors are likely to be among the first to be transformed as autonomous driving technology improves [13].

#### *Planting and Planning*

Sowing seeds used to be a difficult task. Sowing machines, which can cover the world much faster than humans, have advanced modern agriculture. These, on the other hand, often employ a dispersal strategy that can be ineffective and disastrous if the seeds do not fall in the proper place. Active sowing necessitates two flexible controls: planting seeds at the right depth and dividing plants at the right distance without allowing for good growth. To provide information to farmers in the future, existing precision seeds will be combined with separate tractors and IoT-enabled systems.

#### *Weed and Crop Care*

Plant protection and autonomous robot operations both include herbicides and pest control and need caring that can be easy with the help of C.A.M. [14].

## 5.2 *Reducing Activity, Increasing Reversion, and Efficiency*

The basic aim of deploying autonomous robots in agriculture is to reduce dependency on labor while ameliorating production and productivity [15]. Future farmers will spend time doing tasks like repairing equipment, fixing robotic code errors, analyzing data, and planning farm operations, rather than doing hard labor like their forefathers. All of these bots agree that having a robust sensory spine and IoT installed into farm infrastructure is critical. The ability of all the machinery and sensors to interact independently with the farmer, even though they work independently, is critical to a truly “smart” farm [16].

## 5.3 *CAM and Farming*

### *Illustration Drones and Planting*

With advancements in imaging technology, you are no longer limited in your visual acuity while still photographing. From regular imaging to infrared, ultraviolet, and hyperspectral imaging, there’s something for everyone. Camera systems are available. Many of these cameras also have video recording capabilities. In both of these ways of thought, image correction has improved.

### *Planting from Air*

To meet the need for manual labor, prototype drones are built using advanced technology and then tested to see if they can be used in sowing and planting. Several companies, for example, are developing drones that can burn pills containing fertilized vegetable seeds and nutrients directly into the soil with compressed air [17]. Drone-Seed and Biocarbon are two companies that develop drones with a module that burns tree seeds in strategic locations in the ground.

### *Real-Time Monitoring and Analysis*

Monitoring and evaluating fields and crops are some of the most useful activities for drones. Consider the benefits of using fewer drones rather than a large group of staff who spend long hours walking or traveling back and forth through a field to inspect the vegetation [18].

### *Connected Farm: Sensors and IoT*

Agriculture bots and drones are becoming more automated, but the Internet of Things will really turn the future farm into a “smart farm.” The Internet of Things (IoT) has developed into a term that refers to the idea of linking computers, machinery, equipment, and devices of all kinds, as well as data sharing and communication, to create a “smart” infrastructure [19]. On smart farms, sensors will be installed in every stage of the farming process, as well as in all machinery. Throughout the fields, the sensors can collect data on light levels, soil conditions, drainage, air quality, and

temperature. The data will be sent back to the farmer or to the agriculture bots in the field [20].

#### ***5.4 The Role of SaaS-Based Cloud Software Farming***

In today's world, financial and farm activities are managed using cloud-based software. Farmers used to hold long records on paper to store data before computers. But here we speak about the role of SaaS-based cloud software:

##### *Data Collection*

Data collection and retrieval is one of the most important cloud software applications in agriculture. Weather cycles, planting patterns, soil quality, harvesting, and satellite imagery are just some of the data that cloud software can provide with pinpoint accuracy and speed. All of the farm's data is stored in the cloud and is therefore easily available. So, if the plants were infected with the same symptoms in the future as they did 10 years earlier, the data could be used to identify a cure that was used at the time.

##### *Data Processing/Analysis*

To allow for a higher degree of decision-making, database management in cloud computing requires all invalid results of all forms of data available in relation to the farm. Climate data, market data, farm data, G.I.S., and water availability are all carefully analyzed until the correct number of seeds, water requirements, and pesticides are given on the farm.

##### *Data Storage and Distribution*

Previous research relied heavily on data preservation. Previously, data storage was backed up by hardware, which necessitated diligent maintenance and care. When hardware is lost, data is lost forever.

#### ***5.5 IoT (Internet of Things) or SaaS (Software as a Service) Solutions for Cloud used for 'Smart' Agricultural Environments in a Developing Economy Like India***

Although the Internet of Things is still in its infancy, agricultural governments that power the Economy are investing in cutting-edge technology like the Internet of Things, artificial intelligence, and learning machines by developing smart agricultural solutions. IoT implementation in agriculture has its own collection of advantages and challenges in agricultural-based economies like India. To begin with, farmers are hesitant to go high-tech because they are unfamiliar with the applications of

agricultural technology. Aside from that, the sensors, robots, and drones used in the development of IoT solutions are costly and time-consuming to operate, requiring technically skilled staff. The data gathered must be processed, which can be accomplished by taking it to a lab or by using farm equipment. And different sensors are needed to collect data on different parameters that must be evaluated separately, which is why they make high-priced products. As a result, considering the various farm sizes, engineered solutions should be less costly and more intimidating.

Advantages of Smart Farming via SaaS solutions:

- Easily accessible and precisely manageable via Smartphones, tablets, and P.C.s.
- Alert Log and Management (like pest infestation etc.).
- It accounts for end-to-end solutions from farm tracks to fork.
- A robust and flexible farm management system.
- Satellite and weather-based advice.
- High yield as input is prepared and monitored regularly.
- Tracking and Release.
- Investment and understanding reports—easy and mobile reporting.
- Better quality due to being in strict order with dietary standards and nutrition compliance.
- Less waste due to customization procedures for calculating direct use of resources and thus reducing production costs.

## 6 Opportunities and Future Scope

Smart farming has the potential to provide an integrated way out of locked technologies and practices marked by heavy diversification and market segregation. It paves the way to sustainable agriculture by using a range of technology, crop and livestock production systems, and networks for all agricultural food industry participants. There is no single policy solution that can help and promote the successful use of technology. Instead, the aim must be to find the best ways to stress or threaten the long-term use of technology, as well as to choose the most suitable practices across the world. This can upshoot in improved financial access and direct investment support. Furthermore, funding for collaborative farm surveillance technology or investment in education and training will help to ensure that these technologies are used in a sustainable manner. However, in all situations, the policy environment should have straightforward, legal requirements. I.C.T. opportunities lead to recognized forms of agriculture, management advice will be given even if farmers have never developed a specific crop before, and loss of farmer's life and situations like famine will be avoided in India. I.C.T. opportunities lead to recognized forms of agriculture; management advice will be provided even if farmers have never developed a specific crop before. Facilitates the invention of technology that contributes to segregation. Using a variety of production methods, current resistance problems such as those with antibiotics and pesticides can be avoided. Even though the "Internet of Things," such as agricultural machinery, can manage normal farming conditions,

the farmer must still serve as a scientist and watchdog, keeping an eye out for unexpected circumstances. Indian Farmers may use their spare time to invest in digital innovation for disease treatment or for tracking and handling livestock in novel ways. Pests and diseases must be treated only when such thresholds are reached, which are decided by new I.C.T. systems. However, the deliberate increase in diversity necessitates convincing consumers and farmers that they will get advantages of these technological advances. Furthermore, a new data transmission system with various transparent functions is required: administrative and the government and the transmission of output information to suppliers must be open to farmers. In addition, a consumer can gain knowledge of the entire food supply chain. Farmers may use new devices to share desired information, form alliances, conduct peer reviews, and even develop informational information systems to supplement the formal information management system. The flow of such information between farmers and between farmers and consumers will be self-contained and unrestricted by national borders. Shared use of equipment and applications like Airbnb and Uber could promote private sharing of sowing, repair, and harvesting operations. Specific policies and a clear data management system will be required, however, because regulatory authorities will need access to other aspects of the collected data. In India, only the adoption of this new and technologically advanced machinery may take a little while and capital. However, once everything is ready to be functional, the growth will be immense, as was the case with the Green Revolution led by the then Prime Minister, Mrs. Indira Gandhi.

## 7 Conclusion

In the current research, the author/s have discussed various modern farming methods that can be used to increase the efficiency of the output, in turn generating more credit. Millions of tons of production eventually get discarded through various reasons like improper management due to shortage difficulties. In an Agriculture-based economy like India, the scope of using the benefits of the processes of Smart Farming can be huge. As spoken in the paper earlier, manufacturing is also one of the fast-growing sectors of the Indian Economy. Using tools like C.A.M., CAD, and F.M.S. just like we did in the past, but in the Farming sector, we can also produce massive gains. The author has even proposed some easy ways through which the adoption of Smart Farm at least initiates from a point. In India, the advantages of smart farming are numerous. These smart farming strategies have a lot of advantages and can help increase farm productivity. People believe that the methods or ancient practices that have been used in agriculture since ancient times are the best. However, as the population grows and technology advances, strategies must evolve as well. Farmers in India must implement advanced technologies to improve smart farming in order to achieve this. Following are the advantages that can benefit the Agriculture dependent Economy of India. By adopting Smart farming following can be achieved:

**Increase in Efficiency:** Farmers can improve their productivity by using smart farming techniques. Farmers can now deliver more commodities in a shorter amount of time, thanks to advanced technology. They are quickly inspected, foresee problems before they occur, and make critical decisions to keep them at bay.

**Expansion:** Agriculture improves thanks to the use of smart farming technologies. All agricultural operations are completed on time and to a high standard. From these techniques, the short food chain is completed on time, and everybody in the country receives proper food at an affordable price.

**Proper use of resources:** Smart farming innovations make the most of available resources. Power, water, and land are among the resources. By using data obtained from sensors, IoT farming data can be used to assign the most resources to the plants.

**Improved product quality:** Crop sensors, field imaging, and aerial drones are all used to further increase product quality. The best conditions for increasing the value of nutritional goods are created by smart farming technologies.

## References

1. Abhishek D et al (2018) Estimates for world population and global food availability for global health. Book chapter, *The role of functional food security in global health*, 2019, pp 3–24. Elder M, Hayashi S (2018) A regional perspective on biofuels in Asia. In: *Biofuels and sustainability, science for sustainable societies*. Springer
2. Khan J, Mishra A (2019) Role of CAD/CAM in designing, challenges facing in manufacturing industry and developing manufacturing in modern manufacturing technology, pp 453–457
3. Huangfu D, Pei X (2010) Research on the key technologies of CAD/CAM integrated system. *Int Conf Mech Autom Control Eng* 2010:667–670. <https://doi.org/10.1109/MACE.2010.5535721>
4. Balic J (2006) Intelligent CAD/CAM systems for C.N.C. programming—an overview. *Adv Prod Eng Manag* 1(1):13–22
5. Zhang L, Dabipi IK, Brown WL (2018) Internet of things applications for agriculture. In: Hassan Q (ed), *Internet of things A to Z: technologies and applications*.
6. Mufticjev V, Ziatdinov R, Nabiyeu R (2020) Multi-criteria assessment of shape quality in cad systems of the future, *C.E.U.R. Work Proc* 2744:1–16. <https://doi.org/10.51130/graphicson-2020-2-3-68>
7. Usman MM et al (2016) Application of CAD/CAM tools in the production of investment casting Part. *I.O.S.R. J Mech Civil Eng* 13(1):2278–1684. <https://doi.org/10.9790/1684-13143840>
8. Navulur S, Sastry ASCS, Giri Prasad MN (2017) Agricultural management through wireless sensors and internet of things. *Int J Electr Comput Eng (I.J.E.C.E.)* 7(6):3492–3499
9. Sisinni E, Saifullah A, Han S, Jennehag U, Gidlund M (2018) Industrial internet of things: challenges, opportunities, and directions. *IEEE Trans Ind Inf* 14(11):4724–4734
10. Ayaz M, Ammad-uddin M, Baig I, Aggoune EM (2018) Wireless possibilities: a review. *IEEE Sensors J* 18(1):4–30
11. Lin J, Yu W, Zhang N, Yang X, Zhang H, Zhao W (2017) A survey on internet of things: architecture, enabling technologies, security and privacy, and applications. *IEEE Internet Things J* 4(5):1125–1142
12. Hi X, An X, Zhao Q, Liu H, Xia L, Sun X, Guo Y (2019) State-of- the-artinternet of things in protected agriculture. *Sensors* 19:1833

13. Elijah O, Rahman TA, Torikumi I, Leow CY, Hindia MN (2018) An overview of internet of things (I.O.T.) and data analytics in agriculture: benefits and challenges. *IEEE Internet Things J* 5(5):3758–3773
14. Thea K, Martin C, Jeffrey M, Gerhard E, Dimitrios Z, Edward M, Jeremy P (2017) Food safety for food security: Relationship between global megatrends and developments in food safety". *Trends Food Sci Technol* 68:160–175
15. Khanna A, Kaur S (2019) Evolution of Internet of Things (I.O.T.) and its significant impact in the field of precision agriculture. In: *Computers and electronics in agriculture*, vol. 157, February 2019; In: Younis A, Katsoulas N, Bartzanas T, Kittitas C (eds) *Internet of things in agriculture, recent advances and future challenges*
16. Cerchecci M, Luti F, Mecocci A, Parrino S, Peruzzi G, Pozzebon A (2018) A Low power IOT sensor node architecture for waste management within smart cities context. *Sensors* 18:1282
17. Nguyen T, Roehrig F, Grosjean G, Tran D, Vu T (2016) Climate-smart agriculture in vietnam; international. In: Jayaraman P, Yavari A, Georgakopoulos M, Arkady Z (eds) *Internet of things platform for smart farming: experiences and lessons learnt*. *Sensors*, vol 16, pp 1804–1282
18. Zhang X, Zhang J, Li L, Zhang Y, Yang G (2017) Monitoring citrus soil moisture and nutrients using an I.O.T. based system. *Sensors* 17:447
19. Hicham K, Ana A, Otman A, Francisco, F (2017) Characterization of near-ground radio propagation channel for wireless sensor network with application in smart agriculture. In: *Proceedings of the 4th international electronic conference on sensors and application*, SolelyOnline, 15–30 November 2017
20. Bi Y, Bhatia R, Kapoor S (2019) *Advances in intelligent systems and computing* 1038 intelligent systems and applications, vol 2(Ibiza), pp 415–425

# Accident Detection and Prediction with Notification Alert System



Sajal Gupta, Manish Rawat, and A. S. Rao

## 1 Introduction

Interruption of road streams causes lost time, costlier fuel expenses, and missed gains. Officials are operating around the clock to build conventional support inspections as soon as attainable to keep lanes clear and present secure travel. At present, car wrecks are among the most important reasons for disruption to the normal flow of traffic. Harassment prevention is important, however, it is very difficult to implement a structure for traffic-free passage. Although it is not feasible to have a mapped interval from inside and outside injuries, early disclosure and adverse results are important to save lives and overcome trauma-related losses. This document is meant to bring such a structure in which the elements of the road are preserved and where a mishap is predicted before any alert of a mishap emerges from the place. For instance, we have aided provincial authorities to dispatch problem-solving parties to low-risk areas, avoid hazards by taking further steps, check costs completely, and better prepare for the future.

In Segment Two, similar tests regarding the distribution of the road, the recognition of vehicles using different methods, methods are given. The details, location, and extensive information preparation strategies currently in place are set out in Segment Three accompanied by Segment Four which gives information testing and outlines the evacuation strategies. Our Accident Detection and Prediction system will work on such an algorithm that can analyze the collision of vehicles and accidents, over the CCTV cameras, and in turn predict areas that are prone to such damage and also, the chances of it happening by accident.

We have included:

---

S. Gupta · M. Rawat (✉) · A. S. Rao  
Engineering Physics Department, Delhi Technological University, Shahbad Daulatpur Village,  
Main Bawana Road, Delhi 110042, India  
e-mail: [manishrawat\\_2k17ep38@dtu.ac.in](mailto:manishrawat_2k17ep38@dtu.ac.in)



- A. Tensorflow object Detection API (object detection).
- B. Socket.io (for real-time communication).
- C. Node.js (server side programming).
- D. Prediction Models.

## 2 Prior Research

There has been a number of investigations on the transport and transportation structure; however, the majority of them focus on basic development and physical development. Then a few investigations center around some specific keen transportation framework segments, for example, the subjects of mishap avoidance, traffic stream estimation, occasion location, course enhancement, and so on. The aforementioned tests are due to our many concerns.

In one research, Lee concentrated on diminishing the quality of road data gathered by several road sensors and studied the difficulties of achieving precise, solid information. He gave strategies to recognize a portion of these mistakes and tried these models utilizing genuine information. Wang supports the use of Street Traffic Microwave Sensors (RTMS) to get traffic data from Traffic Management Systems and protected several Ontario models. Supervisors et al. have delayed the local time zone structure COMPASS, produced in the Toronto region, which relies on computational estimates, street dwellers, and speed preparation to recognize unusual information. Feng et al. used comparable data to link the normal outbound time using the Bayes model. Pascale et al. concentrated on street limit judgments and supported methods to build effectiveness. Vehicle Ad Hoc Networks network is increasingly used in rush hour gridlock information models, but accounting and information supply are not easy under a variety of road situations. More and more experts are analyzing traffic streams and occasional/incorrect identification.

Baiocchi et al. suggested a structure for regulating traffic patterns using GPS data and won. In the identical article, Terroso-Saenz et al. studied the force of the stream. Hojati et al. presented a standard for judging the preceding time between an accident event and, clearing dependably on several road conditions and baseline measurements. Comprehensive computer arrangements have also been a part of the suggested structure for road traffic estimation, risk association, and so on. Neural Systems, Support Vector Machines, and the Hidden Markov Model are used in this research. The main motive for this procedure is to have the option to implement a perpetual traffic assessment structure that can identify the next risk after an event so that we can play it cautiously ahead of time under the conditions.

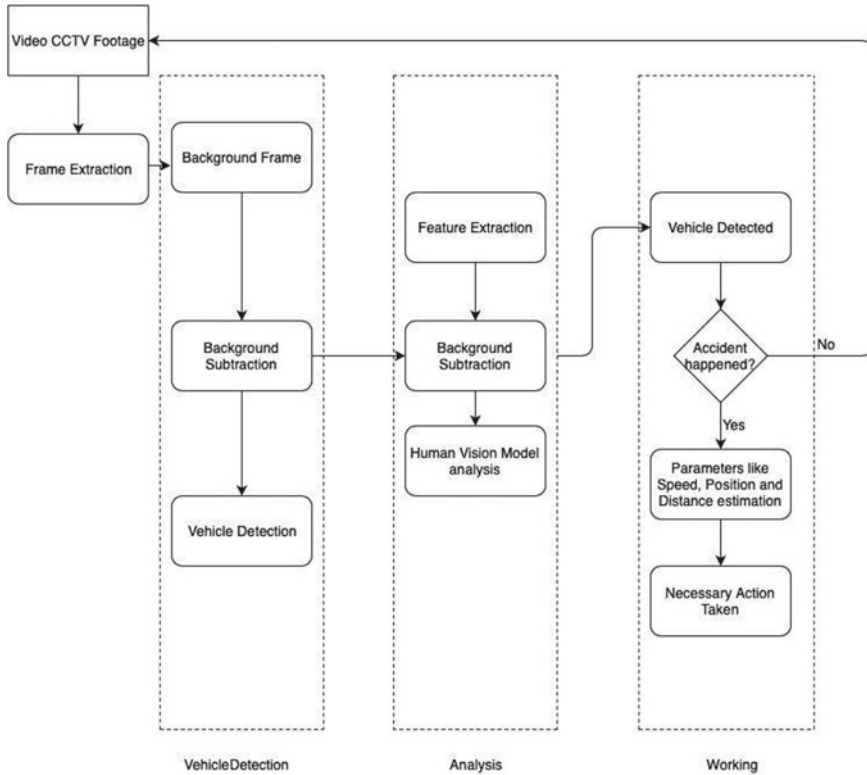


Fig. 1 Data flow diagram for the software

### 3 Design and Specification

The following diagram represents the flow of the project pipeline with all the necessary steps followed (Fig. 1).

### 4 Data Pre-processing

The data utilized in this research was made using Google images and also used other scrubbing algorithms to generate a database of various hazards suitable for model training according to the Indian road standard. The prediction module database is obtained from ARCGIS and extracted from the geo-JSON file. There are about 400 CCTV images that supply data throughout the city, however, using the initial variant of our design, we have elected to leave the data into separate regional images with high-quality cameras. The reason for this is due to poor maintenance such as robots, sharp turns, stop signs, etc. Therefore, we assumed that if a drop or stop was seen in

traffic, it should be due to a road traffic disruption (accident, passage development, motor vehicle, etc.).

The resulting information pieces were collected from the original database.

- A. Number of vehicles moving from the specific road section.
- B. Average speed of the vehicles passing by.
- C. Average occupancy proportion of the path.
- D. Date/time details of accidents in the region including the numerous occurrences used in our research.

The event database has time-varying location, chance of accidents, major or minor accident, continuous road activity, wrecked vehicle in a visual report.

## 5 Accident Detection Model

The Detection Module contains two major models first for collision detection and second for license plate detection. To perform the collision we developed an algorithm such that it can first detect the cars traveling over the road and calculate the total surface area of the rectangle formed around them. Then it calculates the collision threshold by enumerating the areas of two rectangles of a car forming a bigger rectangle together at the time of the collision. The threshold is the  $0.6 \cdot \sqrt{\text{area of rectangle of two cars}}$  and if this threshold came out to be greater than the area of two rectangles together then we can say that these two cars had a collision since they have the overlapping planar coordinates with the threshold.

For license plate detection we used `frozen_east_text_detection` model to detect the number plate and `PyTesseract` to convert the detected number plate into a string. The license plate is detected by converting the image into monochrome and marking out the bounded rectangle plate and having text inside it with a probability rate of detection.

TensorFlow is a structure for creating models in machine learning providing different tools and toolkits at your preferred level to construct models using data binding. Lower level APIs can be used (like `tf.estimator`) to create models by defining a set of mathematical procedures. Alternatively, you can apply higher ones, consisting of APIs specifying predefined structures, such as linear regressors or neural networks.

### 5.1 *Tensorflow Object Detection API*

The TensorFlow Object Detection API is an open-source structure developed within TensorFlow that promotes the development, preparation, and distribution of object acquisition models.

We planned to feed the real-time video footage coming straight from the CCTV to our model to predict the probability of accidents. The model we used for the detection purpose is ‘**ssd\_mobilenet\_v1\_coco\_11\_06\_2017**’.

The prototype is served with real-time videos and images as well, and it detects the accident by the cars that are colliding with each other. Wherever an accident is detected, a rectangle is seen over the collision of the cars which depicts that an accident has occurred over there. The model accuracy has increased in the case of the detection module and hence, accident detection is made possible in our project on real-time systems that can be really helpful to the authorities and organizations using it.

## ***5.2 License Plate Recognition***

The license plate detection and text recognition algorithm are done using OpenCV and PyTesseract Library. The Detection algorithm helps in detecting the license plate in any kind of image, be it blurry, low light, or even a high-quality image. The plate’s **Region of Image (ROI)** is then masked out and cropped automatically with correct dimensions and improved accuracy. The dataset for testing the license plate algorithm is then preprocessed using image thresholding algorithms and segmentation algorithms in OpenCV and using the scikit-learn library of Python. The Text on the detected license plate is recognized using Tesseract-OCR, a Google API. It is easily implemented using PyTesseract API that is a wrapper library for **Tesseract Google-OCR API**.

## **6 Notification Alert System**

Whenever an accident takes place, a lot of time is wasted for it to be reported, so the concerned department doesn’t even get to know that such a crucial incident had taken place and hence it gets unnoticed, which further blocks the road and is the major reason for traffic these days.

Alerting with the location of the accident took place and time, properly generated report, can help the Government and the concerned authorities to keep a firm check on the dangerous locations, as this algorithm will mark the danger prone areas and vicinities so that authorities can pay more attention to these marked positions and hence, can take action at the right time by providing medical aid and reducing the amount of traffic that gets accumulated after any chaos happens. Our Algorithm will help them to be informed about the accidents that have recently succumbed, even the authorities can install this system on their part to place a keen and firm vision on the roads to avoid nuisance.

## **6.1 *Socket.io***

After the detection of the accident, we want the authorities to get informed of the accident that has taken place along with the coordinates of the location where it happened. Socket.io is a JavaScript library for real-time web applications. It enables real-time communication, including two-way associations among network clients and servers. It has two components: a separate dependent library, plus a separate Node library. Using Socket.io, we are sending a notification, live to the mobile phones of the authorities or person whose number is verified with Twilio.

## **6.2 *Twilio***

Our Accident Detection System helps the authorities to stay aware every time and get alerted whenever the public needs their help and reach the accident locations in time!

Twilio is an API through which we can send notifications and alerts, just like a report in which the location of the accident, the time at which it took place is notified, also, along with the valid and correct location coordinates Socket.io helps communicate with Twilio API and the alerts are sent to the people on their phones.

# **7 Accident Prediction Model**

## **7.1 *Objectives***

The main purpose of the Prediction System of Road accidents is: to analyze the accidents already occurring in the area which will be helping us in determining the major accident-prone area and helping in establishing the immediate necessary help/support for them. Making predictions based on weather, pollution, road structure, etc.

## **7.2 *Problem Statement***

There are many problems with current practices for the prevention of accidents occurring in areas. The database we use is officially available by many institutions and government websites. The data collected will be analyzed, integrated, and grouped based on various constraints using the most favorable algorithm. This estimate will help analyze and identify the causes of faults and accidents. It will also be helpful

when constructing roads and bridges as a reference to avoid similar problems encountered earlier. The forecasts made will be very useful for planning the management of such problems.

### ***7.3 Logistic Regression***

Logistic regression, or most commonly, the sigmoid function, is the regression analysis and dependent upon the variables is binary numbers, i.e., (0 s and 1 s), All regression study, the logistic regression is a prediction analysis, helps in contributing and predicting continuous values variables. Logistic regression is used to obtain information about the data and to clearly define the relationship between binary variables that are dependent on different independent variables. Sometimes logistic regressions are difficult to describe the statistics tools are easily conducted and analyze the datasets, then in others, plain words are as it is displayed in the output.

### ***7.4 Random Forest Model***

Random forest includes a large number of single judgment trees clubbed together that work as a group and are working on the principle of ensemble learning. Each tree in a random forest spits out a step-by-step forecast with many votes becoming the prediction of our model. The ultimate concept behind this algorithm is that a large number of approximately uncorrelated models (trees) working as a committee will better any of the single constituent models, and the judgment score is the average of individual scores from the tree.

## **8 Results**

All designs and modules are very accurate in detecting and predicting accidents, however, false positivity rate is high considerably. But, to deal with the Bias-Variance tradeoff, we raise the inclination for reducing these wrong signals, the rate begins to go downward positively. The result in predicting road accidents is to find out the percentage of accidents in a particular area. Having a low number of features helps in rapidly modifying the algorithm and increasing accuracy. The result in predicting road accidents is to find out the percentage of accidents in a particular area. Then we apply logistic regression on these characteristics and obtain the least error. The random forest model then underwent a logistic regression model to give better accuracy.

## 9 Conclusion

We have shown you a promising approach to intelligent road accident detection and early planning. This can produce an early response to uncertainties and save lives and precious time/resources. Preceding outcomes show that such a model may be used live in the Transport Department. Many types of computer intelligence can be modified and tested in advance.

For future work, other features can also be added such as weather limits, road construction details, related location, and road conditions (direction of the sun, nearby structures, roadway signs, service paths, inclusions, availability of emergency routes, etc.). And much analysis needs to be done with personal details, External points can be removed by involving domain experts. Some computer algorithms can be modified. The model can be chosen as a serial time problem, administration of time can be utilized, and neural network designs are built. Finally, the outcomes from various methods can be joined to shape the forecast more precisely and efficiently.

## References

1. Akoz O, Karşlıgil ME (2014) Traffic event classification at intersections based on the severity of abnormality. *Mach Vis Appl* 25(3):613–632
2. Baiocchi A, Cuomo F, De Felice M, Fusco G (2015) Vehicular ad-hoc networks sampling protocols for traffic monitoring and incident detection in intelligent transportation systems. *Transp Res Part C: Emerg Technol* 56:177–194
3. Buyukozcu D (2012) Discretized categorization of high-level traffic activities in tunnels using attribute grammars. Master's thesis
4. Cetiner BG, Sari M, Borat O (2010) A neural network-based traffic-flow prediction model. *Math Comput Appl* 15(2):269–278
5. Feng Y, Hourdos J, Davis GA (2014) Probe vehicle based real-time traffic monitoring on urban roadways. *Transp Res Part C: Emerg Technol* 40:160–178
6. Hojati AT, Ferreira L, Washington S, Charles P, Shobeirinejad A (2014) Modelling total duration of traffic incidents including incident detection and recovery time. *Accid Anal Prev* 71:296–305
7. Jain V, Sharma A, Subramanian L (2012) Road traffic congestion in the developing world. In: *Proceedings of the 2nd ACM symposium on computing for development, ACM, 2012*, p 11
8. Koc,kan C (2008) Communication between vehicles. Ph.D. thesis, Istanbul Technical University, 2008
9. Lu J, Chen S, Wang W, Ran B (2012) Automatic traffic incident detection based on foil. *Expert Syst Appl* 39(7):6547–6556
10. Lu J, Chen S, Wang W, van Zuylen H (2012) A hybrid model of partial least squares and neural network for traffic incident detection. *Expert Syst Appl* 39(5):4775–4784
11. Masters PH, Lam JK, Wong K (1991) Incident detection algorithms for compass-an advanced traffic management system, in *Vehicle Navigation and Information Systems Conference, 1991*. *IEEE* 2:295–310
12. Pascale A, Hoang TL, Nair R (2015) Characterization of network traffic processes under adaptive traffic control systems. *Transp Res Part C: Emerg Technol* 59:340–357
13. Russell SJ, Norvig P (2010) *Artificial intelligence - A modern approach* (3. internat. ed.). Pearson Education, 2010. ISBN: 978-0-13-207148-2.

14. Singliar T, Hauskrecht M (2007) Learning to detect adverse traffic events from noisily labeled data. In: European conference on principles of data mining and knowledge discovery. Springer, pp 236–247
15. Terroso-Saenz F, Valdes-Vela M, Sotomayor- Martinez C, Toledo-Moreo R, Gomez-Skarmeta AF (2012) A cooperative approach to traffic congestion detection with complex event processing and vanet. *IEEE Trans Intell Transp Syst* 13(2):914–929
16. Wang J, Case E, Manor D (1992) The road traffic microwave sensor (rtms). In: The 3rd international conference on vehicle navigation and information systems, 1992. VNIS., IEEE, pp 83–90
17. Yildirim U, Ozcan U (2015) Analysis of traffic accidents in the city of ankara: an artificle neural network model. *Gazi Univ J Econ Adm Sci Sch* 17(1):35–63
18. Yuan Q, Liu Z, Li J, Zhang J, Yang F (2014) A traffic congestion detection and information dissemination scheme for urban expressways using vehicular networks. *Transp Res Part C: Emerg Technol* 47:114–127
19. Zeng Y, Li D, Vasilakos AV (2016) Opportunistic fleets for road event detection in vehicular sensor net- works. *Wireless Netw* 22(2):503–521
20. Ozbayoglu M, Kucukayan G, Dogdu E A real-time autonomous highway accident detection model based on big data processing and computational intelligence. Computer Engineering Department, TOBB Univ. of Economics and Tech. Ankara, Turkey. <https://arxiv.org/pdf/1712.09227.pdf>



# Heat Transfer Analysis of Engine Cylinder Fins by Varying Fin Geometry and Material



Mmehul Bhayana, Mohit Bhanekar, Neeraj Saini, and N. A. Ansari

## 1 Introduction

“Almost all of the present two wheelers use air-cooled engines, because air-cooled engines are the only option due to the impressive advantages like lighter weight and lesser space requirement. In air-cooled motorbikes engines, waste heat is dissipated through the cooling fins to the cooling airflow created by the relative motion occurring due to the movement of bike. One of the important engine subsystems is the cooling system” [1]. “Most of the air-cooling mechanism depends on the Fin design of the cylinder head and the block. One of the other aspects it depends on is the velocity of the vehicle and the ambient temperature” [2].

“This heat transfer from the fin is due to many fixed and variable constraints mainly fin array, fin geometry and shape, fluid flow velocity, and material etc. There are many experimental methods available in literature to analyze the effect of these factors on the heat transfer rate” [3].

“The effect of cooling of internal combustion engine cylinder in free air has been studied, and various results are noted and analyzed. To increase the heat transfer rate, analysis of fin is very important” [4]. “After carrying transient thermal analysis model and heat flow analysis, improvements are there in fin efficiency by changing fin geometry, fin pitch, number of fins, fin material and climate condition” [5].

“Out of these, wavy fins are particularly attractive because they are simple to manufacture, have the potential for enhanced thermal hydraulic performance and are easy to use in both plate-fin and tube-fin type exchangers” [6]. Heat flows from high-temperature region to low temperature region. Thus, heat is always transferred from high-temperature body to low-temperature body spontaneously (Clausius Statement of the second law of thermodynamics). “Three basic mechanisms of heat transfer that

---

M. Bhayana · M. Bhanekar (✉) · N. Saini · N. A. Ansari  
Delhi Technological University, Delhi, India

are often referred as modes of heat transfer are conduction, convection and radiation. But, in practical applications, it may be the combination of above” [7].

### 1.1 Governing Equation

The governing equation for the heat conduction through a solid is given by: [8, 9]

$$k(\partial^2 T / \partial x^2 + \partial^2 / \partial y^2 + \partial^2 / \partial Z^2) + q = \rho c \partial T / \partial t \tag{1}$$

where,

$k$  = thermal conductivity (in  $W/K \cdot m$ ).

$t$  = time  $T$  = temperature (in  $K$ ).

$q$  = rate of heat flux/convection/radiation/internal heat generation inside the volume (in  $W$ ).

$\rho$  = density of the material (in  $kgTm^3$ ).

$c$  = specific heat of the material (in  $JTkg \cdot K$ ).

### 1.2 Fin Materials

“Most commonly used material for manufacturing of fins is aluminum alloy. Now are present aluminum alloy is being replaced with Aluminum alloy 6061 and Magnesium alloy ZC63A.”

#### Chemical Mixture of Aluminum Alloy

See Table 1.

**Table 1** Chemical mixture of AL alloy 6061 [10, 11]

Element	Weight %
Al	Balance
Cr	$10^{(-1)}$
Cu	$10^{(-1)}$
Fe	$35 * 10^{(-1)}$
Mg	$45 * 10^{(-1)}$
Mn	$10^{(-1)}$
Si	$2 * 10^{(-1)}$

**Table 2** Chemical composition of Mg Alloy [12]

Elements	Weight %age
Zn	$83 \times 10^{-1}$
Mg	3
Cu	$24 \times 10^{-1}$
Fe	$1.5 \times 10^{-1}$
Zr	$1.5 \times 10^{-1}$
Si	$1.2 \times 10^{-1}$
Mn	$10^{-1}$

### Chemical Composition of Magnesium Alloy

See Table 2.

### 1.3 Model Overview

The fins geometry is selected based on the experiments conducted by various researchers and is as per the standards [13, 14]. Cylinder-fin model is created in SolidWorks with straight fin profile.

Various parameters are rightly taken for further simulation by Ansys.

Aluminum and Magnesium are selected as fin materials for subsequent analysis in ANSYS software.

Aluminum is a light metal having significantly low specific weight. The use of Aluminum in automobiles reduces the dead weight and energy consumption significantly while increasing load capacity. Aluminum also reflects visible light and heat. Aluminum possesses better corrosion resistance, thermal conductivity, impact resistance, ductility, is odorless and is recyclable as well. Magnesium alloys are not only lighter but have other benefits as well. They are shock resistant and have greater edge over Aluminum to damp noise and vibrations [15–18].

### 1.4 Methodology

1. Used Transient Thermal Analysis model for analysis of imported geometry
2. Imported finned cylinder geometry to ANSYS Design Modeler.
3. Selected material (Aluminum alloy and Magnesium alloy).
4. Generated mesh and tuning up analysis settings.
5. Selected relevant faces in the geometry for heat flux and convection.
6. Calculated the solution by gradually iterating the possible iterations in Ansys software.
7. Determining the results and coming to a conclusion.

## 1.5 Fin Specification

The cylinder density of aluminum alloy =  $2773 \text{ kg/m}^3$ .

Density of magnesium alloy =  $1800 \text{ kg/m}^3$ .

Length (L) of the fin =  $130 \text{ mm} = 0.13 \text{ m}$ .

Width (b) of the fin =  $130 \text{ (mm)} = 0.13 \text{ m}$ .

Thickness (y) =  $3 \text{ (mm)} = 0.003 \text{ (m)}$ .

Initial temperature (room condition) =  $293 \text{ K}$  or  $20^\circ\text{C}$ .

Time for analysis =  $60 \text{ s}$ .

Heat transfer coefficient =  $0.000025 \text{ (W/mm}^2 \times \text{K)}$ .

### Cylinder specification (empirical formulas)

Bore diameter =  $55 \text{ mm}$ .

Length of stroke =  $1.25 D = 68.75 \text{ mm}$ .

Length of cylinder =  $1.15 * 68.75 = 79.05 \text{ mm}$ .

Thickness =  $0.045D + 1.6 = 4.075 \text{ mm}$ .

Dimensions for fins and cylinders are calculated using the empirical relations. Some changes were made to the standard dimensions according to the needs of the project. Dimensions like length of stroke, thickness and bore diameter are modified accordingly.

## 2 Results and Discussion

### 2.1 Analysis of Rectangular Shaped Fin

#### 2.1.1 Analysis of Aluminum Alloy in Rectangular Shaped Fins

See Figs. 1 and 2, and Table 3.

#### 2.1.2 Analysis of Magnesium Alloy in Rectangular Shaped Fins

Figures 3 and 4 and Tables 3.

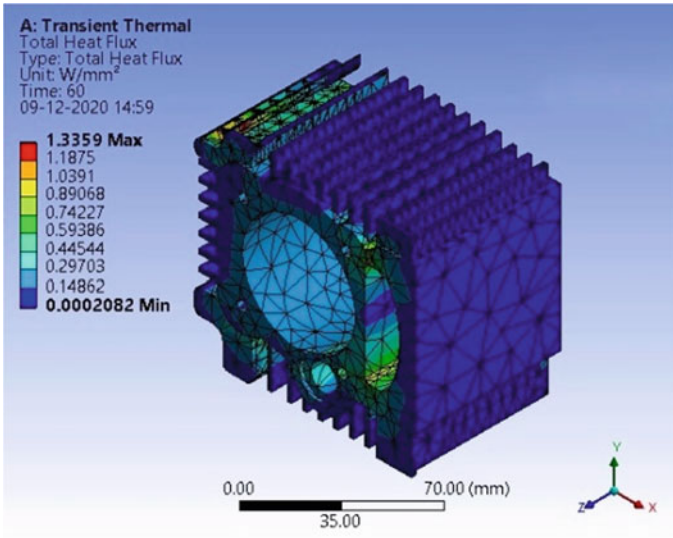


Fig. 1 Shows the variation of the total heat flux inside the rectangular fin of Al alloy

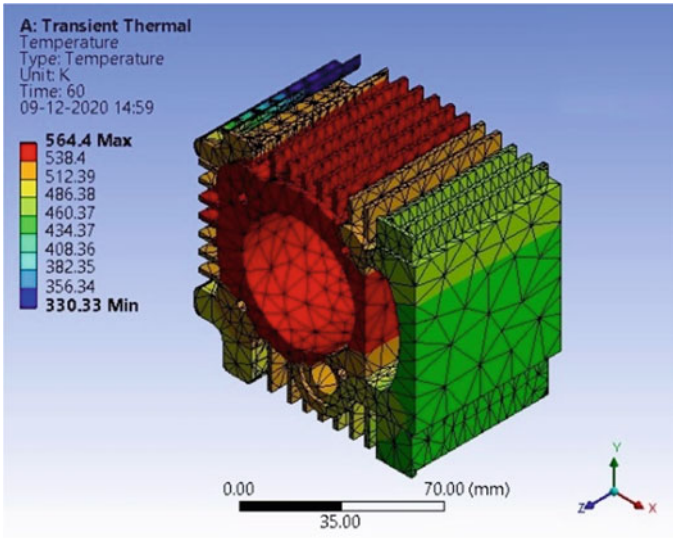


Fig. 2 Shows the variation of the temperature inside of the rectangular fin of Al alloy

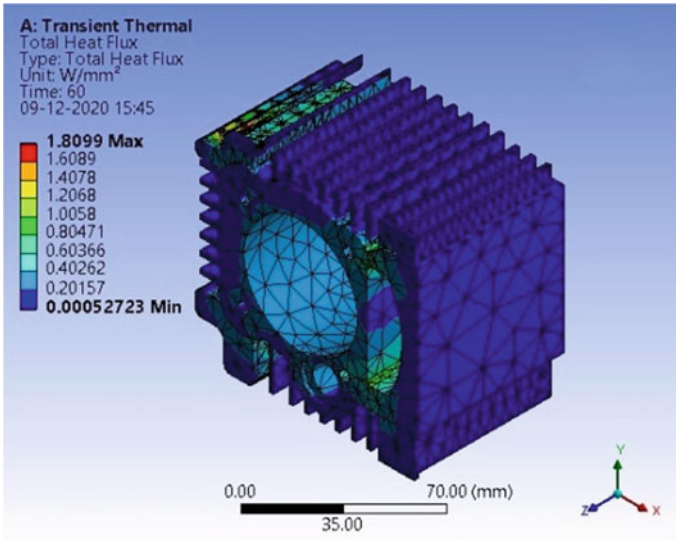


Fig. 3 Shows the variation of total heat inside the rectangular fin of Mg alloy

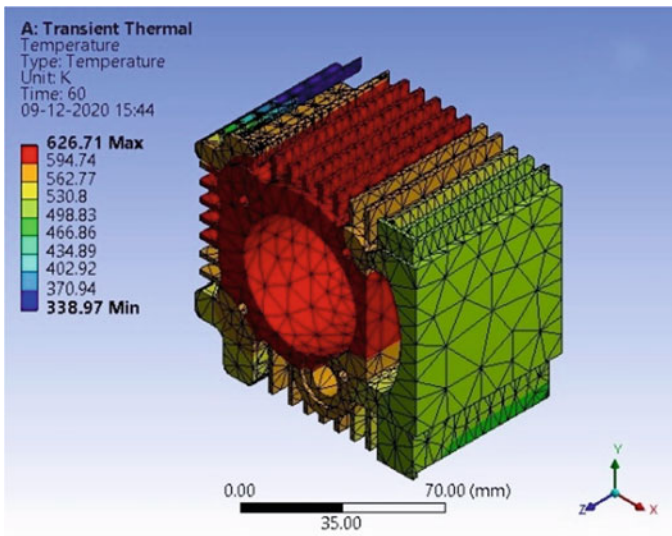


Fig. 4 Shows the variation of temperature inside the rectangular fin of Mg alloy

**Table 3** Properties of rectangular shaped fin

	Maximum temperature (K)	Minimum temperature (K)	Maximum heat flux (W/mm <sup>2</sup> )	Minimum heat flux (W/mm <sup>2</sup> )	Mass (kg)
Al Alloy 6061	564.4	330.33	1.3359	0.0002082	0.84211
Mg Alloy	626.71	338.97	1.8099	0.00052723	0.7455

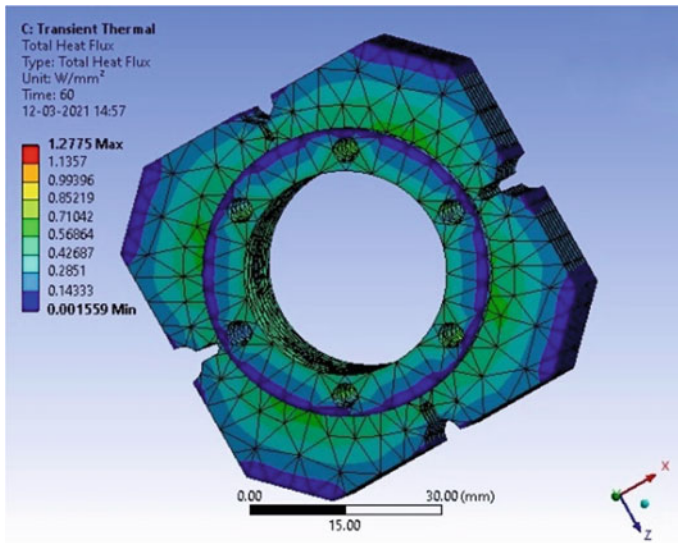
**Table 4** Properties of Circular shaped fin

	Maximum temperature (K)	Minimum temperature (K)	Maximum heat flux (W/mm <sup>2</sup> )	Minimum heat flux (W/mm <sup>2</sup> )	Mass (kg)
Al Alloy 6061	708.27	674.76	1.2775	0.001559	1.0233
Mg Alloy	797.48	757.97	1.407	0.002393	0.988

## 2.2 Analysis of Circular-Shaped Fin

### 2.2.1 Analysis of Aluminum Alloy Circular-Shaped Fins

See Figs. 5 and 6, and Table 4



**Fig. 5** Shows the variation of total heat in modified circular-shaped fin of Al alloy

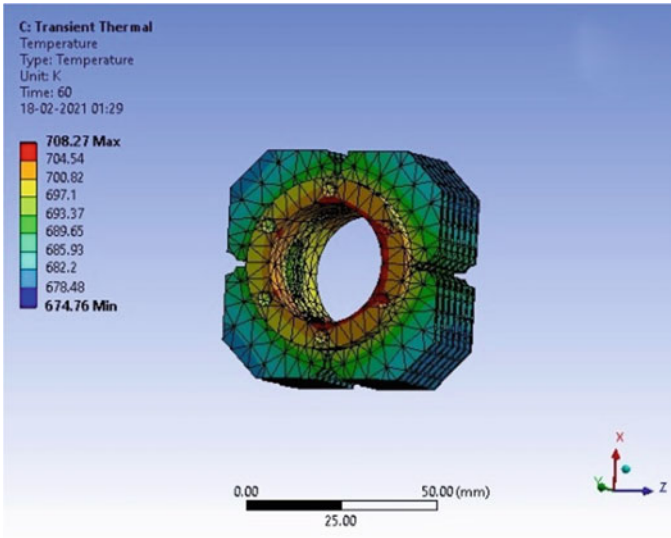


Fig. 6 Shows the variation of temperature in the modified circular-shaped fin of Al alloy

### 2.2.2 Analysis of Magnesium Alloy in Circular Shaped Fins

See Figs. 7 and 8, and Table 4.

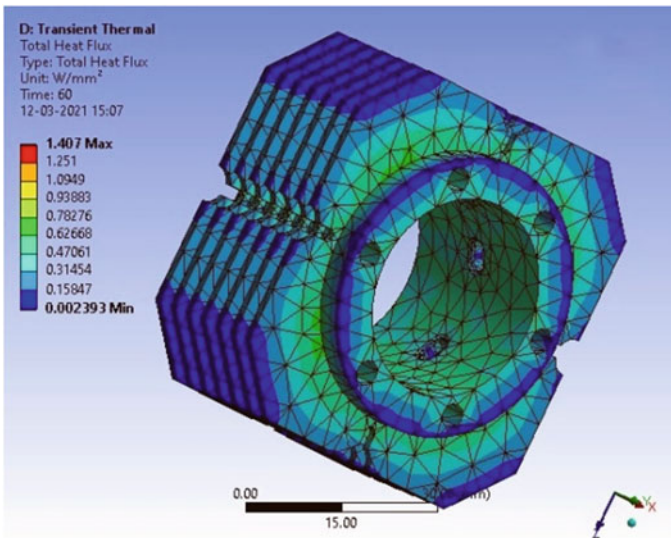
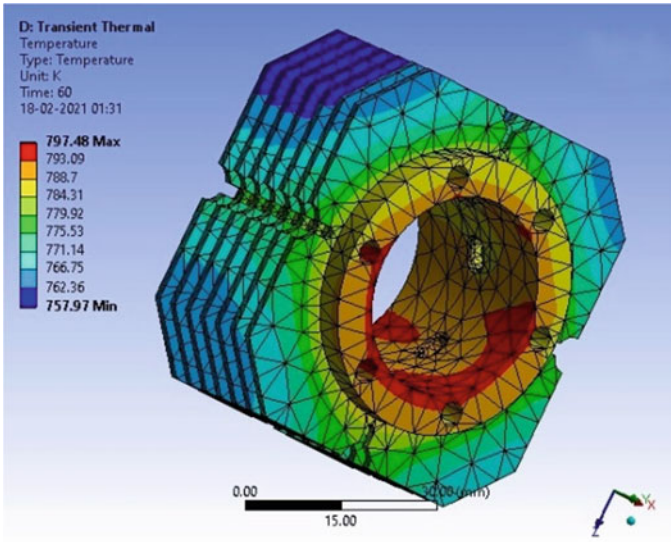


Fig. 7 Shows the variation of total heat inside the modified circular shaped fin of Mg alloy





**Fig. 8** Shows the variation of temperature inside the modified circular shaped fin of Mg alloy

### 2.3 Analysis of the Proposed Model Shaped Fin

#### 2.3.1 Analysis of Aluminum Alloy in the Proposed Shaped Fins

See Figs. 9 and 10.

#### 2.3.2 Analysis of Magnesium Alloy in the Proposed Shaped Fins

See Figs. 11 and 12 and Table 5.

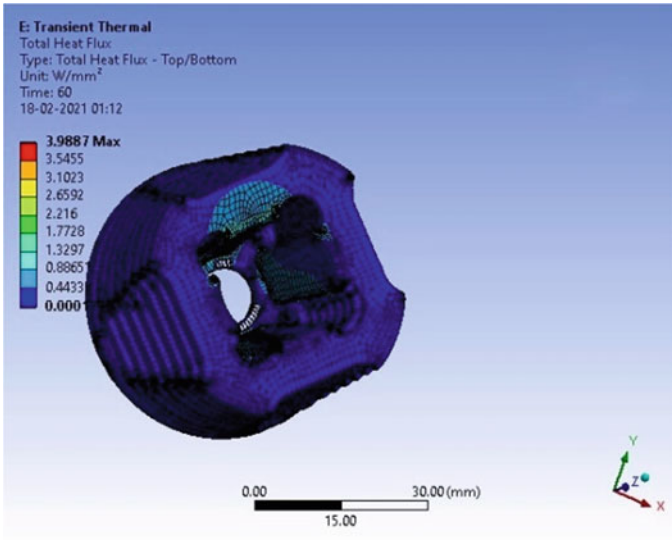
## 3 Model Validation

See Tables 6 and 7

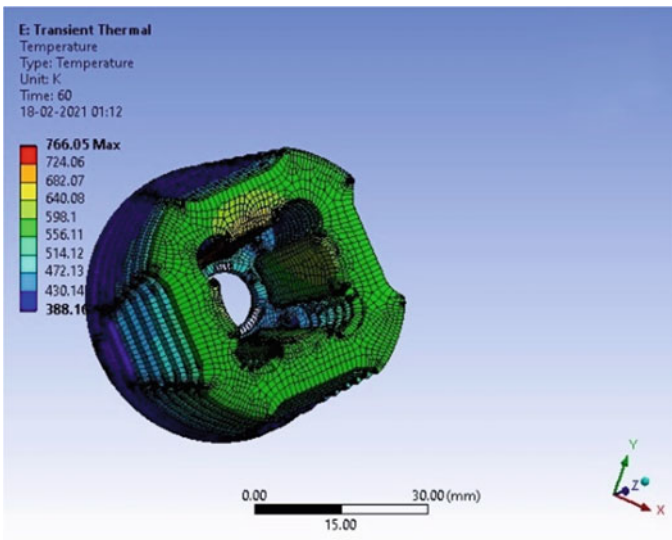
**Hence, the modifications done in the model have led to a huge improvement in heat analysis.**

**Owing to similar modifications, the results of the proposed design are extremely efficient.**

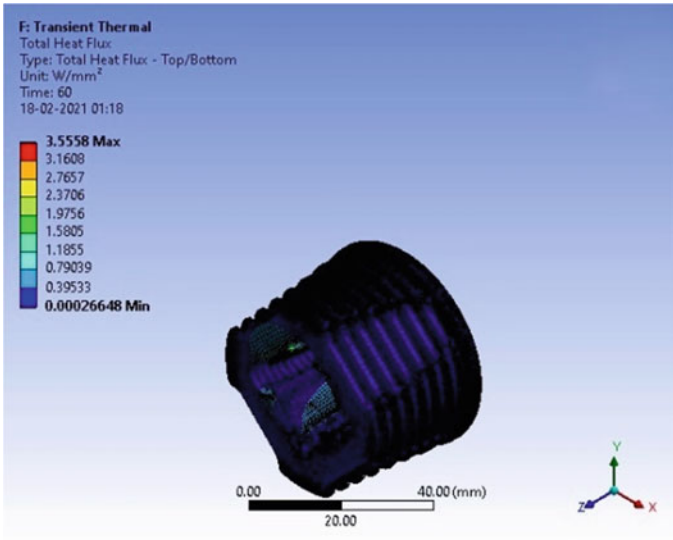
See Tables 8 and 9



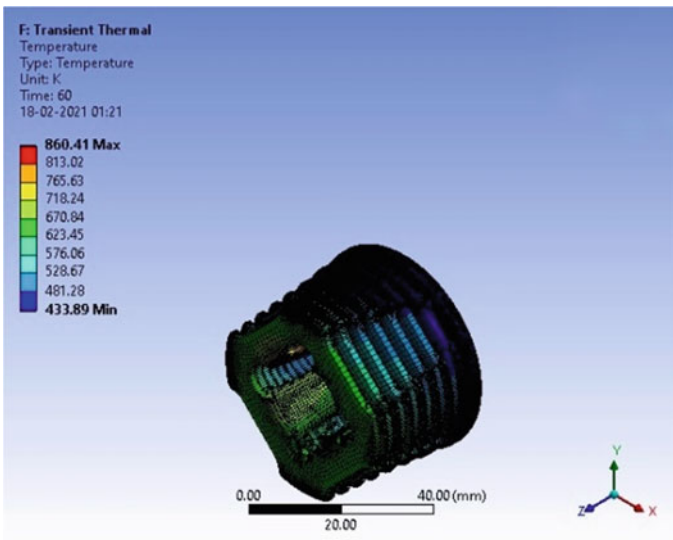
**Fig. 9** Shows the variation of Total heat in the proposed model of fin of Al alloy



**Fig. 10** Shows that variation of temperature in the proposed model of fin of Al alloy



**Fig. 11** Shows the variation of total heat inside the proposed model of fin of Mg alloy



**Fig. 12** Shows that variation of temperature in the proposed model of fin of Mg alloy

**Table 5** Properties of proposed model shaped fin

	Maximum temperature (K)	Minimum temperature (K)	Maximum heat flux (W/mm <sup>2</sup> )	Minimum heat flux (W/mm <sup>2</sup> )	Mass (kg)
Al Alloy 6061	766.05	388.16	3.9887	0.0001	1.03
Mg Alloy	860.41	433.89	3.5558	0.000266	0.972

**Table 6** Value of Thermal Flux for circular fin

Thermal Flux (W/mm <sup>2</sup> )	Normally used	Babu and Lavakumar [2]		Result by present work		Result by the modification in design	
		Al Alloy 2024	Al Alloy 6061	Mg Alloy	Al Alloy 6061	Mg Alloy	Al Alloy 6061
Circular Fin	0.723258	0.738145	0.716357	0.63876	0.70347	1.2775	1.407

**Table 7** Value of Thermal Flux for rectangular fin

Thermal Flux (W/mm <sup>2</sup> )	Babu and Lavakumar [2]		Result by present work		Result by the modification in design	
	Al Alloy 6061	Mg Alloy	Al Alloy 6061	Mg Alloy	Al Alloy 6061	Mg Alloy
Rectangular Fin	0.571051	0.463962	0.523876	0.60347	1.3359	1.8099

**Table 8** Results of proposed design

	Maximum temperature (K)	Minimum temperature (K)	Maximum heat flux (W/mm <sup>2</sup> )
Al Alloy 6061	766.05	388.16	3.9887
Mg Alloy	860.41	433.89	3.5558

**Table 9** Comparison with other work

Mass of cylinder fin(Kg)	Babu and LavaKumar [2]		Result by present work	
	Al alloy 6061	Mg alloy	Al alloy 6061	Mg Alloy
Rectangular fin	0.97395552	0.89459618	0.845	0.735
Circular fin	1.1423490	1.0492687	1.0233	0.988
Proposed fin			1.03	0.9172

Heat transfer to the cylinder walls of IC engines is recognized as the most important factor that influences both engine parameters and its functioning and operations. Only some part of the energy supplied to the internal combustion engine is utilized and transformed into useful work, and the remaining energy is rejected in the below-mentioned ways:

1. Heat from the engine boundaries due to radiation, convection and to a small extent conduction,
2. Exhaust heat, and
3. Heat rejected to coolant.

The engine cooling is necessary for the below-mentioned reasons, First, the lubricating oil used determines the maximum engine temperature that can be used. Depending upon the type of lubricating oil used, this temperature ranges from 450 to 500 K. Above these temperatures, the lubricating oil deteriorates very rapidly with temperature increase, and it might lead to piston seizure. The strength of the materials usually decreases with an increase in temperature and, thus, establishes an upper limit for the temperatures at various points of the engine. High engine temperature may result in a very hot exhaust valve, which, in turn, may give rise to pre-ignition and detonation. Temperature inside the cylinder is maximum as actual combustion takes place there. There exists a temperature difference between cylinder and ambient, hence heat transfer. Temperature reduces as we go radially outwards as amount of heat energy reduces (30–40% usage work, 33% heat to exhaust gases).

It was observed from Figs. 1 and 2 that the temperature change within the rectangular fins of aluminum alloy was from 564.4 K to 330.33 K. It was observed that total heat flux has a maximum value of 1.3359 W/mm<sup>2</sup>. Also, it was observed from Figs. 3 and 4 that the temperature change within the rectangular fins of magnesium alloy was from 626.71 K to 338.97 K. It was observed that the total heat flux has a maximum value of 1.8099 W/mm<sup>2</sup>.

It was observed from Figs. 5 and 6 that the temperature change within the modified circular-shaped fin of aluminum alloy was from 708.227 K to 674.76 K. It was observed that total heat flux has a maximum value of 1.2775 W/mm<sup>2</sup>. Also, it was observed from Figs. 7 and 8 that the temperature change within the modified circular-shaped fins of magnesium alloy was from 797.48 K to 757.97 K. It was observed that the total heat flux has a maximum value of 1.407 W/mm<sup>2</sup>.

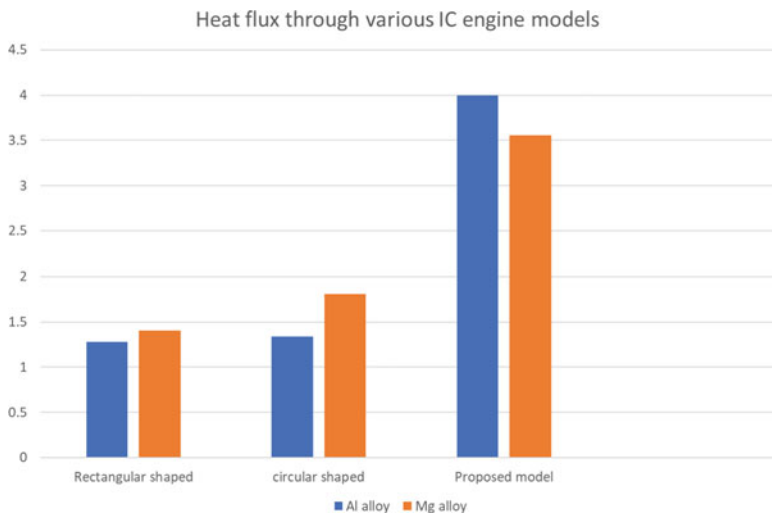
It was observed from Figs. 9 and 10 that the temperature change within the proposed model of fin shape of aluminum alloy ranges from 766.05 K to 388.16 K. It was observed that the total heat flux has a maximum value of 3.9887 W/mm<sup>2</sup>. Also, it was observed from Figs. 11 and 12 that the temperature change within the proposed model of fin shape of magnesium alloy was from 860.41 K to 433.89 k. It was observed that the total heat flux has a maximum value of 3.558 W/mm<sup>2</sup>.

The probable reason for an increase in heat transfer rate in case of magnesium alloy would be the high thermal conductivity  $k$ , as effectiveness (performance) of fins depends directly on  $k$ .

The hot combustion gases give part of their heat to cylinder liner, piston and piston rings, cylinder head, exhaust valves and exhaust ports. Most of this heat is carried

away by the cooling system, while some are lost by direct irradiation from the engine surfaces. It is clear that to promote heat transfer to its highest value, the surface coefficient of the film should be maximum, and the material used for cylinder walls should be highly conductive, and the wall thickness should be maximum but consistent with strength, wear and other similar requirements. The material of the cylinder liner is chosen from the consideration of its thermal conductivity, strength, wear-resisting properties and density. The quantity of the heat transferred also depends upon the area of the heat-transmitting surface and the temperature difference. The area (in the cylinder) exposed to hot gases depends upon the design of the combustion chamber, the cylinder and the cylinder head. The cylinder wall area is exposed to the hot gases varies with the piston position. In this project, it can be seen that in Figs. 6 and 8, area exposed to flux is more, hence the heat transfer is maximization.

The proportion of the time for which an area remains in contact with the hot gases is virtually independent of speed because the decrease in the hot gases is virtually independent of speed because the decrease in the time available for heat transfer with increase in speed is compensated by the increased number of cycles per unit time. The length of the fins and the spacing between them is quite important for efficient cooling. Larger inter-spacing between the fins offers larger area for cooling air but the heating of the air is less, so more cooling air is required. Smaller interspacing between the fins results in the smaller area for cooling air and hence air is heated more. However, the pressure drop required for the flow is also more. Therefore, a spacing less than **2.5 mm** is not used (Fig. 13).



**Fig. 13** Shows the comparison between various fin model

## 4 Conclusion

The use of fins on a surface cannot be recommended unless the increase in heat transfer justifies the added cost and complexity with fins. The following factors TO be considered for optimum design of fins are as follows:

1. Cost
2. Manufacturing difficulties
4. Consideration
5. Weight consideration.

This project has compared the materials aluminum alloy 6061 and magnesium alloy ZC63A with varying shapes of engine cylinder. The fin geometry is modeled using the SOLIDWORKS 2018 and then thermal analysis is done on ANSYS workbench.

1. By simply changing the shape of the fins and also by changing the material of fin; the fin performance is increased as well as the weight is reduced. The weight of the fin is very important, when designing the fins for automobiles and aircrafts. For a given dimension, weight is reduced when magnesium alloy is used. This can also be seen in Table 7.
2. It was observed that the total heat flux has a maximum value of  $3.9887 \text{ W/mm}^2$  within the proposed model of fin shape of aluminum alloy from. Also, it was observed the total heat flux has a maximum value of  $3.558 \text{ W/mm}^2$  for the proposed model of fin shape of magnesium alloy. This clearly conclude that heat transfer hence the cooling is improved.
3. When analyzed on software, the modified cylinder 3 (proposed model) has shown better results than other two, as surface area is increased that leads to increased heat rate. But manufacturing of this type of fins will not be economical because of the complexity of the design.
4. Hence, conclude that using magnesium alloy material is better, and fins shape should be longitudinal.

## References

1. Babu G, Lavakumar M (2013) Heat transfer analysis and optimization of engine cylinder fins of varying geometry and material. Research Paper- IOSR J Mech Civil Eng. (E-ISSN 2278-1684, p- ISSN 2320-334X) 7(4):24–29
2. Sachdeva RC Fundamentals of engineering heat and mass transfer. New Age International Publishers
3. Sorathiya AS, Joshi MB, Rathod PP (2014) Heat transfer augmentation of air cooled 4 stroke si engine through fins. Int J Recent Dev Eng Technol 2(1). ISSN 2347-6435
4. Raviulla AM (2015) Corporate institute of science and technology, Bhopal (M.P.). Heat transfer analysis of engine cylinder fins of varying geometry. Int J Sci Res (IJSR)ISSN (Online): 2319-7064. Index Copernicus Value (2016): 79.57 | Impact Factor (2015): 6.391.

5. Ansys- Intro to Transient Thermal Analysis • DECEMBER 2019- Thermal Capacitance in Heat Transfer Analysis – Lesson 1(December 2019).
6. Varalakshmi P, Lavakumar M (2015) Steady state thermal analysis of engine cylinder fin by changing geometry ISSN NO. 2348-4845 (August 2015)
7. Sorathiya AS, Hirpara HP, Rathod PP (2014) An effect of different parameters of fins. IOSR J Mech Civil Eng (IOSR-JMCE) e- ISSN: 2278-1684, p-ISSN: 2320-334X, 11(3) Ver. I, PP 63–71(May- Jun. 2014).
8. Mishra AK, Nawal S, Thundil Karuppa Raj R (2012) Heat transfer augmentation of air cooled internal combustion engine using fins through numerical techniques. RJES 1(2):32–40. ISSN 2278-9472
9. Ali1 MA, Kherde2 SM (2014) A review on design modification and analysis of two wheeler cooling fins. IJEAS 5(01)
10. Vijayakumar MD, Sathish T, Veeman D, Muthu G (2021) Experimental study of chemical composition of Aluminium alloys. Mater Today
11. Dobrzanski LA, Bamberger M, Totten GE (2021) Magnesium and its alloys: technology and applications
12. Sanders JC (1942) Cooling test of an air-cooled engine cylinder with copper fins on the barrel. NACA Report E-103-Resport and results
13. Shekhada V, Jain S Jayesh undaniya: experimental analysis of transient heat transfer in air-cooled ic engine fin using FEA. International Journal of Scientific Progress and Research Paper Article. ISSN: 2349-4689
14. Deshpande AC, Razik M (2015) Design and finite element analysis of two wheeler engine fins. ISSN: 2277-9655 research paper
15. Ashok Reddy K, Seshi Reddy TV, Satpagiri S (2015) Heat flux and temperature distribution analysis of I C engine cylinder head using ANSYS. Int J Adv Res Found Res Paper Article
16. González AM, Vaz M, Zdanski PSB (2018) A hybrid numerical-experimental analysis of heat transfer by forced convection in plate-finned heat exchangers. <https://doi.org/10.1016/j.applthermaleng.2018.11.068>
17. Chavan L, Purane N (2013) Thermal analysis of pin fin using different materials and forms. Int J Sci Res (IJSR) ISSN (Online): 2319-7064 Index Copernicus Value: 6.14 | Impact Factor (2014):5.611 (2013)
18. Hussaina AA, Freegaha B, Khalafa BS, Towsyfyhan H (2018) Numerical investigation of heat transfer enhancement in plate-fin heat sinks: effect of flow direction and fillet profile. <https://doi.org/10.1016/j.csite.2020.100638>



# Managing Healthcare Supply Chain During Epidemic and Pandemic



Amit Kaushik, Shivam Kumar Mishra, Romesh Yadav, and Girish Kumar

## 1 Introduction

In the contemporary times, human society had been exposed to number of epidemic and pandemic situations ranging from SARS, Ebola, Zika, Swine flu, to the current COVID-19 [1]. The foreseen impact has been increasing in intensity with time, thereby leading to disruption of normal functioning of the society [2]. They not only impact socially by restricting the movement, isolation and losses of life but also affect the economy and environment thereby presenting a challenge to the world in common and third world country in particular [1]. As a result, an urgent need has been arisen for an efficient and effective Healthcare Supply Chain Management (SCM) system, which would help in making healthcare system resilient to tackle these epidemic and pandemic like biological disaster situations.

Healthcare SCM comprises the activities and operation, which would help in seamless and continuous delivery of products, orders, information and services for healthcare delivery [3]. It is especially required during a biological disaster to plan, manage and control key resources through integrated processes for efficient handling of situation [3, 4]. In an epidemic, there are occurrences of more health-related issues then faced by health sector in normal circumstances due to various reasons [5]. Whereas a pandemic is an epidemic occurring widespread across the globe and affecting people at worldwide scale similar or alike to COVID-19 [6].

Number of studies had been conducted in the area of supply chain management design under disruption in a variety of domains, such as fashion supply chain [7], blood supply chain [8], reverse supply chain [9], etc. Also, the research in the domain of epidemic and pandemic impact on healthcare supply chain [10, 11] is limited for tackling the unforeseen situations COVID-19.

---

A. Kaushik (✉) · S. K. Mishra · R. Yadav · G. Kumar  
Delhi Technological University, Shahbad Daultpur, Delhi 110042, India  
e-mail: [amitkaushik\\_2k17ae07@dtu.ac.in](mailto:amitkaushik_2k17ae07@dtu.ac.in)

The current study is towards mapping of challenges, which occurs in healthcare SCM during epidemic and pandemic situations. A multiple-criteria decision-making (MCDM) technique, Best and Worst Method (BWM), is employed in this work. The BWM helps in evaluating alternatives to criteria and also finds the importance of criteria in an efficient and effective manner.

The remaining paper is structured as follows. In Sect. 2, the challenges in healthcare SCM during epidemic and pandemic are identified on the basis of extensive literature review and research. In Sect. 3, the methodological approach undertaken is introduced. Results and Discussion are discussed in Sect. 4. Finally, Sect. 5 concludes the work and provides future research directions.

## 2 Challenges in Healthcare SCM During Epidemic and Pandemic

Through an extensive study of literature review and research of healthcare SCM during epidemic and pandemic, nine possible issues that affect directly or indirectly on it have been identified that will further be studied with the help of Best and Worst Method (BWM). The issues are briefly discussed as follow:

*Inefficient executive leadership (MHSC1):* While execution of Healthcare Supply Chain, there had been inefficiency in leadership for handling supply chain network during crisis. This led to delay in recovery via improper cooperation between different stakeholders [12].

*High cost due to ineffective supply chain (MHSC2):* Improper coordination in supply chain networks leads to shortfall or excess of medical supply, thereby raising the supply chain costs [13, 14].

*Lack of supply chain education (MHSC3):* Low awareness about supply chain management especially in healthcare further exposes the vulnerability [15]. Particularly, managers are ill-informed to control supply of medication in healthcare sector.

*Lack of integration in enterprises and inter departments (MHSC4):* For handling the crisis situation, there had been improper coordination between supplier and retailer in enterprises. Also, casual attitude of policymakers in formulation of right policies for healthcare sector supply chain further aggravates the situation [16, 17].

*Absence of Buffer Inventory (MHSC5):* Companies are in a practice of maintaining lean supply chain, for reducing cost and timely delivery of goods in manufacturing sector. As a result, there are less inventory builds for buffer stock, thereby leading to disruption of supply chain during crisis situation. During COVID-19, there was shortage of personal protective equipment in India.

*Lack of digital supply network (MHSC6):* Many organizations still practice conventional linear supply chain model. This leads to unintegrated network, which would delay and interrupt the seamless flow of information and analytics [11].

*Inadequate Distribution Infrastructure network (MHSC7):* In a crisis situation, the important part is the distribution network of necessary supply. Therefore, improper handling of transport, logistics and communication may further increase the vulnerability of the situation [18].

*Shortage of healthcare providers (MHSC8):* During epidemic and pandemic, the healthcare staffs play the crucial role. Furthermore, a smaller number of hospitals, nursing homes, doctors, medical staff during normal times in under developed and developing country further expose the health sector vulnerability during crisis situation [19].

*Improper handling of demand and supply (MHSC9):* During crisis situation, there is rise in demand of medical devices, equipment's, medicines, etc., thereby leading to shortage of essential medical supply in short term and further making situation more vulnerable [20].

### 3 Methodology

After an intensive literature evaluation and research, nine predominant challenges were identified. Consecutively, we want to prioritize them and clear up on a concern foundation for handling the healthcare deliver chain throughout epidemic and pandemic. So, on this segment, we're going to address the method followed for identity, prioritization and categorization of demanding situations in healthcare deliver chain throughout epidemic and pandemic. Here, this takes a look into incorporate phases. The first segment is the identity of demanding situations on the idea of literature evaluation and dialogue with area experts. In the second one segment the prioritization and categorization of demanding situations is executed the usage of BWM (Big worst Method) that is a MCDM approach.

Although there are numerous MCDM (Multi-standards selection evaluation approach) techniques which include VIKOR (Vise Kriterijumska Optimizacija I Kompromisno Resenje) approach wherein on the idea of a selected degree of "closeness" to the perfect solution, the rating index is formulated through the usage of linear normalization, Analytic hierarchy process (AHP) wherein hierarchy analyses the distribution of a aim a number of the factors which as a end result is in comparison and judged which detail has a more impact on that aim.

The Best Worst Method (BWM) is a multi-standard selection evaluation approach, and it turned into proposed through Dr Jafar Rezaei in 2015. Rezaei (2015) used this approach to select the first-rate providers thinking about financial standards and environmental standards, and next additionally, they used this approach to discover the first-rate freight bundling configurations for transporting freight from outstation to airports. Some different BWM software are provider selection, transportation mode selection, measuring the performance of university-enterprise PhD tasks and comparing enablers of technological innovation.

This methodology is predicated on systematic pairwise comparison of the choice criteria. In comparison to different multicriteria decision analysis methods, BWM has two key advantages:

- BWM results are a lot of compatible compared to other MCDM methods. BWM uses structured thanks to engender the pairwise comparison that ends up in reliable results.
- BWM needs less pairwise comparisons to develop a whole pairwise comparison matrix.

Due to these advantages, BWM is employed in this study. Steps involved in BWM are as follows:

**Step 1.** Categorize a set of decision-making criteria.

In the following step, a set of criteria  $d_1, d_2, d_3, \dots, d_n$  are chosen for making a decision.

**Step2.** Find out the worst criterion (e.g., least important, least desirable) and the best criterion (e.g., most important, most desirable).

In the following step, worst criteria and best criteria are determined with the help of decision-maker.

**Step 3.** Now we've to try a Pairwise comparison.

On the score between one and nine, preference of the simplest criterion over the opposite criteria is determined, wherever a score of 9 suggests that the acute preference of the best criterion over the other criterion and a score of 1 means equal preference between the best criterion and another criterion. The results of the subsequent step are that the vector of Best-to-Others (BO), which might be  $P_b = (p_{b1}, p_{b2}, p_{b3}, \dots, p_{bn})$ , where  $p_{bk}$  indicates the preference of the best criterion Q over criterion k, and it can be deduced that  $p_{bb} = 1$ .

**Step 4.** Set the preference of all criteria over the worst criteria.

On the score between 1 and 9, the preference of all criteria over the worst criterion is determined. The results of the subsequent step are that the vector of Others-to-Worst (OW) might be

$$P_w = (p_{1w}, p_{2w}, p_{3w}, \dots, p_{nw})^T$$

where  $p_{kw}$  shows the preference of the criterion k over the worst criterion W. It also can be concluded that  $p_{ww} = 1$ .

**Step 5.** Determine the best weights.

The optimal weights ( $w_1^*, w_2^*, w_3^*, \dots, w_n^*$ ) are calculated. Each criterion's optimal weight can satisfy the subsequent requirements: for every combination of  $w_b/w_k$  and  $w_k/w_w$ , the best state of affairs is wherever  $w_b/w_k = p_{BK}$  and  $w_k/w_w = p_{kw}$ . Therefore, to succeed in a lot of getting ready to the ideal situation, we should always minimize the most among the set of  $\{|w_b - p_{BK}w_k|, |w_k - p_{kw}w_w|\}$ , and, therefore, the equation is often expressed as follows:

$$\min \max_k \{|w_B - p_{BK}w_k|, |w_k - p_{kw}w_w|\}$$

Subject to

$$\sum_k w_k = 1 \tag{1}$$

$$w_k \geq 0, \text{ for all } k.$$

The above-named equation is reborn to the subsequent LPP (linear programming problem):

Minimize

$$\xi^L$$

Subject to.

$$|w_b - p_{bk}w_k| \leq \xi^L \text{ for all } k,$$

$$|w_k - p_{kw}w_w| \leq \xi^L$$

$$\sum_k w_k = 1 \tag{2}$$

$$w_k \geq 0, \text{ for all } k.$$

After determination the on top of problem, the best weights ( $w_1^*, w_2^*, w_3^*, \dots, w_n^*$ ) and  $\xi^{L*}$  are obtained.  $\xi^{L*}$  can be seen as a direct-indicator of the comparison system’s consistency. The nearer the worth of  $\xi^{L*}$  is to zero, the upper the consistency, and, consequently, the additional reliable the comparisons become.

### 4 Results and Discussion

The methodology discussed in the previous section is applied for this study. Nine factors/criteria affecting the health sector SCM were identified as discussed in Sect. 2. Further, based on expert responses, “Inefficient executive leadership (MHSC1)” and “Lack of integration in enterprises and inter departments (MHSC4)” are found to be the best and worst criteria. Vector of Best-to-Others (BO) and Others-to-Worst (OW) were constructed. These are shown in Tables 1 and 2. Final results of the problem formulated in line with step 5 of previous section are presented in Table 3. The study collected responses from six experts that include three medical practitioners, two logistics experts and one professor, and have experience ranging from 10 to 35 years.

**Table 1** Preference of best criteria over other criteria

Criteria	MHSC1	MHSC2	MHSC3	MHSC4	MHSC5	MHSC6	MHSC7	MHSC8	MHSC9
Ranking as compared to Best criterion (MHSC1)	1	5	6	8	3	4	2	2	4

**Table 2** Preference of other criteria over worst criteria

Criteria	MHSC1	MHSC2	MHSC3	MHSC4	MHSC5	MHSC6	MHSC7	MHSC8	MHSC9
Ranking as compared to Worst criterion (MHSC4)	8	3	3	1	4	7	6	7	4

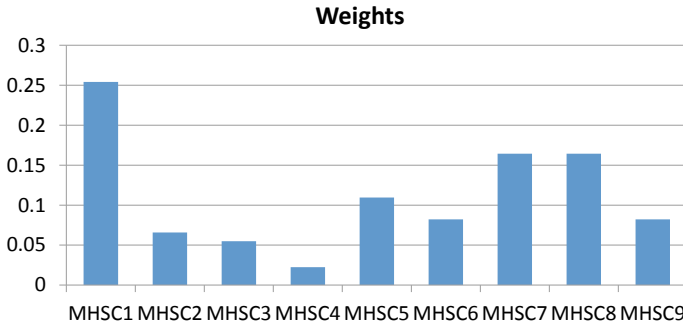
**Table 3** BWM results

Criteria	HSC code	Criteria weightage
Inefficient executive leadership	MHSC1	0.254
Inadequate understanding related to high cost	MHSC2	0.065
Lack of supply chain education	MHSC3	0.054
Lack of integration in enterprises and inter departments	MHSC4	0.022
Absence of buffer inventory	MHSC5	0.109
Lack of digital supply network	MHSC6	0.082
Inadequate distribution infrastructure network	MHSC7	0.164
Shortage of healthcare providers	MHSC8	0.164
Improper handling of demand and supply	MHSC9	0.082

These results provide an insight in managing healthcare supply chain during epidemic and pandemic. From Table 3, “Inefficient executive leadership (MHSC1)” has the highest weight of 0.254. The inefficient executive leadership is the most important criterion to make healthcare supply chain sustainable and resilient during epidemic and pandemic. The next important criteria are “Inadequate Distribution Infrastructure network (MHSC7)” and “Shortage of healthcare providers (MHSC8)”, both with criteria weightage of 0.164. This result indicates that inefficient executive leadership requires the urgent organizational attention in managing healthcare supply chain resilient during crisis. Once the inefficient executive leadership has been handled and improved, it will set a tone for development and inclusion of remaining criteria, and thus resulting in the improvement of the entire system. The data suggest that to make supply chain sustainable, organization should start by focusing on improving corporation between stakeholders and executive leaderships to enhance the efficiency of leadership and helps in quicker decision-making during crisis. According to Queiroz [18], during crises, the distribution network of necessary supply chain is the most important part, and the improper handling can further increase the vulnerability of the situation. Also, according to Jain [19], the healthcare staff are the most crucial elements, and it exposes the healthcare sector shortcomings during crises. Therefore, monitoring these activities can significantly reduce the shortcoming and strengthen the healthcare supply chain in epidemic and pandemic.

“Lack of integration in enterprises and inter departments (MHSC4)” has the criteria weightage of 0.022, and it is ranked lowest in the importance of criteria, which is unexpected as the ineffective executive leadership (rank one) is closely related to this criteria. The possible reason can be that in healthcare supply chain, the inter-relation between departments is highly affected by the cooperation between leadership, which is previously taken into account, and also, this criterion affects the efficiency of the system but has little impact in making it resilient and sustainable. This indicates that healthcare supply chain sector is still in immature stage when it comes to the implementation of healthcare supply chain criteria as the main focus for enhancing and managing healthcare supply chain comes from more fundamental





**Fig. 1** Relative criteria weightage

criteria (leadership). “Absence of Buffer Inventory (MHSC5)” is the fourth most crucial criteria with a weightage of 0.109, this may be due to the fact that organizations are focused on following new and cost-efficient inventory management techniques but during crises, the inventory falls apart and make system vulnerable. MHSC9, MHSC6, MHSC2 and MHSC3 are ranked in the order from 5 to 8th with weightage 0.082, 0.082, 0.065 and 0.054, respectively, which suggests that issues related to education and dataset are not considered highly important in managing healthcare supply chain during epidemic and pandemic.

The results of the study are in line to prior studies on healthcare supply chain. According to a study [22],—“top leadership commitment and support” is among the top-ranked criteria in a study on CSF of sustainable supply chain, and the same is indicated by our study as the “inefficient executive leadership” is our highest ranked criteria. In another study, [23] indicated the importance digitalization and data in supply chain and similar criteria—MHSC6 and MHSC9—are also present in our study (Fig. 1).

## 5 Conclusion and Future Scope

The managing of healthcare supply chain has a huge impact on overall health sector around the globe, particularly during crisis like COVID-19. In addressing healthcare supply chain issues, several organizational as well as government agencies have taken number of initiatives. There are various studies that are attempting to address the managing of healthcare supply chain during epidemic and pandemic. However, these initiatives and studies tend to focus from a broader point-of-view and are inclined towards single scenario of the situation, rather than making healthcare supply chain resilient and sustainable during the crises of epidemic and pandemic.

In this study, nine criteria were identified based on expert opinions and extensive literature review, which are being faced by healthcare supply chain during epidemic and pandemic. A multi-criteria decision-making (MCDM) method—BWM (Best

Worst Method)—is being employed for determining and prioritizing the criteria based on relative weightage. The results obtained through the process are being used in managing healthcare supply chain during crisis.

The final results show that “*Inefficient executive leadership*” was the most crucial criteria in terms of healthcare supply chain during crises, while “Lack of integration in enterprises and inter departments” was considered least favorable. The proposed study can help organization and government agencies in making healthcare supply chain resilient and sustainable during an epidemic and a pandemic. The study can also help stakeholders, industry experts and managers in right and quicker decision-making towards managing supply chain.

There are still some limitations of this study, and these limitations provide scope for future research in this field. This analysis was done considering nine major criteria and with limited expert entries from a smaller pool of domain, but more criteria and larger pool of experts can be taken into account in future research. There are some limitations and drawbacks to BWM, thus other MCDM techniques can also be explored.

## References

1. Chakraborty I, Maity P (2020) COVID-19 outbreak: migration, effects on society, global environment and prevention. *Sci Total Environ* 728:138882
2. Kaur H, Singh SP (2019) Sustainable procurement and logistics for disaster resilient supply chain. *Springer J* 283:309–354
3. Lee SM, Lee D, Schniederjans MJ (2011) Supply chain innovation and organizational performance in the healthcare industry. *Int J Oper Prod Manag* 31(11):1193–1214
4. Shou Y (2013) Perspectives on supply chain management in the healthcare industry. In: 2nd international conference on science and social research, pp 1951–6851
5. Principles of Epidemiology (Third ed.) (2012) Centers for disease control and prevention. Atlanta, Georgia
6. Porta M (Ed.) (2008) Dictionary of epidemiology. Oxford University Press, p 179. ISBN 978-0-19-531449-6
7. Zhao T, Xu X, Chen Y, Liang L, Yu Y, Wang K (2020) Coordination of a fashion supply chain with demand disruptions. *Transp Res* 134
8. Hamdan B, Diabat A (2020) Robust design of blood supply chains under risk of disruptions using Lagrangian relaxation. *Transp Res Part E: Logist Transp Rev* 134. ISSN 1366-5545
9. Hosseini-Motlagh S-M, Nouri-Harzvili M, Choi T-M, Ebrahimi S (2019) Reverse supply chain systems optimization with dual channel and demand disruptions. *Inf Serv* 503:0020-0255
10. Govindan K et al (2020) A decision support system for demand management in healthcare supply chains considering the epidemic outbreaks: a case study of coronavirus disease 2019 (COVID-19). *Transp Res Part E, Logist Transp Rev* 138:101967
11. Iyengar KP, Vaishya R, Bahl S, Vaish A (2020) Impact of the coronavirus pandemic on the supply chain in healthcare. *Br J Healthc Manag* 26(6):1–4.
12. Salem M, Van Quaquebeke N, Besiou M, Meyer, L (2019) Intergroup leadership: how leaders can enhance performance of humanitarian operations. *Prod Oper Manag* 28(11):2877–2897
13. Parvin H, Beygi S, Helm JE, Larson PS, Van Oyen MP (2018) Distribution of medication considering information, transshipment, and clustering: Malaria in Malawi. *Prod Oper Manag J* 27:774–797

14. Mamani H, Chick SE, Simchi-Levi D (2013) A game-theoretic model of international influenza vaccination coordination. *Informa Pubsonline J* 59(7):1650–1670
15. Lauer C (2004) Excellence in supply chain management. *Mod Healthc* 34(50):29–32
16. Khokhar SG, Min Q, Su C (2015) Bird flu (H7N9) outbreak and its implications on the supply chain of poultry meat in China. *J Appl Poultry Res* 24(2):1056–6171
17. Hessel L (2009) Pandemic influenza vaccines: Meeting the supply, distribution and deployment challenges. *Influ Other Respire Viruses* 165–170
18. Queiroz MM, Ivanov D, Dolgui A et al (2020) Impacts of epidemic outbreaks on supply chains: mapping a research agenda amid the COVID-19 pandemic through a structured literature review. *Ann Oper Res* 1572–9338
19. Iyengar KP, Jain VK, Vaishya R (2020) Current situation with doctors and healthcare workers during COVID-19 pandemic in India. *Post-Grad Med J Publ Online First*
20. MIT Sloan Management Review (2020) Three scenarios to guide your global supply chain recovery. <https://sloanreview.mit.edu/article/three-scenarios-to-guide-your-global-supply-chain-recovery>
21. Rezaei J (2015) Best-worst multi-criteria decision-making method. *Omega J* 53:0305–0483
22. Prasad DS, Pradhan RP, Gaurav K, Sabat AK (2020) Critical success factors of sustainable supply chain management and organizational performance: an exploratory study. *Transp Res Procedia* 48:2352–1465
23. Pereira MM, Frazzon EM (2021) A data-driven approach to adaptive synchronization of demand and supply in omni-channel retail supply chains. *Int J Inf Manag* 57:0268–4012

# Trajectory Planning and Optimization of Robotic ARM



Aachman Garg, Aashish Yadav, Abhishek Mishra, and Vikas Rastogi

## 1 Introduction

Living in the world of twenty-first century where the technology has advanced to the point that, anything other than automation or self-intelligence is now considered obsolete. Consequently, humans have also evolved themselves in terms of their way of solving the real-world challenges. Humans are now incorporating modern technologies as a handy tool to solve problems. More and more trust and reliance are seen in the adoption of better technologies such as the solution to material handling problems, where industrialists and experts have expressed their confidence in the use of robotics and automated guided vehicles, among other things [1, 2]. Similarly, the capabilities of the robotic technology have impressed the other segments of society whether it is in manufacturing and production side, or in service side where robot has its application in defense and space exploration, educational and very importantly in medical healthcare.

The development of robust technology accompanied with miniaturization of components and precise control mechanisms; robots are now becoming a reliable asset for doctors. Over the course of time starting from their application in 1985s, robots now make an impact in laparoscopy, neurosurgery, orthopedic surgery, emergency response, and various other medical disciplines [3]. Adding to its scope, this paper has tried to develop a solution to automate sample collection from a highly communicable disease patient using a robotic arm.

This paper aims to present the design of a robotic manipulator with an end effector for use in coronavirus testing and use the concepts of forward and inverse kinematics to plan an optimal trajectory for the robot. The definition of the optimality concept

---

A. Garg · A. Yadav (✉) · A. Mishra · V. Rastogi  
Department of Mechanical Engineering, Delhi Technological University New Delhi, Delhi  
110042, India  
e-mail: [aashishyadav\\_2k17me05@dtu.ac.in](mailto:aashishyadav_2k17me05@dtu.ac.in)

is divided into many directions. Some scientists focus on a time-optimal trajectory to increase productivity [4, 5], while others work on the smoothness of trajectories [6, 7], taking into account reducing cycle time by implementing fast trajectories combined with optimal jerk values in order to reduce the excitation of the resonant frequencies and limit the vibrations of the mechanical system [8–10]. With rise in electricity prices, along with the expected heavy workload that the manipulator is to perform, it is of paramount importance that the robot minimizes energy consumption and forces on its joints in order to have a longer life cycle. Hence, using the concept of via-points, a trajectory optimization algorithm is developed for the designed robot to meet the above-mentioned criteria.

## 2 Methodology

This project is divided into three parts:

- (a) Design: Physical modeling of the robot manipulator using SolidWorks and MATLAB.
- (b) Trajectory Planning: Calculating a time-based trajectory for the manipulator consisting of joint positions, velocities and accelerations by defining the boundary conditions at selected waypoints.
- (c) Trajectory Optimization: Computing the trajectory that minimizes the chosen performance parameter to meet the objective subject to certain constraints.

### 2.1 Design Overview

The preliminary design of the robot was done using SolidWorks software. Keeping the design requirements in mind, robotic arm is designed to have the following capabilities:

- (a) Picking the swab stick from the kit loading point.
- (b) Positioning the end effector according to patient face and mouth positions.
- (c) Traversing inside the patient's mouth.
- (d) Taking sample, i.e., rotation of swab while in contact with mouth surface.
- (e) Carefully delivering the sample inside the storage box.

The robot has in total 9 degree of freedom (5 in manipulator and 4 in end effector) with T-R-R-T-R manipulator configuration. Links and joints are connected in vertically articulated fashion (similar to human arm). Manipulator consists of a swivel base and three links connected to the end effector through another joint. The End effector utilizes two jaw-type grippers for its action and is actuated by means of two mechanisms, i.e., lead screw mechanism and Wire tension method.

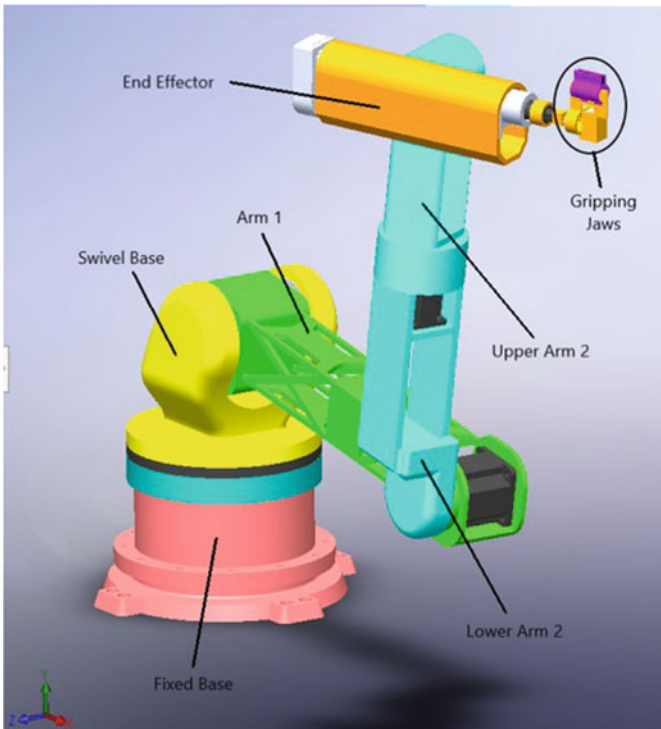
## Modeling

The designed robot was exported to a simulation environment (MATLAB) for further motion and trajectory planning [11].

Each kinematic pair is uniquely defined, a parent–child relation is established, and all the parameters associated with joint are defined.

Different types of joints used in the robot are:

- (a) Twisting Joint: This joint allows relative rotational motion between the two connected links in a direction parallel to their axes.
- (b) Rotational or Revolute Joint: This joint allows the relative rotational motion between the two links but the direction of motion is perpendicular to axes of both the links.
- (c) Linear or Prismatic Joint: This joint allows the relative translational motion between the two connected links in a direction parallel to their axes (Figs. 1 and 2).



**Fig. 1** Robotic Arm with components

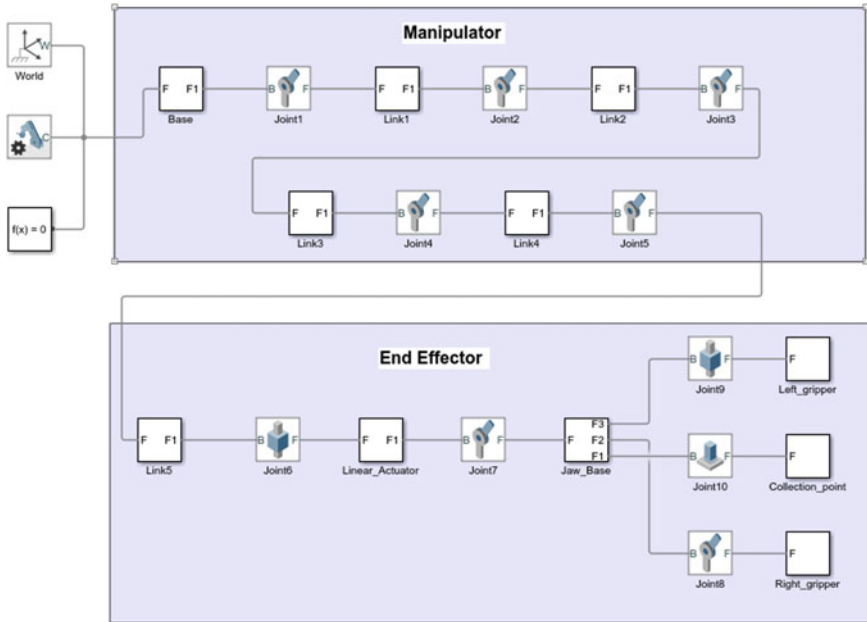


Fig. 2 Kinematic structure of robotic Arm

## 2.2 Motion Planning

The typical hierarchy of motion planning is as follows:

- (a) Task planning
- (b) Path planning
- (c) Trajectory planning.

### Task Planning

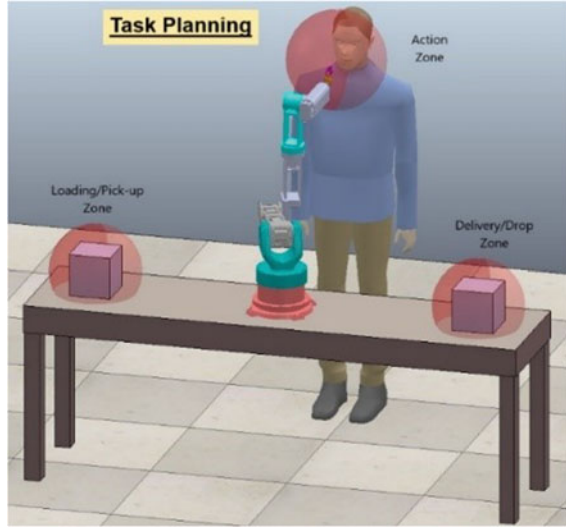
A certain goal or objective is selected, which is to be executed while following the trajectory. For example, there may be a task of picking and loading, or reaching to a particular location etc. After identifying the goal, a set of waypoints are decided, which need to be followed to execute a particular task.

For this paper, a simplified path is chosen with three desired waypoints. The first waypoint is for the pick-up, middle one is for the action and the end point is for the drop/delivery (Fig. 3).

### Path Planning

Path planning is a generation of a feasible path from a start to a goal point. It consists of a set of connected waypoints. The feasibility of the path depends upon the joint constraints of the model as well the geometry of the model and the working environment.

**Fig. 3** Task plan for manipulator



The flow of the path planning algorithm is as follows:

1. Specifying the waypoints in the task space along with orientation of end effector according to the desired requirement.
2. Estimate intermediate waypoints in the task space using curve fitting or interpolation methods.

In this case, the Cartesian coordinates and orientation (in Euler angles) of three desired waypoints from ground reference frame are:

Reference Coordinate System (with Z as principal axis)

$$\text{Position as } [xyz], \text{ Orientation as } [\alpha\beta\gamma] \tag{1}$$

$$\text{Start Point (S)} = [0\text{m}\ 0.7\text{m}\ 0\text{m}], [0^\circ\ 180^\circ - 90^\circ] \tag{2}$$

$$\text{Mid Point (M)} = [0.6\text{m}\ 0\text{m}\ 0.7\text{m}], [0^\circ\ 90^\circ\ 0^\circ] \tag{3}$$

$$\text{End Point (E)} = [0\text{m} - 0.7\text{m}\ 0\text{m}], [0^\circ\ 180^\circ\ 90^\circ] \tag{4}$$

**Trajectory Planning**

It involves the generation of a time schedule for a way to follow a path given constraints like position, velocity, and acceleration. In trajectory planning, there are two ways of preparing a time scheduled trajectory:



- (a) **Joint-Space Trajectory**—In this method, first waypoints are selected in a Cartesian coordinate frame at a particular moment of time, then using inverse kinematics, joint configuration is evaluated and finally an interpolation is made in between them. In this, inverse kinematics is performed only at the waypoints and that makes it a faster execution method.
- (b) **Task-Space Trajectory**—While in task space trajectory method, interpolation is first done between the waypoints stated in Cartesian coordinate frame, and then for each interpolated point, inverse kinematics is executed to create a time scheduled trajectory. This method ensures the better handling of obstacles and collisions and makes it easier to predict the robot motion path; however, this method leads to slower execution.

In given case, joint space trajectory is implemented for trajectory planning using cubic polynomial interpolation method to prepare the trajectory between the way points.

### *Cubical Polynomial Trajectory*

MATLAB offers a functionality for generating cubical polynomial trajectory using “cubicpolytraj” function [12]. This function works by interpolating the piecewise cubical polynomial through the waypoints. The benefit of using cubical trajectory is that the jerk in the trajectory is definite, which results in reduced wear of the joints. The three primary waypoints are fed to the algorithm for interpolation to get a set of intermediate points following the time based cubic polynomial trajectory.

Using inverse kinematics of robot, joint angles of each joints are computed from the desired waypoints coordinates.

$$\{\theta_1, \theta_2, \theta_3 \dots \theta_9\} = \text{RobotInverseKinematics}(x, y, z, \alpha, \beta, \gamma) \quad (5)$$

After calculating the joint coordinates of all the waypoints (i.e., from initial to end point), the time-dependent trajectory for the robot is calculated using cubic interpolation methods. Using this interpolation function, the trajectory at different time samples from start to end time is found. This will give the joint angles, velocities and accelerations as output on the defined number of time samples.

$$\text{Position} : \theta(t) = a_0 + a_1t + a_2t^2 + a_3t^3 \quad (6)$$

$$\text{Velocity} : \dot{\theta}(t) = a_1 + 2a_2t + 3a_3t^2 \quad (7)$$

$$\text{Acceleration} : \ddot{\theta}(t) = 2a_2 + 6a_3t \quad (8)$$

The interpolation function generated by MATLAB “cubicpolytraj” function consists of piecewise cubic polynomials connected together at the breakpoints.

Figure 4 shows the smooth cubic trajectory executed in the task space, and (Fig. 5) shows the same in the joint space.

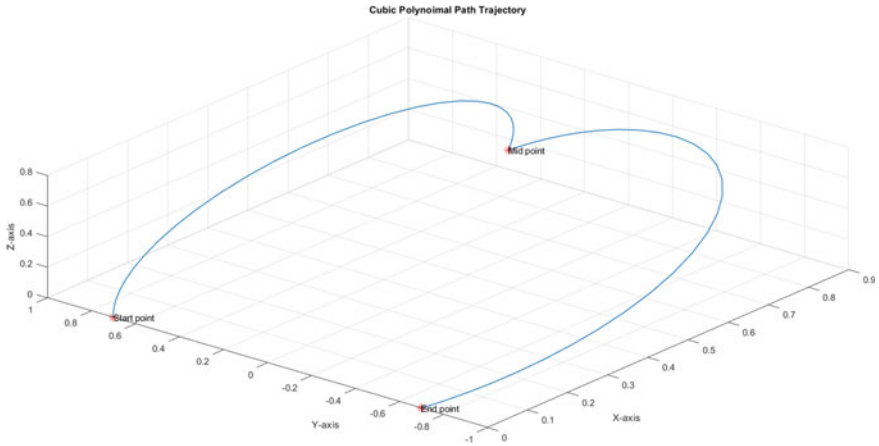


Fig. 4 Cubic polynomial trajectory

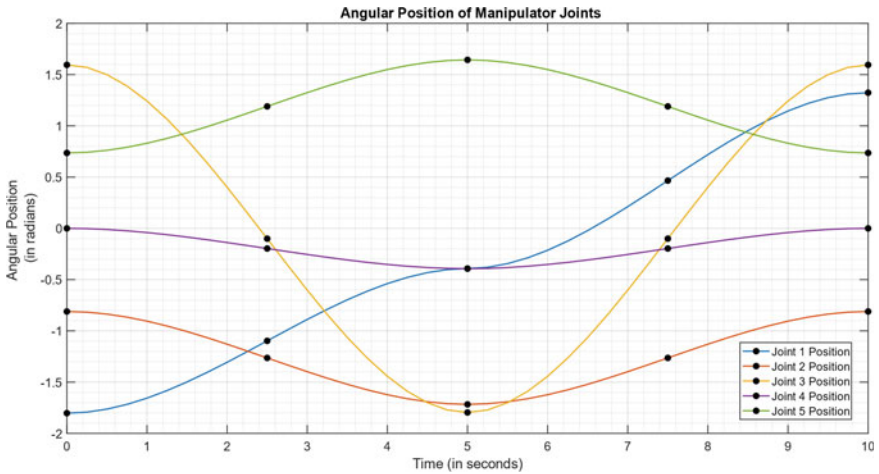


Fig. 5 Angular positions of manipulator joints

The results of the cubic trajectory have been shown using the Simulink simulations of the manipulator, which shows the smooth velocities (Fig. 6) and accelerations (Fig. 7) of the joints.

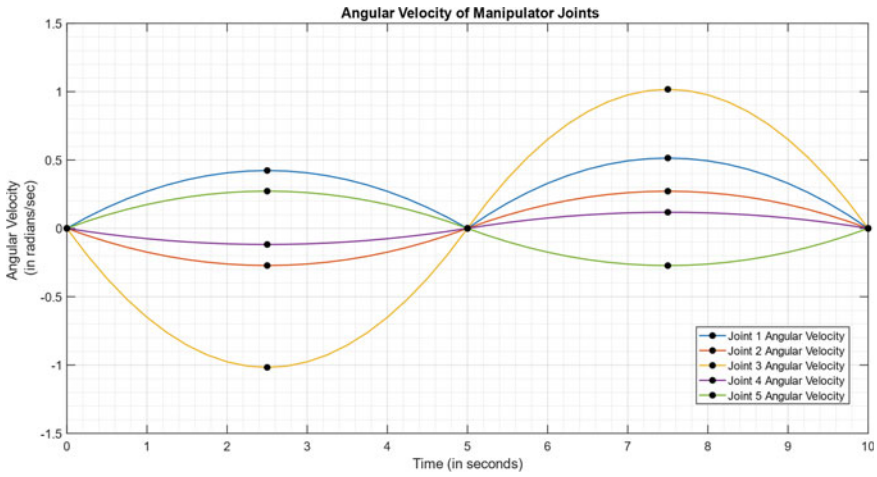


Fig. 6 Angular Velocities of manipulator joints

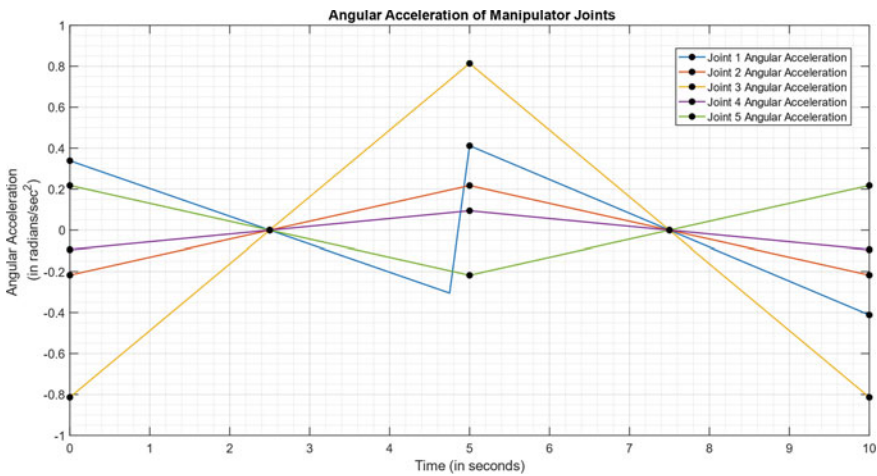


Fig. 7 Angular accelerations of manipulator joints

### 2.3 Trajectory Optimization

The generated trajectory is just one of the many possible cubic trajectories from the initial to the final waypoint. The task of the optimization algorithm is to find a cubic trajectory, which minimizes the energy consumption and the torques on the joints. This type of problem comes under the domain of constrained non-linear optimization. By exploiting the MATLAB optimization solver's capabilities, solution

to this problem is evaluated. In this paper, FMINCON solver is utilized to solve the trajectory optimization problem [13, 14].

**Algorithm** To optimize the trajectory, a set of intermediate points (via-points) are defined along the path, one each in between start to mid and mid to endpoint of the trajectory. Only two via-points are considered in a given case in order to make the algorithm computationally efficient. The joint variables at these via-points are the design variables (i.e.,  $x$ ). To solve this problem, an initial guess value (i.e.,  $x_0$ ) for these variables is extracted from the reference cubical polynomial trajectory. The joint limits are used as a constraint to provide a value range of design variables as lower and upper bounds. Next, a well-formulated objective/cost function is defined, which takes design variables as input and returns a scalar cost value. This cost value is then iteratively minimized through SQP method used by the FMINCON solver. The algorithm structure of the problem is shown in (Fig. 8).

**Cost Function**

In the minimization problem, the algorithm attempts to minimize the energy consumption of the manipulator. Therefore, after each iteration, value of total energy consumption (E) is reduced.

Energy consumption is calculated in the following manner:

First, power consumed for each joint during specific time sample  $t_i$  is found  $\{P_j(t_i)\}$ , then the total consumption of the robot at that time sample is calculated by summing up all the joints’ energy consumption.

$$P_j(t_i) = \tau_j(t_i) \times \dot{\theta}_j(t_i) \tag{9}$$

$$P(t_i) = \sum_{j=1}^9 P_j(t_i) \tag{10}$$

where  $t_i$  is a specific time sample and  $P_j(t_i)$  is the power consumed by  $j$ th joint at time  $t_i$ .

Then, total energy consumption over whole trajectory, i.e., from  $t = 0$  to  $10$  sec is calculated by applying Riemann sum as shown in (11). It is assumed that the energy consumption remains constant during the time interval  $t_i$ .

$$E = \int_{t=0}^{t=10} P(t)dt \cong \sum_{i=1}^m P(t_i) \times l_{t_i} \tag{11}$$

where  $l_{t_i}$  is the length of time interval  $t_i$ , which is one of the  $m$  intervals of time  $t = 0-10$  secs.

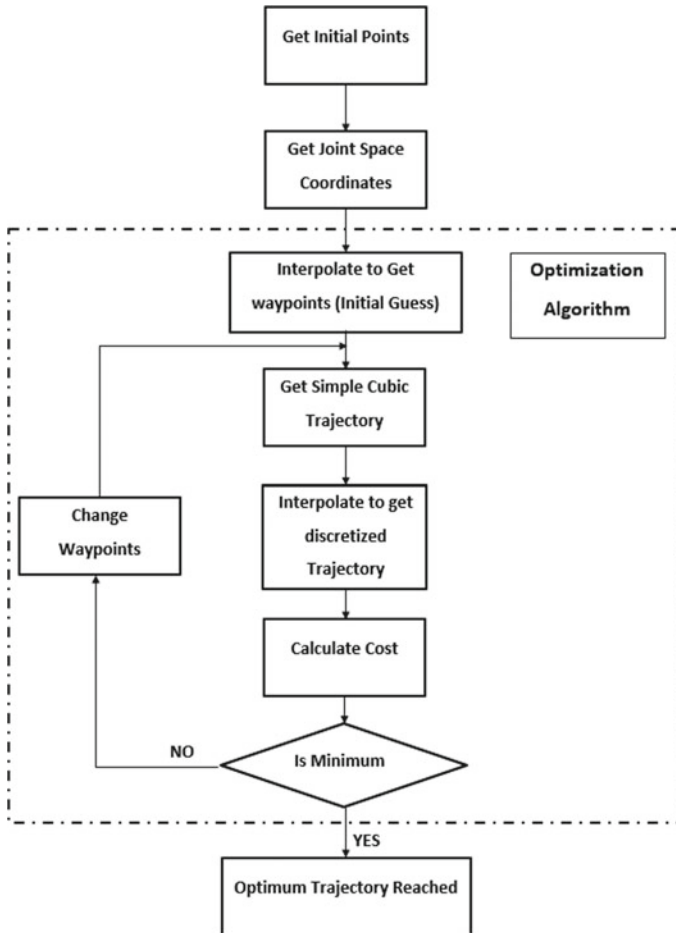


Fig. 8 Optimization algorithm flowchart

### 3 Results

In the test case, the energy consumption of the robotic manipulator is minimized iteratively by considering the dynamics of the first five joints of the manipulator as the joints in the end effector mechanism have no effect on the trajectory. This was done in order to reduce the computational load and to increase the execution speed of the algorithm. The velocity of the joints at the waypoints was set at zero and those at via-points were calculated by the algorithm.

As can be seen in Fig. 9 using the FMINCON solver, a minimum in energy consumption is reached in only a few iterations. Figure 10 shows the initial and optimum trajectories of the manipulator. Table 1 shows the changes in the trajectory in

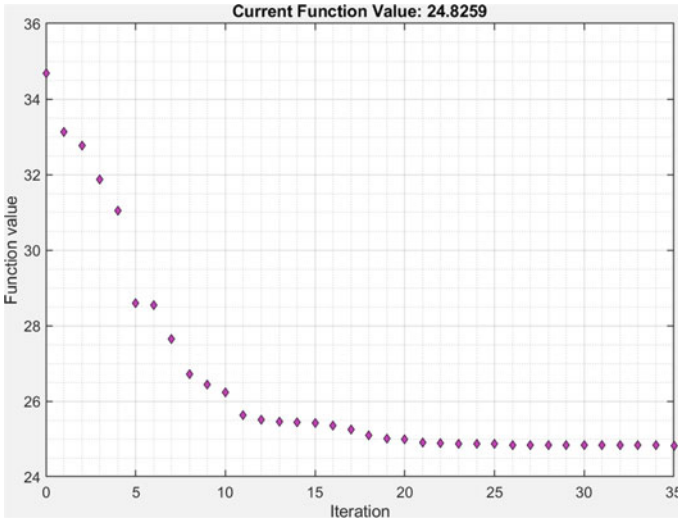


Fig. 9 Cost function value after each iteration

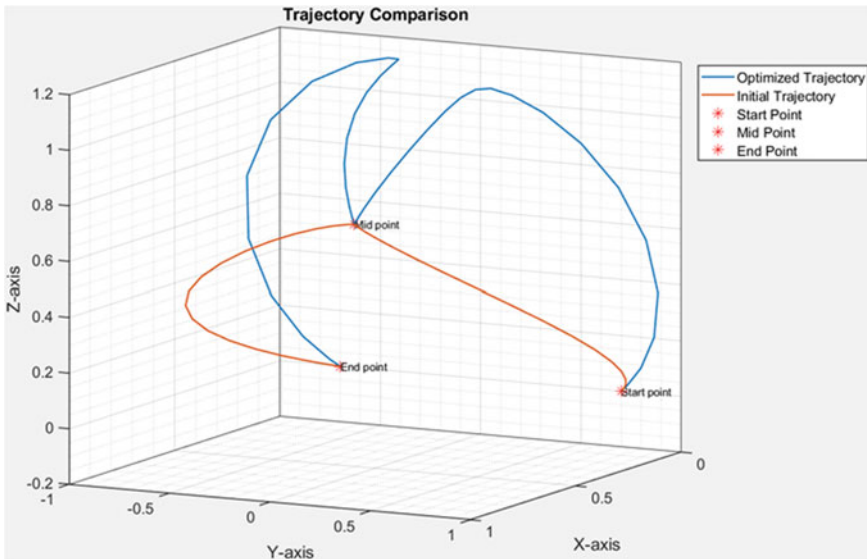


Fig. 10 Initial and final trajectories

form of angular positions and velocities at the two intermediate via-points. The energy cost and torque cost for the initial and final trajectories are also given illustrating the decrease in energy achieved using the algorithm.

**Table 1** Comparison of Initial and Optimum Trajectory Design Parameters

	Joint number	Initial trajectory		Optimum trajectory	
		position ( $\theta$ ) (rad)	Velocity ( $\dot{\theta}$ ) (rad/sec)	position ( $\theta$ ) (rad)	velocity ( $\dot{\theta}$ ) (rad/sec)
Via-Point 1	1	-1.09	0.42	-1.19	0.33
	2	-1.26	-0.27	-0.81	0.00
	3	-1 -10	-1.01	-0.71	-0.26
	4	-0.19	-0.11	-0.08	-0.01
	5	-1.19	0.27	0.76	0.01
Via-Point 2	1	0.46	0.51	0.59	0.47
	2	-1.26	0.27	-0.81	0.00
	3	-1.10	1.01	-1.03	0.05
	4	-0.19	0.11	-0.10	0.03
	5	1.19	0.27	0.70	0.00
Energy cost		34.67 N.m/s		24.82 N.m/s	
Torque cost		901 (N.m) <sup>2</sup>		547 (N.m) <sup>2</sup>	

The energy consumption for the initial trajectory was 34.67 N.m/s, which was reduced to 24.82 N.m/s for the optimized trajectory. Therefore, the optimization resulted in 28.4% reduction in energy consumption.

## 4 Conclusion

The paper illustrates a systematic approach to robot design problem and applies the various concepts to solve a practical problem. It also highlights the usefulness of digital tools for modeling and simulation in the field of robotics. The simplified via-point-based approach to trajectory optimization utilized in this paper enables fast execution and can be easily scaled up to plan more complex paths by increasing the number of via-points. The algorithm's scope can be further expanded to solve a variety of optimizations by changing the cost function. By including path constraints and joint limits, obstacle avoidance capability algorithm can be programmed to suit the requirement. Further work on the paper would involve obtaining waypoints from robot's machine vision system to further improve the robot-environment interactivity and automate the trajectory planning process.

## References

1. Benotsmane R, Dudás L, Kovács G (2020) Survey on new trends of robotic tools in the automotive industry. In: Vehicle and automotive engineering 3; VAE 2020. Lecture notes in mechanical engineering. Springer, Singapore, pp 443–457
2. Benotsmane R, Kovács G, Dudás L (2019) Economic, social impacts and operation of smart factories in Industry 4.0 focusing on simulation and artificial intelligence of collaborating robots. *Soc Sci* 8:143
3. Beasley RA, Janabi-Sharifi F Medical robots: Current systems and research directions. <https://doi.org/10.1155/2012/401613>
4. Kim J, Kim S-R, Kim S-J, Kim D-H (2010) A practical approach for minimum-time trajectory planning for industrial robots. *Ind Robot Int J* 37:51–61
5. Perumaala S, Jawahar N (2012) Synchronized trigonometric S-curve trajectory for jerk-bounded time-optimal pick and place operation. *Int J Robot Autom* 27:385–395
6. Avram O, Valente A (2016) Trajectory planning for reconfigurable industrial robots designed to operate in a high precision manufacturing industry. *Procedia CIRP* 57:461–466
7. Macfarlane S, Croft EA (2003) Jerk-bounded manipulator trajectory planning: design for real-time applications. *IEEE Trans Robot Autom* 19:42–52
8. Gasparetto A, Lanzutti A, Vidoni R, Zanotto V (2012) Experimental validation and comparative analysis of optimal time-jerk algorithms for trajectory planning. *Robot Comput Integr Manuf* 28:164–181
9. Liu H, Xiaobo L, Wenxiang W (2013) Time-optimal and jerk-continuous trajectory planning for robot manipulators with kinematic constraints. *Robot Comput Integr Manuf* 29:309–317
10. Martínez JRG, Reséndiz JR, Prado MÁM, Miguel EEC (2017) Assessment of jerk performance s-curve and trapezoidal velocity profiles. In: Proceedings of the XIII international engineering congress, Universidad Autónoma de Queretaro, Santiago de Queretaro, Mexico, 15–19 May 2017, pp 1–7
11. Corke P (2017) Robotics, vision & control: fundamental algorithms in MATLAB, 2nd edn. Springer, Victoria, Australia
12. <https://www.mathworks.com/help/robotics/ref/cubicpolytraj.html>
13. Byrd RH, Hribar ME, Nocedal J (1999) An interior point algorithm for large-scale nonlinear programming. *SIAM J Optim* 9(4):877–900
14. Mathworks (2014) Matlab Optimization Toolbox



# Investigation of Flexural Strength of Abaca and Neem Twisted Natural Fiber Composites



S. J. Rithik, K. Thileepan, R. Dharmaseelan, and B. Vijaya Ramnath

## 1 Literature Review

Applications of natural fiber composites are increasing over synthetic fiber composites in recent times. Mechanical properties (tensile strength, flexural strength, etc.) of natural fiber composites are low when compared to synthetic fiber composites, in addition to that natural fiber composite are low cost, biodegradable, and high corrosive property have made them more preferable. Natural fibers are still high in cost and this limits their applications. Subrata Chandra Das et al. [1] analyzes the incorporation of wood charcoal as filler in natural fibers composites to improve its overall strength. To manufacture the composite, jute was used as fiber, polyester resin, and wood charcoal as bio filler. Improved tensile properties were shown with a 4 wt.% wood charcoal modification. It showed that the addition of bio-fillers can be a better solution for increasing tensile properties Jonathan Dawit et al. [2] fabricated a polyester composite reinforced with novel Acacia fiber. Their tensile and flexural properties were determined; the fabrication was done by hand layup process. The results were that composite with lower fiber content (15 wt.%) showed higher tensile, lower flexural strength compared with higher fiber content (30 wt.%) samples. Charles Kuranchie et al. [3] reviewed the properties of polyurethane composite foams reinforced with natural fibers. To improve interfacial adhesion, fibers are induced with chemical changes. This paper also studies the chemical effects due to the modification of these fibers for interfacial adhesion. Hariprasad et al. [4] investigated the properties of fibers from milkweed, kusha grass, sisal, banana, and hay for composite preparation mixed with polypropylene (PP) 10:90 (wt.%). Mechanical properties, water absorption studies acoustic characterization have been studied. An scanning electron microscope (SEM) has analyzed the microstructures of milkweed fiber. Bambach [5] experiment results state that moisture ingress leads to material degradation,

---

S. J. Rithik (✉) · K. Thileepan · R. Dharmaseelan · B. V. Ramnath  
Mechanical Engineering Department, Sri Sairam Engineering College, Chennai, India

increase in susceptibility to compression. Habib Awais et al. [6] reviewed the properties of plant-based fibers, textile technologies, thermoplastic matrices, mechanical properties natural fiber-reinforced thermoplastic composites reinforced with natural fibers. Sathees Kumar [7] found that adding sisal, sorghum bicolor, and coconut coir increased the mechanical properties of polyester composites. The mechanical dataset has provided weight percentages of sorghum bicolor and coconut coir which shows its mechanical properties. Azmi et al. [8] fabricated a Kenaf/X-ray/Epoxy hybrid composite and studied the velocity impact and projectile shapes of the composite. Using hand layup method-treated Kenaf fiber and perforated X-ray films were fabricated which is then compressed and subjected to which velocity impact test followed by dye penetration inspection. The result showed that high energy absorption was exhibited by hemispherical projectile, lowest residual strength and produced the most damage compared to the other projectile types which make these suitable for ballistic purposes. Vijaya Ramnath et al. [9] research investigates the effect of twisting along with mechanical properties of the green biodegradable composite. Vacuum-assisted compression moulding technique is used for fabrication. Twisted neem and kenaf are laminated by glass fiber on both ends. The composite with twisted fiber and 45° orientation showed enhanced mechanical properties. Alkalizing the fibers accounted for this enhanced property. Vijaya Ramnath et al. [10] fabricated a jute, flax, GFRP hybrid composite and compares its mechanical properties with jute GFRP composite. Using the hand layup method, jute layer was sandwiched between flax fibers which were then laminated by GFRP on both sides. This research clearly shows that hybrid natural composite possesses superior properties. Vijaya Ramnath et al. [11] compared the mechanical properties of two types of composites (hybrid and mono natural fiber composites). Tensile test, flexural test, impact test, double shear test, and delamination tests were executed. Failure morphology analysis was done. Results showed hybrid composite excelled mono composites in overall mechanical properties. Kaliappan et al. [12] developed three varieties of composites and investigated their hybridization effect and mechanical properties. Fiber distribution, fiber breakage, crack propagation, and fiber pull out were found out by morphological analysis. The fibers with 45° inclined orientation showed enhanced mechanical properties over other composites. Vijaya Ramnath et al. [13] using the hand layup process developed the abaca-*raffia* hybrid composite and investigated its mechanical properties. Abaca fiber strength is higher than kenaf, banana, and sisal fibers. The internal microstructure is analyzed using an SEM. Among other combinations, it concluded that abaca with *raffia* and GFRP showed better double shear properties and high hardness. This makes it a better substitute for automotive applications. Srinivasan et al. [14] tested flax and kenaf single fiber and hybrid composite flexural properties. Fabrication was done by hand layup process. Comparison of hybrid composite with single fiber showed the effect of hybridization. SEM used to analyze internal structure and crack propagation. It is concluded that hybrid composites are far better than mono composites. Niranjana Raja et al. [15] developed abaca fiber with epoxy resin, a natural fiber composite. Abaca is placed alternatively in horizontal and vertical orientation are arranged with GFRP as an outer layer and fabricated by hand layup method. Flexural and tensile tests are done, results show that natural

fiber's strength determine the tensile strength of composite. Abaca shows excellent resistance to corrosion. Vijaya Ramnath et al. [16] developed hybrid natural fiber composite and compared it with mono natural fiber composite (abaca and jute). Glass fiber as outer surface provides the composite more strength and finishing, horizontally and vertically arranged natural fibers provided the strength on all sides. The experiment concludes that hybrid composites have better mechanical properties compared to abaca fiber composite.

## 2 Materials and Methods

**Abaca.** It is acquired from Manila hemp that belongs to the banana family. These fibers show better mechanical strength and it is light in weight. Apart from those properties, they have some characteristics which include non-slipping and anti-static qualities, resistance to fire, corrosion resistance, and pest resistance. These properties have resulted in its increasing importance as better reinforcement for composites.

**Neem.** It is obtained from neem tree. These have high tensile strength compared to much natural fiber which is being used recently. These fibers have some characteristics which make them good reinforcing fiber in polymer composites. Usage of neem fibers in composites has improved the mechanical properties.

**Glass fiber.** Glass fiber consists of fine fibers of glass. It is obtained from heat and softened glass. It has advantageous properties like more bulk strength and good weight properties when compared with metals. The individual strands are clumped together in large numbers to make fiber. It is used as a reinforcing agent for composite materials widely.

**Hardener and Resin.** Epoxy resin is used in improving the adhesive properties. The epoxy resin (LY 556) is used at normal temperature. To enhance the strength of the composite, hardener (HY 951) is used along with epoxy resin in prescribed ratio.

**Hand Layup Method.** This composite is fabricated using hand layup method. Glass fiber layers are used as the first and last layers of the composite. For effective bonding, each and every layer are applied with mixture of epoxy resin and hardener. At first, the fibers are sun dried. Polyvinyl alcohol is applied on the mold. A small amount of resin is spread on the board. Abaca fiber and twisted neem fibers are placed alternatively. For every layer, a resin hardener mixture is applied and spread evenly across the surface. The last layer of fiber is placed followed by the glass fiber. Now a weight (8–10 kg) is placed for 8–12 h on the mold. After the mold dries, the required composite is cut out.

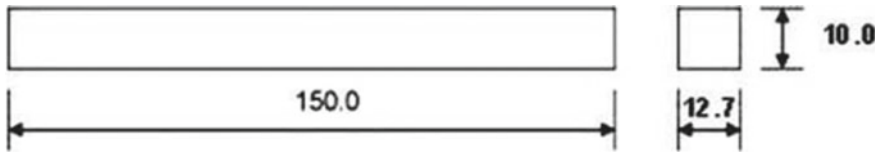


Fig. 1 Flexural test specimen

### 3 Testing of Composite

#### 3.1 Flexural Test

The flexural test, also known as a transverse beam test, is used to measure the behavior of materials subjected to simple beam loading. The maximum stress in the outermost layer of the composite lamination is called flexural stress. Maximum fiber stress and maximum strain are calculated for increments of load. A stress–strain graph is plotted from the results obtained. As per the Standard of American Society for Testing Materials: D790, a 3-point flexural test was carried out. The flexural load is applied at the center of the beam of the composite of length 150 mm. The weight was applied until the breaking point of the beam. The flexural strength and strain was calculated with the help of breaking load and displacement.

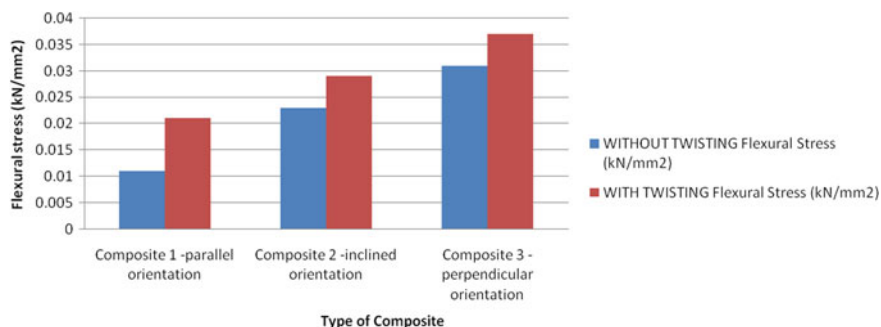
### 4 Result and Discussion

From Fig. 1, it is clear that twisting the fiber affects the flexural strength of fabricated composites. Moreover, twisting makes the fibers of the composites twin among them and avoid a fiber breakage which increases the flexural strength. It is also concluded from the figure that composite 3 which contains fibers arranged in perpendicular orientation has more strength than other fiber orientation (Fig. 2 and Table 1).

### 5 Conclusions

This work has three types and two categories of composites are fabricated using abaca and neem fibers with and without twisting fabricated with hand layup method. The test results are concluded as below:

1. The flexural strength of composite 3 (perpendicular orientation) is higher in both categories.
2. Twisted fibers provide more flexural strength than non-twisted fibers in all the three types of orientation.



**Fig. 2** Comparison of flexural stress of composites

**Table 1** Results of type I composite

Type of composite	Without twisting	With twisting
	Flexural stress (kN/mm <sup>2</sup> )	Flexural stress (kN/mm <sup>2</sup> )
Composite 1 (Parallel orientation)	0.011	<b>0.021</b>
Composite 2 (Inclined orientation)	0.023	<b>0.029</b>
Composite 3 (Perpendicular orientation)	0.031	<b>0.037</b>

3. The perpendicular orientation has shown better flexural strength than other arrangements.

From the above-mentioned statements, it can be concluded that twisted fiber composite with perpendicular orientation composite laminated has better flexural behavior than parallel orientation and inclined orientation laminates.

## References

1. Das SC, Ashek-E-Khoda S, Sayeed MA, Paul D, Dhar SA, Grammatikos SA On the use of wood charcoal filler to improve the properties of natural fiber reinforced polymer composites. Mater Today: Proc
2. Dawit JB, Lemu HG, Regassa Y, Akessa AD (2021) Investigation of the mechanical properties of Acacia tortilis fiber reinforced natural composite. Mater Today: Proc 38:2953–2958
3. Kuranchie C, Yaya A, Bensah YD (2021) The effect of natural fiber reinforcement on polyurethane composite foams – a review. Sci Afric 11: e00722

4. Hari prasada K, Ravichandran K, Jayaseelan V, Muthuramalingam T (2020) Acoustic and mechanical characterisation of polypropylene composites reinforced by natural fibers for automotive applications. *J Mater Res Technol* 9(6):14029–14035
5. Bambach MR (2020) Durability of natural fiber epoxy composite structural columns: high cycle compression fatigue and moisture ingress. *Compos Part C: Open Access* 2:100013
6. Awais H, Nawab Y, Amjad A, Anjang A, Akil HM, Abidin MS (2021) Environmental benign natural fiber reinforced thermoplastic composites: a review. *Compos Part C: Open Access* 4:100082
7. Sathees Kumar S (2020) Dataset on mechanical properties of natural fiber reinforced polyester composites for engineering applications. *Data Brief* 28:105054
8. Azmi AMR, Sultan MTH, Jawaid M, Shah AUM, Nor AFM, Majidd MSA, Muhamad S, Talib ARA (2019) Impact properties of kenaf Fiber/X-ray films hybrid composites for structural applications. *J Mater Res Technol* 8(2):1982–1990
9. Ramnath BV, Rajesh S, Elanchezhian C, Shankar AS, Pandian SP, Vickneshwaran S, Rajan RS (2016) Investigation on mechanical behaviour of twisted natural fiber hybrid composite fabricated by vacuum assisted compression molding technique. *Fibers Polym* 17(1):80–87
10. Ramnath BV, Elanchezhian C, Nirmal PV, Kumar GP, Kumar VS, Karthick S, Rajesh S, Suresh K (2014) Experimental investigation of mechanical behavior of jute-flax based glass fiber reinforced composite. *Fibers Polym* 15(6):1251–1262
11. Ramnath BV, Sharavanan R, Chandrasekaran M, Elanchezhian C, Sathyanarayanan R, Raja RN, Kokan SJ (2015) Experimental determination of mechanical properties of banana jute hybrid composite. *Fibers Polym* 16(1):164–172
12. Kaliappan P, Kesavan R, Vijaya Ramnath B (2017) Investigation on effect of fiber hybridization and orientation on mechanical behaviour of natural fiber epoxy composite. *Bull Mater Sci* 40(4):773–782
13. Ramnath BV, Elanchezhian C, Manickavasagam VM, Prasad SG, Swamy SA, Raj RK (2016) Experimental investigation on shear and hardness of abaca based hybrid composites. In: *MATEC web of conferences*, vol 74, p 00039
14. Srinivasan VS, Boopathy SR, Ramnath BV (2015) Investigation of flexural property of kenaf-flax hybrid composite, vol 10, No. 13, July 2015 ISSN 1819-6608.
15. Niranjan RR, Junaid Kokan S, Sathya Narayanan R, Rajesh S, Manickavasagam VM, Ramnath BV (2013) Fabrication and testing of abaca fiber reinforced epoxy composites for automotive applications. *Adv Mater Res* 718–720:63–68
16. Ramnath BV, Kokan SJ, Raja RN, Sathyanarayanan R, Elanchezhian C, Prasad AR, Manickavasagam VM (2013) Evaluation of mechanical properties of abaca–jute–glass fiber reinforced epoxy composite. *Mater Design* 51:357–366

# Investments in the Long-Term Electric System to Encourage the Use of Plug-In Hybrid Electric Vehicles



Md. Zahid Anwer, Deepanshu Bhatia, and P. Suresh

## 1 Introduction

Conveyance addresses the second-most immensely colossal wellspring of nursery discharge (GHG) outflows inside the US. Just the electrical force area is responsible for more GHG outflows [1]. The module half-breed electric conveyance is a promising invention for reducing GHG outflows associated with the US conveyance sector (PHEC). Exemplary crossbreed EVs (HEVs, for example, the Toyota Prius) drive some piece of their complete force from a battery or other electric memory gadget, yet they can likewise run on petroleum, diesel, or for all intents and purposes some other fuel [2]. PHEVs can drive abstracts similar to conventional fuel-controlled movements since they can run on either completely electric or crossbreed in light of the fact that the batteries of the vehicles can be charged on the standard electric. The way that PHECs are generally associated with a divider hotspot for charging conquers a possible problem accompanied by the averment framework intended HEV electric battery [3]. As per Samaras and Meisterling [4], 61% of energy in the United States depends on excursions of under 50 km (30 miles). PHEVs have the capacity to beat countless customary trucks and cars, particularly in urban areas for driving purposes. The essential impact of PHECs is to interface the transportation and force frameworks in the United States. We researched the likelihood that PHECs could be slanted to give energy and potentially rule organizations to the system (assumed Conveyance to Grid or V2G applications). This will, nonetheless, require a more prominent spotlight on foundation, particularly for interface gear in homes and stopping structures. In a circumstance where an enormous number of PHECs are polarizing power, from the electrical structure, the faint would assist off-top electric interest and extend the extent [5]. The everyday load bend would be leveled, yet because of burden ascend during off-top periods and not because of

---

Md. Zahid Anwer (✉) · D. Bhatia · P. Suresh  
Department of Mechanical Engineering, Galgotias University, Greater Noida, India

pinnacle shaving or request decrease regardless of whether the electrical framework has been intended to deal with top requests (implicatively insinuating that at some arbitrary time, there's a presumable extra limit inside the framework), impacts on the subsisting power substructure are ineluctable and need examination and alleviation. This paper provides details regarding two examinations pointed toward deciding such framework ventures consequential to avail the defragmentation of GHG emanations by designates of astronomically immense scope PHEC charging (that is, controlling conveyances from the network in lieu of utilizing customary gas or diesel energies). We examine the provincial examination of the evening time PHEC charging, and we likewise research the impacts of smoothing the everyday load bend (through expanded off-top interest) on an essential part of structure instrumentation, the oil color-cooled station electrical device. Although that is typically a similar incipient discovery region, here is little indicating visually exploring the electrical framework's inhibition to cope with PHEC charging demands, as well as natural impacts. Both [6] and [7] measure the quantity of regular movements that will be unstuck by PHECs while disregarding structure limit restraints. Utilizing information from that NERC part stage, [6] computes which risen to 73 percent of the heavy-commitment movement fast in the United States could exist supplanted by PHECs upheld by the new electric grid, or 43% if averment was limited to the 12-h time frame between 6 p.m. furthermore, 6 a.m. A more traditionalist ingress number of fifty is estimated by Denholm and Short [7]. Provincial outflows impacts from scope appropriation of PHECs are assessed in [4, 6, 8–10]. As shown by the new etching, cross-country transmissions of two or three essential poisonous substances (CO<sub>2</sub>, NO<sub>x</sub>, and others) will be reduced stood out from a circumstance wherein gas-controlled vehicles were used. Moreover, with carbon catch and sequestration, Samaras and Meisterling state in [4] that PHECs have higher GHG discharge diminishes than coal-to-fluids fills. Both [6] and [9] make a point that typical age blends may have territorial spreads impacts that aren't overall identical to the customary. Samaras and Meisterling [4] take a gander at the effects of PHEVs on the methods cycle, as well as effects from electric battery prompted, research the affectability about GHG transmissions profit by PHECs inculcated of the power of fluctuating carbon power, and evaluate the effects of future biofuel use in PHEVs.

## 2 The Geological Investigation of PHECs

The latest examinations of PHECs' ordinary effects rely upon essential data from the NERC district. NERC territories, of course, are in a state of progress, as cutoff points shift and changes are made conflicting with extreme quality standards. Close from the beginning about the exciting reconstitution inside the United States, a perceivably more grounded unit of examination has been the Regional Transmission Organization (RTO). The RTO is tops to the NERC district commonly considering the way that all ages inside the RTO's impression are dispatched at the same time. For the most part, this has achieved extended usage of straightforward age outlets [11]. The use

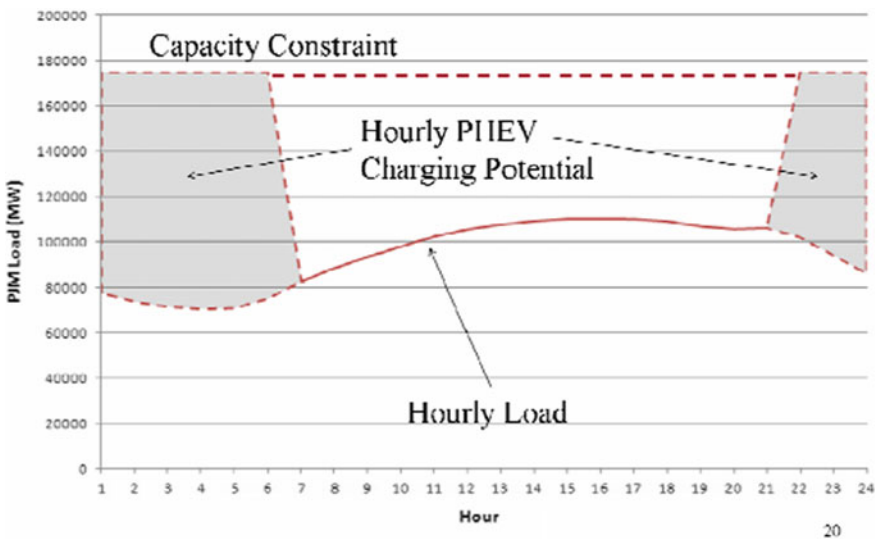


of PHECs for normal developments moves some GHG releases from the tailpipe to the power station's place of union. Each RTO's off-top age combination is as such basic in picking the regular impacts of evening PHEC charging.

**2(a). Quandary Analysis and Emission posits**

We see existence-period discharges from outside-topmost PHEC averment in 3 RTOs: PJM (which covers the vast lion's share about the Middle Ocean also environs about the Middle west), MISO (which covers a sizable fragment of the extra Midwest), and ERCOT (which covers a sizable section of the abundance Midwest) (Texas). We portray PHEC charging limit as the qualification between the absolute best hourly degree of off-top and the most horrendous hourly degree of off-top notwithstanding the most terrible hourly degree of off-top notwithstanding the most frightful hourly degree of off-top notwithstanding the most ghastly hourly degree of off-top notwithstanding the sales and in this manner the quintessential construction cutoff of focal station age. This is routinely depicted possibly inside Fig. 1. Close that action, we get which around 30 percent about the actual standard transport team may be present cleared away PHECs (that is as indicated by [8]).

The basic wellsprings of releases for PHECs are power age and fuel started. The mining/extraction, planning, transport, and utilization of oil subordinates are all important for the continuous example of these discharges. For coal extraction, stockpiling, and passing on, Jaramillo et al. [12] gauge CO2 outflows about 11.6 pounds per million BTU. The improvement of the battery similarly incorporates PHEC radiations. We get our battery-related CO2 outflows figures from [4], which



**Fig. 1** A calculated portrayal about the range limitation, in light of PJM results

gauges yearly CO<sub>2</sub> discharges of 800 to 2,400 pounds for PHECs utilizing lithium-molecule batteries. Over the two regions, we expect the radiations identified with the battery just as upstream outpourings related to coal caused to be undefined.

## 2(b). Used plant-level data to estimate regional emissions

To calculate the local regular effects of evening PHEC charging, we play out a super-session test. We focus on CO<sub>2</sub>-equivalent radiations. The off-busy time is depicted as hours going from 2300-2400 and 0100-0600. We impersonate evening PHEC averment requests away get-together by the hour interest collection appropriate to the 3 RTOs we examine and expanding requests through our party portrayed outside-top period of time consistently. Next [4] we expect which all electric transport takes 0.2 kWhr of force (plant life-to-machine) to movement 1 km; tolerating that all electric development ventures 50 km each time on electric battery ability only, the gross step-by-step interest is 10 kWhr per tense transport. In addition, the GHG outpourings on account of PHEC charging are normally made as [4] We agree which the RTO marking age assets in deserve requests before they are done around there. We also expect that the authenticity requesting would be managed by cost limits (toward the day's end, we recognize that the completion of the RTO markets fuses entirely genuine commitment and regarding). Using routine warmth record data from the United States the EPA's grid informational collection [12], We make the little-trial irrelevant expense (SRMC) turns for all about the 3 RTOs we see by fitting close by fuel costs as in [13] and fitting area fuel costs as in [13]. For every one of the three RTOs, we use subtleties from 2006. We decide (utilizing the SRMC twist) which causes units to be dispatched to finish an aim each hour (checking PHEC charging) as seen in Figs. 2 and 3. We expect that all engenderers will be dependably accessible when called upon to give power and that the system won't have any transmission necessities. Therefore, we construct an unadulterated monetary dispatch. We use CO<sub>2</sub> commensurable releases information from the eGrid information assortment to reenact outright CO<sub>2</sub> releases from each engenderer at every hour, with and without extra PHEC charging requests. On account of PHEC load, the release distinction thusly portrays CO<sub>2</sub> same releases. Figure 4 shows our outcomes intended PJM, MISO, and ERCOT.

We additionally show life-cycle CO<sub>2</sub> identical emanations for an assortment of other movement propels for examination. Except for coal-to-fluids (CTL), which comes from [14], the entirety of the numbers come from [4]. Our discoveries uncover critical regional contrasts in the ordinary outcomes of PHEC charging in the evening. Emanations are a lot more moderate within the ERCOT area, whatever is overflowed with the atomic ability and vaporous petroleum, than in PJM or MISO, which hold more than fossil fuel in their age mixture. MISO, then again, has a bigger number of radiations identified with evening PHEC charging than PJM.

Most essential are connections between basic GHG discharges from PHECs and the outpourings that appeared in Fig. 5 for standard fuel transports and traditional crossover developments, (for example, the Metropolis Prius). Within both PJM and ERCOT, eliminating standard fuel developments with PHECs would decrement CO<sub>2</sub> commensurable outpourings by someplace in the scope of fifty and seventy grams

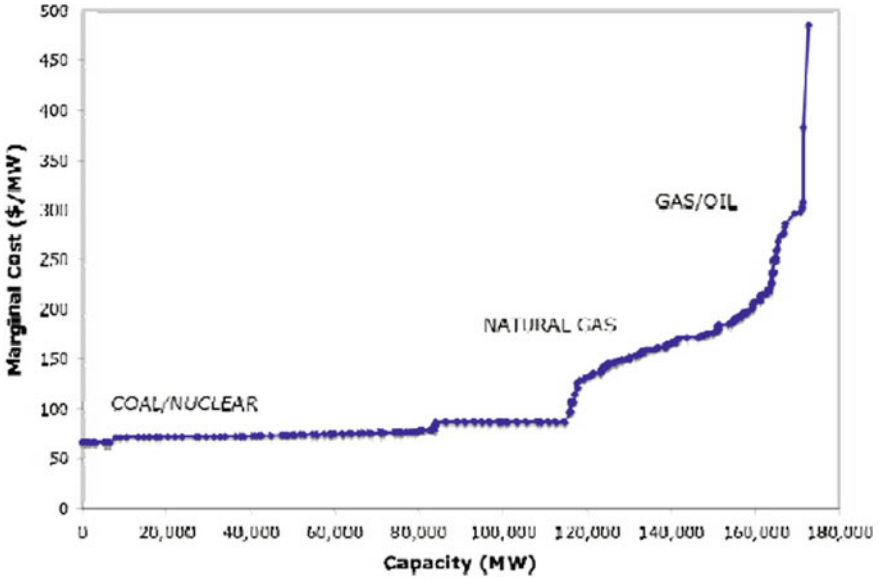


Fig. 2 The PJM short-term minimum price curvature

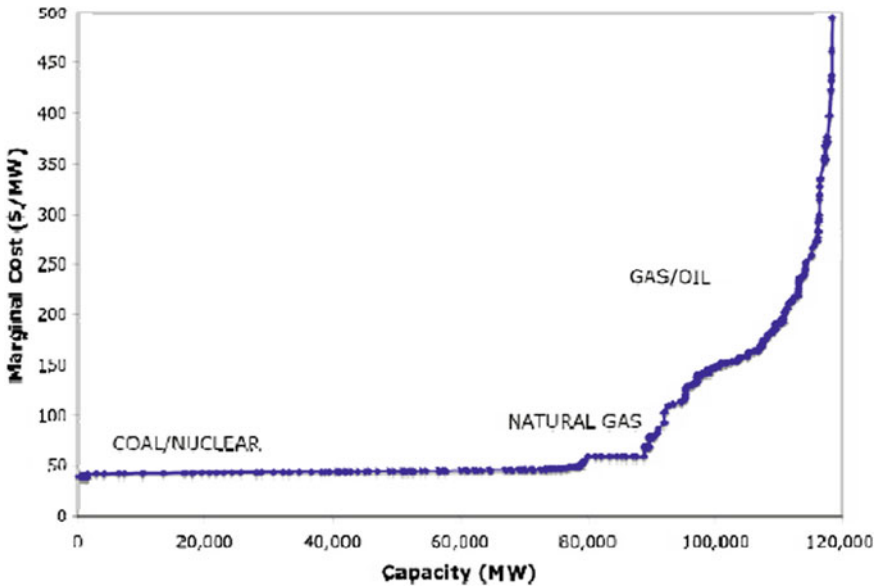


Fig. 3 Middle west ISO's short-term minimum price curvature

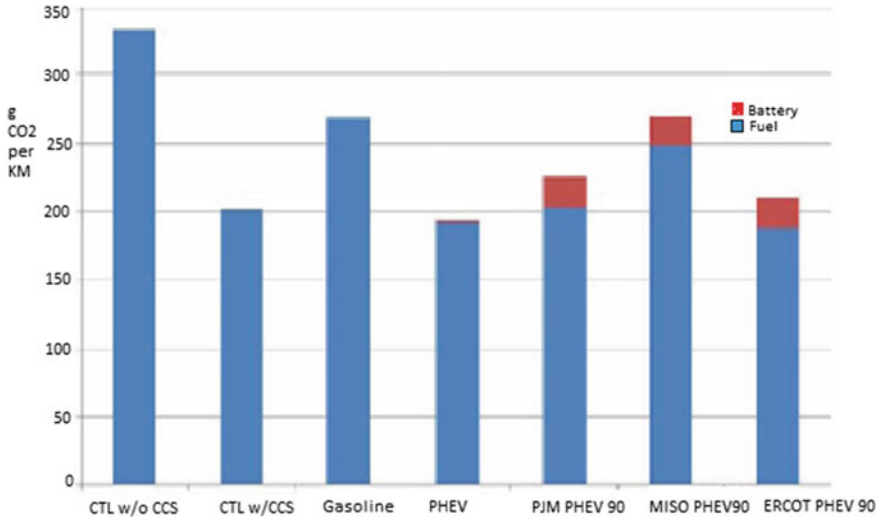


Fig. 4 PHEC life-cycle discharges in PJM, MISO, and ERCOT comparative with customary fuel motors, conventional HEVs, and coal-to-fluids

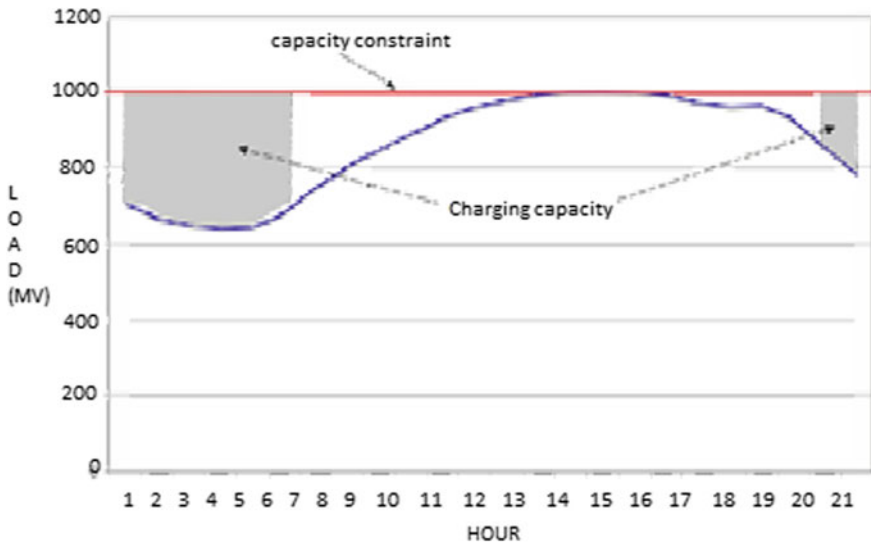


Fig. 5 PHEC averment capability intended a hypothetical electrical circuit

for each km voyaged. Inside MISO, regardless, there is just an insolent separation between discharges from PHECs and radiations from standard gas developments. Deliveries in MISO are from an overall perspective more horrendous when showed up distinctively comparable to standard HEVs.

### 3 Results and Discussion

PHEVs will conceivably lessen CO<sub>2</sub> outpourings from the US development region, yet to the level which releases can be diminished in the power age locale [4]. Breaking down PHEC averment in RTOs convinces that PHECs can't achieve their natural targets until carbon-concentrated RTOs are essentially decarbonized. We furthermore develop the disclosures of [14] by raising that, even without CCS, CO<sub>2</sub> transmissions from PHECs in PJM, MISO, and ERCOT are basically let down than those from fossil fuel-to-fluids power plants (mark which discharges from PHECs in need of CCS in ERCOT look like coal-to-fluids accompanied by CCS). Along these lines, an attainable strategy, rather than coal-to-fluid, would support the decarburization of the limit an area to give PHECs. As of late discussed, evening PHEC charging has the effect of smoothing the stack curve by extending off-top trust in power instead of debilitating the top. Hence, the electric-framework base can be used even more regularly for a more standard reason. Since an immense piece of the transmission and spread bottleneck in the United States is sufficiently sitting inert for extended lengths of the year, extended PHEC charging settles something of a capacity secure, coursing regular costs over a more conspicuous proportion of kilowatt-hours. PHEVs will conceivably lessen CO<sub>2</sub> outpourings from the US development region, yet to the level which releases can be extent diminished in the power age locale [4]. Breaking down PHEC averment in RTOs convinces which PHECs can't achieve their natural targets until carbon-concentrated RTOs are essentially decarbonized. We furthermore develop the disclosures of [14] by raising that, even without CCS, CO<sub>2</sub> transmissions from PHECs in PJM, MISO, and ERCOT are basically let down than those from coal-to-fluids power plants (mark which discharges from PHECs in need of CCS in ERCOT look like fossil fuel-to-fluids accompanied by CCS). Along these lines, an attainable strategy, rather than coal-to-fluid, would support the decarburization of the limit an area to give PHECs. As of late discussed, evening PHEC charging has the effect of smoothing the stack curve by extending off-top trust in power instead of debilitating the top. Hence, the electric-framework base can be used even more regularly for a more standard reason. Since an immense piece of the transmission and spread bottleneck in the United States is sufficiently sitting inert for extended lengths of the year, extended PHEC charging settles something of a capacity secure, coursing regular costs over a more conspicuous proportion of kilowatt-hours.

$$L = De^{-p\theta} \tag{1}$$

Here D and p are both constants (D in years, p in °C-1); the transformer protection's valuable life is sliced down the middle with consistency that passes [15]. The temperature has ascended by 6 degrees Celsius. We can tackle for the steady p utilizing this information. Because of p = 0.1155 °C-1 Characterize  $\theta_n$  as the temperature at which the transformer protection's future should be normal. The maturing element would then be able to be depicted as follows:

$$K = \frac{De^{-0.1155\theta\pi}}{De^{-0.1155\theta}} \tag{2}$$

When  $\theta_n = 98 \text{ }^\circ\text{C}$  and life expectancy is standard, we can solve for the aging factor as

$$K = e^{0.1155(\theta-98)} \tag{3}$$

By separating some regions of (4) accompanied by honor to  $\theta$ , we can see the importance of the aging factor:

$$\frac{dK}{d\theta} = \frac{d}{d\theta} e^{0.1155(\theta-98)} = 0.1155e^{\theta-98} \tag{4}$$

At the point when an electrical device is presented to a fundamental measure of  $\theta_n \neq \theta$  intended  $y$  hours, it is equal to  $yK(\theta)$  long periods of administration at common fundamental measure  $\theta_n$ . We may infer a recipe utilizing the maturing element's property. The connection among a taken over-burden fundamental measure  $\theta^*$  and some other temperature  $\theta$  an alternate temperature on a taken daytime. Assume the temperature is in degrees Fahrenheit for  $h$  hours and in degrees Celsius for 24 h. From that point forward, from (4), we get

$$24 = he^{p(\theta-98)} + (24 - h)e^{p(\theta'-98)} \tag{5}$$

Later few use, we may calculate for  $\theta^*$  as

$$\theta^* = \frac{1}{p} [\ln(24 - he^{p(\theta-98)}) - \ln(24 - h) + 98] \tag{6}$$

Lastly, the relation between temp and power throughput is taken by

$$\Delta\theta = P.R_T \tag{7}$$

where  $R_T$  is the thermic opposition about the electrical device isolation.

Given a fixed over-trouble temperature and throughput trouble time, conditions (6) and (7) basically give a basic measure of PHEC charging that can happen. To put it another way, the boundaries characterize a practical charging cap instead of an all-out charging limit (in Fig. 1). We layout this basic on a hypothetic oil color-cooled electrical device on top of a electrical circuit accompanied by a step-by-step top weight (and cutoff prerequisite) of 1KMW and an entire PHEC averment breaking point of 200 MW, as shown in Fig. 5.

## 4 Conclusion

Evening charging of PHEVs associates the US transport framework with the electric power framework. We optically campaign two significant enhancements to the US electrical framework that ought to be made with the end goal for PHECs to make a significant commitment to lessening outpourings. We explore the CO<sub>2</sub> identical outflows from the evening time charging consistently as a feature of a food circle of PHEVs. Likewise in places like ERCOT, which has a lot more prominent extent of low-level-carbon age capital than PJM or MISO, indispensable de-carbonization old enough is needed, earlier releases can be decreased fit beneath those of normal fuel transports or customary HEVs. We research the impact of evening PHEC averment on a specific piece of far-off association hardware, the oil color-cooled electrical device. These quondam are intended to have higher-than-typical pyrexias during top hours however are permitted to cool to ordinary or lower-than-ordinary temperatures during off-top hours. This everyday working cycle would be upset by PHEC industry invasion. Transformers would either should be supplanted all the more regularly, raising costs, or nascent rampart instruments should be facilitated. All through this article, we've accepted a basic charging plan in which PHECs are connected during the evening's eight off-top hours. As well as being limited, such a charging model can incidentally hurt the transport structure foundation, for reasons illustrated in Section III. It's not difficult to envision a sharp control structure that would charge PHECs on occasion when the biological or system impacts are least (regardless of whether at off-top hours or at different occasions) and may even think about PHECs to relegate fundamental organizations to the system. Such a control plan would require further interests in bleeding-edge innovation trades and control structures.

## References

1. U.S. Environmental Protection Agency. U.S. Greenhouse Gas Inventory: 1999 – 2005. Report. <http://www.epa.gov/climatechange/emissions/usinventoryreport.html>
2. Frank AA (2007) Plug-in hybrid vehicles for a sustainable future. *Am Sci* 95(2):158–165
3. Lave LB, MacLean HL (2002) An environmental-economic evaluation of hybrid electric vehicles: Toyota's Prius vs. its conventional internal combustion engine Corolla. *Transp Res Part D-Transp Environ* 7(2):155–162
4. Samaras C, Meisterling K (2008) Life cycle assessment of greenhouse gas emissions from plug-in hybrid vehicles: implications for policy. *Environ Sci Technol*. In-press
5. Kempton W, Tomic J (2005) Vehicle-to-grid power fundamentals: calculating capacity and net revenue. *J Power Sources* 144(1):268–279
6. Kintner-Meyer M, Schneider K, Pratt R (2006) Impact assessment of plug-in hybrid vehicles on electric power grids and regional utilities. Working paper, Pacific Northwest National Laboratory
7. Denholm P, Short W (2006) An evaluation of utility system impacts and benefits of optimally dispatched plug-in hybrid electric vehicles. NREL Technical report TP-620-40293
8. Stephan CH, Sullivan J (2008) Environmental and energy implications of plug-in hybrid-electric vehicles. *Environ Sci Technol*. <https://doi.org/10.1021/es062314d>

9. Environmental assessment of plug-in hybrid electric vehicles, Volume 1: Nationwide greenhouse gas emissions. EPRI, Palo Alto, CA, Palo Alto 1015325, 2007
10. Environmental assessment of plug-in hybrid electric vehicles, Volume 2: United States air quality analysis based on AEO-2006 assumptions for 2030. EPRI, Palo Alto, CA, Palo Alto 1015326
11. Douglas S (2006) Measuring gains from regional dispatch: coal-fired power plant utilization and market reforms. *Energy J* 27(1):119–138
12. U.S. Environmental Protection Agency eGRID Emissions & Generation Resource Integrated Database, eGRID2006 Version 1.0 Plant File (Year 2004 Data). <http://www.epa.gov/cleanenergy/egrid/index.htm> (January 1, 2007)
13. Newcomer A, Blumsack S, Apt J, Lave LB, Morgan MG (2008) Short- run effects of a price on carbon emissions from U.S. electric generators. *Environ Sci Technol*. In-press
14. Jaramillo P, Samaras C, Wakeley H, Meisterling K (2008) Greenhouse gas implications of using coal for transportation: life cycle assessment of coal-to-liquids, plug-in hybrids, and hydrogen pathways. *Energy Policy*, Submitted Feb 9
15. Kulkarni S, Khaparde S. *Transformer engineering: design and practice*. Marcel Dekker, New York



# Refrigeration Performance Analysis Using Artificial Neural Network



Lavnish Singh Bisht, Sourav Kumar Singh, Ankit Kumar, and Akhilesh Arora

## 1 Introduction

Nowadays, refrigerants that are environmentally friendly and possess no harm to the ozone layer are being used and preferred worldwide. The use of Refrigerants which are Ozone friendly and have low GWP and also the use of renewable sources of energy for adsorption systems are also gaining popularity as compared to the traditional ones which may soon be eliminated owing to all the environmental implications [1, 2]. Now with new evolving technologies like Artificial neural networks which give us the ability to maximize the output using advanced optimization algorithms, considering all these factors, we can go for the ANN-based VCERS system as an alternative to the conventional refrigeration system [3].

Although lack of research in this field poses a challenge for the commercialization of ANN-based VCERS systems as compared to conventional systems.

This report aims to explore a new method that can be used to predict the performance of VCERS without actually performing the experiment but by using a computer algorithm (ANN) to do so. The main benefit of using neural networks instead of performing the actual experiment is that it is much faster, cost-effective, simple, its ability to continuously learn and perform large no. of simulations and also, they have the ability as a universal approximator to fit nonlinear systems [4, 5].

Boon Chiang Ng [6] uses nonlinear autoregressive neural networks with exogenous inputs (NARX) to optimize the Air conditioning system used in automobiles.

Ertunc [7] utilizes ANN for predicting the performance parameters of refrigeration systems with an evaporative condenser with reasonably high accuracy, and the result verifies that high complexity refrigeration systems can be modeled using the ANN algorithm [8].

---

L. S. Bisht (✉) · S. K. Singh · A. Kumar · A. Arora  
Delhi Technological University, Rohini, India

Alamir [9] utilizes ANN for predicting the cooling temperature and performance of Thermoacoustic Refrigeration systems, and he further improves the accuracy of the ANN by adjusting the no. of neurons in the hidden layer.

Mohanraj et al. [10] prepared an ANN model to predict the performance parameter of direct expansion solar-assisted heat pump with high accuracy.

To train an ANN model, initially data is needed to be fed so that it can learn through the data, and once trained, it can be used to make predictions. For training our neural network, the data is obtained by using Engineering Equation Solver (EES) software which was simulated for 50 different values of input parameters to obtain the Performance (COP) of the VCR cycle for 15 different refrigerants.

## 1.1 ANN

Artificial neural network (ANN), which is also called neural networks (NNs), is a computing system that is developed by artificially replicating the biological neural networks which are similar to the animal brain [11].

An ANN is nothing but an amalgamation of connected units called nodes, which is based on neurons present in our brain. Each synapse is the same just like the ones present in our brain, which sends a signal to other connected neurons. Artificial neurons first receive a signal, and after processing it, it sends it to other connected neurons. A nonlinear function is used to compute the output given by each neuron. These connections present in the network are called edges. The weights allocated to these connections keep on changing and improving as learning continues. The strength of a connection is determined by the weight allocated to it.

Sometimes neurons may also have a lower limit, i.e., there should be a certain amount of accumulation of signals for transmission to occur. Neurons are generally arranged in the form of layers and different layers perform different operations on their input signals as signals travel from the input layer to output one by passing through multiple layers.

First of all, an ANN goes through a training, where it undergoes learning such as pattern recognition in the given data and continuously keeps on improving using techniques such as backpropagation, where it tries to reduce the difference between actual and desired output by reallocating the weights assigned at each connection between units until the difference cannot be reduced any further.

With the help of neural networks, we can find the solution for those problems for which an experimental method is not economically viable or does not exist. Neural networks can also learn by example, so we do not need to program them to that extent. Neural networks have high accuracy and are significantly faster than conventional methods.

## ***1.2 Vapor Compression Refrigeration System***

A vapor compression refrigeration system works on the continuous expansion and compression of a liquid refrigerant in a closed environment resulting in its phase change from liquid to vapor and vice versa.

During this entire process, heat is either being fed or being removed from the refrigerant and it causes the air in the vicinity of the system to change its temperature. In this process, the temperature of the space that is to be cooled reduces and the heat absorbed from this space is rejected outside [12].

A VCRS system is made up of four components namely: evaporator, condenser, compressor and expansion valve. Both evaporator and condenser are series of coils which provides increased surface area for refrigerant to change its phase. On the other hand, compression and expansion valves are mechanical devices that are there to provide control over temperature and pressure changes that occur in between I stage and II stage.

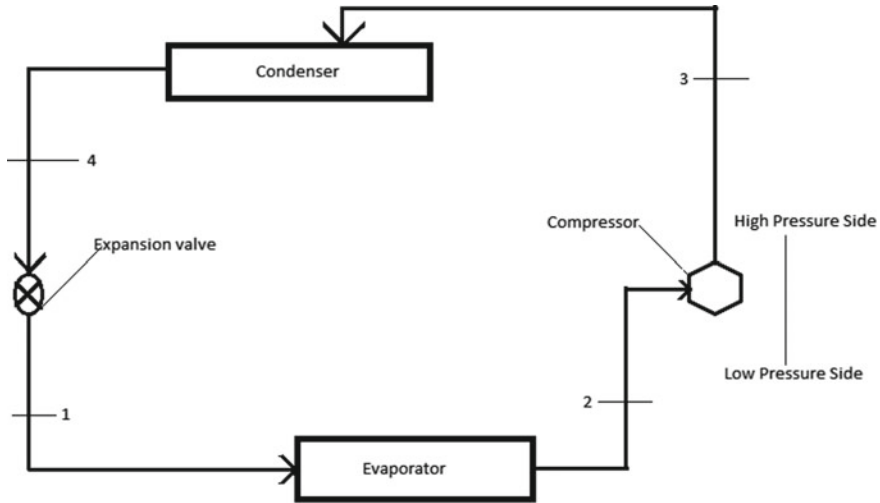
## ***1.3 Working of VCRS***

In the beginning, the required operating pressure for the given refrigerant is achieved then the refrigerant passes through the compressor, where it is converted into a high-pressure, high-temperature vapor. After that, it passes through the condenser where it is made to cool down and facilitate the phase change, i.e., from vapor to liquid [13].

As the external air flows across the coils present in the condenser, it takes away the excessive heat present in the vapor. After that, the liquid passes through the expansion valve, where it is expanded into a low-pressure vapor. This sudden drop in pressure causes a sudden drop in refrigerant pressure too, and because of this, a supercooled refrigerant is made to pass through the evaporator and there's a fan present inside the component which makes the air to flow through the supercooled coil into the region which requires cooling. During this transaction of heat, the temperature of the refrigerant increases as it takes up the heat present in the region that required cooling. After the refrigerant has absorbed the heat from the region which requires cooling, it is sent back to the compressor for the extraction of heat and the cycle continues.

## **2 Description of the Experiment and Experimental Data**

Vapor Compression Refrigeration cycle is based on the Joule–Thomson effect where cooling is achieved by repeated compression and expansion of coolant fluid. Almost all the big refrigeration systems nowadays use the Vapor Compression Refrigeration (VCR) cycle.



**Fig. 1** Refrigeration cycle

VCR cycle is used in HVAC systems, air conditioners, etc. Vapor Compression Refrigeration cycle consists of four components namely evaporator, compressor, condenser and expansion valve (Fig. 1).

## 2.1 Refrigerants

In the past few years, there has been a rise in discussion on the proper selection of refrigerants keeping in mind their environmental impact as well. The need for such discussion has arisen because of the adverse effects of CFCs and HCFs, and currently, the world is moving toward newer compounds as a refrigerant that do not generate chlorine in the atmosphere [14]. As we move toward newer refrigerants, there will be a need to know how efficient they are when operated upon at some temperature and pressure. The parameter we use to find the efficiency of the VCR cycle is called COP, coefficient of performance. COP is the ratio of heat absorbed at low temperature by the evaporator to work supplied to the compressor. COP is used to determine the plant performance, that is higher the COP, the more efficient is the machine and vice versa. Monitoring COP of the system allows us to continuously improve upon its performance and also to control its operating cost.

COP of Vapor Compression Cycle:

$$\text{COP} = (\text{Heat Extracted at lower temperature})/(\text{Work supplied}) \quad (1)$$

(From T-s diagram)

Heat extracted at lower temperature (process 1–2)

$$Q_e = h_1 - h_4 \quad (2)$$

Work of compressor

$$W = h_2 - h_1 \quad (3)$$

$$\text{COP} = (h_1 - h_4)/(h_2 - h_1) \quad (4)$$

For an ideal VCR cycle, COP is the function of evaporator and compressor temperatures only and is independent of the properties of the working fluid.

$$\text{COP} = Q_e/W_{\text{net}} = T_e/(T_c - T_e) \quad (5)$$

But practically this is not the situation and there are multiple parameters that affect the COP of the system. The physical and chemical properties of refrigerant that is being used in the VCR cycle affects COP.

The different properties could be viscosity, density, molar heat capacity, thermal conductivity, molecular weight, critical temperature, etc. In order to get higher COP, we need a combination of higher values of thermal conductivity, latent heat and vapor density while lower values of molecular weight and liquid viscosities [15].

## 2.2 EES Software

Engineering Equation Solver is the equation solving software that can solve thousands of numerical equations, nonlinear algebraic and differential equations. It can also solve integral equations and also do optimization, perform linear and nonlinear regression, can be used to check and convert units as well. It has various other functionalities which facilitate and ease data lookup and also let us to operate upon a number of fluids and refrigerants already present in its memory. Mehmet Altinkaynak et al. [16] had used EES software for the thermodynamic analysis of VCRC cycle as an alternative to the conventional experimental setup, and here, we take that forward for the analysis of COP of a refrigeration cycle.

This could be used to find COP of the VCR cycle by writing the equations involved without actually performing the experiment on a physical setup (Fig. 2).

Datasets like  $T_h$ ,  $T_c$ , COP and all other thermo-physical properties of the refrigerants calculated on EES software for the VCR cycle are written in an MS Excel sheet. Data for 50 different temperature and pressure conditions of over 15 refrigerants is taken from EES software (Fig. 3).

All these datasets along with the properties of different refrigerants have been fed into the ANN model in order to train it. In the future, if we want to know the COP of the VCR cycle operating upon a refrigerant whose thermo-physical data is not

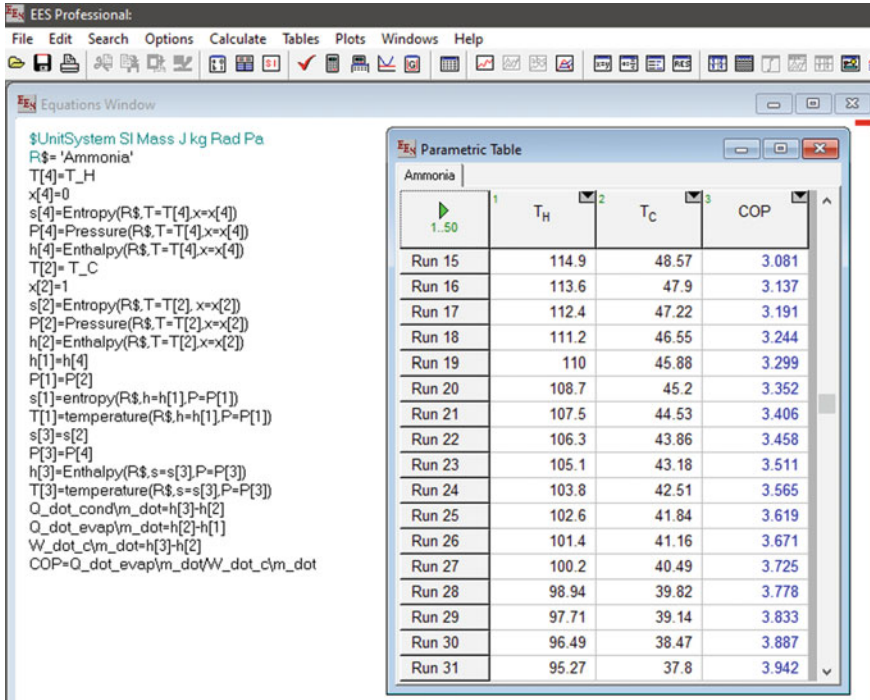


Fig. 2 Snapshot of the EES window with the program code which we used to evaluate the COP

	A	B	C	D	E	F
1	Refrigerant	T <sub>h</sub>	T <sub>c</sub>	COP	Thermal conductivity [W/mK]	Viscosity [kg/ms]
300	R11	56.82	12.41	5.594	0.01286	0.00001094
301	R11	56	12	5.647	0.01286	0.00001094
302	R12	110	45	1.64	0.009675	0.00001257
303	R12	109.2	44.49	1.742	0.009675	0.00001257
304	R12	108.4	43.98	1.833	0.009675	0.00001257
	G	H	I	J	K	
1	MW [kg/ mol]	c temp [C]	c pressure [kPa]	saturation press [kPa]	specific heat [kJ/kgK]	
300	137.4	198	4408	105.6	0.5882	
301	137.4	198	4408	105.6	0.5882	
302	120.9	112	4114	651.1	0.6164	
303	120.9	112	4114	651.1	0.6164	
304	120.9	112	4114	651.1	0.6164	

Fig. 3 Snapshot of table from MS Excel sheet

available in the EES software, our trained ANN model would be able to predict the COP accurately.

### ***2.3 Artificial Neural Network Design***

Artificial neural network is a very powerful and popular algorithm of Machine learning which is widely used to solve complex nonlinear problems which are very difficult to solve by other machine learning algorithms. These networks are basically an attempt to replicate the network of neurons through which are brain functions and thereby an attempt to replicate the working of the human brain but with more processing power. The human brain can understand and solve complex problems with less amount of data and slow processing power compared to a computer. So, if there could be a way through which computers with their abundant processing power and capacity to work with large amounts of data can learn to function in a way a human brain does, then it could become a very powerful and useful tool. The human brain consists of a network of billions and billions of neurons connected with each other. These neurons have chemicals through which they receive, transmit information and process the complex information.

The ANN works in a similar way; it has an input layer, several hidden layers and output layers and each hidden layer has several neurons in them because of the addition of these hidden layers, the complexity of the equation can be increased. These neurons are basically combinations of different attributes from the input layer. Different weights are assigned to each neuron in every hidden layer which defines how much contribution does that neuron have in the output.

After the output is obtained, a cost function is calculated which is basically the sum square of error, and the goal of the ANN is to reduce the cost function. The back Propagation technique is used by the ANN model to update the weights with the aim to reduce the cost function. This updating of weights can be done by brute force method or by gradient descent methods in which the slope of the curve between the cost function and the weights is considered to obtain the global minima.

Some statistical methods are used to check the accuracy of the predictions, RMSE, RMSLE and Mean Residual Deviance.

## **3 Model Design**

In this experiment, the ANN model is trained to predict the Efficiency via the Coefficient of Performance (COP). The algorithm is developed in R programming language by using the H2O Package from CRAN. H2O Package connects the R environment with the open-source platform named H2O which is a very popular platform among data scientists to apply Deep Learning and Artificial Intelligence algorithms to solve complex problems. The H2O offers lots of deep learning and several Supervised and

Unsupervised Machine Learning algorithms which we can call from our computer using any programming language like R where we use H2O package. This sends the data we need to train the model to the source platform where the ANN algorithm is trained, and whenever we need to use the algorithm for prediction on a new dataset, we need to again send the new dataset to the source platform (i.e., H2O) which then predicts and sends back the predictions. ANN requires heavy processing power to run which most normal computers don't have so this H2O library also helps in that sense as the processing is done at the server in the source platform there.

Initially, the data which contains the inputs and efficiency which is the outcome that we desire has been imported in R programming language and converted into Data Frame format from Excel format.

The inputs contain the Condenser Temperature (T\_C), Evaporator Temperature (T\_H) and the properties of Refrigerant: Thermal conductivity, Viscosity, Molecular weight, Critical Temperature, Critical Pressure, Saturation Pressure and Specific heat.

The properties are selected by considering their ability to affect the cop so that the algorithm can identify the relationship between the properties of the refrigerant and COP it gives at given input parameters. In this way, it can predict the COP of any refrigerant by just its properties and the input temperature conditions without any for the refrigerant itself.

For Training the model, 15 refrigerants have been chosen and their properties and Coefficient of Performance at different condenser and evaporator conditions are imputed for which the data has been collected from the EES software.

About 750 observations have been taken of those 15 refrigerants. Out of which 85% data have been used for training and the remaining 15% of the data have been used for testing (Fig. 4).

	Refrigerant	T_h	T_c	EFFICIENCY	Thermal conductivity [W/mK]	Viscosity [kg/ms]	MW [kg/mol]
17	Water	84.37	32	4.747	0.594800	8.905e-04	1.802e+01
18	Water	82.00	32	4.893	0.594800	8.905e-04	1.802e+01
19	R410A	71.57	27	2.535	0.013330	1.288e-05	7.258e+01
20	R410A	68.14	25	3.557	0.013330	1.288e-05	7.258e+01
21	R410A	66.43	23	3.794	0.013330	1.288e-05	7.258e+01
22	R410A	61.29	19	4.338	0.013330	1.288e-05	7.258e+01
23	R410A	60.00	18	4.454	0.013330	1.288e-05	7.258e+01
24	R410A	54.86	14	4.868	0.013330	1.288e-05	7.258e+01
25	R410A	53.14	13	4.993	0.013330	1.288e-05	7.258e+01
26	R134a	98.29	48	2.808	0.013940	1.186e-05	1.020e+02
27	R134a	96.00	47	3.149	0.013940	1.186e-05	1.020e+02

Fig. 4 A fraction of the data frame which was used to train the ANN model



In the Artificial Neural Network model, 80 hidden layers are taken and 100 neurons in each hidden layer are fed in the algorithm. Since the complexity of the problem here is very high so and also on increasing the number of neurons has shown better performance, so a large number of hidden layers and neurons of each hidden layer are selected.

The Rectifier activation function is used in the algorithm which returns the output as the input itself when the input is positive and returns the output as Zero when the input is negative. The activation function is used in the algorithm before the output node which basically decides in what manner the weighted sum of the inputs is to be transformed into the output.

Gradient Descent method is used in the algorithm for the Back Propagation. After the forward propagation, the cost function is calculated which is basically the sum of squares of errors in the output, and in order to minimize the cost function, Back Propagation is done to update the weights assigned to each neuron.

Gradient descent is the optimization algorithm used in the ANN model to minimize the no. of iterations required to find the best weights for the neurons, and this is done by finding the local minima by moving in the opposite direction of the gradient of the slope at the given point.

After the Preparation of the ANN model, the Dataset has been given for training and then predictions are made on the testing data, and Efficiency (COP) given by the test data and training data has been compared to check the accuracy of the model. The graph has been plotted between the real COP and Predicted COP in R programming to visually see the accuracy of the model.

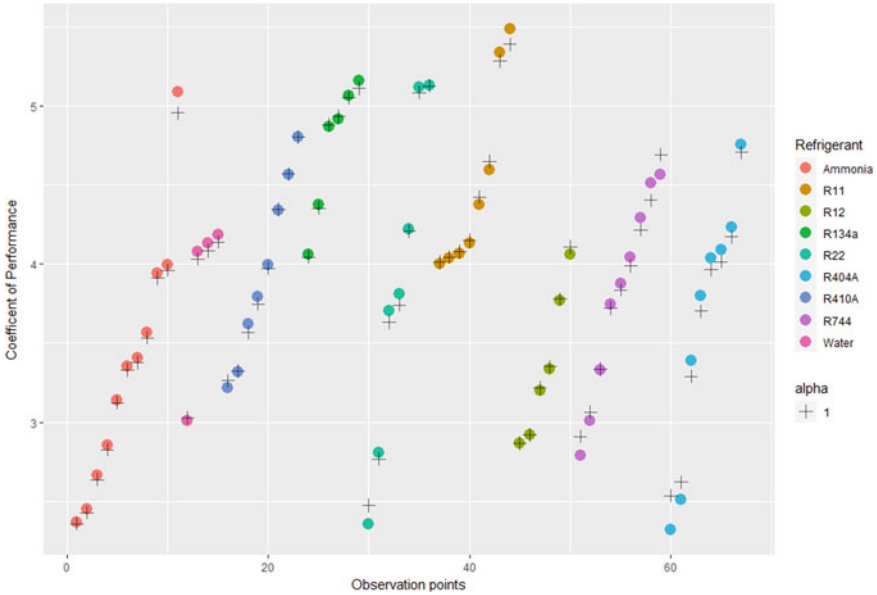
The model has been further utilized to find the Refrigerant out of the given refrigerants which provides the best COP for the given temperature conditions. This is done by plotting the simulations of COP of different Refrigerants at the same temperature conditions for which the value of COP has been calculated by the ANN model.

## 4 Results

The test set consists of 68 observation points being randomly selected from the original dataset obtained from the EES software. Predictions are made for the COP using the ANN model, and those predicted values are then compared with the original values of the COP. The following results were obtained:

1. The plot of Original COP obtained from EES software (represented by colored dots) versus the Predicted COP from the ANN algorithms (represented by black plus sign) has been shown below (Fig. 5).

This plot shows the colored dots and the Black Plus sign of the corresponding observation point being very close to each other if not coincidental shows that the model is very accurate.



**Fig. 5** Original COP versus Predicted COP

$$RMSE : 0.0889381 \quad RMSE = \sqrt{\frac{\sum_{i=1}^N (x_i - \bar{x}_i)^2}{N}} \tag{6}$$

Root mean squared error of 0.0889 is obtained which is much below the acceptable value of 0.5 which shows the model can predict with very high accuracy. RMSE is a suitable metric to judge the accuracy here because it gives more weightage to the large errors, which we obviously do not require while we predict the Coefficient of Performance of the System.

It also gives a Mean Absolute Error of 0.04675756.

The Maximum error shown in the predictions is below 5%.

And the Average error is equal to 0.14%.

1. This plot compares the values of COP of different refrigerants at same temperature conditions varying from 50 °C to 70 °C temperatures (for the evaporator) while keeping the T<sub>C</sub> (condenser temperature) constant at 25 °C (Fig. 6).

This plot is made by plotting the multiple simulations of COP of different Refrigerants at the same temperature conditions using the Ggplot package in R programming. For the plot, the value of COP has been calculated by using the ANN model which we have trained earlier.

From the plot, we can observe that R11 gives the best COP and R404 gives the worst COP out of all the refrigerants on the given temperature range.

Similarly, this method can be used to analyze and compare any given refrigerants in any given temperature conditions to find out the best refrigerant out of all.

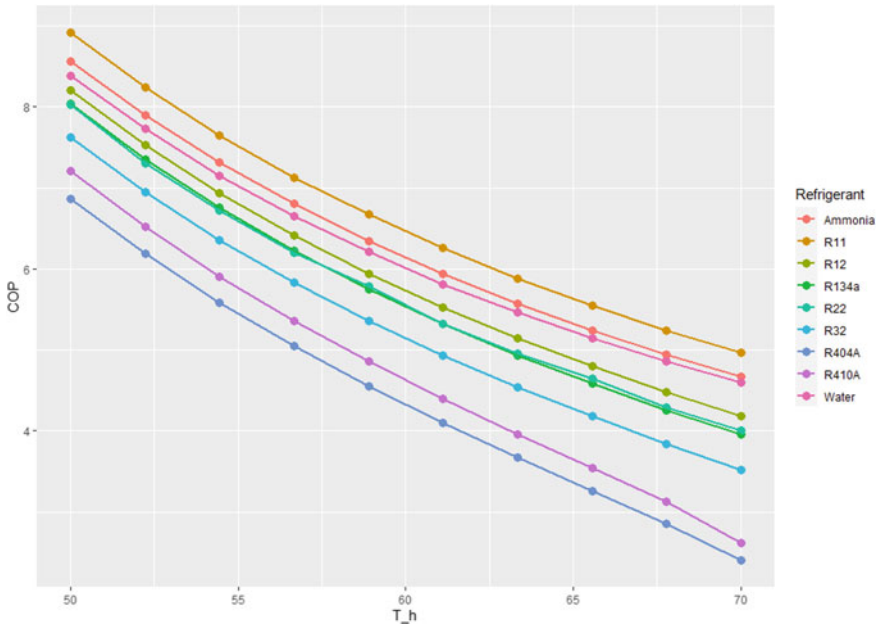


Fig. 6 Comparison of different refrigerants' COP for same temperature conditions

## References

1. Chang YS, Kim MS, Ro ST (2000) Performance and heat transfer characteristics of hydrocarbon refrigerants in a heat pump system. *Int J Refrig* 23:232–242
2. Calm JM (2008) The next generation of refrigerants—Historical review, considerations and outlook. *Int J Refrig* 31:1123–1133
3. Baiju V1, Muraleedharan C (2013) Application of neural network for the performance. *Int J Eng Res Technol*
4. Hornik K, Stinchcombe HW (1989) Multilayer feedforward networks are universal approximators. *Neural Netw* 2:359e366
5. Narendra KS, Parthasarathy K (1990) Identification and control of dynamical systems using neural networks. *IEEE Trans Neural Netw* 1:4e27
6. Chiang Ng B, Zaurah Mat Darus I (2014) Dynamic modelling of an automotive variable speed air conditioning system using nonlinear autoregressive exogenous neural networks. *Appl Thermal Eng* 73:1253e1267
7. Ertunc HM, Hosoz M (2006) Artificial neural network analysis of a refrigeration system with an evaporative condenser. *Appl Therm Eng* 26(5–6):627–635
8. Hosoz M, Ertunc HM (2006) Modelling of a cascade refrigeration system using artificial neural network. *Int J Energy Res*: 1200–1215, Nov
9. Alamir MA (2021) An artificial neural network model for predicting the performance of thermoacoustic refrigerators. *Int J Heat Mass Transf* 164:120551, Jan
10. Mohanraj M, Jayaraj S, Muraleedharan C (2011) Modeling of a direct expansion solar assisted heat pump using artificial neural networks. *Int J Green Energy*:520–532
11. Dase RK, Pawar DD (2010) Application of artificial neural network for stock market predictions: a review of literature. *Int J Machine Intell* 2(2): 14–17. ISSN: 0975–2927

12. Austin N, Diaz PM, Manoj Abraham DS, Kanthavelkumaran N (2014) Environment friendly mixed refrigerant to replace R-134a in a VCR system with exergy analysis. *Adv Mater Res* 984–985:1174–79, July
13. Nikhil Babu P, Mohankumar D, Manoj Kumar P, Makesh Kumar M, Gokulnath M, Gurubalaji K, Harrish G, Ashok M (2021) Energy efficient refrigeration system with simultaneous heating and cooling. *Materials Today: Proceedings*. ISSN 2214-7853
14. Oruç V, Devecioğlu AG (2021) Experimental investigation on the low-GWP HFC/HFO blends R454A and R454C in a R404A refrigeration system. *Int J Refrig*. ISSN 0140-7007
15. Prapainop R, Suen K (2012) Effects of refrigerant properties on refrigerant performance comparison: a review. *Int J Eng Res Appl (IJERA)* 2(4):486-493. ISSN: 2248-9622, July-August
16. Altinkaynak M, Olgun E, Şencan Şahin A (2019) Comparative evaluation of energy and exergy performances of R22 and its alternative R407C, R410A and R448A refrigerants in vapor compression refrigeration systems. *El-Cezerî Fen ve Mühendislik Dergisi Cilt 6(3):659–667*

# Factors Affecting Production System in Additive Manufacturing



Kamal, Gaurav Deshwal, Ayush Kumar, and Mahendra Singh Nirranjan

## 1 Introduction

The use of advances in the manufacture of added substances in various associations has dramatically expanded over the years. Henry Ford introduced the flexible sequential advancement structure which involved a huge degree of accomplishing dubious things in the twentieth century. Today, the production of added substances improves and supports the development of moderate to huge segment proportions that can be changed on their own. Advances in the production of added substances are opening new doors from the point of view of creation and convey probable results. Reunion events will be reduced to a very basic level, new plans will be less likely to air, and customer requests will be met even more quickly (Table 1).

## 2 Brief Description of Critical Factors of Additive Manufacturing

**1. Cost:** Two enormous elevating courses of action for looking at added substance producing costs. the first is to separate added substance conveying measures with other standard cycles [1–3].

**2. Inventory:-**A reduction in holding costs can influence lowering the probability of stock-outs when the traditional credit expense for spare parts is minimal and the Time decreasing will negatively affect stock-out likelihood [4].

---

Kamal (✉) · G. Deshwal · A. Kumar · M. S. Nirranjan  
Department of Mechanical Engineering, Delhi Technological University, New Delhi, India

**Table 1** Critical factors of additive manufacturing

Factor No	Factors description	Authors
1	Cost	Thomas and Gillbert [1], Daniel et al. (2017), [3–5]
2	Inventory	[26, 32], Faweett and Walter (2014), Holmstorm et al. [25]
3	Material	[5, 24], Berman (2012), [27], Dwivedi et al. [36], Ford and Despeissem [13]
4	Designer and education	Ian Gibsona, Aniruddha Srinath (2015), Sebastian Hällgrena, Lars Pejrydb, Jens Ekengrenb (2016)
5	Flexibility	Daniel et al. (2017), [26, 29–31], Ruffo et al. (2007), Daniel et al. [35]
6	Wastage	Lopes [8], Wohlers and Caffery (2013), Horn and Harryson (2012), [10, 28], Roberson (2013)
7	Complexity	[9], Lopes [8], Liu et al [32], [10]
8	Machinery	Ruffon and Hague [11], [12], Ford and Despiessie [13]

**3. Material:** At present, 3D printing movements can be utilized with a wide degree of materials including metals, fired creation, polymers, and composites. In any case, by then, the accessibility of reasonable materials remains possibly as far as possible to utilizing added substance production as a creative strategy [5].

**4. Designer and Education:** As far as possible, AM allocation is the current limit opening. A 2016 report by Deloitte incites that by a long shot most producers are battling to enrol labourers with the correct limits. The limited inadequacy, at that point, is one looked at by social affairs considering everything.

**5. Flexibility:** Flexibility is an indispensable execution objective for accumulating tasks, permitting them to react to changing necessities in questionable and certifiable general business zones.

**6. Wastage:** AM utilizes simply essential material to make parts; in this manner, it prompts the least material waste. Considering less wastage AM ends up being a practical elective for making complex parts that customarily need more reconnaissance [6–8].

**7. Complexity:** The essentials and working norm of AM a few advantages, including close net-shape limits, overpowering strategy, and numerical versatility, innovative multi-material creation, reduced tooling and fixturing more restricted cycle term for plan and gathering, second neighbourhood creation at an overall scale, and material, energy, and cost profitability [9, 10].

**8. Machinery:** Added substance Manufacturing has undeniably added the worth in Industry 4.0 by fast prototyping, speedy gathering, and fast tooling. With the upside of passing on changed and complex game plan parts, Additive Manufacturing has

served the undertakings like the clinical, vehicle, flight, protection, tooling, jewels, style orchestrating, and so forth [11–13].

### 3 Methodology

#### 3.1 Interpretive Structural Model Formation

Interpretive fundamental showing is utilized for appearing of elements and to discover the interrelationship among these parts. The relationship among the components of inaccessible working is confusing and hard to see yet utilizing ISM procedure; it winds up being clear the unusualness of information taking an interest in any connection. Along these lines, a course of the relationship is set up and each factor is examined for its central purpose and reliance through a wide highlight technique. In applying the ISM framework, the sections of information e sharing are seen, and a brief timeframe later, a rational relationship is set up among them. The SSIM (covered-up self-interaction structure) is associated with making a pair-wise relationship between the elements. From SSIM a reachability structure is made, and it is checked for transitive affiliations, hoping to be any. The last reachability cross-segment is then evolved which joins transitive affiliations. The elements are then isolated at various levels [14–16].

#### 3.2 Structural Self-Interaction Matrix (SSIM)

The primary self-communication grid was created by the utilization of specialists’ assessment. In this paper, the SSIM for ISM was loaded up with the assistance of specialists nearby, who are working at the centre level. Pair-wise correlation is done among the variables to know the course of their relationship. Table 2 is made considering the assessment of specialists. The path of the link between the components I

**Table 2** Structural Self-intersection Matrix (SSIM) of additive manufacturing factors

S.No	Factors	8	7	6	5	4	3	2
1	Cost	A	A	A	A	A	A	A
2	Inventory	A	A	A	A	O	O	
3	Material	V	X	V	V	V		
4	Designer	O	A	O	X			
5	Flexibility	A	A	V				
6	Wastage	O	A					
7	Complexity	V						
8	Machinery							

**Table 3** Initial reachability matrix of additive manufacturing factors

Factors	1	2	3	4	5	6	7	8
1	1	0	0	0	0	0	0	0
2	1	1	0	0	0	0	0	0
3	1	0	1	1	1	1	1	1
4	1	0	0	1	1	0	0	0
5	1	1	0	1	1	1	0	0
6	1	1	0	0	0	1	0	0
7	1	1	1	1	1	1	1	1
8	1	1	0	0	1	0	0	1

and j) is shown by four images: V: factor I will help factor j achieve its goal; A: factor j will achieve its goal; X: factors I and j will help one another achieve their goals; 0: factors I and j are unimportant.

### 3.3 Reachability Matrix

By replacing X, A, V, and O with 1 and 0, the SSIM has been transformed into a two-part architecture known as the reachability network. Its transitivity is tested at that moment. If factor I triggers factor j, and factor j triggers factor k, factor I will have an impact on factor k. The addition of transitivity results in a different reachability network. (Table 3). If the SSIM segment is V, the (i,j) component of the reachability network receives 1 and the (j,i) fragment receives 0. ( b) If the SSIM section is A, the reachability network’s (i,j) passage becomes 0 and the (j,i) section becomes 1. (c) If the component in the SSIM is X, the reachability grid’s (i,j) section receives 1 and the (j,i) portion gets 1. (d) If the passage in the SSIM is O, by at that point (i, j) fragment in the reachability cross-area becomes 0.

Table 4 shows the iteration of this matrix into a final reachability matrix. The ultimate reachability matrix is obtained by including transitivity. If enabling A is connected to B and B is linked to C, then is also linked to C. The resulting transitivity reachability matrix is shown in Table 4. 1\* entries are used to incorporate transitivity and fill in any gaps in the views collected throughout the development of SSIM.

### 3.4 Level Partitioning

From the last show up at limit cross-area (Table 5), the reachability set and a prime example set for each empowering sway were settled. The reachability set contains the empowering sway itself and those which it might assist with accomplishing.



**Table 4** Final reachability matrix of additive manufacturing factors

Factors	1	2	3	4	5	6	7	8	Driving power
1	1	0	0	0	0	0	0	0	1
2	1	1	0	0	0	0	0	0	2
3	1	1*	1	1	1	1	1	1	8
4	1	1*	0	1	1	1*	0	0	5
5	1	1	0	1	1	1	0	0	5
6	1	1	0	0	0	1	0	0	3
7	1	1	1	1	1	1	1	1	8
8	1	1	0	1*	1	1*	0	1	6
Dependence	8	7	2	5	5	6	2	3	

**Table 5** Levels of factors of additive manufacturing factors

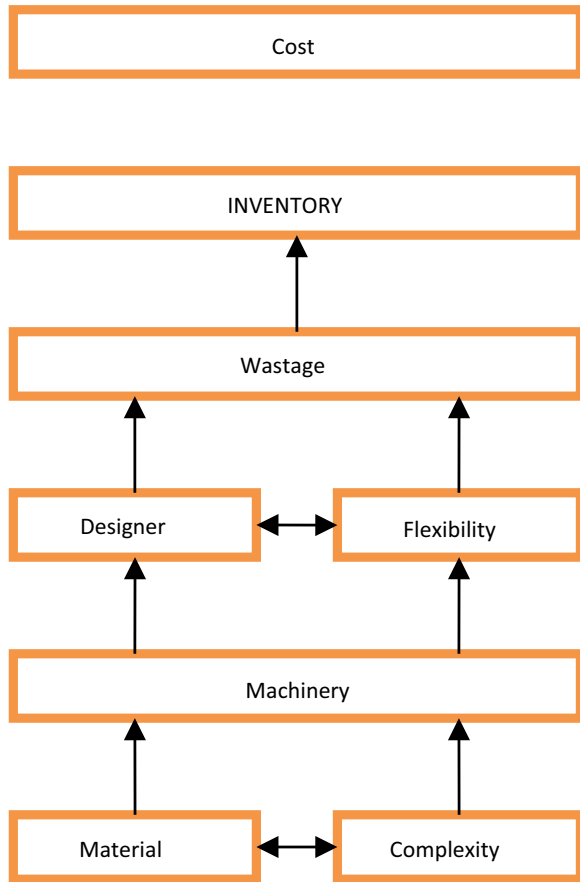
Factors	Reachability Set	Antecedent Set	Intersection	Level
1	1	1,2,3,4,5,6,7,8	1	I
2	1,2	2,3,4,5,6,7,8	2	II
3	1,2,3,4,5,6,7,8	3,7	3,7	VI
4	1,2,4,5,6	3,4,5,7,8	4,5	IV
5	1,2,4,5,6	3,4,5,7,8	4,5	IV
6	1,2,6	3,4,5,6,7,8	6	III
7	1,2,3,4,5,6,7,8	3,7	3,7	VI
8	1,2,4,5,6,8	3,7,8	8	VI

The envoy set incorporates the empowering sway itself and those which may help in accomplishing it. The get-together of these sets is settled for every one of the drawings in subject matter experts. The factor by which the reachability and gathering sets became indistinguishable is the final element in the ISM chain of priority. The solicitation’s final factor has no bearing on the achievement of any other element above it. This partnership will continue until the levels of each element are seen. These obvious thresholds aid in the construction of the map as well as the final model. In this case, the segments close to their reachability range, harbinger set, blend set, and levels are there in Table 5. The affiliation was accomplished in six emphases. The Development of the ISM Model of Additive Manufacturing.

### 3.5 Manufacturing Factors

The secret model is produced using Table 5 as demonstrated by the particular degrees of parts. Factor (1), which is at level I, is set at the most raised sign of the model.

**Fig. 1** ISM-based structural model for factors of production affecting additive manufacturing



Essentially factor (3), factor (7), and factors (8) which are at level VI are factors put at the base chain of importance. Figure 1 shows the ISM model of Additive Manufacturing factors. The parts which are at a lower level in the development have an incredibly high principal force and the elements which are at the most critical sign of the chain of command have a high reliance power. Only the full-scale number of elements (checking) is the essential force for each component, which it may aid in achieving. As shown in Table 4, reliance is defined as the total number of items (counting) that can assist in achieving the goal.

### 3.6 Fuzzy MICMAC Analysis

In the direct ISM model, there may exist backhanded and hide relationships among the components which may influence the presentation of the construction. The standard

ISM model neglects to show the aberrant and disguised relationship and as such padded MICMAC should be formed with ISM so that impact of shrewd and hid relationship is obvious. Direct connections analysis can demonstrate that indications with a significant direct impact may be concealing concealed markers, which can have a very simple influence on the system's common sense on occasion [17, 18]. These relationships between affiliations can be investigated, and their work and leadership can be evaluated using the MICMAC theory [19, 20]. MICMAC is an abbreviation for the following French explanation: It is used to examine hidden and covered-up connections between project elements acquired using the ISM method [21].

### 3.7 MICMAC Principle

The MICMAC rule is based on framework addition features. If pointer I has an unmistakable influence on marker k, and k has an unmistakable influence on pointer j, any modification affecting pointer I can have an influence on marker j. The standard MICMAC warm set hypothesis was created to manufacture its affectability. Regardless of the way that MICMAC contemplates a twofold kind of relationship, in comfortable MICMAC, an extra responsibility of probability of correspondence between the fragments is presented [17]. By including the probability of correspondences into the Fuzzy MICMAC assessment, the direct relationship network (DRM), which is derived from digraph—a head obligation to MICMAC—is enhanced. It is, therefore, referred to as a comfy direct relationship structure (FDRM), and it is based on the manner that a commitment is evaluated by MICMAC; rather than utilizing Boolean augmentation of matrices to change the positions, padded association duplication is utilized [17].

#### 3.7.1 Stabilization of Fuzzy Matrix

**Fuzzy MICMAC Analysis**—The direct link between the components listed in Table 3 is used to generate a DRM. As shown in Table 6, the DRM is produced by setting the diagonal entries to zero and disregarding transitivity.

#### Development of FDRM

The binary DRM now has the probability of reachability. In fuzzy MICMAC analysis, additional feedback on the probability of interaction between the components is included. On a 0–1 scale, Table 7 demonstrates how the chance of interaction may be expressed qualitatively.

The likelihood of a numerical value of reachability has now been placed on the DRM to achieve an FDRM. Table 8 contains the FDRM for the current case report.

**Table 6** Binary direct relationship matrix

Factors	1	2	3	4	5	6	7	8
1	0	0	0	0	0	0	0	0
2	1	0	0	0	0	0	0	0
3	1	0	0	1	1	1	1	1
4	1	0	0	0	1	0	0	0
5	1	1	0	1	0	1	0	0
6	1	1	0	0	0	0	0	0
7	1	1	1	1	1	1	0	1
8	1	1	0	0	1	0	0	0

**Table 7** Possibility of numerical value of the reachability

Possibility of reachability	No	Negligible	Low	Medium	High	Very High	Full
Negligible	0	0.1	0.3	0.5	0.7	0.9	1

**Table 8** Fuzzy direct relationship matrix

Factors	1	2	3	4	5	6	7	8
1	0.0	0.3	0.7	0.3	0.0	0.0	0.0	0.5
2	1.0	0.0	0.5	0.0	0.5	0.3	0.1	0.3
3	1.0	0.5	0.0	0.7	0.7	1.0	0.9	0.7
4	0.7	0.0	0.1	0.0	1.0	0.3	0.3	0.0
5	1.0	0.9	0.0	1.0	0.0	0.7	0.3	0.5
6	1.0	1.0	0.5	0.0	0.0	0.0	0.3	0.0
7	1.0	0.9	0.9	1.0	0.5	1.0	0.0	0.7
8	1.0	0.7	0.0	0.0	0.9	0.5	0.1	0.0

**Stabilization of Fuzzy Matrix**

For the improvement process, the FDRM is employed as a starting point [17]. The networks were increased multiple times till the driving power and dependability improvements were established. The padding Matrix standard has improved, according to the extension process. The primary function of the parts in MICMAC is restricted. By including bits of possible after-effects of collaborative efforts in the lines, the segments’ dependencies are determined by combining the parts of possible effects of relationship in the bits. The locations of the elements’ guiding Power choose the chain of sense of Criterion in the framework [22]. The sensible out structure in MICMAC for Factors of information sharing is developed in the 6th stage and are factors that appeared in Table 9.

**Table 9** Fuzzy MICMAC stabilized matrix

Factors	1	2	3	4	5	6	7	8	Driving power
1	0.3	0.1	0.1	0.1	0.1	0.1	0.1	0.1	1.0
2	0.7	0.5	0.1	0.1	0.1	0.1	0.1	0.1	1.8
3	0.3	0.3	0.7	0.5	0.5	0.5	0.7	0.7	4.2
4	0.3	0.5	0.1	0.5	0.7	0.7	0.1	0.1	3.0
5	0.3	0.5	0.1	0.7	0.3	0.7	0.1	0.1	2.8
6	0.5	0.7	0.1	0.1	0.1	0.7	0.1	0.1	2.4
7	0.3	0.3	0.7	0.5	0.5	0.5	0.5	0.7	4.0
8	0.3	0.5	0.1	0.7	0.7	0.5	0.1	0.3	3.2
Dependence	3.0	3.4	2.0	3.2	3.0	3.8	1.8	2.2	

#### 4 Classification of Factors Affecting Additive Manufacturing in Production System Through Four Clusters of Driving and Dependence

The Matrix I (Autonomous): These are the elements of the Manufacturing fragile driver and ward abilities. They are found close to the reason and well separated from the structure. This has no impact on the mechanism and is unaffected by the structure.

The Matrix II (Dependent): They are essentially based components. Their fragile main thrust is how they are viewed. This is the order of segments 1 (Cost), 2 (Inventory), and 6 (Wastage).

The Matrix III (Linkage): The linkage variables in the second rate class provide a heavy key impetus and dependency. This category includes segments 4 (Designer) and 5 (Flexibility).

The Matrix IV (Independent): The fourth classification combines autonomous components with good drivers but vulnerable dependency. This arrangement includes components 3 (Material), 7 (Complexity), and 8 (Machinery).

##### 4.1 Integrated Model

An organized model was created using the MICMAC seat cushioned structure using driver powers and partial dependence [23] (Table 10). The real estate is paid for in every factor by subtracting the dependency on the controller power. The model’s most abundant fragments are planned at the bottom, while the portions that fit the least are coordinated at the top. “Complex layout and material” were considered as a free base level main factor driving the production of beneficial added substance towards “Cost” and room main factors were considered in the model. The MICMAC fuzzy analysis of the points of the sections subject to their critical motive reveals that content, complexity, and machinery are the primary pieces with stronger driving

**Table 10** Difference in driving power and dependence

S.No	Factors	Driving power	Dependence power	Effectiveness = (Driver Power–Dependence)
1	Cost	1.0	3.0	–2.0
2	Inventory	1.8	3.4	–1.6
3	Material	4.2	2.0	2.2
4	Designer	3.0	3.2	–0.2
5	Flexibility	2.8	3.0	–0.2
6	Wastage	2.4	3.8	–1.4
7	Complexity	4.0	1.8	2.2
8	Machinery	3.2	2.2	1.0

force but weak reliance; similarly, these fragments should be regarded for additive manufacturing execution.

## 5 Result and Discussion

The result of this research paper is to anticipate key influencing factors that affect the production side of Additive Manufacturing. Influencing factors have been identified by thorough research and discussion. A mathematical model was moreover developed which can be helpful for a relationship to find the impact factor of a particular factor on the creation structure. Mathematical modelling of these factors is followed after the identification of impactful factors. Firstly reachability matrix table was obtained through which the VAXO table (Table 3) has been generated for all the factors. The dependency of these factors was identified through this table. Due to transitivity again a reachability matrix was formulated (Table 4). With this (Table 4) a level partition was done and factors got their respective levels (Table 5). A binary matrix is made (Table 6) with the help of Table 4. As per the possibility of factors to influence the process, a numerical value between 0 to 1 was given in Table 7. The end step of modelling these factors was the generation of a Fuzzy MICMAC (Table 8) in which the probability of dependency was given to each factor and later a stabilized matrix (Table 9) was made. At last, a graph (Fig. 2) was made between Driving power and Dependency. The result of this research paper is to give an idea of dependency of major factors on the production system of Additive Manufacturing and to make a systematic approach of the manufacturing process so that consumption of time could be reduced, cost-effective methods can be followed, and more profit generation would be a consequence through this approach.

**Fig. 2** Driving power and dependence power graph of factors

D R I V I N G  P O W E R	3,7					
		IV	8		III	
				4,5		
					2,6	
		I			II	1
	DEPENDENCE					

## 6 Conclusion

Through this assessment, the fundamental contemplations which impact the creation side of Additive Manufacturing were recognized and a relationship among the factors was set up and researched.

- Factors that affect the production system of Additive Manufacturing were identified and levels were assigned according to their driving power on the basics of which it would be easier for any organization to focus on factors that affect the production system most.
- With the ISM relations among all 8 factors are established and transitivity is also found which was hidden but influences the relation between factors.

## References

1. Thomas D, Gilbert S (2014) Costs and cost effectiveness of additive manufacturing, Special Publication (NIST SP), National Institute of Standards and Technology, Gaithersburg, MD
2. Ryan MJ, Eyers DR, Potter AT, Purvis L, Gosling J (2017) 3D printing the future: scenarios for supply chains reviewed. *Int J Phys Distrib Logist Manag* 47(10):992–1014
3. Yoon HS, Lee JY, Kim HS, Kim MS, Kim ES, Shin YJ, Chu WSH, Ahn SH (2014) A comparison of energy consumption in bulk-forming, subtractive, and additive processes: review and case study. *Int J Precis Eng Manuf Green Technol* 1(3):261–279
4. Fawcett SE, Waller MA (2014) Supply chain game changers – mega, nano, and virtual trends – and forces that impede supply chain design (i.e., building a winning team). *J Bus Logist* 35(3):157–164
5. Achillas C, Aidonis D, Iakovou E, Thymianidis M, Tzetzis D (2015) A methodological framework for the inclusion of modern additive manufacturing into the product portfolio of a focused factory. *J Manuf Syst* 37(1):328–339
6. Wohlers T, Caffrey T (2013) Additive manufacturing: going mainstream. *Manuf Eng* 151(6):67–73
7. Horn TJ, Harrysson OL (2012) Overview of current additive manufacturing technologies and selected applications. *Sci Prog* 95(3):255–282

8. Lopes da Silva JV (2013) 3D technologies and the new digital ecosystem: a Brazilian experience. In: Proceedings of the fifth international conference on management of emergent digital eco systems, ACM, Luxembourg, pp 278–284
9. Hopkinson N, Dickens P (2001) Rapid prototyping for direct manufacture. *Rapid Prototyp J* 7(4):197–202
10. Reeves P (2008) How rapid manufacturing could transform supply chains. *Supply Chain Quart* 2(4):32–336
11. Ruffo M, Hague R (2007) Cost estimation for rapid manufacturing simultaneous production of mixed components using laser sintering. *Proc Instit Mech Eng, Part B: J Eng Manuf* 221(11):1585–1591
12. Goodridge RD, Tuck CJ, Hague RJM (2012) Laser sintering of polyamides and other polymers. *Prog Mater Sci* 57(2):229–267
13. Ford S, Despeisse M (2016) Additive manufacturing and sustainability: an exploratory study of the advantages and challenges. *J Clean Prod* 137:1573–1587
14. Luthra S, Kumar V, Kumar S, Haleem A (2011) Barriers to implement green supply chain management in automobile industry using interpretive structural modeling technique: an indian perspective. *J IndustrEng Manag* 4(2):231–257
15. Haleem A, Sushil QMA, Kumar S (2012) Analysis of critical success factors of world-class manufacturing practices: an application of interpretative structural modeling and interpretative ranking process. *Prod Plan Contr* 23(10–11):722–734
16. Kumar S, Luthra S, Haleem A (2013) Customer involvement in greening the supply chain: an interpretive structural modeling methodology. *J Industr Eng Int* 9(1):1–13
17. Saxena JP, Sushil, Vrat P (1990) Impact of indirect relationships in classification of variables –A MICMAC analysis for energy conservation. *Syst Res* 7(4):245–253
18. Abbasi SA, Arya DS (2000) Environmental impact assessment: available techniques. Discovery Publishing House, Emerging Trends
19. Duperrin JC, Godet M (1973) Methode de Hierarchisation des Elements d'un Systeme, Rapport Economique du CEA, R-45-41, Paris
20. Kanungo S, Duda S, Srinivas Y (1999) A structured model for evaluating information systems effectiveness. *Syst Res Behav Sci* 16(6):495–518
21. Khan MI, Khan U, Haleem A (2014) Corporate social responsibility: modeling of critical factors using an integrated ISM and fuzzy-micmac approach. *Int J Global Bus Compet* 9(1):1–13. Print ISSN: 0973-4619. Online ISSN: 0976-1888
22. Khan U, Haleem A (2015) Improving to smart organization: an integrated ISM and Fuzzy-MICMAC modelling of barriers. *J Manuf Technol Manag* 26(6):807–829
23. Khan U, Haleem A (2012) Smart organizations: modeling of enablers using an integrated ISM and fuzzy-MICMAC approach. *Int J Intell Enterpr* 1(3/4):248–269
24. Vinodh S, Sundararaj G, Devadasan SR, Kuttalingam D, Rajanayagam D (2009) Agility through rapid prototyping technology in a manufacturing environment using a 3D printer. *J Manuf Technol Manag* 20(7):1023–1104
25. Holmström J, Partanen J, Tuomi J, Walter M (2010) Rapid manufacturing in the spare parts supply chain: alternative approaches to capacity deployment. *J Manuf Technol Manag* 21(6):687–697
26. Tuck C, Hague R, Burns N (2006) Rapid manufacturing: impact on supply chain methodologies and practice. *Int J Serv Oper Manag* 3(1):1–22
27. Roberson DA, Espalin D, Wicker RB (2013) 3D printer selection: a decision-making evaluation and ranking model. *Virtual Phys Prototyp* 8(3):201–212
28. Campbell RI, De Beer DJ, Pei E (2011) Additive manufacturing in South Africa: building on the foundations. *Rapid Prototyp J* 17(2):156–162
29. Petrovic V, Vicente Haro Gonzalez J, Jorda Ferrando O, Delgado Gordillo J, Ramon Blasco Puchades J, Portoles Grinan L (2011) Additive layered manufacturing: sectors of industrial application shown through case studies. *Int J Prod Res* 49(4):1061–1079
30. Liao S, Wu MJ, Huang CY, Kao YS, Lee TH (2014) Evaluating and enhancing three dimensional printing service providers for rapid prototyping using the DEMATEL based network process and VIKOR. *Math Prob Eng* 2014. Article ID 349348, 16pp



31. Rosen DW (2014) Research supporting principles for design for additive manufacturing: this paper provides a comprehensive review on current design principles and strategies for AM. *Virtual Phys Prototyp* 9(4):225–232
32. Liu P, Huang SH, Mokasdar A, Zhou H, Hou L (2014) The impact of additive manufacturing in the aircraft spare parts supply chain: supply chain operation reference (scor) model-based analysis. *Prod Plan Contr* 25(13–14):1169–1181
33. Kandasamy VWB (2007) Elementary fuzzy matrix, theory and fuzzy models for social scientists, pro quest information & learning, university of microfilm international, Copyright 2007 by Automaton
34. Tuck CJ, Hague RJ, Ruffo M, Ransley M, Adams P (2008) Rapid manufacturing facilitated customization. *Int J Comput Integr Manuf* 21(3):245–258
35. Eyers DR, Potter AT, Gosling J, Naim MM (2018) The flexibility of industrial additive manufacturing systems. *Int J Oper Prod Manag*
36. Dwivedi G, Srivastava SK, Srivastava RK (2017) Analysis of barriers to implement additive manufacturing technology in the Indian automotive sector. *Int J Phys Distrib Logist Manag* 47(10):972–991

# Evaluation of Emerging Smartphone Manufacturing Countries by Fuzzy MCDM



Dhruv Singh Rathore, Sachin Mann, Vaibhav Panchal, and M. S. Niranjana

## 1 Introduction

The increasing sensitivity of supply chains has led many companies to reduce their dependence on one source in current times. A need for alternate sourcing is at its peak amidst the US-China trade war [1]. For companies moving out, selecting the best alternative is a primary concern to ensure smooth operations. Companies must analyze these alternative countries to maximize profits.

Due to the rising labor cost, the US's trade tension with China, and the shift in the prioritization of consumer markets, big smartphone companies are stopping production in China and are starting to move out of the country.

Smartphone manufacturer giant, Samsung, has already shut down its manufacturing units in China and is looking for other Asian countries as alternatives. Apple is also encouraging its suppliers to move more than 30% of iPhone production in China. It is investing to expand in India. Other contract manufacturers are also setting up production units in Vietnam, Thailand, and Indonesia.

Companies usually consider a group of factors for deciding the country to set up their manufacturing hub. These factors can be government legislative and support, customer base, labor cost, infrastructure, Research and development funding, etc. These factors can help companies to compare different countries and choose the best option available according to their growth plans.

This has pressured vendors to consider other options, such as India, Taiwan, and Vietnam for setting up manufacturing hubs [2].

This study could provide an opportunity and learning for different countries on where they can focus to attract smartphone manufacturers to come to their country. For example, India is among one of the few developing countries in the world

---

D. S. Rathore (✉) · S. Mann · V. Panchal · M. S. Niranjana  
Department of Automobile Engineering, Delhi Technological University, Delhi 110042, India  
e-mail: [dhruvsinghrathore\\_2k17ae17@dtu.ac.in](mailto:dhruvsinghrathore_2k17ae17@dtu.ac.in)

which has the least labor cost. This could be an added advantage for India to attract smartphone manufacturers. Similarly, on the basis of other factors, countries can be ranked.

## 2 Literature Review

In this study, we will be deciding the best alternative South Asian country for manufacturing smartphones for the mobile phone companies, which were earlier manufacturing in China. We will be comparing and ranking among the three countries; India, Vietnam, and Taiwan, for the best option for setting up manufacturing hubs based on 10 factors.

Reasons for choosing these three countries are as follows:

- Taiwan has been excelling as a smart manufacturer because of its Government's incentives and rebates on taxes. Taiwan is the greatest manufacturer of semi-conductors and chips, which are essential parts for manufacturing smartphones [3].
- The Indian government is bringing out new incentive plans to bring in phone manufacturers and promoting schemes such as "Make in India".
- Vietnam has cheap resources such as water supply, electricity, and labor. Factors that have given Vietnam as the emerging smartphone manufacturing hub are competitive cost and better quality. Many companies and users favor Vietnamese components over Chinese components [4].

There are major factors based on which phone manufacturing companies can decide in which countries they need to set up their manufacturing unit for the maximum profit. Not only tangible, but intangible/subjective attributes, for example, large consumer base, physical infrastructure, R&D funding, etc. play an important role in deciding. Different experts from big smartphone companies have contrasting perceptions toward the ease of manufacturing phones on a large scale.

The challenge faced is in relationship with measuring the intangible factors that affect the setting up of manufacturing units in a country. The fuzzy set theory provides a way out from this problem and helps convert these intangible factors into quantitative values that can be compared with each other. These values that can help to conclude are regarded as lingual expressions. These characteristics of lingual expressions can be used in Fuzzy set theory to analyze the decision maker's preference structure. The subjective judgment of human beings offers ambiguity when measuring some attributes quantitatively. Fuzzy set theory helps in overcoming this issue.

Different evaluators view different linguistic variables, and conducting their evaluation in an uncertain fuzzy environment becomes crucial.

The research is segregated into two major portions; the primary portion constitutes the crucial aspects for the evaluation of factors that affect setting up a manufacturing hub and then the evaluation substructure and procedure are presented.

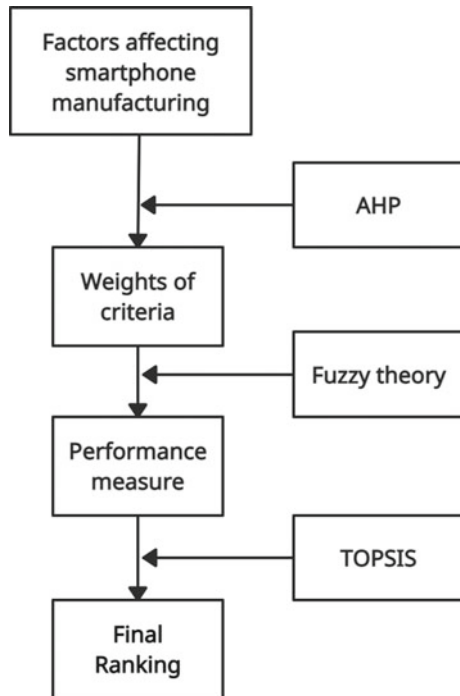
### 3 Structure for Evaluation of Smartphone Manufacturing Hubs

Steps used in the study of the evaluation process are shown in Fig. 1. Using literature review, we identify the major factors that can help us decide the preferred location of a manufacturing hub. Then the fuzzy set theory is applied to measure the performance related to each factor. Finally, the TOPSIS method is used to find the culminating unique ranking of the factors. Each step mentioned above is explained briefly in the following sections.

#### 3.1 Assessment Aspects and Standards

The main objective of the multiple criteria evaluation problem is to look into a variety of factors that can contribute to determining the rank of emerging hubs. While considering the factors, we must ensure that they have a direct impact on the company’s costs or operations. To ensure a comprehensive study, major as well as some relatively minor factors must be taken into account. These can be tax regulations

**Fig. 1** Multi-criteria decision making of smartphone manufacturing hubs



in the form of government support, operational aspects can be considered by looking into the availability of trained manpower, etc.

### ***3.2 Analytic Hierarchy Process***

AHP forms our basis in this research to calculate the corresponding significance of each factor related to smartphone manufacturing. By literature review, we were able to identify the ten most relevant and important factors, but some factors were observed to be of greater value as compared to others. Hence, more important factors must be assigned a greater percentage share while calculating the final ranking. This can be brought into account by allocating appropriate weightage to individual factors with the help of AHP [5]. Experts were asked to rate the importance of one factor over the other for each pair on a scale of 1–9. Where, 1 stands for similar significance, 3 stands for medium significance, and so on 9 means very high importance. If the factor comes out to be less important, then it is shown as a fraction like  $\frac{1}{3}$ ,  $\frac{1}{5}$ , till  $\frac{1}{9}$  for least important. For ten factors, the number of pairs formed was  $10(10-1)/2 = 45$ . A pair-wise matrix was formed listing all the pairs with their ratings. While comparing factors, there can be some contradicting or conflicting pairs which may lead to inconsistencies in the data. This method allows us to bring the inconsistencies down for the data to become consistent and okay to use for further purposes. This is done by introducing a consistency ratio whose permissible limit is 0.1. If the consistency ratio comes out to be less than 0.1, then the data is considered good to use. For calculating the consistency ratio, we normalize the pair-wise matrix to obtain the weights of each criterion. By multiplying each criterion with their respective weights, we get the weighted normalized matrix, This will help us in calculating the consistency index (C.I). On calculating C.I / Random Index (R.I = 1.49 for  $n = 10$  [6]), we finally get the consistency ratio, which should be less than 0.1. AHP takes into account the consistency factor which makes it an appropriate model for our research.

### ***3.3 Fuzzy Set Theory***

Terms used in daily life such as “Somewhat clear”, “probably so”, and “very low” are really common. The absence of fixed numeric values not only makes the process of quantitative analysis difficult but also brings in some inconsistency which brings questions about the accuracy of the results. A lot of research has been done in previous times to take into account this diffused range of answers into fixed numeric values so that meaning can be retained without disturbing the quantitative aspect of the study [7]. We will be facing the same problems; hence, using fuzzy set theory will take into account the linguistic terms as well as help in ranking with the help of TOPSIS. Its applications are explained in detail below:

**Fuzzy numbers** are the set of real numbers, which unlike real numbers have a connected set of possible values and these values have their individual weights. This weight is also known as the membership function. The variable “Government and legislative support” represents a linguistic variable for this study. Values like “moderate” can be taken by variable, the triangular fuzzy numbers (TFN)  $\mu_A \times (X) = (L, M, U)$  [8] within the scale range of 1–9 represents the above linguistic variable, and the officials can presuppose their unique range for the linguistic variable  $\mu_A(\text{very high}) = (7, 9, 9)$ . In accordance with the Likert scale, applying TFN gives the study a more versatile approach in the present scenario.

**Linguistic variable** gives us the means to convert human fuzziness into crisp numeric values to make meaningful interpretations. For instance, the linguistic variable is “Government and legislative support” in our study. It means the evaluation will be made by the official considering the legislative support and laws that can facilitate the smartphone manufacturing industry. The possible values for this variable could be: “very less”, “less”, “moderate”, “high”, and “very high” [9]. The officials were asked to fill out the survey and respond to the above possible values, and all these variables can be represented by using triangular membership functions in the range of 1–9. The range can be adjusted by the evaluator as it will not render the results.

### 3.4 TOPSIS

Hwang and Yoon were the first to propose TOPSIS in 1981 [10]. TOPSIS is a methodology to rank a given set of observations based on two mainly two factors: Distance from the positive and negative ideal solution. To find the distance, we must first find the ideal solutions, both positive and negative. Theoretically, the ideal solution consists of two parts namely: cost criteria and benefit criteria. From common logic, we know that the best solution will be to minimize cost factors and amplify the benefit factors, and the worst solution will be to amplify the cost factors and lessen the benefit factors. These best and worst solutions are named as positive ideal and negative ideal solutions. Ranking the countries with the help of TOPSIS will not just be based on FPIS or FNIS but on the relative similarity. When we take the relative similarity to an ideal solution, we can overcome the possibility of the same similarity to both solutions. While determining the final ranking, we will consider a closeness coefficient  $C_i^*$  that will assign rank one to the country that is closest to FPIS and farthest from FNIS. Similarly, the last rank will be assigned to the country that is farthest from FPIS and closest to FNIS. To compute the ranking, the followed procedure is proposed:

**Normalizing fuzzy decision matrix:** Single matrix entries are merged using a normalized fuzzy decision matrix. The initial decision matrix can be assumed as [11]

$$\mathbf{X} = (X_{ij}) \forall i, j, \tag{1}$$

where  $X_{ij}$  is the performance of country  $i$  to factor  $j$ .

**Creating the weighted normalized fuzzy decision matrix:** The weighted normalized performance matrix according to TOPSIS can be defined as [12]

$$V = (V_{ij})\forall i, j, \tag{2}$$

$$V_{ij} = w_j \times r_{ij}\forall i, j, \tag{3}$$

where  $w_j$  is the weight of factor  $j$ .

**Calculating fuzzy positive ideal solution (FPIS) and fuzzy negative ideal solution (FNIS)**

These equations are used to calculate ideal solutions [13]:

$$A^* = \{(max V_{ij}|j \in J), (min V_{ij}|j \in J'), i = 1, 2, \dots, m\}, \tag{4}$$

$$A^- = \{(min V_{ij}|j \in J), (min V_{ij}|j \in J'), i = 1, 2, \dots, m\}, \tag{5}$$

where

$$j = \{j = 1, 2, \dots, n | j \text{ belongs to benefit criteria}\},$$

$$j' = \{j = 1, 2, \dots, n | j \text{ belongs to cost criteria}\}.$$

**Calculating the distance between FPIS and FNIS for each country [13]**

$$S_i^* = \sqrt{\sum_{j=1}^n (V_{ij} - V_j^*)^2} i = 1, 2, \dots, m, \tag{6}$$

$$S_i^- = \sqrt{\sum_{j=1}^n (V_{ij} - V_j^-)^2} i = 1, 2, \dots, m. \tag{7}$$

**Calculating the closeness coefficient  $CC_i$**

$$CC_i = \frac{S_i^-}{S_i^* + S_i^-} i = 1, 2, \dots, m, \tag{8}$$

where  $0 \leq CC_i \leq 1$ , that is, a country  $i$  is closer to  $A^*$  as  $CC_i$  approaches to 1 [14].

**Ranking the countries:** Rank one will be given to the country with the highest value of  $CC_i$ , and the lowest rank will be given to the country with the lowest  $CC_i$  [15].

## 4 Empirical Study of Emerging Smartphone Manufacturing Hubs

### 4.1 Survey

While conducting the survey, 400 polls were sent to industry experts in the field of smartphone manufacturing from 10 different global companies. The reason for choosing these respondents was their professional background and knowledge about the challenges a company can face while expanding its operations. Most of the respondents were at managerial level or higher positions in manufacturing-related departments like product planning, supply chain management, etc. Out of the 400 questionnaires sent, 187 responded which is a 46% response rate. The average work experience of the respondents was 5.4 years in the industry [16, 17].

To determine the corresponding importance of each factor and the performance of selected countries concerning each factor, two questionnaires were sent to experts. For finding the relative importance (weights) of each factor, AHP was used. For measuring the performance of countries w.r.t each factor, linguistic expressions like “very less”, “less”, “moderate”, “high”, and “very high” were asked in the questionnaire. TMF on a scale of 1–9 is used to convert the linguistic terms into fuzzy numbers [18–20].

The three most suitable alternatives for China were identified by literature review namely India, Taiwan, and Vietnam. The reasons for picking up these countries are the majority population lying in the young age group, low labor costs, policy environment in favor of manufacturing, quality of infrastructure, qualification of engineers, economic growth, and a broad internal consumer base.

### 4.2 Weights of Each Factor

The following flowchart shows the relative weights of each factor associated with the growth of smartphone manufacturing; this was found using AHP [5]. The weights for each factor are Large consumer base (0.27), Government and legislative support (0.04), Trained manpower (0.14), Foreign direct investment (0.02), R&D funding (0.09), Physical Infrastructure (0.07), Product design (0.05), Global competitiveness (0.018), Supplier network (0.09), and Customer willingness to pay (0.18). Looking at the weights of each factor, we can see that companies prefer to manufacture where a large consumer base with high purchasing power already exists (Fig. 2).

As seen from the data, companies prefer countries with low government interference, an already existing consumer base, and trained manpower over product design and global competitiveness. This becomes especially important when we look at countries with very high taxes and too many government curbs. A large consumer base will ensure that companies can maximize their profits by avoiding import duties as they are manufacturing domestically.



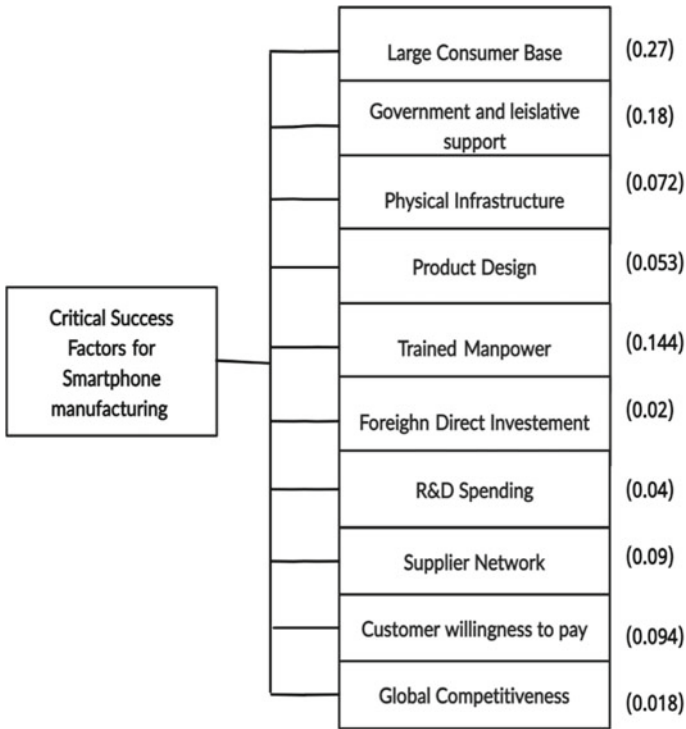


Fig. 2 Weights for ten critical factors for smartphone manufacturing

### 4.3 Performance of Countries w.r.t Factors

By employing the weights calculated using the AHP, the performance of the three south Asian countries w.r.t each factor is measured in terms of fuzzy numbers using a triangular membership function [8]. The below-mentioned table gives the output (Table 1).

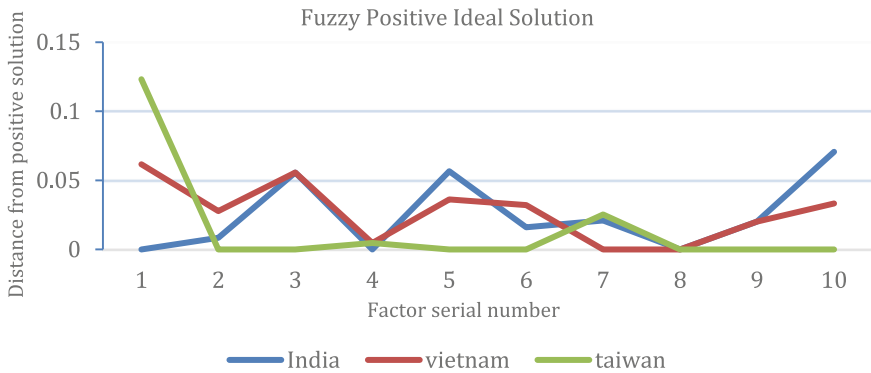
In general, from the above table, we can see that India performs better when we take volume-based factors like consumer base and FDI. Whereas Taiwan succeeds in factors that are more business-oriented, for example, government support and infrastructure [3] (Figs. 3 and 4).

### 4.4 Final Ranking

The final ranking was found by combining all the methods used for the study, and in the end, TOPSIS [10] gives out the closeness coefficient [14] from the positive and negative ideal solutions which are used to obtain the result (Table 2).

**Table 1** Fuzzy performance measures of countries

S.No	Critical success factors	India	Vietnam	Taiwan
1	Large consumer base	(15.4, 21.56, 27.72)	(9.24, 15.4, 21.56)	(3.08, 9.24, 15.4)
2	R&D funding	(2.56, 3.59, 4.61)	(0.51, 1.54, 2.56)	(3.59, 4.61, 4.61)
3	Trained manpower	(4.82, 8.03, 11.24)	(4.82, 8.03, 11.24)	(11.24, 14.45, 14.45)
4	Foreign direct investment	(1.15, 1.62, 2.08)	(0.69, 1.15, 1.62)	(0.69, 1.15, 1.62)
5	Customer willingness to pay	(1.04, 3.13, 5.22)	(3.13, 5.22, 7.31)	(7.31, 9.4, 9.4)
6	Physical infrastructure	(2.41, 4.01, 5.62)	(0.8, 2.41, 4.01)	(4.01, 5.62, 7.22)
7	Product design	(1.77, 1.06, 0.76)	(5.3, 1.77, 1.06)	(1.06, 0.76, 0.59)
8	Global competitiveness	(0.78, 1.31, 1.83)	(0.78, 1.31, 1.83)	(0.78, 1.31, 1.83)
9	Supplier network	(3.02, 5.03, 7.04)	(3.02, 5.03, 7.04)	(5.03, 7.04, 9.05)
10	Government and legislative support	(6.11, 10.19, 14.26)	(10.19, 14.26, 18.34)	(14.26, 18.34, 18.34)

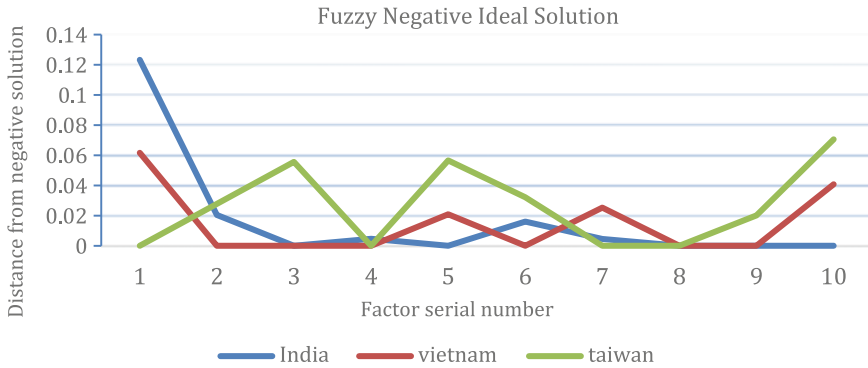


**Fig. 3** FPIS

### 5 Conclusion

There are a lot of factors that companies look into before setting up manufacturing plants in different countries because of the large amount of capital investment that is needed. There are obvious cost-related reasons but apart from that, the geo-political factors also have a significant impact in deciding the best-suited alternative.

For covering all the aspects, we employ procedures to find the most relevant factors for smartphone manufacturing and capture expert opinions for three smartphone manufacturing hubs. The steps in the process of ranking are as follows: (1) Identify



**Fig. 4** FNIS

**Table 2** Final ranking of countries

Country	S*	S <sup>-</sup>	C <sub>i</sub> <sup>*</sup>	Rank
India	0.248222663	0.168894839	0.404909499	2
Vietnam	0.271277898	0.148561781	0.353853597	3
Taiwan	0.153124447	0.262771395	0.631820202	1

the critical success factors for smartphone manufacturing; (2) Determine the relative gravity (weights) of each factor by using AHP; (3) Convert the linguistic terms used in the survey into fuzzy numbers using triangular membership function; (4) Using TOPSIS, the closeness coefficient from the ideal solution was found to give the final ranking.

- The most important findings from the data cover many perspectives of the experts. Companies don't only look at the cost factors related to manufacturing but the government volatility and political stability of the countries also came out to be of significant importance.
- For countries that wish to lure foreign companies for manufacturing must not only focus on cost incentives but also internally ensure they have a good supplier network, a population that can provide trained manpower, and become customers for the same company.
- The final rankings show that Taiwan being a small country with a very less population came out to be the most preferred destination for smartphone manufacturing companies followed by India and finally Vietnam. The critical reason for Taiwan's success came out of its government support, trained manpower, and physical infrastructure.

## References

1. Liu T, Woo WT (2018) Understanding the US-China trade war. *China Econ J* 11(3):319–340
2. Jena J, Pradhan R, Shankar R (2016) A comparative study of indian smartphone manufacturing ecosystem with global best practices for strategic insights. *Global J Enterpr Inf Syst* 8(4):1–10
3. Chen YF, Chen BC, Chen WY, Tsai CW, Lin WH (2012) Optimal strategy for the smartphone industry in Taiwan: HTC case study. *Int J Intell Inf Technol (IJIIT)* 8(4):62–79
4. Cao Q (2014) Case company software potential in the second hand smartphone market in the Philippines, Taiwan, and Vietnam
5. Saaty TL (2008) Decision making with the analytic hierarchy process. *Int J Serv Sci* 1(1):83–98
6. Lin ZC, Yang CB (1996) Evaluation of machine selection by the AHP method. *J Mater Process Technol* 57(3–4):253–258
7. Zimmermann HJ (2011) *Fuzzy set theory—and its applications*. Springer Science & Business Media
8. Pedrycz W (1994) Why triangular membership functions? *Fuzzy Sets Syst* 64(1):21–30
9. Hellmann M (2001) *Fuzzy logic introduction*. Université de Rennes, 1
10. Lai YJ, Liu TY, Hwang CL (1994) Topsis for MODM. *Eur J Oper Res* 76(3):486–500
11. Seghier ML, Ramlackhansingh A, Crinion J, Leff AP, Price CJ (2008) Lesion identification using unified segmentation-normalisation models and fuzzy clustering. *Neuroimage* 41(4):1253–1266
12. Ashtiani B, Haghhighrad F, Makui A, ali Montazer, G. (2009) Extension of fuzzy TOPSIS method based on interval-valued fuzzy sets. *Appl Soft Comput* 9(2):457–461
13. Li DF, Yang JB (2004) Fuzzy linear programming technique for multiattribute group decision making in fuzzy environments. *Inf Sci* 158:263–275
14. Li DF (2011) Closeness coefficient based nonlinear programming method for interval-valued intuitionistic fuzzy multiattribute decision making with incomplete preference information. *Appl Soft Comput* 11(4):3402–3418
15. Buckley JJ (1985) Ranking alternatives using fuzzy numbers. *Fuzzy Sets Syst* 15(1):21–31
16. Ahmed S (2012) Supply chain lessons for the new millenium: a case of micromax informatics. *Integr Rev: A J Manag* 5(2)
17. Wang Y, Wang J, Wang X (2020) COVID-19, supply chain disruption and China's hog market: a dynamic analysis. *China Agr Econ Rev*
18. Hutchinson MO (1998) The use of fuzzy logic in business decision-making. *Deriv Q* 4:53–66
19. Dittrich K, Duysters G (2007) Networking as a means to strategy change: the case of open innovation in mobile telephony. *J Prod Innov Manag* 24(6):510–521
20. Tang L, Murphree M, Breznitz D (2016) Structured uncertainty: a pilot study on innovation in China's mobile phone handset industry. *J Technol Transf* 41(5):1168–1194

# Electric Vehicles Challenges, Opportunities, and Future Scope: The Recent Review



Ranjan Verma, S. K. Srivastava, and Aishvarya Narain

## 1 Introduction

Supreme uses of fossil fuels in the production of electricity and various objectives like automotive industries result in a decrement in reserves of fossil fuels, consistently. Thus, relevant alternatives like renewable resources are demanded most widely. For now, the replacement of fossil fuel with electricity by automotive industries as modern technology for vehicles [1]. Therefore, electrical energy is used as a driving tool for modern vehicles as a better option to overcome conventional drawbacks. Electric Vehicles were used at the beginning of the twentieth century and taken into consideration over the decades, mainly in the U.S. [2]. A few days later, even though the status of EVs in the market was enough superior, the procedure terminated and there was dramatically increment in the use of conventional vehicles [3]. Lower acceleration, higher cost, and short driving ranges of electric vehicles were some extent reasons for the reduction of EVs and promoted the development of the conventional vehicle [4]. Making use of electric vehicle planning took up to overcome a part of challenges in major automotive industries [5].

## 2 Market Structure

On the authority of demands and regulations, several market frameworks are planned in various countries. In case, independent system operators (ISOs), utility companies, and generation companies create a market framework in the United States. The owner of the market framework is an independent system operator in the US. According

---

R. Verma (✉) · S. K. Srivastava · A. Narain  
Electrical Engineering Department, Madan Mohan Malaviya University of Technology,  
Gorakhpur, India

to Europe, there is an almost similar market framework, but the only difference is the independent market operator [6]. Different countries having different market structures can be found in [7, 8]. In Europe, the classes of market structure depend on mandatory provisions, bilateral market, hybrid market, organized market, free offer, mandatory offer, and mandatory provisions with eliminating reservation. For instance, transmission system operators (TSOs) and a grid customer negotiate a bond for a price system and proposed service in a market that is bilateral [9].

There is a scheme for market framework at the distribution level for services like voltage regulation and congestion management by controlled operation of active power [10]. Yet, there is no scheme on segments such as load shifting, valley filling, and peak shaving. Till now, reactive power supports have not been discussed regarding commercial markets, the evaluation of economic incentive on active power support only. A lot of work conveys voltage regulation services and loading by modulation of active energy of electric vehicles. Yet, such services might not be followed by some of the EVs users by the reason of delay in the process of charging, which results in their consolation [11]. In respect of reactive power support, the use of EVs causes voltage regulation due to the injection of reactive power into the grid, it may be in high potential. The charging phenomena of electric vehicles are not influenced by reactive power, and this is one of the causes that continues users' consolation.

The market layout is a dormant concern for advanced studies regarding EV-Distribution System Service as long as acquired services from the different groups are not being allowed by nearly all of the Distribution system operators, yet [11]. Active and reactive electric vehicle distribution system services are enabled by the design of the recent markets.

### 3 Economic Aspects

Various researches concern on EV strategy orderly to show voltage and loading issues, eliminating the features of economic aspects, for example, the interest for dispensing resources to the Distribution System Operators (DSO). One of the viable causes might be that those analyses are mainly based on the regulation scheme, socio-economic, and environmental situations of different countries. Although, many kinds of research concentrated on strategy development, method of working, and algorithm for EV charging strategy while profitable aspects for EV-DSS are disregarded. Defining the price signal concerning the economic angle of EV-DSS is the major problem, ensuring results satisfy every stakeholder.

In Denmark, as per results of simulation executed in [12] employing actual distribution system, customers of EVs may not get sufficient profit per annum for imparting assistance to the distribution system operators, surveying single charging phenomena per EVs per solar day. Regarding the DSOs, evaluation of profit is not straightforward to compute as different groups participated in the retail market of electricity with analogous to revenue distribution. For instance, in Denmark, the injection of reactive power into the grid is abled by chargers of EVs [13]. Therefore, many kinds

of research on such a point are strengthened for undertaking to answer the different question which is still disputed. Estimation of economic containing aspects like possible remuneration strategies for service providers and benefit analysis for all stakeholders are still open for further analysis.

## 4 Reliability Aspects

As demands for electric vehicles increase in the market, car manufacturers have remodeled their plans and policy. Reliability assessment is one of the major unsympathetic issues regarding electric vehicles, which is classified into two sub-division, i.e., reliability appraisal of recent electrical network with EVs and reliability appraisal of the internal structure of electrical vehicles [14]. The reliability appraisal of the intramural structure of EVs is criticized in this paper. Manufacturer's, seller's, and customer's perspectives to be included for the estimation of the reliability concept. Important points which are mentioned above regarding reliability assessment play a vital role in setting up an lifetime operation of electric vehicle's integrant containing electronics converter, motor drives, and battery pack [20]. Nowadays, malfunctioning, breakdown of electrical components, and imperfection in battery capacity for nearly 54% of all vehicle failures are the most dominating parameter regarding reliability conception for electric vehicles integrant [15, 16]. Accordingly, the safety of the electrical unit of EVs and improvement in reliability are required by the market. Safety and reliability enhancement will be challenging aspects due to various sub-elements of EVs. The following elements should be taken into consideration to a superior appraisal of reliability:

- 4.1 To display the elements of a system, parametric models were used in the traditional methods [17]. Even so, the theory that reliability features attend to probability distributions is commonly disregarded. Therefore, the operation may not be assured.
- 4.2 The conclusive decline logic system was implemented, which neglects the unwanted gates in traditional reliability methods [18]. Of course, environmental conditions might cause hidden failure mode in the EVs integrant model resulting in the logic gate being fairly noisy. In this way, the results of failure logical structure set off unpredictable.
- 4.3 Use of traditional techniques to evaluate the quotient's reliability applying the constant logical composition described by professionals [19].

## 5 Charging Infrastructure

As stated by the International Council for Clean Transportation, requirements of the advanced charging station and enhancement in the workplace should be implemented by 400 % in the upcoming five years. In this way, projections of EVs in large

numbers will be on the road. The requirement for charging stations is increasing in large proportionally because of the higher population as well as positive results of EV adoption. In Los Angeles, 35000 additional chargers will be demanded which is seven times that were installed in 2017. City leaders sacrifice the parking zone of a conventional vehicle to develop the charging infrastructure for EVs. 2/3 of U.S. mayors are agreed according to a survey of Boston University regarding the approved proposals. The initial cost is a very challenging task about the infrastructure. According to the Rocky Mountain Institute, the installation cost of a charger is nearly three to five times the cost of chargers themselves. Various issues can be focused on during installation including building constructions. The research by Pacific gas and electric observed that installing charging capacity throughout the construction may minimize the fare per EVs charging area by approximately 75%. Developers have their intention over such an issue and guidelines for comprising charging ability in high locality area and merchandise are involved in assigned modification to the International Energy Conservation Code.

## 6 Battery Technology

Lithium-ion battery technology incorporates a group of chemistry that commissions different types of combinations using anode and cathode material. The most outstanding technology for electric vehicle applications is lithium-nickel-cobalt-aluminum (NCA), lithium-nickel-manganese-cobalt (NMC), lithium-manganese spinel (LMO), lithium titanate (LTO), and Lithium-iron phosphate (LFP). Lithium-ion battery technology can be compared along six dimensions as shown in Fig. 1, i.e., safety, performance, life span, cost, specific power, and specific energy. Still now, the cell has not the technology to win all six parameters simultaneously. Some of them may be high and some parameters may be small. From a business point of view, higher cost remains a crucial issue.

### 6.1 Cathode Materials

- **Lithium-Iron-Phosphate (LFP):** The cost of raw material is less in the manufacturing of cathode using lithium with a large amount of phosphorous and iron. The cell is costly in terms of cost/kWh because of lower capacity as well as lower voltage inherently.
- **Lithium-Nickel-Cobalt-Aluminum oxide (NCA):** The material used for the manufacturing of cathode has higher energy. Nowadays, the main focus is to enhance the energy density using a higher content of nickel as well as minimizing the usage of cobalt to lower down the cost/kWh. Tesla uses NCA most widely.
- **Lithium-Nickel-Cobalt-Manganese Oxide (NCM):** The content of nickel, cobalt, and manganese in equal proportion is beneficial for excessive power



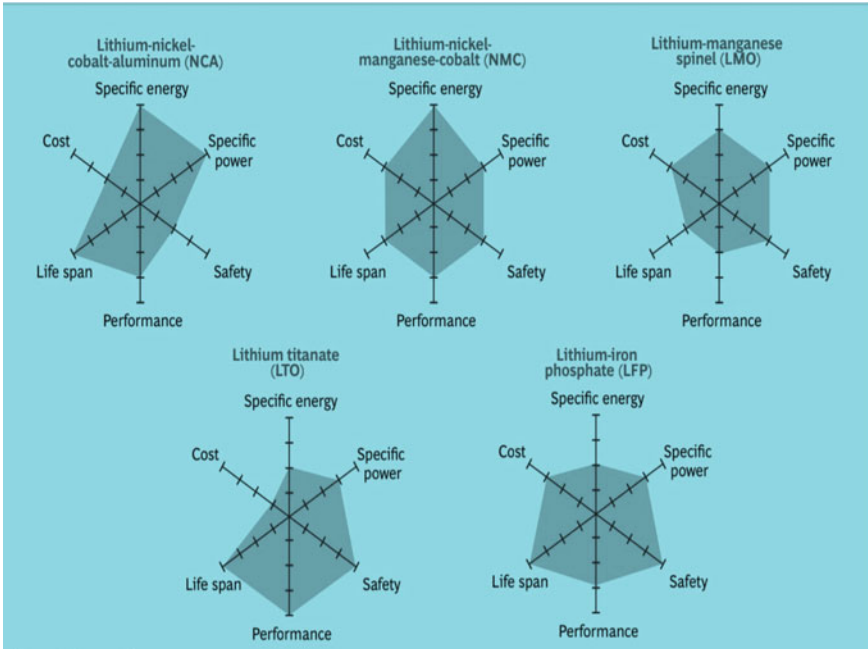


Fig. 1 Tradeoff among the five primary lithium-ion battery technologies

demands. The content of nickel is kept higher to enhance the energy density and at the same time reduce the dependency on cobalt. Nowadays, the better option for cathode materials is nickel, cobalt, and manganese with lithium in the production of all EVs.

- **Lithium-Manganese Oxide (LMO):** LMO has similar property as LFP because it may also provide power in a large amount. While there is a lack of energy density. Lower stability is the disadvantage of such a cathode.
- **Lithium-Cobalt Oxide (LCO):** The cells have larger volumetric energy density. While power density, as well as cyclic capability, is quite low using LCO. The cost will be a larger issue if the cathode is mainly made of cobalt.

## 6.2 Anode Materials

The selection of anode is mainly based on carbon because it is cheaper and has higher energy ability. But they have less voltage v/s lithium ions. Nowadays, the popular technology regarding anode material is based on carbon. It may be altered with innovative ideas including fresh lithium and fresh silica anode. The charging phenomena of anode containing lithium titanate oxide will be extremely fast. Therefore, the cells

can show a full charge in nearly five minutes. The initial cost is quite higher. Also, they have a low energy capacity.

## 7 Service and Maintenance Support

Even if, electric vehicles have known for not so great maintenance and also not to need so much repair. Still, it is important to find professional mechanics in the required field. Woefully, more than 90% of mechanics are not chartered to work on electric vehicles. On the other hand, the remaining of them work for dealerships. Even if a large number of hybrid vehicles are available in the market, the requisite maintenance regimes are similar to conventional gas-powered vehicles. It may explain that for persons who have been certified for working on hybrid vehicles, it may not necessary to know about every single-electric model. Woefully, there is a lack of maintenance support and infrastructure (charging station) for electric vehicles but it will be demanded more in the future. Electric vehicle owners have a few options for professional mechanics. Greatfully, electric vehicle owners need not search for their mechanics because their vehicles have lesser fluid (such as transmission fluid and oil) and also have limited moving parts.

## 8 Future Energy Consumption

Here, analysis in detail has been done to predict energy utilization in the future if the automotive is electrified. If the charging phenomena would be taken place, then that will smash electrical system infrastructure. Governments have a proposal with aim of 20–30% of EVs in the market that replies huge energy utilization would be needed. The analysis is performed in Table 1 considering battery capacity and Wh/km. The available data describes the mean of the different classes by a different manufacturer in the market. Scenarios of 20%, 30%, and 100% are grabbed by observing the different extent of evolution regarding EV. The average distance traveled by two-wheeler is 20 km/day, three-wheeler travels 80 km/day, four-wheeler travels 100 km/day while the commercial vehicle travels 250 km/day are taken for consideration [21].

**Table 1** Different types of vehicles and their battery specifications

Type	Battery(kWh)	Range(km)	Wh/km
Commercial	32	156	195
Four-wheeler	32	156	195
Three-wheeler	1.1	85	13
Two-wheeler	1.2	70	18

Energy utilization per day for different percentages of EVs is discussed in Table 2. It may be concluded that energy utilization per annum is 14TWh/year for 20%, 22TWh/year for 30%, and 75TWh/year for 100% EVs use.

## 9 Electric Vehicle Grid Integration and Future Development Trend

Electrification in the transport sector has considerably obstructed the traditional business model of the electrical system. In general, EVs have led both merits and demerits for the distribution grid including several challenges. The distribution grid can be influenced by the following factor such as load profile, voltage and frequency imbalance, stability, and harmonic injection due to excessive integration of electric vehicles. While excessive penetration may lead to issues like power regulation and power quality [22]. EVs can work as electrical load (G2V), working as an energy source for other EVs (V2V), energy storage system for buildings (V2B), and energy storage system for the grid (V2G), which differs in function from transportation tools. Various technologies are introduced within the automobile sector which results in growth and effectiveness toward the use of the distribution grid. Wireless Power Transfer (WTP), autonomous driving, and connected mobility (CM) come under modern technologies and will be revolutionized in the future. The link between vehicle to vehicle, vehicle to the passenger, vehicle to a traffic signal, etc. such an idea represents the concept of connected mobility. EVs may take part in the growth of energy internet technology [23]. The concept of EI represents the energy conversion of cooling and heating using chillers and boilers to organize the definite power, gas, transportation, and thermal system in a unique policy [24].

## 10 Conclusion

This paper presents a review of some recent researches concentrating on future scope and challenging aspects regarding electric vehicles. Some modifications would be required in the market structure like different countries should have some similarity index to operate in a parallel manner. Organizations may require some changes in their plan and policies so that users get motivated toward EVs. Advance infrastructures like flash Charging stations, battery swapping systems, and qualified mechanics in large numbers are still demanded. Battery technology that can be utilized using six dimensions to optimize the performance is discussed. Also, the description of the reliability concept and prediction of future energy consumption are explained above. However, further development and research are still needed to overcome the various problems regarding the electric vehicle.

**Table 2** Energy utilization per day for different percentages of EVs

Type	Outline of 20% EV in 2030			Outline of 30% EV in 2030			Outline of 100% EV in 2030		
	20% EV	kWh/km	kWh/day	30% EV	kWh/km	kWh/day	100% EV	kWh/km	kWh/day
Commercial	262203	51130	12782500	393304	76694	19173500	1311013	255648	63867000
Four-wheeler	1310189	255487	25548700	1965284	383230	38323000	6550945	1277434	127743400
Three-Wheeler	246762	3208	256640	370144	4812	384960	1233812	16040	1283200
Two-Wheeler	7921479	142587	2851740	11882218	213880	4277600	39607394	712933	114258660
Total	9740633	452412	41439580	14610950	678616	62159060	42152219	2262055	307152260

## References

1. Paska J (2007) Methodologies and tools for electric power system reliability assessment on HL I and HL II levels. In: 9th international conference electrical power quality and utilisation, Barcelona, October 9–11, pp 1–7
2. Deilami S, Masoum AS, Moses PS, Masoum MAS (2011) Real-time coordination of plug-in electric vehicle charging in smart grids to minimize power losses and improve voltage profile. *IEEE Trans Smart Grid* 2(3):456–467
3. Salmasi FR (2007) Control strategies for hybrid electric vehicles: evolution, classification, comparison, and future trends. *IEEE Trans Vehic Technol* 56(5):2393–2404
4. Teixeira ACR, Sodre JR (2018) Impacts of replacement of engine powered vehicles by electric vehicles on energy consumption and CO<sub>2</sub> emissions. *Transp Res Part D: Transp Environ* 59:375–384, Elsevier
5. Clerck Quentin D, van Lier T, Messagie M, Macharis C, Van Mierlo J, Vanhaverbeke L (2018) Total cost for society: a persona-based analysis of electric and conventional vehicles. *Transp Res Part D: Transp Environ* 64:90–110, Elsevier
6. Jensen TV, Pinson P (2017) RE-Europe a large-scale dataset for modeling a highly renewable European electricity system. *Sci Data* 4:170175
7. Rebours YG, Kirschen DS, Trotignon M, Rossignol S (2007) A survey of frequency and voltage control ancillary services—Part I: technical features. *IEEE Trans Power Syst* 22(1):350–357
8. Rebours YG, Kirschen DS, Trotignon M, Rossignol S (2007) A survey of frequency and voltage control ancillary services—Part II: economic features. *IEEE Trans Power Syst* 22(1):358–366
9. ENTSO-E M (2017) Survey on ancillary services procurement, balancing market design 2016. [https://www.entsoe.eu/Documents/Publications/Market%20Committee%20publications/WGAS\\_Survey\\_final\\_10](https://www.entsoe.eu/Documents/Publications/Market%20Committee%20publications/WGAS_Survey_final_10), 3
10. Zhang C, Ding Y, Christian Nordentoft N, Pinson P, Østergaard J (2014) FLECH: a Danish market solution for DSO congestion management through DER flexibility services. *J Modern Power Syst Clean Energy* 2(2):126–133
11. Knezović K, Marinelli M, Zecchino A, Bach Andersen P, Traeholt C (2017) Supporting involvement of electric vehicles in distribution grids: lowering the barriers for a proactive integration. *Energy* 134:458–468, Elsevier
12. Gadea A (2017) Technical investigation and economic assessment of DSO based services from electric vehicles. Technical University of Denmark, Risø, Roskilde, Denmark
13. Altug Karabiber O, Xydis G (2019) Electricity price forecasting in the Danish day-ahead market using the TBATS, ANN and ARIMA methods. *Energies* 12(5):928
14. Association internationale pour l'évaluation du rendement scolaire. *Global EV Outlook 2017. Two million and counting*. IEA (2017)
15. Suci G, Pasat A (2017) Challenges and opportunities for batteries of electric vehicles. In: 2017 10th international symposium on advanced topics in electrical engineering (ATEE), pp 113–117, IEEE, March
16. Wang H, Tao Z, Si N, Fu Y, Li T, Xiao H (2018) Failure analysis of cathode materials for energy storage batteries in overcharge test. In: MATEC web of conferences, Vol 142, p 01007. EDP Sciences
17. Zhong X, Zeng W, Qiu L (2013) A proactive system reliability analysis framework of electric vehicles. In: Proceedings of the 2nd international conference on computer science and electronics engineering. Atlantis Press, March
18. Hanke C, Hülsmann M, Fornahl D (2014) Socio-economic aspects of electric vehicles: a literature review. Evolutionary paths towards the mobility patterns of the future. Springer Berlin Heidelberg
19. Behjati H, Davoudi A (2012) Comparative reliability study of hybrid energy storage systems in hybrid electric vehicles. In: 2012 IEEE transportation electrification conference and expo (ITEC) IEEE, June, pp 1–6

20. Gandoman FH, Ahmadi A, Van den Bossche P, Van Mierlo J, Omar N, Nezhad AE, Mayet C (2019) Status and future perspectives of reliability assessment for electric vehicles. *Reliab Eng Syst Saf* 183. Elsevier
21. Jain A, Jariwala HR, Mhaskar U (2019) Feasibility analysis for the penetration of electric vehicles in india in future. In: 2019 international conference on computation of power, energy, information and communication (ICCPEIC), IEEE, March, pp 68–72
22. Das HS, Rahman MM, Li S, Tan CW (2020) Electric vehicles standards, charging infrastructure, and impact on grid integration: a technological review. *Renew Sustain Energy Rev* 12:109618, March
23. Cao J, Yang M (2013) Energy internet towards smart grid 2.0. *Networking and distributed computing (ICNDC)*, fourth international conference on IEEE
24. Zheng Y, Luo Y, Shi Y, Cai N, Jiao L, Guo D, lyu Y, Yin H (2017) Design of energy internet based on information internet. In: *IEEE conference on energy internet and energy system integration (EI2)*

# Robust Control Design of Active Suspension System for Quarter Car with Neural Network and Ziegler–Nichols Tuning Method



Danish Saifi and Pramod Kumar

## 1 Introduction

For a lengthy period of duration, suspension systems were in use, chiefly in automobile industry for a passenger car. Nowadays, researchers or scientists are trying to make good and smooth driving for the passenger. Active suspension is suitable for this type of condition. The most important technology used in large deluxe vehicles like Audi, BMW, etc. This system will be suitable for small car like a passenger car. [1, 2].

It also includes springs and dampers. The active suspensions are also attached with the vehicle chassis and tire of a car. The damper is used to absorb the vibrations that are come from road to tire. PID control is used in the control system to control various operations functions. PID control (Ziegler–Nichols tuning method) includes the parameters like proportional, integral, and derivative. It is denoted as P, I, and D [3, 4].

Hagan and Menhaj have presented the Levenberg–Marquardt algorithm for neural networks. LM algorithm was made to reduce the detriment Gauss–Newton method and gradient descent algorithm. Gauss–Newton method is become so much fast due to quadratic convergence properties. Also used for training the Neural Network is Gauss–Newton [5, 6].

There are millions of Neurons in the Neural Network. The neural network is an artificial neural network that is made up of artificial nodes. In short, it is made from real biological neurons. But researcher or scientists uses for determining artificial intelligence problems. In the research paper, I have used to control the active suspension system for various aspects like overshooting, steady-state error and resting time, etc. [7, 8].

---

D. Saifi (✉) · P. Kumar

Department of Mechanical Engineering, Galgotias University, Greater Noida, Uttar Pradesh 203201, India

## 2 Mathematical' Model for Quarter Car

In the above figure, this system is also known as the 2 Degree of freedom system. It has the Damper which is Denoted by “D”, Spring which is denoted by “K”, and Tire. It has two masses unsprung and sprung masses respectively. Sprung mass is known as Mass of Car body, and unsprung mass is knows as suspension mass. Sprung mass is attached with mass of car body and unsprung is also attached with suspension mass.

“X” shows the car body’s position, and “y” shows the suspension mass’s position. “R” shows the position of the Road (Table 1).

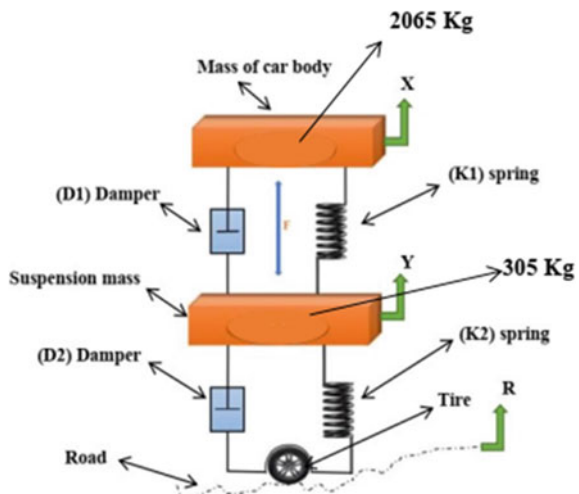
From the dynamic studied, the mathematical equation for Fig. 1 or Mathematical' model for Quarter car.

$$M_c \ddot{x} = -K_1(x - Y) - D_1(\dot{x} - \dot{Y}) + F \tag{1}$$

**Table 1** Data for quarter car model

	Symbols	Unit and data	Parameters
1	Mc	2065 kg	Mass of car body
2	Ms	305 kg	Suspension mass
3	K1	70,000 N/m	spring for suspension system
4	K2	500,000 N/m	Spring for wheel
5	D1	450 N-s/m	Damper for suspension system
6	D2	16,500 N-s/m	Damper for wheel
7	F	N	Control forces

**Fig. 1** Mathematics' model for Quarter car





$$M_s \ddot{y} = K_1(X - Y) + D_1(\dot{X} - \dot{Y}) - K_2(Y - R) - D_2(\dot{Y} - \dot{R}) - F \tag{2}$$

Taking Laplace on both sides in Eqs. 1 and 2,

All initial condition is zero.

We get,...

$$X(s)M_c \cdot s^2 + K_1 + D_1 \cdot s = Y(s)Z_1 + K_1 \cdot S + F(s) \tag{3}$$

$$Y(s)M_s \cdot s^2 + (K_1 + Z_2) + s(D_1 + D_2) = X(s)K_1 + D_1 \cdot S + RK_2 + D_2 \cdot s - F(s) \tag{4}$$

The following equation (Eqs. 3 and 4) will control the vertical movement of the Quarter car.

### 3 Control Systems

In the paper, two types of control systems have been used. First, PID control with Ziegler–Nichols tuning method, and second, RNN control system. RNN stands for Robust neural network. The Robust control design is on the optimal control problem. It will control the Quarter car. Due to this design, riders will feel comfortable.

#### 3.1 PID Control with Ziegler–Nichols Tuning Method

In this method, PID controller is also used with Ziegler–Nichols method. It is formulated by John G. Ziegler and Nathaniel B. Nichols. There are 3 variables used in the PID controller which is like this first of all Proportion that is Denoted by “P”, Second one integral “I” and last one Derivative “D”. This is done at the zero I and D parameter [9] (Fig. 2).

The equations can be used in the active suspension method for the Quatre car (Table 2).

$$u(t) = K_p[e(t) + 1/T_i \int_0^t [e(\tau) + T_d \cdot de(t)/dt] \tag{5}$$

$$u(s) = K_p[1 + 1/T_i \cdot s + T_d \cdot s]e(s) = K_p[T_d \cdot T_i \cdot s^2 + T_i \cdot s + 1/T_i \cdot s]e(s) \tag{6}$$

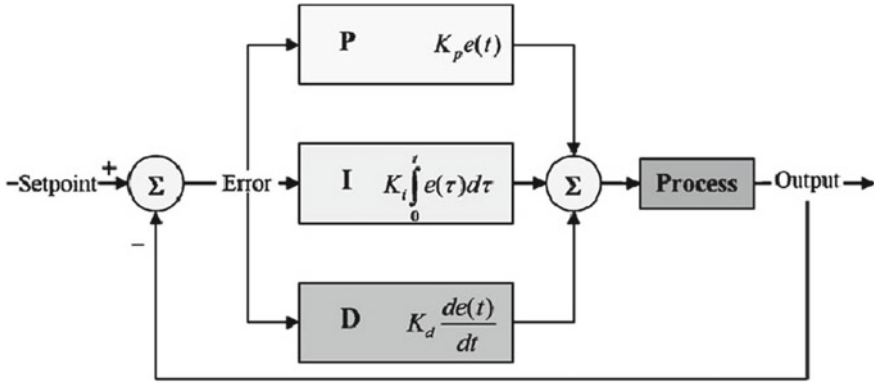


Fig. 2 PID control with Ziegler–Nichols tuning method

Table 2 Ziegler-Nichols method

Control type	$K_p$	$K_i$	$K_d$	$K_i$	$K_d$
P	$0.5 K_u$	–	–	–	–
PI	$0.45 K_u$	$0.80 T_u$	–	$0.54 K_u/T_u$	–
PD	$0.8 K_u$	–	$0.125 T_u$	–	$0.10 K_u/T_u$
Classic PID	$0.6 K_u$	$0.5 T_u$	$0.125 T_u$	$1.2 K_u/T_u$	$0.075 K_u/T_u$
Pessen integral rule	$0.7 K_u$	$0.4 T_u$	$0.15 T_u$	$1.75 K_u/T_u$	$0.105 K_u/T_u$
Some overshoot	$0.33 K_u$	$0.50 T_u$	$0.33 T_u$	$0.66 K_u/T_u$	$0.11 K_u/T_u$
No overshoot	$0.20 K_u$	$0.50 T_u$	$0.33 T_u$	$0.40 K_u/T_u$	$0.066 K_u/T_u$

### 4 RNN Control System

It stands for Recurrent neural network and whose work it is to keep all the parameters under control. It also contains a strong feedback controller and a predicting controller for the Neural Network. Equations for the control regime.

$$F(t) = F_{fb}(t) + F_{nn}(t), \tag{7}$$

where

$F_{fb}$  = Robust feedback controller force,

$F_{nn}$  = Neural Network predictive controller force.

### 4.1 Neural Network Predictive Controller

It has a two-step system classification and control design. It has a two-step method of recognizance and control formation. In the system identification, neural predictive control can train neural networks for forwarding dynamics (Fig. 3). Figure 4 shows ten layered feedforwards neural networks. Input and output for Neural Network are attached to prediction error to train neural network single [10].

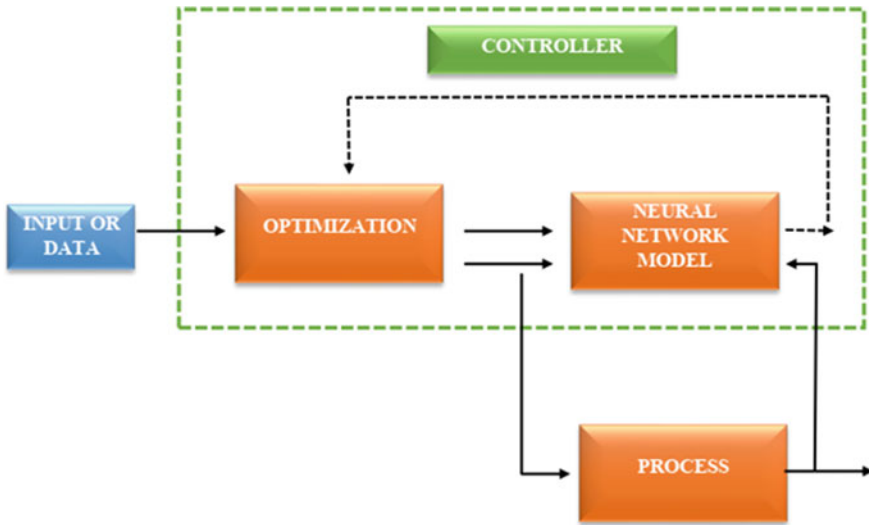


Fig. 3 Neural network predictive controller

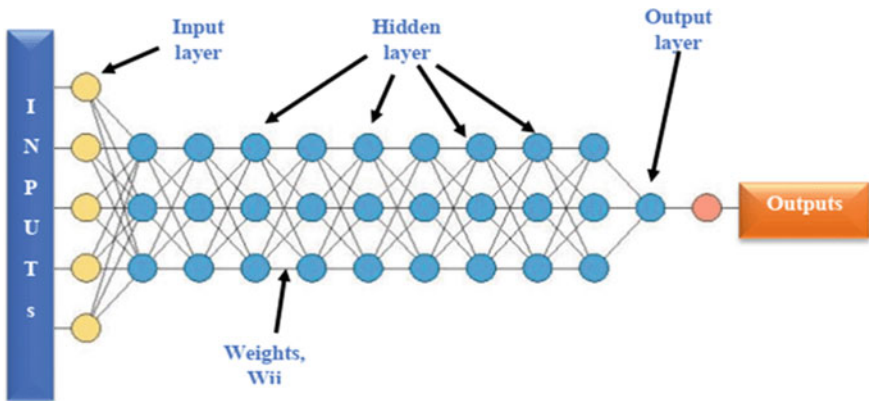


Fig. 4 Artificial neural networks

### 4.2 Levenberg–Marquardt (LM) Algorithm (Artificial Neural Networks):

Hagan and Menhaj have presented this algorithm for the Neural Network for training purposes. It was created to find the drawbacks of the Gauss–Newton method and gradient descent algorithm. By using this algorithm, the calculation becomes so fast.

This formulating was made to realign the weights of the Erratic weight circumstances for the neural network. This algorithm also has a feed-forward network.

An artificial neural network is important for a dynamic system or object. By using this help of this artificial neural network creates various tools or models. An artificial neural network is important for a dynamic system or object. An artificial neural network is the collection of nodes known as artificial neurons. And all artificial neurons are connected and pass information. The output of all neurons is computed by a non-linear function of the input data. These connections are known as the edge in neurology. Neurons and edge include weights. Weights learn self and also can decrease and increase indications. Neurons have thousands or millions of neurons layer in which data pass. It contains three-layer kinds, such as input, concealed layer, and output layer. With the help of we can calculate thousands of input data [4].

## 5 Results

From the closed-loop, we can understand concerning for (Fig. 5).

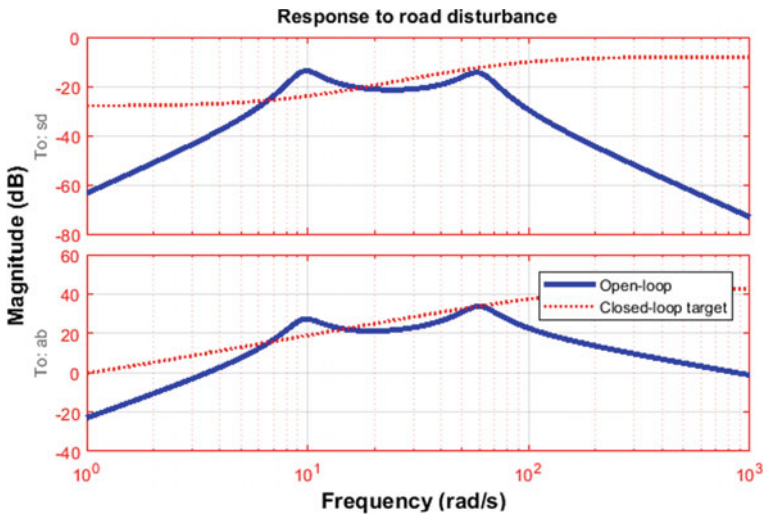
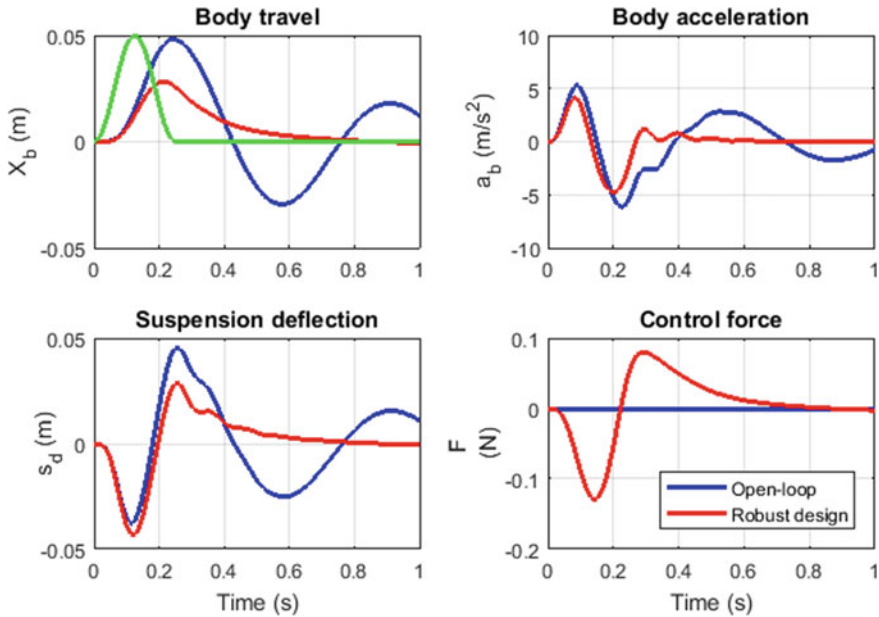


Fig. 5 Response to Road disturbance



**Fig. 6** Body acceleration, Body travel, Suspension deflection and control forces

- Road disturbance to deflection manes suspension deflection.
- Actuator and imaginary axis we can see disturbance below 10 rad/s.

We can see various graph (Fig. 6) that body travel, control force, body acceleration, and suspension deflection. It can also be used to create an active suspension system. This technique is known as  $H_\infty$  controllers (Fig. 7).

All results based on neural network. For the Robust control design, the figure shows body accelerating, body travel, suspension deflection, and robust design.

We can say that this active suspension system is in robust control design. Robust control design for better performance: 0.9056 (Fig. 8).

## 6 Conclusion

In the research paper, we can say that our design is a control design. It is also knowing as two degrees of free system. I have also used PID control with Ziegler–Nichols tuning method and neural network. This controller feedforward is attached to the neural network. By using this Robust control design, some factors controlled like peak response value (overshoot), settling time, rise time, and steady-state error. In the PI chart, the peak value response is 5% and settling time is 1.04 s, the rise time is 0 s and steady-state error is 0 s. We can say that this active suspension system is in robust control design.

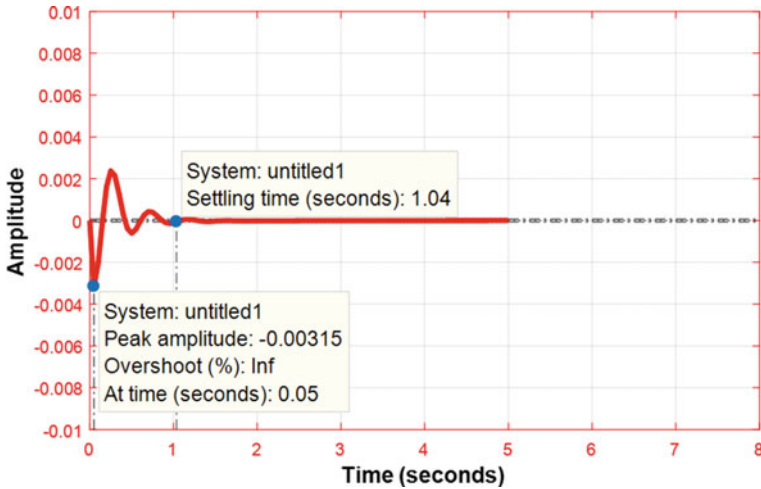


Fig. 7 Based on Levenberg–Marquardt (LM) algorithm

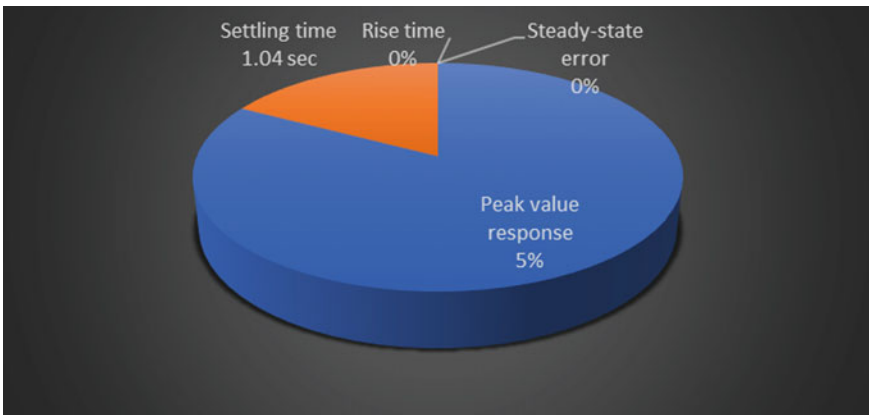


Fig. 8 Peak value response is 5% and settling time 1.04 s, the rise time 0 s and steady-state error 0 s

### References

1. Fateh MM, Alavi SS (2009) Impedance control of an active suspension system. *Mechatronics* 19(1):134–140
2. Lin J, Lian R-J (2010) Intelligent control of active suspension systems. *IEEE Trans Industr Electron* 58(2):618–628
3. Van der Sande TPJ et al (2013) Robust control of an electromagnetic active suspension system: simulations and measurements. *Mechatronics* 23(2):204–212
4. Yoshimura T et al (2001) Construction of an active suspension system of a quarter car model using the concept of sliding mode control. *J Sound Vib* 239(2):187–199

5. Biswas A et al (2009) Design of fractional-order  $PI\lambda D\mu$  controllers with an improved differential evolution. *Eng Appl Artif Intell* 22(2):343–350
6. Yin Tang C et al (2009) Research on suspension system based on genetic algorithm and neural network control. In: 2009 second international conference on intelligent computation technology and automation. Vol. 1. IEEE
7. Al-Holou N et al (2002) Sliding mode neural network inference fuzzy logic control for active suspension systems. *IEEE Trans Fuzzy Syst* 10(2):234–246
8. Liu YJ et al (2018) An adaptive neural network controller for active suspension systems with hydraulic actuator. *IEEE Trans Syst Man Cybern Syst* 50(12): 5351–5360
9. Hassan F, Zolotas AC, Smith T (2017) Optimized Ziegler-Nichols based PID control design for tilt suspensions. *J Eng Sci Technol Rev* 10(5):17–24
10. Moradi SM, Akbari A, Mirzaei M (2019) An offline LMI-based robust model predictive control of vehicle active suspension system with parameter uncertainty. *Trans Inst Meas Control* 41(6):1699–1711
11. Eski I, Yıldırım Ş (2009) Vibration control of vehicle active suspension system using a new robust neural network control system. *Simul Model Pract Theory* 17(5):778–793
12. Fayyad SM (2012) Constructing control system for active suspension system. *Contemp Eng Sci* 5(4):189–200
13. Gao H, Sun W, Shi P (2009) Robust sampled-data  $H_{\infty}$  control for vehicle active suspension systems. *IEEE Trans Control Syst Technol* 18(1):238–245
14. Gysen BLJ et al (2009) Active electromagnetic suspension system for improved vehicle dynamics. *IEEE Trans Vehic Technol* 59(3):1156–1163
15. Gysen BLJ et al (2011) Efficiency of a regenerative direct-drive electromagnetic active suspension. *IEEE Trans Vehic Technol* 60(4):1384–1393
16. Ikenaga S et al (2000) Active suspension control of ground vehicle based on a full-vehicle model. In: Proceedings of the 2000 American control conference. ACC (IEEE Cat. No. 00CH36334). Vol 6. IEEE
17. Kim C, Ro PI (1998) A sliding mode controller for vehicle active suspension systems with non-linearities. *Proc Instit Mech Eng Part D: J Automob Eng* 212(2):79–92
18. Kumar MS (2008) Development of active suspension system for automobiles using PID controller
19. Priyandoko G, Mailah M, Jamaluddin H (2009) Vehicle active suspension system using skyhook adaptive neuro active force control. *Mech Syst Signal Process* 23(3):855–868
20. Rao MVC, Prahlad V (1997) A tunable fuzzy logic controller for vehicle-active suspension systems. *Fuzzy Sets Syst* 85(1):11–21
21. Sam YM, Osman JHS, Ghani MRA (2004) A class of proportional-integral sliding mode control with application to active suspension system. *Syst Contr Lett* 51(3–4):217–223
22. Suda Y, Nakadai S, Nakano K (1998) Hybrid suspension system with skyhook control and energy regeneration (development of self-powered active suspension). *Veh Syst Dyn* 29(S1):619–634
23. Sun W, Gao H, Kaynak O (2010) Finite Frequency  $H_{\infty}$  Control for Vehicle Active Suspension Systems. *IEEE Trans Control Syst Technol* 19(2):416–422
24. Ting C-S, Li T-H, Kung F-C (1995) Design of fuzzy controller for active suspension system. *Mechatronics* 5(4):365–383
25. Vasičkaninová A et al (2011) Neural network predictive control of a heat exchanger. *Appl Thermal Eng* 31(13):2094–2100
26. Yamashita M et al (1994) Application of  $H_{\infty}$  control to active suspension systems. *Automatica* 30(11):1717–1729
27. Yoshimura T et al (1999) Active suspension of passenger cars using linear and fuzzy-logic controls. *Control Eng Pract* 7(1):41–47
28. Yu M et al (2006) Study on MR semi-active suspension system and its road testing. *J Intell Mater Syst Struct* 17(8–9):801–806
29. Ziegler JG, Nichols NB (1942) Optimum settings for automatic controllers. *Trans ASME* 64(11)

30. Georgiou G, Verros G, Natsiavas S (2007) Multi-objective optimization of quarter-car models with a passive or semi-active suspension system. *Veh Syst Dyn* 45(1):77–92
31. Mehra RK et al (1997) Active suspension using preview information and model predictive control. In: *Proceedings of the 1997 IEEE international conference on control applications*. IEEE



# Design of an Unmanned Aerial Vehicle for Search and Rescue Operations



Ayush Muktibodh, Dinesh Kumar, Vishal Dhiman, and Vikas Rastogi

## 1 Introduction

The currently available unmanned aerial vehicles utilized for such operations can only be deployed to assist authorities in the close vicinity of a natural disaster. Olga Petrucci illustrates the impact of natural disasters [1] in different economic frameworks and their growing prevalence. Agoston Restas has very aptly described the different kinds of natural disasters that can greatly benefit from an Unmanned Aerial Vehicle solution; hazardous material or nuclear accidents, earthquakes, floods, and forest fires [2]. Among these, forest fires have demonstrated to be the most practical application for such drones. This has limited applicability since it may not always be feasible to provide an unmanned aerial solution in such a scenario. To solve this issue, we envisioned a transitional model that is capable of changing flight dynamics from a tri-rotor configuration with the propeller thrust being used directly to balance the weight of the vehicle to a fixed wing configuration with the propeller thrust being produced perpendicular to the weight of the vehicle. The advantage of this dynamic configuration is that it would solve the range and endurance constraints that came about from currently designed vehicles, while also providing the dexterity and capability of a tri-rotor hovering vehicle [3]. A lightweight design will permit the carriage of more payload or avionics which will increase mission time. Saharudin has stressed the importance of material selection and structural analysis in the design of a tilt-rotor drone [4]. Milan Erdelj and Enrico Natalizio highlight the importance of networking and valuable data transmission including the deployment of an ad-hoc sensor network [5] onboard the drone to resume cellular networking in areas of disruptions. Remotely sensing signs of life among the survivors of a natural disaster

---

A. Muktibodh (✉) · D. Kumar · V. Dhiman · V. Rastogi  
Department of Mechanical Engineering, Delhi Technological University, Shahbad Daultapur,  
Main Bawana Road, New Delhi 110042, India  
e-mail: [ayush\\_2k15me44@dtu.ac.in](mailto:ayush_2k15me44@dtu.ac.in)

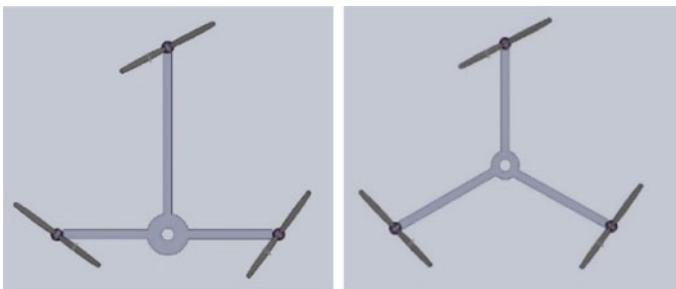
will also allow most of the resources in relief operations to be properly utilized [6]. The practical applications of such systems have been demonstrated and well documented to an accuracy of 100%. Response Time is perhaps the most critical factor in search and rescue operations. Drones are able to be deployed remotely, quickly, and economically in such scenarios to greatly improve the response time in areas that are readily inaccessible to humans [7]. This will allow for timely deployment into remote areas well before first responders arrive at the scene of the natural disaster.

## 2 Conceptual Design

A source of inspiration for the design was the Bell XV-15 Tilt Rotor Research Aircraft [8]. A concept decade ahead of its time has been given a new life as its increased applicability in drones. Tilt rotor drones offer the benefits of conventional fixed wing drones along with the hovering capabilities of quad rotor drones. To accomplish this change in flight dynamics, a simple control system can be employed and the design principles can be extended to multi-rotor designs. Conventional PID sensors may be replaced with low-cost linear controllers for better performance outputs and controllability [9]. Based on our requirements, it was decided that a tri-rotor configuration will be optimum. There are usually two configurations that make use in tri-rotor vehicles; the T-configuration, and the Y-configuration (Fig. 1).

A list was created to determine the most optimum configuration for the vehicle where points were assigned to each factor impacting the designing process. The results are tabulated as follows (Table 1).

One of the major areas of optimization has always been to improve the performance of the vehicle in the cruise phase of flight. Flying wings are known to be supremely efficient and exhibit a low overall drag profile due to the absence of a horizontal and vertical tail [10]. Therefore, we decided to proceed with the Y tri-rotor flying wing design. To cater for the loss in stability due to the absence of the tail, sufficient wing sweep is provided. To ensure stability in all regimes of flight it is

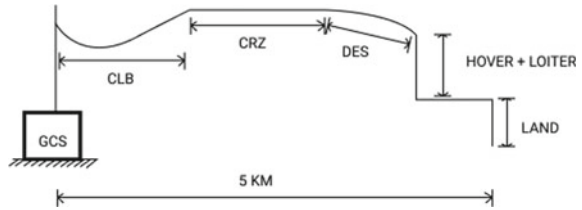


**Fig. 1** T-configuration versus T-configuration for a tri-rotor drone

**Table 1** Y-configuration versus T-configuration

Criteria	Y-configuration	T-configuration
Stability	10	5
Weight and size	7	8
Hand flying characteristics	7	9
Design complexity	9	6
System integration	9	6
Total	42	34

**Fig. 2** Figure depicting mission flight path



**Table 2** Conceptual design parameters

Parameter	Quantity
All up weight	8 kg
Cruise speed	28 m/s
Chord Reynolds Number	535,000
Range	5 km
Wingspan	1 m

important to keep the center of gravity (CG) at an appropriate position in the vehicle [11] (Fig. 2).

From the extensive review done on the subject, most of the vehicles operating in the above conditions exhibited the following parameters that helped compile a final list that is depicted below (Table 2).

### 3 Propulsion System

As stated earlier, there are two different flight regimes for the vehicle in different phases of flight. Since the hovering/loitering stage of the mission is more critical to the power system requirements, it will be the primary reference stage. During the hovering/loitering phase, there is no immediate requirement for quick acceleration, and therefore it was decided to cap the maximum Thrust to Weight (T/W) ratio to 1.5.

Therefore, the maximum thrust required to be produced is

$$(1.5)(8\text{kg}) = 12\text{kg} \quad (1)$$

The maximum thrust required to be produced by each motor is

$$(12\text{kg})/3 = 4\text{kg}. \quad (2)$$

The maximum acceleration of vehicle is

$$(4)(9.8) / (8) = 4.9\text{m/s}^2. \quad (3)$$

### ***3.1 Battery Selection***

Lithium powered batteries come in standard sizes. They are usually represented as 4 s, 6 s, 8 s, etc. where the number denotes the number of individual cells joined in a series connection. The higher the number, the higher the voltage supplied to the system. For the same motor and propeller combinations it was found that the higher the voltage, for the same thrust, the current drawn from the power source is lesser. However, batteries with high voltage and high capacity (10 s, 12 s, etc.) possess a high weight. The gain in endurance does not outweigh the weight of these batteries, and hence it was decided to proceed with the 8 s LiPo battery.

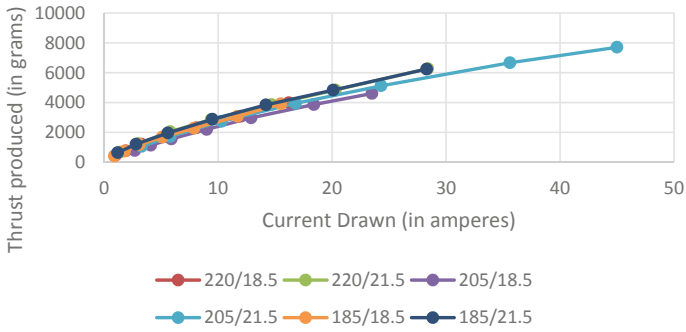
### ***3.2 Propeller Selection***

Primarily there are two types of propellers for application in such vehicles: two-blade and three-blade propellers. Three-blade propellers are capable of producing more thrust, but they tend to draw more current from the power source to overcome the additional drag from the third blade. Two-blade propellers on the other hand draw a lot less current from the power source. The following propellers were considered for the vehicle:

1. 18.5-inch
2. 21.5-inch

### ***3.3 Motor Selection***

Since a DC power source is used for the vehicle, there are primarily two types of DC motors: brushed and brushless. While brushed motors are more cost-effective, brushless motors offer lower maintenance costs, higher efficiency, and boast a high degree of reliability. Hence it was decided to choose brushless DC motors. The next



**Fig. 3** Thrust produced by different motor propeller combinations versus current drawn

factor that contributed to the choice of motor was the velocity constant (kv). This is a quantity that represents the theoretical RPM at which the motor rotates for every volt applied to it. The following motors were considered for the vehicle:

1. 220 kV
2. 205 kV
3. 185 kV

These motors [12–14] were used as a benchmark to compare the different motor sizes and corresponding propellers for the most efficient performance for our purpose. Taking into account the previously mentioned constraints, the following data was computed and analysed (Fig. 3).

From the plot above, it is clear that for a maximum thrust requirement of 4 kg there are two favorable combinations: 220 kV with a 21.5-inch prop and 185 kV with a 21.5-inch prop. However, during lower thrust settings, it is clear that the 220 kV motor performs a lot better. Hence, the propulsion system is decided as follows:

- Battery: 3 LiPo 8 s 12000 mAh batteries for each motor
- Propeller: 21.5-inch two blade propeller
- Motor: 220 kV Brushless DC Motor

## 4 Wing Design

The main purpose of the wing is to generate lift. Further, wings have a substantial impact on the stability of the drone. Hence, this is a crucial phase of the design process. The conceptual design performed earlier helped to provide a feasible starting point in the design of the wing [4]. Detailed criteria for the selection of an appropriate airfoil were formulated as below:

1. The airfoil should generate enough lift to make flight possible.
2. The airfoil should generate minimum drag in flight because to overcome this the motors will have to generate more thrust thereby reducing mission endurance.

**Table 3** List of airfoils [15] used in Xfoil analysis [16]

S. No	Airfoil	Maximum thickness	Maximum camber
1	E471	Max thickness 6.3% at 29.8% chord	Max camber 4.5% at 53.5% chord
2	AH7476	Max thickness 5.9% at 20% chord	Max camber 6.2% at 50% chord
3	E71	Max thickness 5.2% at 25.7% chord	Max camber 4.4% at 54% chord
4	E216	Max thickness 10.4% at 26.2% chord	Max camber 4.7% at 59% chord
5	E385	Max thickness 8.4% at 29.6% chord	Max camber 5.3% at 47.5% chord
6	E59	Max thickness 5.6% at 25% chord	Max camber 5.2% at 50% chord

3. The airfoil should have a sufficiently negative pitching moment coefficient.
4. The range of a drone is directly proportional to the ratio of the lift coefficient to the drag coefficient. An airfoil that is operating at a particular angle of attack that gives maximum range is ideal.

Based on the above criteria, a list of suitable candidate airfoils was prepared for analyzed using the software XFLR5 (Table 3).

After analyzing the various plots for all the airfoils, it was decided to choose the Eppler 71 (E71) airfoil [1]. Similarly, a detailed analysis of the E71 airfoil was performed to ascertain some important values (Fig. 4).

The minimum value of the drag coefficient, maximum value of the ratio of the lift coefficient to the drag coefficient, and most negative value of the pitching moment coefficient are all obtained at an angle of attack of 2.0 degrees. Therefore, it was decided to set the angle of incidence of the wing relative to the axis of the fuselage at 2.0 degrees.

#### 4.1 Main Wing

To reduce the overall drag footprint of the drone, it was decided to move forward with a tail-less design. The vertical tail in a conventional aircraft contributes greatly to its stability, but also produces drag. To avoid this, one work around is using swept wings. These not only create a more ‘elliptical’ lift distribution which is more efficient, but also add stability to the drone. The following equation was used to calculate the dimensions of the wing [17].

In cruise flight,

$$Lift(L) = Weight(W) = 8kg = 78.4N. \quad (4)$$

Also,

$$L = (0.5)(\rho)(V^2)(C_L)(A_{wing}), \quad (5)$$

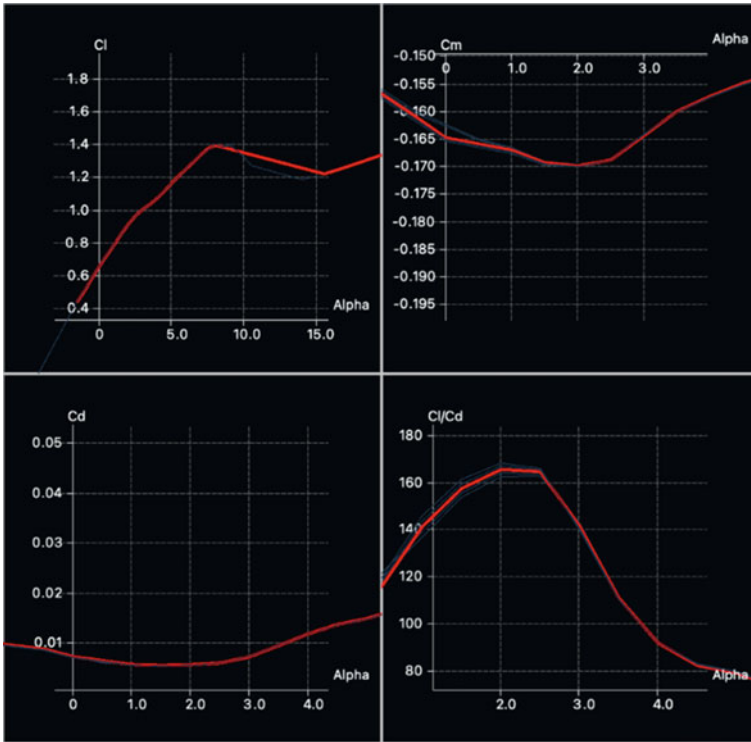


Fig. 4 Plots of various parameters of Xfoil analysis on E71 airfoil

$$L = (0.5)(1.225)(28^2)(0.8)(A_{wing}) = 78.4N. \tag{6}$$

Therefore,

$$A_{wing} = 0.204m^2. \tag{7}$$

For a velocity of 28 m/s a good starting point for calculations is a low Aspect Ratio (AR) of 6.5 [18]. Now,

$$AR = b^2/A_{wing} \tag{8}$$

Solving the above equation, we get a wingspan of 1.14 m.

The Y-configuration of the tri-rotor frame requires that an angle of 120 degrees to be maintained between the motors. It was therefore decided to set the root to tip wing sweep angle as 30 degrees to correspond with this requirement. Finally, with a taper ratio of 3.0 the root and tip chord were calculated to be:

- Root chord: 0.3 m
- Tip chord: 0.1 m

## 4.2 Canard

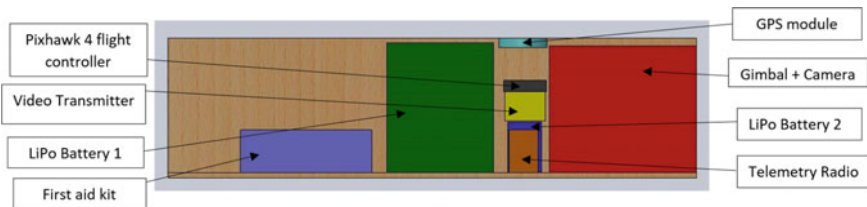
In case of a failure of the propulsion system it is always advisable to have the center of gravity (CG) of the drone ahead of the aerodynamic center of the wing. This will generate a constant nose down pitching moment that will prevent the drone from stalling. However, in normal flight, this nose down pitching moment is usually balanced by a smaller lifting surface with a longer moment arm. In this case, a canard was used with the same airfoil profile. The dimensions of the canard are as follows:

- Mean Aerodynamic chord (MAC): 0.2 m
- Span: 0.7 m

## 5 Fuselage Design

The fuselage was designed as one solid body made out of EPP foam which is a common material used for such applications. Above this, a rectangular box (housing the avionics and payload) was placed that will rotate by 90 degrees during the hover phase to become perpendicular with the fuselage. This achieves two things; the CG is now all balanced at the centroid of the 3 motors which will make controllability a lot easier and during cruise, the rectangular box lays flat with the fuselage to minimize the profile drag in flight (Fig. 5).

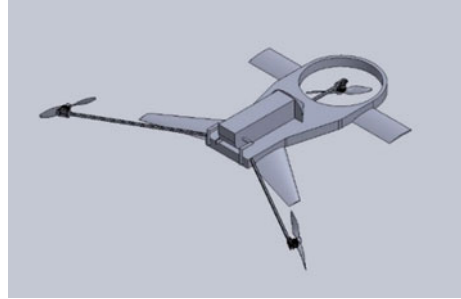
The rectangular box is to be constructed out of Balsa wood, given its high strength to weight ratio making it an ideal choice. The rotation of the rectangular box is achieved through a rack and pinion system that is supplied power through a high torque servo motor. The rotation of the carbon fiber members is accomplished through the use of high torque servos attached directly to the member through a simple gear assembly. At the end of each member is a motor mount which serves as a platform to attach the motor to the drone (Fig. 6).



**Fig. 5** Lateral view of avionics and payload bay



**Fig. 6** Isometric view of vehicle modelled in solidworks

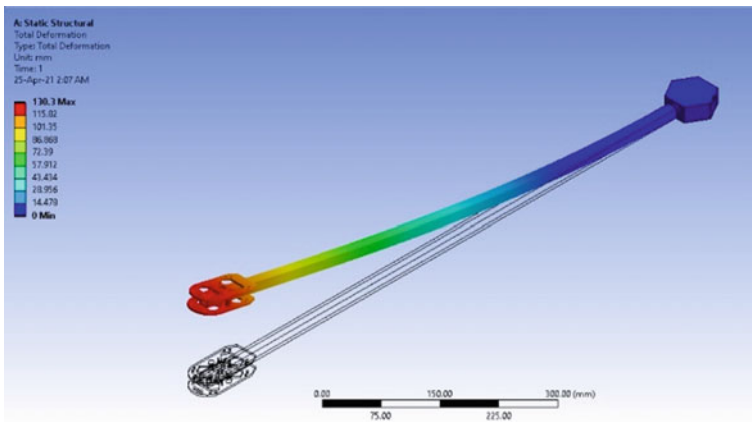


## 6 Simulation Results in ANSYS

### 6.1 Static Structural Analysis

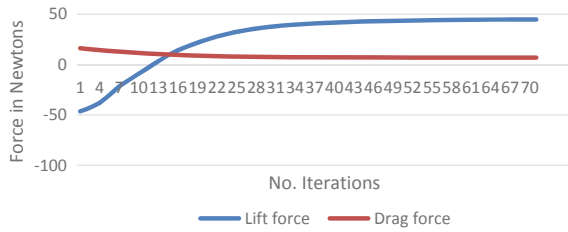
To simulate the forces on the tri-rotor drone Y-frame, a static structural analysis was performed. At the end of each carbon fiber member is motor mount. These will help attach the motors to the vehicle. Since the hovering mode of the vehicle will produce the maximum load on the members, it was used for analysis. A steady force of 50 N was applied on the surface of the motor mount, while the other end of the member was kept fixed. The materials assigned to all the components were that of a low modulus carbon fiber material. The results of the simulation are as follows (Fig. 7).

A maximum deformation of 130.3 mm was reported, while a maximum shear stress of 45 MPa was found at the other end of the carbon fiber member. Both these values are well within limits of the material properties.



**Fig. 7** Total deformation under load

**Fig. 8** Plot of lift and drag force versus iterations on quarter model



## 6.2 Fluent Analysis

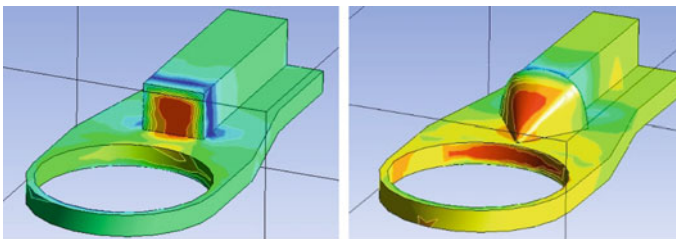
The model geometry was further simplified and divided halfway through the center due to its symmetric nature and then further down for easy meshing. A mesh was created with elements of high orthogonal quality. Due to its high robustness, k-omega SST model was used for viscous analysis with a turbulence intensity of 10% and an inlet velocity of 28 m/s. The results of the model analysis are depicted below (Fig. 8).

The exact value of lift was reported as 44.89 N at the last iteration, whereas the exact value of drag was reported as 7.012 N. Extrapolating this for the entire drone, the total lift produced is about 89.78 N which is enough to support a weight of 9.161 kg in cruise flight. Further analysis was done on the fuselage section and the reported drag for this was 51.4 N. On further inspection it was observed that it was due to an adverse pressure gradient formed at the face of the rectangular section which was slowing down the flow (Fig. 9).

To solve this, a shell was constructed to smoothen out the airflow. The next round of simulations with the shell showed a dramatic reduction in drag to 7.4 N. Therefore, we can summarize the results of the simulations for the entire vehicle as follows:

- Total lift produced: 89.78 N
- Total drag produced: 21.4 N

This demonstrates that the drone is capable of steady flight along with the desired payload at a speed of 28 m/s.



**Fig. 9** Pressure gradient analysis of fuselage before and after implementation of shell

## 7 Conclusion

1. The requirement to design an Unmanned Aerial vehicle to be deployed for reconnaissance operations while carrying payload to be deployed has been achieved.
2. A significant reduction in drag was obtained after modelling the shell.
3. The final weight estimation of the drone leads to a final all up weight of 8.9 kg.
4. Future work may include the stability and control analysis of this vehicle and make use of advanced electronics to limit the constraints put on the design of such systems.

## 8 Notations Used

L—Lift force

GCS—Ground Control Station

$\rho$ —Density of air

CLB—Climb

V—Speed of vehicle

CRZ—Cruise

$C_L$ —Lift coefficient

DES—Descent

$A_{wing}$ —Wing planform area

CG—Center of Gravity

AR—Aspect Ratio of wing

b—Wingspan

## References

1. Petrucci O (2012) The Impact of natural disasters: simplified procedures and open problems
2. Restas A (2015) Drone applications for supporting disaster management. *World J Eng Technol* 3:316–321
3. Sababha B, Alzubi H, Rawashdeh O (2015) A rotor- Tilt-free tricopter UAV: design, modelling, and stability control. *Int J Mechatron Autom*
4. Saharudin M (2016) Development of tilt-rotor unmanned aerial vehicle (UAV): material selection and structural analysis on wing design. *IOP Conference Series: Materials Science and Engineering* 152:012017

5. Erdelj M, Natalizio E (2016) UAV-assisted disaster management: applications and open issues. 1–5
6. Al-Naji A, Perera AG, Mohammed SL, Chahl J (2019) Life signs detector using a drone in disaster zones. *Remote Sens* 11:2441
7. Mayer S, Lischke L, Woźniak PW (2019) Drones for search and rescue. In: 1st international workshop on human-drone interaction, Ecole Nationale de l'Aviation Civile [ENAC], May 2019, Glasgow, United Kingdom
8. Maisel M, Giulianetti D, Dugan D (2000) The history of the XV-15 Tilt rotor research aircraft from concept to flight
9. Chen Z, Jia H (2020) Design of flight control system for a novel tilt-rotor UAV. *Complexity* 2020. Article ID 4757381, 14 pages
10. Wood R, Bauer S (2001) Flying wings/flying fuselages. In: 39th aerospace sciences meeting and exhibit
11. Tuna M, Inel S, Ozdemir S (2020) Longitudinal stability analysis of aircrafts. *J Sci Eng Res* 7:45–51
12. KDE6815XF-205 Brushless DC Motor Performance Data. [https://cdn.shopify.com/s/files/1/0496/8205/files/KDE\\_Direct\\_XF\\_Brushless\\_Performance\\_Testing\\_KDE6815XF-205.pdf?1072](https://cdn.shopify.com/s/files/1/0496/8205/files/KDE_Direct_XF_Brushless_Performance_Testing_KDE6815XF-205.pdf?1072). Last Accessed 2 May 2021
13. KDE6213XF-185 Brushless DC Motor Performance Data. [https://cdn.shopify.com/s/files/1/0496/8205/files/KDE\\_Direct\\_XF\\_CF\\_Brushless\\_Performance\\_Testing\\_KDE6213XF-185.pdf?665](https://cdn.shopify.com/s/files/1/0496/8205/files/KDE_Direct_XF_CF_Brushless_Performance_Testing_KDE6213XF-185.pdf?665). Last Accessed 2nd May 2021
14. KDE5215XF-220 Brushless DC Motor Performance Data. [https://cdn.shopify.com/s/files/1/0496/8205/files/KDE\\_Direct\\_XF\\_CF\\_Brushless\\_Performance\\_Testing\\_KDE5215XF-220.pdf?761](https://cdn.shopify.com/s/files/1/0496/8205/files/KDE_Direct_XF_CF_Brushless_Performance_Testing_KDE5215XF-220.pdf?761). Last Accessed 2nd May 2021
15. Selig MS (1996) UIUC airfoil data site. Urbana, Ill. Department of Aeronautical and Astronautical Engineering University of Illinois at Urbana-Champaign
16. Drela M (1989) XFOIL: an analysis and design system for low reynolds number airfoils. In: Mueller TJ (eds) *Low reynolds number aerodynamics*. Lecture Notes in Engineering, vol 54. Springer, Berlin, Heidelberg
17. Sadraey MH, Design A (2013) *A systems engineering approach*. Wiley, Chichester, West Sussex, U.K.
18. Raymer DP (1989) *Aircraft design: a conceptual approach*. American Institute of Aeronautics and Astronautics, Washington, DC

# Construction and Validation of a Low Cost Thermal Conductivity Measurement Device



Raviratna Subir, Rishabh Goswami, Vikrant Singh, Deepak Kumar, and Pushpendra Singh

## 1 Introduction

Insulators have found important applications in different fields including industries and households. We come across a lot of insulating materials in our daily life. Why though? Well, a short answer is that they, i.e., highly insulation materials reduces wastage of energy by not letting heat of the system to the environment to waste. It is due to this cause that a demand for high-performance insulation is high nowadays. From the second law of thermodynamics. It can be concluded that the exergy of heat is more at high temperatures. Hence thermal barrier coatings plays a vital role in increasing the efficiency of the steam. A thermal barrier coating gives us an advantage of operating the turbine at much more higher temperatures which may not be possible without Thermal barrier coating due to the metallurgical restrictions of the turbine material [1]. At the elevated high temperatures the turbine material can reach up to its upper temperature limits At high temperatures the possibility of high temperature corrosion is there which can be a constraint to the working of the system [2]. In such cases various coating can be very advantageous to increase the upper temperature limits for operation as well as providing some barrier to corrosion of turbine material [2]. This will increase the efficiency as well as decreases the maintenance cost of the turbine.

On the contrary, insulation on electrical wires in the range of critical radius of insulation is done to maximize the heat loss which is produced due to the flow of current [3]. These were the examples where insulation was helpful, but there are many cases where large conductivity is required. Wires used in electrical circuits must possess high conductivity so that a large current will flow. In the VCR (Vapour Compression Refrigeration) cycle, the conductivity of the condenser and evaporator material should be high to increase the value of heat exchange.

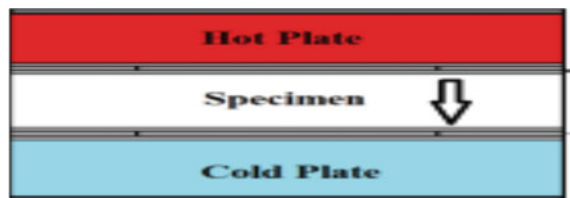
---

R. Subir · R. Goswami · V. Singh · D. Kumar · P. Singh (✉)  
Department of Mechanical Engineering, Delhi Technological University (DCE), Delhi, India

In order to find the perfect material we must have the info most important for such equipment. That is the thermal conductivity of material in order to produce the optimum part. But in the industry and laboratories the machines and methods available for conducting this measurement are far from low cost, and they are costly machines. For measuring this quantity, i.e., thermal conductivity many great minds have suggested many different and versatile techniques giving the answers up to certain level of accuracy. Broadly these techniques are divided into steady state (slow but accurate) and unsteady state methods, which are based on the state of the system in which the measurement is being taken. Heat flow meters are a type of steady state method [5], in which heat flux is observed by sandwiching the sample inside our two hot plates that can be seen in Fig. 1, and that is used to calculate thermal conductivity using Fourier law.

Unsteady state methods are usually applied because they are fast methods and they are much more accurate than steady state methods [4]. They work on a feedback system, meaning a stimulant/sign is introduced and its response is judged/observed. Hot disk method is an unsteady method which gives/observes conductivity and diffusivity and then calculating those to find specific heat. An all-in-one measurement apparatus. Another unsteady state method is laser flash method, in this the lower side of the plane parallel sample, then the temperature change occurring on the other side is measured using an Infrared sensor/detector. Thermal property calculation can also be done using ASTM test methods, but they have some measurement limitations but despite having these limitations they provide an excellent starting point [6]. In another method the recognized thermal conductivity of the substrate material is used as the reference material for heat-flow measurement in a steady-state, comparative measurement process [7]. Using a modified slug calorimeter configuration, a new method for measuring the apparent thermal conductivity of thin coatings has been developed by Robert B. Heimann b, which involves measuring the heat flux through the coatings as well as the external heat transfer coefficient of an uncoated sample [8]. In another method studied there is the development of a non-destructive approach by Ted D. Bennett and Fengling Yu for determining the thermal properties of thermal barrier coatings. A laser is used to create harmonic heating of the film, and the process of thermal emission from the front surface is measured as a function of laser frequency. In this work the approach is to make a conductivity measurement machine using simple technique and materials which lead to a much less expensive machine. Steady state method has been utilized to measure the thermal conductivity of the coating. Steady state method works when the sample or workpiece attains the

Fig. 1 [5]



steady state. Steady state methods are based on the Fourier's law of heat conduction [5]. In this paper guarded hot plate method is utilized as a steady state method to measure the thermal conductivity of the materials and has then be compared by well-known conductivity values of these materials in order to compare the accuracy of our machine.

## 2 Experimentation Method and Procedure

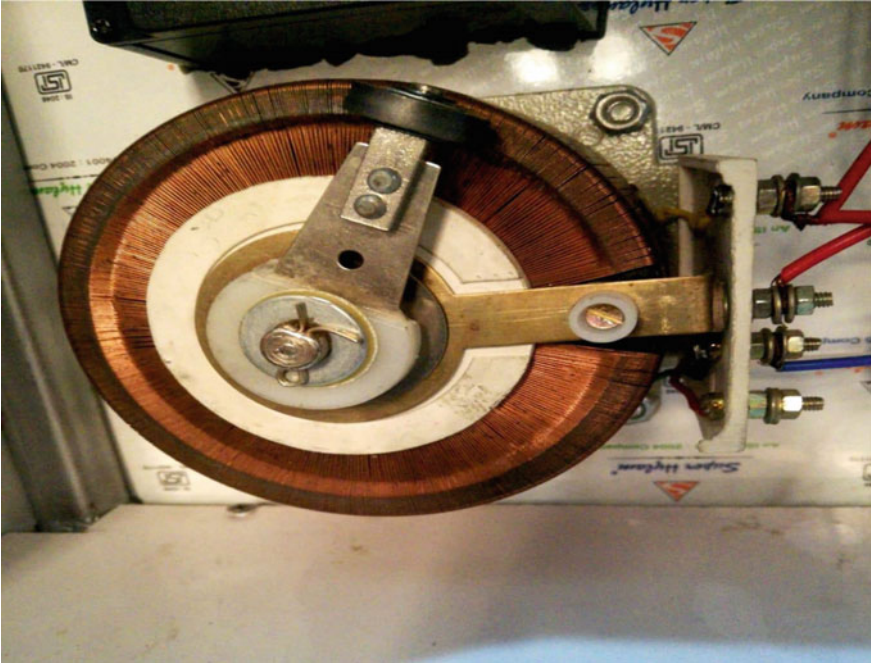
### 2.1 Working Principle

The working of the machine is based on the guarded hot plate method which is further based on the Fourier's law of conduction. The guarded hot plate method is one of the most effective and commonly method for measuring the thermal conductivity. Using the steady state method one can take measurements regarding our thermal conductivity of the material implied via a guarded hot plate apparatus. Steady-state method works only when we maintain a steady-state, i.e., steady environment for the system to be studied and its surroundings, and steady meaning a thermal equilibrium being present. Only then do we acquire accurate result via this method. The basic apparatus has to be of this type, having two samples of the material being examined which are used to provide a sandwich enclosure for the heating plate, which is guarded on all lateral sides, used to create the steady state. Another component called a "cold plate" which is basically an unheated piece, whose purpose is to create the low side for achieving steady state. This is affixed on the open sides of the both testing material. After steady state is reached, as we know every data needed for the cold plate, we can calculate our materials thermal conductivity based on temperature rise of cold plate. This is calculated via basic Fourier law meant to show thermal conductivity.

The device constructed for thermal conductivity measurement is based on the Fourier's law of heat conduction. In Fourier's law of conduction two points should be taken care of first the Fourier's law is defined only of one dimensional heat conduction and second that the system should be in steady state only then one can apply the Fourier's law of heat conduction. Key components of the device is explained below and the working is explained later.

### 2.2 Construction of the Device

A voltmeter of 220 V AC, 50 Hz and range 0–750 V is used to measure the voltage and utilize that value in the equation  $P = VI$  to calculate the heat transferred to the heater plate per unit time. A digital ammeter (20 Hz, 220 V, 20 A) is utilized to calculate the power supply which in turn is used to calculate heat supplied (watts) to the heater plate by Joule's Law. A variable auto transformer (Fig. 2) whose the purpose is to



**Fig. 2** Variable auto transformer

control the voltage given to the heater plate so that we can change the amount of heat per unit time. A temperature controller (“J” “K” Pt 100 type) (Fig. 3) is used to measure the temperature of the upper and lower side of the substrate which is the most important parameter to calculate the conductivity of the substrate material. The heater plate of a kettle is used for heating purposes. It is used to heat the substrate material from beneath (Figs. 4 and 5).

### **2.3 Workpiece Material**

Stainless Steel SS 304 is used as the first workpiece material for the validation of this device.

#### **Dimensions of the workpiece.**

Diameter of the workpiece plate = 100 mm.

Area of the workpiece plate = 0.00785 m<sup>2</sup>.

Thickness of the workpiece plate = 3 mm.



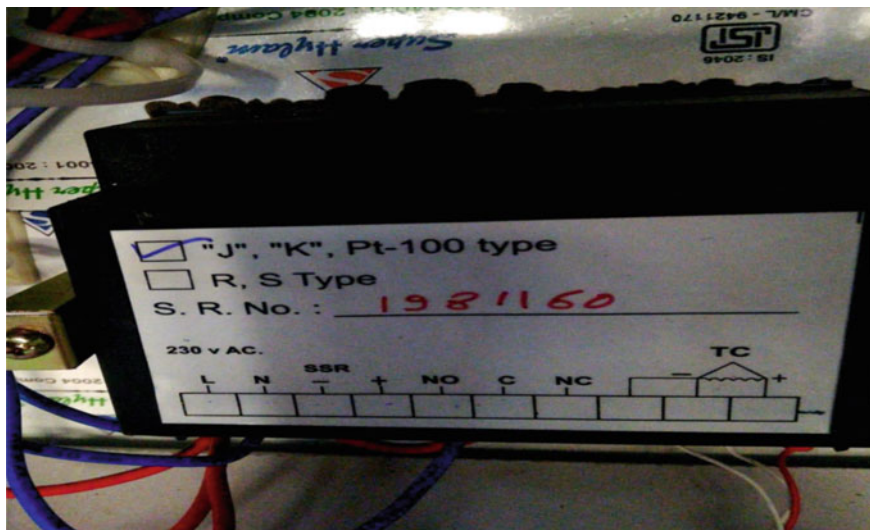
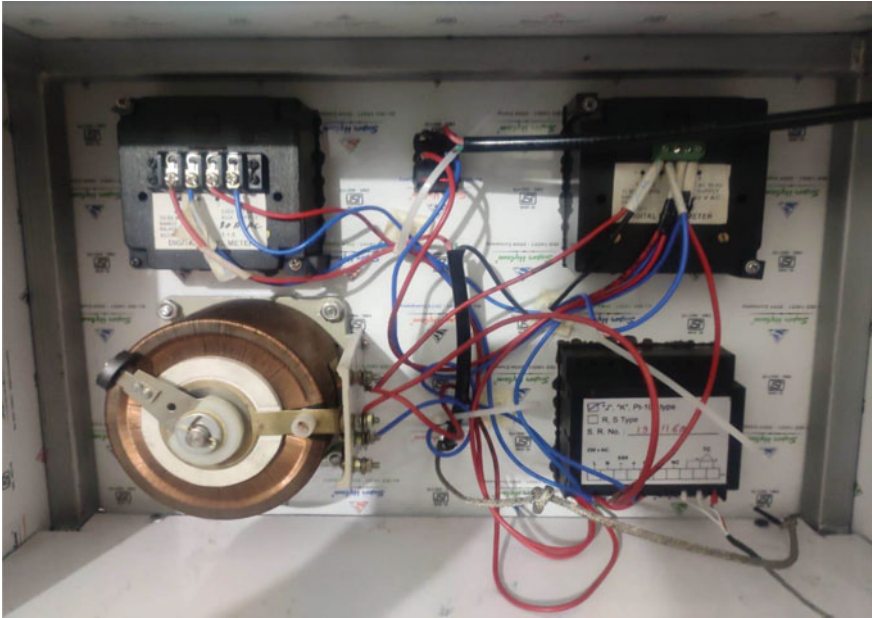


Fig. 3 Temperature controller



Fig. 4 Front view of the device



**Fig. 5** Back view of the Device

Thermal conductivity of Stainless Steel 304 as founded by Sweet [9] using flash diffusivity technique is 14.5 W/mk.

Steel 4340 is used as the second workpiece material for the validation of this device.

**Dimensions of the workpiece.**

Thickness = 6 mm.

Diameter = 100 mm.

Area of the workpiece = 0.007853 m<sup>2</sup>.

Thermal conductivity of Steel 4340 as founded by Parker [10] using flash method technique is 33.44 W/mk.

**2.4 Calculation Method**

For the application of this Law we need to make sure that the heat flow should be one dimensional in the workpiece. To achieve this we can use a thin plate with some insulation on the sides or some other arrangement to reduce the heat loss from the sides.

Workpiece is first clamped on the device using the vice type arrangement. The work piece is placed above a heater plate. The workpiece should be clamped tightly or otherwise any type of air gap will reflect error in the experimental readings. After clamping the workpiece properly place the temperature sensors at the location where you want to measure the temperature of the workpiece. Switch on the power supply and wait for the system to reach the steady state.

As soon as the system reaches steady, take the reading of each sensor attached to the workpiece. Take the readings of the voltmeter and ammeter also. Using all these readings we can calculate the thermal conductivity of the workpiece. The calculation part is shown in the calculations section. Repeat the above steps with some different voltage difference.

Voltage = V.

Current = I.

$T_1$  = Temperature given by the sensor at the top.

$T_2$  = Temperature given by the sensor at the bottom.

K = Thermal conductivity.

### Formula used

Thermal conductivity is calculated by the Fourier's law of conduction as follows:

$$K = \frac{\frac{Q}{A}}{\frac{dT}{dX}}$$

Error is calculated by

$$\text{Errorin\%} = 100 * \frac{(\text{theoreticalvalue} - \text{experimentalvalue})}{\text{theoreticalvalue}}$$

## 3 Result and Discussion

See Tables 1 and 2.

All the components were successfully assembled and circuits were connected successfully.

All the measurements were done properly along with the proper precautions.

The average thermal conductivity of the SS 304 workpiece was found to be 13.43 W/mk.

The mean error calculated for SS 304 Plate is 7.53%.

The average thermal conductivity of the Steel 4340 workpiece was found to be 29.03 W/mk.

**Table 1** Observation table of SS 304 material plate

S.No	Voltage (V)	Current (I) A	Temperature difference Of top and bottom sensor reading ( $^{\circ}\text{C}$ ) ( $T_2 - T_1$ )	Thermal conductivity W/mK	Error In %
1	77	0.09	0.2	13.24	8.68
2	85	0.12	0.3	13.29	10.41
3	91	0.12	0.3	13.91	4.06
4	105	0.14	0.4	14.04	3.17
5	100	0.14	0.4	13.37	7.79
6	110	0.16	0.5	13.45	7.24
7	121	0.17	0.6	13.10	9.65
8	126	0.17	0.6	13.64	5.93
9	135	0.18	0.7	13.26	8.55
10	144	0.19	0.8	13.07	9.86

Mean error for SS 304 plate is 7.53%.

**Table 2** Observation table of Steel 4340 material plate

S.No	Voltage (V)	Current (I) A	Temperature difference Of top and bottom sensor reading ( $^{\circ}\text{C}$ ) ( $T_2 - T_1$ )	Thermal conductivity W/mK	Error In %
1	72	0.10	0.3	27.51	17.73
2	95	0.12	0.3	29.03	13.18
3	100	0.13	0.4	24.83	25.74
4	107	0.14	0.4	28.61	14.44
5	115	0.18	0.5	31.63	5.41
6	118	0.16	0.5	28.85	13.72
7	121	0.18	0.6	27.73	17.07
8	124	0.19	0.6	30.01	10.28
9	129	0.19	0.6	31.21	6.67
10	135	0.21	0.7	30.94	7.47

Mean error for Steel 4340 plate is 13.17%.

The mean error calculated for steel 4340 Plate is 13.17%.

## 4 Conclusion

In this work, different steady and unsteady methods to measure thermal conductivity is studied and a method was proposed out of them. Guarded hot plate method was finally employed in the proposed device. This is based upon the Fourier's law of

heat conduction. In order to use Fourier's law of heat conduction, thin plates were used. Guarded hot plate method is one of the simplest and conventional methods to measure thermal conductivity. This method requires steady state at which the amount of heat entering and leaving is same. To achieve this, the device takes time. Thus this method is time consuming.

A comparative evaluation was done between the experimental value with the reference values of the workpiece materials. According to the experimental readings it has been found that the device gives an error of 8–9% (for thermal conductivity values less than 20 W/mk) which is understandable due to heat dissipation to the environment or to the other parts of the device via conduction. For materials with conductivity above 20 W/mk the error is quite high. The error is high because the least count of the temperature measurement unit is 0.1 °C. To decrease the heat loss and to increase the accuracy of the device more insulation could be used which will be a little costly. The device can also be useful to measure the thermal conductivity greater than 20 W/mk if a temperature measurement device with a least count of 0.01 °C will be used.

## References

1. Sonntag RE, Borgnakke C, Van Wylen GJ, Van Wyk S (2003) Fundamentals of thermodynamics: Wiley New York
2. Gleeson B (2008) High-temperature corrosion of metallic alloys and coatings. <https://doi.org/10.1002/9783527619306.ch14>
3. Cengel YA, Ghajar AJ (2014) Heat and mass transfer: fundamentals and applications (5th ed.). McGraw-Hill Professional
4. Hattori M, Sanada K, Kajita Y (2020) Experimental measurement and finite element analysis of the thermal conductivity of alumina/silicone polymer composites. In: 2020 36th semiconductor thermal measurement, modeling & management symposium (SEMI-THERM), pp 143–146. <https://doi.org/10.23919/SEMI-THERM50369.2020.9142837>
5. The review of some commonly used methods and techniques to measure the thermal conductivity of insulation materials. <https://doi.org/10.5772/64157>
6. Tzeng JJ, Weber TW, Krassowski DW (2000) Technical review on thermal conductivity measurement techniques for thin thermal interfaces. In: Sixteenth annual IEEE semiconductor thermal measurement and management symposium (Cat. No.00CH37068), San Jose, CA, USA, pp 174–181. <https://doi.org/10.1109/STHERM.2000.837081>
7. Slifka AJ (2000) Thermal-conductivity apparatus for steady-state, comparative measurement of ceramic coatings. *J Res Natl Inst Stand Technol* 105(4):591–605. <https://doi.org/10.6028/jres.105.050.PMID:27551628;PMCID:PMC4877160> Aug 1
8. Litovsky E, Kleiman J, Shagalov M, Heimann RB (2014) Measurement of the thermal conductivity of cold gas dynamically sprayed alumina-reinforced aluminum coatings between – 150 °C and + 200 °C: New test method and experimental results. *Surf Coat Technol* 242. <https://doi.org/10.1016/j.surfcoat.2014.01.033>.
9. Assael M, Gialou K (2003) Measurement of the thermal conductivity of stainless steel AISI 304L up to 550 K. *Int J Thermophys* 24:1145–1153. <https://doi.org/10.1023/A:1025069405106>
10. *J Appl Phys* 32:1679 (1961). <https://doi.org/10.1063/1.1728417>

# A Statistical Study for Optimizing the Challenges in Vaccine Supply Chain During Critical Times Using DEMATEL Method



Mukul Suri, Priyam Srivastav, Abhishek Dhiman, and M. Shuaib

## 1 Introduction

One of the most substantial and rapidly expanding industries globally is the health-care industry today and in it the vaccination market plays a crucial part. There are numerous distinguishing attributes to this vaccination marketplace which increases the intricacy of some processes like procurement, supply, and distribution of vaccines to different destinations. We need a strong and secure supply chain network in order to supply vaccines sustainably and proficiently across corners. Supply chain management consists of the different processes and the approaches and successfully amalgamates suppliers, manufacturers, distributors, and customers to make deep-rooted performance enhancement of individual companies and the whole supply chain in an exhaustive gassed-up business model.

The function of supply chain management of vaccine is to establish a better repository and control of vaccines, appropriate management of stock, cautious control of temperature in the cold chain, and logistics maintenance [1]. The motive is to assure that the standard vaccine supply is continuously available from manufacturing to delivery so that any opportunity to vaccinate are not overlooked due to the unavailability of vaccine stocks. The overall process of a vaccine beginning from the research and development to the vaccine distribution via regulatory acceptance of the vaccine is in itself a very composite process. Before being ready for shipments a vaccine usually advances through various different phases. There are a few vaccines and other crucial medicines whose supply chains are under development strain so that they can function with better efficacy. In order to enhance the performance of the supply chain of vaccination industry it is necessary for the policymakers in the healthcare sector to tackle the main problems and thus take measures in the correct directions [2].

---

M. Suri · P. Srivastav (✉) · A. Dhiman · M. Shuaib  
Delhi Technological University, Shahbad daultapur, Delhi 110042, India

Decision making trial and evaluation laboratory (DEMATEL) is regarded as an efficacious method for discovering the cause-effect chain constituents of an intricate system. It work toward calculating interdependent connections within factors and finding the essential ones via a visual structural model. The DEMATEL approach aids us in acknowledging both direct and indirect criteria and assists in filtering out the best criterion. The DEMATEL can adopt interdependence among factors and assist in the development of a map to contemplate comparative relationships within them and can be used for scrutinizing and solving intricate and intertwined problems. In this paper we will first try to express and talk about, the ongoing challenges and issues in the vaccine supply chain industry. Then we will advance to our analysis which will assist us in recognizing present challenges of vaccine supply chain industry and eventually we will manifest the consequences of several challenges on the performance of the vaccine supply chain that can be implemented to the industry in order to refine its functioning [3].

The purpose of this study is to explore different types of challenges faced by the vaccine supply chain industry and use DEMATEL approach to analyze the problem. The remaining part of this paper is structured as follows: Sect. 2 presents a review of related literature in the field of vaccine supply chains and DEMATEL and other statistical techniques used. In Sect. 3 we introduce our data and research methodology used to model the challenges in vaccine supply chain. Section 4 includes the results obtained after applying the DEMATEL technique and in the least section, we will give our final conclusion of the research along with some policy recommendations and scope for future work.

## **2 Literature Review**

This section points down all the previous work that has been published in the field of vaccine supply chain. Many researchers have done the research on wastage, temperature, storage, coverage, shortage, etc. of the vaccine in different parts of different countries and pointed out the key issues involving generalizing a vaccine supply chain. We have divided this section into 2 parts, firstly we will talk about the work done in supply chain in the vaccine market and in the later section we will mention how DEMATEL technique is used in various domains.

### ***2.1 Vaccine Supply Chain***

A supply chain is a web that connects an organization and its different distributors or suppliers to produce and disperse a product to the customer in need. This web includes all sorts of information, people, activities, entities, and resources. The supply chain also tells the steps, in a chronological, it takes to get the product or service

from raw material state to the customer as a final product. Supply chain is a crucial part of any organization and determines the major cost of the product or service.

According to Chandra and Kumar, demand forecasting, communication between the all the members of the supply chain and proper planning as well as scheduling are the 3 most important points to be taken care of in a vaccine supply chain. After carefully reviewing their results, we found that demand forecast is the most impactful factor among these and hence was considered in our list of factors [4].

On the other hand, Julian de Meyrick, in 2003, used Delphi to identify pitfalls (weakness) in vaccine supply chain [5]. We found this research to be very helpful as only a few researchers talked about factors as a strength or weakness and since Delphi is a good source for experts' information, we selected a few of these strengths and weakness in our list. Evelot Duijzer, Willem, and Rommert in 2018, tried a different approach by classifying the vaccine supply chain into 4 factors which are, product, production, allocation and distribution and analyzed the problems in decision for existing versus (vs) sudden outbreaks in developing versus developed country [2]. They also identified shooting uncertainties in both supply and demand, and different mindset or alignment of goals and decisions between supplier, public health organizations, and end customer.

Stef Lemmens, Catherine, Nico, and Mauro studied that whether or not the decisions at strategic, operational, and tactical levels are able to solve the major problems in vaccine supply chain such as cold chain distribution and limited shelf life. They also explained how uncertainty is allowing to incorporate lead time, epidemics in diseases, tender procurement, and demand variability [3].

## **2.2 *Decision Making Trial and Evaluation Laboratory (DEMATEL)***

Decision making trial and evaluation laboratory (DEMATEL) was first introduced in the Geneva Research Centre by the Battelle Memorial Institute in the year 1973, and it is a method that is used to identify or classify the factors into cause or effect in a complex system. It works by identifying the interdependencies between the factors and gives out a result showing critical factors in a chronological order through a visual structural model. The DEMATEL approach helps us understand both direct and indirect factors and then suggests us the most important factors among them. The approach considers factor's, their causal relationship with each other, and then helps in the development of a web which takes into consideration as them being a cause or an effect and after that, it helps us solve complex and intertwined problems.

DEMATEL has been widely used in healthcare sector, for example, Anil Kumar, Kavian, Eleonora, Manoj Kumar, and Edmundas Zavadskas [6] combined DELPHI and DEMATEL to investigate that what role social media played in the prevention of Polio in India.



Thomas K. Dasaklis and Costas P. used DEMATEL to classify the most critical success factors in the implementation of cholera vaccine during emergencies [7]. DEMATEL has also been used to assist vaccine supply chain in Indonesia by A.C. Sudramin and Ardi in 2020, they developed and integrated DEMATEL and then used analytical network process technique to assess their goal [8]. Fatma Altuntas and Mehmet used DEMATEL analysis to optimize quarantine decisions for Turkey and also gave the result that Turkey's neighboring country Istanbul has an essential impact on Turkey's rest. They proved that DEMATEL provides very accurate and possible solutions for decision related to quarantine during a pandemic [9–11]

### 3 Data and Methodology

#### 3.1 Data

To begin with, first various challenges affecting the vaccine supply chain were identified with the aid of an extensive review of literature and past studies in the field of vaccine development and vaccination challenges and referring to expert opinions of the various stakeholders in the industry [3, 12]. Upon analysis, the various factors identified as potential roadblocks in vaccine supply chain and vaccination programs are listed in Table 1.

After selecting the 10 factors which affecting the most to conducting successful vaccination and running an efficient vaccine supply chain, we moved toward the initial part of our analysis, which was to collect data from different stakeholders to implement in our DEMATEL model. For this purpose, a questionnaire was prepared and sent to 60 individuals involved in the field of vaccines, drug industry, healthcare industry, and supply chain management. The questionnaire was focused on assessing

**Table 1** List of factors identified as challenges in vaccine supply chain

Index	Factor
P1	Allocation priority for vaccination—Who should be vaccinated first?
P2	Location of manufacturing and distribution facility
P3	Monitoring the vaccinated population
P4	Storage of perishable products and maintaining the cold chain—distribution—Limited shelf life of vaccine and its components
P5	Vaccine selection—which vaccine to take from different vaccines available
P6	Disease and epidemiological dynamics
P7	Forecasting demand—How much vaccine is needed
P8	Transportation disruptions—Vaccine distribution in case of disruptions or faults
P9	Information systems and combating fake news propaganda
P10	Economic costs, R&D and sustainable financing

the impact of one roadblock (say P1) on the other roadblock (say P2) on a scale of 0 to 4 where 0 indicating that the factor has the least influence whereas 4 indicating that the factor has a very high influence on the other factor.

### 3.2 Implementing the DEMATEL Technique

The DEMATEL (Decision Making Trial and Evaluation Laboratory) is a statistical tool was in its most nascent form was originated by Fontela and Gabus in 1972 in the research center of Geneva located in the Battelle Memorial Institute with an aim visualize the contextual inter relationships between the factors and further quantify that relationship among factors with the help of matrices and causal diagrams [11]. The indigenous DEMATEL technique searched for integrated solutions to fragmented and antagonistic societies around the world. The DEMATEL method has recently become very popular all over the world primarily because of its ability to pragmatically identify relationships between qualitative factors and providing a systematic way to deal with it [8]. The biggest advantage of using DEMATEL is that it helps to uncover complex contextual relationships between the facts and helps us to prioritize and categorize those challenges for an efficacious way to surmount them.

Data collected from various experts and stakeholders was presented in the form of a  $10 \times 10$  matrix A where each cell  $a_{ij}$  of the matrix represents the impact in terms of the linguistic score of a challenge i on another challenge j on a scale as defined in Table 2. The major steps involved in conducting the DEMATEL process are shown below:

STEP 1: Calculating the average direct relation matrix with the help of response gathered from different individuals.

Experts were asked to present their opinions based on the linguistic scale of 0–4 as shown in Table 2 for quantifying the impact of one factor on other factors with the responses collected in the form of a matrix A. Here,  $a_{ij}$  represents the extent to which a factor i impact the other factor j. For each indicator, a response  $n \times n$  matrix can be given as

$$A_r = [a_{ij}^x]_{n \times n} \tag{1}$$

**Table 2** Impact in terms of the linguistic score

Linguistic terms	Influence score
No impact or relation	Zero
Very Low impact (VL)	One
Low impact	Two
High impact (HL)	Three
Very High impact (VH)	Four

Here, ‘x’ is the number of individuals who took part in the questionnaire cum survey and  $a_{ij}$  represents the extent to which a respondent believes that  $i$ th criteria impacts the  $j$ th criteria. For summarizing the opinions of all ‘x’ respondents, we simply calculated the average of all the respondents to form the average direct relation matrix.

$$B = [b_{ij}]$$

$$b_{ij} = \frac{1}{m} \sum_{r=1}^m a_{ij}^x$$

Here,  $n$  is the number of pitfalls (challenges) considered in our problem statement and for  $i = j$ , it interprets how one factors impacts itself which is practically an ambiguous statement. Hence, the diagonal elements for the matrix  $A$  are set to zero (Table 3).

STEP 2: Normalizing the matrix formed in Eq. 1 by calculating the normalized direct relation matrix ‘N’, this matrix is calculated by dividing all the elements of the matrix by the maximum sum of rows calculated to each row of the matrix (Table 4):

$$N = D \times B \tag{2}$$

where  $D = \frac{1}{\max(\sum_{j=1}^n b_{ij})}$ .

STEP 3: Estimate the Total Relationship Matrix ‘T’ using Eq. 3, here  $I$  denoted the identity matrix of order  $n$  and  $T$  is calculated as

$$T = N(I - N)^{-1} \tag{3}$$

**Table 3** Average direct relation matrix

	P1	P2	P3	P4	P5	P6	P7	P8	P9	P10
P1	0.00	1.80	1.83	2.11	1.54	1.61	1.87	1.87	2.28	1.78
P2	2.00	0.00	1.98	2.17	2.33	1.96	1.98	2.17	1.72	2.00
P3	2.15	2.15	0.00	2.07	1.83	1.87	2.26	2.37	2.04	1.96
P4	2.11	1.85	2.09	0.00	1.76	1.65	2.07	2.13	2.67	2.41
P5	2.22	2.48	2.65	2.59	0.00	2.59	2.39	2.52	2.30	2.22
P6	2.72	2.33	2.35	2.65	2.59	0.00	2.43	2.33	2.39	2.41
P7	2.54	2.15	2.17	2.26	2.59	2.52	0.00	2.41	2.50	2.26
P8	2.48	2.39	2.43	2.50	2.48	2.70	2.61	0.00	2.50	2.52
P9	2.35	2.70	2.33	2.50	2.26	2.85	2.74	2.52	0.00	2.20
P10	2.61	2.37	2.37	2.35	2.37	2.61	2.39	2.52	2.54	0.00

**Table 4** Normalized direct relation matrix

	P1	P2	P3	P4	P5	P6	P7	P8	P9	P10
P1	0.000	0.080	0.081	0.093	0.068	0.071	0.083	0.083	0.101	0.079
P2	0.088	0.000	0.088	0.096	0.103	0.087	0.088	0.096	0.076	0.088
P3	0.095	0.095	0.000	0.091	0.081	0.083	0.100	0.105	0.090	0.087
P4	0.093	0.082	0.092	0.000	0.078	0.073	0.091	0.094	0.118	0.107
P5	0.098	0.110	0.117	0.114	0.000	0.114	0.106	0.112	0.102	0.098
P6	0.120	0.103	0.104	0.117	0.114	0.000	0.108	0.103	0.106	0.107
P7	0.113	0.095	0.096	0.100	0.114	0.112	0.000	0.107	0.111	0.100
P8	0.110	0.106	0.108	0.111	0.110	0.119	0.115	0.000	0.111	0.112
P9	0.104	0.119	0.103	0.111	0.100	0.126	0.121	0.112	0.000	0.097
P10	0.115	0.105	0.105	0.104	0.105	0.115	0.106	0.112	0.113	0.000

where I is the identity matrix (Table 5).

**STEP 4: Developing the causal diagram.**

The sum of rows and sum of columns are denoted by D and R respectively and are calculated from the Total Direct Relation Matrix ‘T’. Then the prominence metric which is (D+R) and the Relation metric which is (D–R) are computed which will help us to prioritize and categorize the challenges in different cause and effect groups. The factor comes in the ‘Cause’ group if the D–R metric comes out to be positive, and it comes in the ‘Effect’ group if the D–R metric comes out to be negative. Thus, DEMATEL helps us to classify the factors into different stimulus and response groups. Now, to prioritize the factors, we will use the Prominence parameter. Higher the prominence parameter, i.e., (D+R), higher is the influence of factor over other factors. The scatter plot obtained from the data (D+R, D–R) is the casual diagram.

**Table 5** Total relation matrix

	P1	P2	P3	P4	P5	P6	P7	P8	P9	P10
P1	0.760	0.802	0.802	0.846	0.776	0.799	0.822	0.825	0.845	0.787
P2	0.909	0.793	0.873	0.916	0.869	0.877	0.892	0.903	0.891	0.859
P3	0.930	0.894	0.806	0.927	0.865	0.889	0.918	0.925	0.919	0.872
P4	0.933	0.888	0.895	0.848	0.867	0.886	0.916	0.921	0.947	0.893
P5	1.066	1.034	1.040	1.080	0.915	1.043	1.054	1.062	1.061	1.007
P6	1.092	1.036	1.036	1.090	1.025	0.948	1.063	1.063	1.072	1.021
P7	1.058	1.004	1.003	1.049	1.000	1.022	0.939	1.039	1.048	0.990
P8	1.103	1.058	1.058	1.105	1.040	1.074	1.089	0.989	1.096	1.044
P9	1.091	1.062	1.047	1.097	1.026	1.072	1.086	1.082	0.988	1.025
P10	1.088	1.038	1.037	1.079	1.017	1.052	1.061	1.070	1.077	0.925

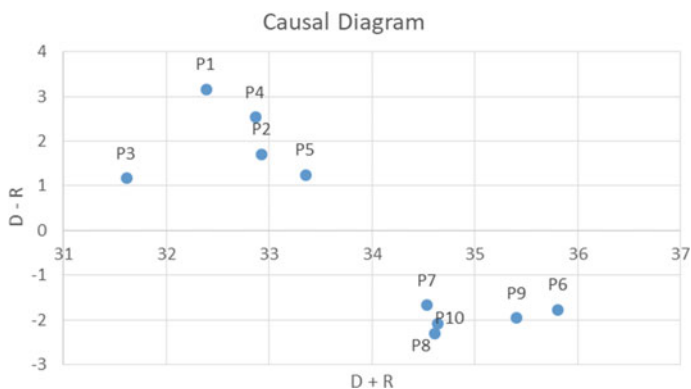
## 4 Results

Table 6 shows the results of the DEMATEL techniques applied over the data obtained from the questionnaire. Here, on calculating the values of D & R which are the sum of rows and sum of columns respectively, we subsequently calculated the D+R and D–R. Here, D–R which is known as ‘Relation’ metric helps us to categorize the factor into cause and effect groups. Here, we can see that for the factors P1 (Allocation priority for vaccination), P2 (Location of manufacturing and distribution facility), P3 (Monitoring the vaccinated population), P4 (Storage of perishable products and maintaining the cold chain distribution), and the value of D–R is negative which signifies that these criteria come into the ‘effect’ group which interprets that these challenges are highly impacted by other factors. Now, for the factors P5 (Vaccine selection), P6 (Disease and epidemiological dynamics), P7 (Forecasting demand), P8 (Transportation disruptions), P9 (Information systems and combating fake news propaganda), P10 (Economic costs, R&D and sustainable financing), these factors have a positive D–R value which signifies that these factors come into the cause group interpreting that these factors can greatly influence other factors.

Now, coming to the D+R values, the ‘Prominence’ metric tells us how much is one factors influences the total decision making ability, higher the D+R value, more is the influence of the factor over other factors. Here, as we can see in Table 6 that factors P8 (Transportation disruptions) and P9 (Information systems and combating fake news propaganda) have the highest D+R values which are 20.537 and 20.521 respectively. This shows that factors are the most influential over the other factors. The factors P1 (Allocation priority for vaccination) and P2 (Location of manufacturing and distribution facility) have the lowest D+R values which are 18.092 and 18.389 respectively. These factors have the lowest influence or are least related with other factors. A causal diagram shows in Fig. 1 shows a scatter plot between (D+R) and (D–R) values.

**Table 6** The table shows D+R and D–R values calculated using the matrix ‘T’

Factor	D	R	D+R	D–R
P1	8.063	10.029	18.092	–1.966
P2	8.781	9.608	18.389	–0.827
P3	8.944	9.597	18.542	–0.653
P4	8.992	10.037	19.029	–1.045
P5	10.363	9.400	19.762	0.963
P6	10.447	9.663	20.110	0.784
P7	10.152	9.840	19.992	0.312
P8	10.657	9.880	20.537	0.778
P9	10.576	9.944	20.521	0.632
P10	10.444	9.421	19.866	1.023



**Fig. 1** Causal diagram of  $(D+R)$  and  $(D-R)$  value

## 5 Conclusion

The study uses data in the form of responses collected from 60 individuals over the impact of different challenges faced in the vaccine supply chains and governmental mass vaccination programs for harmful infectious diseases over other challenges and used a statistical tool, DEMATEL to form an efficacious way to surmount those challenges. On application of DEMATEL in this case, we were able to categorize the challenges in various cause and effect groups, this categorization could help governments and organizations involved in vaccination programs to better understand which challenges to focus more as compared to other challenges. DEMATEL also tells us the priority order in which each challenge is related to other challenges, here the factors ‘transportation disruptions’ and ‘Information systems and combating fake news propaganda’ are the factors that come out with highest relative importance as compared to other factors. This is also relevant to the current scenario of COVID-19 vaccination drive where various fake news, and misbeliefs are spread through distinguished social media platforms which halts a successful vaccination program. In the end, we would like to recommend that working on fake news and managing the transportation and other logistics of vaccine are the most important challenges which should be overcome in order to ensure a successful vaccine supply chain.

## References

1. Zaffran M, Vandelaer J, Kristensen D, Melgaard B, Yadav P, Antwi-Agyei KO, Lasher H (2013) The imperative for stronger vaccine supply and logistics systems. *Vaccine* 31:B73–B80
2. Duijzer LE, van Jaarsveld W, Dekker R (2018) Literature review: the vaccine supply chain. *Eur J Oper Res* 268(1):174–192
3. Lemmens S, Decouttere C, Vandaele N, Bernuzzi M (2016) A review of integrated supply chain network design models: key issues for vaccine supply chains. *Chem Eng Res Des* 109:366–384

4. Chandra D, Kumar D (2018) Analysis of vaccine supply chain issues using ISM approach. *Int J Logist Syst Manag* 31(4):449–482
5. de Meyrick J (2003) The Delphi method and health research. *Health education*
6. Kumar A, Kaviani MA, Bottani E, Dash MK, Zavadskas EK (2018) Investigating the role of social media in polio prevention in India: a Delphi-DEMATEL approach. *Kybernetes*
7. Dasaklis TK, Pappis CP (2018) Critical success factors for implementing cholera vaccination campaigns in humanitarian emergencies: a DEMATEL-based approach. *EURO J Decis Process* 6(1):1–20
8. Sudarmin AC, Ardi R (2020, December) DEMATEL-Based Analytic Network Process (ANP) approach to assess the vaccine supply chain risk in Indonesia. In: 2020 IEEE international conference on industrial engineering and engineering management (IEEM), pp 726–730. IEEE
9. Altuntas F, Gok MS (2021) The effect of COVID-19 pandemic on domestic tourism: a DEMATEL method analysis on quarantine decisions. *Int J Hospit Manag* 92:102719
10. Arifoğlu K, Deo S, Irvani SM (2012) Consumption externality and yield uncertainty in the influenza vaccine supply chain: interventions in demand and supply sides. *Manag Sci* 58(6):1072–1091
11. Abdel-Basset M, Manogaran G, Gamal A, Smarandache F (2018) A hybrid approach of neutrosophic sets and DEMATEL method for developing supplier selection criteria. *Des Autom Embed Syst* 22(3):257–278
12. Sodhi MS, Tang CS (2020). Supply chain management for extreme conditions: research opportunities. *J Supply Chain Manag*

# Impact of COVID-19 Lockdown on Noise Levels in Delhi and Mumbai



Reuben Sewak, Sankalp Kumar, Aviral Agarwal, and Rajeev Kumar Mishra

## 1 Introduction

In the year 2020, the world was hit with a deadly virus (SARS-CoV-2). The virus is responsible for COVID-19 (coronavirus disease), and by the end of May 2020, 3,67,166 deaths have been recorded worldwide [1]. Due to the large-scale spread of the virus and the mortality resulting from the concurred disease, the world's governing bodies resolved toward lockdowns to curb down the spread of the virus.

The lockdown resulted in a visible reduction in environmental pollution worldwide. Since then, several studies have quantified and analyzed the improvements in air and water quality [2, 3]. However, no such study has been conducted to quantify and analyze the effect of lockdown on ambient noise levels in India.

Noise pollution can be defined as any disturbing or unwanted noise that interferes with or harms humans or wildlife. It is a pollutant in the environment that has a detrimental effect on people's quality of life, health, and well-being. It is considered a pollutant under the Prevention and Control of Pollution Act, 1981 of India. Motor vehicles are the key sources of urban noise levels, accounting for about 55% of overall noise. Noise pollution and its related health effects are becoming more common, and they can cause both short- and long-term psychological and physiological disorders [4, 5]. According to the World Health Organisation (WHO), over 1 million health years are lost per year in the European Union and Western European countries due to traffic noise [6]. Moreover, 10% of the world's population is subjected to sound levels that may cause noise-induced hearing problems. Environmental noise has several psychological effects, including irritation, anxiety, depression, and severe health consequences, such as cardiovascular disease. Similarly, noise pollution causes

---

R. Sewak · S. Kumar · A. Agarwal · R. K. Mishra (✉)

Department of Environmental Engineering, Delhi Technological University, Delhi 110042, India  
e-mail: [rajeevkumarmishra@dtu.ac.in](mailto:rajeevkumarmishra@dtu.ac.in)



hearing loss, high blood pressure, insomnia, and poor work performance, among other things [7–9].

The significant reduction in anthropogenic activities resulted in air and water quality improvements; some studies conducted in other parts of the globe indicated that lockdown also reduced ambient noise levels during the lockdown [10, 11].

India being a major partake in the rapid urbanization and industrialization has resulted in massive urban noise pollution. Several studies have indicated the hazardous noise levels in Indian cities and studied the auditory and non-auditory impact of noise pollution [12, 13]. Similar studies concerning air and water pollution have been published widely; however, no study has been conducted to assess the impact of COVID-19 induced lockdown for Indian cities. Therefore, it has become integral to study the effect of the lockdown on noise levels in Indian cities. The present study analyses the impact of reducing anthropogenic activities on the noise levels in two metropolitan Indian cities, namely Delhi and Mumbai. The study will assist policymakers and government bodies in identifying areas where there is a scope of reducing noise levels and understanding the noise level patterns in Indian cities.

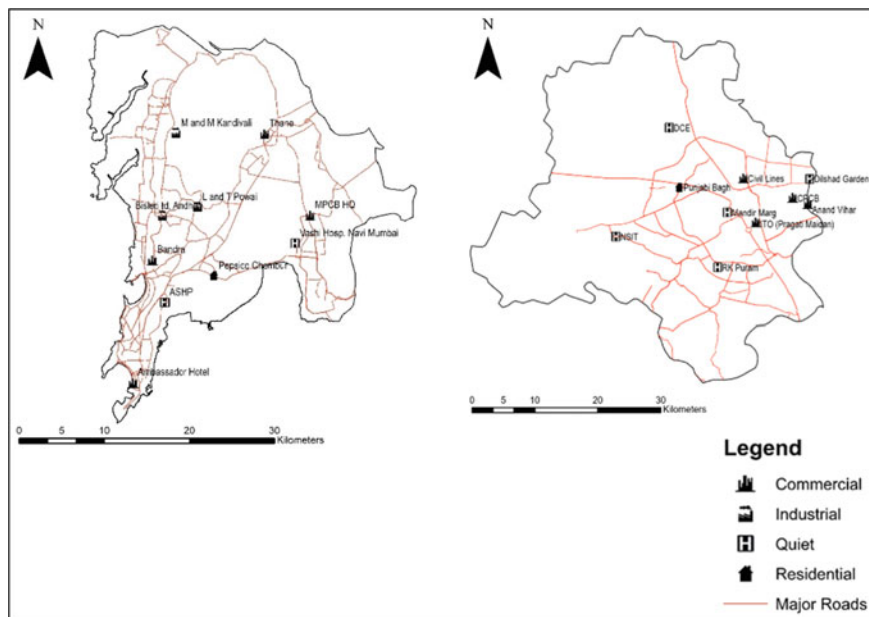
## 2 Methodology

### 2.1 Site Selection

The Central Pollution Control Board (CPCB) of India has a network of 70 noise monitoring stations across India in major metropolitan cities under the National Ambient Noise Monitoring Network (NANMN). CPCB has categorized the stations in four different categories, viz. Industrial Zone, Commercial Zone, Residential Zone, and Silence Zone based on the monitors' location around the city [14].

### 2.2 Data Collection and Interpretation

The present study utilizes hourly data from 20 monitoring stations (ten in each city) for the period 1st February–31st May for 2019 and 2020. The data has been examined for any obscure values and removed if found negative or beyond the explainable range for the analysis. The data is primarily bifurcated into two periods, Before Lockdown (BL)—1st February–24th March and After Lockdown (AL)—25th March–31st May for 2019 and 2020. The percentage changes in noise levels during the lockdown in 2020 is estimated with respect to the  $AL_{2019}$  period and  $BL_{2020}$  period. Percentage change with respect to  $AL_{2019}$  is denoted as  $AL_{2020}/AL_{2019}$  and with respect to  $BL_{2020}$  is denoted as  $AL_{2020}/BL_{2020}$ . The noise monitors are also plotted on the respective city's map (Fig. 1) to identify the primary noise generating sources, such as major roads, railway stations, and other public spaces.



**Fig. 1** Location of ambient noise monitoring monitors in Delhi and Mumbai

### 2.3 Parameters Analyzed

CPCB noise monitors provide several noise level parameters; however, for the present study, data for  $L_{eq}(A)$  (A-weighted, equivalent continuous sound level),  $L_{10}$  (noise level exceeded 10% of the time), and  $L_{90}$  (noise level exceeded 90% of the time) is collected.

In addition to the above-given parameters, Noise Climate (NC) has been calculated to analyze the sound level fluctuations within an hour. Equation 1 is used to estimate NC for a particular station within an hour [15]:

$$NC = L_{10} - L_{90} \quad (1)$$

## 3 Results and Discussion

### 3.1 Mumbai

Mumbai comprises of four commercial, three industrial, two silence, and one residential noise monitoring stations. During the lockdown, monitoring stations in Mumbai,

on average, recorded a drop of 2.23% (1.47 dB(A)) compared to BL<sub>2020</sub>, while there was a decrease of 2.05% (1.90 dB(A)) compared to AL<sub>2019</sub> in the Leq (A), as evident in Table 1. As evident from Figs. 2 and 3, diurnal values observed in silent, commercial, and residential zones for AL<sub>2020</sub> are less than BL<sub>2020</sub> and AL<sub>2019</sub>. In silence zone, values observed in AL<sub>2019</sub> are significantly higher than values observed for the year 2020, before and after the lockdown. For Industrial Zone, BL<sub>2020</sub> values are higher than both AL<sub>2019</sub> and AL<sub>2020</sub>. The most significant change in AL<sub>2020</sub> diurnal values are observed for the residential zone, indicating that due to the lockdown, all sources of noise pollution typical in a residential were on halt due to the lockdown; hence there was a significant impact on noise pollution values.

For Leq (A), during the Lockdown MPCB (Maharashtra Pollution Control Board) HQ, recorded the highest drop of 11.15% (7.6 dB (A)) compared to BL<sub>2020</sub>. In contrast, Vashi Hospital Navi Mumbai recorded the highest drop, 20.67% (15.46 dB(A)) compared to AL<sub>2019</sub>. MPCB HQ is surrounded by major roads and is located in a commercial zone. During the lockdown, all activity in commercial zones was at a halt; the significant decrease in noise pollution is attributed to the fact that all the commercial zones were shut down due to the nationwide lockdown. Vashi Hospital in Navi Mumbai is located in a quiet zone; hence due to the lockdown, there was a further decrease in noise levels compared to AL<sub>2019</sub>. Compared to BL<sub>2020</sub> in Lockdown, two locations Ambassador Hotel and Bandra recorded a significant increase of 6.13% in Leq (A). During the Lockdown Bisleri td. Andheri in the industrial zone had the highest average Leq (A) level, 76.89 dB (A), while ASHP recorded the lowest average Leq (A) level, 49.81 dB (A).

Among the ten stations installed in Mumbai, three stations are proficient at monitoring and recording percentile levels in noise. The Noise Climate at these monitoring stations presiding in Mumbai increased; the percentage increase with respect to BL<sub>2020</sub> was 79%, while the increase with respect to AL<sub>2019</sub> was 65%. Bisleri Andheri recorded the highest average NC was 12.79 dB (A) during the lockdown, while the lowest was 5.9 dB (A) and was recorded at Pepsico Chembur, Mumbai. Among these three monitoring stations, two stations recorded an increase in NC compared to AL<sub>2019</sub>, with an average increase of 112%. In comparison, one station recorded a decrease of 29% in NC compared to AL<sub>2019</sub>. Whereas in comparison to BL<sub>2020</sub>, an average increase of 123% was observed at two stations and a decrease of 8% was observed at the remaining station (Table 2).

### 3.2 Delhi

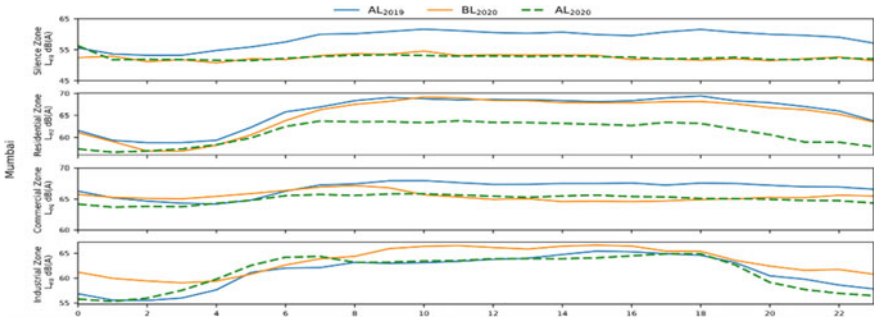
Delhi comprises of five Silence, four Commercial, and one Residential noise monitoring stations as observed in Figs. 4 and 5, which recorded the diurnal and daily variation in noise stations of Delhi for the four-time periods. The trend in Fig. 5 Daily shows that after lockdown, commercial zones observed a sharp decline in noise levels. Similarly, Residential zones also recorded noise levels below the 2019 values. Whereas silence zones hardly observed any change even after lockdown.

**Table 1**  $L_{eq}$  (A) during 2019/2020 and percentage drop during lockdown

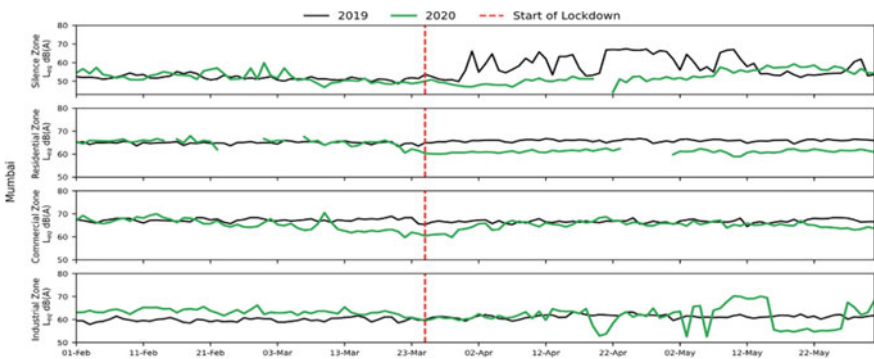
City	Zone	Station	BL <sub>2019</sub> dB (A)		AL <sub>2019</sub> dB (A)		BL <sub>2020</sub> dB (A)		AL <sub>2020</sub> dB (A)		AL <sub>2020</sub> /AL <sub>2019</sub> (%)		AL <sub>2020</sub> /BL <sub>2020</sub> (%)		Average AL <sub>2020</sub> /AL <sub>2019</sub> (%)		Average AL <sub>2020</sub> /BL <sub>2020</sub> (%)		
			Mean	Mean	Mean	Mean	Mean	Mean	Mean	Mean	Mean	Mean	Mean	Mean	Mean	Mean	Mean	Mean	
Delhi	C	Anand Vihar	64.75	64.09	63.42	63.87	53.87	15.94	15.05	1.26	2.64								
	C	CPCB	62.38	62.6	62.19	56.63	9.54	8.94											
	C	Civil Lines	60.62	60.37	59.59	57.67	4.47	3.22											
	C	ITO (Pragati Maidan)	71.83	71.37	72.96	77.42	-8.47	-6.11											
	S	DCE	55.11	61.2	57.77	58.93	3.72	-2											
	S	Dilshad Garden	58.13	55.65	66.28	66.9	-20.21	-0.93											
	S	Mandir Marg	55.17	54.35	53.82	57.27	-5.38	-6.42											
	S	NSIT	56.73	56.65	57.62	52.72	6.94	8.5											
Mumbai	S	RK Puram	57.76	57.67	59.24	57.16	0.88	3.51											
	R	Punjabi Bagh	56.29	56.54	55.05	53.6	5.2	2.64											
	C	Ambassador Hotel	70.3	70.33	61.98	65.78	6.47	-6.13											
	C	Bandra	61.12	60.42	61.98	65.78	-8.87	-6.13											
	C	MPCB HQ	68.69	68.22	68.18	60.58	11.21	11.15											
	C	Thane	69.33	67.9	68.52	67.72	0.26	1.16											
	I	Bisleri td. Andheri	67.14	70.43	77.34	76.89	-9.16	0.59											

(continued)





**Fig. 2** Mumbai zone wise diurnal variation in noise levels from 1st February 2020 to 31st May 2020



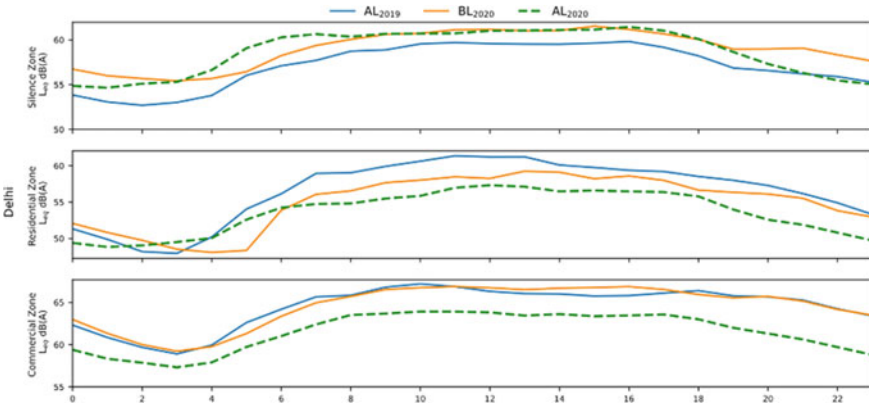
**Fig. 3** Mumbai zone wise daily variation in noise levels from 1st February 2020 to 31st May 2020

Commercial zones observed noise levels below the  $AL_{2019}$  and  $BL_{2020}$  noise levels (Fig. 4). However, in silence zones, there was not a significant difference in the noise levels. The maximum decrease in noise levels with respect to  $BL_{2020}$  and  $AL_{2019}$  was observed in commercial stations with an average decrease of 5% (4 dB (A)) Table. The Anand Vihar noise monitoring station recorded the maximum decrease in noise levels which decreased by 16% (11 dB (A)) as compared to  $AL_{2019}$  and 15% (10 dB (A)) as compared to  $BL_{2020}$ . This sharp decline can be attributed to the fact that Anand Vihar is in proximity to the train, bus, and metro stations. However, Silence zones in Delhi observed the least change –2.81% with compared to  $AL_{2019}$ . Dilshad Garden recorded –20.21% (11 dB (A)) change in the silence zones.

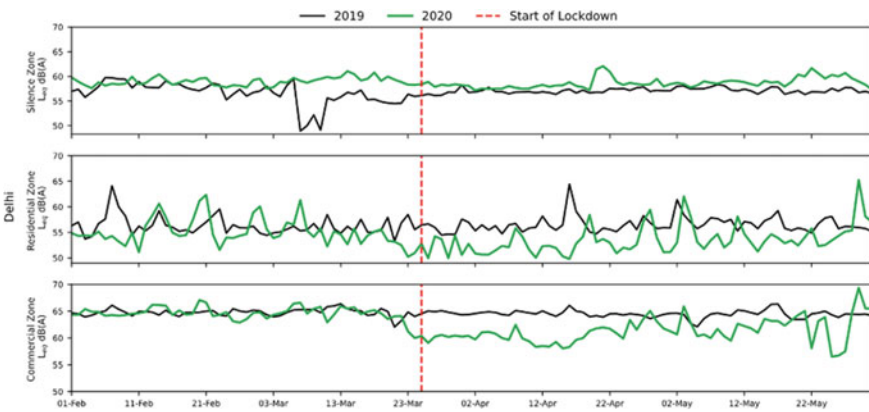
Among the ten stations installed in Delhi, four stations record monitoring and recording percentile levels in noise. The Noise Climate at these monitoring stations presiding in Delhi decreased; the percentage increase with respect to  $BL_{2020}$  was 2.83%, while the increase with respect to  $AL_{2019}$  was 4.65%. Mandir Marg recorded the highest average NC was 8.31 dB (A) during the lockdown, while the lowest was 4.14 dB (A) and was recorded at RK Puram. Among the four stations, two stations

**Table 2** Noise climate during 2019/2020 and percentage drop during lockdown

City	Zone	Station	BL <sub>2019</sub> dB (A)		AL <sub>2019</sub> dB (A)		BL <sub>2020</sub> dB (A)		AL <sub>2020</sub> dB (A)		AL <sub>2020</sub> /AL <sub>2019</sub> (%)	AL <sub>2020</sub> /BL <sub>2020</sub> (%)	Average AL <sub>2020</sub> /AL <sub>2019</sub> (%)	Average AL <sub>2020</sub> /BL <sub>2020</sub> (%)
			Mean	Mean	Mean	Mean	Mean	Mean						
Delhi	C	Anand Vihar	7.15	7.22	6.93	6.35	6.35	12.06	8.46	4.65	2.83			
	C	Civil Lines	7.07	5.62	6.46	6.77	6.77	-20.54	-4.76					
	S	Mandir Marg	7.71	7.23	6.84	8.31	8.31	-14.92	-21.53					
	S	RK Puram	7.71	7.13	5.84	4.14	4.14	42	29.15					
Mumbai	C	Ambassador Hotel	11.06	10.62	NA	NA	NA	NA	NA	NA	-65.34		-79.41	
	I	Bisleri id. Andheri	3.88	4.29	4.18	12.79	12.79	-198.07	-206.07					
	I	L and T Powai	5.9	6.96	6.29	8.82	8.82	-26.6	-40.28					
R		Pepsico Chembur	8.7	8.24	6.4	5.88	5.88	28.63	8.12					



**Fig. 4** Delhi zone wise diurnal variation in noise levels from 1st February 2020 to 31st May 2020



**Fig. 5** Delhi zone wise daily variation in noise levels from 1st February 2020 to 31st May 2020

recorded increased NC during AL<sub>2020</sub> as compared to AL<sub>2019</sub> with an average of 17.5%. In comparison, the other two stations recorded an average decrease of 27% in NC compared to AL<sub>2019</sub>. The increase in NC indicates that the sound level fluctuations have increased during the lockdown [8]. The decrease in Leq (A) and the increase in NC in the silence zones demonstrates that the background noise levels have decreased primarily because of reduced traffic and commotion in these areas.



## 4 Conclusion

The lockdown implemented to curb the spread of COVID-19 in 2020 led to an extensive curtailment of anthropogenic activities, contributing to a considerable reduction in environmental pollution worldwide. The present study delves deep into quantifying and analyzing the effect of the lockdown on noise levels in urban cities across India. Significant findings of this study are as follows:

- Among the 20 stations, 14 stations observed a reduction in noise levels with respect to  $AL_{2019}$  and 13 stations with respect to  $BL_{2020}$ .
- Seven monitoring stations monitoring fluctuations in noise levels recorded an increase of 25.35% compared to  $AL_{2019}$  and 32.42% compared to  $BL_{2020}$  in Noise Climate (NC).
- The Silence and Industrial zone stations experienced the slightest change during lockdown with an average change in noise levels ~ less than 2 dB (A) compared to  $BL_{2020}$  and  $AL_{2019}$ .
- The Residential zone stations observed an average noise level change of ~3 dB (A) with respect to  $BL_{2020}$  and ~4 dB (A) with respect to  $AL_{2019}$ .
- The Commercial zone stations recorded an average change of ~2 dB (A) with respect to  $BL_{2020}$  and  $AL_{2019}$ .
- The highest drop in  $Leq$  (A) compared to  $AL_{2019}$  and  $BL_{2020}$  was recorded at Vashi Hosp. Navi Mumbai (20.67%) and Anand Vihar (15.05%), respectively.
- Among the two cities, the maximum drop with respect to  $AL_{2019}$  was observed in Mumbai ~2 dB (A), followed by Delhi ~1 dB (A).

**Acknowledgements** The authors are incredibly grateful to Advance Air & Acoustics Research Laboratory, Delhi Technological University, Delhi (India), to encourage to conduct this research and provide all the facility to compile this work.

## References

1. WHO: Coronavirus disease (COVID-19) Situation Report – 132. (2020)
2. Fu F, Purvis-Roberts KL, Williams B (2020) Impact of the COVID-19 pandemic lockdown on air pollution in 20 major cities around the world. *Atmosphere* 11:1189. <https://doi.org/10.3390/atmos11111189>
3. Agarwal A, Kaushik A, Kumar S, Mishra RK (2020) Comparative study on air quality status in Indian and Chinese cities before and during the COVID-19 lockdown period. *Air Qual Atmos Health* 13:1167–1178. <https://doi.org/10.1007/s11869-020-00881-z>
4. Banerjee D, Chakraborty SK, Bhattacharyya S, Gangopadhyay A (2008) Evaluation and analysis of road traffic noise in asansol: an industrial town of eastern India. *Int J Environ Res Public Health* 5:165–171. <https://doi.org/10.3390/ijerph5030165>
5. Sinha S, Sridharan PV (1999) Present and future assessment of noise level in the Neyveli region. *J Environ Stud Policy* 2:1–14
6. WHO: Burden of disease from environmental noise: Quantification of healthy life years lost in Europe. World Health Organization. Regional Office for Europe (2011)

7. Öhrström E (2004) Longitudinal surveys on effects of changes in road traffic noise—annoyance, activity disturbances, and psycho-social well-being. *J Acoust Soc Am* 115:719–729
8. Pathak V, Tripathi BD, Mishra VK (2008) Dynamics of traffic noise in a tropical city Varanasi and its abatement through vegetation. *Environ Monit Assess* 146:67–75. <https://doi.org/10.1007/s10661-007-0060-1>
9. Luxon LM, Prasher D eds (2007) Noise and its effects
10. Basu B, Murphy E, Molter A, Sarkar Basu A, Sannigrahi S, Belmonte M, Pilla F (2021) Investigating changes in noise pollution due to the COVID-19 lockdown: the case of Dublin Ireland. *Sustain Cities Soc* 65:102597. <https://doi.org/10.1016/j.scs.2020.102597>
11. Asensio C, Pavón I, de Arcas G (2020) Changes in noise levels in the city of Madrid during COVID-19 lockdown in 2020. *J Acoust Soc Am* 148:1748–1755. <https://doi.org/10.1121/10.0002008>
12. Gray A (2021) These are the cities with the worst noise pollution. <https://www.weforum.org/agenda/2017/03/these-are-the-cities-with-the-worst-noise-pollution/>. Last Accessed 21 Jan 2021
13. Jamir L, Nongkynrih B, Gupta SK (2014) Community noise pollution in urban India: need for public health action. *Indian J Commun Med* 39:8. <https://doi.org/10.4103/0970-0218.126342>
14. CPCB: CPCB ENVIS | Control of Pollution. [http://www.cpcbenvnis.nic.in/noise\\_quality\\_data.html](http://www.cpcbenvnis.nic.in/noise_quality_data.html). Last Accessed 21 Jan 2021
15. Hunashal RB, Patil YB (2012) Assessment of Noise Pollution Indices in the City of Kolhapur, India. *Procedia Soc Behav Sci* 37:448–457. <https://doi.org/10.1016/j.sbspro.2012.03.310>

# Evaluation of Metal Removal Rate in EDM Machining of AISI P20 Steel



Tariq Zafar, Shivam Rawat, Satyam Tiwari, Abhishek Singh, Anurag Shanu, and Shrikant Vidya

## 1 Introduction

EDM machining is a non-traditional process of machining which is employed for the fabrication of electrically conductive tough materials with the help of spark produced between workpiece and cutting tool [1–3]. AISI P20 steel is a pretty choice for many industries due to their high strength [4, 5]. AISI P20 steel is used to produce thermoplastic molds, injection molds, die casting dies, and extrusion dies. It is also used to prepare structural components of automobiles. As far as machinability of AISI P20 steel is concerned, traditional machining processes exhibits poor process performance when the MRR and surface finish is of utmost important criteria. It is indeed a challenge for increasing the surface quality of the machining as well as improving the metal removal rate. Since AISI P20 steel possesses high strength, an advanced machining technology like EDM is required for machining purposes. Burr free edges are often made with very good surface finish with contact free machining process of EDM [4, 6, 7]. A dielectric medium is used in the form of fluid to initiate a spark between tool electrode and workpiece material [8]. Though EDM has merits, its tool wear is very high [9, 10]. AISI P20 steel has been selected as work piece (anode) for machining in EDM process, and copper has been taken as cutting tool (cathode) [11].

Fred and Weingaertner [12] reported that the customers develop their process parameters by doing many experimental tests in the tooling industry. They conducted a test on EDM of AISI P20 steel with two different cutting tools. They got the best MRR with EDM negative graphite electrodes.

---

T. Zafar · S. Rawat · S. Tiwari · A. Singh · A. Shanu (✉) · S. Vidya  
Department of Mechanical Engineering, Galgotias University, Noida, India  
e-mail: [anurag.shanu@galgotiasuniversity.edu.in](mailto:anurag.shanu@galgotiasuniversity.edu.in)

Kiyak and Çakır [13] examined the influence of machining factors on the quality of surface in machining of AISI P20 tool steel. Pulse-on-time, current, and pulse-off-time were chosen as the parameters. The pulse current was the dominating parameter, and pulse time was the second most influencing. They concluded that higher values pulse current affects the surface roughness. Dewangan and Shailesh Kumar [14] optimized tool wear rate of EDM with the help of Grey relational method (GRA). They chose AISI P20 steel as work piece, and they applied Taguchi method with L27 Orthogonal array (OA). They suggested that MRR is affected by electrode lift time. Dadvandipour [15] reported the “evaluation of process parameters of EDM in AISI P20 steel” with three different cutting tools such as brass, graphite, and copper. They took three parameters (pulse-on-time, voltage, peak current) for analyzing the rate of material removal, tool wear, and roughness of the produced surface. Nevertheless, EDM can replace traditional machining in terms of performing very hard material; still it has disadvantages of poor MRR. Hence much research is going on to evaluate the parameters of EDM for the better metal removal rate [16–19].

The present study is focused on some vital parameters which influence the EDM performance such as pulse-on-time, current, and pulse-off-time for fabrication of AISI P20 steel toward improving the MRR. Since EDM has poor MRR when compared to other advanced machining technology, present focus is to improve the MRR by analyzing the effects of parameters through ANOVA [20–23].

## 2 Experimental Setup

The AISI P20 steel has high strength and conventional machining cannot perform machining operation with ease and hence one of the advanced machining technologies known as EDM process was selected for machining the AISI P20 work piece. The entire experimentation was conducted on an EDM machine of model ELECTRONICA-(500 × 300 ZNC) which is shown in Fig. 1. Here the work piece

**Fig. 1** EDM machine for experiment



**Table 1** Properties of AISI P20 steel

Density	7.85 gm/cm <sup>3</sup>
Specific gravity	7.86
Modulus of elasticity	207 GPa
Hardness, Brinell	300
Ultimate tensile strength	1000 MPa
Tensile-yield	850 MPa
Compressive strength	850 MPa
Poisson’s ratio	0.27–0.30
Elastic modulus	200 GPa

is kept as anode as more metal removal is done only in anode. Copper is used as an electrode, and it acts as cathode. Hydrocarbon oil is used as dielectric fluid, and it cools the work surface and electrode and also maintains the spark gap in EDM. Removal of EDM chips is mainly carried out by dielectric fluid.

**2.1 Selection of Material and Tool**

AISI P20 steel is selected as work piece, and it has higher hardness and plasticity. Variety of molds is made with AISI P20 steel. So, it can be used to make a variety of molds. Table 1 represents the mechanical properties of the selected work material, AISI P20 steel.

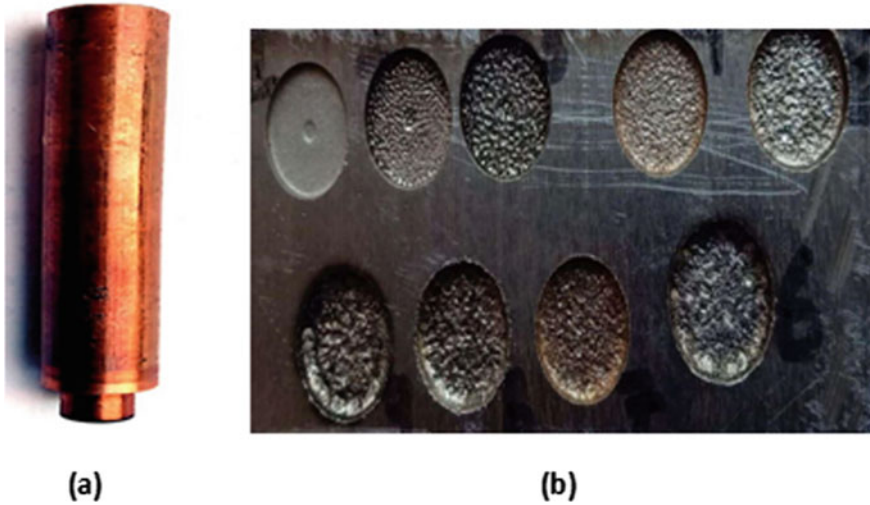
The chemical composition of workpiece material is presented as follow:

C (%)	0.30–0.40
Si (%)	0.30–0.70
Cr (%)	1.50–2.00
Mo (%)	0.35–0.55
Mn (%)	0.60–1.00

EDM use different tool like copper, graphite, silver alloys, etc. Copper is selected as tool material, and it is shown in Fig. 2. The form of copper is cylindrical with diameter 6 mm.

**2.2 Evaluation of MRR**

Thermal energy produced is responsible for material removal in EDM process. Removal rate of material is expressed as the ratio of change in weight difference



**Fig. 2** a Copper-tool after machining b Machined holes over AISI P20

divided by duration of machining, and it is given in Eq. 1. Machined work part is shown in Fig. 2.

$$\text{MRR} = (W_1 - W_2)/t_m \times \rho, \quad (1)$$

where

- $W_1$  weight before experiment
- $W_2$  weight after experiment
- $\rho$  density of material = 7.85 gm/cm<sup>3</sup>
- $t_m$  machining time.

### 2.3 Design of Experiments (DoE)

Taguchi Method based on L9 Orthogonal Array (OA) has been chosen for conducting the experiment so as to improve the MRR. Taguchi Method is employed in the quality control methodology to achieve a good design by combining control charts and process control with product and process design. Taguchi design is intended to minimize the variability of the product. The DoE is employed to create a best combination of parameters in OA. In this experiment three important parameters were used namely pulse-on-time (in  $\mu\text{s}$ ), pulse-off-time (in  $\mu\text{s}$ ) and, current (in Ampere). Machining parameters and their level is shown in Table 2.

**Table 2** Parameters of machining and their levels

Machining factors	Unit	Levels		
		1	2	3
Current	A	1	15	30
Pulse-on-time (T <sub>ON</sub> )	μs	100	1500	3000
Pulse-off-time (T <sub>OFF</sub> )	μs	1	6	12

**Table 3** Experimental results for MRR

Exp. no	Current	T <sub>ON</sub>	T <sub>OFF</sub>	MRR (mm <sup>3</sup> /min)
1	1	100	1	0.1698
2	1	1500	6	0.2070
3	1	3000	12	0.0871
4	15	100	6	4.2460
5	15	1500	12	7.1330
6	15	3000	1	1.3500
7	30	100	12	12.7380
8	30	1500	1	11.8900
9	30	3000	6	2.5478

### 3 Results and Discussion

Results from the experiment have been discussed by analyzing the three different parameters on MRR, and its result is illustrated in Table 3. Plot for mean is produced in Fig. 3. In the main effects plots for means, the MRR value increases with the current value. The rate of increase in value of MRR is slightly more for the range of current (15–30 A) than the range of current (1–15 A). The MRR increases very slightly as the values of pulse on time increases from 100 to 1500 μs. The MRR value declines more quickly as the T<sub>ON</sub> is increased from 500 to 1000 μs. As the value of T<sub>OFF</sub> increases from 1 to 6 μs, MRR decreases. MRR, on the other hand, improves after 6 μs.

The residual plots for MRR shown in Fig. 4 expresses the normal probability against the standardized residuals in which the straight line indicates that the model is valid and there is no abnormality. Response table is portrayed in Table 4.

Similarly, for response table for means is presented in Table 5. ANOVA for MRR is shown in Table 6.

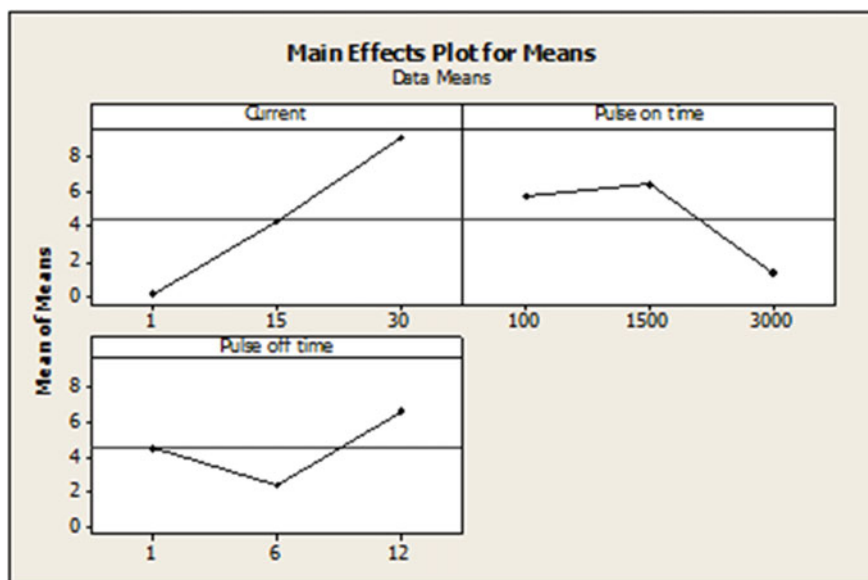


Fig. 3 Main effects plots for means

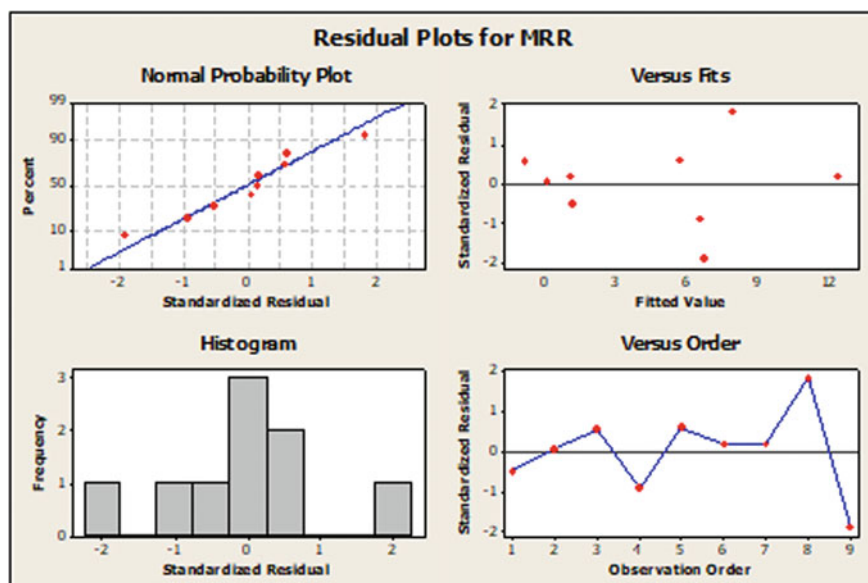


Fig. 4 Residual plots for material removal rate



**Table 4** Response table for S/N ratios for larger is better

1	-16.760	6.240	2.903
2	10.744	8.296	2.334
3	17.243	-3.490	5.989
Delta	34.003	11.786	3.655
Rank	1	2	3

**Table 5** Response table for means

Level	Current	T <sub>ON</sub>	T <sub>OFF</sub>
1	0.1546	5.7179	4.4699
2	4.2430	6.4100	2.3336
3	9.0586	1.3283	6.6527
Delta	8.9040	5.0817	4.3191
Rank	1	2	3

**Table 6** Variance analysis for material removal rate

Source	DoF	Seq SS	Adj SS	Adj MS	F	P	% of Contribution
Current	2	119.185	119.185	59.593	16.74	0.056	59.63
T <sub>ON</sub>	2	45.572	45.572	22.786	6.40	0.135	22.80
T <sub>OFF</sub>	2	27.983	27.983	13.992	3.93	0.203	14
Error	2	7.120	7.120	3.560			3.5
Total	8	199.860					

$S = 1.88678$

$R\text{-Sq} = 96.44\%$

$$MRR = 0.76 + 0.307 \text{ Current} - 0.00154 T_{ON} + 0.216 T_{OFF} \tag{2}$$

Experimental = 10.252

Predicted = 13.105

From Table 6, it is evident that P value is significantly influenced by current mainly whose value is almost equal to 0.05. The p-values greater than 0.1 denote unimportant model terms and P value of T<sub>ON</sub> and T<sub>OFF</sub> is bigger than 0.05. Hence the vital parameter is current. The contribution of T<sub>ON</sub>, current, and T<sub>OFF</sub> in percentage are 59.63, 22.80, 14 respectively. The percentage of error is 3.5 and lies within 5%; hence the mathematical findings are in the acceptable range. The regression equation is calculated as Eq. (2).

## 4 Conclusions

With the three important parameters of EDM process, experiments were performed successfully with the help of Taguchi's L9 Orthogonal array. AISI P20 steel was chosen as a workpiece (anode) and copper electrode (cathode) as a tool. The purpose of the present work was to find MRR and the effects of parameters on the responses using a statistical tool called ANOVA. It was found that the current has significance value (59%) for higher MRR. Pulse-on-time (22.80%) has a little role on MRR, and similarly the pulse off time (14%) is very least important. The optimal input parameters are found as A3, B2, and C3. Also, it is proved from the ANOVA table that only current has significance value as its P value is almost equal to 0.05. The P-values greater than 0.1 denote unimportant model terms. The most vital parameter is current. The percentage of error is 3.5 and lies within 5%, hence the statistical conclusions are in the acceptable range.

## References

1. Shankar S, Maheshwari S, Pandey PC (2004) Some investigations into the electric discharge machining of hardened tool steel using different electrode materials. *J Mater Process Technol* 149(1–3): 272–277
2. Singh N, Raghukandan K, Rathinasabapathi M, Pai BC(2004) Electric discharge machining of Al–10% SiCP as-cast metal matrix composites. *J Mater Process Technol* 155:1653–1657
3. Dwivedi A, Choudhury SK (2016) Effect of tool rotation on MRR, TWR, and surface integrity of AISI-D3 steel using the rotary EDM process. *Mater Manuf Process* 31(14):1844–1852
4. Lin YX, Lin H, Han ZW (2014) Effect of cutting speed on wear property of TiAlN PVD coated tools in high-speed milling of AISI P20 mold steel. *Key Eng Mater* 621:75–81. Trans Tech Publications Ltd
5. Kumar A (2015) Machining performance OfAisi P20 steel with graphite and tungsten based electrode on EDM. PhD diss, MNIT Jaipur
6. George PM, Raghunath BK, Manocha LM, Warriar AM (2004) EDM machining of carbon–carbon composite—a Taguchi approach. *J Mater Process Technol* 145(1):66–71
7. Subramaniam K, Natarajan A, Vinayagam N, Muthiya J, Rajendiran R (2020) Optimization of wire cut EDM process parameters of Al/SiO<sub>2</sub> composites using Taguchi method. No 2020-28-0426
8. Ming QY, He LY (1995) Powder-suspension dielectric fluid for EDM. *J Mater Process Technol* 52(1):44–54
9. Bleys P, Kruth J-P, Lauwers B, Zryd A, Delpretti R, Tricarico C (2002) Real-time tool wear compensation in milling EDM. *CIRP Ann* 51(1):157–160
10. Bleys P, Kruth J-P, Lauwers B (2004) Sensing and compensation of tool wear in milling EDM. *J Mater Process Technol* 149(1–3):139–146
11. Aligiri E, Yeo SH, Tan PC (2010) A new tool wear compensation method based on real-time estimation of material removal volume in micro-EDM. *J Mater Process Technol* 210(15):2292–2303
12. Amorim FL, Weingaertner WL (2007) The behavior of graphite and copper electrodes on the finish die-sinking electrical discharge machining (EDM) of AISI P20 tool steel. *J Braz Soc Mech Sci Eng* 29(4):366–371
13. Kiyak M, Çakır O (2007) Examination of machining parameters on surface roughness in EDM of tool steel. *J Mater Process Technol* 191(1–3):141–144

14. Dewangan SK (2010) Experimental investigation of machining parameters for EDM using U-shaped electrodes of AISI P20 tool steel. Department of Mechanical Engineering, National Institute of Technology Rourkela (India)
15. Dadvandipour S (2013) On the experimental study of electric discharge machining (EDM) of P20 type tool steel. In: 2013 IEEE 11th international symposium on applied machine intelligence and informatics (SAMII), pp 245–248. IEEE
16. Kumaravel S, Alagumurthi N (2020) Material removal characteristics of Al–SiO<sub>2</sub> composite in WEDM. *Epitoanyag-J Silicate Based Compos Mater* 72(1)
17. Pradhan MK, Biswas CK (2008) Modelling of machining parameters for MRR in EDM using response surface methodology
18. Jabbaripour B, Sadeghi MH, Faridvand Sh, Shabgard MR (2012) Investigating the effects of EDM parameters on surface integrity, MRR and TWR in machining of Ti–6Al–4V. *Mach Sci Technol* 16(3):419–444
19. Das MK, Kumar K, Barman TK, Sahoo P (2013) Optimization of surface roughness and MRR in EDM using WPCA. *Proc Eng* 64:446–455
20. Asal VD, Patel RI, Choudhary AB (2013) Optimization of process parameters of EDM using ANOVA method. *Int J Eng Res Appl* 3(2):1119–1125
21. Sivaraj M, Selvakumar N (2016) Experimental analysis of Al–TiC sintered nanocomposite on EDM process parameters using ANOVA. *Mater Manuf Process* 31(6):802–812
22. Tosun N, Cogun C, Inan A (2003) The effect of cutting parameters on workpiece surface roughness in wire EDM. *Mach Sci Technol* 7(2):209–219
23. Singh A, Kumar A, Kumar S, Kumar A, Vidya S (2018) A review on research aspects and trends in electrical discharge machining (EDM). *Int J Eng Technol Sci Res* 5:2394–3386

# Floating Solar Power Plant System



Bhanu Pratap Bhandari, Yati Sharma, and Altaf Hasan Tarique

## 1 Introduction

The most disturbing issue in our nation is forced emergency. Almost seventy percent of coal is utilized in the time of electrical power. Water framework, industry creation also gets influenced because of difficulty shedding, step-by-step conclusion, etc. So we need to move toward manageable force sources to deliver power. As of now, a day's reasonable force sources are developing fast not only in India but rather also in other nations. Daylight-based energy is the extraordinary, practical, and bountiful wellspring of elective energy. The utilization of sun-controlled energy Sun-based energy diminishes nursery sway [1, 2].

Zone-wise seventh most prominent nation in India and has extraordinary sunlight. Sun-arranged energy can't avoid being energy conveyed by the sun made through an atomic communication and this cycle container energy and magnetic radiation. That magnetic radiation has the power which appears on the land. Sun-arranged energy is the wandering wellspring of power as we need 2 fundamental parts: from the very start, the ability to amass radiation that comes from the sun and changes it into the electric power structure, other than limit units like emissions are moving into the environment. For addressing the power emergency, sun-filled energy will be a fabulous course of action yet to use land mounted close-by planetary gathering is the need for the earth that is excessive and little accessible for getting it. India will make 1.75 GW sunlight-based forces from the doable power source and 1 GW of solar arranged force for moving toward ten years. As demonstrated by Pandit Jawaharlal Nehru Public Sunlight-based Mission around five thousand Mega Watt have been affirmed to date in various pieces of the country. For making the country

---

B. P. Bhandari (✉) · Y. Sharma · A. H. Tarique  
Department of Mechanical Engineering, Galgotias University, Greater Noida 203201, India  
e-mail: [bhanu.bhandari01\\_2017@galgotiasuniversity.edu.in](mailto:bhanu.bhandari01_2017@galgotiasuniversity.edu.in)

© The Author(s), under exclusive license to Springer Nature Singapore Pte Ltd. 2022  
R. M. Singari et al. (eds.), *Advances in Mechanical Engineering and Technology*,  
Lecture Notes in Mechanical Engineering,  
[https://doi.org/10.1007/978-981-16-9613-8\\_42](https://doi.org/10.1007/978-981-16-9613-8_42)

461

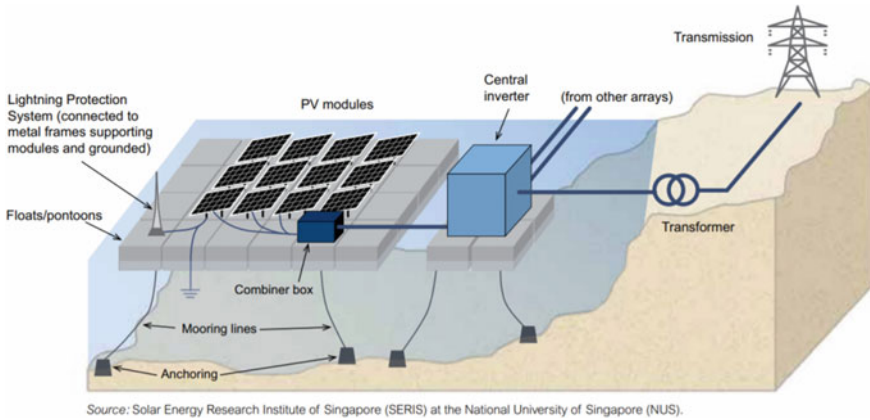
devouring green force on the planet, the progress isn't simply palatable and needs hard endeavors by each state and state division [3, 4].

Drifting close planetary frameworks have photovoltaic concentrators that are incredibly lightweight and this coasts over a water body, situated on got freight ships skim ostensibly of water structure streams, water supplies, quarry lakes, and following lakes. A portion of the constructions exists in France, India, Japan, Korea, the Unified Realm, and the US [5].

The floating close planetary framework diminishes the need for excessive land in a territory, it also saves the drinking water that would by one way or another be lost as a result of dissemination, reducing the advancement of green development. The close-by planetary gathering shows the highest capacity like the heaps up is placed inside a cool temperature then they will be shorewards locale. The drifting stages can be recycled a hundred percent, using higher thickness polyethylene that may withstand splendid columns and may be used [6, 7].

## 2 Fundamentals and Outline of Floating Solar PV Plants

The drifting sun-fueled plant is presented over water archives as dam, lake, streams, and oceans. The sun put together sheets are mounted concerning for to skimming stages which are gotten solidly to with the objective that it won't get injured significantly under the more woeful ecological conditions. Additionally, research proposes that sun-based sheets presented aground surfaces achieve the diminishing of gains like the land prepares and impacts the back surface of the sun arranged board. Studies furthermore suggest that if the back surfaces of daylight put together sheets are put concerning the most elevated place of the water, the sun-fueled sheets will need for cooling themselves much higher competently that gathers they will last more and they may cover the water they coast on which lessens dissipating by subordinate upon seventy percent, and their capacity for making energy go up as higher as to sixteen percent. The mix of photovoltaic plant improvement and skimming headway gives a photovoltaic drifting force age. That blend of the novel idea includes a floating framework which is a gliding body (structure + floater) that permits the establishment of the PV module, PV framework, for example, PV age gear, as electrical union boxes that are introduced on top of the skimming structure and brought down association which moves the made capacity to the PV framework movement as shown in Fig. 1. Drifting sun-arranged shows are PV structures that skim apparently of drinking water supplies, quarry lake, water system channels, or remediation and following lakes. Very few such frameworks exist in France, India, Japan, South Korea, the Unified Realm, Singapore, and the US. The framework is said to have benefits over the photovoltaic plants on a solid surface. The expense for the surface is even much costly, and there are fewer principles and rules for the structure subject to streams not utilized for amusement. Not in the least like most land-based daylight-based plants, skimming bunches can be unpretentious considering the way that they are stowed away from general perceivability. They achieve higher efficiencies than PV sheets aground, in



**Fig. 1** Floating solar power plant [10]

light of the fact that water cools the sheets, the sheets have a one-of-a-kind covering to thwart rust or disintegration [8, 9].

### 2.1 Idea of Floating PV System

This is a novel plan for introducing a solar-based photovoltaic framework on the water body by utilizing drifting innovation. The force ages result through the blend of photovoltaic plant innovation and drifting innovation. This innovation changes the establishment of a PV force plant on the important surface. The gliding photovoltaic plant comprises a Barge or different buoys, securing framework, sunlight-based boards, and links (Fig. 1). As indicated by an exploration, having this powerful concealment from the barge and the PV boards on the supplies brought about a decrease of water vanishing through the repository. Exploration inside Australia proposes that up to forty percent of open repository’s water might be lost at the time of vanishing. The main boundary considered for the exhibition assessment of the FPV is the photovoltaic successful change productivity in employable condition, which influences the power age and in this manner much important result of the segment. We can give the change productivity of a photovoltaic module by the proportion between the created electric force and the occurrence of sun-based radiation power, as per the accompanying articulation:

$$\eta_{el} = \frac{P_{max}}{SXA_{Pv}} \times 100\%$$

where

$\eta_{el}$  is the electric effectiveness (%),  $P_{max}$  is the energy created by photovoltaic module (W),  $S$  is the sun-based radiation power occurrence over the photovoltaic module ( $W/m_2$ ), and  $A_{pv}$  is the front photovoltaic module land present for the sun-based radiation intensity ( $m_2$ ).

### **3 Components of Floating Power Plant**

It is an imaginative idea in power advancement to address the issues inside late memory. The coasting PV framework is another technique for sun-based energy age using water plane accessible on dams, supplies, and different bodies of water coming about because of the blend of PV innovation and skimming innovation. The coasting PV plant comprises a drifting framework, securing framework, PV framework, and submerged links. The gliding sunlight-based force framework likewise gives other natural advantages like avoidance of dissipation of water. The frameworks can likewise improve water quality. Sun-powered boards go about as rooftops for the water bodies, so the water won't be presented to the sun and environment; it adds beneficitation for drinking water plants.

#### **3.1 Pontoon/Boat**

It is a gliding structure. The boat has light enough to skim on water and back a hefty burden. The construction is planned, for example, it can hold a number of boards. Drifting design permits the establishment of a PV module.

#### **3.2 Mooring Structure**

A getting structure is a suffering arrangement that gets skimming advancement. The getting gives thwart the free progression of floating development over the water. An anchor getting fixes a floating improvement's position near with a point on the lower part of a stream without interfacing the skimming setup to drift. This awards changing water level vacillations at the same time keeping up its situation toward the south heading.

#### **3.3 Solar Module**

It is a PV production gear, like electric intersection boxes, which are introduced at the peak of the drifting framework. A solitary sun-based unit can create just a

restricted measure of force; most establishments contain various modules. A photovoltaic framework normally incorporates a board or a variety of sun-based modules, a sunlight-based inverter, and here and there a battery as well as a sun-powered tracker and interconnection wiring. Generally, glass-like sun-based PV modules have been utilized for drifting sun-oriented frameworks.

### **3.4 Cabling**

It is utilized to move produced energy from the water body to the substations. Taking into account their outside use, sun-arranged associations are explicitly proposed to keep secured against Ultra-Violet radiations and staggeringly more against Ultra-Violet radiations and staggeringly more temperature insecurities. Those are usually unchanged by the climate.

## **4 Environmental Effects of Floating Solar**

The floating sunlight-based stage permits standard PV boards to be introduced on enormous waterways like drinking water supplies, quarry lakes, water system channels, or remediation and following lakes. the basic and reasonable drifting sun-oriented stage is especially well appropriate for energy and water-serious enterprises who can't bear to squander both surface and water. The winery, dairy farm, fish farm, mining associations, wastewater treatment plant, water framework territories, and water workplaces are organizations that may benefit from the helpful energy that skimming nearby the planetary group makes among sun and water.

## **5 Conclusions**

The research provided in this paper can be used to help improve floating photovoltaic systems in the future. To revolutionize floating solar, threats must be recognized and properly monitored. Floating solar energy, on the other hand, seems to have a promising future. It is essential to develop a solar tracking device that can adjust the tilt and azimuth angle of a floating PV system.

When designing a solar panel, the maximum wind speed, water current, temperature cap, snow load, cyclone, and typhoon must all be taken into account. The efficiency of a floating solar plant is 11% higher and decreases water evaporation by 70%, but the cost of such a power plant is 1.2 times that of a conventional solar plant.



## References

1. Sharma P, Muni B, Sen D (2015) Design parameters of 10 KW floating solar power plant. In: Proceedings of the international advanced research journal in science, engineering and technology (IARJSET), National conference on renewable energy and environment (NCREE-2015), Ghaziabad, India, vol 2
2. Majid ZAA, Ruslan MH, Sopian K, Othman MY, Azmi MSM (2014) Study on performance of 80 Watt floating photovoltaic panel. *J Mech Eng Sci* 7:1150–1156
3. Sahu A, Yadav N, Sudhakar K (2016) Floating photovoltaic power plant: a review. *Renew Sustain Energy Rev* 66:815–824
4. Zhou X, Yang J, Wang F, Xiao B (2009) Economic analysis of power generation from floating solar chimney power plant. *Renew Sustain Energy Rev* 13(4):736–749
5. Goswami A, Sadhu P, Goswami U, Sadhu PK (2019) Floating solar power plant for sustainable development: a techno-economic analysis. *Environ Progr Sustain Ener* 38(6):e13268
6. Mittal D, Saxena BK, Rao KVS (2017) Floating solar photovoltaic systems: an overview and their feasibility at Kota in Rajasthan. In: 2017 international conference on circuit, power and computing technologies (ICCPCT), pp 1–7. IEEE
7. Oliveira-Pinto S, Stokkermans J (2020) Assessment of the potential of different floating solar technologies—overview and analysis of different case studies. *Ener Conver Manage* 211:112747
8. Singh AK, Boruah D, Sehgal L, Ramaswamy AP (2019) Feasibility study of a grid-tied 2MW floating solar PV power station and e-transportation facility using ‘SketchUp Pro’ for the proposed smart city of Pondicherry in India. *J Smart Cities* 2(2):49–59
9. Gaikwad OD, Deshpande UL (2017) Evaporation control using floating pv system and canal roof top solar system. *Int Res J Eng Technol* 4(4)
10. From Google homepage. <https://images.app.goo.gl/TKD35KwkdrntjnU9>

# Convolution Neural Network for Structural Failure Detection of Wind Turbine Blade: A Review



Ameya Gajbhiye and Vilas Warudkar

## 1 Introduction

The increasing carbon footprint of various energy-producing industries has increased the use of wind turbines. Wind turbine farms when built near settlements cause discomfort (noise due to vibration) to a resident of the settlements, hence they are built in remote locations (mountain, grassland, away from settlement, etc.). The twenty-first century has seen growing trends of wind turbines being built offshore. The main reasons for building offshore wind turbines are better and stable wind speed, ease of transport of huge parts, less visual hinderances and less potential of conflicts of interest. However, when compared to onshore wind turbines, the cost of maintenance of offshore wind turbines is significantly high. If the optimal performance of wind turbines is considered during their average life of 20–25 years, the maintenance cost is around 25% of installation cost in offshore wind turbines [1].

Offshore wind turbines though more economical for power generation suffer high maintenance costs due to the challenging environment of the sea. Wind turbines which are situated in remote locations are difficult to access for maintenance. The condition of wind turbines is monitored remotely by condition monitoring (CM). CM is an integral part of operation and maintenance (O&M). Condition monitoring makes use of sensors and drones to examine components' operation and condition. Data collected by CM is analyzed to predicted the failure of the component. Currently, failure by variation in data by humans or predefined mathematical architecture is proven to be effective but up to a certain extend. Deep learning and neural network are an alternative to solve such kinds of problems.

Observing performance parameters of components to identify changes in operation which indicate the development of fault is called condition monitoring (CM).

---

A. Gajbhiye (✉) · V. Warudkar

Department of Mechanical Engineering, Maulana Azad National Institute of Technology, Bhopal, Madhya Pradesh, India

Defects are predicted before they occur, so implementation of CM should significantly reduce Operation and Maintenance (O&M) costs [2]. CM approaches rely upon investigations of specific estimations and parts of the activity (for example, vibration investigation, strain estimation, thermography and acoustic discharges). Ongoing advancements in sensors and sign preparing frameworks, large information the executives, AI (ML), and enhancements in computational capacities have opened up promising circumstances for coordinated and top to bottom CM examination, where various sorts of information can work with solid, practical, and vigorous dynamic in CM.

Deep learning and neural network are proven to limit human intervention for failure prevention and prediction. This paper investigates convolutional neural network' (CNN) integral part of deep learning and neural network for failure prediction of wind turbine blade and can it be used for prediction of crack and breakage. This paper does not consider the time taken by the algorithm to detect or predict failure; it only focuses on whether it can predict failure or not.

## 2 Condition Monitoring of Wind Turbine Blade

Observing the components of a wind turbine to identify changes in operation that can be indicative of a developing fault is called condition monitoring (CM). Condition observing is a basic piece of the Operation and Maintenance (O&M) of wind turbines which comprises the board, checking, and significant level coastal control of wind ranch site, while support covers intercessions needed to upkeep the establishment. Maintenance is of three sorts, responsive, preventive, and prescient [3]: receptive (or remedial, rush to-disappointment) is the most costly sort and doesn't use CM with parts being supplanted when deformities happen or aggregate; under preventive (planned) support, segments are supplanted at the following mediation, ideally, before a connected issue happens; a prescient support system dependent on CM can educate support about segments that are probably going to come up short and have them supplanted in due time.

When selecting components to monitor the level of failure and rate to failure should be consider. Importance is given to parts that have a high probability of failure or that can lead to long periods of low downtime, as they can have a significant potential impact. Pfaffel collected data from several studies of the annual failure rate of wind turbine sub-system and found that out of total mechanical failure 83% is caused due to blade/pitch [4]. Carroll has investigated 300 overseas wind turbines and concluded that the rate of failure of each coastal operator per year is approximately 12, which includes 80% incident requiring repairs costing less than one thousand Euro labeled as minor repairs, 17.5% incident requiring repairs costing between one to ten thousand Euro labeled as major repairs and a substantial exchange rate of 2.5% (>10 k Euro) [5]. They have identified blade damage as one of the major causes of wind turbine failure.



**Fig. 1** Breakage and surface defect [6]

After going through a number of research papers based on vibration analysis and condition monitoring of blades, we can categorize condition monitoring based on vibration analysis and visual inspection (sometimes done through drones). Frequency measurement is done through an accelerometer. Spectrums for vibration are obtained through Fourier transformation on the time waveform. Visual inspection is either done by the supervisor by going near the wind turbine or by surveillance through a drone (Fig. 1).

## ***2.1 Vibration Monitoring***

Vibration analysis detects repetitive motion of a surface of rotating or oscillating machines. The repetitive motion is caused by unbalance, misalignment, resonance and varying load. We are interested in vibration caused by varying wind speed load. Wind turbine blade can be assumed as a cantilever beam with uniformly distributed load [7]. Rupali conducted experiments on crack and uncrack beams indicating vibration spectrum (FFT curve) of the crack beam is different from that of an uncrack beam.

Joshuva [8] performed an experiment on wind turbine blades in good condition, blades with crack, pitch twist, erosion and bend. They concluded that vibration signals for a good blade and blade with defect are different. They also indicated that neural network and machine learning can be used to predicted failure. Crabtree [9] concluded that although there are various types of CM systems in use, there is no uniformity in the direction of propagation for future research. They found that CM-propelled air is now more reliant on innovative methods borrowed from conventional machinery industries. The most common CM methods include methods designed to measure acoustic, monitor electrical effects, energy quality and temperature monitoring, oil waste monitoring, vibration analysis [10, 11], physics-based data analytics [12], etc. (Fig. 2).

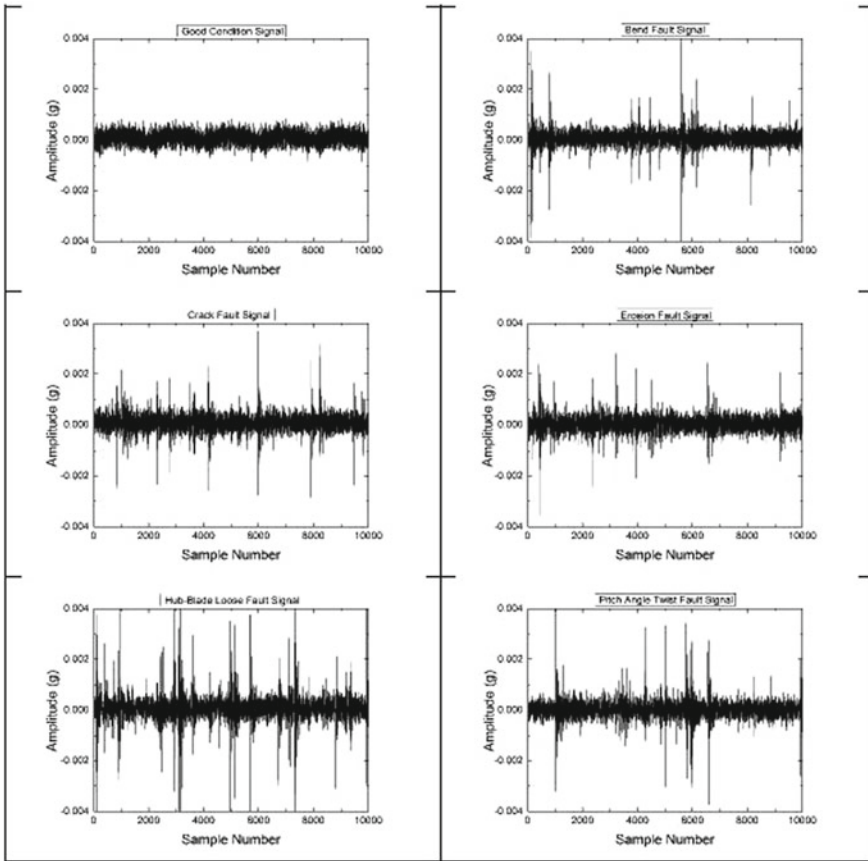
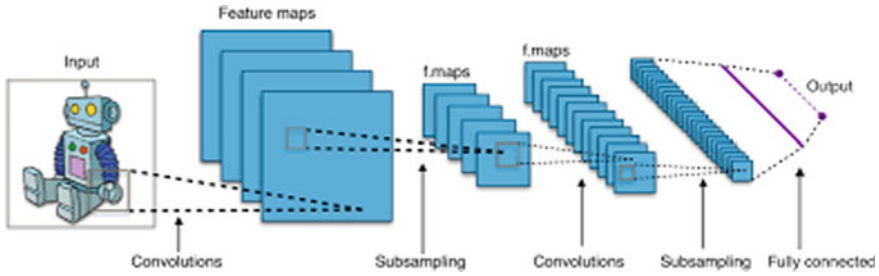


Fig. 2 Vibration Signals [6]

### 3 Convolution Neural Network (CNN)

CNN is an unsupervised learning algorithm which can take input image pixel data, assign learnable weights and biases to various aspects/objects in the image and can differentiate one object from the other [13]. CNN is mainly used for image classification and segmentation. Just like humans, CNN can predict an object inside the image just by looking at it which is the reason we are considering it for structure defect detection.



**Fig. 3** Layers of convolution neural network [6]

### 3.1 CNN Architecture

Convolution layer in CNN consists of filters having weight in matrix form which are applied to the image matrix to get the required feature. Padding is done by applying zeros at the border of the image matrix to avoid loss of data. During pooling, we take a small portion of the input image matrix from which we take the average value called average pooling or maximum value called max pooling. The activation function is then applied to determine whether the neuron will fire or not (Fig. 3).

During implementation, we have to handle many things like the number of layers, size of filter, padding type, activation function and many more. The solution for such types of problems is to use a pretrained architecture like inception, Visual Geometry Group (VGG), etc. VGG-16 is the most widely used architecture; it can solve any classification problem [14]. VGG-16 has 16 layers that have some weight and accuracy of 92.7%. VGG-16 has a filter size of  $3 \times 3$  and a pool size of  $2 \times 2$  in all layers.

### 3.2 CNN for Crack and Breakage Detection

CNN can be applied for detecting surface defects. Cha et al. used CNNs to detect cracks in concrete blocks and obtained better results compared to traditional crack detection methods [15]. Masci detected surface defects and cracks on steel structures using CNN and demonstrated its superiority over old methods which depended on feature-based engineering and support vector machines (SVM) [16]. Nicolas has detected cracks on building surfaces by employing CNN on camera images taken from a drone (UAV) and obtained an overall accuracy of 96% for classification [17].

Acquiring a data set which is large enough for training is the most challenging part while applying CNN. Transfer learning, i.e., using a pretrained architecture on image classification is considered as one of the potential solutions [18]. Gopalakrishnan used VGG-16 as a pretrained architecture and successfully detected cracks in Portland cement concrete (PCC) and hot-mix-asphalt (HMA) [19, 20]. Jung compared pretrained architectures like DenseNet121 and VGG-16 to detect various surface

defects on wood surfaces [21] and found superiority of VGG-16 over DenseNet121 [22]. In the case of wind turbine blades, there are CNN approaches for surface defect detection, but there is no CNN approach yet. Dimitri has applied CNN for surface defects on wind turbine rotor and obtained 98% effectivity using VGG-16 pretrained architecture [23].

## 4 Conclusion

Traditional condition monitoring methods use experts to identify irregularity in vibration signals and images acquired through UAVs. The involvement of experts means human intervention in fault detection which can be eliminated by the application of the CNN network indirectly reducing the maintenance and operating cost. Convolution neural network can be successfully applied to surface defect and crack detection of wind turbine blades. CNN works on the principle of image comparison which is suitable for fault detection for vibration analysis of blades as vibration signals of blades in good health are different from that of damaged blades. There are many pretrained architectures to implement with CNN but through our review, we consider VGG-16 most suitable for crack and breakage detection. Accuracy of CNN with VGG-16 for crack detection in wind turbines is a matter of further investigation. The implementation is hindered by a lack of a database set based on which new architecture can be trained. Considering the CNN architecture with VGG-16, it should be able to distinguish the vibration signal of crack and uncrack blade.

## References

1. Wiggelinkhuizen E, Braam H (2017) Offshore windfarm condition monitoring and maintenance (position paper)
2. Helsen J, Devriendt C, Weijtjens W, Guillaume P (2015) Condition monitoring by means of SCADA analysis. EWEA 2015 annual event, No. 18
3. Tchakoua P, Wamkeue R, Ouhrouché M, Slaoui-Hasnaoui F, Tameghe TA, Ekemb G (2014) Wind turbine condition monitoring: state-of-the-art review, new trends, and future challenges. *Energies* 7(4):2595–2630
4. Pfaffel S, Faulstich S, Rohrig K (2017) Performance and reliability of wind turbines: a review. *Energies* 10(11)
5. Carroll J, McDonald A, McMillan D (2016) Failure rate, repair time and unscheduled O&M cost analysis of offshore wind turbines. *Wind Energy* 19(6):1107–1119
6. Nikolov I, Nielsen M, Garnæs J, Madsen C (2020) Wind turbine blade surfaces dataset. Mendeley Data, V1. <https://doi.org/10.17632/jrmm82m4mv.1>
7. Schubel PJ, Crossley RJ (2012) Wind turbine blade design. *Energies* 5(2016):3425–3449
8. Crabtree CJ, Zappala´ D, Tavner PJ (2014) Survey of commercially available condition monitoring systems for wind turbines vol 44, pp 11–22
9. Dias H, De Azevedo M, Araújo AM, Bouchonneau N (2017) A review of wind turbine bearing condition monitoring: state of the art and challenges. *Renew Sustain Energy Rev* 56:368–379
10. Huang S, Wu X, Liu X, Gao J, He Y. Overview of condition monitoring and operation control of electric power conversion systems in direct-drive wind turbines under faults

11. Luo H (2017) Physics-based data analysis for wind turbine condition monitoring. *Clean Energy* 1(1):4–22
12. Joshuva A, Sugumaran V (2017) Classification of varies wind turbine blade faults through vibration signals using hyper-pipes and voting feature interval algorithm. *Int J Perform Eng* 13:247–258
13. Sumit S (2020) A comprehensive guide to convolutional neural networks- the ELI5 way. <https://towardsdatascience.com/a-comprehensive-guide-to-convolutional-neural-networks-the-eli5-way-3bd2b1164a53>
14. Cha Y-J, Choi W, Büyüköztürk O (2017) Deep learning-based crack damage detection using convolutional neural networks. *Comput Aided Civil Infrastruct Eng* 32(5):361–378
15. Cordts M et al. (2016) The cityscapes dataset for semantic urban scene understanding. <http://arxiv.org/pdf/1604.01685v2>
16. Cortes C, Vapnik V (eds) (1995) *Machine learning: support-vector networks*. Kluwer Academic Publishers, Boston
17. Vazquez-Nicolas JM, Zamora E, Gonzalez-Hernandez I, Lozano R, Sossa H (2018) Towards automatic inspection: crack recognition based on Quadrotor UAV-taken images. In: 2018 International conference on unmanned aircraft systems (ICUAS). Dallas, TX, USA, pp 654–659
18. Yosinski J, Clune J, Bengio Y, Lipson H () How transferable are features in deep neural networks? <https://arxiv.org/abs/1411.1792>. Accessed 21 Dec 2018
19. Gopalakrishnan K, Khaitan SK, Choudhary A, Agrawal A (2017) Deep convolutional neural networks with transfer learning for computer vision-based data-driven pavement distress detection. *Constr Build Mater* 157:322–330
20. Simonyan K, Zisserman A (2014) Very deep convolutional networks for large-scale image recognition. <http://arxiv.org/pdf/1409.1556v6>
21. Jung SY, Tsai YH, Chiu WY, Hu JS, Sun CT (2018) Defect detection on randomly textured surfaces by convolutional neural networks. In: 2018 IEEE/ASME international conference on advanced intelligent mechatronics (AIM), Auckland, New Zealand, pp 1456–1461
22. Huang G, Liu Z, van der Maaten L, Weinberger KQ (2016) Densely connected convolutional networks. <http://arxiv.org/pdf/1608.06993v5>
23. Ren R, Hung T, Tan KC (2018) A generic deep-learning-based approach for automated sur-face inspection, (eng). *IEEE Trans Cybern* 48(3):929–940
24. Madsen BN (2019) Condition monitoring of wind turbines by electric signature analysis. A cost effective alternative or a redundant option for geared wind turbines, pp104–118
25. Qiao W, Lu D (2015) A survey on wind turbine condition monitoring and fault diagnosis part II: signals and signal processing methods. *IEEE Trans Ind Electron* 62(10):6546–6557



# A Literature Survey on the Design and Development of Work-Holding Fixtures



Syed Haider Abbas Abidi, Adarsh Kumar Verma, and Abdul Gani

## 1 Introduction

Fixture is a mechanical device used for supporting the workpiece in holding during the manufacturing process. It helps in growing the production figure of similar parts and brings down our efforts required for manufacturing these similar products. We already know that a center Lathe Machine is an ideal machine tool for producing products of various shapes and sizes. A fixture is used in various industrial manufacturing because of its advantages and unique feature. The design of the fixture consists of a body, locators and clamps. The basic work of locators is to decide the arrangement, orientation and position of our workpiece. Clamps exert acting forces on the workpiece so that it can be pressed easily with locators.

The fixture design process is a highly complicated process. It requires knowledge of materials, machine design, etc. The design of the fixture is an important part of manufacturing. An appropriate design of the fixture is important for a product with perfection in quality, surface finishing and error-free machined parts. Currently, there are various designs of the fixture, so the aim of this work is to study various design approaches and outline considerations while designing fixtures in terms of their properties, application, etc. [1, 2].

---

S. H. A. Abidi (✉) · A. K. Verma · A. Gani  
School of Mechanical Engineering, Galgotias University, Greater Noida, India

© The Author(s), under exclusive license to Springer Nature Singapore Pte Ltd. 2022  
R. M. Singari et al. (eds.), *Advances in Mechanical Engineering and Technology*,  
Lecture Notes in Mechanical Engineering,  
[https://doi.org/10.1007/978-981-16-9613-8\\_44](https://doi.org/10.1007/978-981-16-9613-8_44)

475

## 2 Commencement of Fixture Design

An accurate and perfect fixture design always requires a systematic plan. The workpiece, operations, tools and machine may affect the amount of planning required.

Initiating analysis can take some amount of time as it depends on the complication of fixture designs [3]. While designing a fixture, some important steps (Fig. 1) have to be kept in mind to solve a fixture design problem. These is a list of steps for detailed analysis following operative requirement should be kept in mind while designing a fixture [4].

(a) Balanced resting, (b) Accuracy in locating (Fig. 2), (c) support reinforcement, (d) Secure clamping, (e) foreclosure and (f) quality performance.



**Fig. 1** Steps for Beginning of Fixture Design Process [1, 9]

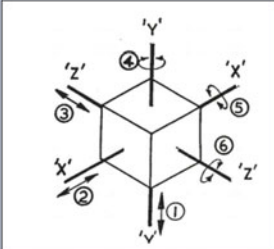
Understanding the location principles	Defining Degree of Freedom	Selecting Appropriate Locator
<p>➤ Location should be performed on most accurate surface of workpiece. Machined surface should be used instead of roughed one. Locate the most accurate surface.</p> <p>➤ Location should prevent any type of motion of the workpiece make from automation.</p> <p>➤ Location should have easy and fast process of attaching the workpiece in the fixture.</p> <p>➤ A redundant location is defined as when two locators are trying to constrain one freedom from two location points. These must be avoided.</p>	<ol style="list-style-type: none"> <li>1. Move along 'Y-Y'</li> <li>2. Move along 'X-X'</li> <li>3. Move along 'Z-Z'</li> <li>4. Rotate about 'Y-Y'</li> <li>5. Rotate about 'X-X'</li> <li>6. Rotate about 'Z-Z'</li> </ol> 	<ul style="list-style-type: none"> <li>• Flat locator</li> <li>• Jack pin locator</li> <li>• Drill bush locator</li> <li>• Vee locator</li> </ul>

Fig. 2 Location principle, degree of freedom, and types of locators [9, 10]

### 2.1 Design Consideration in Fixture

The joints in the main body that should remain fixed in the fixture must be fused together instead of putting screws. Screw only those parts that may need frequent changing or opening [1, 5].

(a) Clamping should take less time and effort. (b) Arrange the clamp in a manner such that its availability and removal should be easy. (c) The frame of fixture should be rigid to overcome deflection. This cause for this deflection is various forces acting from operations happening on it. (d) All attached parts should be clearly noticeable to the machinist for arranging, cleaning or screwing. (e) All clamps and support points that have any type of fastener that requires to be adjusted during operations should be the same size for less tooling and fast operation. (f) The piece of work should be tight when it is attached to the fixture to avoid disturbance from movements. If the surface of the part is unmachined or rough, then we should provide 3 fixed support points because it has good grip but if the workpiece is smooth then it can slip due to forces. In this case, we have to provide more than 3 fixed support points. (g) Three support points should give on work-piece to hold with fixture and also maintain the center of mass of the workpiece. (h) Try to make the area as small as possible on which the fixture is acting pressure to avoid damage.

### 3 Location and Errors

The effect of location deals with the accuracy of the final product. It will help in restricting movements of the workpiece in any direction. Before finalizing the locating points, and should be checked for all-possible degrees of freedom (Fig. 2). It should ensure that the degree of freedom is restrained by making some proper positioning devices known as locators. It should completely constrain the workpiece or eliminate as many of the six degrees of freedom noticing what is necessary for the operation to be completed with the desired accuracy [6]. There are two types of errors, that is, Locating and Machining errors [7]. Locating Error—Variation of Locating Position and Clamping Deformation. Machining Error—Spring Back, Inaccuracy of Machine, Deformation in Tool Holder, Workpiece Twist and Tool Wear.

### 4 Clamping

The purpose of these devices is to hold work in the accurate relative position in the fixture and to make sure that the workpiece is not moved by operational forces. It is also necessary for clamping for the jig to the work (Fig. 3) [8].

### 5 Recent Developments in Fixture Design

Corrado and Polini [11] compared tools used for tolerance analysis in Fixture Design. This study compared Geometrical Model with the Variation model, Vector loop model, and CAT software. The criteria for comparison were Localization error, or datum establishment error which is misalignment error in between datum surface and machine tool. The reason for error is the deviation from its specification of contact in between locator and workpiece. Variation from a minimal specification of the locator is known as fixel. The result of the study showed that the CAT software package adds the deviation of the fixels to workpiece sides. The maximum overestimation is observed in the variation model while the vector loop model had minimum overestimation. Similarly, Geometrical Model reduces the deviation from the minimal of the drilled hole.

WU et al. [12] achieved high accuracy in production from fixture and control deformation. This research overcomes low stiffness and positioning difficulty. The evaluation criteria included the overall deformation, maximum deformation, and system stiffness. A cutting experiment was performed on FEA based on the ANSYS platform. From the results, it was concluded that deformation of the blade is rigid-body displacement; the main deformation of the blade-fixture system occurs on the four clamping heads, and this fixture can effectively protect the blade from local deformation. The clamping-sequence method which was proposed in this research

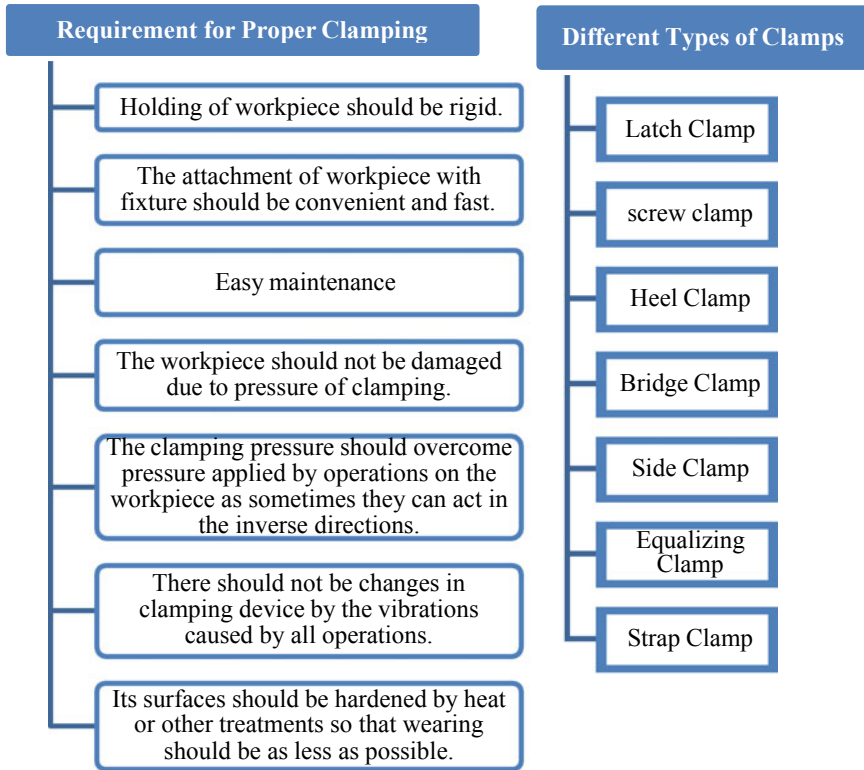


Fig. 3 Location principle, degree of freedom, and types of locators [9, 10]

was reliable and had effective control on the maximum deformation of the blade. It also introduced different materials and multipoint support structures which is an advanced strive for manufacturing a blade fixture.

Tyagi et al. [13] propose a design of fixture layout which supports in minimizing the product dimensional variations which are caused by different operations and labor. The Multi Station Assembly requires fixtures and clamps to hold and locate the workpiece accurately in the desired position. A state-space model is used for detecting the variation in the final product. An Electric optimality criterion is used here for better accuracy in results. This study proposed an intelligent HOT-inspired heuristic, and it can be concluded from research that the proposed heuristic can lead us in solving complex optimization problems.

Wang et al. [6] proposed a method for identifying the error and calculating it. Two types of inaccuracies occur during fixture development, that is, Locating Error and Surface Error. This used Finite Element Analysis (FEA) to identify and calculate locating errors and Coordinate Measurement Machine (CMM) for machining error. Turbine blade is a sample part. First, they located surface error sources (Fig. 4), after this they located variation in locating positions. After calculating Locating Error,

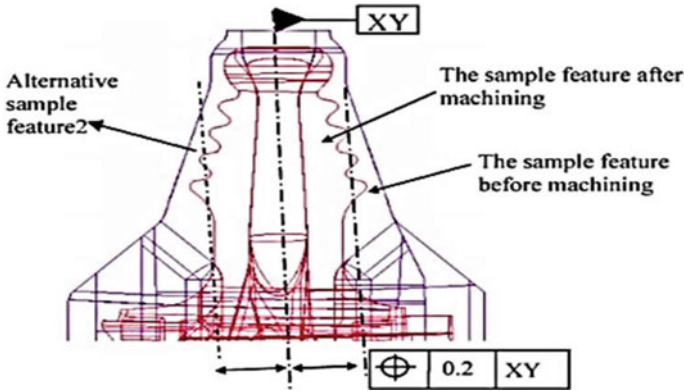


Fig. 4 Tolerance of sample feature [6]

they calculated error caused by machining processes. After analyzing the error in a sample feature, they decompose error sources for the identification of reasons for failure. A methodology for the calculation of surface and error decomposition is presented in this paper. Dimitrov and Szecsi [14] analyze the fixture setup methods and causes of datum error in manufacturing. The datum error occurs because of the difference between process datum and design datum. While machining of shafts when different shoulders of CNC are in operation, it is obligatory to acquire the precision in all automatically since re-setup of the machine will consume time. The datum error requires the trimming of press tolerance, which will increase production costs. The procedure of holding the piece of work and inaccuracy in holding the cutting tool also results in datum error. They concluded with tables showing data of inaccuracy for technological components and Error range for the eight cases which the authors took for their considerations. They analyzed all factors that contribute to machining errors in independent non-systematic with normal distributions. Gonzalo et al. [15] performed analyses for identifying the reasons for the static deformations while the process of clamping and also a methodology for correction in the distortion of the clamped workpiece by evaluating the reaction forces on the points on which clamping is done. The purposed clamping gives an alternative to combine the locator and clamp in one part which can control the force created by reaction and the distortion of the workpiece at the holding point. This helps in positioning of the holding point to minimize the deformation and distortion in the final product. The purposed clamping unit was tested in different technical conditions by which is evaluated the ability regarding positioning and reaction force.

Zeng et al. [16] concern with the suppressing of the mechanical vibrations by designing a fixture layout. A prototype is designed in which cutting force was used as disturbance input, and the element of the fixture was used as a control input. With this designed model, the first time the sound produced by cutting force was suppressed. The effectiveness was tested and verified with the help of a machining example. The impact hammer process was used as a machining experiment and results

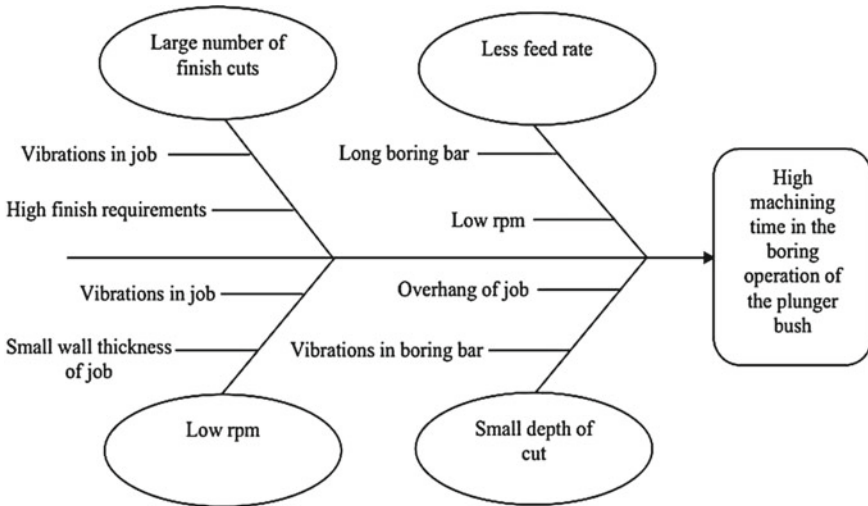


Fig. 5 Ishikawa diagram of high machining time in boring [17]

of measured vibrations were compared to acknowledge the changes. Ghatorka et al. [17] concern the utilization of lean manufacturing in the industry of press manufacturing for improving productivity by increasing the rate of removal of material in the boring operation. A flange fixture was designed which has reduced the time taken in machining by doubling the material removal rate. Ishikawa diagram (Fig. 5) was used to understand and analyze the cause and effect of the process. The authors collected data directly from operators and supervisors and analyzed that boring operations take more machining time in comparison to others.

Aphale et al. [18] purposed an implementation on an assembly line which can decrease human efforts, time taken and labors effort. This can reduce required labors in half and can improve productivity. The design and development of fixtures is specifically for engine door assembly. The problems were analyzed and a fixture is designed to overcome these issues. The design process of the fixture was completed using CAFD with FEA validation. For testing, the designed fixture was manufactured and used in Assembly, and this led to the improvement of the total profit of manufacturing and finest product. This fixture also reduced time in assembly by 40%. Förstmann et al. [19] present an approach for solving rapid product development and arrangement of equipment. The proposal consists of an idea of fixture design which consists of designing rules which are developed with the goals of an automated design. With these rules, which permit to be implanted in algorithms, the freedom of designing in 3D printing and possibilities for production resources emerge. The growth in algorithm and execution of this approach in software were required. With the use of software, the process can be increased faster. For more complicated designed fixtures which are used for welding and milling, more research was required to be conducted. With implementations of this design approach, the fixtures

can be provided in minimum time and can be rearranged as needed if product design is needed to modify. Hunter et al. [20] presented a development to give ease in the automation of the fixture design process. In this research, the MOKA methodology has been adopted for knowledge of fixtures. IDEF0 and UML are utilized for representation of the fixture design process. The methodology proposed in this research is in the fixture design procedure which is based on five phases. These are Functional Essential Development, Defined Fixture Design Functions, Functional Design Solution, Elaborated Design Fixture Solution and Fixture Concluding Design Solution authorize.

Radhwan et al. [21] analyze the design of jigs and fixtures to numb work processing. For analyses, the data was taken from the operations. A design was developed using Unigraphics software. The design was analyzed with FEA, which shows the Von Mises stresses and translational displacement for each part. The results were stable with tolerance. With ergonomic analysis, the risk factors were calculated and removed. It was concluded that a noticeable time was saved by a change in the handling process. Lastly, with the help of cost analysis, a big amount of cost was also saved. Apoorva [22] developed a fixture in which machining can be performed on both sides for performing operations easily on any certain angle. A minimum number of parts were used in the fixture as an increase in the number of parts leads us to high maintenance. The static force acting on the fixture and the total deformation and stress acting on the fixture were analyzed and it was observed from results that the design of this fixture was within the safe limits of operations. Khond et al. [23] present a fixture design for operations boring and facing in real industry square block components. Four jaw chucks were used in industry for holding square block for these operations which costs more than a fixture which was designed for this purpose. The designed fixture was tested in Computer-Aided Fixture Design (CAFD) giving satisfactory results which concluded in reducing of manufacturing lead time and cost.

Kumara and Ram [24] designed a new fixture for Brake Drum machining. There were many drawbacks in the previous one. The design of the old fixture was complicated and it was difficult to modify with the desired changes. In the new fixture, pads were provided instead of buttons, and this was also suitable for drums having a slot on the top face. In the trail run, it was noticed that this lathe fixture was more comfortable during operations. Waghmare & K, n.d. [25] proposed a fixture design for holding cylindrical bodies for turning. The authors designed a fixture specifically for the purpose of holding cylindrical parts and evaluated it against the operational forces which are acting on it. After satisfactory results, they fabricated the evaluated design. It was concluded that the time consumed in material loading and unloading is decreased and the new model is easy and user-friendly. The weight is also less in comparison to previous devices used. The new model is assembly type so it can be disassembled in case of a problem and emergency.

Maniar and Vakharia [26] presented the design of rotary fixture. Mass balancing of the fixture was used in this research. By this, unsymmetrical products can also be handled. The results of this research showed three different methodologies for the Computer-Aided Mass Balancing Method. These methods make work for fixture



designer easy and decrease the time of the process. Siva et al. [27] designed a fixture to deal with the alteration for the planet carrier component. They created a design on SOLIDWORKS and analyzed it on ANSYS. Renishaw probe technique is a solution for inspection of the finished part. It was concluded that the quality and repetition of the component have risen. The fixture modifications were introduced in two stages. The first stage has given rigid holding while in operation because of grip and long clamping. The second stage has used the Renishaw Probe Technique to measure the exact initial size of the part to ensure stock allowance for Mapal tool machining.

Cecil [8] proposed a clamping design in which the part of the process with designing of clamping involves identification of points and surfaces to be clamped. With locator designed to hold it on fixed position while operations. A model was designed with the CAD program; its specifications and features mentioned in the completed product, points for fixture and many other parts. Kumar et al. [28] designed a fixture that represents reducing time which can achieve a product manufacturing plan and shows both views of this as an aspect like a positive and negative. A mixture of production's method and fine quality by demand of customer and it is over with production's method through good economical graph of product manufacturing plan. Time is the main role in this product manufacturing plan in all working time machines. The concept of designing and fabrication of fixture include integration of introduction of an additional fourth axis in the fixture design so fixtures are given table rotation of 360-degree. Balaykin et al. [29] proposed a method of machine tooling utilized on manufacturing elements with the help of multi-axis CNC machining focus on a middle point in the manufacturing method. The process permits to decrease the design time of tooling while creating modification in an element's geometric parameters. This can decrease the time taken in design and pre-manufacturing with control programs for CNC equipment and control and measuring machines, and automate the release of design and engineering documentation. Variance parameterization supports optimizing the construction of elements as well as machine tooling using integrated CAE systems. An analysis review of papers on parametric modeling to prove the relevance of this focus on real manufacturing process of aircraft engines. Chetan Appasab et al. [30] designed fixture for differential carriers R149.5 and R149.7. This fixture was produced according to the design specified and conditions of both. 2D and 3D modeling was carried out on AutoCAD and CREO and analysis was done on ANSYS. The total deformation, Von Mises stress and Von Mises elastic strain were calculated. After that, the fabrication process was carried out and its implementation was carried out successfully.

## 6 Conclusion

In this study, fixture design principles, techniques and methodologies were reviewed. Some recent works in this field were also reviewed. Major concerns in the design of fixtures are minimizing location and surface error, reducing clamping force without

compromising the quality of clamping, decreasing human efforts, reducing mechanical vibrations and increasing productivity by reducing production time. Concerns regarding the localization error are addressed by utilizing vector loop methods. The clamping sequence method is an effective and reliable method to reduce the local maximum deformation. Present work provides a brief to the industry practitioner for developing a design plan for fixtures which can be integrated into the overall manufacturing plan.

## References

1. Pachbhai SS, Raut LP (2014) A review on design of fixtures. *Int J Eng Res Gen Sci* 2:126–46. Issn: 2091-2730
2. Boyle I, Rong Y, Brown DC (2011) A review and analysis of current computer-aided fixture design approaches. *Robot Comput Integr Manuf* 27:1–12. <https://doi.org/10.1016/j.rcim.2010.05.008>
3. Hoffman EG (2005) Jigs and fixture design. delmar learning drafting series
4. Attila R, Stampfer M, Imre S (2013) Fixture and setup planning and fixture configuration system. *Proced CIRP* 228–233. Elsevier B.V. <https://doi.org/10.1016/j.procir.2013.05.039>
5. Basha VR, Salunke JJ (2015) An advanced exploration on fixture design 5:30–33
6. Wang Y, Chen X, Gindy N (2007) Surface error decomposition for fixture development. *Int J Adv Manuf Technol* 31:948–956. <https://doi.org/10.1007/s00170-005-0270-z>
7. Prakash Hiralal Joshi DA (2010) Jigs and fixtures, 3rd edn
8. Cecil J (2001) A clamping design approach for automated fixture design. *Int J Adv Manuf Technol* 18:784–789. <https://doi.org/10.1007/s001700170003>
9. Venkataraman, K.: *Design of Jigs, Fixtures and Press Tools*. John Wiley & Sons, Ltd (2015). <https://doi.org/10.1002/9781119191414>.
10. Nagyszalanczy S (2014) *Taunton's complete illustrated guide to jigs & fixtures—sandor nagyszalanczy—google books*. Taunton Press, Incorporated, 2014.
11. Corrado A, Polini W (2020) Tolerance analysis tools for fixture design: a comparison. *Proced CIRP* 92:112–117. <https://doi.org/10.1016/j.procir.2020.05.174>
12. Wu D, Zhao B, Wang H, Zhang K, Yu J (2020) Investigate on computer-aided fixture design and evaluation algorithm for near-net-shaped jet engine blade. *J Manuf Process* 54:393–412. <https://doi.org/10.1016/j.jmapro.2020.02.023>
13. Tyagi S, Shukla N, Kulkarni S (2016) Optimal design of fixture layout in a multi-station assembly using highly optimized tolerance inspired heuristic. *Appl Math Model* 40:6134–6147. <https://doi.org/10.1016/j.apm.2015.12.030>
14. Dimitrov D, Szecsi T (2016) Machining accuracy on CNC lathes under the lack of unity of the process and design data. *Proced CIRP* 41:824–828. <https://doi.org/10.1016/j.procir.2015.10.001>
15. Gonzalo O, Seara JM, Guruceta E, Izpizua A, Esparta M, Zamakona I, Uterga N, Aranburu A, Thoelen J (2017) A method to minimize the workpiece deformation using a concept of intelligent fixture. *Robot Comput Integr Manuf* 48:209–218. <https://doi.org/10.1016/j.rcim.2017.04.005>
16. Zeng S, Wan X, Li W, Yin Z, Xiong Y (2012) A novel approach to fixture design on suppressing machining vibration of flexible workpiece. *Int J Mach Tools Manuf* 58:29–43. <https://doi.org/10.1016/j.ijmactools.2012.02.008>
17. Ghatorha KS, Sharma R, Singh G (2019) Application of root cause analysis to increase material removal rate for productivity improvement: a case study of the press manufacturing industry. *Mater Today Proc.* 26:1780–1783. <https://doi.org/10.1016/j.matpr.2020.02.374>

18. Aphale S, Nandurdikar V, Desale S (2021) Design and deployment of fixture on assembly line to improve productivity. *J Phys Conf Ser* 1803. <https://doi.org/10.1088/1742-6596/1803/1/012025>
19. Förstmann R, Wagner J, Kreisköther K, Kampker A, Busch D (2017) Design for automation: the rapid fixture approach. *Proced Manuf* 11:633–640. <https://doi.org/10.1016/j.promfg.2017.07.161>
20. Hunter R, Rios J, Perez JM, Vizan A (2006) A functional approach for the formalization of the fixture design process. *Int J Mach Tools Manuf* 46:683–697. <https://doi.org/10.1016/j.ijmachtools.2005.04.018>
21. Radhwan H, Effendi MSM, Farizuan Rosli M, Shayfull Z, Nadia KN (2019) Design and analysis of jigs and fixtures for manufacturing process. *IOP Conf Ser Mater Sci Eng* 551. <https://doi.org/10.1088/1757-899X/551/1/012028>
22. Apoorva MV (2016) Design and fabrication of CNC Fixture For A Spring Sheet Component, vol 4, pp 106–110
23. Khond V, Gedekar VR, Rewatkar HS, Parate KL (2017) Design and fabrication of CNC lathe fixture for square block, pp 2986–2993
24. Kumara, B., Ram, M.M.: DESIGN AND FABRICATION OF LATHE FIXTURE FOR BRAKE DRUM ( cargo ) MACHINING. 4, 1–5 (2014).
25. Waghmare SN, Prabhavalkar MS, Dongare VK Design and fabrication of turning fixture for CNC lathe machine. *Ijirse Com* 10:42–48
26. Maniar NP, Vakharia DP (2014) Design & development of rotary fixture for CNC with computer aided mass balancing method as pre-mortem tool. *Proced Technol* 14:397–404. <https://doi.org/10.1016/j.protcy.2014.08.051>
27. Siva R, Siddardha B, Yuvaraja S, Karthikeyan P (2020) Improving the productivity and tool life by fixture modification and renishaw probe technique. *Mater Today Proc* 24:782–787. <https://doi.org/10.1016/j.matpr.2020.04.386>
28. Kumar SR, Dinesh Krishna S, Gowthamaan KK, Mouli DC, Chakravarthi KC, Balasubramanian T (2020) Development of a re-engineered fixture to reduce operation time in a machining process. *Mater Today Proc* 37:3179–3183. <https://doi.org/10.1016/j.matpr.2020.09.056>
29. Balaykin AV, Bezsonov KA, Nekhoroshev MV, Shulepov AP (2018) Developing parametric models for the assembly of machine fixtures for virtual multiaxial CNC machining centers. *IOP Conf Ser Mater Sci Eng* 302. <https://doi.org/10.1088/1757-899X/302/1/012009>
30. Chetan Appasab C, Kiran K, Rajgopal Anantharaja MH (2014) Design and fabrication of a fixture for differential carriers R149.5 and R149.7. *Int J Res Adv Technol* 2:117–123. E-ISSN 2321-9637

# Design of Storage System for Local Gardeners: A Case Study



Prakash Kumar and Sirish Taneeru

## 1 Introduction

One of the biggest challenges in the design field, today, is to come up with innovative solutions giving due consideration to the sustainability aspects. Design for sustainability pillars on three broader domains, i.e., society, economy, and environment [1]. When we consider the social sustainability aspect of design, it mostly deals with social impact of the design [2]. This owes importance as most of the present design endeavors are catering to only a small section of society with a good purchasing capacity [3]. In contrast, the larger section of the underprivileged population, at the bottom of the pyramid, is ignored [4, 5]. When we talk about environmental sustainability, the main concerns are the justified use of depleting non-renewable resources, wastage reduction, and disposal of the used or waste materials [6, 7]. One of the ways to dispose of materials is to reuse them, and there is a huge scope of reusing the waste materials innovatively. Hence, the goals of sustainability can be achieved by striking a balance between economic, social, and environmental concerns [8]. There are many daily life problem areas around us that require problem-solving through a sustainable approach. One such area that we identified was related to storage issues faced by the small gardeners. Gardeners used different types of tools and equipment during their daily gardening work, but keeping them safely after their work is very challenging. Moreover, they also have certain belongings that need to be stored carefully while they are in the field. The literature shows that there has been research that reported on the design and development of different farm tools, but there has hardly been any research related to designing a proper storage system for garden equipment fulfilling the requirements of small Indian gardeners [9–13]. Hence, an effort was made to understand and address their problems through a new solution. The design

---

P. Kumar (✉) · S. Taneeru  
Department of Design, Shiv Nadar University, Dadri 201314, Uttar Pradesh, India  
e-mail: [Prakash.kumar@snu.edu.in](mailto:Prakash.kumar@snu.edu.in)

and development are based on inputs and responses from two gardeners, working at Shiv Nadar University. Their participation and inputs were sought during various stages of the design development process.

## 2 Method

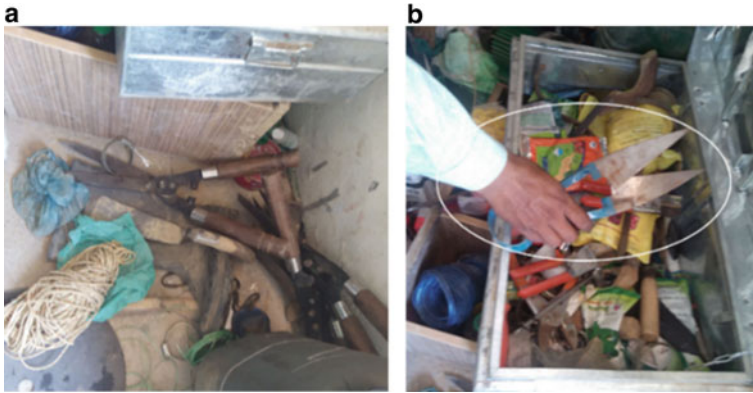
The section broadly presents the method adopted for the design development of the solution and describes various stages of assessment related to the product. The process started with a general discussion with the gardeners at the university campus. The overall scenario was tried to be understood based on the gardeners' input. During the interactions, they described the storage-related problem they faced.

### 2.1 *General Work Scenario*

The gardeners have specific needs regarding the storage of their gardening tools and equipment. Their work started in the morning where they had first to change to the uniform and the shoes. They would keep their lunch and drinking water at a place and start with various gardening tasks. These include watering plants, digging up pits for new plants, spraying pesticides, preparing the ground, spreading seeds, making water drains and hedges, pruning leaves and plants, making nodes, grass cutting, etc. In between, they would stop, take some rest, and have their lunch. They used tools and equipment for different tasks, put in a small aluminum box, acting as their storage system. This was not a very effective solution for the storage purpose, and the gardeners faced a lot of difficulties while placing and taking different tools out of it. Firstly, it was tough to place all the equipment, properly, because of the lack of proper provisioning or order for placing the tools. It was also difficult to find small tools, placed haphazardly in the box, and tended to sink to the bottom. Even retrieving the tools at the top was difficult and time taking. Sometimes, it also resulted in injuries. Due to improper space management, the tools were left outside. And there was always a risk of losing them (Fig. 1a). Since all tools were kept one over another, they often got entangled and damaged or worn out. There was no proper provision for putting the clothes, purse, valuables, and shoes safely. Since the box contained many sharp tools, materials like cloth, shoes, etc. were more likely to get damaged (Fig. 1b). If not careful, one might even cut his hands.














### 2.2 *Study of Existing Solutions*

Based on the prevailing storage-related issues of gardeners at the campus, efforts were made to find available alternate solutions in the local market, studies done, or



**Fig. 1** a Tools lying outside due to lack of space management; b Sharp tools kept inside the box may be dangerous.

efforts made to address the issues of similar nature. A Survey of the local market showed that there was no specific solution, locally available for the gardening tool storage, except the aluminum box that was presently used by the gardeners, though exploring similar solutions on the Internet did show that there were a couple of storage solutions available at other places outside India (Fig. 2).

 Lifetime 60012 Extra Large Deck Box Lifetime Products <del>\$199.99</del> <b>\$158.99</b>	 Rubbermaid 5E39 Extra Large Deck Box with Seat, Sandstone Rubbermaid <del>\$212.00</del> <b>\$129.00</b>	 Keter Rockwood Deck Box, 150-Gallon Keter <b>\$164.99</b>	
 Suncast DBW9200 Mocha Wicker Resin Deck Box, 99-Gallon Suncast <del>\$149.99</del> <b>\$121.73</b>	 Suncast SS1000 Storage Seat Suncast <del>\$49.99</del> <b>\$29.49</b>	 Keter Deck Box, 110-Gallon Keter <b>\$115.99</b>	
 Suncast Deck Box, 127-Gallon Suncast <del>\$146.60</del> <b>\$101.99</b>	 Keter Woodland Storage Shed Keter <del>\$229.00</del> <b>\$154.13</b>	 Suncast DCP2000 Outdoor Prep Station Suncast <del>\$420.00</del> <b>\$98.74</b>	
 <del>\$364.00</del> <b>\$312.00</b> <a href="#">Arrow Brentwood 6x4 Metal Storage Shed</a>	 <del>\$360.00</del> <b>\$334.00</b> <a href="#">Arrow 6x5 Sentry Metal Storage Shed Kit</a>	 <del>\$436.00</del> <b>\$385.00</b> <a href="#">Arrow 6x5 Hamlet Metal Storage Shed Kit</a>	 <del>\$460.00</del> <b>\$391.00</b> <a href="#">Arrow 6x5 Woodlake Metal Storage Shed Kit</a>

**Fig. 2** Details of available options online

The storage solutions found online were quite expensive, and most of them were not very relevant to local gardeners' context as the shapes and sizes of the used tools and equipment varied. Hence, it was decided to develop a solution to cater to the specific needs of the small gardeners like those working at the university.

### **2.3 Design Development Process**

Having decided to design a new solution, the specific details of items the gardeners used and kept, or aspired to keep, were listed. These details would help in conceptualizing a better and effective solution. So, at first, a detailed study of the local tools and equipment, used for gardening, was recorded along with the important dimensions and their typical shapes.

#### **2.3.1 Detailed Study of the Tools and Equipment Locally Used**

As the gardeners at the campus do different types of gardening jobs, they have a large number of local tools with varying shapes and sizes. Some of them were *Khurapi* (Hand Hoe Trowel), *Tasla* (Rounded Container), *Favada* (Spade), *Kudaal* (Hoe), Spray machine, Pipe, Scissors (small), Scissors (big), *Gaiti* (pickaxe), Cutter (small), Cutter (big), Funnel, Measuring cylinder, Pesticide bottles, Water sprinkler, etc. Different tools and equipment were studied for their important dimension to make proper accommodation of the tools in lesser space (Fig. 3).

The dimensions of important tools and gardening equipment, to be stored, were determined to get a fair idea of the space requirements to be considered (Table 1).

Also, other space-related requirements of the gardeners (i.e., provision for keeping shoes, clothes, purse, mobile, food, and water) were included. Also, an effort was made to use cheaply available local material (with due consideration of quality and strength) to reduce the price and lower the impact on the environment. Hence, the product concepts were generated considering all these factors.

#### **2.3.2 Conceptualization**

On the basis of inputs on specific requirements, the ideation process started and different solution concepts were generated. The concepts were mainly focused on making the storage system compact and ensuring maximum utilization of the given space.



**Fig. 3** Study of different gardening equipment used at SNU


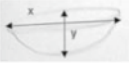

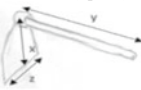

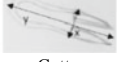

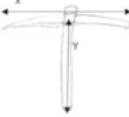
### 2.3.3 Fabrication

These concepts were then evaluated based on ease of use, simplicity of the design, fast and easy access to tools, and provision for keeping other accessories like clothes, shoes, valuable items, etc. Eventually, it was found that “concept 5” was better than all the other concepts. After finalizing the concept, it was further detailed with the inputs from the study of important tools and their dimensions and then fabrication of the model was started in the design studio using the waste wooden packaging material (Fig. 4). The fabrication consisted of some processes involving mainly carpentry-related processes and to retain the original wooden look, varnishing was done on the plain wooden surface.

During this process, trials were done to improve the design and ensure that all essential tools and equipment fit into it. After fabrication, the new solution and its different features were shown to the gardeners and they were asked to rate it on different criteria.



**Table 1** List of common tools and their important dimensions

Sr. no	Tools/equipment	Important dimensions (cm)		
		x	Y	z
1	 <i>Khurapi</i> ( Hand Hoe Trowel)	30	10	10
2	 <i>Tasla</i> (Rounded Container)	42	15	42
3	 <i>Favada</i> (Spade)	30	70	5
4	 <i>Kudaal</i> (Hoe)	30	65	24
5	 Spray machine	15	32	15
6	 Cutter	8	20	1
7	 Scissors (big)	15	35	6
8	 <i>Gaiti</i> (pick-axe)	44	60	8




(continued)

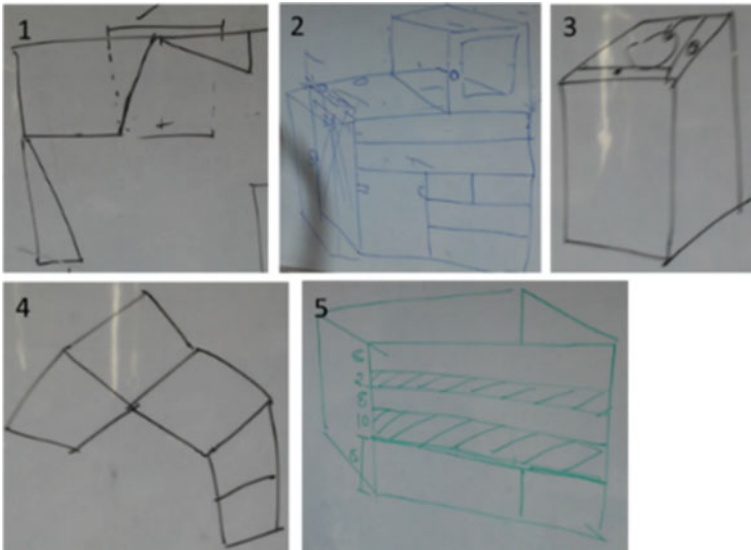
### 2.3.4 Evaluation

During the evaluation, the product was deployed to the gardener’s workplace, and feedback was taken from them. A comparative study was carried out between their assessment-based ratings for the new and the old storage system (Fig. 5). A 7-point rating scale was used for assessment where 1 and 7 were the minimum and maximum values, respectively (Fig. 6).

Since the sample consisted of only two gardeners at the university, a mean value of the rating was used for comparing both solutions. The result showed that for many aspects, the mean ratings of the new solution was higher.

**Table 1** (continued)

Sr. no	Tools/equipment	Important dimensions (cm)		
		x	Y	z
9	 Hasiya (Sickle)	30	12	3
10	 Water Sprinkler	42	24	10
11	 Funnel	10	15	10



**Fig. 4** Concept 1—solution with rotating racks, Concept 2—solution with sliding drawer, Concept 3—storage with glass top sliding door, Concept 4—Solution with foldable compartments, Concept 5—solution with fixed compartments (front and top)

### 3 Results

#### 3.1 Reliability Test

At first, the uniformity of data was checked using an inter-rater reliability test. Since the sample size was very small and consisted of responses of only two subjects, the data was assumed not to be uniformly distributed, and hence, the Spearman



**Fig. 5** Detailing and fabrication process



**Fig. 6** Assessment of new solution by gardener overview of various features of the solution

correlation coefficient [14] was used for the inter-rater reliability test. Also, the internal consistency of the responses was checked using a split-half reliability test [15]. The two-tailed Spearman correlation coefficient was found to be considerably high with the magnitude of 0.87 suggesting a strong correlation, whereas the Guttman split-half reliability coefficient was found to be 0.96 indicating high consistency (Table 2). After ascertaining the reliability of the obtained data, a comparison was made between the mean rankings of the new and old storage solutions against the needs and aspirations of the respondents that were to be fulfilled.

**Table. 2** Result of the reliability tests

	Tests	Values	Remarks
Inter-rater reliability Test	Two-tailed Spearman coefficient	0.87	High positive value indicating strong correlation
Internal consistency	Guttman split-half reliability coefficient	0.96	High positive value indicating higher reliability

### 3.2 Comparison Between New and Old Storage Solutions

Based on user feedback, the old and new storage systems were compared considering various task-related aspects. On the rating scale, the mean rating for a new solution (mrn) was found to be considerably better than the mean rating of the old existing storage solution (mro) on criteria, i.e. inefficient tool arrangement (mro = 2.5, mrn = 6), security of belongings and accessories of the gardener (mro = 1, mrn = 6.5), fastness and safety placing and retrieval of the tool during work (mro = 2, mrn = 7 and mro = 2.75, mrn = 6.26, respectively), overall ease of use (mro = 2.75, mrn = 6.5), and the level of satisfaction (mro = 2.25, mrn = 6.25). For all the above requirements, the mean ratings were higher for the new solution t of the old one. For the locking aspect (w.r.t. ease and security), both the solutions had a similar rating with the new solution marginally above (mro = 5.75, mrn = 6.25) as both the solutions had a fast and effective locking system (Table 3).

## 4 Discussion

The paper presented the process of designing a storage system for the gardener population and then, evaluated how effective the new outcome was, as compared to the old one, in addressing the storage-related issues. It also looked at the issues more holistically from a sustainability perspective. From a social perspective, the new solution effectively addressed users' needs and aspirations. The solution was also looked upon from an economic and environmental perspective and was found to be better. During the study, the local market survey was done to explore the existing solutions and also the available solutions were searched online. Though there were hardly any solutions available in the local market, there were some options available online, the price details of which have been shown in Fig. 2. For the economic aspect of the new design, a detailed cost break-up of expenditure incurred over manufacturing of the new design was listed (Table. 4). It was found that the cheapest product option, with a similar capacity and construct, available online, was 1.5 times costlier than the new solution excluding the shipment charges. As far as environmental sustainability is concerned, the main raw material for the storage system is the waste wood pieces that were left over after unpacking the materials.

**Table 3** Mean ratings of new and old solutions with respect to different task-related aspects

Sr. no	Task-related aspects	Mean rating for old solution (mro)	Mean rating for new solution (mrn)	Inference
1	Locking of storage system (w.r.t. ease and security)	5.75	6.25	New solution is marginally better than the old one
2	Efficient tool arrangement	2.5	6	New solution is considerably better than the old one
3	Retrieving tool during work (w.r.t. ease and fastness)	2	7	New solution is considerably better than the old one
4	Keeping gardeners' clothes and other accessories	1	6.5	New solution is considerably better than the old one
5	Having safety while placing/retrieving tools	2.75	6.25	New solution is considerably better than the old one
6	Reducing frequency of tool damage due to improper keeping of tools	3.25	6.25	New solution is considerably better than the old one
7	Reducing mismanagement/loss of tool	3.25	6.25	New solution is considerably better than the old one
8	Overall ease of use	2.75	6.5	New solution is considerably better than the old one
9	Level of satisfaction	2.25	6.25	New solution is considerably better than the old one

## 5 Conclusion

The paper presents the process of designing a low-cost innovation, i.e., a gardener's storage system catering to the specific requirements of the Indian gardener population, a section that is, generally, ignored. The study also establishes the efficacy of the new design in meeting the needs and aspirations of the users' population. The work motivates and paves the path for research looking into the various issues of similar sections of the society, falling at bottom of the pyramid. The present study can be furthered in terms of exploring other waste materials that can be used to make the design more effective, cheap, simple, and eco-friendly.

**Table 4** Cost break-up of the expenditure incurred on fabrication

Particulars	Cost (in Rs.)
Waste wood from packaging	1500/-
Plywood	500/-
Nails	30/-
Screws and washers	70/-
Handles	20/-
Locking system	30/-
Hinges	60/-
Hangers and holders	30/-
Varnish	200/-
Misc	500/-
Labor charges	1000/-
Total	3940/-

## References

1. Diehl JC, Crul M, Ryan C (2009) Design for sustainability: a step-by-step approach. In: UNEP—DTIE Sustainable Consumption and Production Branch, Milan
2. Eizenberg E, Jabareen Y (2017) Social sustainability: a new conceptual framework. *Sustainability* 9(68):1–16
3. Clarkson P, Coleman R, Keates S, Lebbon C (2003) *Inclusive design: design for the whole population*, 2nd edn. Springer, London
4. Tromp N, Hekkert P (2019) *Designing for society: products and services for a better world*. Bloomsbury Publishing, Great Britain
5. Prahalad CK, Hart SL (2004) *Fortune at the bottom of the pyramid*. Wharton School Publishing, New Jersey
6. Morelli J (2011) Environmental sustainability: a definition for environmental professionals. *J Environ Sustain* 1(1):1–10
7. Weaver P, Jansen L, van Grootveld G, van Spiegel E, Vergragt P (2000) *Sustainable technology development*. Greenleaf Publishing, UK
8. Spangenberg JH (2005) Economic sustainability of the economy: concepts and indicators. *Int J Sustain Dev* 8(1):47–64
9. Nag PK, Gite LP (2020) Ergonomics application in design of farm tools and equipment. In: *Human-centered agriculture. Design science and innovation*. Springer, Singapore
10. Bello S (2012) *Horticultural machinery: equipment and safety*. Createspace, US
11. Niemiera AX (2016) Gardening equipment. *Extension horticulturist Virginia tech* 426–315
12. Gie LP, Mehta CR, Tiwari PM, Potdar R (2013) *Hand book of agricultural engineering*. Directorate of Knowledge Management in Agriculture, ICAR, New Delhi
13. Patel T (2017) Importance of human factors and ergonomic principles in agricultural tools and equipment design. *J Ergon* 7(s6):1–2
14. Gauthier TD (2001) Detecting trends using Spearman's rank correlation coefficient. *Environ Forensics* 2(4):359–362
15. Johnson RL, Penny J (2005) *Encyclopedia of social measurement*. Elsevier, Texas

# A 30-h Observation of Electric-Vehicle-To-Grid Technology in the Presence of Residential and Industrial Inductive Loads



Raju Chintakindi

## 1 Introduction

In the energy sector, incorporating electric vehicles (EVs) into the supply chain is an eco-friendly way to approach the technical performance issues that conventional combustion engine (IC) automobiles face. Whenever an EV is connected to the system, it can act as a load or an energy source, but when it is used as an energy source, the system is referred to as vehicle-to-grid (V2G) [1, 2]. Because electric vehicles emit almost no exhaust gases and make no noise, they have grown in popularity among the industrial sector and researchers, proving that this modern technology is completely good for the environment and reduces the consumption of oil [3]. However, while using electric vehicles has many consequences for society and the economy, introducing many EVs into the retail sector can be difficult for the grid and causes many challenges and limitations [4]. Because of the large number of EVs in an area causing eminent power requirements, power, voltage fluctuations, and supply shortages are all may probable [5]. Active power from a diesel generator, solar and wind turbines with base-load and peak-load configurations are all taken into account. When we integrate the wind power farm into the grid [6], simultaneously various situations, such as the solar farm's lighting level, need to be observed [7]. A standard aggregation of electric vehicles is simulated. We have simulated the vehicle-to-grid technology for 30 h of observation, with a rated power of 40 kW, a rated capacity of 85 kWh, and a system efficiency of 90%.

We examine the interconnection of the electrified vehicle with renewable energy sources in the smart grid and assess their potential effects on the power network [8, 9]. The micro-grid is composed of four major components. Initially, the size of the PV farm's covered area, the efficiency of a solar panel, and the solar irradiation content all contribute to the amount of energy produced [10]. Second, a streamlined

---

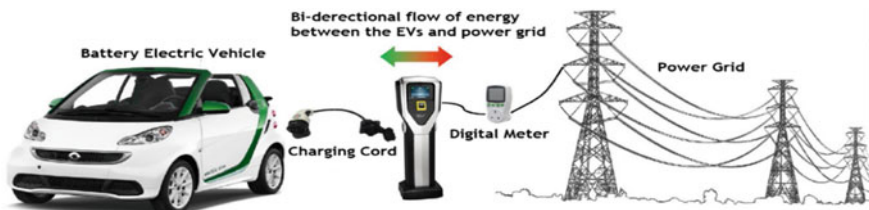
R. Chintakindi (✉)  
Vaagdevi College of Engineering, Warangal, India

windmill model generates electricity in a linear association with the wind. The wind farm generates the rated power whenever the airflow reaches the specified limit [11]. Whenever the velocity contains a high wind value, the power plant disconnects from the power system until the velocity returns to normal [12].

### 1.1 Overview of the Simulation Study

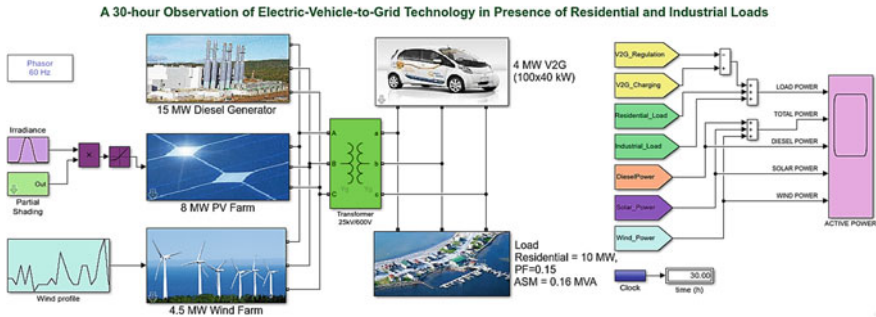
The proposed approach, the basic model of which can be found in the Simulink 2019b library, is composed of various power plants [13]. In this system, two renewable resources (PVF and WF) are there, which can be referred to as a micro-grid [14]. It consists of a 15 MW diesel engine, a 4.5 MW wind turbine, an 8 MW solar power plant with shading regulation, loads, and an EV aggregator that interacts with a large number of electric vehicles to provide ancillary services to the grid as needed [15]. When the sun shines, photovoltaic arrays are made of solar cells that produce an 8 MW solar power plant that generates energy from the sun. A wind farm is a collection of wind turbines, which produce power from wind velocity. The wide range of accumulated electric vehicles is assumed to be around 100 in this simulation study, and they act with different characteristics. DG is unaffected by any atmospheric conditions and is completely unaffected by wind gusts, rainfall, or anything else [16]. A 30-h scenario can be quickly simulated using the phasor-mode of commissioned electrical systems. Execute the illustration model for 30 h and monitor the power profile (production and utilization). Figure 2 shows the 30-h observation of 4 MW electric-vehicle-to-grid technology (4 MW) by integrating 10 MW, 0.95-power factor residential load, and 0.16 MVA, 0.15 power factor industrial inductive load as the asynchronous machine. Figure 1 depicts a simulation model of Vehicle-to-Grid (V2G) technology, illustrating the bidirectional energy balance between both the electric car and the power grid.

The 15 MW diesel generator maintains a balance between the amount of energy consumed and the amount of energy produced. The grid frequency deviation can be determined by observing the synchronous machine's rotor speed. This case illustrates how a 4 MW electric-vehicle-to-grid platform can be used to control the frequency of incidents on a micro-grid over the course of 30 h.



**Fig. 1** A simplified model of V2G technology with its bidirectional energy-flow concept [5]





**Fig. 2** Schematic diagram of an electric-vehicle-to-grid technology in the presence of residential and industrial loads [13]

### 1.2 Functions and Executions of Vehicle-To-Grid Technology

The V2G primarily serves multiple functions, which are as follows. When a daytime event occurs, the grid is regulated by controlling the charge of connected batteries and utilizing the available power. Five separate car-user options are enforced in the frame. In the form of a flowchart, Fig. 3 shows the activities and operations of vehicle-to-grid technology.

- Option 1. People go to work who have the option of charging their car at work.
- Option 2. People go to work with the option of charging their car at work, but with a longer commute.
- Option 3. People go to work who don't have access to a charging station at their place of employment.
- Option 4. People who prefer to stay at home.
- Option 5. People who work nightshifts.

The load is made up of 10 MW, 0.95 power factor residential loads, as well as an 0.16 MVA, 0.15 power factor asynchronous machine that simulates the influence of an industrial inductive load (such as a ventilation system) on the micro-grid. The active and reactive power flow variations at the residential load utility are depicted in Fig. 4a. The housing load is pursuing a consumption characteristic with a specified power factor. A square relationship between the rotation speed and the mechanical torque controls the asynchronous machine. Figure 4b depicts the active and reactive power flow variations at the industrial inductive load utility. The simulation will go on for a total of 30 h. A small voltage drop between  $7.997e^4$  and  $7.998e^4$  seconds was discovered.

The solar radiation tends to follow a standard distribution, with the peak occurring at midday. The wind changes dramatically throughout the day, with characteristic peaks and lows. The housing load follows a pattern that is analogous to that of traditional domestic consumption. Throughout the day, consumption is low, but it

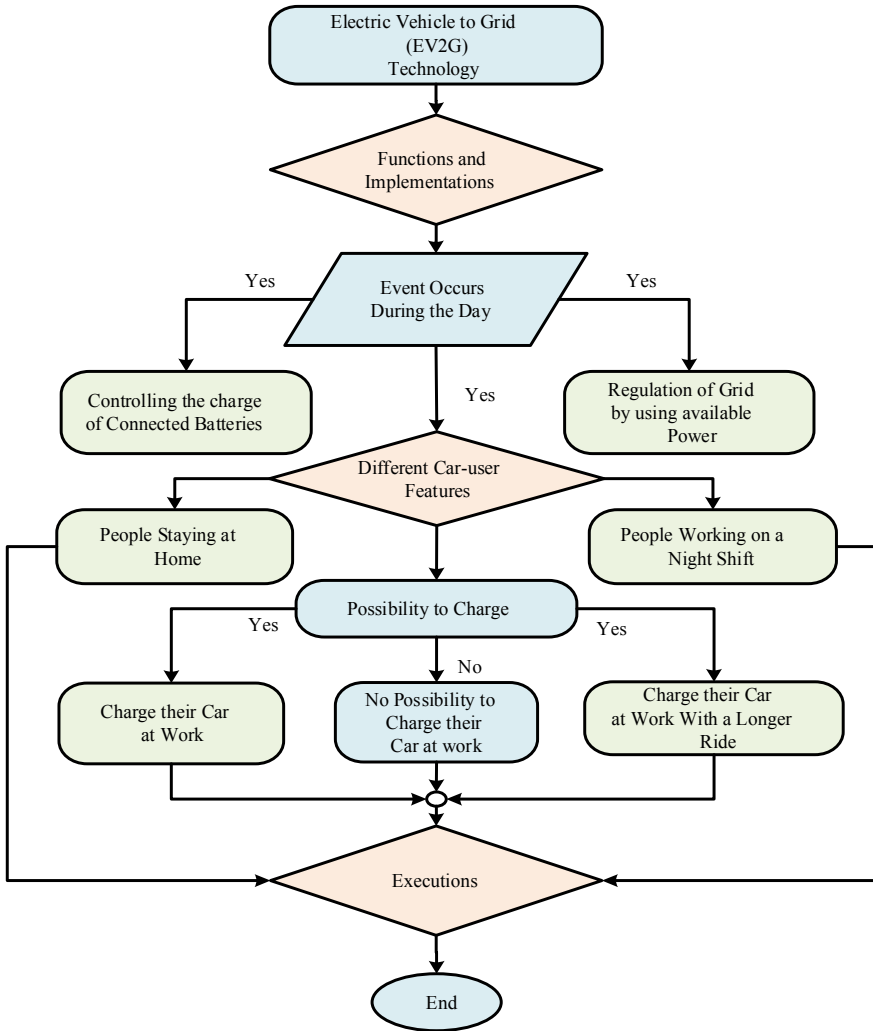
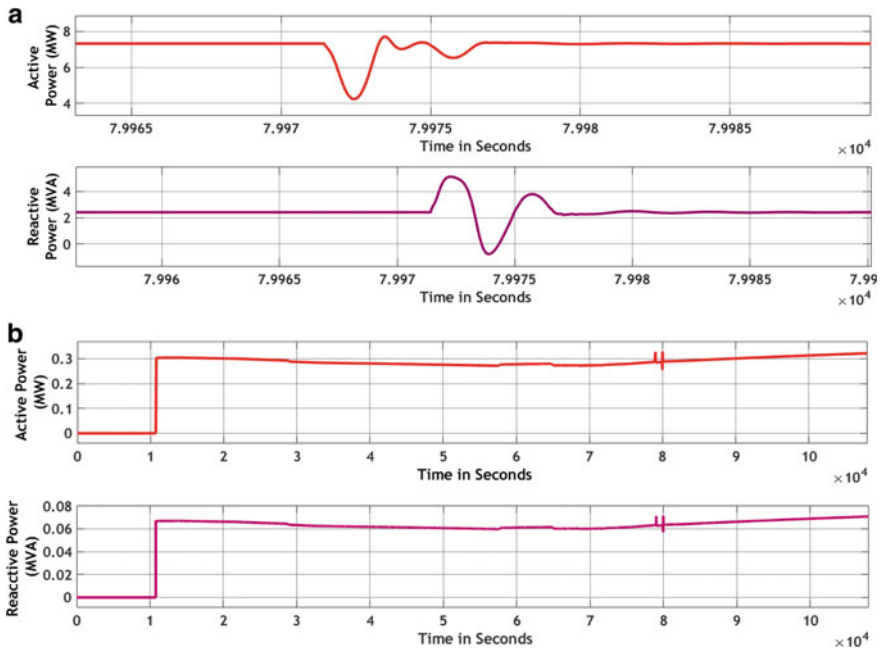


Fig. 3 Activities and operations of vehicle-to-grid technology

rises to a peak in the evening and then gradually declines throughout the night. The grid frequency will be affected by three events throughout the day.

1. The asynchronous machine started up early in the third hour.
2. Partial shading harms the generation of solar energy at midday.
3. When the wind exceeds the specified wind power authorized limit, the wind farm trip normally begins at 22 h.

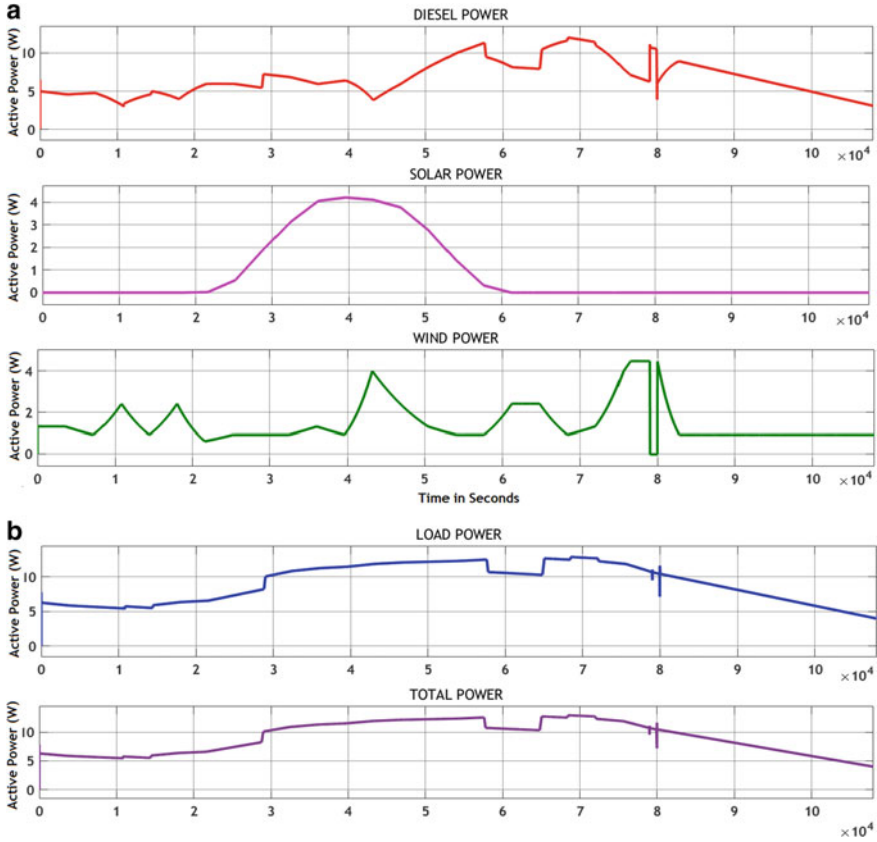


**Fig. 4** a Active and reactive power flow variations at the residential load utility [13]. b Active and reactive power flow variations at the industrial load utility [13]

### 1.3 Outcomes of a Fundamental Simulation Model

Solar farms are the most unpredictable for power production, because there is no assurance of when shading will occur, which shows the solar farm will not be capable of producing continuous power when needed. As a result, solar shadow (shading factor) is taken into account here and is used to evaluate the functionality. The shading factor is the percentage of the solar power plant that is shaded in relation to its total area. The solar shading of the PV plant, as well as the use of such a different pattern of EVs in the process, has an impact on power production. The outcome of the total PV system varies when the shading factor or period of shading is changed, and thus the overall production varies. The power responses of the various plants, such as 15 MW diesel, 8 MW solar, and 4.5 MW wind generators, were calculated using the simulation, and then are showcased below with a shading factor of 0.7.

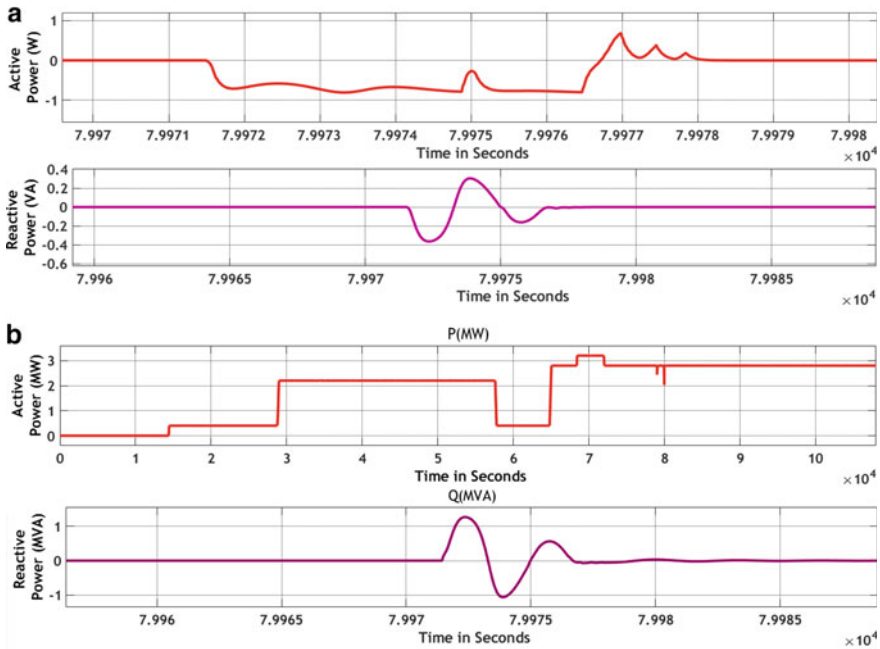
The red color represents the power generated by the DG in the first graph, as shown in Fig. 5a. The pink graph in the second depicts the output power of the solar plant, which simply shows the shading of the solar plant. The green graph in the third depicts the wind farm’s output, which is entirely dependent on the weather profile in the location. We can see the power dropping at  $8e^4$  seconds due to weather and wind flow availability in a windmill’s location.



**Fig. 5** a Active power flow variations of 15 diesel, solar, and wind power generation sources. b Variations in load power and total power flow at the vehicle-to-grid technology [13]

Variations in active power flow of diesel, solar, and wind power generation sources, as well as variations in load power and total power flow at the vehicle-to-grid technology, are depicted in Fig. 5a, b. We plotted the total load power first in blue, then the total active power generated by all grid sources in violet, as shown in Fig. 5b. This figure shows the load profile, which emulates the grid performance, specifically the graph of total power produced in the V2G-based micro-grid, as it should, demand and supply must be equal. Figure 6a depicts the active and reactive power flow variations of an electric vehicle under V2G regulation. Between  $7.9971e^4$  and  $7.9978e^4$  seconds, there was a minor active power deviation. Similarly, reactive power deflection took place between  $7.9970e^4$  and  $7.998e^4$  seconds. We depicted the real and reactive power stream differences of an EV under a V2G charging scenario in Fig. 6b.

To charge and discharge the EV battery is equivalent to deploying the EV as a dispatchable load resource, allowing bidirectional power flow between the EV and



**Fig. 6** a Active and reactive power flow variations of electric vehicle under V2G regulation [13].  
 b Active and reactive power flow variations of electric vehicle under V2G charging [13]

the power system. For this V2G phenomenon, we considered a total of 100 cars. Those are depicted in Fig. 7a in terms of regulation and charging.

When the performance of the solar plant drops or the PV plant is shaded, the power generated should be equivalent to the amount required. The V2G aggregators of the electric vehicle fleet enable regulatory power solutions to the grid, ensuring system stability. This shows that the EVs are constantly charging and discharging. However, the EVs are integrated into the power grid. When there is a power drop, the state-of-charge (SoC) of the EVs must be regulated. Figure 7b shows that multiple grid-connected electric vehicles, ranging from EV1 to EV5, have different state-of-charge characteristics for V2G or G2V activity.

A standard aggregation of electric vehicles is modeled. Modeled vehicle-to-grid technology with a rated power of 40 kW, rated capacity of 85 kWh, and system efficiency of 90%. The vehicle-to-grid (V2G) process can provide substantial benefits to the system by utilizing the battery life of interlinked vehicles [17]. The SoC ranges from negative 100 percent to positive 100 percent, with a negative correlation indicating vehicle-to-grid function, and a positive correlation indicating grid-to-vehicle function. A negative state-of-charge shows whether the vehicle is on the roadway.

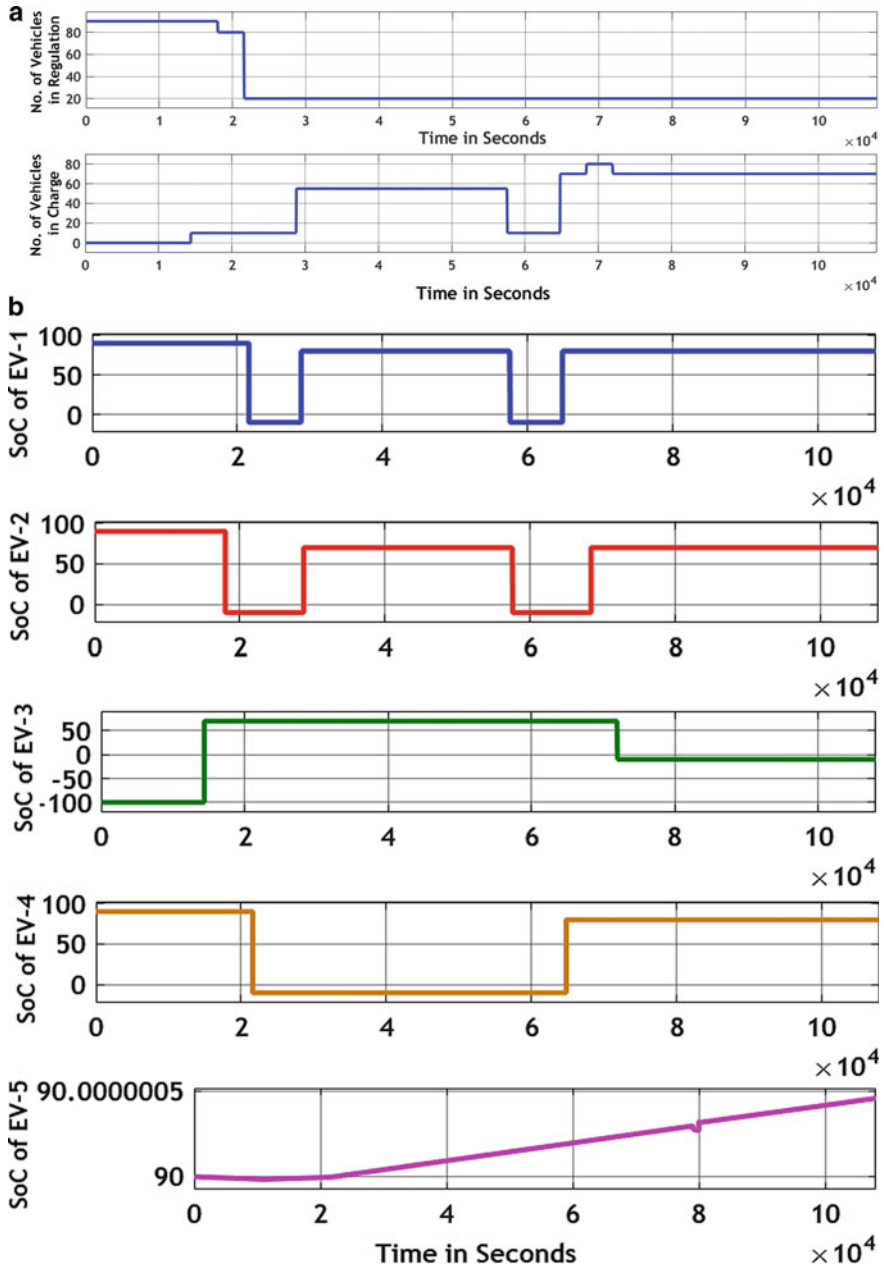


Fig. 7 a Number of vehicles in regulation and charging under V2G technology [13]. b Number of vehicles in regulation and charging under V2G technology

## 2 Conclusions

The introduction of vehicle-to-grid (V2G) advancements as portable energy, as well as their assimilation with RESs and smart grid, is the most effective solution for removing potential demand and supply complications. Electric cars are forecast to expand in popularity during the next few decades, due to their potential economic benefits. We examined the consequences of charging electric vehicles on the transient behavior of power grids in this study. A simple V2G example model was simulated for 30 h of observation using the MATLAB-Simulink platform to understand the electric-vehicle-to-grid operation and its effects. We observed that after a variation in the operation of the micro-grid, the output characteristics were comparable to the standard one because of its potential V2G performance, based on comprehensive simulation results. This study examined the 100 electric cars' integration in V2G technology, which aids in identifying grid parameters like active and reactive powers. It is very helpful to understand how parameters change with solar shading, wind flow subjected to time variation. The simulation results can be used to support future investigations into the technical and financial aspects of V2G hardware at the technical grid level.

## References

1. Chintakindi R, Mitra A (2020) Execution of real-time wide area monitoring system with big data functions and practices. In PIICON 2020—9th IEEE power India international conference
2. Hemmati R, Mehrjerdi H, Al-Emadi NA, Rakhshani E (2019) Mutual vehicle-to-home and vehicle-to-grid operation considering solar-load uncertainty. In: 2nd international conference on smart grid and renewable energy (SGRE)
3. Shaukat N, Khan BK, Alia S, Mehmooda CA, Khana J, Farida U, Majidb M, Anwarc SM, Jawadd M, Ullaha Z (2018) A survey on electric vehicle transportation within smart grid system. *Renew Sustain Energy Rev* 81(1):1329–1349
4. Chintakindi R, Mitra A (2020) PMU-based real-time load balancing strategy for lights-out case in India—a case study. In: First IEEE international conference on smart technologies for power, energy and control, no September, pp 5–10
5. Bijan Bibak HT-M. A comprehensive analysis of vehicle to grid (V2G) systems and scholarly literature on the application of such systems. *Renew Energy Focus* 36
6. Shrimali B, Maherchandani JK, Chhipa AA (2021) Vehicle to grid system integration for frequency regulation of renewable based microgrid. In: International conference on sustainable energy and future electric transportation (SEFET)
7. Huang H, Ogbodo M, Wang Z, Qiu C, Hisada M, Abdallah AB (2021) Smart energy management system based on reconfigurable AI chip and electrical vehicles. In: IEEE international conference on big data and smart computing (BigComp)
8. Aboshady FM, Pisisca I, Axon CJ (2021) Stochastic modeling of vehicle arrival for the UK's first electric vehicle charging forecourt. In: IEEE power & energy society innovative smart grid technologies conference (ISGT)
9. Hajebrahimi A, Mohseni-Bonab SM, Moeini A, Kamwa I (2020) A corrective integrated transmission and distribution co-simulation for scenario analysis of different technology penetration. In: IEEE PES innovative smart grid technologies Europe (ISGT-Europe)

10. Chintakindi R, Rajesh SPS (2013) Vital role of FBG sensors—2012 developments in electrical power systems. In: Proceedings of 2013 international conference on power, energy and control, ICPEC 2013
11. Mitra A, Chatterjee D (2016) Active power control of DFIG-based wind farm for improvement of transient stability of power systems. *IEEE Trans Power Syst* 31(1):82–93
12. Yan Yang; Rong-Jong Wai (2021) Design of adaptive fuzzy-neural-network-imitating sliding-mode control for parallel-inverter system in islanded micro-grid. *IEEE Access* 9:56376–56396
13. I. The MathWorks (2019) 24-hour simulation of a vehicle-to-grid (V2G) system. MATLAB®
14. Yada HK, Murthy MSR, Chintakindi R (2017) A dual second-order SOGI based control algorithm for UPQC under distorted grid and load conditions. *Int J Appl Eng Res* 12(10)
15. Kouvelas N, Venkatesha Prasad R (2021) Efficient allocation of harvested energy at the edge by building a tangible micro-grid—the texas case. *IEEE Trans Green Commun Netw* 5(1):94–105
16. Robin Chola SBS (2021) A case study on 24-h simulation of V2G system. In: Dewan L, Bansal RC, Kalla UK (Eds) *Advances in renewable energy and sustainable environment*, Lecture notes, pp 131–140. Springer, Singapore
17. Neofytos Neofytou YK, Blazakis K, Stavrakakis G (2019) Modeling vehicles to grid as a source of distributed frequency regulation in isolated grids with significant RES penetration. *Energies* 12(4)



# Study and Modal Analysis of Induction Motor by Using ANSYS



Siddhant Bhadouria, Brahma Nand Agrawal, Sudhir Kumar Singh, and Pawan Kumar Singh Nain

## 1 Introduction

In this paper, different modes at which a motor could deform are calculated through modal analysis and FEM. A high power density induction motor presents a promising potential to be used in heavy machinery; this is due to various factors, high efficiency, rugged construction, and less mechanical losses. Operational performance plays a huge role in the stability of the motor. The losses in a motor system can happen due to various reasons: electromagnetic noise, radial force ripple, torque ripple, switching noise, shaft eccentricity, sliding contact between rotors, and bearings. This leads to unbalanced mechanical coupling and causes vibration. The non-linear vibrations induced in the motor can be determined through finite element analysis. However, this may result in variation in actual results.

A strong understanding of the mathematical model is required to find the hidden oscillation which has a damaging effect as it has a very small area of attraction; such oscillations are difficult to integrate into computer modeling [1, 2]. Various methods have been applied to detect faults in the system; one such system is a Neural Network which is made using a Vibration Spectrum model it can capture the Non-linear dynamic system and doesn't require a mathematical model for it, which can generate some faulty values. It varies effectively for diagnosing electrical faults [3–5]. A very small exposure to vibration could have a greater impact on the mechanically moving system; it slows down the system and affects the efficiency of the machine [6, 7]. Vibration with higher frequencies (>150 Hz) induces stress of the overall motor units; stress is highest at a medium level, though the spread of vibration is limited beyond 100 Hz; thus, high-frequency vibration with low intensity is much preferred that could cause less resonance, thus, high-threshold components are always preferred over the

---

S. Bhadouria · B. N. Agrawal (✉) · S. K. Singh · P. K. S. Nain  
Department of Mechanical Engineering, Galgotias University, Greater Noida, India  
e-mail: [brahma.agrawal@galgotiasuniversity.edu.in](mailto:brahma.agrawal@galgotiasuniversity.edu.in)

© The Author(s), under exclusive license to Springer Nature Singapore Pte Ltd. 2022  
R. M. Singari et al. (eds.), *Advances in Mechanical Engineering and Technology*,  
Lecture Notes in Mechanical Engineering,  
[https://doi.org/10.1007/978-981-16-9613-8\\_47](https://doi.org/10.1007/978-981-16-9613-8_47)

509

lower threshold components; they reduce the probability of fatigue in the system [1, 8, 9]. Dynamic eccentricity is the main cause for the vibration in the motor; it is the gap between rotor and stator; when the rotor rotates, the small deviation from the axis can cause vibration; a no-load system is best to determine the eccentricity in the system [10–12]. As the flux density increases, an imbalance in the mass increases which results in the resonance at a very lower frequency [13]. There are various methods to mitigate the effect of vibration; some of them are vibration isolation devices, use of alignment tools, including elastic damping methods, dynamic rotor balancing, and application of axial load with springs [14, 15]. There is a need for avoiding the resonance between the static force and magnetic force. The main reason for the resonance could be that spatial distribution matches the existing forces with stator and rotor structural modes [7, 16].

Thus, it is important to know what effects could cause it to break down. So, this paper studied a Modal analysis for this purpose, which tells about the deformation of a motor at different frequencies. The motor consists of different parts that are made of different materials that have different thermal, structural, and electrical properties. Different parts will have different natural frequencies, and thus will undergo different deformations. This deformation is important to calculate to prevent breakdown. The result will help us understand the effect of vibration under different frequencies in different parts of the motor.

The main objective of this paper is to calculate the natural frequencies and the mode shapes of induction motor, under different dynamic loading conditions. The different shapes have been considered which a motor might undergo during the deformation. It will also help in determining the natural frequencies and vector shapes of the motor. The motor is subjected to balanced and unbalanced loads under different frequencies to get the desired result. That will help engineers in designing a better machine.

## **2 Material and Method**

### ***2.1 Materials Used***

The materials which was used in this study are shown in Table 1, while the properties of the material are as shown in Table 2.

### ***2.2 Specification of Motor***

The specification of the motor used in this study is shown in Table 3.

**Table 1** Material of component

Component	Material used
Back cover	Stainless steel
Box top	Structural steel
Enclosure	Stainless steel
Rotor	Stainless steel NL
Stand	Gray cast iron
Stator	316 stainless steel

**Table 2** Properties of material

Material	Density (kg/m <sup>3</sup> )	Young’s Modulus (Pa)	Poisson’s ratio	Specific heat constant pressure (J/kg °C)	Isotropic thermal conductivity (W/m °C)	Isotropic resistivity ohm-m
Structural steel	7850	2e+11	0.3	434	60.5	1.7e-7
Stainless steel	7750	1.93e+11	0.31	480	15.1	7.7e-7
Gray cast iron	7200	1.1e+11	0.28	447	5.2	9.6e-8

**Table 3** Specifications of Motor

Mark	GAMAK
Model	AGM2E 132 S 2b
Phase	3 Phases
Power	7.5 KW
Rotor rotation speed	2910
Nominal current	13.6 A
Moment	24.6 N
Number of poles	2
Power factor	0.9
Efficiency	88.5%

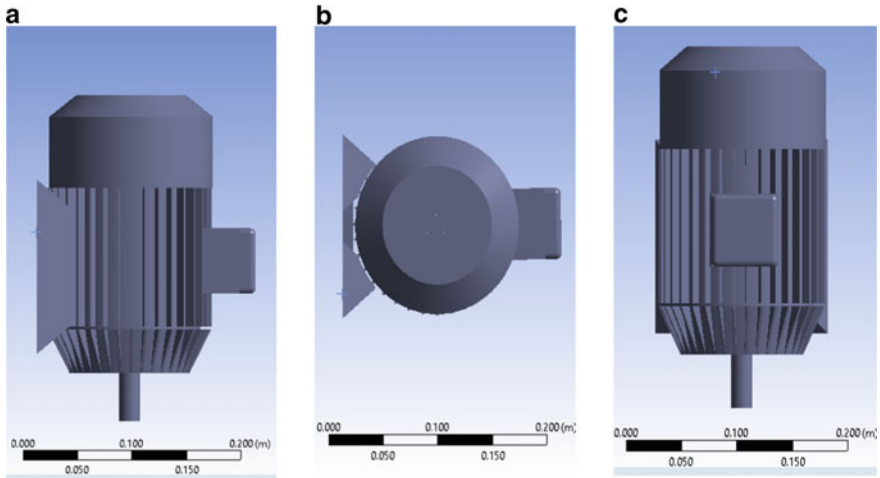
### 2.3 Method Used

In this study, Ansys 2020 R1 is used for the design and modal analysis of the induction motor.

Modeling size

Length X: 0.20471 m

Length Y: 0.21651 m



**Fig. 1** a Side view. b Back view. c Top view

Length Z: 0.29891 m (Fig. 1).

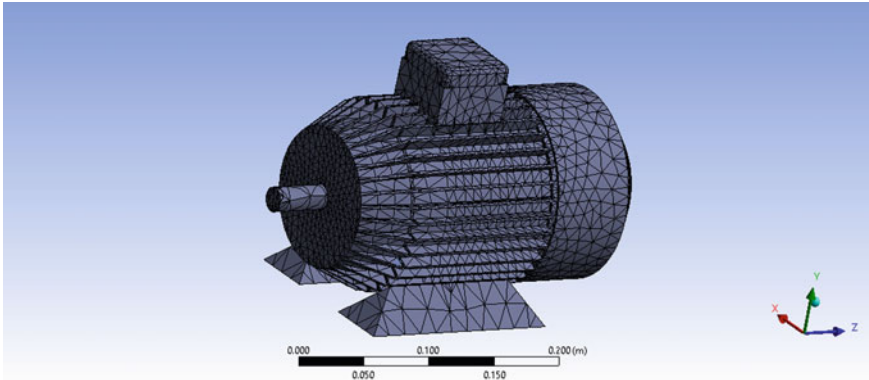
## 2.4 Meshing

The model has been meshed in Ansys with the following parameters:

Nodes—53,416  
 Elements—23,192  
 Bounding Box Diameter—0.42205 m  
 Average Surface Area—6.147e-004 m<sup>2</sup>  
 Minimum Edge length—3.495e-005 m (Fig. 2).

## 2.5 Modal Analysis

Modal Analysis is a way to determine the natural frequencies of a system. It is used to find out which frequency could be catastrophic for the system. This analysis helps us find out at which particular frequency, deformation can occur in the system. The system has six parts: Back cover, Box top, Enclosure, Rotor, Stand, and Stator. Each component will be deformed differently according to a different frequency. The stand of the model is fixed and cannot move. The material of all the components is different and is explained in the above table. It is necessary to note that all the components of the mode shape are real numbers with only a sign and amplitude difference between any two of them. The phase relationships are either in-phase or out-of-phase at 180°. Thus, these mode shapes are also called real modes. All points



**Fig. 2** Meshed model of induction motor

on the structure pass through their equilibrium positions simultaneously. Therefore, undamped modes have well-defined modal points or lines.

In the absence of damping and external forces:

$$M\ddot{X}(t) + KX(t) = 0 \tag{1}$$

Generally, Eq. (1) has the form as follows:

$$x(t) = \varphi \sin(\omega t + \phi) \tag{2}$$

Double differentiation of Eq. (2) becomes

$$X(f) = -\omega^2 \varphi \sin(\omega t + \phi) \tag{3}$$

Substituting Eqs. (2) and (3) into Eq. (1) to get results

$$K - (\omega^2 M)\varphi = 0 \tag{4}$$

Calculating the algebraic eigenvalue with this will help to find the natural frequency

$$|K - \omega^2 M| \tag{5}$$

Equation 5 is used to find the different natural frequencies at different eigenvalues. Eigenvector represents the mode shapes.

### 3 Result and Discussion

At different frequencies, the deformation in the motor occurs due to vibration. These deformations are shown at different frequencies at different modes. A total of six modes have been calculated which results in different frequencies. The deformation is different at each frequency and mode, which has been shown as follows.

#### 3.1 Deformation in Various Modes

In mode 1, the maximum deformation is in the stator which is almost 0.5 m. The frame, base, and back cover of motor are not much deformed. The frequency is almost 24 Hz. The vibration is compressed in a particular area. In mode 2, the maximum deformation is again in the stator; as the frequency increases up to 25 Hz, the deformation increases up to 0.556 m, and also the average deformation starts increasing which means that the effect of vibration is spread across the surface of the motor. The back end of the stator is severely affected. In mode 3, the maximum deformation is decreased and average deformation is increased resulting in an overall effect over the frame of the motor. The frequency in this mode was 122 Hz. The maximum deformation decreased to 0.43 and the average deformation increased to 0.17. The area which is being affected the most is the spindle of the motor; at this vibration, the motor vibrates in the sideways direction on the X-axis. In mode 4, the frequency is 143 Hz and the maximum deformation is 0.58 m and the average deformation is 0.13. The most affected area is the stator, but the effect on the rest of the motor is quite uniform, thus not much deformation. In mode 5, the frequency is 252 Hz. The maximum deformation increases up to 0.768 m and the average deformation to 0.39 m. The most affected area is the box top and the back cover. In mode 6, the frequency is 272 Hz and the maximum deformation increased to 0.82 m. The most affected area is the box top. The effect of vibration is more evenly distributed and the intensity of vibration is increased as shown in Table 4 (Figs. 3, 4, 5, 6, 7 and 8).

**Table 4** Data for various modes

Parameters	Mode 1	Mode 2	Mode 3	Mode 4	Mode 5	Mode 6
Frequency	24.19 Hz	24.575 Hz	122.08 Hz	143.06 Hz	252.13 Hz	272.88 Hz
Maximum deformation	0.55532 m	0.556 m	0.4786 m	0.586 m	0.76851 m	0.82228 m
Average deformation	7.921e-002 m	7.90e-002 m	0.17133 m	0.13137 m	0.3933 m	0.34805 m
Object with maximum deformation	Stator	Stator	Stator	Stator	Back cover	Box top

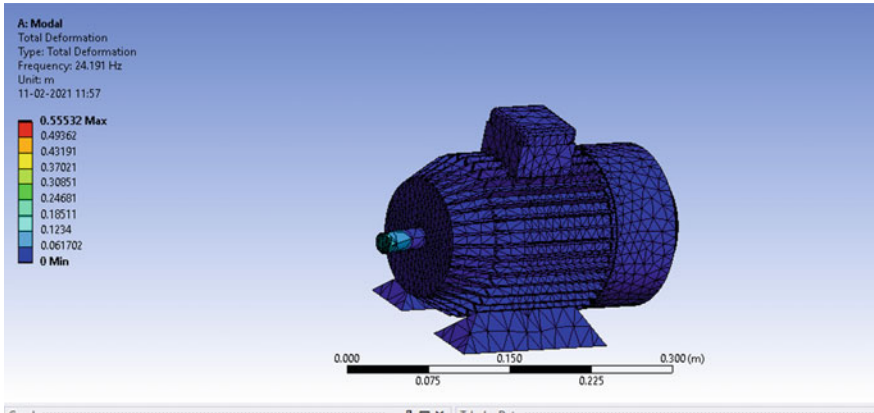


Fig. 3 Deformation in mode 1

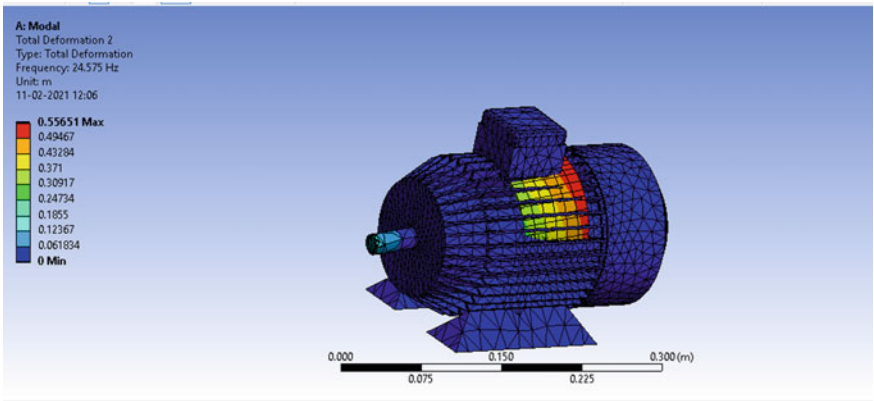


Fig. 4 Deformation in mode 2

### 3.2 Participation Factor

The participation factor tells how much mass of certain modes is moving in the same direction as the excitation. A high value in the direction indicates that the modes will be excited by the forces in that direction.

It is clear from Table 5 that mode 4 is making a meaningful contribution in the Z-direction when the frequency is 143.06 Hz; in the X-direction, mode 1 is maximum, and in the Y-direction mode 2 has the highest value.

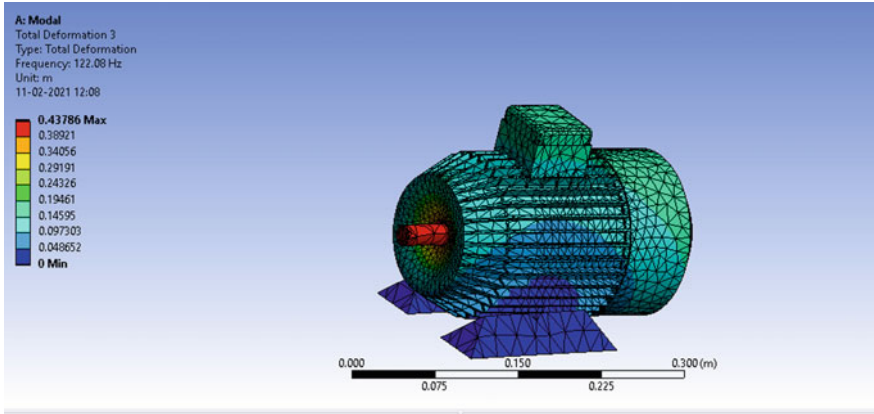


Fig. 5 Deformation in mode 3

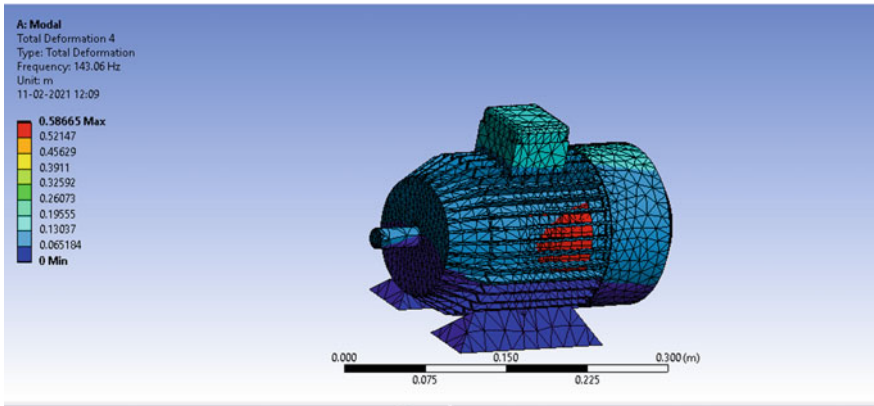


Fig. 6 Deformation in mode 4

### 3.3 Ratio Effective Mass to Total Mass

The mass which is moving in X-, Y-, and Z-directions at different frequencies and different modes (from mode 1 to mode 6) are shown in Table 6. This shows that the maximum amount of mass moving in the X-direction is about 71%.

## 4 Conclusion

This paper concluded the following points:



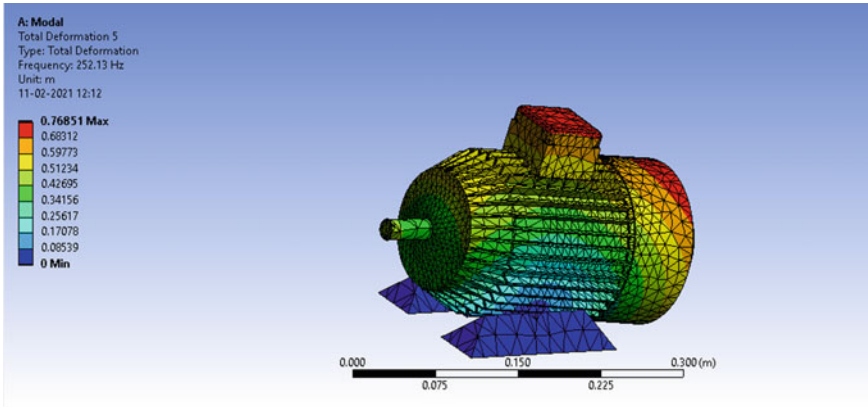


Fig. 7 Deformation in mode 5

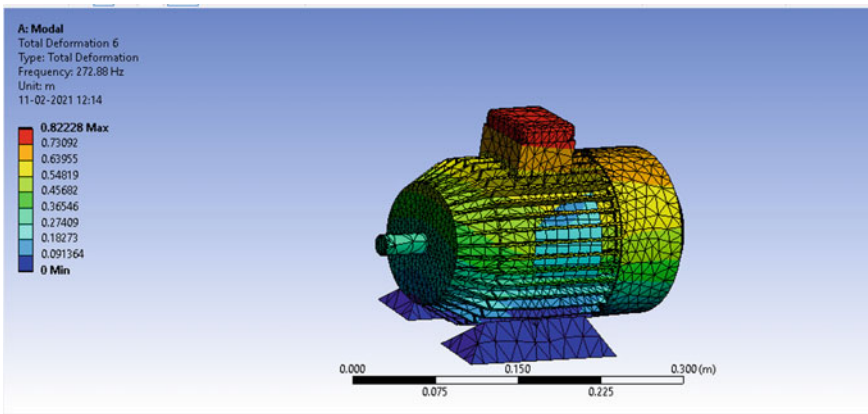


Fig. 8 Deformation in mode 6

Table 5 Participation factor

Modes	Frequency	X-direction	Y-direction	Z-direction
1	24.19	2.3088	0.50371	-1.4e-002
2	24.575	-0.52113	2.37	-6.17e-002
3	122.08	-0.3628	-4.6363e-004	4.4025e-003
4	143.06	-1.2038e-002	-4.599e-002	2.5595
5	252.13	1.6553	-1.34e-002	3.274e-002
6	272.88	-9.88e-003	-0.281	1.0898

**Table 6** Ratio effective mass to the total mass

Mode	Frequency	X-direction	Y-direction	Z-direction
1	24.19	0.448	2.136e−002	2.13e−002
2	24.575	2.2867e−002	0.421	0.42138
3	122.08	1.1083e−002	1.81e−008	1.81e−008
4	143.06	1.43e−005	1.78e−004	1.78e−004
5	252.13	0.23071	1.512e−005	1.512e−005
6	272.88	8.234e−006	6.6849e−003	6.68e−003
Sum		0.7153	0.4496	0.65205

- As the stator is the most affected part, it must be designed in such a way that it could bear the load and sustain the deformation.
- Box top and back cover are also experiencing high deformation between 200 and 250 Hz, and thus are designed accordingly.
- As the vibration frequency increases, the deformation spreads all over the body of the motor. The difference between average and maximum deformation increases.
- Frequencies between 100 and 150 Hz affect the rotor and stator motor; thus for these frequencies, respective components must be designed accordingly to avoid the breakdown.
- The motor frame is most stable around 150 Hz, and between 100 and 130 Hz it is mildly affected, and above 200 it is most affected.
- The highest impact in the Z-direction of the motor is obtained in mode 4.

## References

1. Rodríguez PVJ, Belahcen A, Arkkio A, Laiho A, Antonino-Daviu JA (2008) Air-gap force distribution and vibration pattern of induction motors under dynamic eccentricity. *Electr Eng* 90(3):209–218
2. Su H, Chong KT, Kumar RR (2011) Vibration signal analysis for electrical fault detection of induction machine using neural networks. *Neural Comput Appl* 20(2):183–194
3. Gangsar P, Tiwari R (2019) Diagnostics of mechanical and electrical faults in induction motors using wavelet-based features of vibration and current through support vector machine algorithms for various operating conditions. *J Braz Soc Mech Sci Eng* 41(2):71
4. Martin BJ, Park HS (1997) Analysis of the tonic vibration reflex: influence of vibration variables on motor unit synchronization and fatigue. *Eur J Appl Physiol* 75(6):504–511
5. Kumar P, Shankar A (2020) Review on machine learning algorithm based fault detection in induction motors. *Arch Comput Methods Eng*. <https://doi.org/10.1007/s11831-020-09446-w>
6. Chen X, Yuan S, Peng Z (2015) Nonlinear vibration for PMSM used in HEV considering mechanical and magnetic coupling effects. *Nonlinear Dyn* 80(1):541–552
7. Leonov GA, Kuznetsov NV, Kiseleva MA, Solovyeva EP, Zaretskiy AM (2014) Hidden oscillations in mathematical model of drilling system actuated by an induction motor with a wound rotor. *Nonlinear Dyn* 77(1–2):277–288

8. Güçlü S, Ünsal A, Ebeoğlu MA (2017) Vibration analysis of induction motors with unbalanced loads. In: 2017 10th international conference on electrical and electronics engineering (ELECO), November. IEEE, pp 365–369
9. Li Y, Wu H, Xu X, Cai Y, Sun X (2019) Analysis on electromechanical coupling vibration characteristics of in-wheel motor in electric vehicles considering air gap eccentricity 67:851–862. <https://doi.org/10.24425/bpasts.2019.130882>
10. Mohammed OA, Abed NY, Ganu S (2007). Modeling and characterization of induction motor internal faults using finite element and discrete wavelet transform. In: The 2007 IEEE electric ship technologies symposium, May. IEEE, pp 250–253
11. Zuo S, Liu Z, Hu S (2020) Vibration reduction of switched reluctance motor under static eccentricity with optimised current harmonic 14:1480–1487. <https://doi.org/10.1049/iet-epa.2019.1044>
12. Bouzida A, Abdelli R, Touhami O, Aibeche A (2017) Dynamic eccentricity fault diagnosis in induction motors using finite element method and experimental tests. *Electronics I* 3
13. Kumar P, Isha TB (2016) Electromagnetic field analysis of 3-Phase induction motor drive under broken rotor bar fault condition using FEM. In: 2016 IEEE international conference on power electronics, drives and energy systems (PEDES), December. IEEE, pp 1–6
14. Neves CGC, Carlson R, Sadowski N, Bastos JPA, Soeiro NS, Gerges SNY (1999) Experimental and numerical analysis of induction motor vibrations. *IEEE Trans Magn* 35(3):1314–1317
15. Ayhan B, Chow M-Y, Trussell HJ, Song M-H, Kang E-S, Woe H-J (2003) Statistical analysis on a case study of load effect on PSD technique for induction motor has broken rotor bar fault detection. In: 4th IEEE international symposium on diagnostics for electric machines, power electronics, and drives, 2003. STAMPED 2003. IEEE, pp 119–123
16. Lin F, Zuo S, Deng W (2018) 2827. Impact of rotor eccentricity on electromagnetic vibration and noise of permanent magnet synchronous motor 2018:923–935. <https://doi.org/10.21595/jve.2017.18436>

# The Physical and Chemical Fuel Properties of Jatropha Oil Diesel Blends with Biogas in Dual Fuel Operation



Lalit

## 1 Introduction

Biodiesel addresses a suitable fuel substitute to decrease the contamination outflows created by the burning of diesel got from oil in pressure start motors. Biogas is principally utilized for the creation of warmth and power in cogeneration frameworks [1–4]. Biogas, biomethane, and flammable gas (CNG—packed gaseous petrol, LNG—melted petroleum gas) are delegated methane fuels. This work is mostly focused on ecological advantages coming about because of the utilization of biomethane to control the motor of vehicle, rather than flammable gas or petroleum derivative. Aside from flammable gas, there is research work on biomethane. This restricts its economic intensity contrasted with minimal effort creation of diesel acquired from oil. Appropriately, numerous investigations have been directed lately to distinguish minimal effort crude oil sources like utilized vegetable oil, creature squander fats, crude vegetable oils, or fish squander from fishing-related things [5].

This type of gas, in the wake of fitting refinement to biomethane eminence, can be crushed into the combustible gas scattering association or used as an oil to control streak start and self-start engines of automobiles [6]. The examinations to control automobile endeavored by assessment parts all throughout the planet for quite a long time. Examination in this space is centered around, among others:

- I. discharge of harmful parts in the form of fumes and gases from the motor and natural effect for the duration of the existing pattern of vaporous fuel (from acquiring the crude material, through creation, to its utilization in the motor) [7];
- II. the effect of the adjustment of inception of fuel start of the combination, from diesel oil, effect of ethanol with biodiesel, effect of ethanol with diesel [8];

---

Lalit (✉)

Mechanical Engineering Department, UIET, MDU, Rohtak, Haryana, India

- III. economic impacts of fueling the motor with CNG. The assessment of the gaseous petrol burning cycle in the motor, with the expansion of another gas [9];
- IV. the effect of such a gas fuel (Liquified Petroleum Gas, Compressed natural gas) on motor activity boundaries, contrasted with the traditional fuel [10];

## 2 Physical and Chemical Properties of Jatropha Biodiesel

Each kind of unsaturated fat, for example, methyl esters present in different feed-stocks impact a few chattels of fuels [11]. The Physical and synthetic properties of U.S. furthermore, European determinations for biodiesel (B100) and biodiesel mixes. Biodiesel is for the most part comprised of fourteen unique sorts of unsaturated fats, which are changed into unsaturated fat methyl esters by transesterification measure. Their fundamental particulars including sulfur content, thickness, iodine number, warming worth, corrosive worth, and carbon lingering when transesterification (vegetable oil and biodiesel, individually) was investigated in detail. From their examination, it was noticed that three factors impact the biodiesel creation. As of late, [12] directed a far-reaching examination on biodiesel created from around 28 eatable and 40 non-eatable vegetable oils, of organization and details.

1. **Density:** In reality, it has been found that there exists a relationship among's thickness and NOx outflows, lower densities favor lower NOx, however further specialists have not affirmed a particularly unambiguous pattern. As indicated by ASTM standard passable B100 thickness goes from 870 to 900 kg/m<sup>3</sup> [13, 14]. In the event that a diesel-tuned motor is run on biodiesel, higher thickness of the inferred methyl ester, and more noteworthy fuel mass are because of more unsaturated starting oil showing expansion in the quantity of twofold securities, in this manner builds thickness.
2. **Heating Value:** Late examination contemplates states biodiesel mixes in diesel motor decreases PM/smoke emanation and improves the in-chamber residue oxidation rate [13, 14]. The fuel ignition premise, lower warming worth (LHV), and higher warming worth (HHV) of fuel is estimated.
3. **Viscosity:** According to the ASTM standards, B100 thickness range from 1.9 to 6 mm<sup>3</sup>/s[14].
4. **Flash Point:** Evangelos [13] considers uncovered expansion in a number of twofold bonds and shows a marginally expanding pattern in streak point, as there is a connection between blaze point and level of unsaturation. As per ASTM standard, the passable B100 streak guide goes from 373 K toward 443. From the above detail, we can understand that the proportion over the fuel can be lighted is basically known as The Flash Point (FP) [14].

### 3 Reduction of Viscosity Besides Transesterification

In any case, the high consistency prompted issues in the engine [15–17]. Non-eatable plant oils may give better other options. Canakci and Gerpen [18] considered the creation of biodiesel (methyl esters) from not eatable plant oil or jatropha oil, decreasing consistency is subsequently the significant justification for handling oils of plants to be utilized as biodiesel. The jatropha biodiesel of crude oil with methanol can be utilized ideal sodium hydroxide impetus of one per cent at 65 °C, for 1 hour response time. The properties of delivered biodiesel can be utilized as an unsaturated fat methyl ester inside determination for motor purposes [19]. Strategies for decreasing thickness other than transesterification incorporate mixing, microemulsion, pyrolysis, and reactant breaking [20–23] (Fig. 1).

FP is determined to fill in as a limitation of liquor sum in biodiesel for wellbeing measure in carriage and capacity [23]. Thickness, cloud point, and Cetane number to be examined for fuel quality ascribe jatropha biodiesel properties [24]. The principles control the physical and compound properties of diesel and biodiesel (B100) [25]. Jatropha biodiesel thickness is high contrasting and differs from plant oil, the mix with petro diesel diminished the consistency as far as possible. New D7467 was distributed for B6 to B20 of 6 vol% to 20 vol% [26], the below mentioned Table 1 of Cloud point shows that the fuel can be used at what extent of low temperature, particularly in cool nations [26].

Thickness is determined to bar inconsequential things from being used as biodiesel raw material. It is in like manner used in confirmation of the thickness of biodiesel. The physical and engineered properties of Jatropha appeared differently in relation to the ASTM standard, hence the assessment considered the making of jatropha biodiesel through the reaction of transesterification.

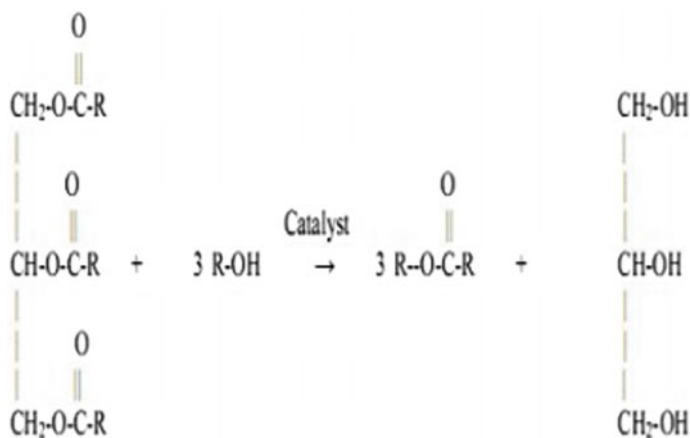


Fig. 1 Reaction of transesterification

**Table 1** Chemical and physical properties of biodiesel and diesel [25, 27]

Physicochemical property	Biodiesel (B6-B20) ASTM D6467	D 975 diesel	D6751 biodiesel (B100)
Flash point (°C)	53 (min)	60–80	130 (min)
Thickness (15 °C)	0.88	0.82-0.87	0.87
Kinematic viscosity (40 °C)	2.9–6.0	1.3–4.1	1.8–6.0
10% distillation of carbon residue	0.36 (maximum)	0.16	0.4 (maximum)
Cetane no	40 (minimum)	40–55	48 (minimum)
Cloud point (°C)	–3 to 12	–15 to 5	–3 to 13
Specific gravity	0.86–0.88	0.86	0.86–0.88

## 4 Biodiesel-Blend in Diesel Engine Its Performance and Emission

Expanding the proportion of jatropha fuel in diesel mix is the monetary decision that decreased the reliance on petroleum derivatives and addressed an elective fuel as a clean source. Discharge in CI motors comprises of hydrocarbon, carbon monoxide, Nitrogen oxide, and particulate matter. The utilization of diesel–biodiesel mixes which prompts an abatement in all the particulates mentioned before contrasted with diesel fuel.

The near aftereffect of every examination identified with the outflow attributes of biodiesel–diesel fuel mixes with diesel fuel separately in various motors archived in Table 2. The emanation level fluctuates as per motor boundaries, fuel quality, working state of the motor, and motor plan.

### 4.1 Emission of HC

HC outflow is marginally lesser than diesel fuel because of rich oxygen substance [34]. Plus, advanced cetane no. of biodiesel and properties of blending of butanol abbreviate the start postpone period and fire engendering which bring about better ignition. For biodiesel mixed fuel, the HC emanation is lower than diesel and diminishes with an increment of biodiesel in the fuel [39]. For Diesel, the HC outflow diminishes with an increment of motor burden, because of the increment in burning temperature related to higher motor burden. In case the biodiesel–diesel mix is utilized as fuel rather than diesel, the HC emanation is declined [29]. Be that as it may, for the biodiesel mixed fuel, the HC discharge, rather than diminishing straightly with motor burden, has a pinnacle esteem at the 40% motor burden.

**Table 2** Result for various test condition of performance and emission

Motor/Engine	R No	Fuel	Experiment	Comparison of diesel fuel					
				HC	CO	Smoke	NO	BSFC	Efficiency
Single cylinder diesel engine	[28]	Pongamia Pinnata oil and mustard oil	(300 rpm) Continuous speed	Higher	Lower	Higher	Higher	Higher	0.9% increase
	[29]	Oil of Rice bran	(1,550 rpm) Continuous speed	Lower	Lower	Lower	Lower	Higher	2% increase
	[30]	Oil of Palm	(16:1, 17:1, 18:1) Variable compression ratio	Lower	Lower	Lower	Higher	Lower	Lower
	[31]	Oil of Rice bran	Different load	Higher	Higher	-	-	Higher	Similar
	[32]	Oil of Rapo seed	(1,500 rpm) Continuous speed and 20 bars of Continuous injection	Lower	Lower	Lower	Higher	Higher	Similar
	[33]	Oil of Palm	(2,000, 2,500, 2,800) rpm of Diverse speed	Lower	Lower	-	Higher	Higher	-
	[34]	Oil of Safflones	1,500 rpm of Constant speed	-	Similar	-	Similar	Similar	Higher
	[35]	Seed (Cotton)	(20, 40, 60, 80, 100%) of Different load	Lower	Similar	Higher	Lower	Lower	Increase
Diesel engine	[36]	Oil of Pongamia	(30, 50, 20, 100%) At diverse loads	Lower	Lower	-	Higher	Higher	Similar
	[37]	Palm (Jatropha meringa)	(100 to 400) rpm Of Diverse speed	Higher	Lower	-	Higher	Higher	-
	[38]	Oil of palm	Different speed (1,000, 1,800, 2,000, 2,500, 3,000 rpm)	Lower	Similar	-	Higher	Higher	-



## **4.2 Emission of CO**

The CO emanation of biodiesel mixes is low as compared to the fuel motor. De Oliveira et al. [40] revealed, utilization of ethanol diminishes the CO discharge by 8.6% low as compared to B7. Utilizing B7E5 CO emanations expanded relatively till motor burden arrived at 30 kW. As the exceptionally premixed charge disseminated consistently in the chamber with the fissure locale and limit layer district close to the chamber liner, where, brings about high carbon monoxide discharges. Alptekin et al. [41] saw that the discharge of biodiesel had expanded Carbon dioxide and Nitrogen oxide, also they emanate low CO when contrasted with diesel fuel. They saw that the complete HC discharge expanded while CO outflow lessens marginally for mix comprised of bioethanol contrasted and B20. The Carbon monoxide outflow diminishes while utilizing biodiesel-diesel mix contrasted the oxidization of fuel is difficult with fuel. Raman et al. [32] tracked down that the Carbon monoxide emanation at lower loads when contrasted and motor activity at greatest burden is higher.

## **4.3 Emission of NOx**

The thickness of vapor smoke raised by 12.89, 5.077, 11.339, and 14.063% for extension of 4% propanol, 8% propanol, 8% butanol and with diesel and 4% butanol, independently. Motamedifar and Shirmeshan [39] reported that the NO surge will be generally outrageous for D100 vane point.

## **4.4 Particulate Matter**

It is discovered that most limit particulate matter of smoke saw for D55 at 20, 40 and 60% troubles [42, 43].

## **4.5 Rate of Heat Release**

The most extreme warmth discharge rate happens at the greatest motor burden nearer to the top right on. Eventually, this brought about a higher warmth discharge rate for diesel. The increment of burden from low to medium the most extreme warmth discharge rate increments, in any case, the contrary wonder happens under high burden [44]. The biodiesel-diesel mix from biodiesels of various beginnings gave a lower top warmth discharge than diesel fuel. Qi and Chen [45] found that the

pinnacle heat discharge pace of biodiesel is high as compared to the diesel fuel under low engine loads, anyway, the opposite is legitimate under high engine troubles [46].

## 5 Conclusion

The utilization of biodiesel will prompt misfortune in motor influence primarily because of the decrease in warming worth of biodiesel contrasted with diesel, and it brings about the increment in biodiesel fuel utilization. The primary biodiesel creation challenge in commercialization is the significant expense of creation contrasted with non-renewable energy source diesel. From the survey, it tends to be reasoned that the utilization of biodiesel favors to decrease carbon store and wear of the key motor parts, contrasted and diesel. This is because of the expense in delivering biodiesel that is vigorously relying upon feedstock cost or crude materials.

## References

1. Shen Y, Linville JL, Urgun-Demirtas M, Mintz MM, Snyder SW (2015) An overview of biogas production and utilization at full-scale wastewater treatment plants (WWTPs) in the United States: Challenges and opportunities towards energy-neutral WWTPs. *Renew Sustain Energy Rev* 50:346–362
2. Gazda W, Stanek W (2016) Energy and environmental assessment of integrated biogas trigeneration and photovoltaic plant as more sustainable industrial system. *Appl Energy* 169:138–149
3. Zuñiga-Díaz J, Reyes-Dorantes E, Quinto-Hernandez A et al (2018) Biodiesel from “Morelos” rice: synthesis, oxidative stability, and corrosivity. *J Chem* 2018. Article ID 4595130, 11 pp
4. Anguebes-Franceschi F, Abatal M, Bassam A et al (2018) Esterification optimization of crude African palm olein using response surface methodology and heterogeneous acid catalysis. *Energies* 11(1):157
5. Rajak U, Verma TN (2018) Effect of emission from ethylic biodiesel of edible and non-edible vegetable oil, animal fats, waste oil and alcohol in CI engine. *Energy Convers Manage* 166:704–718
6. Ray NHS, Mohanty MK, Mohanty RC (2013) Biogas as alternate fuel in diesel engines: a literature review. *J Mech Civ Eng* 9:23–28
7. Rose L, Hussain M, Ahmeda S, Malek K, Costanzo R, Kjeang E (2013) A comparative life cycle assessment of diesel and compressed natural gas powered refuse collection vehicles in a Canadian city. *Energy Policy* 52:453–461
8. Paul A, Bose PK, Panua RS, Banerjee R (2013) An experimental investigation of performance-emission trade off of a CI engine fueled by diesel–compressed natural gas (CNG) combination and diesel–ethanol blends with CNG enrichment. *Energy* 55:787–802
9. Banapurmath NR, Gireesh NM, Basavarajappa YH, Hosmath RS, Yaliwal VS, Pai A, Navale KG, Jog P, Tewari PG (2015) Effect of hydrogen addition to CNG in a biodiesel-operated dual-fuel engine. *Int J Sustain Eng* 8:332–340
10. Selim MYE (2005) Effect of engine parameters and gaseous fuel type on the cyclic variability of dual fuel engines. *Fuel* 84:961–971
11. Hoekman SK, Broch A, Robbins C, Cenicerros E, Natarajan M (2012) Review of bio diesel composition, properties, and specifications. *Renew Sustain Energy Rev* 16(1):143–169

12. Sajjadi B, Raman AAA Arandiyan H (2016) A comprehensive review on properties of edible and non-edible vegetable oil-based bio diesel: composition, specifications and prediction models. *Renew Sustain Energy Rev* 63:62–92
13. Giakoumis EG (2013) A statistical investigation of bio diesel physical and chemical properties, and their correlation with the degree of unsaturation. *Renewable Energy* 50:858–878
14. Panneerselvam N, Murugesan A, Vijayakumar C, Kumaravel A, Subramaniam D, Avinash A (2015) Effects of injection timing on bio-diesel fuelled engine characteristics—an overview. *Renew Sustain Energy Rev* 50:17–31
15. Canoira L, Galean JG, Alacantara R, Lapuerta M, Garcia CR (2012) Fatty Acid Methyl Esters (FAMES) from Castor oil: production process assessment and synergistic effects in its properties. *Renew Energy* 35(1):208–217
16. Demirbas A (2005) Biodiesel production from vegetable oils via catalytic and non-catalytic supercritical methanol transesterification methods. *Progr Energy Combust Sci* 31:466–487
17. Demirbas A (2006) Biodiesel Production via non-catalytic SCF method and biodiesel fuel characteristics. *Energy Conservat Manage* 47:2271–2282
18. Canakci M, Gerpen J Van (2001) Biodiesel production from oils and fats with high free fatty acids. *Am Soc Agri Eng* 44(6):1429–1436
19. Knothe G (2006) Analysing biodiesel: standards and other methods. *JAOCS* 83:823–833
20. Vicente G, Martinez M, Arcil J (2004) Integrated biodiesel production: a comparison of different homogeneous catalysts systems. *Biores Technol* 92:297–305
21. Hirata S, Berchmans HJ (2007) Biodiesel production from crude *Jatropha Curcas L.* seed oil with high content of free fatty acids. *Biores Technol* 99:1716–1721
22. <http://www.astm.org/Standards>. ASTM standard test method for cloud point of petroleum products. 23. Feb. 2015, 8.00 pm
23. Knothe G, Steidley KR (2005) Kinematic viscosity of biodiesel fuel components and related compounds. Influence of compound structure and comparison to petro-diesel fuel Components. *Fuel* 84:1059–1065
24. Knothe G (2005) Dependence of biodiesel fuel properties on the structure of fatty acid alkyl ester. *Fuel Process Technol* 86:1059–1070
25. Kywe T, Oo M (2009) Production of biodiesel from jatropha oil in pilot plant. In: *World Academy of Science, Engineering and Technology*
26. Pramanik K (2003) Properties and use of jatropha curcas oil and diesel fuel blends in compression ignition engine. *Renew Energy* 28:239–248
27. Production process assessment and synergistic effects in its properties. *Renew Energy* 1–10 (2009)
28. Srithar K, Arun Balasubramanian K, Pavendan V, Ashok kumar B 2017 Experimental investigations on mixing of two biodiesel blended with diesel as alternative fuel for diesel engines. *J King Saud Univ* 29:50–56
29. Goga G, Chauhan BS, Mahla SK, Cho H (2019) Performance and emission characteristics of diesel engine fueled with rice bran biodiesel and n-butanol. *Energy Rep* 5:78–83
30. Roshia P, Mohapatra SK, Mahla SK, Cho HM, Chauhan BS, Dhir A (2019) Effect of compression ratio on combustion, performance and emission characteristics of compression ignition engine fuelled with palm (B20) biodiesel blend. *Energy* 178:676–684
31. Chhabra M, Sharma A, Dwivedi G (2017) Performance evaluation of diesel engine using rice bran biodiesel. *Egypt J Pet* 26:511–518
32. Raman AL, Deepanraj B, Rajakumar S, Sivasubramanian V (2019) Experimental investigation on performance, combustion and emission analysis of a direct injection diesel engine fuelled with rapeseed oil biodiesel. *Fuel* 246:69–74
33. Bari S, Hossain SN (2019) Performance and emission analysis of a diesel engine running on palm oil diesel (POD). *Energy Procedia* 160:92–99
34. Celebi Y, Aydin H (2018) Investigation of the effects of butanol addition on safflower biodiesel usage as fuel in a generator diesel engine. *Fuel* 222:385–393
35. Vijayakumar M, Mukesh Kumar PC (2017) Performance enhancement and emissions analysis of diesel engine with biodiesel, N-propanol and 1-butanol blend. *J Appl Fluid Mech* 10:79–84

36. Kumar P, Sharma MP, Dwivedi G (2016) Impact of ternary blends of biodiesel on diesel engine performance. *Egypt J Pet* 25:255–261
37. Kumar K, Sharma MP (2016) Performance and emission characteristics of a diesel engine fuelled with biodiesel blends. *Int J Renew Energy Res* 6:658–662
38. Arumugam K, Sathiyamoorthy V, Anbazhagan R, Suresh R (2017) Performance and emission characteristics of CI engine fuelled with 100% palm biodiesel: an experimental study. *Int J Pure Appl Math* 8:265–273
39. Motamedifar N, Shirmeshan A (2018) An experimental study of emission characteristics from cylindrical furnace: effects of using diesel-ethanol-biodiesel blends and air swirl. *Fuel* 221:233–239
40. De Oliveira A, De Moraes AM, Valente OS, Sodre JR (2015) Combustion characteristics, Performance and emission from a diesel power generator fuelled by B7-Ethanol Blends. *Fuel Process Technol* 139:67–72
41. Alptekin E, Canakci M, Ozsezen AN, Turkcan A, Sanli H (2015) Using waste animal fat-based biodiesel-bioethanol diesel fuel blends in a DI diesel engine. *Fuel* 157:245–254
42. Vijayakumar M, Mukesh kumar PC (2017) Diesel engine with biodiesel, N-propanol and 1-butanol blend. *J Appl Fluid Mech* 10:79–84
43. Verma P, Jafari M, Ashrafur Rahman SM et al (2020) The impact of chemical composition of oxygenated fuels on morphology and nanostructure of soot particles. *Fuel* 259:116167
44. Adu-Jrai A, Yamin JA, Al Muhtaseb AH, Hararah MA (2011) Combustion characteristics and engine emission of a diesel engine fueled with diesel and treated waste cooking oil blends. *Chem Eng J* 172:129–136
45. Qi DH, Chen H (2010) Experimental studies on the combustion characteristics and performance of a direct injection engine fueled with biodiesel-diesel blends. *Energy Convers Manage* 51:2985–2992
46. Lakshmi Narayana Rao G, Durga Prasad B (2007) Combustion analysis of diesel engine fuelled with jatropa methyl ester biodiesel-diesel blends. *Int J Green Energy* 4:45–58

# Design and Analysis of Overhead Ambulance



Sudhir Kumar Singh, Dipul Kumar, Gaurav Kumar Jha,  
and Pawan Kumar Singh Nain

## 1 Introduction

Ambulances play a critical role in the healthcare system, saving millions of lives each year. Emergency response vehicles currently in operation are most frequently caught in traffic jams. According to a World Health Organization survey, road accidents claim the lives of 1.35 million people per year [1]. Regrettably, around 30 percent of deaths result from delayed ambulances. The causes could be—too many road vehicles, people not complying with transport rules, poor road conditions, and much more. In 2016, about 146,133 people have been killed as a result of road accidents in India, according to a study published by the Times of India. More than 50 percent of heart attack cases reach hospitals late, indicating the unavailability of ambulances, but most of these may be attributed to trafficking in patients [2]. Improved road quality and the use of modern technology are two ways to minimize ambulance travel time and injuries, but no matter how much we change these things, ambulances will always run on the road and humans will make mistakes. Nearly 24,012 people die every day due to delays in obtaining health assistance, according to information collected by the National Crime Records Bureau. These deaths include patients with heart attacks, brain bleeding, suicide attempts, injuries, and stroke. The optimal window time for patients with heart attacks is 30 min, but the government reports that the patients with heart attacks, in India, take over 6 h. The first hour is considered a golden hour but the patient was unable to hit the dead time because of traffic congestion, bad roads, bad weather or human error [3].

In order to find out whether patients are able to use or not an autonomous ambulance, Zarkeshev et al. [4] performed t-testing, ANOVA, and mediation analysis. The findings show that education materials relating to preparing future patients for technology for autonomous vehicles must be created and disseminated. Dadfarnia

---

S. K. Singh (✉) · D. Kumar · G. K. Jha · P. K. S. Nain  
Department of Mechanical Engineering, Galgotias University, Greater Noida 203201, India

et al. [5] recommended scientific input to review and strengthen existing standards and practices in ambulance design. With the advance in technology, ambulances evolved further, making them more useful to people. With the ongoing enhancement in automation and artificial intelligence [6], connected and automated vehicles are definitely going to be an important part of future transportation. The healthcare sector is one of the industries that could benefit from connected and automated vehicles technology. The replacement of traditional ambulances by autonomous ambulances contributes to this accelerated growth. Autonomous ambulances reduce the risks associated with driver errors, which are normally the main cause of a vehicle crash.

## 2 Literature Review

A number of studies have been carried out in order to better understand the aerodynamic aspect and flow visualization in the automobile sector. In this section, a few studies have also been reported here related to CFD analysis and structural analysis of vehicles. Each study derives its cope and interpretation in a different way.

The added roof and bars in the ambulance were examined by Taherkhani et al. [7]. They focused on laboratory wind tunnel tests, CFD, and meta-modeling. Findings demonstrate that the aerodynamic drag can be reduced by 20 percent. The decreased drag offers significant benefits in terms of fuel savings and emergency response vehicle emissions. Jadhav et al. [8] considered a popular bus model Volvo 9400 and performed CFD analysis. They found that there is the potential for all sorts of modifications to the existing bus design, including faces, walls, and the chassis. Changed or existing models were used for CFD analysis. Drag increases with velocity a little but decreases with higher velocity. At a speed of 120 km per hour, a modified bus drag coefficient was 0.41 that of the standard one's 0.65. Rubel et al. [9] used Solidworks-2015 to design a spoiler that was mounted on the vehicle's rear side. The aim of this external device was to minimize lift and boost the vehicle's performance. The author used the Autodesk simulation CFD software method to conduct the study and discovered that a 12-degree inclination was the best and the drag coefficient of the lift was the lowest. The research of Wang et al. [10] compares the boundary layer flow on a two-element airfoil concept like the A350XWB with the amount of downward spoiler deflection. The author found that the lift coefficients of L1T2 and GAW airfoil oscillate with spoiler deflection, respectively, in the nonlinear range, while in the linear range, the lift coefficient increases with spoiler deflection. Devang et al. [11] created a 3D car model and used CFD to better understand the effects of car add-ons such as fins, wings, spoilers, and diffusers. In various cases, the author measured and compared lift coefficient, drag coefficient, lift force, and drag force. In a model GT, they observed a maximum reduction of 16.53 percent with the spoiler and diffuser. The final conclusion reached was that different add-on devices would affect aerodynamic drag. Aero-drag reduction of the XAM 2.0-vehicle prototype was first studied using CFD calculations and later validated in a full-scale wind tunnel by Ferraris et al. [12]. The virtual and laboratory tests were compared to check the drag

reduction and the CFD analysis predictive ability. Bansal et al. [13] developed and carried out multiple simulations on a passenger car model. The author was mainly concerned with reducing the aerodynamic drag and gas mileage. The figures indicate that, due to the use of Vortex Generators, the lift coefficient was down to 18.83 percent and the drag coefficient was reduced to 4.35 percent. In order to obtain the distribution diagram of velocity, pressure, resistance, and lift, Yang et al. [14] created a 2D graphic of the automobile and ran numerical simulations. Pressure coefficient and pressure resistance of different models were obtained by simulating the external flow field of several typical vehicles. They recommended the optimized car design by analyzing and comparing the aerodynamic characteristics of various car models. Singh et al. [15] recommended a windshield to increase rider comfort in a TVS pep Scooty. The authors developed four Scooty models using Solid Works software, three with and one without a windshield. Flow analysis was performed on all of the models using ANSYS fluent. The simulation revealed a maximum reduction in drag coefficient value of 1.58 baseline model to 0.95 models 3 at a speed of 60 km per hour. The study confirms that the base model requires a 150 mm windshield height to avoid unwelcome aerodynamic advantages for the rider.

Satish et al. [16] increased the loading capacity of a TATA pickup truck from 1.5 to 2 tons by altering the vehicle body. For various load conditions, the updated models are numerically analyzed. The impact load was determined by dropping the five cylinders in the bottom row from a height of 1 cm. To estimate the impact force, they dropped the cylinders from a height of 1 cm in the bottom row. Since the proposed design was not strong enough to withstand the impact force of the cylinder falling, the sectional modulus was increased to improve strength without affecting vehicle dynamics. They demonstrated that the proposed design was safe when subjected to impact loads. Chethan et al. [17] designed twelve models of stem design and performed static structural analysis to identify the best possible stem design and acetabular stem cup combination. The author found three cross sections (Profile 1, Profile 2, and Profile 3) for analysis in circular, oval, elliptic, and trapezoidal design. Various mesh sizes from 5 mm to 0.25 mm were created and models were meshed with non-structured grids. Based on results, Profile 2 showed 25 percent less deformation and stress compared with Profile 1 and profile 3 compared to other profiles. They concluded that Profile 2 is the least deformed with a trapezoidal stem with CoCr material and is ideally fit for hip joint implants. Singh et al. [18] designed plates on ANSYS workbench and tested two welded plates made of aluminum, copper alloy, stainless steel, and structural steel for tensile and fatigue. In a static structural mechanical solver, 1000 N force was applied to one face of the plates to complete the analysis on all of these materials. In both tensile and fatigue testing, the aluminum alloy showed the least deformation, while the copper alloy showed the most deformation. Rahman et al. [19] studied the global structural analysis of a ship to detect most stress concentration points and deformed areas that would ultimately affect fatigue fractures. Three cases of An ANSYS sys were solved and the findings were presented with strain, stress, deformations. With the same loading of the vessel, it was found that the stress produced by hogging was much higher than

the stress developed by sagging. Gandhi et al. [20] used 3D modeling software Pro-engineering to develop the helmet, which was then imported into ANSYS software for static and dynamic analysis. When the author compared the obtained results to BIS standard values, it was found that all of the data was within reasonable limits. Celik et al. [21] have developed a 3D model of an apple and have investigated the bruising of apple fruits with effects on various materials from several heights. The tests revealed that the yield stress of the apple was 0.38 MPa, and the results of the simulation provided valuable visuals and numerical data for the timely inflammatory phenomenon. Bozkurt et al. [22] used the ABAQUS/Explicit finite element tool to create a 3D virtual test setup for simulating a typical drop-weight effect test on a composite laminate. The results of this study showed that the bottom layer matrix cracking is the initial failure mechanism in a 3D low-velocity impact case, and that the stacking order of the laminates has no bearing on this. Jembere et al. [23] designed the 3D passenger truck chassis model to study the increased chassis capacity and to analyze stress in various transverse areas under different load conditions, taking the stress concentration factor into account. The results revealed that the I-cross-section is the strongest, with the least amount of stress and distortion in a variety of cross sections and load conditions.

No research has been identified for autonomous ambulances from the existing literature. This research would fill a void in the design of overhead ambulances that currently exists. This research has four goals:

- (1) Present the idea of an autonomous ambulance.
- (2) Create an ambulance model and its components.
- (3) Investigate the modeled cabin drag coefficient.
- (4) Examine the ambulance's mounting and cabin for stress and deformation.

In this study, the solid models of the ambulance and its parts are created using the solid works software 2018. The drag coefficients, deformation, and stress of developed models are assessed using ANSYS 2015.

The paper is structured in the following manner. Section 1 begins with a short introduction before moving on to Sect. 2, which is devoted to the literature review. Section 3 discusses the methodology used in the study, while Sect. 4 presents the findings and discussions. Finally, Sect. 5 draws the key conclusions.

## 3 Methodology

### 3.1 Autonomous Ambulance

Figure 1 depicts the planned ambulance, which is based on the idea of aerial tramways. Cabin, upper railroad, and mounting are the three main components of this ambulance. The cabin is connected to the upper railroad by two mountings. This vehicle is designed exclusively for healthcare and will run on rail tracks rather than



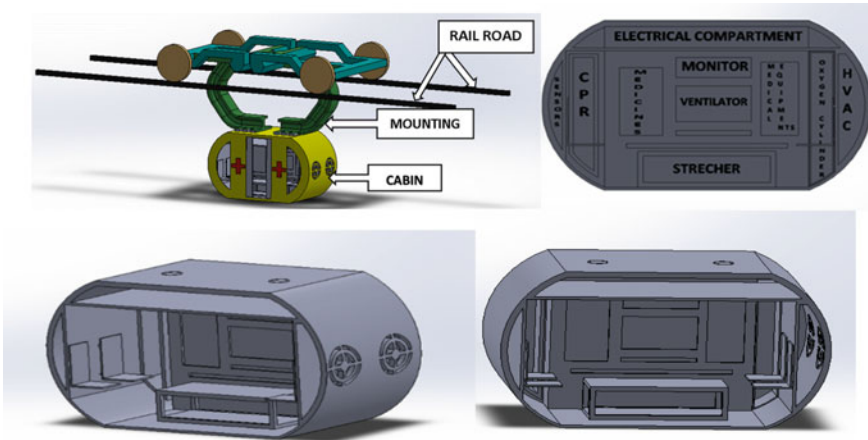


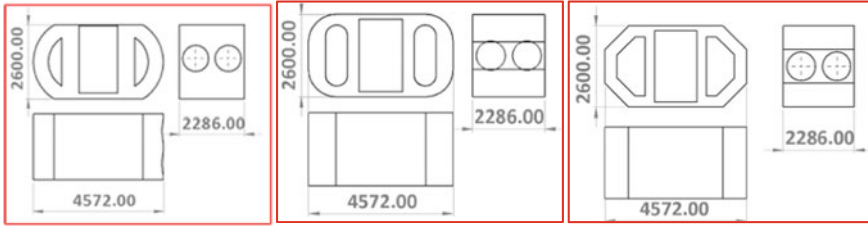
Fig. 1 Model of autonomous ambulance assembly and inside view of ambulance cabin

on the road above the ground at a height of 24 m. Multiple stations should be built in all the entry points of city and accident-prone areas, from where the patient could be transported directly to the closest hospital. The station would be constructed in such a way that it should be accessible to anyone seeking medical help in the metropolis. The electronic control unit and body control unit from the control rooms are used to control and track the autonomous ambulance, ensuring that they are not disturbed. McKinsey and company predict that autonomous technology could reduce casualties by 90 percent by 2050 [24]. A self-sufficient vehicle is able to sense and operate the surroundings without any human intervention. A human passenger is not needed at any time to drive the ambulance and is not required to be present in a vehicle as a driver.

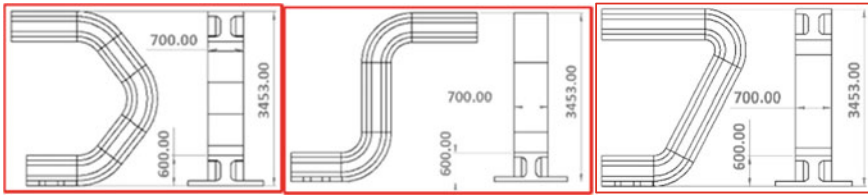
### 3.2 Model Development

For the proposed ambulance, three cabin designs have been built. Model 1 is a capsule, Model 2 is a rectangle with a fillet, and Model 3 is Octagonal. The main goal of various designs is to find the best cabin design with the least amount of drag so that operational performance can be improved. Although the shapes of all cabins differ, the length (4572 mm), breadth (2286 mm), and height (2600 mm) of all cabins (Model 1, Model 2, and Model 3) have been kept the same. In addition, all of the designed models have the same thickness (50 mm). Cabin models for CFD simulation are shown in Fig. 2. The three models developed for the cabin are also used to investigate the behavior of total deformation under impact load.

Figure 3 illustrates three distinct mounting profiles developed for simulation. The three mounting profiles have the same dimensions. The horizontal flanges withstand



**Fig. 2** 2D View of Cabins **a** Capsule-Model 1, **b** Rectangle with fillet-Model 2, and **c** Octagonal-Model 3



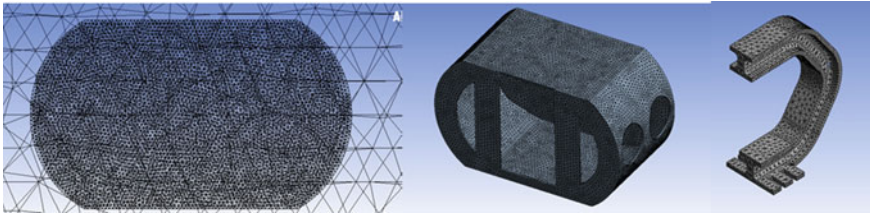
**Fig. 3** 2D View of Mountings **a** Profile 1, **b** Profile 2, and **c** Profile 3

bending moments while the web is stress resistant to shear. The I-shape cross section is preferred for mounting because of its high functionality and because of its shape, which makes it suitable for unidirectional bending parallel to the web [23]. On the other hand, the I-shape reduces the material cost.

### 3.3 Computational Domain, Meshing, and Boundary Conditions

CFD Simulation is commonly used in the analysis of fluid flow over engineered objects. The airflow in the vicinity of an ambulance cabin is dominated by turbulent flow and is subjected to straight winds. In CFD, the K-epsilon ( $\epsilon$ ) turbulence model is the most commonly used for simulating mean flow characteristics in turbulent flow conditions. It's a two-equation model that employs two transport equations to define turbulence in a general way [15]. To solve the cabin models built in this research, the standard k- $\epsilon$  turbulence model in ANSYS software was chosen.

In ANSYS Fluent, the study is performed in an enclosure fluid domain with dimensions of 13000 mm  $\times$  7000 mm  $\times$  7000 mm across the cabin. The cabin models are placed 6.5 m from the front, 3.5 m from the top, and 3.5 m from the right side of the enclosure. A straight wind with a speed of 80 kmph is considered. Following the creation of the enclosure, the Boolean function is used to remove the cabin body from the enclosure for the next stage of simulation in order to make two bodies onto one body. Fluent is used to create the mesh around the enclosure. All



**Fig. 4** **a** Meshed Cabin model 1 for CFD analysis, **b** Meshed Cabin model 1 for structural analysis, and **c** Meshed mounting profile1 for structural analysis

of the models were created using tetrahedral meshing, which ensures a high-quality mesh that is ideal for the durable and automated surface. For the discretization of the model, a mesh size of 50 mm was chosen. This is a requirement for evaluating the data at different nodes in order to obtain finer results.

The meshed model was subjected to boundary conditions, as seen in Fig. 4a, only straight wind conditions at speed of 80 kmph were considered at the computational domain's inlet. Constant inlet velocity conditions were used to simulate constant wind velocity conditions at the inlet similar to those found in wind tunnel experiments. At the computational domain's exit, an ambient static pressure condition was applied. To solve the case, the following conditions were used: material: air, density of air:  $1.225 \text{ kg/m}^3$ , inlet: velocity, outlet: pressure, and no-slip condition. The file is exported to fluent after the boundary conditions are specified in the ANSYS preprocessor. The aforementioned boundary conditions were applied to all the cabin models.

The same three cabins used in the CFD analysis are then tested for static structure analysis under impact load. After importing the model, the mesh has to be generated in order to perform further analysis in ANSYS. A tetrahedral grid is used for analysis because the geometry is complex. The investigation begins with a coarse mesh, followed by a convergence check to ensure that the result is correct. For the discretization of the model, a mesh size of 70 mm was chosen. The impact force acts on three cabins are identical as the dimensions of all cabins are the same. In a static state, the impact force acts on the cabin's bottom exterior surface, while the exterior top surface acts as a fixed support. The impact force conditions (magnitude and direction) are defined in the ANSYS preprocessor and then the file is exported to the solver. The results are calculated using a static structural model. When a cabin drops from a height (h), the impact load works on it as follows:

The 7000 kg total mass of the cabin is detailed here.

1. Mass of the cabin body = 5500 kg.
2. Mass of five persons at the rate of 70 kg = 350 kg.
3. Mass of medical equipment (Ventilator, Stretcher, Oxygen cylinder, and many more) = 500 kg
4. Mass of HVAC system = 100 kg.
5. Mass of electrical sensors, alternator, and wiring = 50 kg.

6. Additional mass of interior work in the cabin = 500 kg.

Before Impact, the velocity of a cabin mass ( $m = 7000$  kg) falling from a height ( $h = 24$  m) is  $v$ .

$$v = \sqrt{2gh} = 21.69 \text{ m/s}$$

The kinetic energy (KE) the cabin possesses before it impacts the ground is the same as the gravitational potential energy (P.E) it possessed from the height it was dropped

$$K.E = P.E = m \times g \times h = 1646400 \text{ J}$$

Nevertheless, this alone does not allow us to compute the force of impact. The cabin travel distance ( $d$ ) after impact is necessary to determine the impact force. The distance traveled by cabin is 0.1 m.

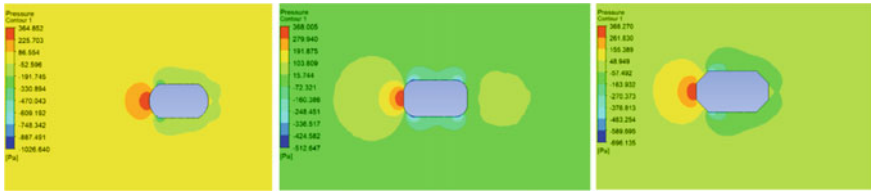
$$\text{Average impact force}(F) \times \text{distance traveled}(d) = \text{change in kinetic energy}$$

$$\text{Average impact force} = 16464000 \text{ N}$$

To perform the simulation, three mounting profiles developed in solid works are imported into ANSYS. Once the mounting profile is imported, the mesh has to be generated for further analysis. Tetrahedral mesh is used because it provides robust and automated surfaces with high-quality mesh. For the discretization of the mounting profile, a mesh size of 70 mm was chosen. After the mesh has been completed, 34,300 N tensile force is applied on the ends of each mount. For all mounting profiles, static structural analysis is performed by applying identical boundary conditions. These are necessary steps for analyzing and obtaining accurate results.

## 4 Result and Discussion

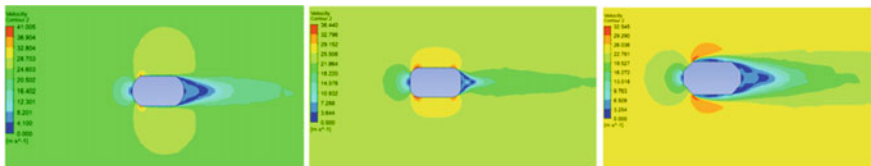
Static pressure contours of the autonomous ambulance cabin model 1, model 2, and model 3 are as shown in Fig. 5 at a speed of 80 kmph. The front part of the cabin is seen clearly with the stagnation points. The cabin frontal area has the most stagnation pressure. The maximum pressure concentration in the frontal area of model 3 is observed. The model 1 simulation pressure contour result shows that there is less pressure concentration on the capsule cabin compared to model 2 (Rectangle with fillet) and model3 (Octagon) on the front face. The simulation results of model 2 and model 3 show that no change in maximum pressure is observed in these models of the cabin. Thus, the capsule model has diminished the pressure drag on the cabin. A sleek and streamlined front-looking nose airflow system would help the autonomous ambulance's aerodynamic efficiency.



**Fig. 5** Pressure contour—**a** Capsule model 1, **b** Rectangular model 2 with fillet, and **c** Octagonal Cabin model 3

Figure 6 depicts the velocity contour obtained from the simulation of three models at a speed of 80 kmph. The left side of the figures is the front of the cabin. In all the models, velocity is much lower in the central portion of the cabin front face. Figure 6a reveals that the velocity around the capsule cabin is 0 m/s, but due to the acceleration of flow, high magnitude velocity is observed near the front upper and lower corners. The edge of the top and bottom face is responsible for the velocity obstruction. As shown in the graph, the velocity decreases next to the edge. Figure 6b shows that the velocity around the rectangular cabin with a fillet is 0 m/s and the high magnitudes are reached on the top and lower surface near the corner because the form of the rectangular fillet cabin has suddenly changed and the flow has been accelerated. A similar pattern of velocity as that of model 2 was seen in Fig. 6c, which is for the shape of the octagonal cabin except for the rare side. The massive and significant reduction in velocity seen in the graph is at the back end of the cabin.

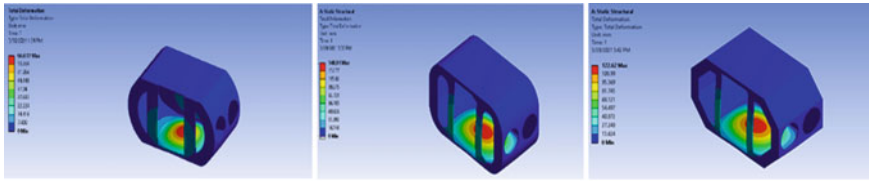
The drag coefficient is the most important parameter in the study of vehicle aerodynamics. Figure 7 portrays the comparison of drag coefficient with different cabin



**Fig. 6** Velocity contour—**a** Capsule model 1, **b** Rectangular fillet Model 2, and **c** Octagonal-model 3

**Fig. 7** Comparison of drag coefficients at various models





**Fig. 8** Total Deformation: **a** Cabin model 1, **b** Cabin model 2, and **c** Cabin model 3

models. For a constant speed, the value of the drag coefficient decreases with an increase in the streamlined design of the cabin. The maximum reduction in drag coefficient value is observed in model 1 at a speed of 80 kmph. The simulation result shows the reduction in the drag coefficient from 0.66 (model 3) to 0.53 (model 1) which is an 18.19 percent improvement compared to model 3. In brief, the overall aerodynamics supremacy of the proposed capsule cabin for the ambulance in this study was measured based on the capacity to attain low values for the drag coefficient.

Structural analysis is performed on all three cabins to determine total deformation when fully loaded cabins drop under static conditions from a height of 24 m. The results are evaluated with an impact force of 16,464 kN in the base of the cabin under static design. Figure 8 depicts cabin deformation under impact load for different models. The various color parameters can be seen for different cabins with varying degrees of deformation. Comparing the three cabins shows the min and max values of deformation for each model. The deformation of cabin model 1 is 66.67 mm, while cabin 2 and cabin 3 are 148.91 mm and 122.62 mm deformed, respectively. It is clearly visible that cabin 1 has less deformity (2.56 percent), while the other two cabins have relatively more deformity, which is 4.99% and 2.99%.

The results for mounting simulation collected in Table 1 indicate that, in comparison with the other two profiles, Profile 1 has shown less total deformation and less von Mises stress. Total deformation is the vector sum of all directional displacements of the systems. The contour plots of total deformation, von Mises stress, and elastic strain for profiles in Figs. 9, 10 and 11 are investigated in greater detail. All profiles display stresses less than the material’s yield strength for 34,300 N loading. In addition, in comparison with the other two profiles, the mounting of profile 1 has a minimum deformation of 0.077 mm and von Mises stress of 1.52 MPa. Equivalent Stress-Minimum stress in profile 1 was observed at point C, which is on the lower

**Table 1** Structure static analysis of mounting

Sl	Material	Profile	Load in N	Total deformation in mm	Equivalent von Mises stress in MPa	Equivalent strain in mm/mm
1	Structural steel	Profile1	34,300	0.077	1.52	7.617e-6
2	Structural steel	Profile2	34,300	0.120	2.23	1.221e-5
3	Structural steel	Profile3	34,300	0.140	2.73	1.371e-5

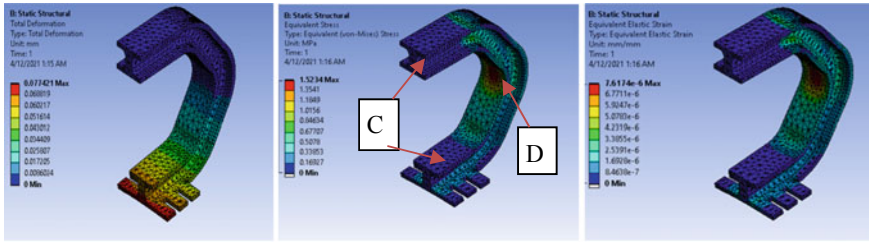


Fig. 9 Mounting profile 1: a Total deformation, b von Mises stress, and c Elastic strain

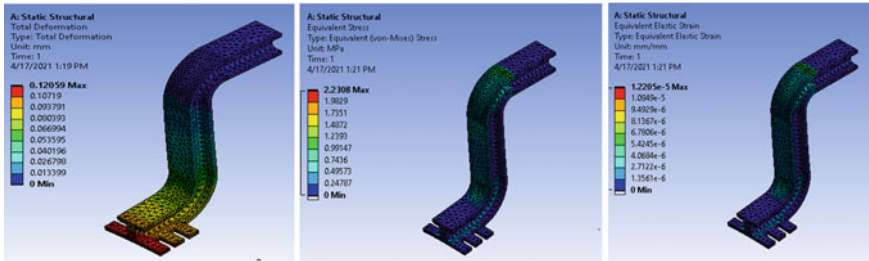


Fig. 10 Mounting profile 2: a Total deformation, b von Mises stress, and c Elastic strain

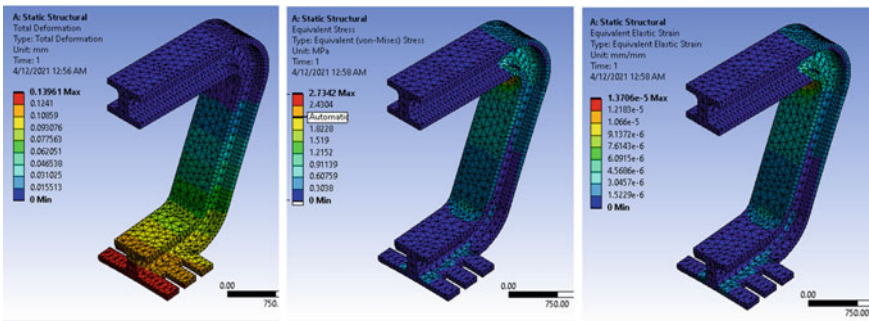


Fig. 11 Mounting profile 3: a Total Deformation, b von Mises Stress, and c Elastic strain

and upper side of members and maximum was observed at point D, which is on the inner side of members. Mounting profile 1 showed 45% less deformation and 44.3% less stress than mounting profile 3. Thus, from the results of this study, it can be concluded that profile 1 is well suited for secure and long-term use as mounting.

## 5 Conclusions

This study looked into the effects of various cabin and mounting designs for an autonomous ambulance. The findings of these investigations were used to create a user-friendly, aerodynamically and structurally efficient ambulance design. The studies led to the following conclusions:

- Using Solid Works software, three different cabin models and three different mounting profiles were developed for the ambulance.
- The Capsule form cabin configuration (Model) observes a maximum reduction of the drag coefficient and lower pressure concentration at a speed of 80 kmph.
- Capsule cabin 1 has a lower total deformation (66.67 mm) than cabin 2 and 3 when subjected to an impact load. Cabin 1 is, therefore, safer and tougher than the other two cabins.
- The mounting of profile 1 is 0.08 mm less deformed and the lowest stress of von Mises is 1.52 MPa in comparison to the other two profiles. Thus, from the results of this study, it can be concluded that profile 1 is well suited for secure and long-term use as mounting.
- The final results show that the proposed capsule cabin configuration and mounting profile 1 are both stable and appropriate for the envisioned autonomous ambulance.
- The proposed autonomous ambulance architecture concept has the potential to revolutionize the healthcare sector by reducing the number of people killed as a result of ambulance delays. The new ambulance concept would be able to replace ambulances that are now operating on the route, resulting in a reduction in the number of ambulances on the road leads to reduce emissions.

## References

1. World Health Organization (2020) Road traffic injuries. <http://www.who.int/news-room/fact-sheets/detail/road-traffic-injuries>. Accessed 24 Feb 2021
2. Shashi Bhushan (2019) 12 November 2019, Ambulance Stuck in traffic, Scary Right? <https://medium.com/@bkshashi9/ambulance-stuck-in-traffic-scary-right-7b539ce518b9last>. Accessed 26 Feb 26
3. The Hindu (2017) 15 April 2017, Helping patients get to hospital on time. <https://www.thehindu.com/news/cities/mumbai/helping-patients-get-to-hospital-on-time/arcle18031300.ece,last>. Accessed 04 March 2021
4. Zarkeshev A, Csizsár C (2020) Patients' Willingness to ride on a driverless ambulance: a case study in Hungary. *Transp Rese Procedia* 44:8–14
5. Dadfarnia M, Lee YT, Kibira D, Feeney AB (2013) Requirement's analysis for safer ambulance patient compartments. *Procedia Comput Sci* 16:601–610
6. Singh L, Kumar S, Raj S, Badhani P (2021) Development and characterization of aluminium silicon carbide composite materials with improved properties. *Mater Today: Proc* 46, 6733–6736
7. Taherkhani AR, deBoer GN, Gaskell PH, Gilkeson CA (2015) Aerodynamic drag reduction of emergency response vehicles. *Adv Autom Eng* 4:1–6



8. Jadhav CR, Chorage RP (2020) Modification in commercial bus model to overcome aerodynamic drag effect by using CFD analysis. *Results Eng* 6:1–7
9. Rubel Chandra Das (2017) Mahmud Riyad: CFD analysis of passenger vehicle at various angle of rear end spoiler. *Procedia Eng* 194:160–165
10. Wang W, Liu P (2017) Numerical study of the influence of spoiler deflection on high-lift configuration. *Theor Appl Mech Lett* 7:159–163
11. Nath DS, Pujari PC, Jain A, Rastogi V (2021) Drag reduction by application of aerodynamic devices in a racecar. *Adv Aerodyn* 3(4):1–20
12. Ferraris A, Airale AG, Berti Polato D, Messana A, Xu S, Massai P, Carello M (2019) City car drag reduction by means of shape optimization and add on devices. *Adv Mech Mach* 15:3721–3730
13. Ram Bansal R, Sharma B (2014) Drag reduction of passenger car using add-on devices. *J Aerodyn* 1–13
14. Yang X, Cai Zh, Ye Q (2019) Aerodynamics analysis of several typical cars. *J Eng Thermophys* 28(2):269–275
15. Singh SK, Agrawal BP, Agrawal BN, Dubey KK, Sharma SK, Phanden RK (2020) Drag reduction of TVS Scooty using a windshield for the rider comfort improvement. *Int J Veh Struct Syst* 12(5):498–502
16. Satish S, John Alexis S, Bhuvendran A, Shanmugam M, Baskar S, Shaisundaram VS (2021) Design and analysis of mild steel mini truck body for increasing the payload capacity. *Mater Today: Proc* 37(2):1274–1280
17. Chethan KN, Mohammad Z, Shyamasunder BN, Satish SB, Chandrakant RK (2019) Static structural analysis of different stem designs used in total hip arthroplasty using finite element method. *Heliyon* 5(6):e01767
18. Singh O (2017) Vika, Satpal Sharma: Analysis and comparison of total deformation of welded plates in tensile and fatigue tests using ANSYS. *Mater Today: Proc* 4(8):8409–8417
19. Rahman MM, Kamol RS, Islam R (2017) Structural analysis of a ship on global aspect using ANSYS. *Am Inst Phys AIP Conf Proc* 1919:020004
20. Gandhi VS, Kumaravelan R, Ramesh S, Venkatesan M, Ponraj MR (2014) Performance analysis of motor cycle helmet under static and dynamic loading. *Mech Mech Eng* 18(2):85–96
21. Celik HK, Ustun H, Erkan M, Rennie AE, Akinci I (2021) Effects of bruising of ‘Pink Lady’ apple under impact loading in drop test on firmness, color and gas exchange of fruit during long term storage. *Postharvest Biol Technol* 179:1115–1161
22. Bozkurt MO, Parnas L, Coker D (2019) Simulation of drop-weight impact test on composite laminates using finite element method. *Procedia Struct Integr* 21:206–214
23. Jembere AK, Paramasivam V, Tilahun S, Selvaraj SK (2021) Stress analysis of different cross-section for passenger truck chassis with a material of ASTM A148 Gr 80–50. *Mater Today: Proc*, in press
24. Bertonecello M, Wee D (2015) Ten ways autonomous driving could redefine the automotive world. <https://www.mckinsey.com/industries/automotive-and-assembly/our-insights/ten-ways-autonomous-driving-could-redefine-the-automotive-world,last>. Accessed 14 April 2021

# Design of Pineapple Peeling Equipment



Prakash Kumar and Debkumar Chakrabarti

## 1 Introduction

Northeast is one of the largest producers of pineapples in India. There are many small fruit processing units located across different northeastern states that process pineapples during peak harvest season [1, 2]. Pineapple has nutritional and medicinal values and it is processed and consumed in different forms like juice, squash, jelly, jam, and canned slices [3]. The canning of pineapple slices requires large investments in infrastructure and equipment. Therefore, many small processing units were, only, engaged in preparing juice and juice-related products which could be accomplished even in a small area. For preparing the juice and juice-related product, the pineapple was first peeled and chopped in small chunks. These chunks are then pulped and then the juice is squeezed out of the pulp. Presently, at almost all such processing units, the peeling and chopping activities are carried out using local knives. In the study, these cumbersome and time-consuming activities were found to be the biggest bottlenecks in the productivity of these units during the peak season [4]. The literature study of the existing solutions showed that there were solutions to solve issues related to processing of different fruits [5–7]. However, there was hardly much of research on addressing the issues related to pineapple peeling faced of the local processing units. The machines were quite fast but were very expensive, required large installation space, and increased the material wastage due to the varying size of pineapples. Most of such machines were foreign-made which could lead to repair and maintenance issues during breakdown situations [8]. Besides, most of the available solutions were

---

P. Kumar (✉)

Department of Design, Shiv Nadar University, Dadri, Uttar Pradesh 201314, India  
e-mail: [prakash.kumar@snu.edu.in](mailto:prakash.kumar@snu.edu.in)

D. Chakrabarti

Department of Design, Indian Institute of Technology Guwahati, North Guwahati, Assam 781039, India

power-driven, which does not suit the local power conditions. Moreover, there were hardly any solutions that could peel and cut the pineapples in small chunks. Hence, based on the findings related to the problem study, to ease the workers' task involved in peeling, a solution was conceptualized, developed, and evaluated by the user for its efficacy.

## **2 Method**

To address the problem of fast and effective peeling and chopping of pineapples, a holistic design approach was taken. At first, a brief was prepared that delineated all the possible needs and issues, the solution would address. The solution was supposed to peel and chop the pineapples fast and without much material wastage. It was supposed to be low cost and affordable for small units and easy to install and work. It should require less effort and preferably work without electricity. Based on this, different concepts were generated.

### ***2.1 Concept Generation***

The concepts were generated with a focus on reducing the material wastage that might occur due to the varying size of the pineapples. The concepts were generated for solutions that could

- peel the whole pineapple at one go
- peel the pineapple slices of different sizes
- Peel the pineapple and then chop it
- Peel and chop the pineapples simultaneously
- Peel pineapple by pressing it on the blades
- Peel pineapple by pressing the blades on the fruit.

Based on the criteria like the task completion time, the force requirement for operation, and the quantity of waste generated, conceptualization started for a solution that could effectively peel the pineapple slices of different thickness and diameter. The concepts were evaluated and, eventually, one of the concepts was detailed (Fig. 1).

### ***2.2 3D Visualization***

Based on the concepts, 3D models of the solutions were made and refined. At first, the concept with the pineapple constant and moving the blade was modeled. A mechanism was devised to ensure that the peeled slice did not stick inside the blade (Fig. 2).

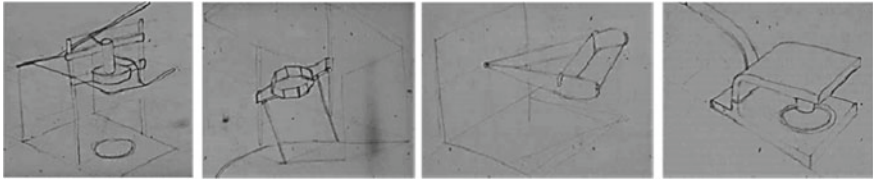


Fig. 1. Initial concept sketches depicting different pineapple peeling solutions

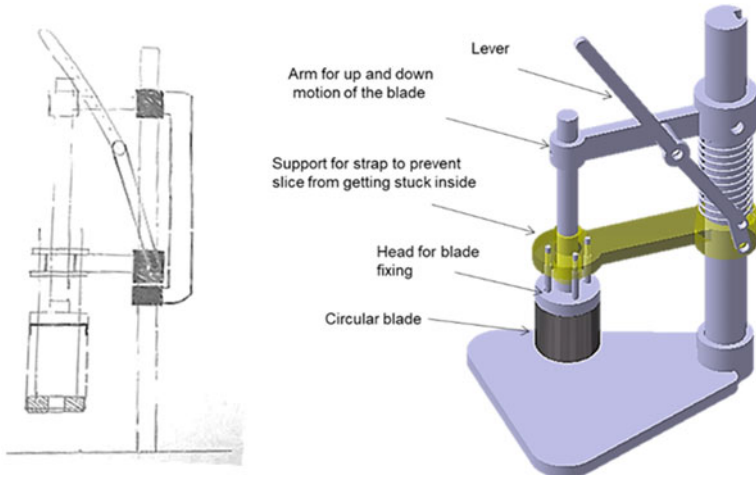


Fig. 2. Detailed 2D and 3D visualization of the selected concept solution

The model was evaluated on different criteria, and based on the user feedback, the model was further refined and made light weight and easy to use, maintain, and clean. Besides, the other concepts, with the stationary blades and moving pineapple over them, were explored. These concept solutions comprised a pressing mechanism operated by a handle. Cutting blades were fixed over a baseplate with a hole, vertically below the pressing plate. This equipment is fixed over a table with a hole. So, different possible variations were made. These were re-evaluated on the criteria like ease of manufacturing, ease of use, time of operation (Fig. 3).

After the evaluation, “option 02” was selected for detailing, and a 3D model for the same was created. The arrangement of blades was also detailed to understand how it would peel and cut the pineapple in a single pressing. When the pineapple slice is placed in the blades and press down, the slice gets peeled and divided into four chunks and falls down in the container placed below the table frame (Fig. 4).

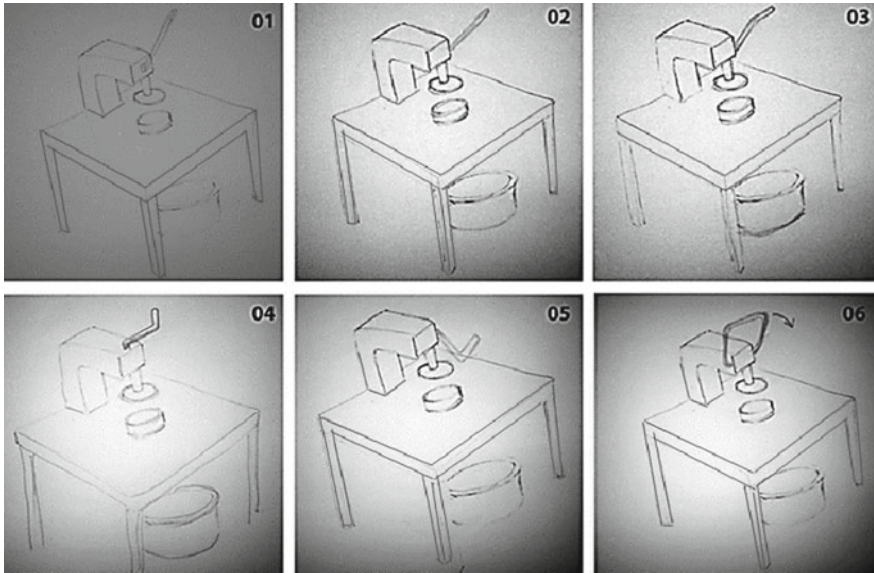
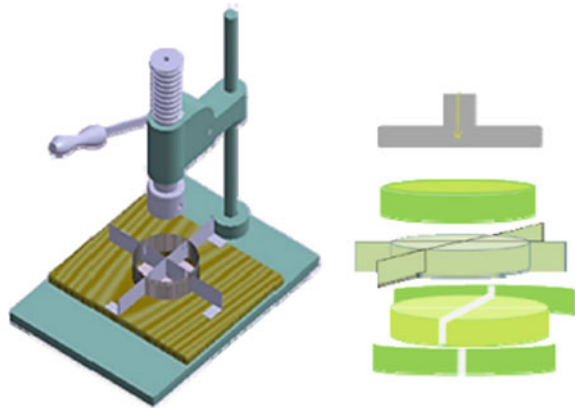


Fig. 3. Different variations for peeling the pineapple slices by pressing it against fixed blade

Fig. 4. 3D visualization of the selected concept and its working

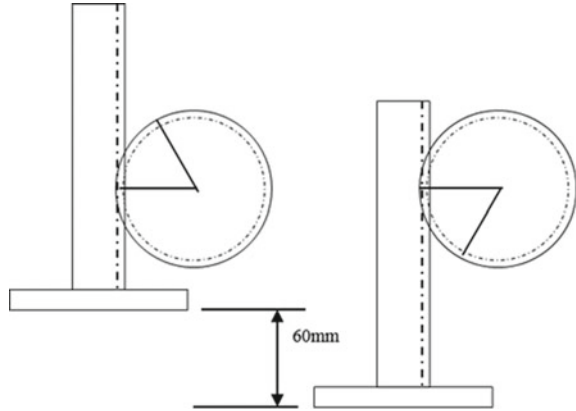


### 2.3 Product Detailing

**Critical dimensions of the Pressing Mechanism.** One critical decision related to the pressing mechanism regarding how much should the lever be rotated to cut peel the fruit comfortably. For this, pitch diameter of the pinion had to be decided. This diameter also decides the dimension of the casted casing of the equipment.

*Pitch radius of the Pinion.* For the comfortable pressing by hand, the lever should not rotate more than 60°. Within this angular rotation of the handle, the ram should

**Fig. 5** Displacement of pressing plate rack and pinion between initial and final position



come down at least by 6 mm. This gap provides space for placing the pineapple slice before pressing it against the blade (Fig. 5).

Therefore, for a linear movement of 60 mm through a lever rotation of 60°, the pitch radius of the pinion was determined to be 60 mm approximately.

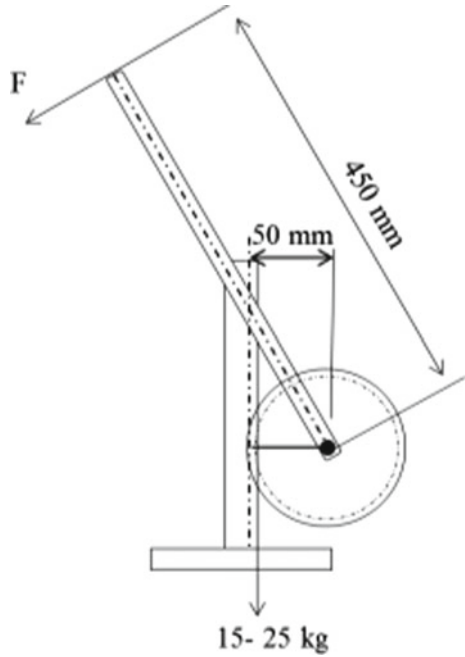
*Length of the Handle for optimum force application.* The optimum force required for repeatedly operating any lever is 2 Kg, the force required for pressing the pineapple slice over the blade was found to be 15 kg–25 kg. Since the pitch diameter of the pinion is 60 mm, we could calculate the optimum length of the lever for operating force of only 2 kg. Making all due considerations, it was calculated to be 450 mm (Fig. 6).

*The diameter of the blades.* Based on the study of the pineapples, it was found that the diameter of the fruit is maximum at its middle height and the diameter decreases gradually giving it an oval shape. Considering the average diameter of the upper, middle, and lower part of the fruit, and the general thickness of the peel, replaceable blades of three diameters, i.e., 90 mm, 94 mm, and 96 mm were designed to peel fruit with varying diameters for reducing wastage.

### 2.4 Fabrication

Based on the product details, proof of concept was fabricated. Its components were fabricated, separately, and then assembled. For the pressing mechanism, modification of an existing machine component was used. A hole was made in the baseplate just below the pressing plate to meet the requirements. Different parts of the blades were made separately, sharpened, and assembled. The configuration of the blades was such that circular blades with different diameters can be easily added or removed. This equipment was mounted on a table having a cut hole with screws (Fig. 7).

**Fig. 6** Optimum length of the lever



**Fig. 7** Fabrication of different components

The proof of concept was assembled and used for peeling and chopping pineapples with a satisfactory quality of output. However, the posture of the hand while pressing the lever was found to be deviating from the neutral axis which would lead to pain if the operation is done continuously for some hours. Hence, an effort was made to improve the solution through virtual simulations (Fig. 8).

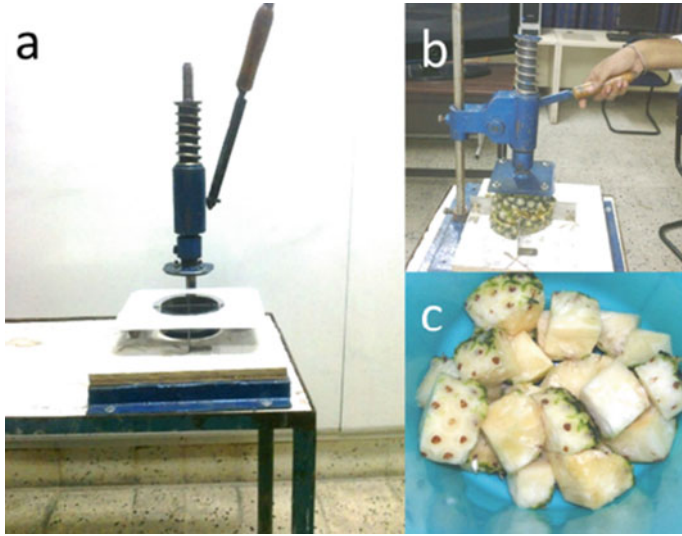


Fig. 8 Proof of concept and its work output

### 2.5 Improvements and Ergonomics Evaluation Using DHM

Using 3D modeling software, two new models were generated with improvised handles (Fig. 9). Both these models were tested for their efficacy through Rapid Upper Limb Assessment (RULA) [9] scores using Digital human modeling (DHM).

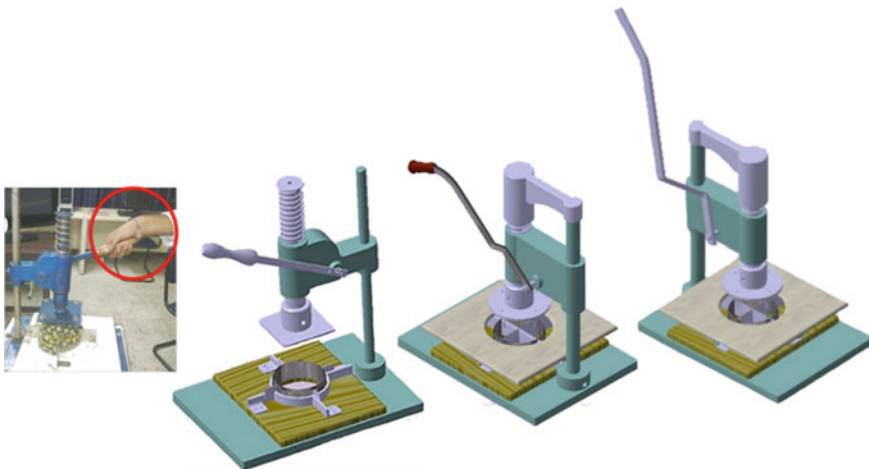


Fig. 9 Handle related ergonomics issues and 3D visualization of the modified solutions





**Fig. 10** RULA evaluation of the first modified solution using Digital Human Modeling

At first, 5th and 95th percentile, mannequins were generated for the male and female Indian population. Then RULA scores were generated for the critical initial and final postures related to the task. When the first improved version was checked, the final RULA score was found to be 6 for both positions (Fig. 10).

Consequently, the RULA score was generated for the second improved version with the 5th and 95th percentile Indian population for both the critical positions. The final RULA scores, in this case, were seen to be 3 which was significantly lesser than the former (Fig. 11).

Based on the RULA score, the changes were incorporated in the equipment and this improved solution was evaluated for its performance through user testing (Fig. 12).

## 2.6 Evaluation

The performance evaluation of solution by participant workers was done objectively as well as subjectively. Objective assessment was done through the determination of Task completion time (TCT), and the subjective evaluation by the workers was done through ratings using NASA TLX (Task Load Index). For better comprehension and precise response, the questions were translated into Hindi. The study was done on 11 participants and they were observed peeling pineapples using old/ traditional solutions, i.e., knife, *Baithi*, etc., and newly designed peeling equipment. The task completion time was recorded. They were asked to give their feedback using NASA TLX (Fig. 13).

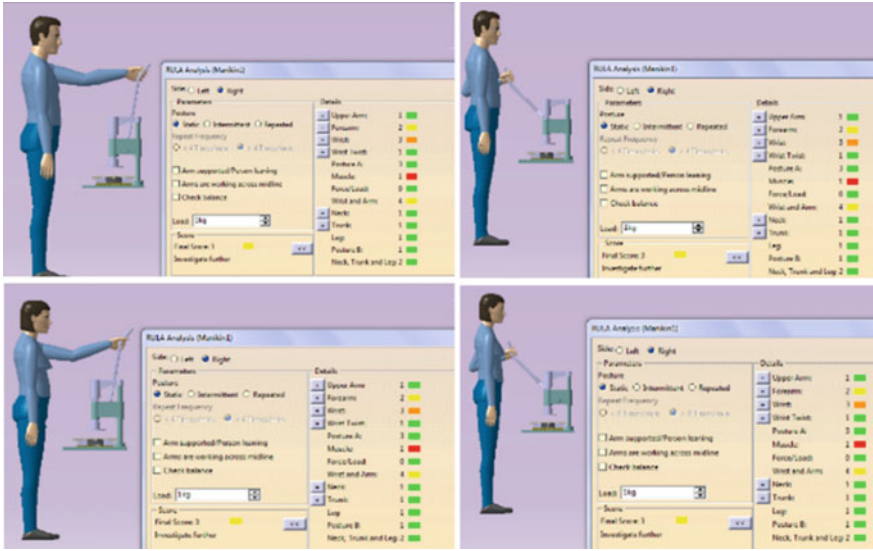
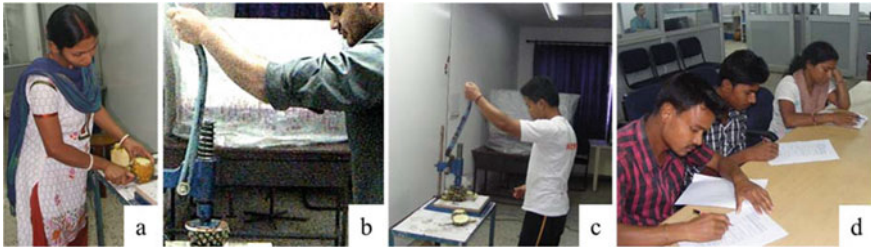


Fig. 11 RULA evaluation of the first modified solution using Digital Human Modeling

Fig. 12 Proof of concept of the modified solution





**Fig. 13** Performance evaluation of the traditional and new peeling solutions by workers; **a** peeling task using traditional work tool, i.e., knife, **b** initial position, and **c** final position of new peeling equipment (illustrating peeling process using new solution)

Since sample size was small and the data unlikely to be normally distributed, Mann Whitney U- test was used to compare the data regarding the two solutions.

### 3 Results

#### 3.1 Task Completion Time

In the “Task Completion Time” study, the time taken by workers using their old peeling method was compared with that required for the new equipment. The average time taken by the group of workers in peeling the fruit using the new technique was found to be lesser as compared to the traditional technique as shown in Table 1.

The standard deviation in the case of the traditional tool was very high as some traditional techniques had a faster rate of peeling (but had higher effort requirement). Since the sample size was not normally distributed, Mann Whitney U- test was used to check if the method with new equipment took lesser time compared to the traditional techniques. It was found that the mean rank for the traditional technique ( $mr = 11.86$ ) was higher than the method using the new technique ( $mr = 11.14$ ). As the sample size was small, the significance level for one-tailed test was found to be 0.41.

**Table 1** Mean TCT for peeling with old and new equipment

Sr. No.	Peeling technique	Mean (in S)	Standard error
1	Using traditional equipment	63.82	$\pm 17$
2	Using new equipment	42.82	$\pm 3.6$

**Table 2** Load score comparison for new and old peeling solution using Mann Whitney U- test

Sr. No.	NASA TLX Subclasses	Mean rank for new equipment (±SD)	Mean rank using for old equipment (±SD)	p-value
1	Mental Demand [TLX-MD]	12.05	10.95	0.35
2	Physical demand [TLX-PD]	13.14	9.86	0.11
3	Performance [TLX-P]	13.41	9.59	0.08
4	Effort [TLX-E]	14.86	8.14	0.01
5	Frustration [TLX-F]	15.55	7.45	0.00

### 3.2 Subjective Workload Assessment Using NASA TLX

After completion of task using the old as well as the new method, respectively, the participants reported the feedback of the used methods using NASA TLX which covers 5 subscales, i.e., Mental Demand [TLX-MD], Physical demand [TLX-PD], Performance [TLX-P], Effort [TLX-E], and Frustration [TLX-F] [9–12]. Since, the data obtained was not normally distributed; we tried to see if there was any significant decrease in the load while using the new solution as compared to the old one, using Mann Whitney U test. For all the subclasses of load, the mean ranking for old machine was greater as compared to the new solution, suggesting that greater load is required for the operation using old technique. It also found to be significant ( $p < 0.05$ ) in case of Performance [TLX-P], Effort [TLX-E], and Frustration [TLX-F]. Since tool which they use previously for peeling was mainly a knife, some users, who were habituated of using knife, felt that mental and physical load required in both the cases are similar. The insignificant difference in case of Mental demand [TLX-MD] and Physical demand [TLX-PD] can be attributed to the above tendency and mean rankings are not found significant in these two cases (Table 2).

## 4 Conclusion

After analyzing the workers’ performance, objectively and subjectively, for old and new solutions, the latter was, by and large, found to be faster and less load requiring method. However, it required further improvement to be converted to a market-ready product. The improved solution is required to be taken out of the lab and field-tested. During initial cost estimation, the total cost came around 5000/- which includes their profit margin of vendors as well. The cost could be further reduced if there is mass production of such equipment. On the contrary, since the above-mentioned cost is one for making the proof of concept, there might be a slight increase in the cost of the

final design. The research also paves the path for addressing other issues prevalent in the local food processing units.

## References

1. Sema A, Maiti CS (2011) Pineapple cultivation in north east India - a prospective venture. *Acta Horticulturae* 902:69–78
2. Rymbai D, Singh R, Sheikh F, Rani PM, Bardoloi R (2019) *Horticulture for economic prosperity and nutritional security in 21st century*, 1st edn. Westville, New Delhi
3. Hossain M (2015) Nutritional value and medicinal benefits of pineapple. *Int J Nutr Food Sci* 4:84
4. Kumar P, Chakrabarti D (2014) Ergonomic evaluation of manually operated pineapple peeling machine. In: Chakrabarti D (ed) *Humanizing work and work environment*. Tata Mc. Graw Hill, , pp 244–247
5. Ugwu B, Chime ER (2020) Ogbuka: review of orange juice extractor machines. *Adv Sci Technol Eng Syst J* 5(5):485–492
6. Nayak PK, Rayaguru K (2017) Design, development and performance evaluation of elephant apple core cutter. *J Food Sci Technol* 54:1–7
7. Nusbir Y, Candra H, Satriardi Susilawati A, Arief D (2016) Design of coconut de-husking machine using quality function deployment method. In: *The 3rd international conference on ocean, mechanical & aerospace -scientists & engineers*. Malaysia, pp 506–510
8. Desai Anoop (2006) Design for maintenance: basic concepts and review of literature. *Int J. Prod Dev* 3:77–121
9. McAtamney L, Corlett EN (1993) RULA: a survey method for the investigation of work-related upper limb disorders. *Appl Ergon* 24(2):91–99
10. Didomenico A, Nussbaum MA (2011) International journal of industrial ergonomics effects of different physical workload parameters on mental workload and performance. *Int J Ind Ergon* 41(3):255–260
11. Sharma V, Simpson RC, Lopresti EF, Schmeler M, Otr L Clinical evaluation of semiautonomous smart wheelchair architecture (Clinical evaluation of semiautonomous smart wheelchair architecture (Drive-Safe System) with visually impaired individuals Clinical evaluation of semiautonomous smart wheelchair 49(1):1–13
12. Yiyuan Z, Tangwen YIN, Dayong D, Shan FU (2011) Using NASA-TLX to evaluate the flight deck design in Design Phase of Aircraft. *Procedia Eng* 17:77–83

# Aerodynamic Design of Heavy Transport Vehicles



Anuj Vaishnav , Vaibhav Prasad , and Brahma Nand Agrawal 

## 1 Introduction

Today, vehicle manufacturing companies are continuously working to cut down emissions done by the vehicles keeping in mind the visionary thought of climate change. Some have also planned to shift to clean energies like CNG and Electric Batteries. But there is also one more approach to achieve the objective and that is the reduction of drag force acting on the vehicles and thus having less fuel consumption, better fuel burning, and thus following the process cutting down the emissions. This paper aims to design of container and driver's cab of Tata 3118 in SolidWorks and then import it into the Ansys Fluent for analyzing and improving the aerodynamic design. There have been several aerodynamic studies done on Formula cars, supercars, and passenger cars, but the emphasis was always less on heavy vehicles. However, some studies have been done by Richard A. Drollinger [1], because of the rise in fuel prices at that time, he studied the aerodynamics of trucks and got the results with the help of an experiment done in the wind tunnel, and thus gave an alternate aerodynamic shape for the truck. Aerodynamic study of state transport bus using computational fluid dynamics was studied by Kanekar et al. [2] studied about the aerodynamics of transport bus and by modifying the design were able to reduce the drag coefficient by 28% taking the speed 80 km/h because of which mileage went up by 20%. Patidar et al. [3] studied about fuel economy by investigating drag resistance.

S. KOPP [4] studied, how trucks are made fuel-efficient in aerodynamic aspects. Ganga Singh and Vinod Kumar [5] of JCDM College studied about reduction of drag forces in intercity buses and reduced 16% drag from a baseline model by modifying the frontal area. Sachin and Rao G. Amba Prasad [6] presented the computational analysis of intercity buses in which they improved the aesthetics and aerodynamic performance for Indian roads. Bayraktar [7] studied the external aerodynamics of

---

A. Vaishnav (✉) · V. Prasad · B. N. Agrawal  
Department of Mechanical Engineering, Galgotias University, Greater Noida, Uttar Pradesh, India

heavy ground vehicles to have better vehicle stability and increased performance. Marco Lanfrit [8] studied and presented the optimum routines and standards for controlling automotive external aerodynamics using “FLUENT” as the primary analysis tool. Imad Shukri Ali and Aws Akram Mahmood [9] studied and stated the improvement of aerodynamics characteristic of heavy trucks to have better output in harsh weather conditions, such as thick air in snowy areas, and to have better fuel efficiency as well. E. Selva Kumar [10] studied “Aerodynamic exterior body design of bus”, in which, the experimental numerical tests were conducted in wind tunnels and the effectiveness of the new concept design. The drag can reduce by 30–40% in the new concept than the existing bus and the test result show that for every 100 km 6–7 L of fuel are used.

A study conducted by Firoz Alama and Harun Chowdhury [11] found that small changes in body shape, extrusions, and accessories are found to cause a considerable volume of aerodynamic air resistance. In spite of popular belief, it was discovered that HPV 1 has lower air resistance than HPV 2. The outcomes of the research aided in the development and refinement of existing upcoming automobiles usage in RACV or comparable motorsport competitions in order to improve aerodynamic efficiency. In a study conducted in 2015 by Mehrdad Khosravi and Farshid Mosaddeghi [12], it was found that the most effective auxiliary part is a deflector, which reduces the drag coefficient significantly at a specific angle. The second finding was that adding two cab vane corners at the two front part corners of the cab results in a large air resistance deduction. Also, the back vanes and base flap have a notable effect on drag reduction, so when all auxiliary pieces are installed in their optimal places, the drag reduction is increased by around 41% in comparison to the simple model. In 2010, a study conducted by Zulfaa Mohamed-Kassim and Antonio Filippone [13], one strategy to improve vehicle fuel efficiency is to create effective routes that avoid interactions with traffic lamps on the road, indicators indicating a halt, road connections, steep splits, a lot of vehicles, and so on. Automobile statistics from an automatic tachograph, for example, can be used to determine how effective a city route is. Furthermore, correct driving etiquette should be enforced to limit the amount of fuel wasted due to excessive acceleration and deceleration. Jeong Jae Kim et al. [14] concluded in the year 2017 that the projected drag lowering consequence of the altered CRF using CFD Analysis is 19.0%, and this is in proximity to the result of the wind tunnel experiment. Furthermore, the drag reduction rates for the CRFs studied in this work tended to be extremely near to the outcome of the research. The CRF curvature affects the vortical formations across the automobile with a CRF.

It was concluded in the year 2019 by Taeseong Hann and Daewook Kim [15] that fuel efficiency can be increased even more by a model he proposed AFP that greatly lowered drag and side force coefficients by 26.5% ( $\phi \frac{1}{4} 0$ ) and 5.3% ( $\phi \frac{1}{4} 15$ ), respectively. The LIAD boat tail and gap fairing were found to satisfactorily postpone airflow separation and lower TKE in the forebody and base body sections using PIV parameters. Besides that, a reduction of 13.4% in fuel consumption was recorded by installing the proposed AFP in a proving ground test using real tractor-trailers. Based on a conservative estimate, a tractor-trailer moving with a speed of 90 kmph might save \$3300 per year in transportation logistics costs. In 2019, Ravi

Kumar B. [16] proved drag reduction from 0.3454 to 0.2322 through his research done in the rear portion of the car by altering rear slot angles from  $0^{\circ}$ – $13^{\circ}$ . In 2016, L. Anantha Raman [17] did tests on a SUV by doing rear fending, adding a rear plate, and by adding a vortex generator. Because of this 6.5% drag reduction by rear plate and 26% by rear plate. In 2014, J. Abinеш [18] analyzed two Volvo intercity buses, the base model and the modified model. And as per the CFD analysis, drag was 10% less for the modified model as compared to the base model.

Aerodynamics is a term which is given less importance when it comes to heavy vehicles, this study shows how to incorporate the best methods to increase the efficiency of heavy transport vehicles, which, in turn, can generate larger profits for the transportation agencies as well as decrease the pollution indexes to a greater extent.

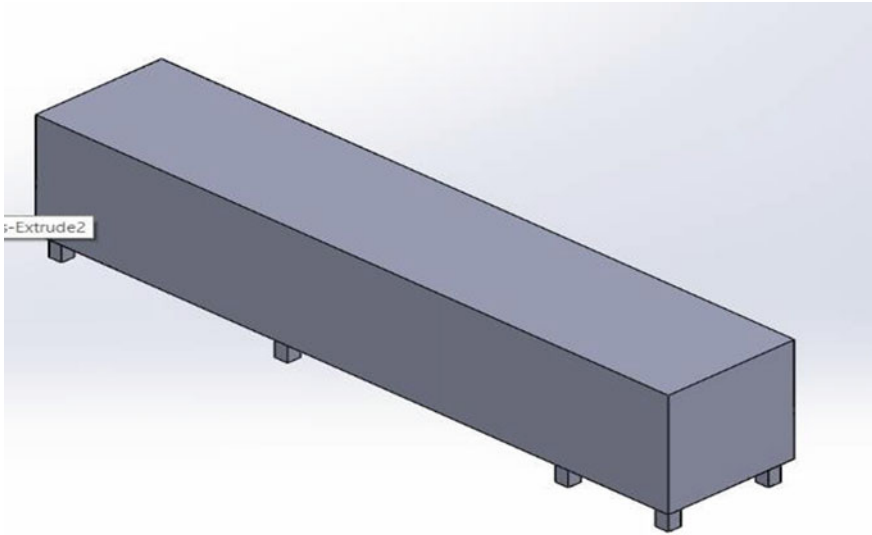
## 2 Methodology

The methodology of this study consists of designing the conventional design of container and driver's cab in Solidworks and analyzing it using Ansys Fluent. Similarly, modified design of container and driver's cab was also designed in Solidworks and analyzed using Ansys Fluent. In this study, two models are used that are conventional and modified to reduce the drag force by doing modifications in conventional design. The vehicle taken in the study is Tata 3118 which has a brick-like design and is widely used pan India for transportation of freight. Main modifications done in the design of the container are giving it a boat like ending by providing a curve in the rear upper part, whereas in the driver's cab, the main modification done is the curve spoiler given at the cab's head which can reduce air drag by providing smooth contours. After designing the models in SolidWorks, analysis to calculate Lift and Drag force was done using the Ansys (FLUENT). First, an enclosure was made to create boundary conditions, and the air was taken as the fluid at the inlet velocity of 25 m/s as per the Indian road regulations. Once the enclosure was complete, tetrahedral meshing was done to create finite element analysis and following the process of lift and drag, forces are calculated by performing over 200 iterations before calculating the final result.

## 3 Results and Discussion

Results were calculated in Ansys fluent and according to the results change in the Drag force because of providing a curve in the rear upper portion to give it a boat like ending was on the conventional container is 5982.786 and on the modified container its value is 4258.223 and similarly for conventional driver's cab the change in drag force because of giving curve like a spoiler at the cab's head was 9582.668 for a conventional design of driver's cab and modified driver's cab it is 8850.428 so observing the values of drag force we were able to consider that our modifications





**Fig. 1** Conventional design of container

were suitable to reduce the drag force and thus providing better stability and less fuel consumption. Analysis was also done in the category like velocity contour distribution on container and driver's cab in interactive color graphics. Results are depicted in the form of graphs taken from Ansys (Fluent).

Figures 1 and 2 show the conventional design of the container and modified design of the container, respectively, designed in SolidWorks.

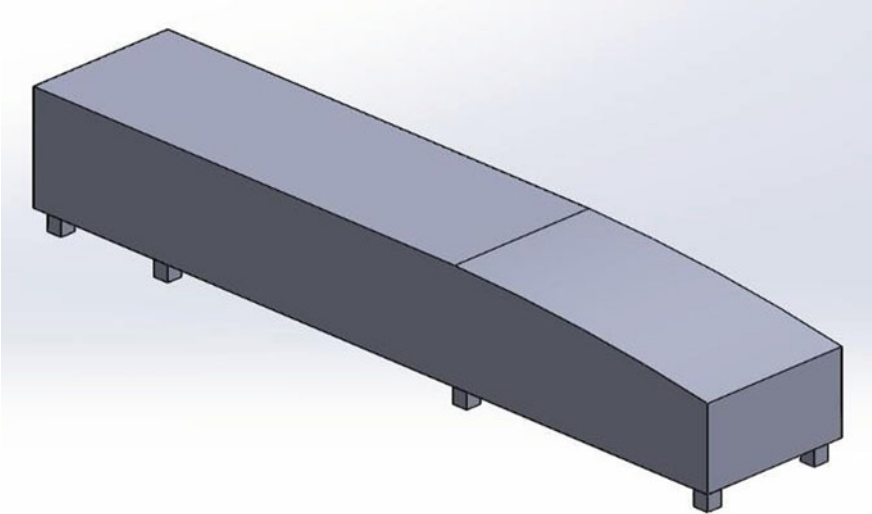
Similarly, Figs. 3 and 4 show the conventional design of the driver's cab and modified design of the driver's cab respectively designed in SolidWorks.

Figure 5 shows the drag force on conventional container calculated by performing 200 iterations and the graph plotted of drag giving the value of drag force, respectively.

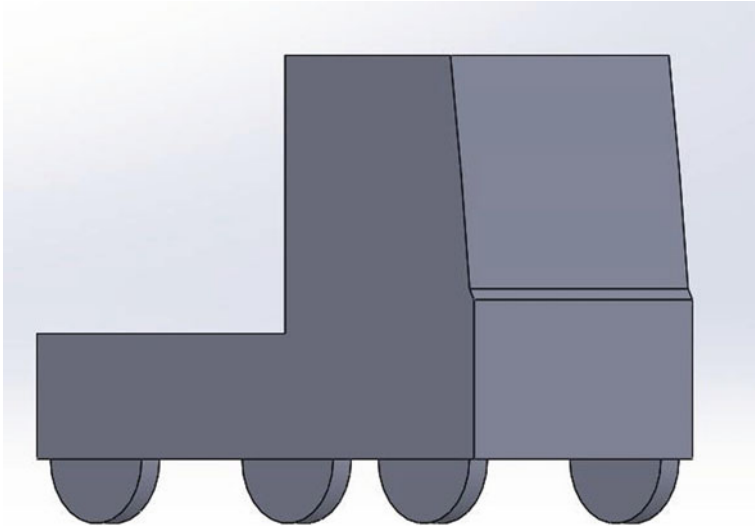
Figure 6 shows the drag force on modified container calculated by performing 200 iterations and the graph plotted of drag giving the value of drag force, respectively.

Figures 7 and 8 are the graphs displaying the drag force acting on the conventional and modified design of the driver's cab, respectively.

As analysis results were studied, it can be plainly stated that the modified designs of container and driver's cab have less drag force acting on them in comparison to the conventional designs of both, respectively, which can further increase the fuel efficiency as presented in the study of state buses done by Ganga Singh and Vinod Kumar.



**Fig. 2** Modified design of container



**Fig. 3** Conventional design of driver's cab

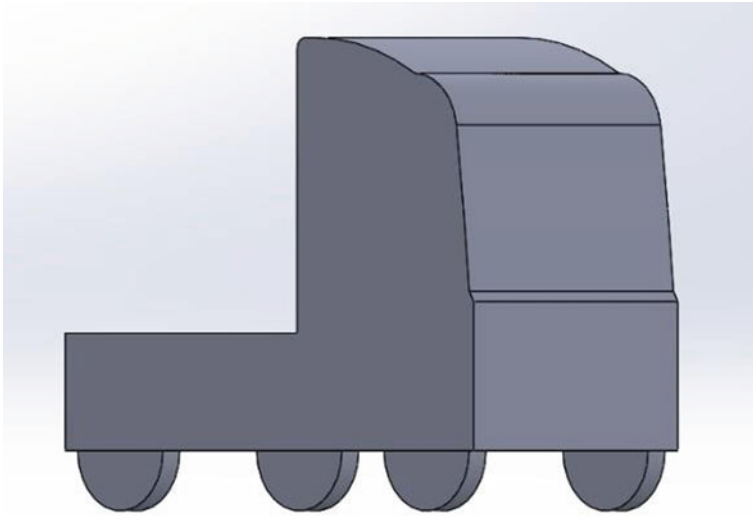


Fig. 4 Modified design of driver’s cab

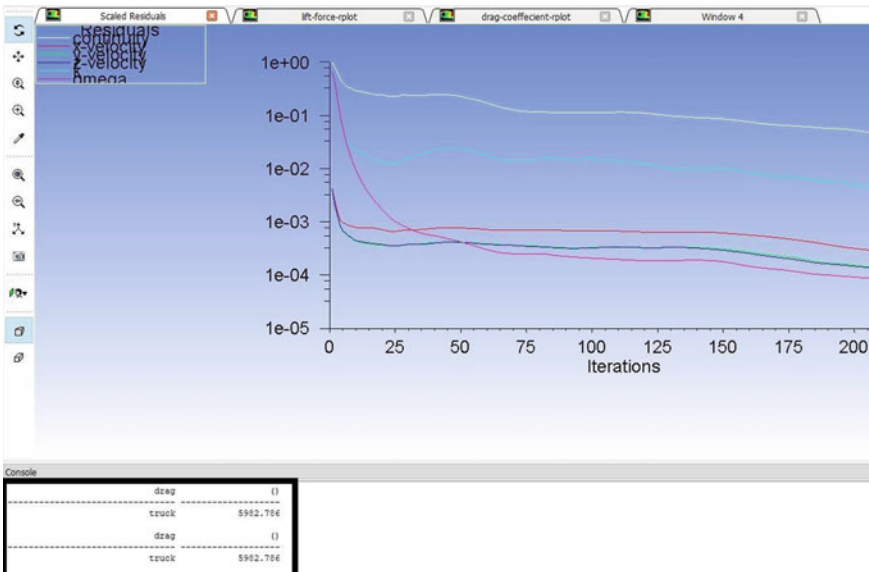


Fig. 5 Drag force graph on the conventional container

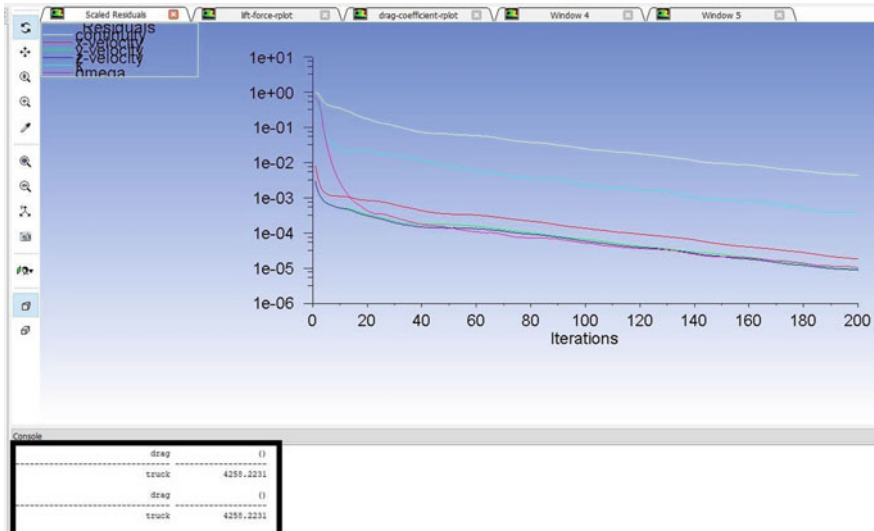


Fig. 6 Drag force graph of the modified container

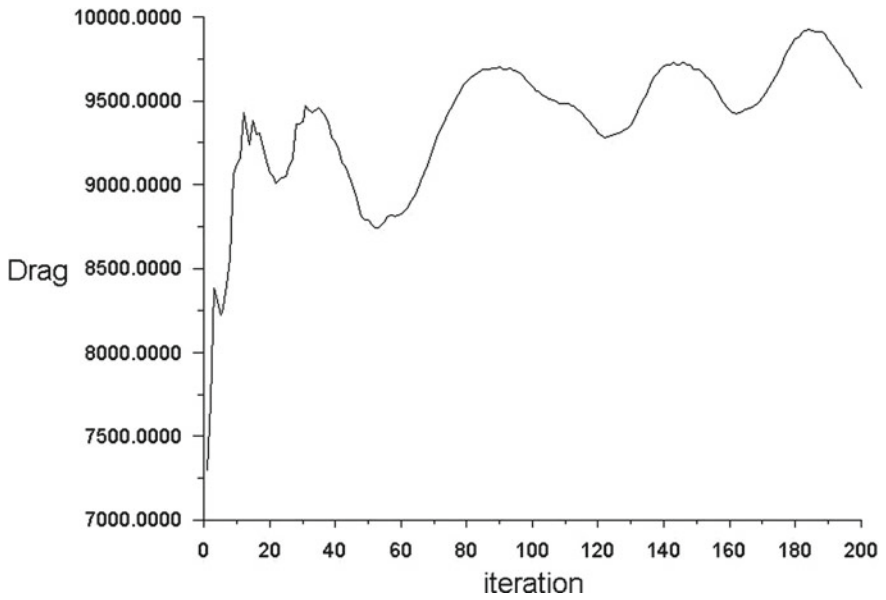
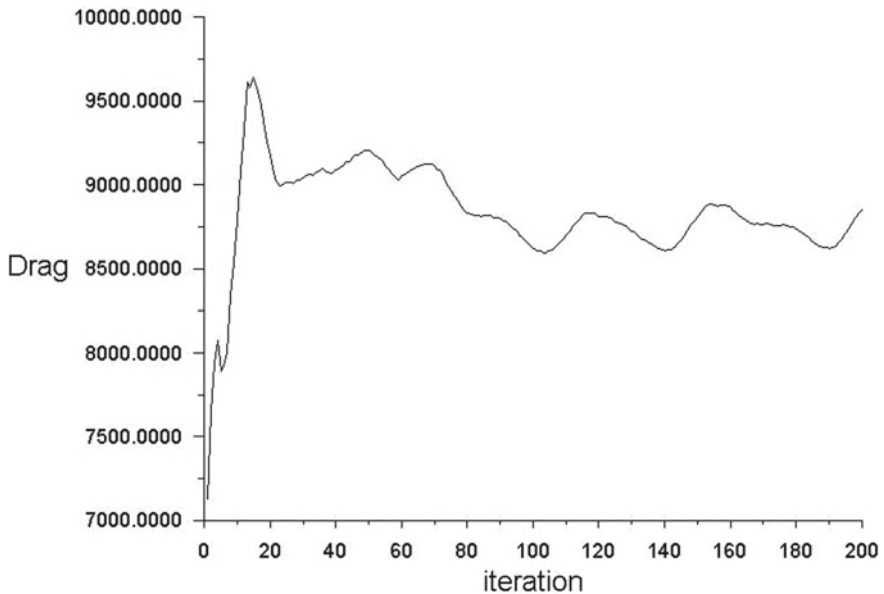


Fig. 7 Drag force of conventional driver's cab



**Fig. 8** Drag force of modified driver's cab

## 4 Conclusion

Taking the conventional model of Tata 3118 and modifying it in SolidWorks in such a way that affects its aerodynamics analysis of both has been done in Ansys Fluent and the results have been compared and conclusions are as follows:

Drag is reduced by outer contour modifications of giving a boat like ending by providing curve in the rear upper part from 5982.786 on the conventional container to 4258.223 on the modified container and in the case of the driver's cab, it was reduced from 9582.668 on conventional driver's cab to 8850.428 on modified driver's cab by giving a curved spoiler at the head of the driver's cab. Reduction in the drag force further leads to an increase in fuel efficiency by providing better stability to the heavy vehicles at operational speeds and cutting down the time and cost of freight transportation from one place to another.

## References

1. Drollinger RA (1987) Heavy duty truck aerodynamics. SAE Tech Pap. <https://doi.org/10.4271/870001>
2. Kanekar S, Thakre P, Rajkumar E (2017) Aerodynamic study of state transport bus using computational fluid dynamics. IOP Conf Ser Mater Sci Eng 263(6): 0–9. <https://doi.org/10.1088/1757-899X/263/6/062052>

3. Patidar A, Gupta U, Bansal A (2015) Fuel efficiency improvement of commercial vehicle by investigating drag resistance. SAE Tech Pap 2015. <https://doi.org/10.4271/2015-01-2893>
4. Hirz M (2011) Environmental impact of aerodynamic optimizations at heavy duty commercial vehicles. EAEC European automotive congress
5. Akash M, Kumar B, Rana P (2018) Int J Adv Eng Res Dev 5(3): 434–439. ISSN 2348-4470
6. Thorat S, Rao GAP (2011) Computational analysis of intercity bus with improved aesthetics and aerodynamic performance on Indian roads. Int J Adv Eng Technol II(III):103–109. Available: <http://www.technicaljournalonline.com/ijeat/VOLII/IJAETVOLIIISSUEIIIJULYSEPTEMBER2011/ARTICLE20IJAETVOLIIISSUEIIIJULYSEPT2011.pdf>
7. Bayraktar I (2002) External aerodynamics of heavy ground vehicles: computations and wind tunnel testing. ProQuest dissertations & theses, p 114. <https://doi.org/10.25777/tgte-np27>
8. Lanfrat M (2005) Best practice guidelines for handling automotive external aerodynamics with FLUENT. FLUENT 2:1–14
9. Ali IS, Mahmood AA (2013) Improvement of aerodynamics characteristic of heavy trucks. In: 3rd international conference on trends in mechanical and industrial engineering, vol 7, no 3, pp 246–255. Available: <http://escholarship.org/uc/item/63g6128j%5Cnpapers2://publication/uuid/55EF5EBD-7CB1-4E84-9889-EDAA3B6E65AD%0Ahttps://e-reports-ext.llnl.gov/pdf/741852.pdf>
10. Roy V, Kumar TS, Kumar RA, Jeeva S, Kumar VV (2018) Aerodynamic design improvement for an intercity bus
11. Chowdhury H, Moria H, Ali A, Khan I, Alam F, Watkins S (2013) A study on aerodynamic drag of a semi-trailer truck. Procedia Eng 56:201–205. <https://doi.org/10.1016/j.proeng.2013.03.108>
12. Khosravi M, Mosaddeghi F, Oveisi M, Khodayari-b A (2015) Aerodynamic drag reduction of heavy vehicles using append devices by CFD analysis. J Cent South Univ 22(12):4645–4652. <https://doi.org/10.1007/s11771-015-3015-7>
13. Mohamed-Kassim Z, Filippone A (2010) Fuel savings on a heavy vehicle via aerodynamic drag reduction. Transp Res Part D Transp Environ 15(5):275–284. <https://doi.org/10.1016/j.trd.2010.02.010>
14. Kim J, Lee S, Kim M, You D, Lee SJ (2017) Salient drag reduction of a heavy vehicle using modified cab-roof fairings. J. Wind Eng Ind Aerodyn 164:138–151. <https://doi.org/10.1016/j.jweia.2017.02.015>
15. Kim J, Kim J, Hann T, Kim D, Roh HS, Lee SJ (2019) Considerable drag reduction and fuel saving of a tractor–trailer using additive aerodynamic devices. J Wind Eng Ind Aerodyn 191(May):54–62. <https://doi.org/10.1016/j.jweia.2019.05.017>
16. Kumar RB, Nitesh Varshan M, Kannan T (2019) Aerodynamic design optimization of an automobile car using computational fluid dynamics approach. Aust J Mech Eng 1–7. <https://doi.org/10.1080/14484846.2019.1654963>
17. Raman A, Hari RH (2016) Methods for reducing aerodynamic drag in vehicles and thus acquiring fuel economy. J Adv Eng Res 3(1):26– 32. Available: [www.jaeronline.com](http://www.jaeronline.com)
18. Abinesh J, Arankumar J (2014) CFD analysis of aerodynamic drag reduction and improve fuel economy. Int J Mech Eng Robot Res 3(4):430–440

# Design, Fabrication and Cost Analysis of Tri-Star Wheel Stair Climber Trolley Load Carrier on Indian Road Context



Rakshit Varshney, Yash Modi, Shrikant Vidya, and Kuldeep Narwat

## 1 Introduction

Carrying weights or loads like food grains, books and so on to keep from the ground, or even patients to move upper level from the ground isn't simple work, particularly where there are no lifting offices (lift, transport and so on) Moreover, in a large portion of the structures on the planet doesn't have lifts or elevators as discussed by Nortan et al. [1]. For this situation, human works are viewed as a solitary arrangement. Work is getting expensive just as tedious in the created nations, where the development rate is decreasing. According to a journal by Sajay et al. [2], this can be made simple by making something that can carry loads over the steps without involving a lot of effort. This load carrier explained in this paper will do the same. Most amount of structures and buildings have small lifts which cannot be used for transporting loads as well as carrying people at the same time, therefore, this step climbing hand trolley can help out in transporting weights/loads using stairs without using a lot of effort in short statues similar to libraries, emergency clinics, etc. The device that can transport heavy loads from one place to the other regardless of the loads to be carried over steps, flat surfaces, rough surfaces is called steps climbing trolley.

Raundal et al. [3] and Subhasis et al. [4] investigated different trial work done in the field of planning and assembling of tri-wheel load carriers that can be used over the stairs with less effort in contrast to travel physically. The most important issues to be taken care of in this are stability and pace of the load carrier during carrying loads on the steps, whereas the height of the stairs will be a significant issue during this project. This device would be generally used to lift heavy commodities that are generally like carrying books in a library, medical equipments in an emergency hospital/clinic, any general commodity used in any organization, or carrying any harmful material for ventures as well as offer opportunity to the impeded individual

---

R. Varshney · Y. Modi · S. Vidya (✉) · K. Narwat  
Department of Mechanical Engineering, Galgotias University, Uttar Pradesh, Noida, India

or disabled peoples to move anyplace irrelevant to going over the stairs. This device has a design involving four wheels to help carry the weights when being used on the stairs.

Problem faced by Murray et al. [5] was understood that it would fit for conveying a hefty burden without enduring any mishappening or nearby breaks in the event that it would go into true creation at an ideal scale. Despite the fact that the underlying expense of the venture appeared to be higher, however, more precise assembling would abbreviate this. There were more than 1,000,000 individuals who are unable to lift heavy loads on their own without any help physically and this count is increasing day by day in this quickly maturing society, and later or sooner, due to the unavailability of helpers, there would be a requirement for robots to carry weights for disabled and elderly people.

According to a study by Rajkumar [6] an electric and manual trolley like this would minimum cost Rs. 15,000 and Rs. 5500, respectively, and our goal was to make an economic chair that can be used by people having not a lot of money to spend on these, and thus to make a trolley when produced in bulk would lie under this budget criteria. According to the Jawaharlal Cards Institute study [7] and Bruno et al. [8], there are numerous issues that should be settled. The most significant and troublesome matter in planning these robots is the manner by which to make the debilitated and older individuals who use robots in their everyday life agreeable. What's more, numerous specialized issues should likewise be addressed. Mabuchi et al. [9] reviewed various experimental work carried out in the field of designing and manufacturing a stair-climbing mobile robot with legs and wheels. In this, there are a pair of legs at the end of the robot in which there are two degrees of freedom in each pair of legs, i.e. 225 mm in the horizontal direction and 135 mm in the vertical direction. The robot assembly contains legs and feet. To prevent from slipping, the robot uses push and pull forces to go up or downstairs and in the upcoming time, a robot enabled inside a wheelchair would be made for old aged or disabled people.

According to Md. Hossain et al. [10], this device can move over any surface, whereas the problem faced in designing is the speed and stabilizing it when it comes to going up the stairs. The main usage of this device would be in transporting medicines, goods in industries, books, etc., and using this device would not only decrease the efforts to carry weights, but also will result in saving a huge amount of money that would have been spent in the form of labour cost. According to Gaikwad Avinash et al. [11], the device is designed and fabricated to be used over the stairs acting over to handle materials. This device is used to travel people/wheelchairs on the stairs up and down for which it is difficult to do so. It is an electric device that uses a DC motor which can be used to run in forward as well as backward direction depending on the polarity of the supply manoeuvred using switches and buttons, a gear mechanism, rope drive and a set of rails to be used as sliding chairs. According to Roshan Alaspure et al. [12], the main aim of the project is a stair climbing Mechanism for load carriers with decreasing efforts. Doing better work with fewer efforts has been the main objective of humans in any field. The modified wheels are designed such that it climbs stairs easily.



## 2 Methodologies

- Selection of Material
- Parameter: Designing, Dimension, Wheel diameters, Size of frames, Fabrication
- Process Used: Plasma Arc Cutting, Arc/Gas Welding, Pipe welding
- Material Selection: Material choice is a stage during the time spent planning any actual article. With regards to the item plan, the principal objective of material choice is to limit cost while meeting item execution objectives. The selection of the material should be done taking care of the competing materials and their properties.

Mild-Steel: It is also known to be plain carbon steel and also the most used kind of steel because comparatively to iron mild-steel being less expensive with properties that are sufficient to fulfil the requirement. Low-carbon steel is flexible and pliable as it has roughly 0.05–0.3% of carbon. Mild steel is most preferred when required in bulk.

Rubber Wheel: Tyres are made of rubbers using silica or carbon black having treads and body. Part of tyre that interacts with road is tread on the other hand at a given moment the part that interacts with road is contact. Treads frequently intend interacting with explicit item promoting positions.

Wheel Frame: To hold the wheels to the shaft, a new and different design is required. According to a journal by Md. Nafees et al. [13], power transmitted in a mono or di-wheeled load carrier isn't successful in moving on the steps because of the structure of the steps. The plan of the straight wheel frame turned out to be more convoluted and should have been altered with its bent circular design to move properly which generates more friction concluding us to use the tri-wheel design of wheels attached at the ends of the frame resulting in flawless movement of the trolley on flat as well as step surfaces. Frame arrangement is reasonable to send a definite speed ratio. It gave higher efficiency and smaller design with dependable assistance. Simpler support was conceivable if there should arise an occurrence of supplanting any deficient parts like nut, bolt and so on.

Straight wheel frames have been used due to ease in building and strength benefits (Fig. 1).

## 3 Processes Involved in Fabrication

- Arc welding: In this process, the electric supply (maybe DC power supply or AC power supply) is used to generate heat between the electrode/filler and the workpiece due to which the semi/fully consumable filler melts and fills the gap between the pieces resulting in joining the workpieces together. Generally, the welded area is enclosed by an idle/semi-idle gas emitted during melting of filler for some time to ensure no environmental gas reacts with the welded area, and in this way, we use the method of Arc-Welding to join metal pieces together.

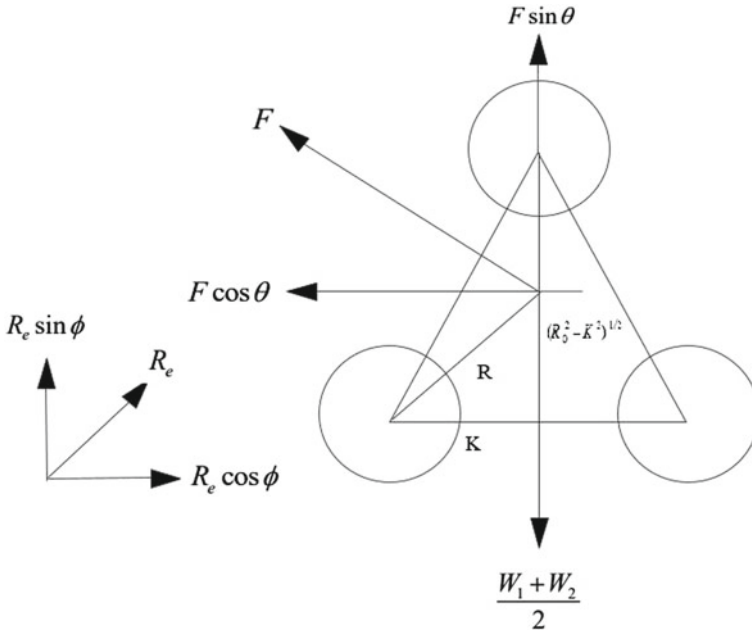


Fig. 1 Tri-star wheel force analysis

- **Welding:** It is the process of joining metal or thermoplastic by melting and adding filler in the gap resulting in the fusion of two or more pieces together. The joint becomes strong as it cools. This method of joining metal pieces is widely used because of its ease, economic as well as strong results. Welding is in contrast with the processes like brazing or soldering.
- **Pipe Bending:** This is a process in which a pipe is stacked in a pipe bending machine that holds the pipe between the dies. There are two dies—the forming die and the clipping block and the pipe is held by two other dies that are pressing and the forming die. These dies hold the pipe and insert pressure to bend the pipe in the desired shape.
- **Plasma Arc Cutting:** It is a process that uses plasma light to cut metals of different dimensions and shapes. In this, an inert gas is blown from a torch and simultaneously an electric arc is being supplied at that nozzle of the gas and when it comes in contact with the gas, it generates plasmas that are hot enough to melt the material and cut it into two pieces and from the molten metal is blown by the fast speed of movement of the plasma.

## 4 Problems Faced in Daily Life and Solutions

### DOMESTIC.

- Carrying domestic load
- Carrying heavy gunny bags.

### INDUSTRIES:

- Lifting of cartons.
- Lifting of bricks.

### Solutions.

After analyzing daily problems faced by different sites, i.e. labour at construction sites, domestic work, industrial level, commercial sectors, wholesale market, etc. We decided to build a TRI-STAR WHEEL TROLLEY that can solve the problems mentioned above (Fig. 2) (Tables 1 and 2):

- For carrying load upstairs, it will shift the load from labour's backbone to their forearms.
- At construction sites, it can be used to carry bricks and heavy gunny bags.
- In industries, it can be used to carry loads from one place to another.
- It is simple to construct and economical in usage.
- It is eco-friendly.
- It reduces the labour cost.

## 5 Conclusions

In spite of the fact that this had some constraint in regards to the strength and work of design, it very well may be viewed as a little step forward, to the extent that step climbing devices are associated. While in the process of this project, it was understood that this was not a bad plan for conveying a substantial burden up the steps. This project will be very much acclaimed if marketed to suit the industrial requirements, whereas the initial cost of setting up the production would be high, but if done with precision, then the bulk production would compensate the set up cost easily. And when it comes to commercial aspects of this product, if produced accurately, then the demand of this product would be way more than expected to be. Moreover, there are not many competitors for this product out in our market that would lead to an advantage for us as well.



**Fig. 2** Images of physical model

**Table 1** Parameters for Dimensional analysis

Design	Parameter values (cm)
Frame height	135
Frame width	45
Handle length	14
Support pipe length	35/45
Pipe diameter	2
Wheel diameter	9
Wheel frame comb length	14
Sheet length	28
Sheet width	45
Sheet thickness	0.3
Shaft length	13

**Table 2** Cost estimation table

Item	Quantity	Price
Wheels	6	$280 \times 6 = 1680$
Pipe	2(20 feet)	$680 \times 2 = 1360$
Plate	1	600
Shaft	2	450
Nut & bolts	2	120
Welding (per joint)	9	$30 \times 20 = 600$
Turning & facing	14	200
Cutting	28	500

## References

1. Norton RL, Wang SSL (2004) Design of machinery: an introduction to the synthesis and analysis of mechanisms and machines. McGraw-Hill Higher Education
2. Muthanna AV, Sajay Krishnan M, Nasruddin PN, Pavan Kumar M (2017) Analysis of tri-star frame in stair climbing hand truck. Int J Eng Sci Comput 7(4): 6444–6449
3. Raundal APV, Galande A, Devkar R, Jiman P, Pathare B (2018) Design and manufacturing of stair climbing trolley. Int J Adv Res Sci Eng 7(3):402–414
4. Shriwaskar AS, Choudhary SK (2003) Stair climbing mechanism. Thesis, Dr B R Ambedkar National Institute of Technology, Jalandhar
5. Lawn MJ, Ishimatsu T (2003) Modeling of a stair-climbing wheelchair mechanism with high single step capability. Trans Neural Syst Rehab Eng 11(3)
6. Rajkumar R, Pranavkarthik KP, Prashanth R (2013) Design and fabrication of staircase climbing wheelchair. International Journal of Mechanical Engineering and Robotics Research 2(2)
7. Gaikwad Avinash, Bhalerao Sachin (2013), “Design and Finite Element Analysis of a Stair-Case Material Handling System”, International Journal of Scientific Engineering and Research (IJSER), Volume 1 Issue 1.
8. Isabelle Laffont, Bruno Guillon, Christophe Fermanian, Sophie Pouillot, Alexia Even-Schneider, François Boyer, Maria Ruquet, Philippe Aegerter, OlivierDizien and Frédéric Lofaso

- (2008), "Evaluation of a Stair-Climbing Power Wheelchair in 25 People with Tetraplegia", *Arch. Phys. Med. Rehabil.*, Vol. 89, October.
9. Murray J Lawn and Takakazu Ishimatsu (2003), Modeling of a stair-climbing wheelchair mechanism with high single step capability, *Transactions on neural systems and rehabilitation engineering*, vol. 11, no. 3
  10. Md. A. Hossain, Mafia A. Chowdhury, Shamiuzzaman Akhtar, 2010, " Design and Manufacturing of a Stair Climbing Vehicle", Department of Mechanical Engineering, MIST, Dhaka-1216, Bangladesh. International Conference on Industrial Engineering and Operations Management Dhaka, Bangladesh
  11. Habib HK (2007) Bioinspiration and robotics walking and climbing robots
  12. Alaspure R, Barmase C, Chambhare S, Mandhre M, Joshi YG (2016) Fabrication of stair climbing wheel mechanism: alternate for lifting goods. *Int Res J Eng Technol (IRJET)*, 3(5)
  13. Chowdhury MA, Linda RI, Akhtar S (2010) Design and manufacturing of a stair climbing vehicle. In: International conference on industrial engineering and operations management Dhaka, Bangladesh

# Longitudinal Speed Control of Electric Vehicle to Reduce Road Speed Limit Violations



Ritanshu Tiwari and A. R. Kulkarni

## 1 Introduction

With the increasing number of vehicles on road, the problem related to road accidents, traffic jam, pollution, and road speed limit violations has become the major concerns in the field of transportation. Considering the limited fuel resources, the electric vehicle (EV) is certainly the new era of transportation and it has proven an alternative for vehicles with combustion engine further reducing their impact on environment.

But one of the major concerns is speed limit violation and in case of EV it can be more prominent as the power delivery in EV is almost instantaneous as compared to non-EV and in very short period the speed of the vehicle can cross the road speed limit. Thus, speed control is necessary to reduce road speed limit violations. Linghui Xu et al. [1] presented speed control of EV using Adaptive Fuzzy PID controller by controlling the armature voltage of the separately excited DC motor (driver system). Anil Kumar Yadav et al. [2] presented an approach for optimal speed control of hybrid EV through various control techniques like PID, Observer-based controller, Linear quadratic regulator [3, 4], Pole placement technique, to maintain a speed according to reference speed. The control techniques like model predictive control [5, 6], motion control through deep learning [7], and adaptive control [8] have been used to control the longitudinal motion of vehicle.

The motive of this paper is to present a comparative study between PI [9, 10], Scheduled PI, and Predictive speed tracking controller implemented through longitudinal driver block in MATLAB Simulink. The motor driving system consists of a PWM controlled voltage block, H-bridge to drive the motor according to the PWM input, and a DC motor which further drives the kinetic model of the vehicle.

---

R. Tiwari (✉) · A. R. Kulkarni  
EE Department, DTU, Delhi 110042, India

The remainder of this paper has the following sections: Sect. 2 includes system model description. Section 3 includes the result and simulations. Section 4 ends the paper with conclusion.

## 2 System Model Description

### 2.1 Longitudinal Dynamic Model

The forward motion dynamics based on Newton’s second law describes the longitudinal dynamic model [11–13] of the vehicle as

$$m\ddot{x} = F_{xr} - F_{aero} - R_{xf} - R_{xr} - mg \sin \alpha \tag{1}$$

Since it is assumed that the vehicle is running over a flat road with no inclinations,  $\alpha = 0$ .

$$m\ddot{x} = F_{xr} - F_{aero} - R_{xf} - R_{xr} \tag{2}$$

where  $m\ddot{x} = F_{xr} - F_{aero} - R_{xf} - R_{xr}$ .

Considering real wheel drive  $F_{xr}$  is traction force,  $F_{aero}$  is aerodynamic drag experienced by vehicle,  $R_{xf}$  and  $R_{xr}$  are rolling resistances of front and rear wheels.

Wheels are modeled using Tire (magic formula) in MATLAB (Table 1).

**Table 1** Parameters for vehicle model

Parameters	Values	Units
Mass of vehicle	1000	Kg
No. of wheels per axle	2	–
Frontal area(A)	3.0	m <sup>2</sup>
Rolling resistance (constant coefficient)	0.015	–
Air Density( $\rho$ )	1.18	Kgm <sup>-3</sup>
Rolling radius of wheel	0.3	m
Drag coefficient( $C_a$ )	0.4	–
Magic formula coefficient [B,C,D,E]	[10, 1.9, 1, 0.97]	–



## 2.2 Controller Model

The controller is modeled using longitudinal driver block which is implemented as a speed tracking controller, and it also represents the dynamic behavior of the driver. The techniques used for controlling the speed limit of vehicle through longitudinal driver block are explained below:

- (A) PI controller with anti-tracking windup with feedforward gain is used to track the reference speed.

$$y = \frac{k_{ff}}{v_{nom}} V_{ref} + \frac{k_p}{v_{nom}} e_{ref} + \int \left( \frac{k_i}{v_{nom}} e_{ref} + k_{aw} e_{out} \right) dt \quad (3)$$

where velocity feedforward  $k_{ff} = 0.05$ ,  $k_p = 15$ ,  $k_i = 1$ , anti-windup gain  $k_{aw} = .1$ , nominal velocity  $v_{nom} = 100$  km/hr

- (B) Scheduled PI with anti-tracking windup with feedforward gain as a function of velocity is used.

$$y = \frac{k_{ff}(v)}{v_{nom}} V_{ref} + \frac{k_p(v)}{v_{nom}} e_{ref} + \int \left( \frac{k_i(v)}{v_{nom}} e_{ref} + k_{aw} e_{out} \right) e_{ref} dt \quad (4)$$

where velocity gain breakpoints = [0 100], velocity feedforward gains  $k_{ff} = [-1 \ .1]$ ,  $k_p = [10 \ 10]$ , Integral gain values  $k_i = [5, 5]$ , nominal velocity  $v_{nom} = 100$  km/hr, anti-windup gain  $k_{aw} = 0.1$

Also, velocity error  $e_{ref}$  is given by

$$e_{ref} = v_{ref} - v \quad (5)$$

Difference between saturated and nominal control output  $e_{out}$  is described as

$$e_{out} = y_{sat} - y \quad (6)$$

where  $y_{sat}$  is described as

$$y_{sat} = \begin{cases} -1 & y < -1 \\ y - 1 & -1 \leq y \leq 1 \\ 1 & y > 1 \end{cases} \quad (7)$$

The braking and acceleration commands are generated using below equations:

$$y_{acc} = \begin{cases} 0 & y_{sat} < 0 \\ y_{sat} & 0 \leq y_{sat} \leq 1 \\ 1 & y_{sat} > 1 \end{cases} \quad (8)$$

$$y_{dec} = \begin{cases} 0 & y_{sat} > 0 \\ -y_{sat} & -1 \leq y_{sat} \leq 0 \\ 1 & y_{sat} < -1 \end{cases} \quad (9)$$

- (c) In Predictive speed tracking control, an optimal single point preview look ahead model (developed by C.C. MacAdam) is implemented using the dynamics as a linear single track (bicycle) vehicle. This model diminishes the previewed error signal at a single point  $T^*$  seconds ahead in time.

For longitudinal motion, the linear dynamics implemented are described by the following equations:

$$x_1 = v \quad (10)$$

$$\dot{x}_1 = x_2 = \frac{k_{pt}}{m} - g \sin(\gamma) + f_r x_1 \quad (11)$$

where  $F_r$  is rolling resistance,  $m$  mass of vehicle,  $x$  is predicted velocity state vector,  $k_{pt}$  is tractive force, and brake limit,  $v$  is longitudinal velocity,  $\gamma$  is grade angle which is assumed to be zero in this paper.

To determine the preview time window, the relation is given below

$$T^* = \frac{L}{v} \quad (12)$$

Here, preview distance ( $L$ ) is 2 m by default in predicting control of longitudinal driver block.

### 2.3 Motor Driver System

Motor driver system includes DC motor of permanent magnet field type. The controlling mechanism mentioned above in the longitudinal controller generates acceleration/deceleration in range 0 to 1 normalized value after comparing the reference velocity and vehicle velocity. Then, the signal passes through controlled voltage source which generates a voltage signal proportional to the input signal.

The output voltage from the controlled voltage source is fed as an input to the controlled PWM generation block which in turn generates a PWM [14] voltage signal. The lower value is set to 0 and higher value is set to 1 of this PWM signal and is fed to H-bridge circuit. The output of the H-bridge is the required controlled

voltage which is used to control the motor speed. Then the controlled output of motor is converted into longitudinal motion of the vehicle by using kinetic model of the vehicle.

### 3 Simulation and Results

For selecting the input reference speed, in this paper a route from DTU (Delhi Technological University) to Indira Gandhi International Airport is chosen from google maps. The route consists of four zones and each zone has its own speed limit. The zone length is selected based on road length, speed limit on that road, and simulation time. The simulation time is set to 2000s (Figs. 1 and 2).

Figures 3, 4, and 5 show the response of PI, scheduled PI, and predictive speed tracking controller. It is observed that the best response is obtained using the Predictive speed tracking controller as there is no overshoot in its response because of its previewed time window which allows it to minimize the error. For tuning of parameter in PI and scheduled PI, hit-and-trial method is used. The response of scheduled

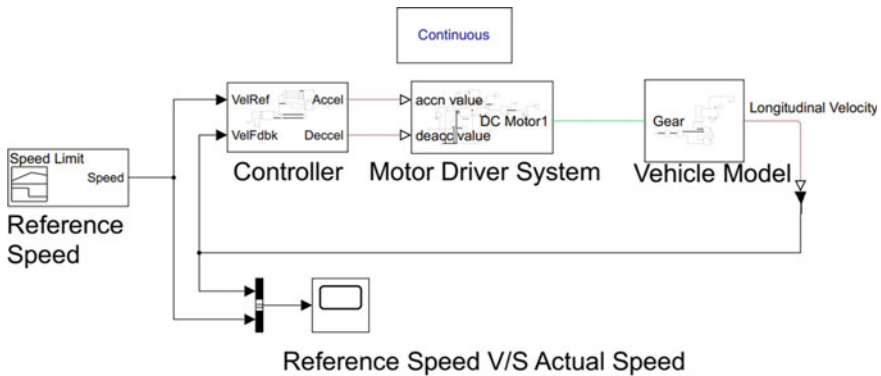


Fig. 1 Simulink model for longitudinal speed control



Fig. 2 Selected route from google maps defining each zone with respective road length in km

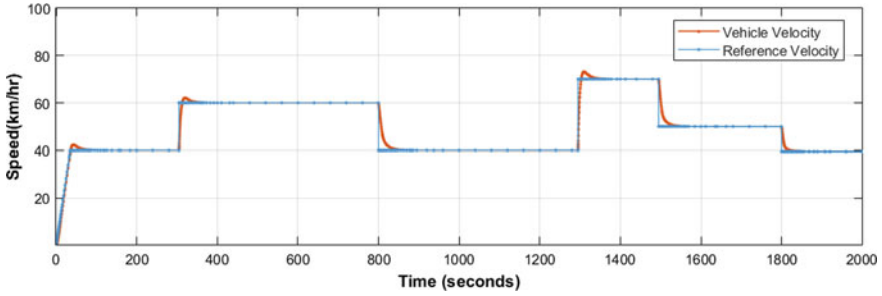


Fig. 3 Vehicle response with PI controller

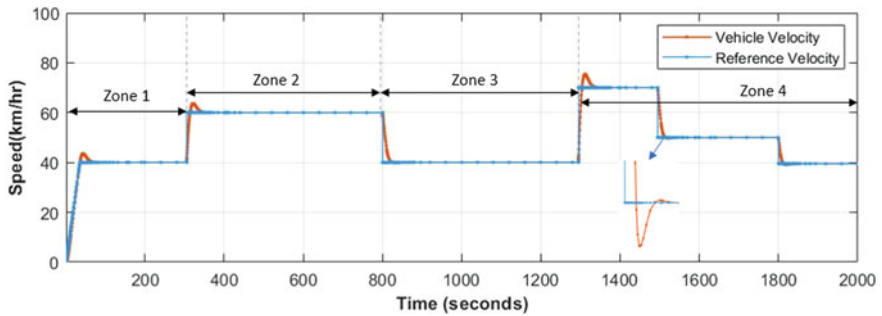


Fig. 4 Vehicle response with scheduled PI controller

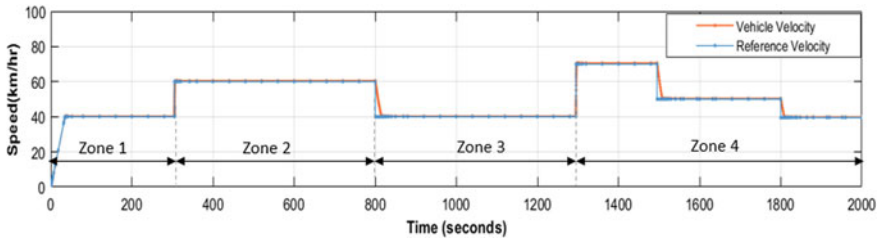


Fig. 5 Vehicle response with predictive speed tracking controller

PI contains more oscillations than that of PI control and it has more overshoot than any of the response because the feedforward gain in scheduled PI controller is the function of vehicle velocity. So, any abrupt change in velocity causes more overshoot and oscillations.

Figures 6, 7, and 8 represent the acceleration and deceleration command generated by the PI, scheduled PI, and Predictive speed tracking controller. The acceleration and deceleration values are the normalized value between 0 to 1. The first acceleration value is generated at 0 s and then it continues with the same value till 300 s where the speed limit changes. Similarly, the first deceleration value is observed at 800 s where

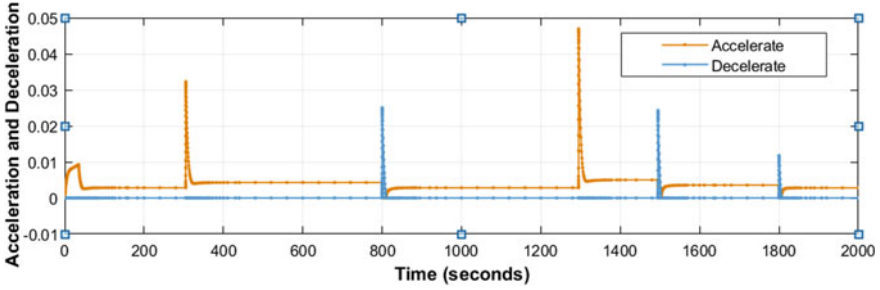


Fig. 6 Acceleration and deceleration response with PI controller

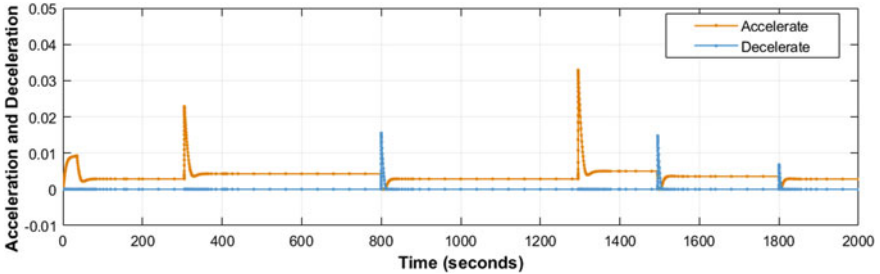


Fig. 7 Acceleration and deceleration response with scheduled PI controller

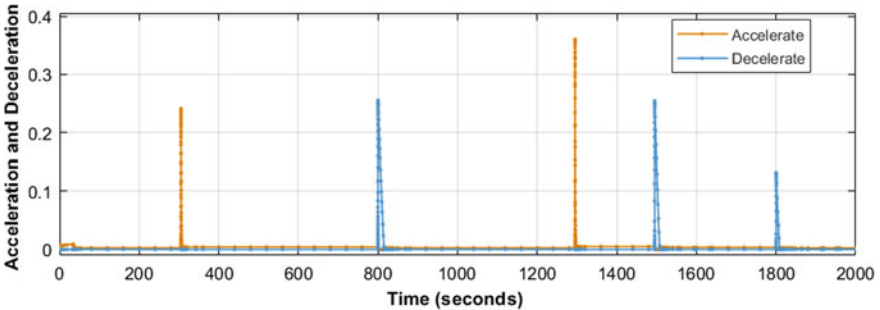


Fig. 8 Acceleration and deceleration response with Predictive speed tracking controller

a sudden decline in speed is observed. The value of acceleration and deceleration is much higher in predictive control as compared to PI and scheduled PI. Thus, the predictive control can track the speed more comprehensively than the other two controllers.

## 4 Conclusion

A comparative analysis of the controllers, namely PI, scheduled PI, and Predictive speed tracking controller for the longitudinal speed control of vehicle is performed. By observing the response of each controller, it can be concluded that the predictive speed tracking controller provides the best result among all the three controllers as there is no overshoot and settling time is much less in comparison to other two techniques. The response is also well calibrated with the reference speed limit. This model can work well with interconnected vehicle environment, i.e., infrastructure to vehicle (I2V) and vehicle to infrastructure (V2I) communication as well as with vehicle to vehicle communication (V2V).

## References

1. Xu L et al (2017) Speed control of pure electric vehicle based on adaptive fuzzy PID controller. Springer, International Symposium for Intelligent Transportation and Smart City
2. Yadav AK et al (2011) Optimal speed control of hybrid electric vehicles. *Journal of Power Electronics* 11(4):393–400
3. Prasad LB et al (2014) Optimal control of nonlinear inverted pendulum system using PID controller and LQR: performance analysis without and with disturbance input. *International Journal of Automation Computing* 11(6):661–670
4. Saeed, M. A., et al. (2016). A comparative study of controllers for optimal speed control of hybrid electric vehicle. 2016 International Conference on Intelligent Systems Engineering (ICISE), IEEE.
5. Mekala, G. K., et al. (2020). Speed Control in Longitudinal Plane of Autonomous Vehicle Using MPC. 2020 IEEE International Conference for Innovation in Technology (INOCON), IEEE.
6. Matute, J. A., et al. (2018). Longitudinal model predictive control with comfortable speed planner. 2018 IEEE International Conference on Autonomous Robot Systems and Competitions (ICARSC), IEEE.
7. Sharma, S., et al. (2019). Lateral and longitudinal motion control of autonomous vehicles using deep learning. 2019 IEEE International Conference on Electro Information Technology (EIT), IEEE.
8. Xue J, Jiao X (2021) Speed cascade adaptive control for hybrid electric vehicle using electronic throttle control during car-following process. *ISA Trans* 110:328–343
9. Ando T et al (2019) Design of longitudinal controller for automated driving bus. *International Journal of Intelligent Transportation Systems Research*: 1–15.
10. Xu S et al (2018) Accurate and smooth speed control for an autonomous vehicle. 2018 IEEE Intelligent Vehicles Symposium (IV), IEEE
11. Rajamani R (2011) *Vehicle dynamics and control*, Springer Science & Business Media
12. Lekshmi S (2019) Mathematical modeling of Electric vehicles—a survey. *Control Engineering Practice* 92: 104138.
13. Hamid UZA et al (2020) Longitudinal Velocity Control Design with Error Tolerance Strategy for Autonomous Vehicle. *RITA 2018*, Springer, pp 1–11
14. Turcian D, Dolga V (2020) Intelligent speed control system for electric vehicle. In: IOP conference series: materials science and engineering, IOP Publishing.

# Design of Adaptive Wheel Driven Pipeline Inspection Robot



Ayush Kaiwart , Nikhil Dhar Dubey , Farman Naseer ,  
Ankush Verma , and Swastik Pradhan 

## 1 Introduction

Pipeline are widely used for the transportation of liquids and gases across the globe as they are one of the safest and economical way to transport them. Crude Oil, fuels, water, and natural gas are among the key materials that are being transported with the help of these pipelines. They play a very crucial for the proper working of various industries and have a significant role in the country's economy.

There is a need of timely inspection of these pipelines for inspection for various types of anomalies that have been developed during its work cycle. Anomalies like aging of pipelines, corrosion, scaling, sludge formation, cracks, dents, misalignment of joints, etc. Regular check and maintenance ensure proper working and optimal efficiency of pipelines. Deteriorated pipelines can cause leakage that can lead to material loss, environmental damage and sometimes can even lead to casualty.

Inspection of these pipelines by conventional method like visual inspection and NDT inspection method on outside periphery of these pipelines does not provide satisfactory level of inspection. Moreover, these pipelines carry toxic chemical, fluids, etc., that lead inspection quite a difficult task for a human to perform. Hence, In-pipe Inspection robot (IPIR) is now being used and is replacing human labor. They ease the process of inspection, provide safe operation and provide good results.

The IPIR robot is designed considering several parameters like type of pipeline, shape and size adaptability, maneuverability, turning radius, number of actuators, analysis of defects, task to be performed inside the pipe, autonomous operation, etc.

Pipeline Inspection Robot can be broadly classified as Out-pipe and In-pipe Inspection robots (IPIR). The Out-Pipe Inspection Robot (OPIR) as the name suggests inspects the outer periphery of the pipes. The robot clamps the outer walls

---

A. Kaiwart (✉) · N. D. Dubey · F. Naseer · A. Verma · S. Pradhan  
Department of Mechanical Engineering, Lovely Professional University, Grand Trunk Rd,  
Jalandhar, Delhi, Phagwara, Punjab 144001, India

of the pipe and move along the pipe. Whereas, the IPIR enables us to inspect the internals of the pipe. They provide information regarding corrosion level, build-up sludge, or any anomaly found inside the pipe. They prove to be very useful in case of underground pipe inspection that is not possible with an OPIR. IPIR can be further classified into six categories according to their fundamental movements.

The wheel-type robot is the most common type. Robot wheels are powered by Actuators/motors that are pressed against the pipe walls with some force to provide traction [2, 16]. The robot can have two-wheel chain [1], three-wheel chain [14], or can be of six-wheel chain [15]. They are simpler in design, efficient, and less bulky. Mostly four-bar link mechanism is incorporated for adaptable mechanism, however [2] employed Shape Memory Alloy (SMA)-based adaptable mechanism.

The next is caterpillar type robot. The Robot has tracks in place of wheels which provide greater traction force [3, 17]. Independent control of each track helps in maneuver at corners and joints [4]. However, maneuverability at corners is quite an issue for them. The use of two module helps to maneuver at joint and avoid motion singularity [18]. Electric putter in pantograph mechanism helps in real-time adjustment of track and traction force generated [19].

Pipe Inspection Gauge (PIG) is fluid-driven pipeline robots designed for single diameter of pipes. The PIG robot has its launching and receiving station. Robot moves with the help of fluid velocity and or with magnetic flux [20]. The robot is incorporated with magnetic flux leakage sensing device for non-destructive testing [6]. The robot kinematic model helped to predict the location and orientation of robot [5]. Butterfly Bypass valve helped in regulating the speed of robot inside pipeline [21]. Following the sequence comes screw type robot that propel forward with continuous rolling motion [22]. It mainly comprises two parts; one is the rotor and the other one is the stator. The wheels are in the trajectory of the rotor and have a tilt angle on which the velocity of the robot is dependent [7]. The proposed robot has three modes of locomotion to navigate through the T-branch easily. These locomotive modes are a mode for screw driving, a mode for steering, and finally a mode for rolling.

Next category is of Walking/legged type robot with multiple legs having several DOF that helps to move inside the pipe. They are bulky and involve a lot of actuators, making them a complex system. Walking type Robot has the advantage that it can step over the obstacle majorly including matter deposits, and helps ease of movement near branches and joints [8, 23, 24].

The slowest driving speed is of Inchworm type robot. Their movement resembles that of an earthworm [25, 26]. Suction cups were used as gripping tool of robot [9]. Pneumatic actuators have been used to provide motion [27–29].

Considering the above factors, we propose a new wheel type in-pipe inspection robot that has two-wheel chain. Four bar link provides adaptability to robot motion. The driving wheel servo motor is mounted on steering servo attachment enabling the robot to simultaneously drive and steer. The proposed model has good Maneuverability capability. The wheel links are located 180 degree apart providing ample space for mounting sensors and other inspection tools on the flat surface of robot. The robot can make Helical motion and 360 rotation at place in addition to translation motion.



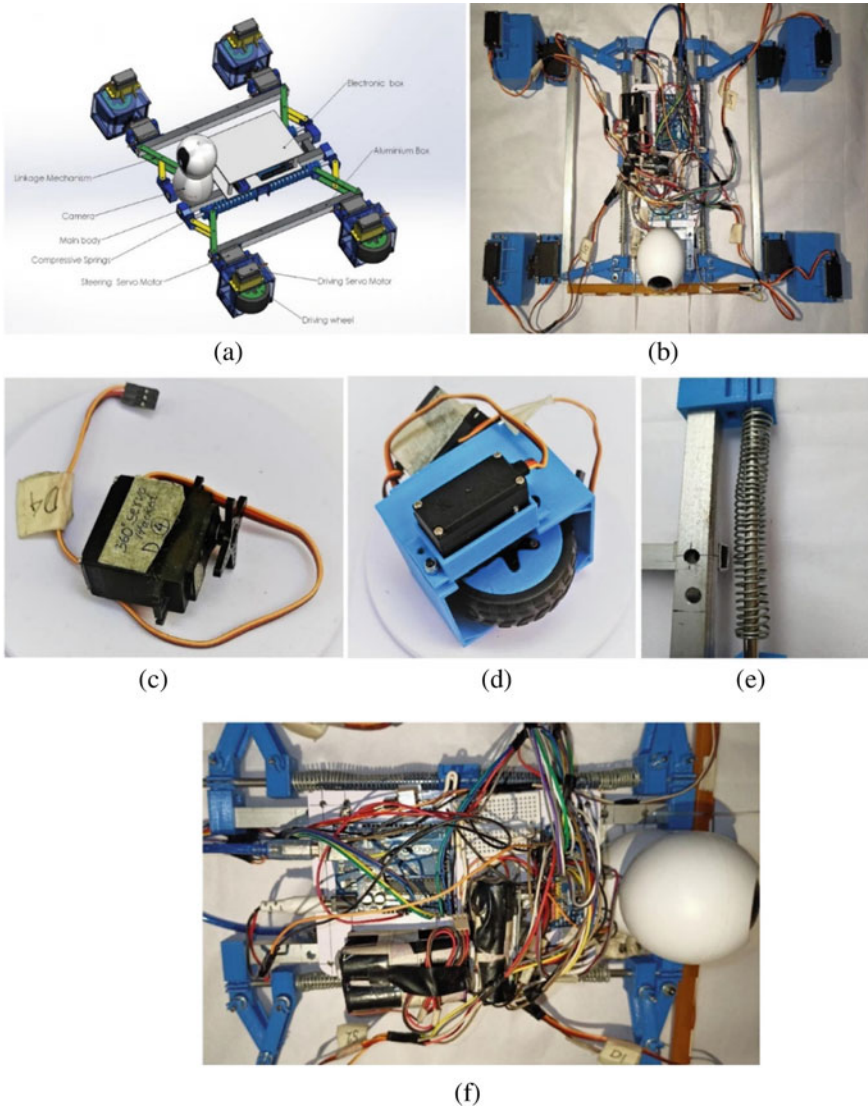
## 2 Methods and Experiments

### 2.1 Robot Characteristics

**Structure**—The Robot Hardware configuration starts with the frame. The 13 mm × 13 mm tubular aluminum frame having a 1.5 mm thickness has been used that will provide good bending stiffness and torsional rigidity. The robot comprises a two-wheel chain connected with the main body. The wheel chain mechanism is embedded with a four-bar link mechanism having a key and slider joint. This helps in the adaptation and folding mechanism of the system. There are 4 compressive springs, one for each Driving wheel. The Springs of the right size were difficult to find hence they were custom made from fencing wire. Both sides of the wheel chain can compress about 4 inches in total, providing adaptability of 4 inches to the robot. Fig. 1e. shows the compressive spring arrangement. The wheel chain comprises a four-bar link mechanism, springs, Steering and Driving servo motors as shown in Fig. 1a. The steering servo motor helps to steer the driving servo in the desired direction. The robot consists has a flat structure allowing space for mounting sensors. For steering and Driving actuators, an MG995 Metal gear servo motor has been used. They provide enough torque to drive the robot. 4 driving servos and 4 steering servos have been used. Each driving servo is mounted on the servo horn of each Steering servo motor. Special enclosure mounts have been designed for steering and driving servo. The steering servo is attached to the aluminum frame. Figure 1c, d shows the MG995 steering and driving steering servo assembly. The front part of robot has a camera that has a pan tilt ability.

**Robot Motion**—The robot needs to pass through a straight, curved, elbow, and T joints. To justify movement through these pipelines; different motion planning has been proposed. The robot has 3 types of primary movement; driving mode, Helical mode, and 360-degree Rotation mode, shown in Fig. 1a–e. In the driving mode, the robot is in linear movement, i.e., Forward and backward movement. The helical mode helps in obstacle avoidance and locating the defects correctly on the inner walls of the pipeline. The helical motion of the robot is achieved by keeping the left and right sides of the drive wheel direction at a certain steer angle. The left and right sides of steer angle need to be opposite. The robot will move then in a helical path. And finally, in 360 rotation motion helps in setting the correct position and orientation during the turning motion.

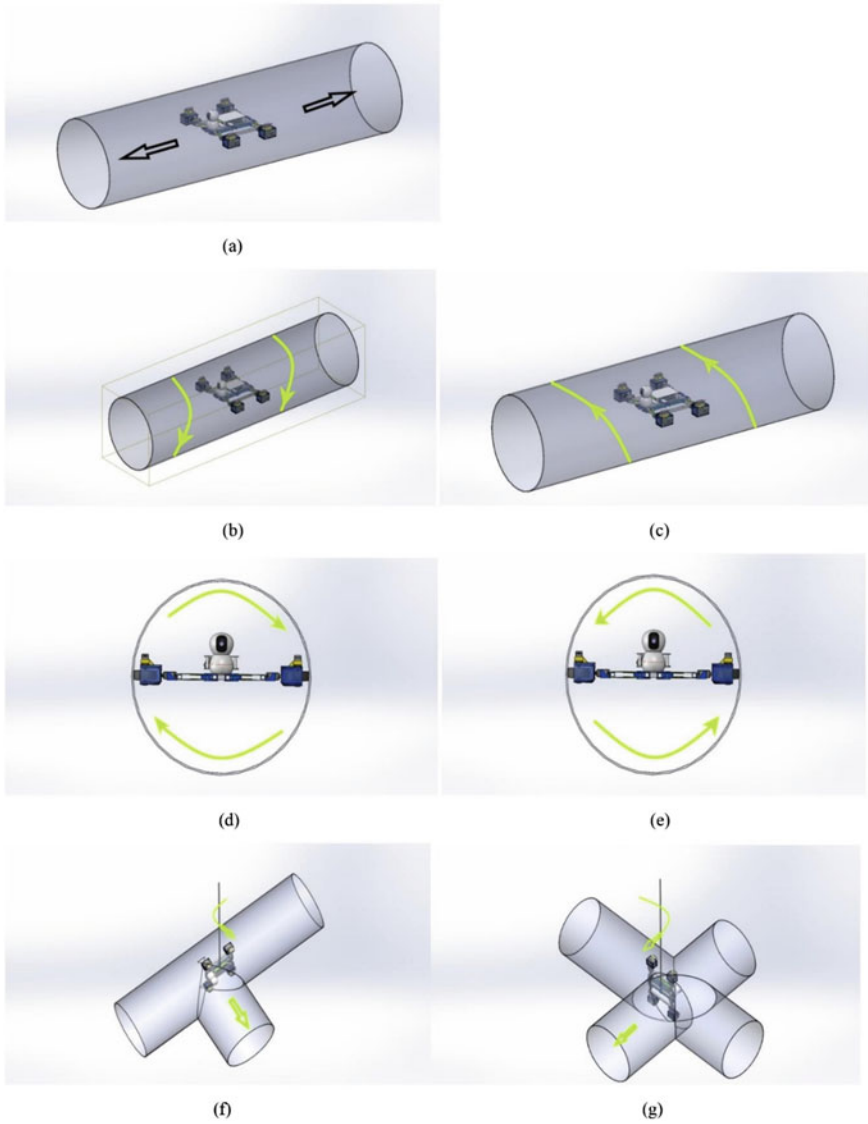
For steering at corners at the elbow joint or T-joint, the front wheels steer at the same angle in the same direction. Similarly, the rear wheels also steer to assist the robot for quick turning. It should be noted that the direction of the front and rear steer will be mirrored. The robot needs to align itself in a correct orientation before proceeding to move through the corners. Figure 2 f, g represents the position of robot during turning at corners.



**Fig. 1** Robot structure with wheel chain mechanism **a** 3d model **b** Prototype model **c** MG995 Servo **d** Steering and driving servo assembly on 3d printed Enclosure. **e** Compressive spring **f** Electronics assembly

### 2.2 Robot Mechanism

**Pipe Analysis**—The robot dimensions were made within the critical dimensions needed in the 24-inch system. The pipeline elbow joint dimension is considered according to the ASME B16.9 protocols. According to it, for long radius elbow



**Fig. 2** Three types of primary motion **a** Translational motion **b** and **c** Helical motion **d** and **e** 360-degree rotation **f** and **g** The motion at joints during left turn and right turn

joint, the elbow centerline radius is 1.5 times the nominal pipe diameter. For short radius elbow joint, elbow centerline radius is the same as its nominal pipe diameter. The short radius elbow joint of the 24-inch system is considered here for the robot system.

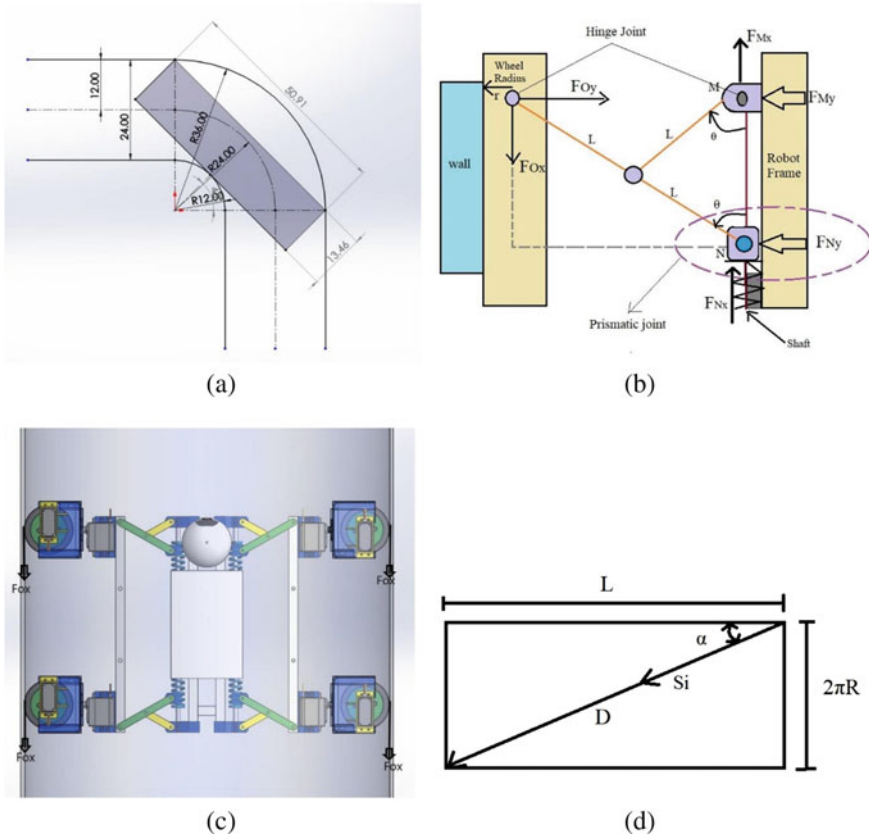
The critical length and height coming out to be 50.91 inches and 13.46 inches respectively as shown in Fig. 3(a) The robot proposed has a length of 12 inches and height of 6 inches which is well defined within the dimensions, hence it will easily pass through the elbow joint. The robot will also be able to maneuver through the Long radius elbow joint and T-joint.

**Kinematic Analysis**—Static analysis of the robot is required to get the required motor sizing and spring stiffness. From Fig. 3(b), we can see  $F_{Oy}$  and  $F_{Ox}$  represents the reaction force and traction force acting on the wheel. Applying the virtual work principle, we get  $F_{Nx}$ ;

$$\delta W = -F_{Oy} \cdot \delta y + F_{Nx} \cdot \delta x = 0 \tag{1}$$

where  $F_{Nx}$  is spring force.

The corresponding displacement of these forces are.



**Fig. 3** a Critical dimensions of robot for 24-inch pipe system b Static analysis c Traction force d The robot helical motion with steering angle  $\alpha$

$$y = 2.L.\sin(\theta) \text{ and } x = 2.L.\cos(\theta) \tag{2}$$

putting 2 in Eq. 1, we get

$$\begin{aligned} \delta W &= -F_{Oy}.\delta(2.L.\sin\theta) + F_{Nx}.\delta(2.L.\cos\theta) = 0 \\ &= -F_{Oy}.2.L.\sin\theta.\delta\theta + F_{Nx}2.L.\cos\theta.\delta\theta = 0 \end{aligned} \tag{3}$$

$$F_{Nx} = F_{Oy} \cdot \left( \frac{\cos\theta}{\sin\theta} \right)$$

On further simplification, we get.

$$F_{Nx} = F_{Oy}.\tan^{-1}\theta \tag{4}$$

This is how reaction force is related to the spring force.  
We also know that

$$F_{Nx} = k.\delta x \tag{5}$$

where k = Spring stiffness.  
 $\delta x$  = spring coil displacement.

When the robot is moving vertically upward, the total weight of the robot will be equal to the traction force generated by all three wheels of the robot. Thus each traction for  $F_{ox}$  is one-fourth the total weight of the robot as shown in Fig. 3c. The minimum torque required for each motor is given by.

$$\begin{aligned} \tau &= F_{Ox} \cdot r = \frac{W.r}{4}; \text{ r represents the radius of the wheel.} \\ \tau &= \frac{2264 \cdot 65}{4 \cdot 2} = 18,395 \text{ gm mm} = 1.8395 \text{ kg cm.} \end{aligned}$$

MG995 servo can easily generate 5–6 kg cm torque at nominal voltage. Hence, it is suitable choice.

### 2.3 Motion Dynamics

**Helical motion**—The robot moves in a straight pipeline and rotates about the z-axis with a steering angle  $\alpha$ .

The steering vector is represented by  $S_i$ .  $L$  represents the distance traveled along the z-axis, while  $D$  is the distance traveled in direction of steering vector  $S_i$  because of the steering angle  $\alpha$ .  $2\pi R$  represents the inner diameter of the pipeline as shown in Fig. 3d.

We get the relation:

$$L = D \cos\theta \text{ and } 2\pi R = D \sin\theta$$

The rotational velocity along the z-axis can be defined as.

$$\omega_x = \frac{2\pi}{t} = \frac{Vi \sin\theta}{t};$$

$D = Vi.t$ ;  $Vi$  is the velocity in the direction of steering.

$t$  = time taken by cover a particular distance.

**Rotational Motion**—The rotational motion in the straight pipeline is executed by making  $\alpha = 90$  degrees. The left and right sides of the wheel chain must have opposite steer angles. Robot will rotate on its axis and will have no translational motion. Figure 2(d) and (e) represents clockwise and anticlockwise rotation respectively.

**Turning Motion**—The angular velocity in the x-axis during turning motion at joints is given by

$$L_x = \frac{Vi}{L_w}$$

where  $L_w$  is the length from wheel to wheel.

Figure 2(f) and (g) shows robot position during turning on Left and Right sides, respectively.

## 2.4 Electronics

The electronics components are chosen that are readily available in the robotics store and which are easy to implement on the robot system. Figure 1(f) shows electronics assembly.

**Microcontroller:** Arduino Uno has been used for control of the robot.

**PCA9685 Module:** To limit the current draw and to safeguard the Arduino board, the PCA9685 module has been used. This module can drive 16 servos simultaneously over I2C with only 2 pins provided with an external power supply connection.

**Rotary Encoder:** This sensor is mounted on one axle of the driving wheel. The movement of the wheel drives the shaft of an encoder which will tell about the robot distance travel and the traveling speed of robot.

**Camera:** A surveillance camera is used for visual feedback. It transmits the visual data to the Laptop wirelessly over Wi-Fi network. The Pan and Tilt facility avails a greater Inspection. The camera is having 1080p resolution capability.

**Power Supply:** Based on the Power requirements of the above components, 18,650 Lithium-ion cells were considered as the right choice. A 2S-2P configuration (7.4 V) battery is used for powering Arduino, PCA9685 module, MG995 servos, and

integrated sensors. A separate power supply 5 V is provided for powering the camera and 3S-1P configuration(12 V) for LED Light.

## ***2.5 Software***

Initially, the CAD model of the robot was designed in Solidworks software. The Programming of the microcontroller Atmega 328P was done Arduino IDE sketch. The sensor data is displayed on Laptop PC using a wired connection with the robot. Cura Ultimaker 4.8.0 has been used for 3D printing platform, and Creality Ender 3 V2 machine has been used.

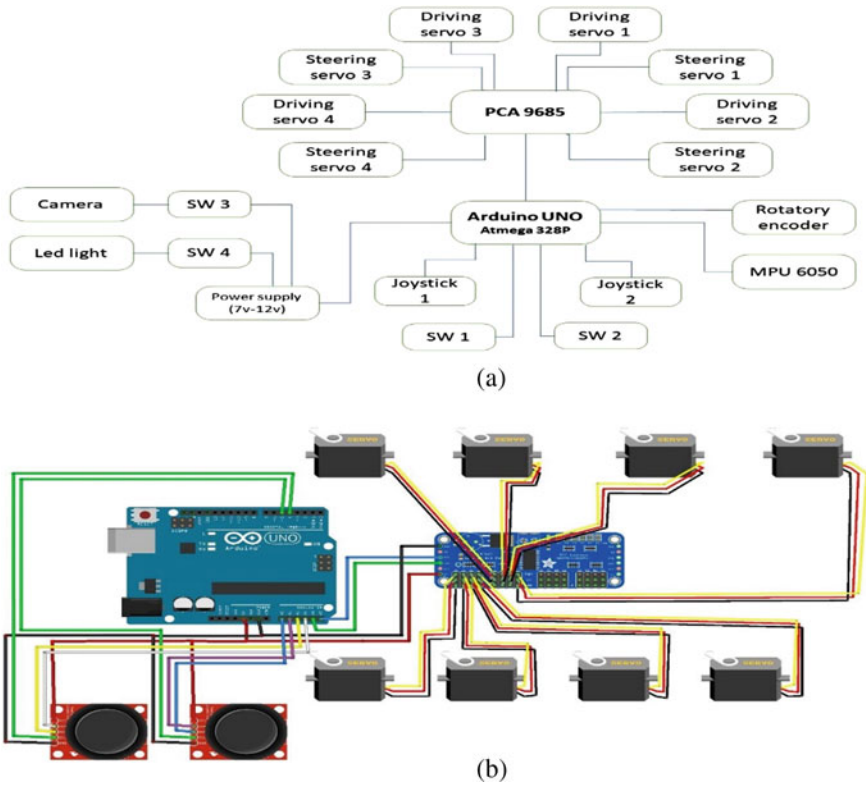
## ***2.6 Control Logic***

The control system comprises a Robot device, control circuit, joystick interface, and a PC laptop. The robot is executed by giving an Analog signal from the joystick. Results are noted down and displayed on the PC laptop screen. In this System, Arduino Uno (ATMEGA 328P) has been used as microcontroller. It calculates the servo position (driving and steering servo) value based on the Analog value received from joystick signal. The PCA9685 module is used up here to drive all the servo. The Rotary encoder code helps in distance measurement. It also calculates orientation through the MPU6050 sensor. The visual inspection is provided by using a Surveillance Camera having pan and tilt ability. The camera has a 1080p resolution that will provide good visual details. The LED lights and Cameras were controlled via the switch on controller remote to turn ON/OFF them whenever required. A lithium-ion battery is used to power the system. Figure 4(a) shows the System Flowchart.

Figure 4(b) shows Pin mapping of Servo motor with PCA9685 module start with steering servo in serial order and then for driving servo. Positive, ground, and signal wires of servo, joystick and sensor are connected accordingly. External power supply of 7.2 V is provided to PCA9685 module to power all the servo sufficiently.

## ***2.7 Experimentation***

The robot is big. Hence, it needs industrial-level pipelines to test it. The test setup arrangement was difficult during the pandemic time, hence the Robot maneuverability was tested on a Standard oil drum having an internal diameter of 22 inches. Test bed 1 is shown in Fig. 5.



**Fig. 4** a System flowchart b Circuit schematic of Arduino Uno, PCA9685, Servo, and joystick interface



**Fig. 5** a Oil drum-22 inches b Robot inside oil drum

The robot speed on a straight horizontal pipeline was experimentally found out to be around 28.63 cm/s with no-load condition. It was around 22 cm/s at working condition. The torque output of servo motor was also dependent on the voltage we



supply in. The 5 V supply was running the servo near ideal power and was insufficient so we supplied 7.2 V to get good torque output.

The robot has three types of motion to test on horizontal pipe testbed 1: Horizontal movement, Helix, and 360-degree rotation. These motions were tested on the testbed successfully.

The ability to pass through elbow joints and T joint can be verified by testing it on a separate testbed. Artificial obstacles were created and tested the robot's adaptive mechanism and obstacle-avoiding ability. The robot ran through different diameters of pipe successfully.

### 3 Results and Discussion

From the test bed 1 results, it was found that the robot successfully passed through the horizontal pipe. It successfully performed the testbed 1 experiments. The mode of operation, i.e., straight, Helix, and 360-degree rotation were tested during the experiments. The robot could pass with different diameters of pipes and obstacle avoidance capability was also tested. The robot flat surface offered good space for mounting other sensors and tools as expected. The proposed motion planning proved to be successful after testing the robot. The robot design gave expected performance and proved to be a potential design in field of pipeline inspection robot. There are some shortcomings that were observed after the tests. This includes bending of the wheel chain link due to the weight of driving and steering module weight. This led to improper traction of wheel with inner surface and the possible danger of the breakage of 3d printed linkage arms. Next shortfall is the inadequate stiffness of the compression spring wire, which led to improper contact of wheels with pipe inner surface. The correct specification of spring is required. Furthermore, there is scope of improvement in communication control. It is recommended to implement wireless communication to drive the robot for long-range application because wired connection increases drag and can also create tangle problem. There is a need to reduce the size of the camera and increase the number of cameras to have a greater visual inspection area. At last, it is required to implement some kind of inspection tool to the proposed robot to make robot what is designed to, that is the implementation of some kind of inspection tool. This shortcoming will be further fulfilled in the next research study.

### 4 Conclusions

This study was to developed a new pipeline inspection robot having a two-wheel chain with an adaptive mechanism for a pipeline having an internal diameter in range of 20–24 inches. The wheel chain can adapt with help of a 4 bar link mechanism and compressive springs. By having this, they can maintain continuous contact with the

inner walls of the pipe having an irregular diameter. All the wheels can be driven and steered separately. This provides good traction and maneuverability to the robot. The robot can move in three different ways is Straight, helix, and 360-degree rotation which is the specialty of the robot.

The flat shape of this robot allows ample space for mounting different sensors tools for inspection. The robot performance is verified through various testbed experiments. It showed potential design, novelty, and its practical implementation of prototype model in the field of pipeline inspection robot.

After the testing of robot, it was found that further improvement can be done on this robot. This includes the inclusion of correct specification of compressive springs, mechanism to support eccentric loading of servo weight, implementation of Wireless communication control, and addition of some Non-Destructive Tool sensors for inspection. These shortcomings will be fulfilled in the next coming study.

## References

1. Kwon YS, Lee B, Whang IC, Kim WK, Yi BJ (2011) A flat pipeline inspection robot with two wheel chains. Proc IEEE Int Conf Robot Autom Published online: 5141–5146. doi:<https://doi.org/10.1109/ICRA.2011.5979712>
2. Hadi A, Hassani A, Alipour K, Askari Moghadam R, Pourakbarian Niaz P (2020) Developing an adaptable pipe inspection robot using shape memory alloy actuators. J Intell Mater Syst Struct 31(4):632–647. <https://doi.org/10.1177/1045389X19898255>
3. Abidin ASZ, Chie SC, Zaini MH, et al (2017) Development of In-pipe robot D300: cornering mechanism. MATEC Web Conf 87. <https://doi.org/10.1051/mateconf/20178702029>
4. Kim JH, Sharma G, Iyengar SS (2010) FAMPER: a fully autonomous mobile robot for pipeline exploration. Proc IEEE Int Conf Ind Technol Published online:517–523. <https://doi.org/10.1109/ICIT.2010.5472748>
5. Mishra D, Agrawal KK, Abbas A, Srivastava R, Yadav RS (2019) Pig [pipe inspection gauge]: An artificial dustman for cross country pipelines. Procedia Comput Sci. 152:333–340. <https://doi.org/10.1016/j.procs.2019.05.009>
6. Pasha MA, Khan TM (2017) A pipeline inspection gauge based on low cost magnetic flux leakage sensing magnetometers for non-destructive testing of pipelines. ICET 2016 - 2016 Int Conf Emerg Technol. Published online 1–5. <https://doi.org/10.1109/ICET.2016.7813212>
7. Nayak A, Pradhan SK (2014) Design of a new in-pipe inspection robot. Procedia Eng. 97:2081–2091. <https://doi.org/10.1016/j.proeng.2014.12.451>
8. Savin S, Jatsun S, Vorochaeva L (2017) Trajectory generation for a walking in-pipe robot moving through spatially curved pipes. MATEC Web Conf 113. <https://doi.org/10.1051/mateconf/201711302016>
9. Wang W, Cai S, Ma C, Li W, Liu J (2020) Multi-objective optimization design of an inch-worm climbing robot. ICARM 2020-2020 5th IEEE Int Conf Adv Robot Mechatron Published online:189–193 <https://doi.org/10.1109/ICARM49381.2020.9195306>
10. Chauhan SS, Khare AK (2020) Kinematic analysis of the ABB IRB 1520 industrial robot using roboanalyzer software. Evergreen. 7(4):510–518. <https://doi.org/10.5109/4150470>
11. Dief TN, Yoshida S (2016) System identification for Quad-rotor parameters using neural network. Evergreen. 3(1):6–11. <https://doi.org/10.5109/1657380>
12. Xu W, Zhang F, Lin D (2021) System identification and adaptive control of micro helicopter. J Phys Conf Ser 1780(1):58–66. <https://doi.org/10.1088/1742-6596/1780/1/012026>

13. Pariaman H, Luciana GM, Wisyaldin MK, Hisjam M (2021) Anomaly detection using LSTM-autoencoder to predict coal pulverizer condition on coal-fired power plant. *Evergreen* 8(1):89–97. <https://doi.org/10.5109/4372264>
14. Mohd Aras MS, Md Zain Z, Kamaruzaman AF, et al (2021) Design and development of remotely operated pipeline inspection robot. Vol 666. Springer Singapore. [https://doi.org/10.1007/978-981-15-5281-6\\_2](https://doi.org/10.1007/978-981-15-5281-6_2)
15. Li H, Li R, Zhang J, Zhang P (2020) Development of a pipeline inspection robot for the standard oil pipeline of china national petroleum corporation. *Appl Sci* 10(8). <https://doi.org/10.3390/APP10082853>
16. Tătar O, Măndru D, Ardelean I (2007) Development of mobile minirobots for in pipe inspection tasks. *Mechanika*. 68(6):60–64
17. Anuar A, Roslin NS, Sahari, Mohamed KS, Aziz MA (2014) Inspection robot for parallel entry boiler header pipe. *Adv Intell Syst Comput* 269:5–7. <https://doi.org/10.1007/978-3-319-05573-2>
18. Kwon Y, Yi B (2012) Design and Motion Planning of a Two-Module. *IEEE Trans Robot* 28(3):681–696
19. Zhao W, Zhang L, Kim J (2020). Design and analysis of independently adjustable large in-pipe robot for long-distance pipeline. *Appl Sci* 10(10). <https://doi.org/10.3390/app10103637>
20. Nguyen TT, Kim DK, Rho YW, Kim SB (2001) Dynamic modeling and its analysis for PIG flow through curved section in natural gas pipeline. *Proc IEEE Int Symp Comput Intell Robot Autom CIRA 2001-Janua*:492–497. <https://doi.org/10.1109/CIRA.2001.1013250>
21. Bin TG, Zhang SM, Zhu XX (2011) Design of the speed regulating pig with butterfly bypass-valve. *Adv Mater Res* 201–203:429–432. <https://doi.org/10.4028/www.scientific.net/AMR.201-203.429>
22. Kurata M, Takayama T, Omata T (2010) Helical rotation in-pipe mobile robot. 2010 3rd IEEE RAS EMBS Int Conf Biomed Robot Biomech BioRob 2010. Published online: 313–318. <https://doi.org/10.1109/BIOROB.2010.5628009>
23. Savin S, Jatsun S, Vorochaeva L (2018) State observer design for a walking in-pipe robot. *MATEC Web Conf*. 161:4–9. <https://doi.org/10.1051/mateconf/201816103012>
24. Savin S (2019) RRT-based Motion Planning for In-pipe Walking Robots. In: 12th Int Sci Tech Conf Dyn Syst Mech Mach Dyn 2018. Published online:1–6. <https://doi.org/10.1109/Dynamics.2018.8601473>
25. Chablat D, Venkateswaran S, Boyer F (2018) Mechanical Design Optimization of a Piping Inspection Robot. *Procedia CIRP*. 70:307–312. <https://doi.org/10.1016/j.procir.2018.02.015>
26. Jeon W, Park J, Kim I, Kang YK, Yang H (2011) Development of high mobility in-pipe inspection robot. 2011 IEEE/SICE Int Symp Syst Integr SII 2011. Published online:479–484. <https://doi.org/10.1109/SII.2011.6147496>
27. Yoon KH, Park YW (2010) Pipe inspection robot actuated by using compressed air. *IEEE/ASME Int Conf Adv Intell Mechatron AIM*. Published online: 1345–1349. <https://doi.org/10.1109/AIM.2010.5695865>
28. Yamamoto T, Sakama S, Kamimura A (2020) Pneumatic Duplex-Chambered Inchworm Mechanism for Narrow Pipes Driven by only Two Air Supply Lines. *IEEE Robot Autom Lett*. 5(4):5034–5042. <https://doi.org/10.1109/LRA.2020.3003859>
29. Hayashi K, Akagi T, Dohda S et al (2020) Improvement of pipe holding mechanism and inchworm type flexible pipe inspection robot. *Int J Mech Eng Robot Res*. 9(6):894–899. <https://doi.org/10.18178/ijmerr.9.6.894-899>

# Designing Mobile App Interfaces for Facilitating Medical Treatment at the Government Hospitals



Prakash Kumar

## 1 Introduction

Government hospitals are the pillars of public healthcare services in India. They have specialized and expert doctors as well as well-trained nursing staff to treat different ailments. They offer genuine treatment to the patients and provide them at almost free of cost, compared to the private hospitals. Many of these government hospitals are also engaged in research to develop new techniques to improve the quality of treatment [1, 2]. Significant research has also been reported on the use of IT-based innovations to enrich the healthcare systems whether it is seeking remote consultation through Telemedicine, administering glucose using IoT system, managing diabetic or elderly patients or Patient-related information, connecting patients to specialized doctors or using cloud computing and mobile OS to manage hospital system [3–13]. However, not much has been reported on navigating patients or attendants within hospitals and addressing their queries related to the hospital norms in real time. Most of these hospitals are in big towns of every province, and every day, a large number of patients from remote places visit these hospitals for different treatments. But, due to inadequate resources, the hospital administration is unable to meet this ever-increasing demand resulting in shortfalls. Getting all relevant information, at times, is not possible. Lack of proper information at every step leaves many patients confused and puzzled, delaying the treatment process, often, leading to altercations and chaos. Many people with higher purchasing power prefer treatment at private hospitals. However, a large section of the population is, still, completely dependent upon these hospitals exerting huge pressure on their infrastructure. After visiting a few of the government hospitals like *Safdarjung* Hospital New Delhi, AIIMS New

---

*Present Address:*

P. Kumar (✉)

Department of Design, Shiv Nadar University, Dadri, Uttar Pradesh 201314, India

e-mail: [prakash.kumar@snu.edu.in](mailto:prakash.kumar@snu.edu.in)

Delhi, and Patna Medical College hospital, it was observed that the patient treatment gets delayed due to different reasons related to the patients and the hospitals. The study tried to capture all such issues and reflected on them to solve them.

## 2 Method

### 2.1 *Problems from Patients' Perspective*

Talking about the patients' perspective, there are several causes because of which the treatment is delayed. Some of them are as following:

**Delays due to issue related to understanding rules, norms, and processes.**

When the patients or attendants arrive at the hospital premises, the first-timers can't directly consult the doctor. They have to undergo procedures starting from registering the patients, followed by the registration slip entry at the concerned department OPD.

Also, for new cases and follow-up cases, there are different registrations. The general process of registering also varies from hospital to hospital. Like for AIIMS Delhi, the first appointment date has to be sought. This is followed by OPD registration on the date of appointment. Whereas in the case of Safdarjung Hospital or Patna Medical College and Hospital, the appointment system is not mandatory. One can directly register and proceed to OPD. Also, there is so much rush everywhere that it is quite possible that a step is skipped and the person gets into the wrong queue. In that case, the person has to return and redo the step before moving forward. Say if the person gets into the queue for registration, mistakenly, and skips the appointment process, he has to start with the appointment seeking process which means standing behind a large queue of people. And, by the time, his turn comes, the appointment for the day is either over, or even if he can get an appointment, a large number of people have already completed the registration process before him. In both cases, the treatment process is delayed. In case of any doubt, if the person wants to enquire at inquiry/reception counter, he finds a big queue there which, eventually, means delay. On the other hand, lack of full acquaintance with the system leads to fair chances that one would miss a process that completely delays the treatment process.

**Delay due to difficulty in finding places within the hospital Premises.** The government hospitals, like Patna Medical College Hospital, are built and spread over a very large area where most of the departments and units are scattered all over the area and also have fixed way and gate. With an inefficient signage system, the Patients find it difficult and lose a lot of time finding the right place. Also, in government hospitals, many passages and doors are blocked. These inconsistencies also add to increasing the time delay.

**Delay due to doctors' schedule and timings.** Unlike private hospitals, even if the patient wants to see a particular doctor, there is no provision to know the weekly schedule of the doctor before reaching the hospital. Moreover, if the patient does not, repeatedly, mention that during the registration, he is often allocated to a

different doctor. Also, each doctor is there for a stipulated time, and then he goes to ward inspection or operation. Finding when the concerned will be available is also a difficult task. As a result, when the patients reach the doctors, they find them unavailable.

**Issues related to availing hospital facilities.** The government hospitals, generally, have the facilities for different tests and diagnoses. But sometimes there are break downs which are not mentioned anywhere and the visitors only come to know about it when they are at the counter after standing in queue for hours. Also, when they require certain assistance, they don't know where to find the concerned person say for stretcher, ambulance, other requirements. Many times, the hospital staffs are not at their seats which makes the situation quite difficult.

## ***2.2 Problem from Hospitals' Perspective***

The government hospitals are running much beyond their handling capacity [14]. The number of patients visiting the hospitals has increased drastically but the infrastructure and resources have not increased that way. Compared to the patient number they are understaffed. In this condition, the administration cannot employ their staff just for guiding and helping the patients. They can hire outsourced people for this work as in the case of AIIMS but that again not possible for all the government hospitals. Also, it is not always possible to monitor all staff if they are doing their duties sincerely. Hence, there is a gap that appears between the requirement of the patients and what is fulfilled by the Government hospitals.

## ***2.3 Consequences***

Due to difficulties and delays in getting proper treatment at the government hospitals, the population, with higher purchasing power, has shifted towards costly private hospitals in recent times. But the larger population that cannot afford costly treatment are still suffering. They have to face delays in treatment which sometimes even becomes fatal for the patients. This sometimes also results in violent exchanges between staff and the attendants.

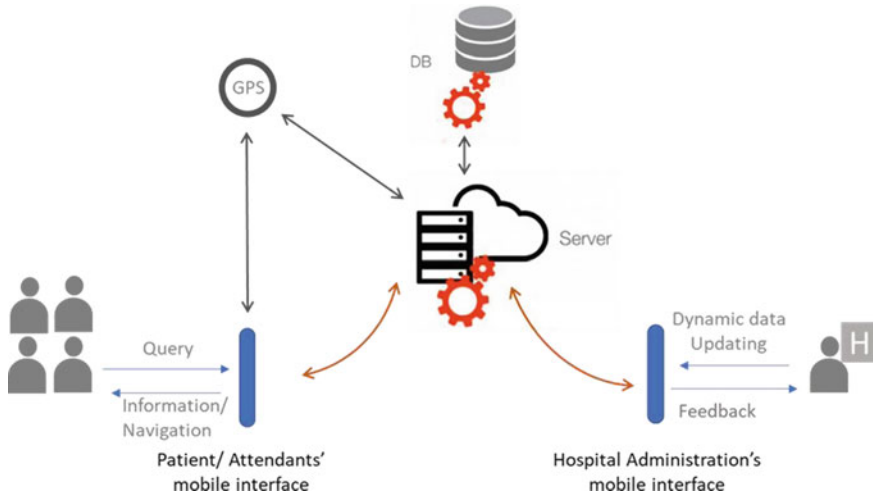
Besides, there are some anti-social elements active in the hospital premises too who try to take advantage of the situation and lure the patients to quacks who not only exploit them financially but also put patient's life at risk. This evades the very mission of the government to ensure public health. Had the patients and attendants been provided the necessary information timely and accurately, the treatment would become easier and faster but also relieve the hospital administration and help to deliver better services. Thus, help in achieving the mission of the government to ensure public health. Besides, it will also prevent innocent people from falling prey to quacks.

### 3 Possible Solutions

The need for the required information to patients and attendants can be solved by different methods. However, the efforts have to be taken to address the issues through system design approach [15, 16]. It can be addressed using proper signage system for guiding patients to their destination [17]. The doctors with their timings and day can be mentioned on a board too. Similarly, the rules and regulations can be printed and given to the patients to guide them. But these solutions have their limitations. Printed signage cannot handle dynamic information. Also printing material will be costly and not very environment-friendly. Also, hardly anybody is interested to read a lot of material when they require just specific information. In this context intervention of Information, Technology can be of great help. In recent times, IT has revolutionized our way of working and provided us with an effective interface that connects two different domains. They have evolved as a platform where relevant information is provided as per users' needs through suitable technology. It has versatile applications. Especially, the use of mobile app for different purposes has changed our lives forever. Apps like UBER have fulfilled the needs of the commuters using the Global Positioning System and IT. Also, the recent studies report a high surge in internet and mobile usage among different strata Indian population irrespective of rural–urban background, age, gender, disparities in income, and education [18]. Hence, a system-supported new mobile app could provide necessary information regarding hospitals to patients.

### 4 The Proposed System Design

The proposed system acts as an interface between the patients/ attendants and the hospital administration. There are two sets of interfaces, one for the patients/ attendant to get information and the other for hospital administration to update information. The patient-related interface provides all the relevant information related to hospital premises surrounding areas to the patients/attendants which would help them get the treatment without delay. This includes stepwise rules and norms of getting treatment at the hospital, location of different departments, counters, wards, blood bank, facilities points (for the ambulance, stretcher, wheelchair, etc.) and contact number of the concerned person, information about break-down of the facility (like an X-ray machine, an Ultrasound Machine, etc.) and tentative time of resumption, availability of different doctors during the week and their consultation timings. Information like availability of beds at any ward is provided to the attendants also guides them as to where to go, whom to meet, and what procedures to follow to get the patient a bed. In addition, it also provides important information regarding the location of interest around the hospital premises like the medicine stores, the general stores, the hotels, the bus stops, etc., that would help the patients during admission. While on the hospital administration's interface, the hospital can update the important dynamic



**Fig. 1** Working of the proposed system design

information like changes in some rules, timings, availability of doctors, availability of beds for admission, temporary shifting of any unit, and similar dynamic information. The hospital’s interface is highly secured and password protected and only an authorized person can do any kind of updating (Fig. 1).

When the app is opened, the GPS gets activated and the phone is connected to the server providing all the relevant information to patients and attendants and navigates them through the different places within the hospital premises wherever they mention to go. The detailed step-wise working of the app has been discussed. In this paper, the working of the patient’s interface has been discussed in detail.

### 4.1 Working of Patients’ Interface of the App

The proposed system works on android enabled mobile phones. After installing, the app will activate the mobile GPS and shows the position of the mobile whenever it is opened. It would identify the patients’ needs, i.e., if the app users want help for some emergency or have to visit the hospital for a follow-up case. It also establishes if they are new visitors to the particular hospital meeting the doctor for some non-emergency serious ailment like arthritis, cataract, respiratory issues, etc. And it provides the information accordingly.

**During an emergency.** During an emergency, the app asks about the kind of emergency, i.e., road accident, heart attack, delivery issues, some stroke, etc. On selecting a particular option, it reflects all the nearby government hospital emergencies that offer treatment for the same. The hospitals are arranged in the order of their proximity. Once the patients select any hospital, the navigation guides them to the



emergency unit so that they don't have to waste time asking anybody. Along with navigation, in the expandable menu, it provides all the information possibly required by the attendants like information regarding all the chemist shops nearby emergency unit, blood bank, the important telephone numbers of the concerned hospital (Fig. 2).

**For the non-emergency diseases/ailments.** In case of non-emergency diseases like arthritis, cataract, respiratory problems, etc., the app has two options. If the patients know which hospital they want to visit they can directly mention the hospital name. Else, they can mention their ailments and the app suggests the hospitals where they can get the treatment for it. Either way, when the patients select the hospitals, the

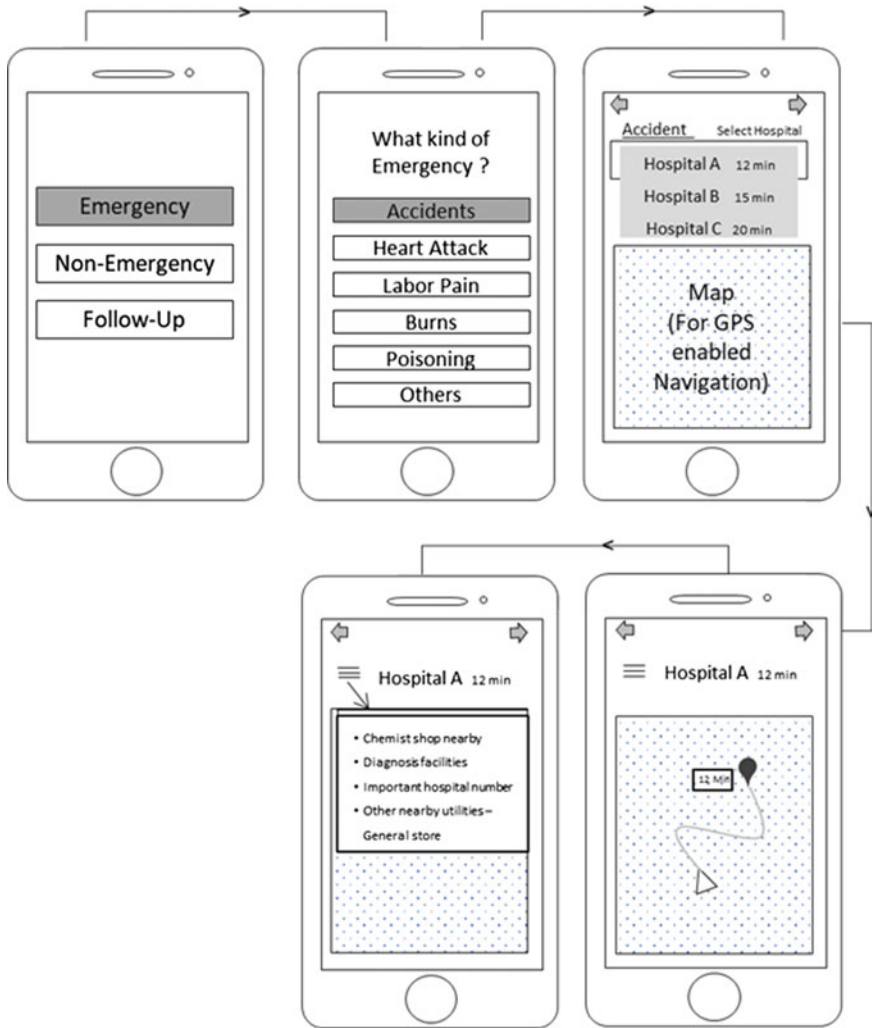
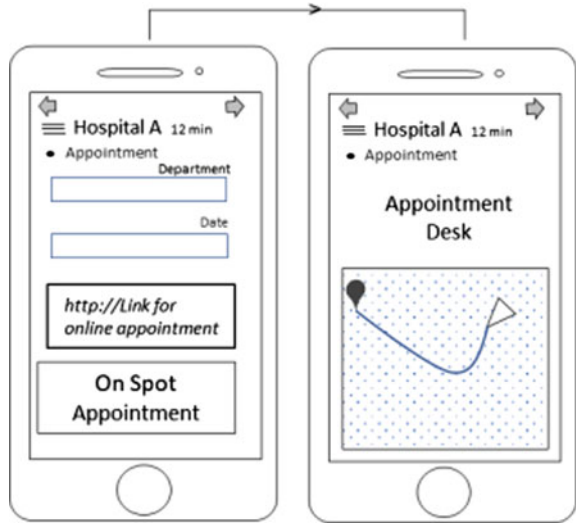


Fig. 2 Wireframes for task performed through app in emergency

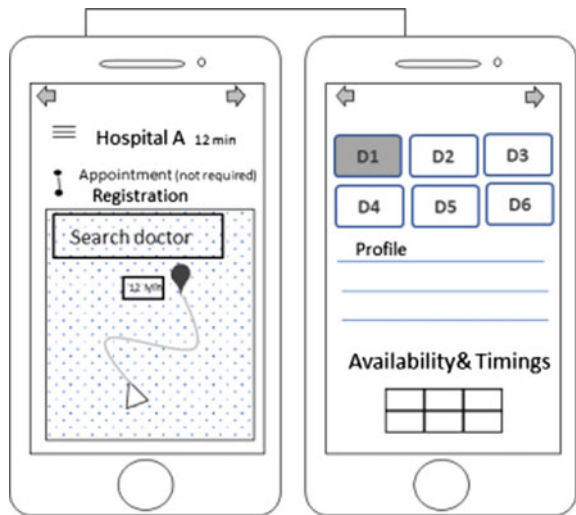
navigation guides them through the processes of that hospital. If the hospital requires an appointment before registration, the patients are shown appointment status for the required day. It also directs them to an online appointment site. If patients want to take an appointment from the counter, the system navigates them to the appointment desk (Fig. 3).

For the hospital without this system, the patients are directly guided to the registration desk. In expandable menu, they are also provided with information regarding doctors' availability on that day and their timings (Fig. 4).

**Fig. 3** Wireframe for seeking appointment through the app



**Fig. 4** Wireframes for searching doctors, their availability, and timings



After OPD registration is done, the patients are guided to the department entry desk as every registration has to be entered with the entry desk. On this interface page, the expandable menu also provides information regarding navigation to different units within department, location of other departments in the case of cross referring (the person is internally referred to the relevant department), information regarding diagnostic facilities of the hospital, etc. (Fig. 5).

**For the old follow-up cases.** Here, the process is similar to the registration process but the department name has to be mentioned just after mentioning the hospital name.

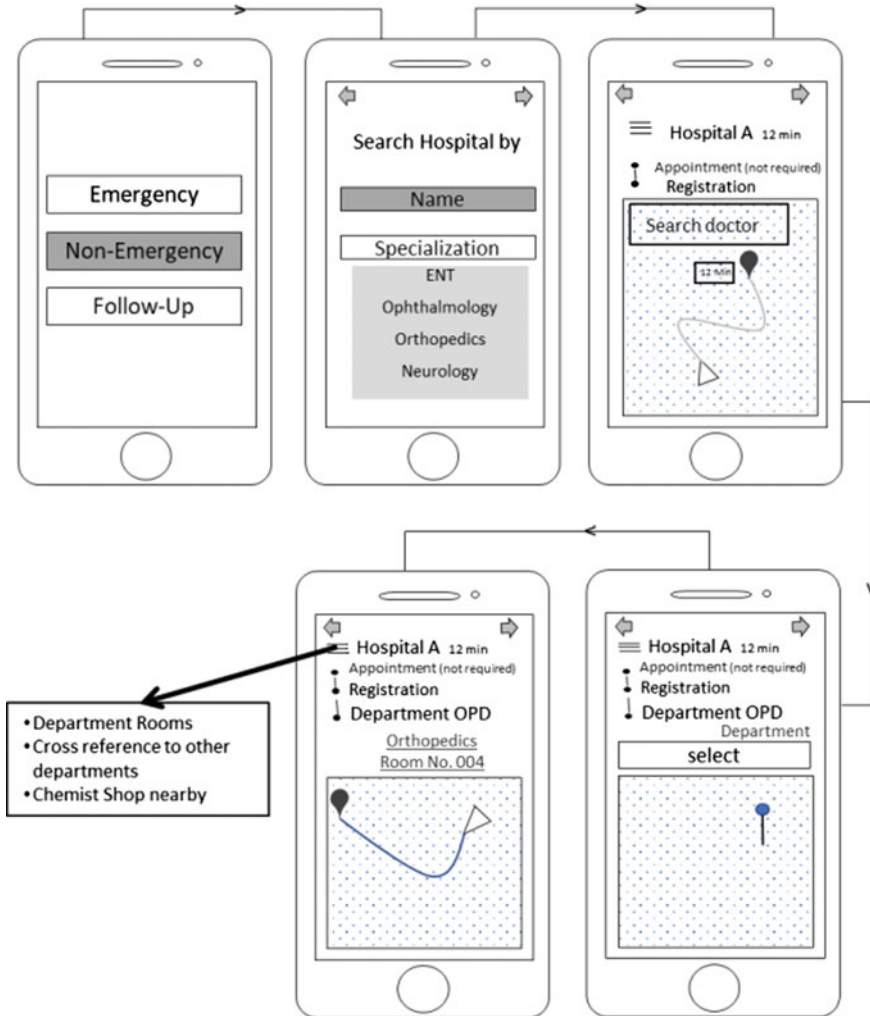


Fig. 5 Wireframes of the overall task performed for non-emergency cases

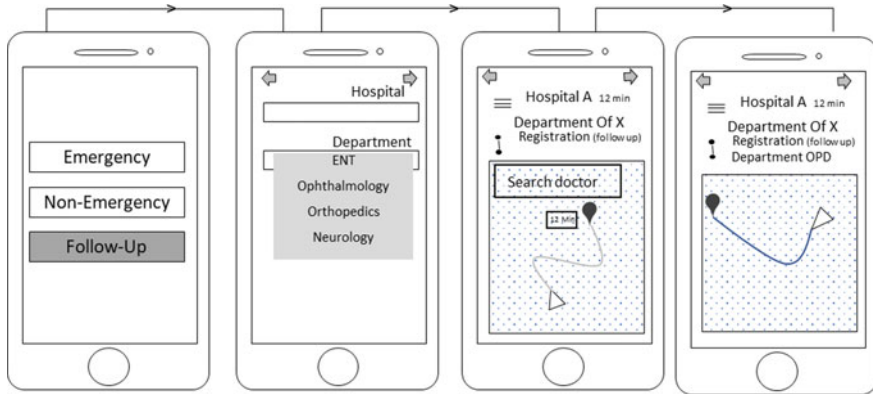


Fig. 6 Wireframes for task performed for follow up cases

The system then navigates patients directly to the registration desk for the old follow-up cases. On the same page, there is a tab to check doctors’ availability. This avoids the wastage of time due to absence of doctor on the day of visit. After registration, they are directed to the department entry desk. The expandable menu other relevant information which the patients might require (Fig. 6).

## 5 Conclusion

Government hospitals are the most important centers of providing inexpensive and reliable treatment to the larger patient population. But, as every hospital does not have the same rules and norms, it takes some time to understand and get acquainted that delays the treatment process. Also, the location of different departments and other units are very haphazard that further adds to delays. Since the inquiry counter, meant to provide reliable information, is limited in number and is always heavily crowded, people get relevant information late. In this paper, the different issues, faced by patients due to the information gaps, were studied. Different aspects of the problems were analyzed through the experiential study of three hospitals, i.e., AIIMS New Delhi, Safdarjung Hospital New Delhi, and Patna Medical college hospital. Based on the experiences, observation, and interactions with patients and doctors at different hospitals, a Mobile-based app was visualized. This mobile app solution could provide all relevant information related to the listed government hospital to the patients and help them navigate inside and around the hospital premises. This type of app finds special relevance in present pandemic situation where every second is critical for saving lives. But this application has some limitations too.

This efficacy of the application is affected by the level of mobile literacy of the user. Also, it can’t work on the old mobile that does not have an android platform. The reliability of this app is also dependent on dynamic information related to

doctor's availability, changing status of hospital's infrastructure (temporary shifting, machinery breakdown, etc.), which has to be updated regularly by hospital authorities. Any problem at the hospitals' end would lead to incorrect information and confusion. The functioning of the app is dependent on the available network signals. In case of connectivity issues, the system will not function properly or stop working. The proposed system only facilitates improving accessibility by providing relevant information from the present system. But it cannot reduce the disparity between the number of patients and doctors. The proposed system would be more effective if the number of doctors is increased to relieve the burden on the existing infrastructure. The app also assumes that doctors and staff are available at the hospital at right time. Any schedule change has to be informed to the concerned authorities and updated. If updates are not regular, the app has no provision to check such discrepancies. The system can be further improved to check such discrepancies through patients' feedback and real-time monitoring of such complaints. Also, integration of the proposed system with the government's initiative of Online Registration System can help in enhancing the experience of the patients by providing hassle-free treatment at government hospitals.

## References

1. Krishna KPR (2011) The efficacy of Ayurvedic treatment for rheumatoid arthritis: Cross-sectional experiential profile of a longitudinal study. *International Journal of Ayurveda Research* 2(1):8–13
2. Sahu B, Chauhan S, Kiran U, Bisoi A, Ramakrishnan L, Nehra A (2009) Neuropsychological function in children with cyanotic heart disease undergoing corrective cardiac surgery: effect of two different rewarming strategies. *Eur J Cardiothorac Surg* 35(3):505–510
3. Thavareesan S (2016) Android Based Patient's Healthcare Management System. *Journal of Information Systems & Information Technology* 1(1):1–9
4. Nourizadeh S, Deroussent C, Song YQ, Thomesse JP (2009) A distributed elderly healthcare system. *MobiHealth*
5. Singh S, Khadamkar P, Kumar M, Maramwar V (2014) Healthcare Services Using Android Devices. *The International Journal of Engineering And Science* 3(4):41–45
6. Spat S, Höll B, Beck P, Chiarugi F (2012) A mobile android-based application for in-hospital glucose management in compliance with the medical device directive for software. In: *International conference on wireless mobile communication and healthcare*. Springer, Greece, pp 211–216
7. Kumar MD, Keerthana K (2018) Healthcare Management System In Android – “meDKare” Application. *International Research Journal of Engineering and Technology* 5(8):843–844
8. Zarka N, Mansour MM, Saleh A (2016) Mobile healthcare system. In: *International conference for young researchers in informatics, mathematics and engineering*. Italy, pp 13–18
9. Al- Hakim L (2007) *Web Mobile-based Applications for Healthcare Management*, 1st edn. IRM Press, US
10. Vinutha S, Raju CK, Siddappa M (2012) Development of Electronic Hospital Management System utilizing Cloud Computing and Android OS using VPN connections. *Int J Sci Technol Res* 1(6):59–61
11. Nalagatla V (2017) *Android mobile application for hospital executives*. Electronic Theses, Projects, and Dissertations. California State University 435, San Bernardino

12. Patterson V, Wootton R, Craig J (2006) Introduction to Telemedicine, 2nd edn. CRC Press, London
13. Erick M, Kasamani BS (2015) Afya App – The Mobile Personal Health Management Platform. International Journal of Research Studies in Science, Engineering and Technology 2(1):58–71
14. Sharma S (2021) India's public health system in crisis: Too many patients, not enough doctors. Hindustan Times. Retrieved from <https://www.hindustantimes.com/india-news/public-health-system-in-crisis-too-many-patients-not-enough-doctors/story>, last accessed 2021/10/05
15. Singh S, Kotzé P (2003) An overview of systems design and development methodologies with regard to the involvement of users and other stakeholders. Hum Comput Interact 37–47
16. Bahill AT, Botta R (2015) Fundamental principles of good system design. Eng Manage J (20) 9–17
17. Rodrigues RSQ, Coelho R, Tavares J (2019) Healthcare signage design: a review on recommendations for effective signing systems. Health Environ Res Des J 12(3):45–65
18. Agarwal S (2018) Internet and mobile association of India: internet users in India expected to reach 500 million by June: IAMAI. The Economic Times, Retrieved from <https://economictimes.indiatimes.com/tech/internet/internet-users-in-india-expected-to-reach-500-million-by-june-iamai/articleshow/63000198.cm>, last accessed 2018/5/16

# Finite Element Analysis of Friction Angle in Friction Drilling Process



Nitin S. Chityal and Sagar U. Sapkal

## 1 Introduction

Friction Drilling is an unconventional heat forming method that employs a conical high-speed rotating tool that creates significant heat energy due to high frictional forces in the tool-work contact zone. This technique is also termed the thermal drilling and flow drilling process due to the workpiece's high thermal power and deformation. Thin sheets are assembled to structural components by using friction drilling operation. Friction angle is one of the critical parameters related to tool geometry, and many researchers found that as the friction angle increases, the thrust force also increases [1]; this leads to the rupture of the coil edges during the drilling process [2]. To generate adequate frictional heat during the friction drilling of aluminum alloys, the machine's settings should be adjusted at high spindle speed and low feed rate because of the high thermal conductivity [3].

The explicit dynamic approach worked well for simulating and analyzing significant deformations in work materials and tool-workpiece contact conditions [4]. Very few research papers are available related to the friction drilling process, and hence the FEM modeling of stir friction welding can be analyzed to expand the ABAQUS/EXPLICIT FEM program to the friction drilling process [5, 6]. The ABAQUS/EXPLICIT 6.14 finite element analysis software has been used to perform an explicit dynamic modeling three-dimensional temperature-dependent model. This research paper contributes to the work carried out by Miller and Shih [7]. They have modeled the friction drilling process by a 3D finite element model and analyzed the axial thrust force, torque, and temperature by varying few machine parameters. Distribution of plastic strain, thermal analysis, stress and deformation were shown, and the workpiece's thermal-mechanical behavior was also investigated. The effect of different coefficients of friction and different feed rates were analyzed on thrust

---

N. S. Chityal (✉) · S. U. Sapkal  
Walchand College of Engineering, Sangli, India

force and torque. This research work extends the work using the same model data to study the effect of varying friction angles on temperature, deformation, thrust force, and torque.

## 2 Literature Survey

Ozler and Dogru[2] showed that the increase of friction angle increases the thrust force and lowers the temperature and length of the bush. Ozek and Demir[3] examined the thermal conductivity of aluminum alloy friction drilling. The larger bush forms were seen at low spindle speeds and high feed rates. Soo et al. [4] have built a 3D FE model that used ABAQUS/Explicit software for friction drilling of an Inconel 718. This paper clarified the details of the contact conditions during the thermal drilling of the workpiece. Sundararajan et al. [5] have built, in ABAQUS/Explicit, a fully coupled three-dimensional thermo-mechanical FE model utilizing the arbitrary Lagrangian–Eulerian formula and Johnson–Cook material law. Schmidt and Hattel [6] have adopted an FE model with less specified boundary conditions and a minimal number of predefined domains than other preset models. Miller and Shih [7] have modeled the friction drilling process using 3D FE analysis, obtained workpiece temperature and material deformation, and done comparative analysis with experimentally workpiece temperature thrust force and torque. Miller et al. [8] have used the friction drill of standard geometric parameters with friction angle i. e.  $\beta = 36^\circ$  tool. Kaya et al. [9] observed increased thrust force and torque with increased friction angle, feed rate, and friction contact area ratio. Dehghan et al. [10] have found that the temperature gradient is high around the tool-work contact region, and it reduces away from the hole region. In the dry friction drilling process, the desired machine parameters should be selected. Karabulut and Bilgin [11] have found some cracks and petals after dry friction drilling of an AA7075-T6 material. Kumar and Hynes [12] reviewed several friction drilling research papers and reported that in many research papers friction angle of friction drill was in the range  $30^\circ$ – $36^\circ$ , and standard drill size of diameter 5.3 mm was used.

## 3 FEM Technique

### 3.1 FEM Preprocessing

The workpiece is modeled as a circular disc plate having dimensions of 10.16 cm diameter and 1.59 mm thickness, as shown in Fig. 1. The workpiece is made fixed at opposite points on the circular periphery by arresting all translational and rotational DOF. The surface of a plate is freely convected by a convective coefficient of  $0.030 \text{ KW/m}^2\text{K}$  and an ambient air temperature of 295 K. The rotational tool speed was



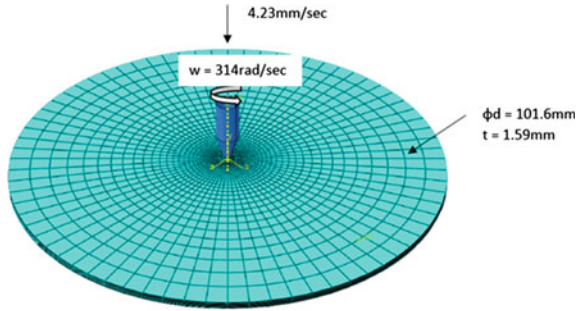


Fig. 1 Modeling of AA6061-T6 material showing all input parameters

Table 1 Temperature-dependent material properties of an AA6061-T6 material [7]

T (K)	310.8	366.3	422	477	533	589	644	700
K (KW/m°C)	0.162	0.177	0.184	0.192	0.201	0.207	0.217	0.223
C (KJ/Kg°C)	0.945	0.978	1	1.030	1.052	1.080	1.100	1.130
$\rho$ (Ton/m <sup>3</sup> )	2.690	2.690	2.670	2.660	2.660	2.630	2.630	2.600
$\epsilon$ (MPa)	68,500	66,200	63,100	59,200	54,000	47,500	40,300	31,700
$\sigma_y$ (MPa)	274	265	248	219	160	66.2	34.5	17.9
$\alpha$ (1/°C)*10 <sup>-6</sup>	23.5	24.6	25.7	26.6	27.6	28.5	29.6	30.7

set at 3000 rpm, i.e., 314 rad/s. The tool feed movement is given in the Y direction at -4.23 mm/s; the negative sign indicates the downward directional movement. In this research work, the temperature-dependent material properties of an AA6061-T6 material are considered for the analysis, as shown in Table 1.

The tool’s geometric parameters are  $\alpha = 90$  deg,  $\beta = 36$  deg,  $h_c = 0.940$  mm, and  $h_n = 5.518$  mm[8]. The tool is assumed to be rigid and has not been meshed. Three different tools are modeled by keeping all the parameters same  $\alpha$ ,  $h_c$ ,  $h_n$  only  $\beta$  angle has been changed with 3 different values of 30°, 36°, and 44° to analyze the effect of variable friction angle as shown in Fig. 2.

Figure 3 shows a rigid hard holder plate that restricts the workpiece in the downward direction. This rigid support plate has an outer radius of 40 mm and an inner radius of 12.25 mm. The nodes present on the workpiece can slide over the rigid plate in the x and z-directions. The thermal boundary condition to the workpiece for the region in touch with the hard plate applied adiabatic heat transfer conditions and the remaining area exposed to the convection of the free surrounding air with a convective coefficient of 30 W/m<sup>2</sup>K.

The workpiece is modeled as a disc plate that is meshed with eight hexagonal node elements. The element type is used as temperature-displacement coupled elements. Three different workpiece meshing was done according to the 3 different cases, case i) workpiece part mesh for  $\beta = 30^\circ$  consists of the number of elements of 22,520, with the number of nodes of 25,181 case ii) workpiece part mesh for  $\beta = 36^\circ$  consists of

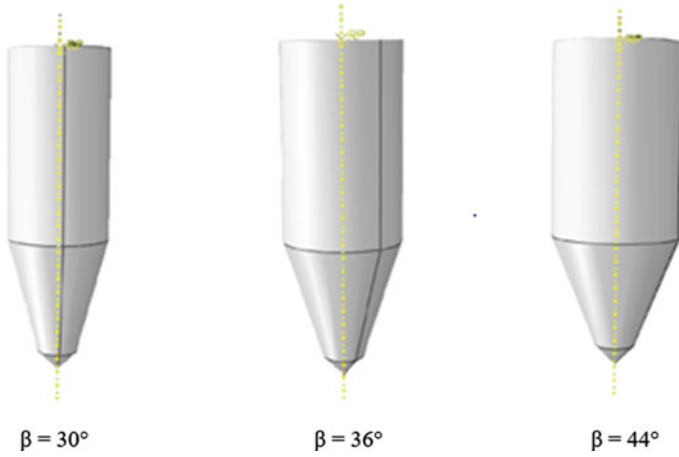


Fig. 2 Modeling of the tool as a rigid analytical body with variation in friction angle

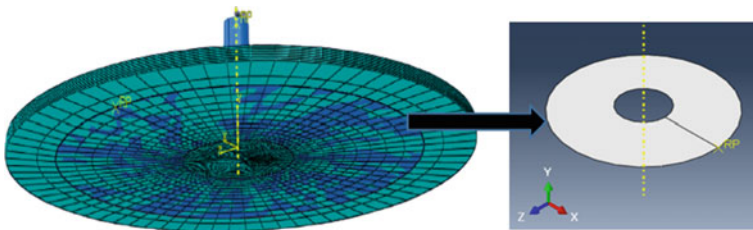


Fig. 3 Modeling of the rigid support plate

the number of elements of 22,640, with the number of nodes of 25,313 iii) workpiece part mesh for  $\beta = 44^\circ$  consists of the number of elements of 22,730, with the number of nodes of 25,523. Each node has degrees of freedom associated with X, Y, and Z displacements and a DOF linked to the nodal temperature. The mesh of the workpiece was more refined in the vicinity of the contact between both the workpiece and the tool, as seen in Fig. 1. In the direction of thickness, 10 rows of elements were created. The mesh size is an essential element to take into account. If the mesh size is too coarse, the elements would be deformed considerably, and if the mesh size is too small, then the computing time would be increased. The ALE adaptive mesh region was selected near the tool–work interaction at which the workpiece is expected to undergo significant deformation, and the frequency was set near about the value of 5.

Different interaction parameters were selected for proper tool–work interaction during friction drilling operation [13]. The first interaction was made by selecting the top surface and subjected to a coefficient of 0.03 (Convective Coefficient) and sink temperature of 295 K. The second was done by selecting the base surface not connected with the supporting plate and applying the same film coefficient and sink temperature parameters. The second interaction was done by selecting the base

surface. A surface set was made for the third interaction by selecting the more refined elements along the thickness direction at the tool-work interaction region. A general contact type was selected with three contact pairs. The interaction properties were selected by selecting the two contact property options; the first is mechanical interaction property, i.e., tangential behavior, and the second is thermal interaction property, i.e., heat generation. For the mechanical interaction property, the constant friction coefficient of 0.7 was selected. For the thermal interaction property, the fraction of heat convected to the slave surfaces was selected by a factor of 0.87.

### **3.2 Convergence Criteria**

In this research, shear damage criteria have been used to maintain the convergence in friction drilling analysis. Elements with excessive significant plastic strain more than a threshold value of 2.2 were deactivated. Stress components will become zero if a value of equivalent plastic strain exceeds 2.2. This is the maximum possible value at which the analysis will terminate the solution and gives the final output result. This research paper uses ALE, adaptive mesh domain region, selected at the tool-work interface region with a frequency value of 5.

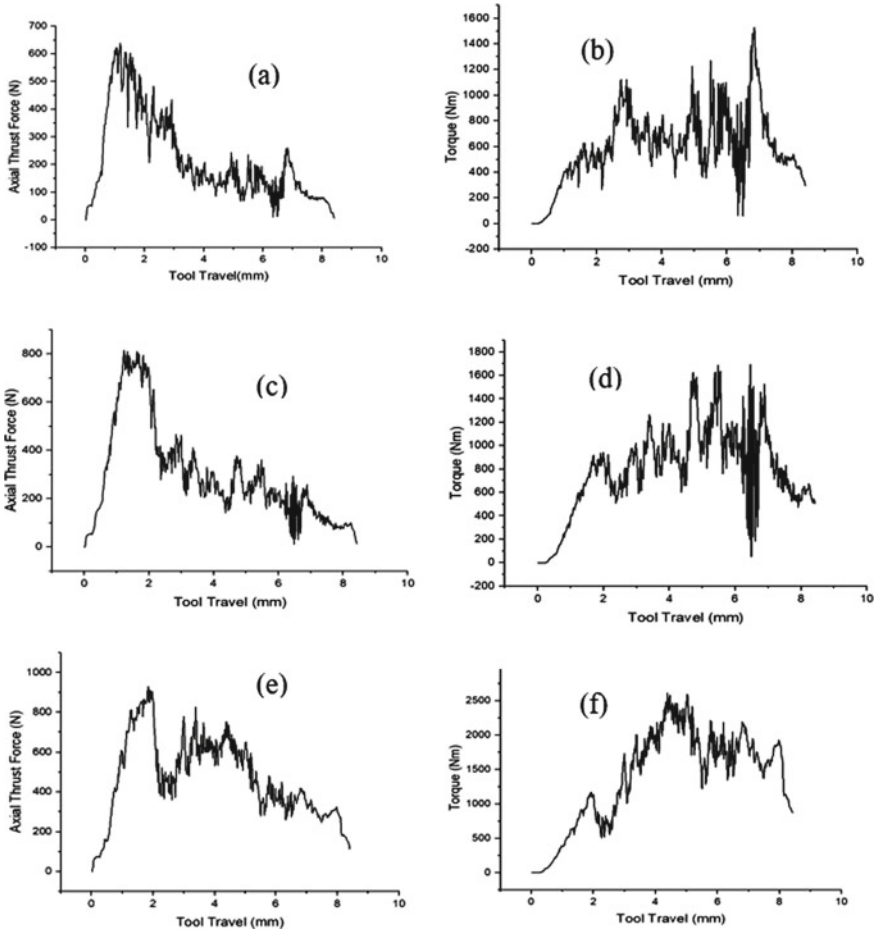
Mass scaling is used to improve the FEM computational efficiency; however, the accuracy will be retained. The mass scaling technique makes adjustments in temperature-dependent density data of the workpiece to reduce the time for the analysis. As there are minimal elements with reduced characteristic lengths of the elements near the tool-work contact region, there will be an increase in simulation time during the deformation of the elements due to tool travel. The stability in iterations and reduction in analysis time is achieved by scaling of density data during simulation. In this research, the mass scaling for every 10 increments was done to achieve a steady increase in at least  $2.5e-6$  s step time of tool travel time.

## **4 Results and Discussion**

### **4.1 Thrust Force and Torque**

Thrust force and torque are essential parameters to be measured for energy consideration in the friction drilling process. The machine parameters' feed rate and spindle speed impact the thrust force and torque, but the tool's geometry and angle also affect the thrust force. The variation in the friction angle ( $\beta$ ) causes the variation of frictional contact area with the workpiece surface. After penetration of tip angle ( $\alpha$ ) at the entry point, because of the variation in friction angle ( $\beta = 30^\circ$ ,  $\beta = 36^\circ$ , and  $\beta = 44^\circ$ ) the elements near the tool-work contact region experience the different stresses.

An increase in the friction angle makes the friction drilling of the workpiece so complex that it becomes resistant for easy penetration; it raises the thrust and torque. In this study, the FE model was carried out by adopting three different models with three different friction angles, i.e.,  $\beta = 30^\circ$ ,  $\beta = 36^\circ$ , and  $\beta = 44^\circ$ . The thrust force and torque plots were produced shown in Fig. 4. The peak thrust forces recorded are 639.38 N, 815.09 N, and 928.593 N. The peak torques recorded are 1526.96Nm, 1694.35Nm, and 2611.35Nm for three different friction angles, respectively.

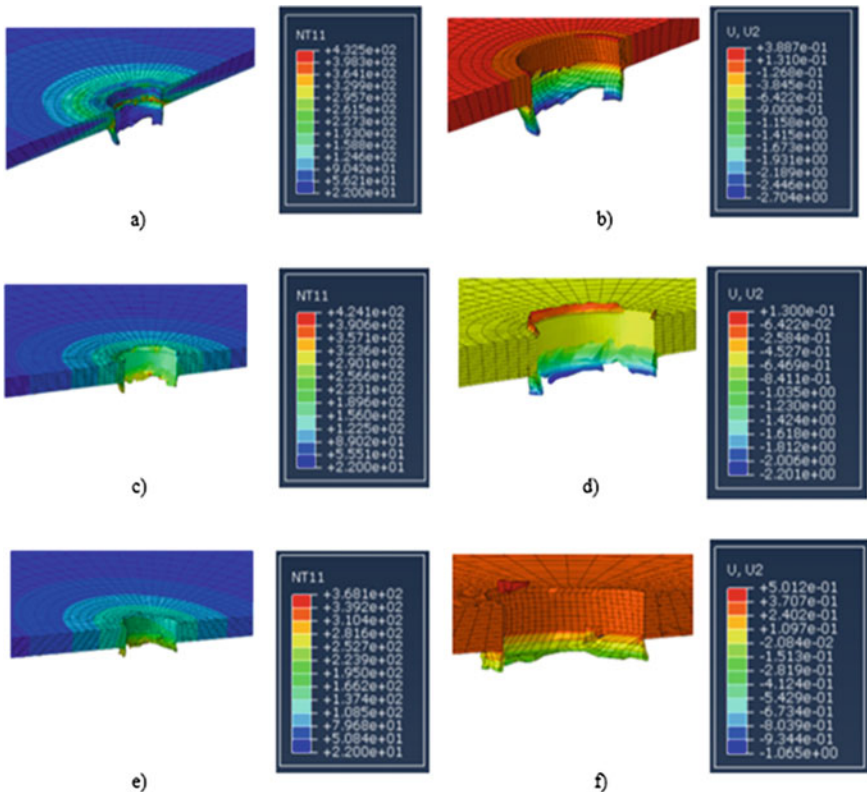


**Fig. 4** FEA Results of Thrust Force and Torque, respectively. **a, b** Thrust force and torque for  $\beta = 30^\circ$  **c, d** Thrust force and Torque for  $\beta = 36^\circ$  and **e, f** Thrust force and torque for  $\beta = 44^\circ$

### 4.2 Temperature and Deformation

The variation of friction angle causes the variation of duration at which the drill bit contacts with the workpiece material during the friction drilling operation.

As tool penetration is easier in smaller friction angles, the tool contacts the workpiece for a longer duration than drill bits with larger friction angles. It results in the rise in hole zone temperature, and hence for smaller friction angle drills, the hole zone temperature is high. The hole zone temperature decreases as the friction angle increases. The maximum temperatures of 432.5 °C, 424.1 °C, and 368.1 °C were recorded by AA6061-T6 workpiece material during friction drilling operation by using 3 different friction drills of friction angles  $\beta = 30^\circ$ ,  $\beta = 36^\circ$ , and  $\beta = 44^\circ$ , respectively. As shown in Fig. 5, near the drill-work contact region, the elements were distorted due to the high rise in temperature. The temperature decreases from the center region to the region away from the center radially. The outer circular



**Fig. 5** FEA Results of temperature and deformation, respectively. **a, b** Temperature and deformation for  $\beta = 30^\circ$  **c, d** Temperature and deformation for  $\beta = 36^\circ$  and **e, f** Temperature and deformation for  $\beta = 44^\circ$

region has the same temperature as the surrounding air temperature, i.e., 22 °C. The deformation of the material mainly depends upon the hole zone temperature. As the temperature is high, the material flow high because the material is subjected to high plastic deformation. Hence, as the friction angle increases, the hole zone temperature decreases, which reduces the deformation of the work material. The maximum deformation of 2.7 mm, 2.2 mm, and 1.065 mm was recorded by AA6061-T6 workpiece material during friction drilling operation by using 3 different friction drills of friction angles  $\beta = 30^\circ$ ,  $\beta = 36^\circ$ , and  $\beta = 44^\circ$ , respectively, as shown in Fig. 5.

## 5 Conclusion

In this research paper, 3D FEM analysis is carried out to predict the temperature and deformation. There are experimental difficulties in measuring the temperature and deformation of the workpiece. The model showed the peak temperature of 432.5 °C and maximum deformation of 2.7 mm by drilling with the drill bit having a friction angle of 30 °C. The practical analysis of material heating and material deformation was achieved by FEA modeling. The friction cone angle has affected the bushing length of the work material. The increase in the friction angle decreases the deformation of the workpiece. The increase of the friction angle does not affect the temperature considerably, but the axial thrust force and torque are increased excessively. The increase in the friction angle decreases the temperature of the hole zone and the workpiece material deformation.

## References

1. El-Bahloul SA, El-Shourbagy HE, El-Bahloul AM, El-Midany TT (2018) Experimental and thermo-mechanical modeling optimization of thermal friction drilling for AISI 304 stainless steel. *CIRP J Manuf Sci Technol* 20:84–92
2. Ozler L, Dogru N (2013) An Experimental Investigation of Hole Geometry in Friction Drilling. *Mater Manuf Processes* 28:470–475
3. Ozek C, Demir Z (2013) Investigate the Friction Drilling of Aluminium Alloys According to the Thermal Conductivity. *TEM Journal* 2:93–101
4. Soo SL, Aspinwall DK, Dewes RC (2004) 3D FE modelling of the cutting of Inconel 718. *J Mater Process Technol* 150:116–123
5. Soundararajan V, Zekovic S, Kovacevic R (2005) Thermo-mechanical model with adaptive boundary conditions for friction stir welding of Al 6061. *Int J Mach Tools Manuf* 45:1577–1587
6. Schmidt H, Hattel J (2005) A local model for the thermo-mechanical conditions in friction stir welding. *Modell Simul Mater Sci Eng* 13:77–93
7. Miller SF, Shih AJ (2007) Thermo-Mechanical Finite Element Modeling of the Friction Drilling Process. *J Manuf Sci Eng* 129:531–538
8. Miller SF, Blau PJ, Shih AJ (2007) Tool wear in friction drilling. *Int J Mach Tools Manuf* 47:1636–1645
9. Mehmet Tuncay Kaya, Alaattin Aktas, Bertan Beylergil and Hamza K. Akyildiz, “An Experimental Study on Friction Drilling of ST12 Steel”, *Transactions of the Canadian Society for Mechanical Engineering*, Vol. 319, pp. 319–329, (2014).

10. Shayan Dehghan, M. I. S. Ismail, M. K. A. Ariffin and B. T. H. T. Baharudin, "Measurement and analysis of thrust force and torque in friction drilling of difficult-to-machine materials", *The International Journal of Advanced Manufacturing Technology*, Vol. 105, pp. 2749–2769, (2019).
11. Karabulut S, Bilgin M (2021) Friction drilling of AA7075-T6 and AZ31B alloys under dry and oil containing ceramic particulates. *J Manuf Process* 65:70–79
12. Kumar R, Jesudoss Hynes R (2019) Thermal drilling processing on sheet metals: a review. *Int J Lightweight Mater Manufact* 2:193–205
13. Abaqus/CAE User's Manual 6.11 (2011) Dassault Systemes Simulia Corp., Providence, RI, USA

# Particle Size Distribution Analysis and Characterization of Cenospheres



Pragnya Pradeep, M. Y. Aravind Rao, J. Dharanish, R. Bheemraj, P. Rajeshwari, and S. Seetharamu

## 1 Introduction

The term “cenospheres” is started from the Greek word “kenos” that signifies “empty circles”. The Greek significance of the cenosphere itself shows the presence of hole encompassed by strong or a punctured mineral shell that is the main element of the cenosphere. The last of microspheres are regularly called network organized cenospheres or “Plerospheres” from the Greek “pleres”—signifies "filled circles" [1].

Even though the cenospheres are smaller in size and shape, it gains its importance in the fraction of the by-products originating from the combustion of the coal. This is due to its low density, spherical shape, high melting temperature, and high mechanical strength. These features make them appreciable uses in wide range of industries. Hence, the coal fired power plants are mainly interested in the cenosphere recovery process. The present work is conducted with M/s. NTPC Simhadri Thermal Power Station, India. Examination of the variables liable for the yield of cenosphere from the fly debris tests is the significant goal of this investigation. Fly debris is delivered as a result of the consuming of the pounded coal in nuclear energy stations. The lighter particles present in the fly debris are only the cenosphere, and they comprise around 1-2 weight level of the fly debris [2].

---

P. Pradeep (✉) · M. Y. Aravind Rao · J. Dharanish · R. Bheemraj  
Department of Mechanical Engineering, National Institute of Engineering, Mysuru 570008, India

P. Rajeshwari  
Department of Industrial Engineering and Management, Dr. AIT, Bengaluru 560056, India

S. Seetharamu  
Central Power Research Institute, Bengaluru 560080, India



Vassilev et al. [3] has detailed that the cenosphere (can have or has) the distance across going from 8  $\mu\text{m}$  to 1000  $\mu\text{m}$ . Kolay et al. [4] connect the normal measurement and thickness, where for particles with thickness lower than  $0.857 \text{ g/cm}^3$ , 80% of them have distance across a range between 50 and 150  $\mu\text{m}$ , 15% of them have width range between 150 and 200  $\mu\text{m}$  and 5% of them have breadth range between 200 and 250  $\mu\text{m}$ . Also, for the particles with thickness lower than  $1.282 \text{ g/cm}^3$ , 10% of them have distance across between 40 and 50  $\mu\text{m}$ , half of them have measurement between 50 and 100  $\mu\text{m}$ , 20% of them have breadth between 100 and 110  $\mu\text{m}$ , and 20% of them have width between 110 and 150  $\mu\text{m}$ .

A blended glass and translucent design is displayed by Cenosphere. As per Vassilev et al. [3] the significant constituents of the cenosphere are 76% of glass, 22% of mineral matter, 2% of burn, and essentially by-alumina–silicate glass, quartz, mullite, calcite, iron oxides, calcium silicates, and sulfates. Development of cenosphere is tantamount to as that of interaction of glass blowing [5]. The silica-toxin for the most part liquefies shows higher thickness and structures the glass when exposed to cooling. Comparable perception was accounted for cenosphere [6]. During the consuming of single particle or during mellowing of fly flotsam and jetsam, the gases are created. These gases grow the relaxed inorganic mineral issue and if the cooling is at a speedier rate, it shapes the amorphous cenosphere. The decay of the calcium and magnesium sulfates, kaolinite, calcium carbonate, dolomite, and pyrite oxidation conveys the gases capable to grow roundabout particle [7]. All of these reactions are occurring at temperatures underneath 1000 °C. Time required for the plan of a 50  $\mu\text{m}$  cenosphere is nearly around 0.3 ms [7].

Vassilev et. al. [3] uncovered that the chlorites and montmorillonites may show some reactant properties for the advancement of cenosphere, while illite capacities as a debilitating subject matter expert. According to Karret. al. [7], at temperature higher than 1500 °C, gas improvement is astoundingly brisk that it may escape from condensing garbage particle.

## 2 Experimental Details

Samples of Indian coal ash [8] cenosphere were harvested from the ash ponds of M/s NTPC Simhadri Thermal Power Station, India. Wet method was used for the Separation. The samples of fly ash were poured into water, subjected to stirring and kept for sedimentation for about 1 hour. Later, the particles that were floating [9] were skimmed, dried at 105°C for 2 h and afterward consumed for 1.5 h at 800 °C. The assortment of the fly debris was performed two times each day at 5:00 AM and at 4:30 PM. In this work, the examples just from Electrostatic Precipitator (ESP) zone-I were considered since about 70% load of all fly debris winds up there. All the examples [10] were gathered inside a significantly brief timeframe. This is on the grounds that the heap and the size of energy creation, these were very much like during that period power plant's activity. The normal mass of each debris test gathered was 400 g. The demineralized water was utilized as partition specialist

henceforth all the gathered cenosphere have thickness lower than  $1 \text{ g/cm}^3$  [11]. A few test were directed for noticing the relationship if any between the structure of fly debris and the yield of cenosphere. The Particle size circulation [12] investigation was accomplished for cenosphere of the fly debris and copper powder utilizing Malvern Master sizer 3000 Particle Size Analyser, X-Ray Diffraction (XRD) was utilized with a PAN scientific diffractometer and  $\text{CuK}\alpha$  radiation, worked at 40 KV and 35 mA with step of 0.05 and a sweep step season of 200 s. The morphology [13] of the cenospheres was noticed utilizing Scanning Electron Microscope (SEM) (Leica make, Q500MC model).

### 3 Results and Discussion

#### 3.1 Characterization of Cenosphere, Fly Ash, and Copper

The details of the characterization [14] carried out using various techniques are discussed. Figures 1 and 2 show the cenosphere samples of magnitude 500X and 1000X, respectively, in which the measured particle size of the cenosphere wall [15] ranges from 5.26 to  $35 \mu\text{m}$ . Moreover, these particles are spherical and have different particle sizes. Figures 3 and 4 show that the fly ash samples of magnification zoomed at 500X and 1000X, respectively. Figures 5 and 6 show pure Copper samples [16] of magnitude 500X and 1000X, respectively. Figure 3 depicts the morphology of fly ash which shows that the particle size is unevenly distributed, and Fig. 4 shows the

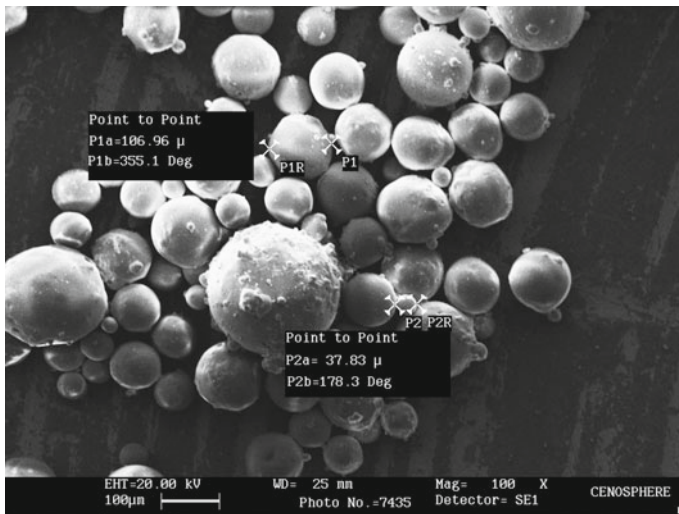


Fig. 1 Cenosphere sample of Mag. 500X

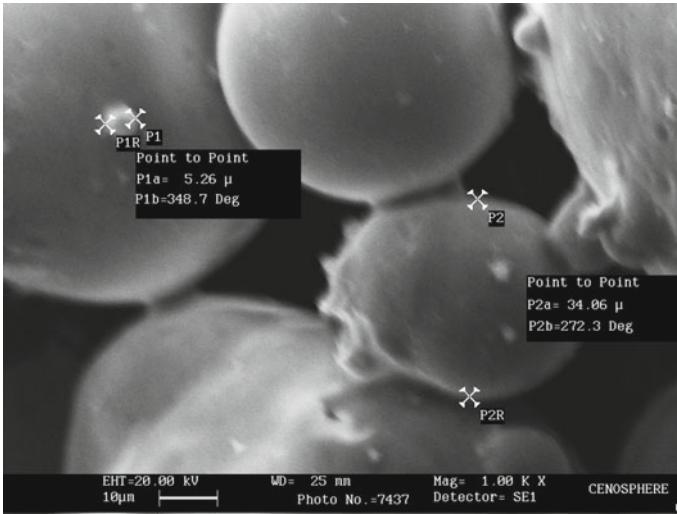


Fig. 2 Cenosphere sample of Mag. 1000X

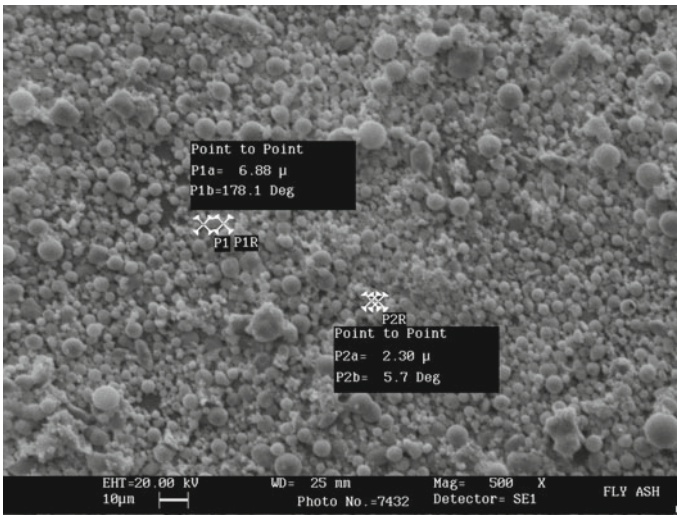


Fig.3 Fly ash sample of Mag. 500X

average particle size is in the range from 1.38 to 5 µm. This is having acceptable consistency with the particle size circulation qualities as portrayed in figure and in the normal size of cenosphere, fly debris and molecule is around 100 µm.

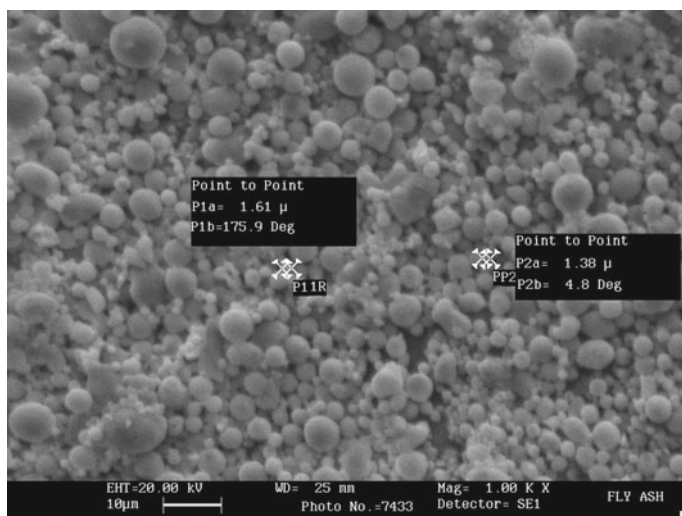


Fig. 4 Fly ash sample of Mag. 1000X

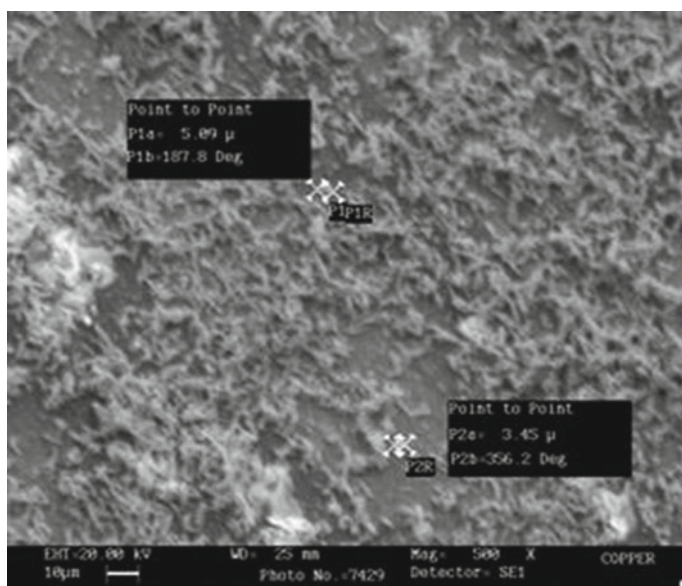
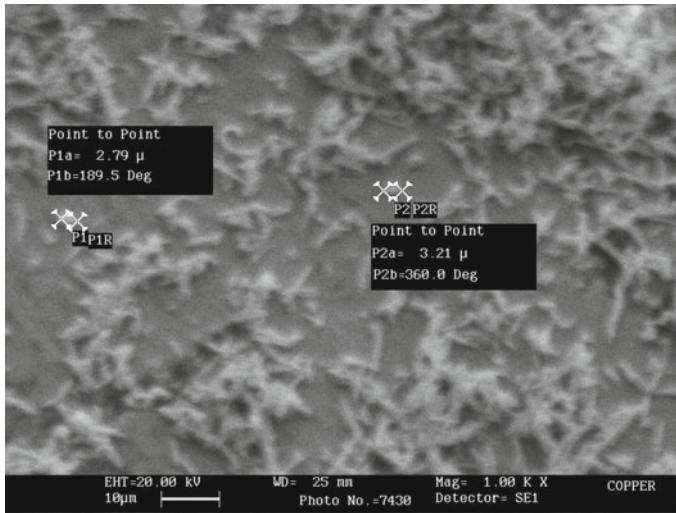


Fig. 5 Pure Copper sample of Mag. 500X



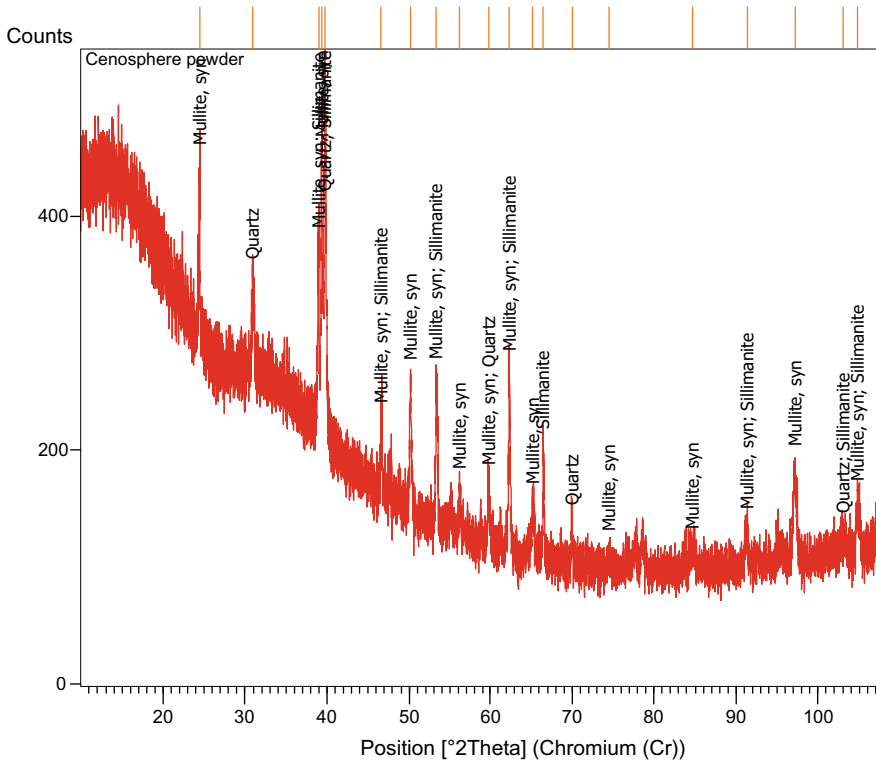
**Fig. 6** Pure Copper sample of Mag. 1000X

### 3.2 X-Ray Diffractometer (XRD)

The presence of crystalline phases in the cenospheres from the XRD analysis studies is quartz, mullite, and calcite which can be comprehended from Fig. 7. A wide void state of the primary bend can be credited to the presence of an amorphous stage, while the sharp pinnacles are related with the presence of translucent stages. Since carbonates like calcite can't be found at high-temperature conditions as calcite is completely deteriorated [17] under 1400 °C [7], its occurrence could be due to the effect of later crystallization. The presence of quartz, mullite, and calcite are in agreement with the composition of cenospheres as described by XRD. Different minerals are identified and are shown in Figs. 7 and 8. It is worth to note here that the primary content of the cenosphere is alumina (SiO<sub>2</sub>) as mentioned in Fig. 7 and Figs. 8 and Fig 9 shows the XRD pattern of Copper.

### 3.3 Particle Size Distribution

The particle size circulation (PSD) shows a rundown of qualities or a numerical capacity that clarifies the overall amount of existing particles that are arranged by size of powder or granular material or particles scattered in liquid [18]. PSD is known to be a grain size conveyance and PSD of the cenosphere test is gotten from dry sieving and utilizing a laser particle size analyzer. The particle size of cenospheres fluctuates from < 0.10 to 3500 μm with lion's share of the particles in the size scope of 90–200 μm. These cenosphere have a strength going from 4000 to 7000 psi. The



**Fig. 7** XRD pattern of cenosphere

size of fly debris particles which are going from 0.010 to 3050  $\mu\text{m}$  thick, when contrasted with the normal size of fly debris particles, has altogether more modest normal breadth than cenospheres. PSD tests of cenosphere, fly debris, and copper were completed utilizing Malvern laser shaft molecule size analyzer gear of which the outcomes are examined in Tables 1, 3, and 5 individually (Table 2).

The cenosphere are bigger than that of fly debris molecule because of the caught air inside the unbending circle. Tables 3 and 4 show the molecule size circulation of the fly debris molecule. The fly debris particles discovered to be a lot more modest in contrast with cenosphere. From Figs. 10, 11, and 12 it is seen that the cenosphere particles are a lot bigger than that of fly debris. It is additionally seen that the molecule size of cenosphere is about 25% of the molecule size range as that of fly debris [18] (Table 6).



**Table 1** Particle size data for cenosphere

Cenosphere Results	
Measurement Details	Measurement Details
Sample Name Average of 'Cenosphere'	Measurement Date Time 04-01-2017 16:44:43
SOP File Name HydroMV.cfg	Result Source Averaged
Analysis	Result
Particle Refractive Index 1.640	Span1.904
Particle Absorption Index 0.100	Uniformity0.583
Dispersant Name Water	D [4,3] 74.080p.m D [3,2] 30.921p.m
Dispersant Refractive Index 1.330	Dv (10) 18.911p.m
Scattering Model Mie	Dv (50) 64.805p.m
Analysis Model General Purpose	Dv(90)142.296p.m
Laser Obscuration 6.95%	Specific Surface Area 194.0 m <sup>2</sup> /kg
	Dv(95)170.265p.m
	Dv (99) 221.414p.m

## 4 Conclusions

In the current work, Fly debris test was gathered from M/s NTPCL Simhadri for additional investigation, prepared with reasonable reagent for additional portrayal study. The light weight empty particles were exposed to mineralogical and morphological examinations. The Particle Size Distributions (PSD) of the compound have been studied. The fly ash-based cenospheres efficiently harvested from the ash pond of coal-fired thermal power stations, upon comprehensive characterization revealed properties par excellence and therefore is a highly resourceful material for effective use in high value products for various engineering applications like metal matrix composites, special concretes, light polymer composites, high temperature refractories both for thermal insulation as well as bulk refractories for cast able applications, etc. The consequences disclosed a strong disproportion in the content of cenosphere from fly ash sample. In view of the outcomes, following ends can be drawn.



**Table 2** Presents data for cenosphere results

Data for Cenosphere Results													
Size (µm)	% Volume In	Size (µm)	% Vol In	Size (µm)	% Vol In	Size (µm)	% Vol In	Size (µm)	% Vol In	Size (µm)	% Vol In	Size (µm)	% Vol In
0.010	0	0.060	0	0.357	0.00	2.131	0.14	12.726	0.98	76.006	7.34	453.960	0.00
0.011	0	0.068	0	0.405	0.00	2.421	0.17	14.458	1.16	86.355	7.05	515.772	0.00
0.013	0	0.077	0	0.460	0.00	2.750	0.20	16.427	1.38	98.114	6.49	586.001	0.00
0.015	0	0.088	0	0.523	0.00	3.125	0.23	18.664	1.66	111.473	5.70	665.793	0.00
0.017	0	0.100	0	0.594	0.00	3.550	0.26	21.205	2.02	126.652	4.75	756.449	0.00
0.019	0	0.113	0	0.675	0.00	4.034	0.29	24.092	2.47	143.897	3.72	859.450	0.00
0.022	0	0.128	0	0.767	0.00	4.583	0.33	27.373	3.02	163.490	2.71	976.475	0.00
0.024	0	0.146	0	0.872	0.08	5.207	0.37	31.100	3.67	185.752	1.78	1109.435	0.00
0.028	0	0.166	0	0.991	0.09	5.916	0.42	35.335	4.39	211.044	1.01	1260.499	0.00
0.032	0	0.188	0	1.125	0.10	6.722	0.47	40.146	5.16	239.780	0.37	1432.133	0.00
0.036	0	0.214	0	1.279	0.10	7.637	0.54	45.613	5.90	272.430	0.00	1627.136	0.00
0.041	0	0.243	0	1.453	0.11	8.677	0.62	51.823	6.56	309.525	0.00	1848.692	0.00
0.046	0	0.276	0	1.651	0.11	9.858	0.72	58.880	7.06	351.670	0.00	2100.416	0.00
0.053	0	0.314	0	1.875	0.13	11.201	0.84	66.897	7.34	399.555	0.00	2386.415	0.00

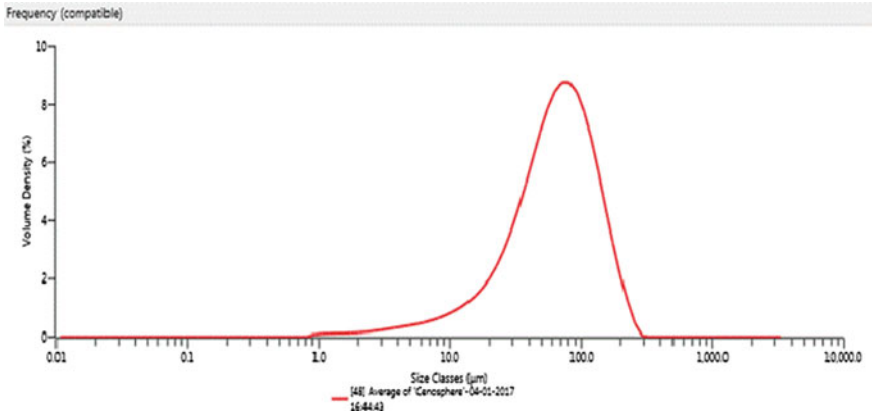
**Table 3** Particle size data for fly ash

Particle Size Data for Fly ash	
Measurement details	Measurement details
Sample Name Average of "Flyash"	Measurement Date Time 04-01-20,176:11:14
SOP File Name HydroMV.cfg	Result Source Averaged
Analysis	Result
Particle Refractive Index 1.640	Span2.930
Particle Absorption Index 0.100	Uniformity 0.922
Dispersant Name Water	D [4,3] 57.069 μm
Dispersant Refractive Index 1.330	Dv(10)5.951 μm
Scattering Model Mie	Dv(50)42.225 μm
Analysis Model General Purpose	Dv(90)129.674 μm
Laser Obscuration 12.72%	Specific surface area 460.9 m <sup>2</sup> /kg
	Dv(95)163.506 μm
	Dv (99) 234.498 μm

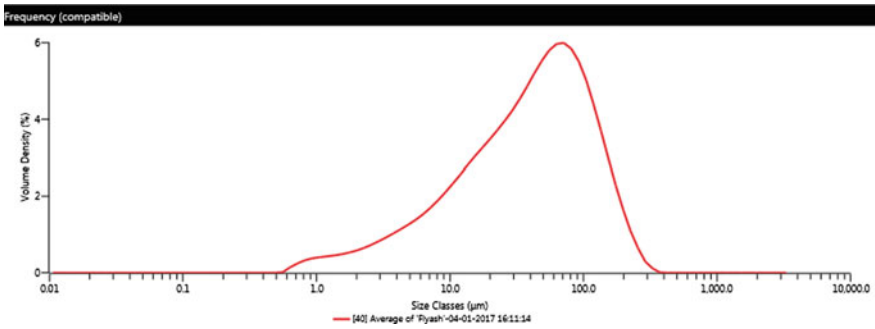
- The cenosphere test displayed particles with more extensive scope of molecule size between 0.010 to 3080 μm. The mean distance across the cenosphere molecule is around 100 μm.
- The more modest particles saw to be generally straightforward, though the bigger particles are somewhat obscure and have various shades
- Cenosphere displayed the higher alumina substance of around 25–27 rate and the construction of cenospheres ended up being primarily nebulous, with the event of glasslike stages, for example, mullite and quartz.
- This investigation likewise reports the event of glass development measure inside the pounded coal ignition heater. From glass arrangement standards, it is known, that to frame an undefined stage, quick extinguishing of a high gooey liquefy is essential. Significant part of cenosphere is silica from which the high thickness comes while quick extinguishing conditions happen inside the heater.
- It was found that copper-based composites are promising material for various applications. Even though several researches on copper-based composites with different reinforcements are available, still researchers are incisive for the promising reinforcement candidate with lower density and cost effective. One such reinforcement is cenosphere. When the difference in density between the matrix and reinforcement is high, for processing the particulate reinforced MMC, powder metallurgy technique is preferred over other processing methods.
- It was found that research work on cenosphere as reinforcement in copper-based composites through powder metallurgy route is scarce. Mechanical properties on copper fly ash composite are not yet addressed by the researchers, and hence this work is proposed.

**Table 4** Data pertaining to fly ash results

Data for Fly ash Results													
Size (µm)	% Vol In	Size (µm)	% Vol In	Size (µm)	% Vol In	Size (µm)	% Vol In	Size (µm)	% Vol In	Size (µm)	% Vol In	Size (µm)	% Vol In
0.01	0	0.06	0	0.357	0	2.131	0.54	12.726	2.34	76.006	4.88	453.96	0
0.011	0	0.07	0	0.405	0	2.421	0.61	14.458	2.53	86.355	4.61	515.772	0
0.013	0	0.08	0	0.46	0	2.75	0.69	16.427	2.72	98.114	4.19	586.001	0
0.015	0	0.09	0	0.523	0	3.125	0.77	18.664	2.91	111.473	3.67	665.793	0
0.017	0	0.1	0	0.594	0.12	3.55	0.86	21.205	3.09	126.652	3.09	756.449	0
0.019	0	0.11	0	0.675	0.2	4.034	0.95	24.092	3.3	143.897	2.48	859.45	0
0.022	0	0.13	0	0.767	0.27	4.583	1.05	27.373	3.52	163.49	1.9	976.475	0
0.024	0	0.15	0	0.872	0.32	5.207	1.16	31.1	3.77	185.752	1.36	1109.435	0
0.028	0	0.17	0	0.991	0.34	5.916	1.28	35.335	4.05	211.044	0.9	1260.499	0
0.032	0	0.19	0	1.125	0.36	6.722	1.42	40.146	4.34	239.78	0.53	1432.133	0
0.036	0	0.21	0	1.279	0.38	7.637	1.58	45.613	4.61	272.43	0.22	1627.136	0
0.041	0	0.24	0	1.453	0.4	8.677	1.75	51.823	4.84	309.525	0.08	1848.692	0
0.046	0	0.28	0	1.651	0.44	9.858	1.94	58.88	4.99	351.67	0	2100.416	0
0.053	0	0.31	0	1.875	0.48	11.201	2.14	66.897	5.01	399.555	0	2386.415	0



**Fig. 10.** Particle size distribution for Cenosphere



**Fig. 11** Particle size distribution for Fly ash

**Table 5** Particle size data for copper

Particle Size Data for Copper	
Measurement Details	Measurement Details
Sample Name Average of "Copper"	Measurement Date Time 04-01-2017,715:55:43
S OP File Name HydroMV.cfg	Result Source Averaged
Analysis	Result
Particle Refractive 0.250	Span2.799
Particle Absorption Index 0.1000	Uniformity0.891
Dispersant Name Water	D [2, 3] 12.105 µm
Dispersant Refractive Index 1.330	D [3, 4] 46.795 µm
Scattering Model Mie	Dv (10) 4.744 µm
Analysis Model General Purpose	Dv (50) 36.292 µm
Laser Obscuration 9.28%	Specific Surface Area 495.7 m <sup>2</sup> /kg
	Dv (90) 106.319 µm
	Dv (99) 162.731 µm

**Table 6** Presents Data for Copper Results

Size ( $\mu\text{m}$ )		% Vol Under		Size ( $\mu\text{m}$ )		% Vol Under		Size ( $\mu\text{m}$ )		% Vol Under		Size ( $\mu\text{m}$ )		% Vol Under		Size ( $\mu\text{m}$ )		% Vol Under		Size ( $\mu\text{m}$ )		% Vol Under	
0.01	0	0.06	0	0.357	0	2.131	3.01	12.726	25.87	76.006	77.36	453.96	100	2711.357	100								
0.011	0	0.07	0	0.405	0	2.421	3.75	14.458	28.36	86.355	82.55	515.772	100	3080.544	100								
0.013	0	0.08	0	0.46	0	2.75	4.61	16.427	30.95	98.114	87.36	586.001	100	3500	100								
0.015	0	0.09	0	0.523	0	3.125	5.62	18.664	33.63	111.473	91.56	665.793	100										
0.017	0	0.1	0	0.594	0	3.55	6.77	21.205	36.42	126.652	94.95	756.449	100										
0.019	0	0.11	0	0.675	0	4.034	8.08	24.092	39.33	143.897	97.45	859.45	100										
0.022	0	0.13	0	0.767	0.08	4.583	9.56	27.373	42.4	163.49	99.06	976.475	100										
0.024	0	0.15	0	0.872	0.22	5.207	11.19	31.1	45.66	185.752	99.91	1109.435	100										
0.028	0	0.17	0	0.991	0.41	5.916	12.96	35.335	49.19	211.044	100	1260.499	100										
0.032	0	0.19	0	1.125	0.66	6.722	14.85	40.146	53.05	239.78	100	1432.133	100										
0.036	0	0.21	0	1.279	0.98	7.637	16.86	45.613	57.27	272.43	100	1627.136	100										
0.041	0	0.24	0	1.453	1.36	8.677	18.96	51.823	61.87	309.525	100	1848.692	100										
0.046	0	0.28	0	1.651	1.83	9.858	21.17	58.88	66.83	351.67	100	2100.416	100										
0.053	0	0.31	0	1.875	2.37	11.201	23.47	66.897	72.05	399.555	100	2386.415	100										

Data for Copper Results

## References

1. Fenelonov VB, Mel'gunov MS, Parmon VN (2010) The properties of cenospheres and the mechanism of their formation during High temperature coal combustion a thermal power plants, Kona powder and particle Journal No.28, PP 189–2083
2. Siddique R (2010) Utilization of coal combustion by-products in sustainable construction materials. *Resour Conserv Recycling* 54:1060–1066
3. Vassilev ST (2004) Phase-mineral and chemical composition of coal fly ashes as a basis for their multi component utilization Characterization of ceramic cenosphere and salt concentrates. *Fuel* 83:585–603
4. Kolay PK (2014) Recovery of hollow spherical particles with two different densities from coal fly ash and their characterization. *Fuel* 117:118–124
5. Ghosal S (1995) Particle size-density relation and cenosphere content of coal fly ash. *Fuel* 74:522–529
6. Shelby JE (1997) Introduction to glass science and technology. The Royal Society of chemistry, Cambridge
7. Karr C (1979) Analytical methods for coal and coal products. Academic Press, New York
8. Matsunaga T, Kim JK, Hardcastle S, Rohatgi PK (2002) Crystallinity and selected properties of fly ash particles, materials science & engineering. A325, 333–343
9. Biernacki JJ, Anil Vazrala K, Wayne Leimer H (2008) Sintering of a class fly ash. *Fuel* 87:782–792
10. Wu G, Huang X, Dou Z, Chen S, Jiang L (2010) Electromagnetic interference (EMI) shielding of Aluminium-cenosphere composition. *Advanc Mater Res* 97–101: 1760–1763
11. Itskos G (2010) Size fraction characterization of highly-calcareous fly ash. *Fuel Process Technol* 91: 1558–1563
12. Baasner A, Schmidt BC, Webb SL (2013) The effect of chlorine, fluorine and water on the viscosity of aluminosilicate melts. *Chem Geol* 357:134–149
13. Zimova M, Webb SL (2007) The combined effects of chlorine and fluorine on the viscosity of aluminosilicate melts, pp 1553–1562
14. Fenelonov VB, Mel'gunov MS, Parmon VN (2010) The properties of cenospheres and the mechanism of their formation during high-temperature coal combustion at thermal power plants. *KONA Powder and Particle*: 189–207
15. Tomeczek J (1994) Coal Combustion, Malabar. Krieger Publishing Company, Florida
16. Vergas S, Frandsen F, Dam-Johansen K (1997) Performance of viscosity models for high-temperature coal ashes [project review]. Technical University of Denmark, Lyngby
17. Kim GH, Sohn I (2012) Effect of Al<sub>2</sub>O<sub>3</sub> on the viscosity and structure of calcium silicate-based melts containing Na<sub>2</sub>O and CaF<sub>2</sub>. *J Non-Crystalline Solids* 358:1530–1537
18. Vynatheya S, Kumar JN, Madhusudhana R, Sagar LC, Raju VB (2017) Preparation and characterization of electroless Ni-P-W coated nano cenosphere/ABS composite for EMI shielding application. *Mater Today Proc* 4: 12130–12137